DEEP ROCK MASS ENGINEERING: EXCAVATION, MONITORING, AND CONTROL

EDITED BY: Zhiqiang Yin, Yilin Gui and Kun Du
PUBLISHED IN: Frontiers in Earth Science

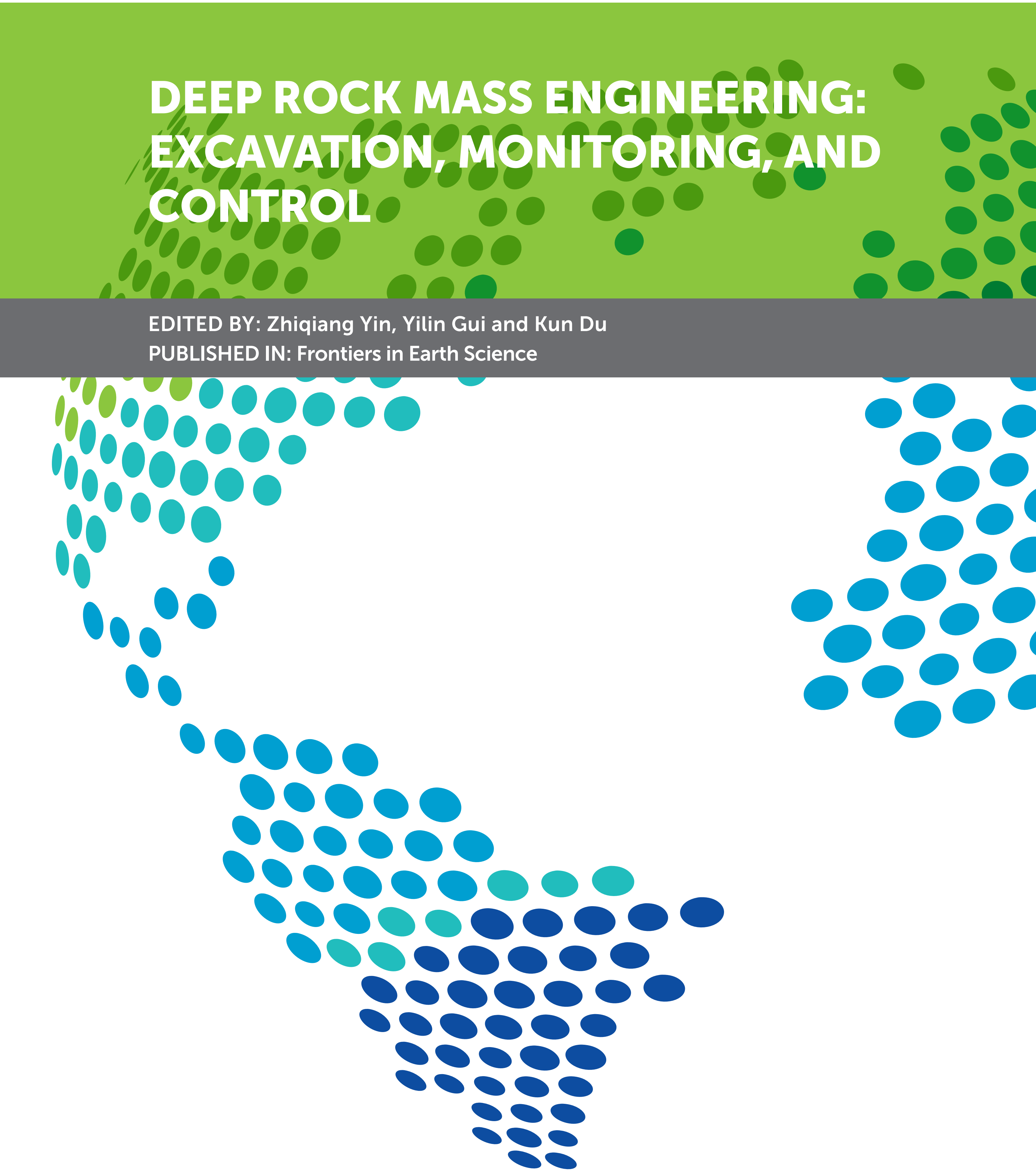

frontiers Research Topics

ISSN 1664-8714
ISBN 978-2-83250-564-9
DOI 10.3389/978-2-83250-564-9

About Frontiers

Frontiers is more than just an open-access publisher of scholarly articles: it is a pioneering approach to the world of academia, radically improving the way scholarly research is managed. The grand vision of Frontiers is a world where all people have an equal opportunity to seek, share and generate knowledge. Frontiers provides immediate and permanent online open access to all its publications, but this alone is not enough to realize our grand goals.

Frontiers Journal Series

The Frontiers Journal Series is a multi-tier and interdisciplinary set of open-access, online journals, promising a paradigm shift from the current review, selection and dissemination processes in academic publishing. All Frontiers journals are driven by researchers for researchers; therefore, they constitute a service to the scholarly community. At the same time, the Frontiers Journal Series operates on a revolutionary invention, the tiered publishing system, initially addressing specific communities of scholars, and gradually climbing up to broader public understanding, thus serving the interests of the lay society, too.

Dedication to Quality

Each Frontiers article is a landmark of the highest quality, thanks to genuinely collaborative interactions between authors and review editors, who include some of the world's best academicians. Research must be certified by peers before entering a stream of knowledge that may eventually reach the public - and shape society; therefore, Frontiers only applies the most rigorous and unbiased reviews.
Frontiers revolutionizes research publishing by freely delivering the most outstanding research, evaluated with no bias from both the academic and social point of view.
By applying the most advanced information technologies, Frontiers is catapulting scholarly publishing into a new generation.

What are Frontiers Research Topics?

Frontiers Research Topics are very popular trademarks of the Frontiers Journals Series: they are collections of at least ten articles, all centered on a particular subject. With their unique mix of varied contributions from Original Research to Review Articles, Frontiers Research Topics unify the most influential researchers, the latest key findings and historical advances in a hot research area! Find out more on how to host your own Frontiers Research Topic or contribute to one as an author by contacting the Frontiers Editorial Office: frontiersin.org/about/contact

DEEP ROCK MASS ENGINEERING: EXCAVATION, MONITORING, AND CONTROL

Topic Editors:
Zhiqiang Yin, Anhui University of Science and Technology, China
Yilin Gui, Queensland University of Technology, Australia
Kun Du, Central South University, China

Citation: Yin, Z., Gui, Y., Du, K., eds. (2022). Deep Rock Mass Engineering: Excavation, Monitoring, and Control. Lausanne: Frontiers Media SA. doi: 10.3389/978-2-83250-564-9

Table of Contents

frontiers | Frontiers in Earth Science

TYPE Editorial
PUBLISHED 07 October 2022
DOI 10.3389/feart.2022.1047612

OPEN ACCESS

EDITED AND REVIEWED BY
Candan Gokceoglu,
Hacettepe University, Turkey

*CORRESPONDENCE
Yilin Gui,
yilin.gui@qut.edu.au

†These authors have contributed equally to this work

SPECIALTY SECTION
This article was submitted to Geohazards and Georisks, a section of the journal Frontiers in Earth Science

RECEIVED 18 September 2022
ACCEPTED 26 September 2022
PUBLISHED 07 October 2022

CITATION
Gui Y, Yin Z and Du K (2022), Editorial: Deep rock mass engineering: Excavation, monitoring, and control. *Front. Earth Sci.* 10:1047612.
doi: 10.3389/feart.2022.1047612

Editorial: Deep rock mass engineering: Excavation, monitoring, and control

Yilin Gui[1]*†, Zhiqiang Yin[2]† and Kun Du[3]†

[1]School of Civil and Environmental Engineering, Queensland University of Technology, Brisbane, QLD, Australia, [2]School of Mining Engineering, Anhui University of Science and Technology, Huainan, Anhui, China, [3]School of Resources and Safety Engineering, Central South University, Changsha, Hunan, China

KEYWORDS

mining engineering, rockburst, rock mechanics, rock excavation, deep rock mass engineering

Editorial on the Research Topic
Deep rock mass engineering: Excavation, monitoring, and control

With the development of the social economy, the depth of underground excavation has seen a significant increase in the fields of mining, tunnelling, hydropower, nuclear waste deep geological storage, and underground protection engineering. In mining engineering, for instance, nearly 200 metal mines have mining depth of more than 1 km, and the deepest one has reached more than 4 km below the ground surface (Li et al., 2017). The excavation of rocks in deep ground is subjected to the state of complicated circumferential loadings, for example, the high *in situ* stress, the high ground temperature, the high hydraulic pressure (high gas pressure), in addition to the dynamic disturbance caused by blasting and mechanical excavation (Zhang and Zhao 2014; Huang et al.). Therefore, the excavation process may cause rockburst, coal and gas outburst, sudden fracture of rock mass and other dynamic phenomena, and cause severe engineering disasters. Therefore, in deep rock excavation engineering, the description of dynamic disaster response induced by excavation, the exploration of hidden disaster sources, and disaster forecasting and control have become the key technologies.

Within this context, continuous progress needs to be done to improve the safety performance of deep rock excavation. To meet the demand of engineering and academic communities in this topic, a Research Topic “*Deep Rock Mass Engineering: Excavation, Monitoring, and Control*” was proposed to the renowned journal *Frontiers in Earth Science*. The aim of this topic was to call for the state-of-the-art research in deep rock mass excavation, particularly in mining engineering, tunnelling, petroleum (gas) engineering and general rock mechanics, and to pulse the research trend in deep rock engineering.

It was a great honour to be invited to serve as a Guest Editor for this Research Topic. Upon the open of this topic, it was even more privileged to receive so great response from relevant academic communities. In total 21 papers collected and published in this Topic. A wide range of research was presented from novel laboratory testing (e.g., Liu et al.; Zhao and Niu; Liu et al.), robust numerical modelling (e.g., Hu et al.; Zhang et al.; Zhu et al.) and new development of models (e.g., Huang et al., 2022, Bu et al.) to case studies (e.g., Wu et al.; Li et al.; Liu et al.).

It was hoped that this special topic would serve as a small but thought-provoking collection for the community through the state-of-the-art review, introducing the new technologies in the industry practices and techniques used in the research field as well as insight to the future of deep rock mass engineering.

Author contributions

All authors listed have made a substantial, direct, and intellectual contribution to the work and approved it for publication.

Conflict of interest

The authors declare that the research was conducted in the absence of any commercial or financial relationships that could be construed as a potential conflict of interest.

Publisher's note

References

Huang, X., Xu, N., Wu, W., Xiao, P., Dong, L., and Li, B. (2022). Instability of an intersecting fault-dyke system during deep rock excavation. *Int. J. Rock Mech. Min. Sci.* 153, 105087. doi:10.1016/j.ijrmms.2022.105087

Li, X., Gong, F., Tao, M., Dong, L., Du, K., Ma, C., et al. (2017). Failure mechanism and coupled static-dynamic loading theory in deep hard rock mining: A review. *J. Rock Mech. Geotechnical Eng.* 9, 767–782. doi:10.1016/j.jrmge.2017.04.004

Zhang, Q. B., and Zhao, J. (2014). A review of dynamic experimental techniques and mechanical behaviour of rock materials. *Rock Mech. Rock Eng.* 47, 1411–1478. doi:10.1007/s00603-013-0463-y

frontiers
in Earth Science

ORIGINAL RESEARCH
published: 25 January 2022
doi: 10.3389/feart.2021.791180

Numerical Simulation of Rock Dynamic NSCB Test Based on a Self-Developed Dynamic Damage Model

Xuelong Hu[1,2,3], Minke Duan[1,2,3], Min Tu[1,2,3], Xiangyang Zhang[1,2,3], Ming Zhang[4,3] and Wenyao Xu[5]*

[1]School of Mining Engineering, Anhui University of Science and Technology, Huainan, China, [2]Key Laboratory of Safety and High-efficiency Coal Mining, Ministry of Education, Anhui University of Science and Technology, Huainan, China, [3]State Key Laboratory of Mining Response and Disaster Prevention and Control in Deep Coal Mines, Anhui University of Science and Technology, Huainan, China, [4]State Key Laboratory of Coal Resources and Safe Mining, China University of Mining and Technology, Xuzhou, China, [5]Metallurgical Mines' Association of China, Beijing, China

Elucidating and understanding the dynamic fracture characteristics of rocks play an essential role in the application of rock engineering and geophysics. In this study, based on a self-developed dynamic damage model, a rock notched semi-circle bend test with the Split Hopkinson Pressure Bar technique is numerically simulated. The study focuses on three aspects including damage evolution, energy evolution, and failure mode of rock under different loading velocities. From the simulated results, the following conclusions can be conducted: 1) the damage range increases gradually with the increase of loading velocity; 2) the crack propagates to the loading point along the symmetry axis of the samples under different loading velocities; 3) the loading velocity has an important influence on the failure mode of straight notch semi-circular marble, whose mechanism can be explained by that the local high strain rate leads to the obvious randomness and uncertainty of crack activation in rock; and 4) the energy evolution of notched semi-circle bend is vitally affected by loading velocity, and the deformation and the failure process of straight notch semicircular marble under dynamic loading can be divided into five stages according to the ratio of internal energy to total energy. The beneficial findings may provide some references in practice design from engineering problems.

Edited by:
Kun Du,
Central South University, China

Reviewed by:
Mingdong Wei,
Nanyang Technological University, Singapore
Xin Cai,
Central South University, China

****Correspondence:***
Minke Duan
duanminke@aust.edu.cn

Specialty section:
This article was submitted to Geohazards and Georisks, a section of the journal Frontiers in Earth Science

Received: *08 October 2021*
Accepted: *31 December 2021*
Published: *25 January 2022*

Citation:
Hu X, Duan M, Tu M, Zhang X, Zhang M and Xu W (2022) Numerical Simulation of Rock Dynamic NSCB Test Based on a Self-Developed Dynamic Damage Model. Front. Earth Sci. 9:791180. doi: 10.3389/feart.2021.791180

Keywords: numerical simulation, notched semi-circle bend test, dynamic damage model, stain rate, energy evolution, failure mode

INTRODUCTION

Studying and understanding the dynamic fracture characteristics of rocks under different loading rates are of great significance for the application of rock engineering and geophysics, and there are many researchers to make efforts in the fracture characteristics of rocks (Dai et al., 2016; Du et al., 2020; Du et al., 2021; Wei et al., 2021; Xia and Yao 2015).

At present, there are many methods to measure rock fracture characteristics (Zhang and Zhao 2013 Yao and Xia 2019), including wedge-loaded compact tension (WLCT) (Klepaczko et al., 1984), notched semi-circle bend (NSCB) (Chong and Kuruppu 1984), short rod (SR) (Franklin et al., 1988), single edge notched bending (SENB) (Tang and Xu 1990), cracked straight through Brazilian disc

(CSTBD) (Kourkoulis and Markides 2014; Nakano et al., 1994), holed-notched cylinder fracture (HNCF) (Wei et al., 2018a; Wei et al., 2018b), three-point chevron bend (CB) (Zhou et al., 2009), cracked chevron notched Brazilian disc (CCNBD) (Dai et al., 2010), cracked chevron notched semi-circle bend (CCNSCB) (Dai et al., 2011), and double cleavage drilled compression (DCDC) (Wang et al., 2016). Compared with other methods, the NSCB method has incomparable advantages (Yao and Xia 2019): 1) the notch of the specimen is straight, which is convenient for the preparation of specimen; 2) in the placement process of the specimen, only two support points of the specimen need to be aligned on the bar side, which simplifies the specimen alignment; and 3) the size of the specimen is so small that it can expedite the dynamic force balance. Because of its merits, the NSCB method was recommended to determine the dynamic fracture characteristics of rocks by the international society for rock mechanics and rock engineering (ISRM) in 2012 (Zhou et al., 2012), and then determine the static type I fracture characteristics of rocks by ISRM in 2014 (Kuruppu et al., 2014). Therefore, the NSCB method is the only ISRM suggested method to determine the static and dynamic mode I fracture toughness of rocks.

So far, the research on rock dynamic fracture behaviors based on the NSCB method has mostly focused on the following aspects: 1) measurement of rock dynamic fracture toughness and crack propagation velocity, for example, Chen et al. (2009) proposed a method to simultaneously measure dynamic fracture parameters such as fracture propagation toughness and fracture velocity using a semi-circular bend technique, and Zhao et al. (2017) studied the influence of bedding angle and loading rate on the initiation fracture toughness of coal using NSCB method; 2) obtaining rock displacement and strain field using the digital image correlation (DIC) technology (Zhang and Zhao 2013; Zhang and Zhao 2014; Gao et al., 2015a; Gao et al., 2015b; Xing et al., 2017); 3) fracture characteristics of deep rock (Yin et al., 2014; Chen et al., 2016; Yao et al., 2019; Li et al., 2020), and 4) the influence of heat, moisture anisotropy, and other factors on rock dynamic fracture characteristics (Yin et al., 2012; Dai et al., 2013; Dai and Xia 2013; Yao et al., 2017; Xu et al., 2018; Zhou et al., 2018; Cai et al., 2018; Wei, et al., 2018c; Shi et al., 2019; Cai et al., 2020a; Cai, et al., 2020b; Wei et al., 2021). Due to the limitation of the measurement technology, there is still a lack of in-depth understanding of the damage evolution law, energy evolution law, and mechanical mechanism of the failure mode in the deformation and the failure process of NSCB rock specimens. Thus, based on a rock dynamic damage model, this study numerically simulates the rock dynamic NSCB test, in order to study the damage evolution law, mechanical mechanism, and energy evolution law of rock under different loading rates.

EXPERIMENT SETUP

Brief Introduction of Dynamic Notched Semi-Circle Bend Experiment

The NSCB method was originally proposed by Chong and Kuruppu (1984) to determine mode I fracture toughness,

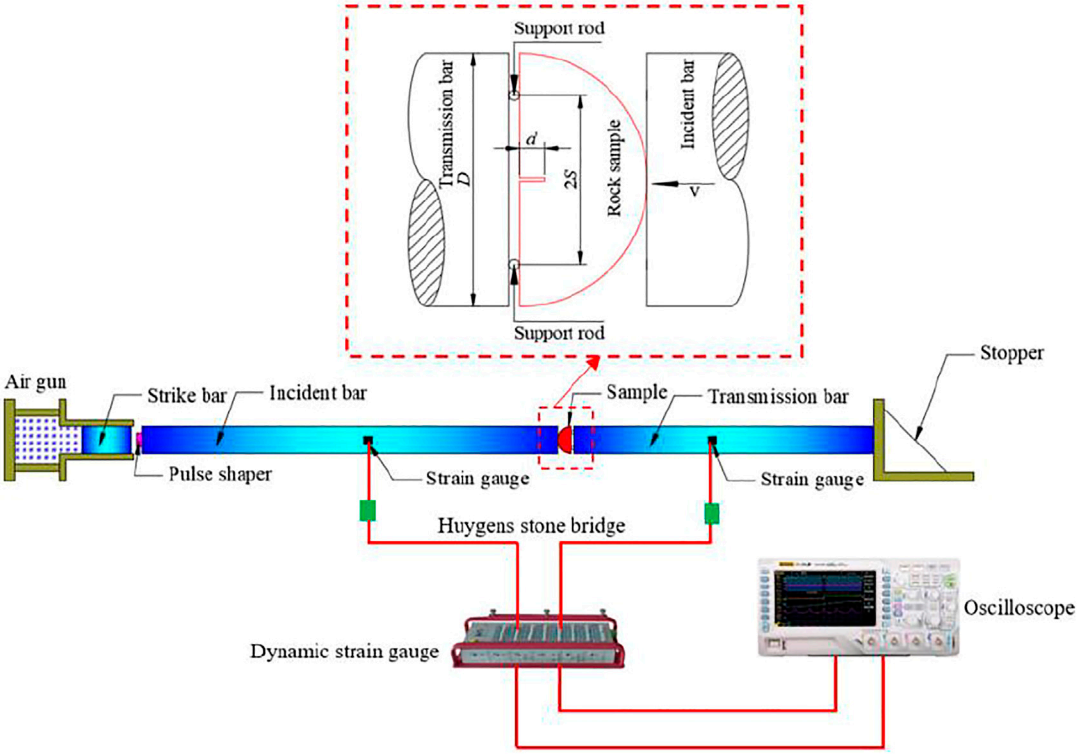

FIGURE 1 | Schematic diagram of the dynamic NSCB test device.

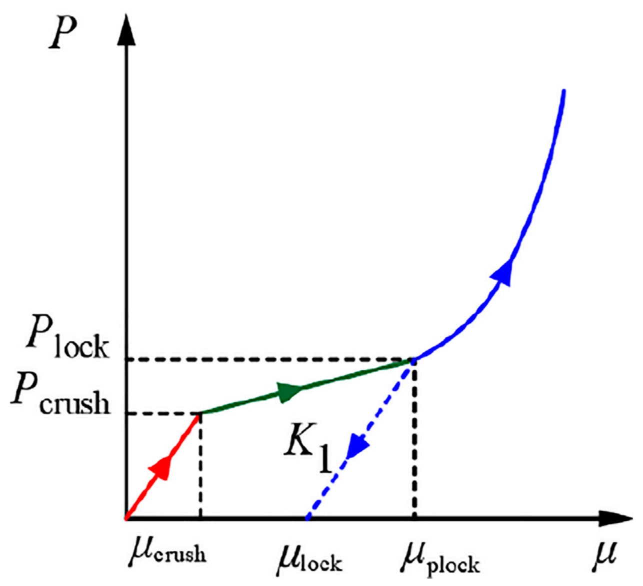

FIGURE 2 | Relationship between P and μ. In linear elastic stage ($0 \le \mu < \mu_{\mathrm{crush}}$), P can be expressed as.

which has been widely used all over the world. The dynamic NSCB test combines the notched semicircle bend (NSCB) test and Split Hopkinson Pressure Bar (SHPB) technique, and the schematic diagram of dynamic NSCB test device is shown in **Figure 1**. The test device is mainly composed of an air gun, strike bar, incident bar, transmission bar, strain gauge, and oscilloscope. The standard rock sample is semicircular, with a radius of 25 mm and a thickness of 20 mm. The length and width of the straight cutting notch are 5 and 0.6 mm, respectively. The span of the support point is $2S = 33.3$ mm. Under quasi-static loading, the stress intensity factor of the sample can be expressed as follows (Chong and Kuruppu 1984):

$$K_{\mathrm{I}} = Y_{\mathrm{I}}(S/R)\frac{P'\sqrt{\pi a'}}{2RB}, \tag{1}$$

where K_{I} is the stress intensity factor, $Y_{\mathrm{I}}(S/R)$ is the geometric factor of mode I fracture, $2S$ is the span of the supporting point of the sample, R is the radius of the sample, P' is the force applied to the sample, a' is the length of the straight cut notch, and B is the thickness of the sample. When $S/R = 0.667$ and $a'/R = 0.2$, $Y_{\mathrm{I}}(S/R)$ can be calculated by the following formula (Lim et al., 1993):

$$Y_{\mathrm{I}}(S/R) = 3.638 - 0.139(a'/R) + 0.039e^{7.387(a'/R)}. \tag{2}$$

Under dynamic loading, the force exerted on the sample turns into a time-dependent force, namely, $P(t)$, then the dynamic stress intensity factor can be expressed as follows (Zhang and Zhao 2013):

$$K_{\mathrm{I}}^{\mathrm{dyn}} = Y_{\mathrm{I}}(S/R)\frac{P(t)\sqrt{\pi a'}}{2RB}. \tag{3}$$

Setup of the Finite Element Model

According to the above brief introduction of the NSCB test, the established numerical model is the same as the experiment. The contact between the rock sample and the incident bar and the contact between the rock and the support bar are through the keyword "contact_2D_AUTOMATIC_SURFACE_TO_SURFACE_ID." The numerical model adopts 2D solid162 element, which is meshed into 15,917 elements in total.

Material Model of Numerical Simulation

The mechanical behaviors of rock are characterized by a self-developed dynamic damage model. The model takes unified strength theory as the strength criterion and considers hardening behaviors, tension-compression damage, and Lode angle effect as well as strain rate effect. The strength criterion of the model can be expressed as

$$\begin{aligned} F = \Bigg\{ & \frac{1}{3}(1-a)I_1 + \frac{1}{\sqrt{3}}\sqrt{J_2}\,\frac{a-b-2ab-1}{1+b}\sin\theta \\ & + \sqrt{J_2}\,\frac{a+b+1}{1+b}\cos\theta - (1-\omega)\kappa, \left(\theta \in \left[-\frac{\pi}{6}, \arctan\frac{\sqrt{3}(1-a)}{3(1+a)}\right]\right. \\ & \times \Bigg)\frac{1}{3}(1-a)I_1 + \frac{1}{\sqrt{3}}\sqrt{J_2}\,\frac{a+2b+ab-1}{1+b}\sin\theta \\ & + \sqrt{J_2}\,\frac{a+ab+1}{1+b}\cos\theta \\ & - (1-\omega)\kappa, \left(\theta \in \left[\arctan\frac{\sqrt{3}(1-a)}{3(1+a)}\right], \frac{\pi}{6}\right) \end{aligned} \tag{4}$$

where a is the ratio of tensile strength to compressive strength, b is the selected parameter which can reflect the influence of the intermediate principal stress on the material failure, φ is the internal friction angle, ω is the damage variable, κ is the yield strength, I_1 is the first invariant of the stress tensor, J_2 is the second invariant of the deviatoric stress tensor, θ is the Lode angle, and J_3 is the third invariant of the deviatoric stress tensor.

In the above formula, κ can be expressed as

$$\kappa = \begin{cases} DIF \cdot \left[\beta_0 + (\beta_m - \beta_0)\dfrac{\gamma^p}{b_1 + \gamma^p}\right]\dfrac{2c\cos\varphi}{1+\sin\varphi}, (p_1 \le 0) \\ DIF \cdot \dfrac{2c\cos\varphi}{1+\sin\varphi}, (p_1 > 0) \end{cases}, \tag{5}$$

where DIF is the dynamic increase factor, β_0 is the initial yield threshold for plastic hardening, β_{m} is the maximum yield threshold for plastic hardening, b_1 is the parameter describing the rate of hardening, and γ^{p} is the generalized plastic shear strain.

And ω and DIF can be shown, respectively, as follows:

$$\omega = \begin{cases} \sum \dfrac{d\gamma^p + d\varepsilon_V^p}{D_1(P^* + T^*)^{D_2}}, (p_1 \le 0) \\ 1 - \exp(-\alpha\gamma^p), (p_1 > 0) \end{cases}, \tag{6}$$

$$DIF = 1 + A(\dot{\varepsilon}/\dot{\varepsilon}_r)^B, \tag{7}$$

where P^* is the standardized hydrostatic pressure, $P^* = P/\sigma_{\mathrm{c}}$, P is the actual hydrostatic pressure, σ_{c} is the uniaxial compressive

TABLE 1 | Model parameters of Fangshan marble.

ρ(kg/m^3)	**E** (GPa)	ν	σ_c (MPa)	σ_t (MPa)	β_0	β_m	b_1	D_1
2800	85	0.30	155	9.5	0.8	1.0	1.80×10^{-4}	0.04
D_2	K_1 (GPa)	K_2 (GPa)	K_3 (GPa)	μ_{crush}	P_{crush} (MPa)	μ_{lock}	P_{lock} (GPa)	α
1.0	320.54	−1980.57	4241.13	0.58×10^{-3}	41.33	0.1	17.54	180
A	B	—	—	—	—	—	—	—
0.0168	0.9896	—	—	—	—	—	—	—

TABLE 2 | Mechanical parameters of 40Cr steel.

ρ(kg/m^3)	**E** (GPa)	V
7697	206	0.28

strength of rock materials, T^* is the standardized tensile strength, $T^* = \sigma_t/\sigma_c$, σ_t is the uniaxial tensile strength of rock materials, D_1 and D_2 are the damage constants of rock materials, p_1 is the hydrostatic pressure, α represents the rock tensile damage parameter, A and B are the strain rate parameters, $\dot{\varepsilon}$ is the effective strain rate, and $\dot{\varepsilon}_r$ is the reference strain rate, which is used to make DIF dimensionless.

The relationship between P and volumetric strain μ can be divided into three stages: linear elastic stage, transition stage, and compaction stage, as shown in **Figure 2**.

$$P = K\mu\left(K = \frac{P_{\text{crush}}}{\mu_{\text{crush}}}\right). \tag{8}$$

In the transition stage ($\mu_{\text{crush}} \leq \mu < \mu_{\text{plock}}$), P can be expressed as

$$P = \frac{(P_{\text{lock}} - P_{\text{crush}})}{\mu_{\text{plock}-\mu_{\text{crush}}}}(\mu - u_{\text{crush}}) + P_{\text{crush}}. \tag{9}$$

In the compaction stage ($\mu > \mu_{\text{plock}}$), P can be expressed as

$$P = K_1\bar{\mu} + K_2\bar{\mu}^2 + K_3\bar{\mu}^3, \tag{10}$$

where K is the volume modulus; P_{crush} is the hydrostatic pressure when the rock reaches its elastic limit; μ_{crush} is the volumetric strain corresponding to P=P_{crush}; P_{lock} is the hydrostatic pressure when the rock is compacted; μ_{lock} is the volumetric strain corresponding to P=P_{lock}; μ_{lock} is the plastic deformation that occurs when the rock is compacted; K_1, K_2, and K_3 are rock material parameters; and $\bar{\mu}$ is the corrected volumetric strain.

The mechanical parameters of Fangshan marble are listed in **Table 1**. The rigid model is used to simulate the incident bar and transmission bar, which are made of 40Cr steel, and the parameters of bars are listed in **Table 2**.

SCHEME DESIGN OF NUMERICAL NOTCHED SEMI-CIRCLE BEND TEST AND VALIDATION

Because this study focuses on the failure mode and energy evolution of rock under different loading rates, the initial velocities of 0.01 m/s, 1.0 m/s, 2.0 m/s, and 3.0 m/s are applied to the incident bar. In order to ensure the validity and correctness of numerical the NSCB test, numerical simulation was carried out with an initial velocity of 2.25 m/s from the experiment conducted by Zhang and Zhao (2013). As the finite element method is based on continuum mechanics and cannot show the process of rock crack propagation, the element deletion technology is adopted in this study; that is, when the element state reaches a threshold, the element is deleted and a

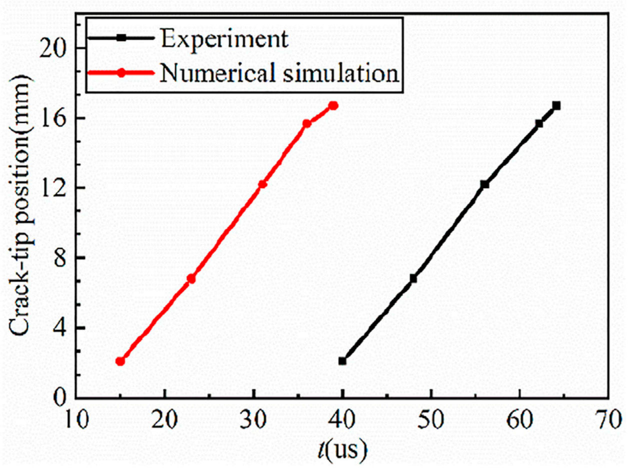

FIGURE 3 | The comparison between numerical simulation results and experimental one of crack tip position.

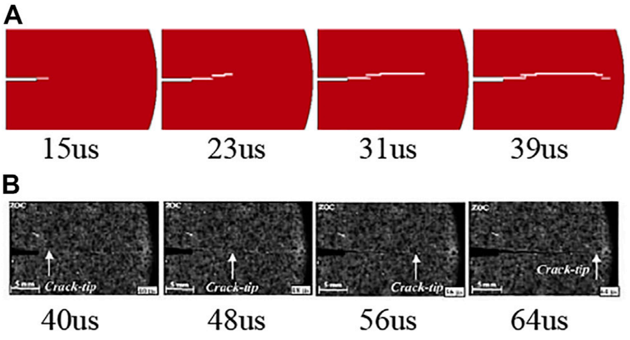

FIGURE 4 | The comparison between numerical simulation results and experimental results of crack propagation process. **(A)** Numerical simulation, **(B)** Experiment Zhang and Zhao (2013).

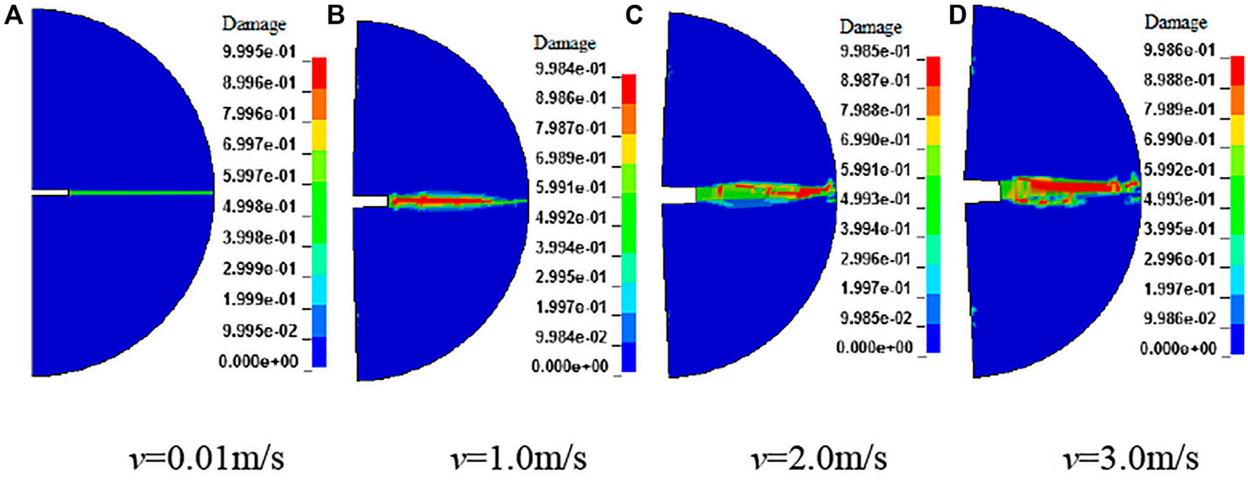

FIGURE 5 | Final damage distribution of NSCB rock samples under different loading velocities. Failure characteristics of marble under different loading velocities. **(A)** v=0.01m/s, **(B)** v=1.0m/s, **(C)** v=2.0m/s, **(D)** v=3.0m/s.

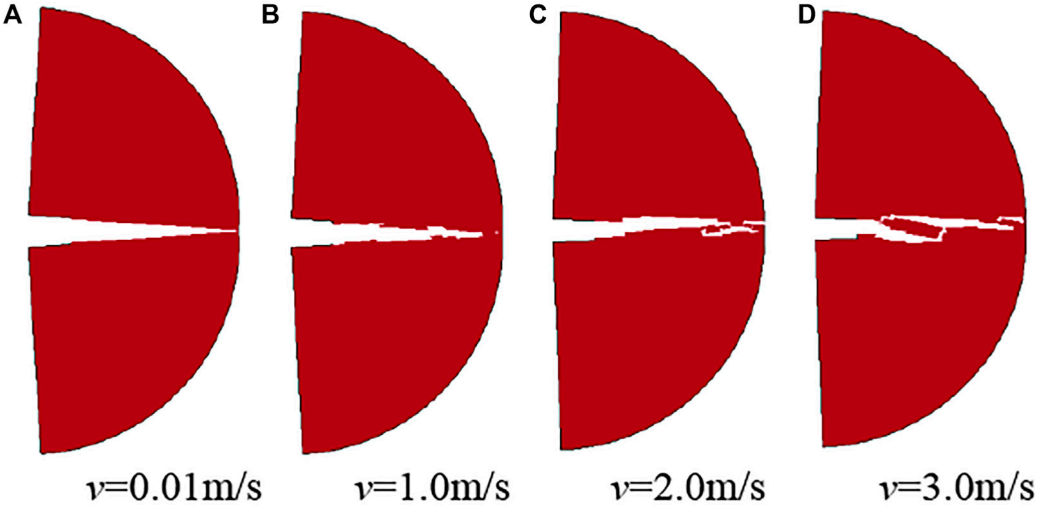

FIGURE 6 | Final failure mode of NSCB rock samples under different loading velocities. Energy evolution law of NSCB rock samples under different loading velocities. **(A)** v=0.01m/s, **(B)** v=1.0m/s, **(C)** v=2.0m/s, **(D)** v=3.0m/s.

failure crack is formed in the visual effect. According to the damage mechanics, when the damage of rock materials accumulates to a certain extent, the rock materials will fail. Therefore, this study uniformly selects the damage variable of the element as the basis for judging the deletion of the element. Based on the comparison between numerical simulation results and experimental results, the damage threshold is set as 0.8; that is, when the damage of rock is greater than or equal to 0.8, the rock will fail and crack.

Figure 3 shows the comparison between numerical simulation results and experimental one of crack tip position. It can be seen that the numerical simulation value of the time when the crack tip reaches the same position is larger than the test value, which is due to the different loading modes of the initial velocity in the numerical simulation and the test. The initial velocity in the numerical simulation is directly applied to the incident bar, while the initial velocity in the test is loaded to the incident bar to improve computational efficiency. There is a pulse shaper between the strike bar and the incident bar, which prolongs the rise time of the incident wave, resulting in a condition where the crack initiation time of the straight notch is later than that of the straight notch in the numerical simulation. Although there are some differences between the numerical results and the experimental value when the crack tip reaches the same position, the time interval of the same length of crack propagation is relatively close; that is, the crack propagation

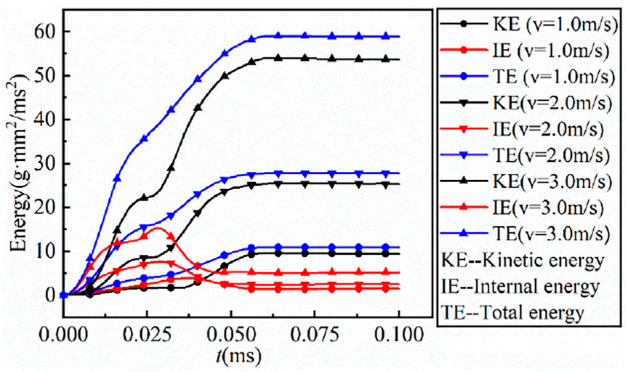

FIGURE 7 | Time history curves of rock energy under different loading velocities.

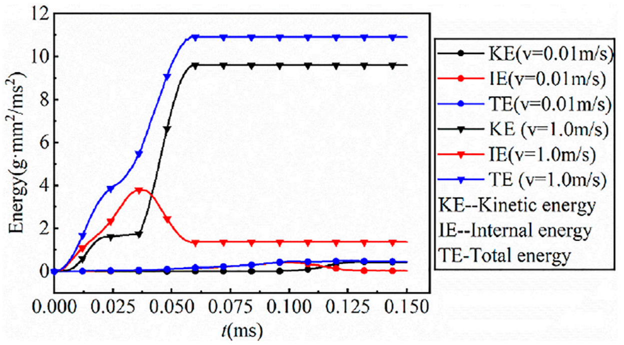

FIGURE 8 | Time history curves of rock energy under quasi-static and dynamic loading.

speed is relatively consistent, so the reliability of the numerical simulation results can be determined.

Figure 4 shows the comparison between the numerical simulation results and the experimental results of the crack propagation process with the initial velocity of 2.25 m/s. From this figure, it can be seen that the crack starts from the notch tip and propagates along the symmetrical pumping direction of the NSCB sample to the loading point. The numerical simulation results of the crack propagation process are consistent with the experimental results.

RESULTS AND DISCUSSIONS

For the purpose of this study, the effects of loading velocities on the damage evolution law, failure characteristics, and energy evolution law of marble are analyzed and discussed below.

Damage Evolution Law of Marble Under Different Loading Rates

Figure 5 shows the final distribution of damage of NSCB rock samples under different loading velocities. From the figure, the damage is distributed along the symmetry axis of the rock samples. The damage distribution of the rocks under dynamic loading is obviously different from that under quasi-static loading. The damage distribution of the rocks under quasi-static loading is in a straight line, while the damage evolves not only to the loading point but also to the direction perpendicular to the symmetrical axis under dynamic loading. With the increase of loading velocity, the damage range of rock samples increases gradually.

Figure 6 shows the final failure mode of NSCB rock samples under different loading velocities. It can be seen from the figure that the rock samples crack from the notch and expand along their symmetrical axial to loading point under different loading velocities, indicating that the notch plays a leading role in the crack propagation direction, which is in good agreement with the test results conducted by Zhang and Zhao (2013). With the increase of loading velocity, the flatness of crack becomes smaller and smaller, and indicates that with the increase of loading velocity, the stability of crack propagation to the loading point becomes worse and worse. This is because Fangshan marble is a rock material with a strong strain rate effect, and its failure is closely related to its dynamic strength. From the meso point of view, the dynamic strength induced by strain rates of different internal parts of the rocks is different under dynamic loading, resulting in notable randomness and uncertainty in the activation of cracks inside the rock, and this randomness is stronger and stronger with the increase of the strain rate, which activates more cracks inside the rock.

Figure 7 shows the time history curves of rock energy under different loading velocities. The total energy comes from the incident bar. According to the law of energy conservation, the total energy is equal to the sum of internal energy and kinetic energy. Internal energy is mainly used for rock deformation, damage, and failure, and kinetic energy is mainly used for rock movement. It can be obtained from the figure that the total energy of rocks under different loading velocities has the same evolution trend, which first increases gradually and then tends to have a stable value. The change of kinetic energy under different loading velocities has the same trend, which first increases gradually and then tends to be stable. The internal energy of rocks under different loading velocities also has the same trend, which first increases gradually, then decreases gradually after reaching the maximum value, and finally tends to a stable value. The stable value of internal energy increases with the increase of loading velocity. Combined with the previous analysis, it can be found that the stable value of internal energy can reflect the damage range of rocks under different loading velocities. The total energy, kinetic energy, and internal energy of rocks increase with the increase of loading velocities, but at the initial stage, the internal energy is greater than the kinetic energy.

Figure 8 shows the time history curves of rock energy under quasi-static and dynamic loading. It can be concluded from the figure that the evolution law of rock energy under quasi-static loading is notably different from that of rock energy under dynamic loading. Under quasi-static loading, the kinetic energy of the rock at the initial stage is almost zero, which

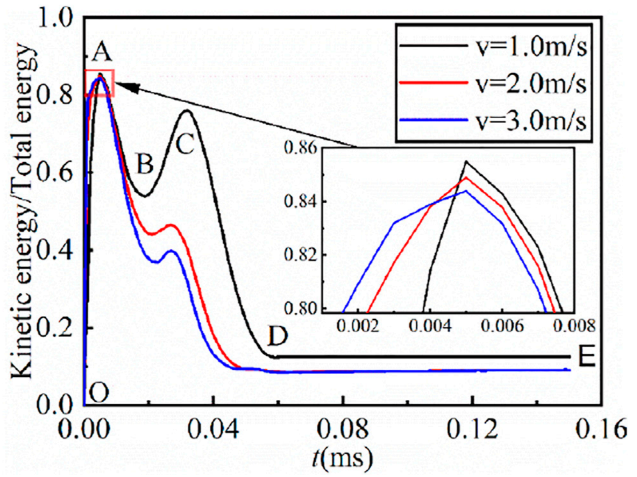

FIGURE 9 | Time history curve of the ratio of internal energy to total energy of NSCB rock samples under different loading velocities.

indicates that the total energy is basically transformed into the internal energy of the rock. The internal energy of the rock at the later stage is zero, indicating that the damage range of the rock is very small after the rock fails along the axis of symmetry. Under dynamic loading, the internal energy and kinetic energy of the rock increase gradually in the initial stage, and tend to be stable in the later stage. This stability value of internal energy is greater than that under quasi-static condition, indicating that the local high strain rate under dynamic loading can cause a wider range of damage.

Figure 9 shows the time history curve of the ratio of internal energy to total energy of NSCB rock samples under different loading velocities. The ratio of internal energy to total energy can reflect the evolution law of energy in the process of rock deformation, damage, and failure. It can be seen that the ratio of internal energy to total energy has a similar evolution law under different loading velocities. The greater the loading velocity, the smaller the maximum value of the ratio of internal energy to total energy, indicating that a higher proportion of internal energy can be obtained by rocks at a lower loading velocity. According to the energy ratio, the process from rock deformation to failure can be divided into five stages, and it is illustrated by taking the initial loading velocity of 1.0 m/s as an example, that is, OA, AB, BC, CD, and DE. In the OA stage, the energy ratio increases sharply in a very short time, and the internal energy of the rock sample increases sharply. This stage is the collision stage between the incident bar and rock sample. In the AB stage, the energy ratio decreases rapidly. At this stage, the rock sample begins to move, the kinetic energy and internal energy increase, and the increase rate of kinetic energy is greater than that of internal energy. In the BC stage, the energy ratio begins to increase gradually. At this stage, the rock sample begins to crack from B and the crack extends to the loading point, but the crack does not reach the loading point, the kinetic energy and internal energy increase, and the increase rate of internal energy is greater than that of kinetic energy. In the CD stage, the energy ratio decreases gradually. At this stage, due to the increase of crack length, the constraint of the rock sample decreases, the kinetic energy of the rock sample increases rapidly, and the internal energy of rock increases first and then decreases. In the DE stage, the crack tip reaches the loading point, the crack penetrates, the internal energy exists inside the samples in the form of plastic deformation energy remaining unchanged, and the kinetic energy tends to be stable.

CONCLUSION

Based on a self-developed dynamic damage model for rocks and element deletion technology, the NSCB test is numerically simulated, and the following conclusions are drawn in this study:

1) In the NSCB test, the loading velocity has an important influence on the damage of rock samples. With the increase of loading velocity, the damage range increases gradually.
2) The loading velocity has an important influence on the failure mode of straight notch semi-circular marble. With the increase of loading velocity, the flatness of cracks becomes worse and worse, and the stability of crack propagation becomes worse and worse. This is because the local high strain rate leads to the obvious randomness and uncertainty of crack activation in rocks.
3) Under different loading velocities, the evolution trends of total energy, kinetic energy, and internal energy of straight notch semicircular marble are similar. The damage range of marble can be evaluated by the stable value of internal energy. The larger the stable value is, the larger the damage range of marble is.
4) The energy evolution of marble under dynamic loading is obviously different from that under quasi-static loading. Under quasi-static loading, the total energy of marble in the initial stage is basically transformed into internal energy, and the internal energy of marble in the later stage is almost zero. Under dynamic loading, in addition to some of the total energy of marble in the initial stage being transformed into internal energy, some of it is also transformed into kinetic energy. The stable value of internal energy in the later stage is much greater than 0, indicating that a larger damage range can be caused under dynamic loading.
5) According to the ratio of internal energy to total energy, the deformation and failure process of straight notch semicircular marble under dynamic loading can be divided into five stages, namely, at the first stage, the energy ratio increases rapidly, and the rock sample collides with the incident rod at this stage; at the second stage, the energy ratio decreases rapidly, the rock sample begins to move, the kinetic energy and internal energy increase, and the increase rate of kinetic energy is greater than that of internal energy; at the third stage, the rock sample begins to crack and the crack extends to the loading point, but the crack does not reach the loading point. Both kinetic energy and internal energy increase, and the increase rate of internal energy is greater than that of kinetic energy; at the fourth

stage, the energy ratio decreases gradually, the crack propagates further, the constraint of rock samples decreases, the kinetic energy increases, and the internal energy first increases and then decreases; at the final stage, the energy ratio is stable, the crack penetrates at this stage, the internal energy exists in the form of plastic deformation energy, and the kinetic energy tends to be stable (Friedman et al., 1972, Hu 2020, Rossmanith et al., 1997).

DATA AVAILABILITY STATEMENT

The data supporting the conclusion of this article will be made available by the first author, without undue reservation.

AUTHOR CONTRIBUTIONS

XH contributed to conceptualization, methodology, software, data curation, validation, writing—original draft, and funding acquisition. MD contributed to data curation, writing—review and editing, and funding acquisition. MT contributed to supervision, writing—review and editing, and funding acquisition. XZ contributed to writing—review and editing, and funding acquisition. MZ contributed to funding acquisition and writing—review and editing. WX contributed to writing—review and editing.

FUNDING

This work was supported by the University natural science research project of Anhui province (KJ2020A0324 and KJ2020A0325), Natural science foundation of Anhui province (1908085QE186), The open research fund of the state key laboratory of coal resources and safe mining (SKLCRSM21KF007), Talent introduction research start-up fund of Anhui university of science and technology (13200364), Collaborative innovation project of Universities in Anhui Province (GXXT-2020-056)and National natural science foundation of China (52074007 and 52074008), which are gratefully acknowledged.

REFERENCES

Cai, X., Zhou, Z. L., Ma, D., Du, X. M., Chen, L., Wang, H. Q., et al. (2018). Water Saturation Effects on Dynamic Fracture Behavior of sandstone. *Int. J. Rock. Mech. Mining. Sci.* 114, 46–61. doi:10.1016/j.ijrmms.2018.12.014

Cai, X., Zhou, Z., Zang, H., and Song, Z. (2020a). Water Saturation Effects on Dynamic Behavior and Microstructure Damage of sandstone: Phenomena and Mechanismsffects on Dynamic Behavior and Microstructure Damage of sandstone: Phenomena and Mechanisms. *Eng. Geology.* 276, 105760. doi:10.1016/j.enggeo.2020.105760

Cai, X., Zhou, Z., Tan, L., Zang, H., and Song, Z. (2020b). Fracture Behavior and Damage Mechanisms of sandstone Subjected to Wetting-Drying Cycles. *Eng. Fracture Mech.* 234, 107109. doi:10.1016/j.engfracmech.2020.107109

Chen, R., Li, K., Xia, K., Lin, Y., Yao, W., and Lu, F. (2016). Dynamic Fracture Properties of Rocks Subjected to Static Pre-load Using Notched Semi-circular bend Method. *Rock. Mech. Rock. Eng.* 49 (10), 3865–3872. doi:10.1007/s00603-016-0958-4

Chen, R., Xia, K., Dai, F., Lu, F., and Luo, S. N. (2009). Determination of Dynamic Fracture Parameters Using a Semi-circular bend Technique in Split Hopkinson Pressure Bar Testing. *Eng. Fracture Mech.* 76 (9), 1268–1276. doi:10.1016/j.engfracmech.2009.02.001

Chong, K. P., and Kuruppu, M. D. (1984). New Specimen for Fracture Toughness Determination for Rock and Other Materials. *Int. J. Fract.* 26 (2), R59–R62. doi:10.1007/BF01157555

Dai, F., Chen, R., and Xia, K. (2010). A Semi-circular bend Technique for Determining Dynamic Fracture Toughness. *Exp. Mech.* 50 (6), 783–791. doi:10.1007/s11340-009-9273-2

Dai, F., Xia, K., and Nasseri, M. H. B. (2013). Micromechanical Model for the Rate Dependence of the Fracture Toughness Anisotropy of Barre Granite. *Int. J. Rock Mech. Mining Sci.* 63, 113–121. doi:10.1016/j.ijrmms.2013.08.011

Dai, F., and Xia, K. W. (2013). Laboratory Measurements of the Rate Dependence of the Fracture Toughness Anisotropy of Barre Granite. *Int. J. Rock Mech. Mining Sci.* 60, 57–65. doi:10.1016/j.ijrmms.2012.12.035

Dai, F., Xia, K., Zheng, H., and Wang, Y. X. (2011). Determination of Dynamic Rock Mode-I Fracture Parameters Using Cracked Chevron Notched Semi-circular bend Specimen. *Eng. Fracture Mech.* 78 (15), 2633–2644. doi:10.1016/j.engfracmech.2011.06.022

Dai, F., Xu, Y., Zhao, T., Xu, N.-w., and Liu, Y. (2016). Loading-rate-dependent Progressive Fracturing of Cracked Chevron-Notched Brazilian Disc Specimens in Split Hopkinson Pressure Bar Tests. *Int. J. Rock Mech. Mining Sci.* 88, 49–60. doi:10.1016/j.ijrmms.2016.07.003

Du, K., Li, X., Tao, M., and Wang, S. (2020). Experimental Study on Acoustic Emission (AE) Characteristics and Crack Classification during Rock Fracture in Several Basic Lab Tests. *Int. J. Rock Mech. Mining Sci.* 133, 104411. doi:10.1016/j.ijrmms.2020.104411

Du, K., Li, X., Wang, S., Tao, M., Li, G., and Wang, S. (2021). Compression-shear Failure Properties and Acoustic Emission (AE) Characteristics of Rocks in Variable Angle Shear and Direct Shear Tests. *Measurement* 183, 109814. doi:10.1016/j.measurement.2021.109814

Franklin, J. A., Sun, Z., Atkinson, B. K., Meredith, P. G., and Bobrov, G. F. (1988). Suggested Methods for Determining the Fracture Toughness of Rock. *Int. J. Rock. Mech. Mining. Sci.* 25 (2), 71–96. doi:10.1016/0148-9062(88)91871-2

Friedman, M., Handin, J., and Alani, G. (1972). Fracture-surface Energy of Rocks. *Int. J. Rock Mech. Mining Sci. Geomechanics Abstr.* 9 (6), 757–764. doi:10.1016/0148-9062(72)90034-4

Gao, G., Huang, S., Xia, K., and Li, Z. (2015a). Application of Digital Image Correlation (DIC) in Dynamic Notched Semi-circular bend (NSCB) Tests. *Exp. Mech.* 55 (1), 95–104. doi:10.1007/s11340-014-9863-5

Gao, G., Yao, W., Xia, K., and Li, Z. (2015b). Investigation of the Rate Dependence of Fracture Propagation in Rocks Using Digital Image Correlation (DIC) Method. *Eng. Fracture Mech.* 138, 146–155. doi:10.1016/j.engfracmech.2015.02.021

Hu, X. L. (2020). *Study of Rock Dynamic Damage Model Based on Unified Strength Theory*. PhD thesis. Beijing: University of Science and Technology Beijing.

Klepaczko, J. R., Bassim, M. N., and Hsu, T. R. (1984). Fracture Toughness of Coal under Quasi-Static and Impact Loading. *Eng. Fracture Mech.* 19 (2), 305–316. doi:10.1016/0013-7944(84)90025-0

Kourkoulis, S. K., and Markides, C. F. (2014). Fracture Toughness Determined by the Centrally Cracked Brazilian-disc Test: Some Critical Issues in the Light of an Alternative Analytic Solution. *Matls. Perf. Charact.* 3 (3), 20130056–20130086. doi:10.1520/MPC20130056

Kuruppu, M. D., Obara, Y., Ayatollahi, M. R., Chong, K. P., and Funatsu, T. (2014). ISRM-suggested Method for Determining the Mode I Static Fracture Toughness Using Semi-circular bend Specimen. *Rock. Mech. Rock. Eng.* 47 (1), 267–274. doi:10.1007/s00603-013-0422-7

Li, Y., Dai, F., Wei, M., and Du, H. (2020). Numerical Investigation on Dynamic Fracture Behavior of Cracked Rocks under Mixed Mode I/II Loading. *Eng. Fracture Mech.* 235, 1–17. doi:10.1016/j.engfracmech.2020.107176

Lim, I. L., Johnston, I. W., and Choi, S. K. (1993). Stress Intensity Factors for Semi-circular Specimens under Three-point Bending. *Eng. Fracture Mech.* 44, 363–382. doi:10.1016/0013-7944(93)90030-v

Nakano, M., Kishida, K., Yamauchi, Y., and Sogabe, Y. (1994). Dynamic Fracture Initiation in Brittle Materials under Combined Mode I/II Loading. *J. Phys. IV France* 04 (C8), C8–C695. doi:10.1051/jp4:19948106

Rossmanith, H. P., Daehnke, A., Nasmillner, R. E. K., Kouzniak, N., Ohtsu, M., and Uenishi, K. (1997). Fracture Mechanics Applications to Drilling and Blasting. *Fatigue. Fract. Eng. M.* 20 (11), 1617–1636. doi:10.1111/j.1460-2695.1997.tb01515.x

Shi, X., Yao, W., Liu, D. A., Xia, K., Tang, T., and Shi, Y. (2019). Experimental Study of the Dynamic Fracture Toughness of Anisotropic Black Shale Using Notched Semi-circular bend Specimens. *Eng. Fracture Mech.* 205, 136–151. doi:10.1016/j.engfracmech.2018.11.027

Tang, C., and Xu, X. (1990). A New Method for Measuring Dynamic Fracture Toughness of Rock. *Eng. Fract. Mech.* 35 (1-3), 783–791. doi:10.1016/0013-7944(90)90162-A

Wang, Q., Ni, M., Zhang, C., and Li, L. (2016). Clarification of Formulas for Stress Intensity Factor for DCDC Specimens. *Int. J. Fract.* 201 (2), 249–250. doi:10.1007/s10704-016-0144-4

Wei, M.-D., Dai, F., Xu, N.-W., Liu, Y., and Zhao, T. (2018a). A Novel Chevron Notched Short Rod bend Method for Measuring the Mode I Fracture Toughness of Rocks. *Eng. Fracture Mech.* 190, 1–15. doi:10.1016/j.engfracmech.2017.11.041

Wei, M.-D., Dai, F., Zhou, J.-W., Liu, Y., and Luo, J. (2018b). A Further Improved Maximum Tangential Stress Criterion for Assessing Mode I Fracture of Rocks Considering Non-singular Stress Terms of the Williams Expansion. *Rock. Mech. Rock. Eng.* 51, 3471–3488. doi:10.1007/s00603-018-1524-z

Wei, M.-D., Dai, F., Liu, Y., Xu, N.-W., and Zhao, T. (2018c). An Experimental and Theoretical Comparison of CCNBD and CCNSCB Specimens for Determining Mode I Fracture Toughness of Rocks. *Fatigue Fract Eng. Mater. Struct.* 41, 1002–1018. doi:10.1111/ffe.12747

Wei, M., Dai, F., Liu, Y., Li, A., and Yan, Z. (2021). Influences of Loading Method and Notch Type on Rock Fracture Toughness Measurements: From the Perspectives of T-Stress and Fracture Process Zone. *Rock. Mech. Rock. Eng.* 54, 4965–4986. doi:10.1007/s00603-021-02541-9

Xia, K., and Yao, W. (2015). Dynamic Rock Tests Using Split Hopkinson (Kolsky) Bar System - A Review. *J. Rock Mech. Geotechnical Eng.* 7 (1), 27–59. doi:10.1016/j.jrmge.2014.07.008

Xing, H. Z., Zhang, Q. B., Braithwaite, C. H., Pan, B., and Zhao, J. (2017). High-speed Photography and Digital Optical Measurement Techniques for Geomaterials: Fundamentals and Applications. *Rock. Mech. Rock. Eng.* 50 (6), 1611–1659. doi:10.1007/s00603-016-1164-0

Xu, Y., Zhang, J. C., Yao, W., and Xia, K. W. (2018). Experimental Study of Dynamic Fracture Energy Anisotropy of Granitic Rocks. Chin. *J. Rock. Mech. Eng.* 37 (S1), 3231–3238.

Yao, W., and Xia, K. (2019). Dynamic Notched Semi-circle bend (NSCB) Method for Measuring Fracture Properties of Rocks: Fundamentals and Applications. *J. Rock Mech. Geotechnical Eng.* 11 (5), 1066–1093. doi:10.1016/j.jrmge.2019.03.003

Yao, W., Xia, K., and Zhang, T. (2019). Dynamic Fracture Test of Laurentian Granite Subjected to Hydrostatic Pressure. *Exp. Mech.* 59 (2), 245–250. doi:10.1007/s11340-018-00437-4

Yao, W., Xu, Y., Liu, H.-W., and Xia, K. (2017). Quantification of Thermally Induced Damage and its Effect on Dynamic Fracture Toughness of Two Mortars. *Eng. Fracture Mech.* 169, 74–88. doi:10.1016/j.engfracmech.2016.11.018

Yin, T., Li, X., Xia, K., and Huang, S. (2012). Effect of thermal Treatment on the Dynamic Fracture Toughness of Laurentian Granite. *Rock. Mech. Rock. Eng.* 45 (6), 1087–1094. doi:10.1007/s00603-012-0240-3

Yin, Z. Q., Ma, H. F., Ma, H. F., Hu, Z. X., and Zou, Y. (2014). Effect of Static - Dynamic Coupling Loading on Fracture Toughness and Failure Characteristics in Marble. *J. Eng. Sci. Tech. Rev.* 7 (2), 169–174. doi:10.25103/jestr.072.25

Zhang, Q. B., and Zhao, J. (2013). Determination of Mechanical Properties and Full-Field Strain Measurements of Rock Material under Dynamic Loads. *Int. J. Rock Mech. Mining Sci.* 60 (8), 423–439. doi:10.1016/j.ijrmms.2013.01.005

Zhang, Q. B., and Zhao, J. (2014). Quasi-static and Dynamic Fracture Behaviour of Rock Materials: Phenomena and Mechanisms. *Int. J. Fract.* 189 (1), 1–32. doi:10.1007/s10704-014-9959-z

Zhao, Y., Gong, S., Hao, X., Peng, Y., and Jiang, Y. (2017). Effects of Loading Rate and Bedding on the Dynamic Fracture Toughness of Coal: Laboratory Experiments. *Eng. Fracture Mech.* 178, 375–391. doi:10.1016/j.engfracmech.2017.03.011

Zhou, X. P., Yang, H. Q., and Zhang, Y. X. (2009). Rate Dependent Critical Strain Energy Density Factor of Huanglong limestone. *Theor. Appl. Fracture Mech.* 51 (1), 57–61. doi:10.1016/j.tafmec.2009.01.001

Zhou, Y. X., Xia, K., Li, X. B., Li, H. B., Ma, G. W., Zhao, J., et al. (2012). Suggested Methods for Determining the Dynamic Strength Parameters and Mode-I Fracture Toughness of Rock Materials. *Int. J. Rock Mech. Mining Sci.* 49 (1), 105–112. doi:10.1016/j.ijrmms.2011.10.004

Zhou, Z., Cai, X., Ma, D., Cao, W., Chen, L., and Zhou, J. (2018). Effects of Water Content on Fracture and Mechanical Behavior of sandstone with a Low clay mineral Content. *Eng. Fracture Mech.* 193, 47–65. doi:10.1016/j.engfracmech.2018.02.028

Conflict of Interest: The authors declare that the research was conducted in the absence of any commercial or financial relationships that could be construed as a potential conflict of interest.

frontiers
in Earth Science

ORIGINAL RESEARCH
published: 07 February 2022
doi: 10.3389/feart.2021.829258

Experimental Study on Fracturing Characteristics of Double-Hole Blasting Under Static Stresses

Hui Chen[1,2]*, Xianyang Qiu*[1]**, Xiuzhi Shi*[1]*, Junhui Zhang*[1,2]*, Xiaofeng Huo*[1] *and Dongping Li*[3]

[1]School of Resources and Safety Engineering, Central South University, Changsha, China, [2]School of Geological and Mining Engineering, Xinjiang University, Urumqi, China, [3]China Nonferrous Metal Mining Group Co., Ltd., Beijing, China

This study aims to investigate the fracturing characteristics of double-hole blasting under the action of coupled static stress and delayed time explosion. A total of thirteen explosive tests were carried out on rectangular concrete blocks with different constraints. The test blocks were wrapped in steel mesh in the test bed to prevent flying away of the cracked blocks after blasting. After blasting, the surface area of the crater was measured, and all pieces of the cracked blocks were collected, screened, and analyzed. The experimental results show that (1) the shape of free-surface craters was affected by static stress. The surface area and overall volume of the craters increased in the direction of loading stress. (2) The crater under simultaneous initiation was larger than that under delayed initiation when the tested block had a single free surface. (3) The fragmentation of blasting is closely related to the static confining pressure and delay initiation applied on the tested specimens. It is believed that this research will contribute to the design of multi-hole blasting in the deep geological body in the respect of the theoretical analysis.

Keywords: ***in situ*** **stresses, double-hole blasting, borehole expansion, delay initiation, fragmentation of blasting**

Edited by:
Zhiqiang Yin,
Anhui University of Science and Technology, China

Reviewed by:
Jianhua Yang,
Nanchang University, China
Jianyu Peng,
Northeastern University, China

Correspondence:
Xianyang Qiu
qiuxianyang_csu@163.com

Specialty section:
This article was submitted to Geohazards and Georisks, a section of the journal Frontiers in Earth Science

Received: *05 December 2021*
Accepted: *30 December 2021*
Published: *07 February 2022*

Citation:
Chen H, Qiu X, Shi X, Zhang J, Huo X and Li D (2022) Experimental Study on Fracturing Characteristics of Double-Hole Blasting Under Static Stresses. Front. Earth Sci. 9:829258. doi: 10.3389/feart.2021.829258

INTRODUCTION

The depletion of shallow resources and increasing demand for metal sources have led to increasing interest in underground mining, featured by high *in situ* stress in deep Earth (Fan et al., 2009). Drilling and blasting are always employed for these underground rock excavations due to their economic cost and effectiveness. However, under high *in situ* stress, the rock breaking produced by underground blasts differs from that generated from open-pit mining and shallow excavation (Yan et al., 2016; Han et al., 2020). To make the fragmentation law clear under the coupling action of high *in situ* stress and blasting, it is of great significance for determining blasting parameters and safe and efficient production in deep ore bodies. They carried out physical experiment research of double-hole blasting to determine the blasting parameters of deep rock mass that are necessary to realize safe and efficient excavation and mining (Yilmaz and Unlu, 2013; He et al., 2018; Jayasinghe et al., 2019). At present, scholars have carried out a lot of research work on rock breaking by blasting under *in situ* stress. Some theories and experiments have been carried out on rock blasting under high ground stress (Xiao et al., 1996).

Many research studies have been carried out on the mechanism of blasting fracture (Zhu et al., 2016). Static stress can reduce the fracture length and the area of the blasting damage zone. Moreover, the tensile strength of rock under the coupling action of static and dynamic loads decreases with the increase in the static prestress, indicating that high ground stress can enhance the fragmentation of rock under blasting excavation (Zhao et al., 2017). The aforementioned studies illustrated the influence of static stress on the blasting fracture of rock materials, and *in situ* stress played a key role in crack initiation and growth. Based on these studies, the influence of *in situ* stress on blasting rock fracture was analyzed and experimentally studied (Li et al., 2021; Wu et al., 2015; Zhang et al., 2017). The results show that the cracks caused by blasting stress wave and gas pressure grow well in the direction of the maximum principal stress of the superimposed stress field (Kutter and Fairhurst, 1971). It calculated the rock breakage caused by blasting under high stress based on fracture mechanics and rock damage criterion. The results showed that the release of strain energy in high-stress rock mass was beneficial to improve the crushing effect. Based on this, they studied the propagation characteristics of blasting crack in dynamic and static stress fields by the caustic experiment. The results showed that *in situ* stress had an important influence on the crack growth caused by blasting (Xiao et al., 2019). When the direction of vertical *in situ* stress was in the direction of crack propagation, the crack growth was restrained. It experimentally simulated the blasting failure characteristics of rock mass under different stress conditions, and the influence of the *in situ* stress value and direction on presplitting blasting was studied (Yang et al., 2019). The damage of the gypsum block decreased with the increase in uniaxial pressure. The article studied the influence law and the response of the main crack induced by blasting the initial static stress field using dynamic and static loading experimental equipment to simulate static stress field, and a digital laser dynamic caustic system was used to collect data (Yang et al., 2021). The findings revealed that the combined action field of the initial static stress and the dynamic blasting stress field gave priority to the maximum crack propagation along the initial static stress direction (Yang and Ding, 2018). The study simulated the blasting disturbance of the underground tunnel through a physical model test and analyzed the influence of the blasting position on surface deformation and failure characteristics (Qiu et al., 2021). The work studied the crater blasting under different confining pressures through theoretical analysis and physical model tests. Under the condition of the uniaxial load, the shape of the crater in the long axial loading direction was elliptical with the increase in the confining pressure, and the opening angle and pit volume in this direction increased (Peng et al., 2020; Zhang et al., 2021).

Some experiments and numerical simulation studies were carried out on rock blasting under high ground stress (Li et al., 2021; Jayasinghe et al., 2019). The research results show that the existence of high ground stress changed the propagation direction and propagation length of explosion-induced cracks. The cracks first radiated outward from the blast hole wall and then gradually extended outward along the direction of the maximum principal stress (He and Yang, 2019). The article used the RHT model in LS-DYNA to simulate the blasting damage characteristics of the high-stress rock mass. Under uniaxial loading, the crater volume increased with the increase in the confining pressure (Huo et al., 2021). The uniaxial static load could change the optimal load and the critical buried depth of charge. The granitic lithology with a complete deep structure has high energy storage capacity (Wang et al., 2019; Zhang et al., 2020). The influence of the confining pressure and ratio of horizontal pressure to vertical pressure on blasting rock fracture was studied through experiments. The results showed that the direction of crack propagation was mainly controlled by circumferential tensile stress and biaxial preload ratio (He and Yang, 2019).

The combined finite-discrete element method (FDEM) was used to simulate the excavation damage area of rock mass caused by contour blasting. It was found that blasting cracks initially spread along the horizontal direction of ground stress under high level of *in situ* stresses. The following study was carried out on the double-hole test. Increasing the millisecond initiation time between adjacent holes could form a better crack network between holes and make radial cracks penetrate through (Zhao et al., 2017). The research results showed that through the field test and numerical analysis it was found that the larger the distance between adjacent holes, the closer the main cracks to the connecting direction of holes (LEI and JIANG, 2019). The blasting of high-stress rock mass was studied using the coupled numerical simulation method of smooth particle hydrodynamics and finite element method. The crack propagation length between the blast holes decreased with the increase in the local stress level, and the crack mainly expanded parallel to the direction of maximum principal stress. Arranging the blast holes along the direction of maximum principal stress and shortening the distance between the blast holes were considered to be beneficial to the connection and penetration of cracks between the blast holes. The influence of the confining pressure and ratio of horizontal pressure to vertical pressure on blasting rock fracture was studied through experiments. The results showed that the direction of crack propagation was

FIGURE 1 | Model manufacture.

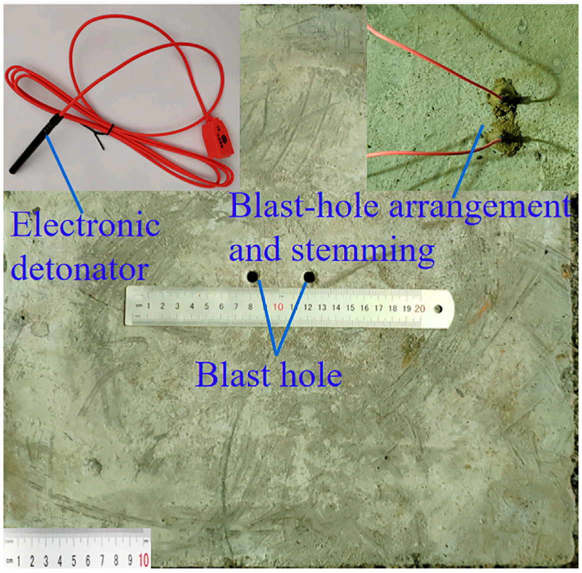

FIGURE 2 | Test block hole layout and plug hole.

mainly controlled by circumferential tensile stress and biaxial preload ratio.

The aforementioned studies were mostly conducted in the numerical simulation experiments of single-hole blasting and double-hole blasting. It is thus critically urgent to conduct the physical model test to further explore the influence of static stress on rock breaking by double-hole blasting. In this study, the influence of static stress on the double-hole crater and fragmentation under the condition of a single free surface was studied by laboratory tests, the main contribution of which is to provide the theoretical foundation to the design of multi-hole blasting in the deep geological body.

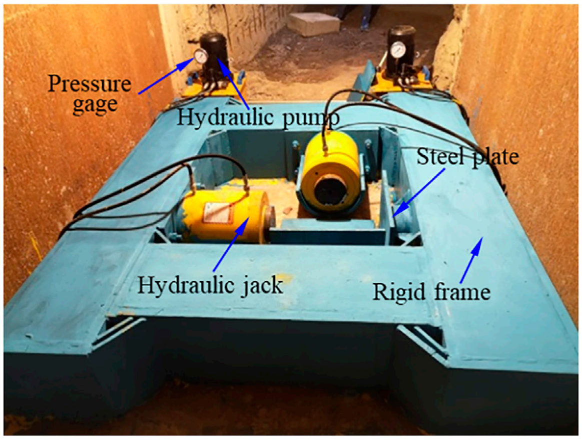

FIGURE 3 | High-stress loading test platform.

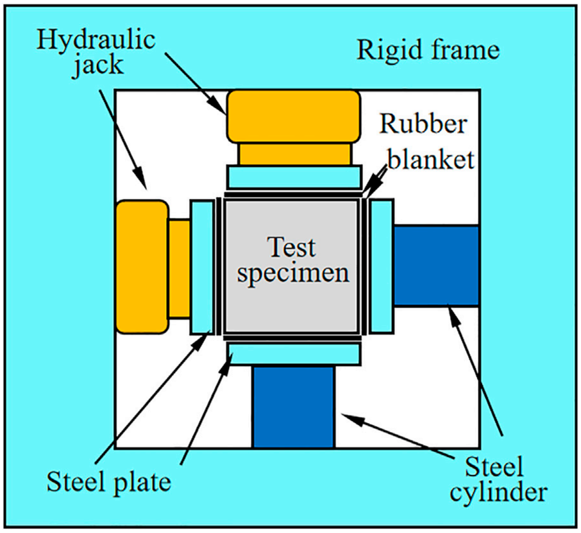

FIGURE 4 | Platform loading form and layout.

BLASTING TEST OF A CONCRETE BLOCK UNDER THE STATIC STRESS

Test Block

Cement blocks are widely used to simulate brittle rocks in blasting tests because cement mortar has the characteristics of homogeneity, isotropy, and designable strength. In this study, a series of blasting model tests were conducted using solid cement mortar and block stones. The test block was made of sand with uniform particle size, ordinary Portland cement (PC42.5), small stones, and water. **Figures 1**, **2** show the geometric dimensions of the model test block. The model test block adopted cuboid specification (**Figure 1**), and its size was 400 × 400 × 200 mm^3. During the preparation of the test block, three groups of 120 × 120 × 120 mm^3 cube test blocks were poured with the same mixture, and the physical and mechanical parameters of the test blocks were measured with the cube test blocks. Compressive strength and elastic modulus were measured using the CSS-YAW3000 electrohydraulic servo pressure frame and the KD7016A static strain test and analysis system. A CTS-25 nonmetal ultrasonic detector was used to measure the longitudinal wave velocity of the mortar. The parameters of the cement mortar block were as follows: density 2,451 kg/m^3, elastic modulus 32.30 GPa, compressive strength 40.8 MPa, Poisson's ratio 0.24, longitudinal wave velocity 3,808 m/s, and shear wave velocity 2,219 m/s.

Blasting Parameters

The blasting hole was located on the central line of the surface of the test block, with a diameter of 7.5 mm and a distance of 4 cm from the bottom of the hole to the free surface and 7.0 cm between holes (**Figure 1**). The experiment used a No. 8 digital electronic detonator to initiate the simulated charge to reduce the influence of the delay time error. The external dimension of the No. 8 digital electronic detonator was φ7.3 × 73 mm^2, and the inner diameter of the electronic detonator shell was 6.1–6.4

TABLE 1 | Experimental scheme of the double-hole crater under the stress condition.

Load direction	No.	Loading stress (MPa)	Delay time (ms)
Loading direction parallel to the bore centerline	S1	0	0
	S2	5	0
	S3	10	0
	S4	20	0
Loading direction perpendicular to the direction of the hole centerline	S1	0	0
	S5	5	0
	S6	10	0
	S7	20	0
Loading direction parallel to the bore centerline	S8	0	1
	S9	10	1
	S10	20	1
	S11	0	2
	S12	10	2
	S13	20	2

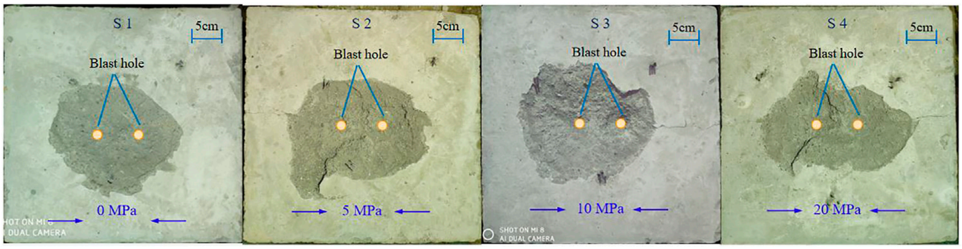

FIGURE 5 | Shape of the crater under parallel hole confining pressure.

cm, the filling length was 15 mm, the density was 1.4–1.6 g/m^3, and the mass was 0.65 g RDX. The hole orifice was plugged with stemming to reduce the influence of stemming on blasting (**Figure 2**), and the plugging was to achieve the ideal rock crushing effect (Zhang et al., 2021).

High-Stress Blasting Test Platform

A new type of blasting test system was set up under high stress in the blasting test chamber of Fankou Lead–Zinc Mine, Guangdong Province, to carry out experimental research, which was used to carry out the biaxial loading test on the square block to achieve the pressurization condition of the model block. **Figure 3** shows that the test platform mainly consisted of a rigid frame, two hydraulic jacks, two hydraulic pumps, and two rigid pressure heads. The hydraulic jack pushed the rigid indenter to make contact with the test block, the hydraulic pump controlled the loading pressure, and the universal testing machine combined with the pressure sensor was used to calibrate the hydraulic jack, ensuring the accuracy of loading static stress. The loading system applied compressive stress in two directions perpendicular to the free surface of the sample, simulating the bidirectional *in situ* stress environment of the deep rock mass. The hydraulic cylinder provided 0–60 MPa pressure in two directions, and the pressure gauge on the hydraulic pump was used to measure the output pressure load. As shown in **Figure 4**, the boundary of the test block was covered with a 20-mm-thick rubber plate to absorb the stress wave at the boundary. Rubber is a kind of polymer material with high elasticity, low impedance, viscoelasticity, shock energy absorption, earthquake resistance, and other mechanical properties. It is often used in structures to reduce the influence of the dynamic load (Qiu et al., 2021). The loading device had a 30-mm-thick steel plate to induce uniform boundary stress. In addition, the unpressurized direction also uses the press to contact the test block.

Experimental Scheme of the Double-Hole Crater Under the Stress Condition

In this study, the experimental research on the double-hole crater was carried out under three different confining pressures: (1) the double-hole crater was detonated simultaneously under unidirectional confining pressure; (2) two-hole simultaneous initiation crater under bidirectional confining pressure; and (3) double-hole short-delay initiation crater under confining pressure loading. A total of sixteen groups of blasting tests were conducted, and the detailed parameters of test confining pressure loading conditions and delay time are shown in **Table 1**. After placing the test block, the boundary was

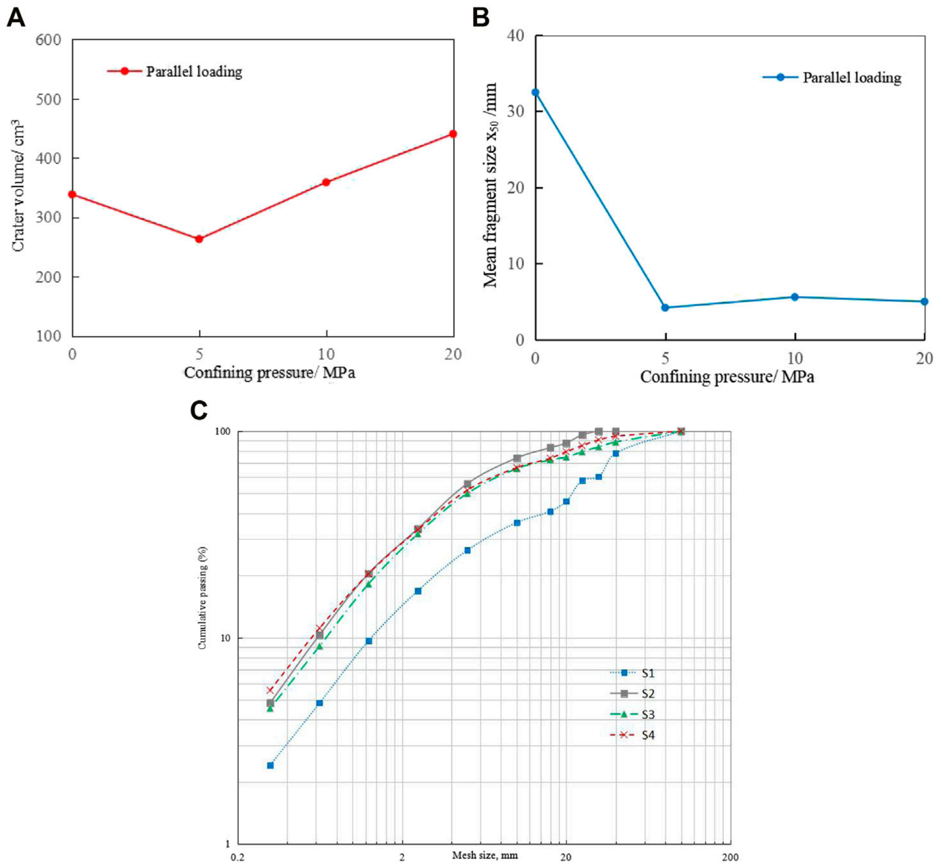

FIGURE 6 | Double-hole simultaneous initiation effect under unidirectional confining pressure. **(A)** Crater volume. **(B)** Average block size (x_{50}). **(C)** Distribution functions fitted to sieving results for the S1 ~ S4 surface profile of the crater.

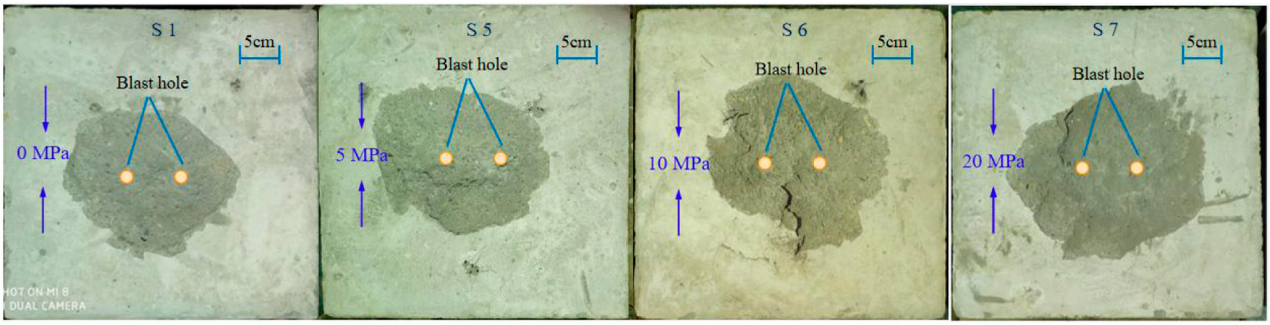

FIGURE 7 | Shape of the crater under vertical hole confining pressure.

covered with a rubber plate, and the rubber plate, in turn, was covered with a steel plate. The confining pressure was loaded to the design value using a loading device. The electronic detonator was inserted into the designed hole, and the surface of the model was covered with a cover plate to facilitate the collection of the test block broken by blasting. The electronic detonator was detonated according to the experimental scheme. After each blasting experiment, the data of the crater were carefully measured, and the test pieces were collected, weighed, and screened. On this basis, the relationship between the particle (fragment) size of each test block and the cumulative mass pass rate (%) was established.

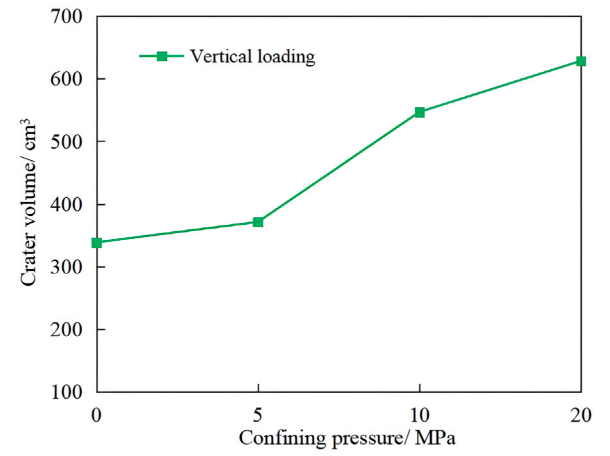

FIGURE 8 | Crater volume.

RESULT ANALYSIS

Double-Hole Simultaneous Initiation Crater Under Unidirectional Confining Pressure

1) Blasting test results and analysis under the condition that the direction of the confining pressure loading was parallel to the direction of the hole-to-heart line.

Figure 5 shows the shape of the double-hole simultaneous initiation crater under unidirectional confining pressure when the direction of the confining pressure loading was parallel to the direction of the hole-to-hole line. When no confining pressure was applied, the crater was smaller, and the length of the crater in the hole-to-heart line direction was slightly longer than that in the other direction. However, applying a unidirectional confining pressure in the direction of the hole-to-heart line caused the crater length to gradually increase in the pressurization direction and reduce in the unpressurized direction, especially when the unidirectional pressure reached 20 MPa, the crater diameter in the pressure direction increased from 23.2 to 27.4 cm. This was because the direction of the hole-to-heart line was consistent with the direction of the confining pressure loading, and a stress blind area appeared between two adjacent holes. The applied confining pressure had little effect on the blasting breakage between two holes, but it could promote the breakage around the holes. The volume of the crater first decreased and then increased with the increase in the unidirectional confining pressure, among which the volume of the crater with 5 MPa loading stress was the smallest. This phenomenon shows that low static stress inhibits blasting breakage in the direction parallel to the hole loading. Similar results were reported by Zhang et al. (Zhang et al., 2021). Under the condition of low static stress, the cracks inside the test block are closed. With the increase of static stress, the reflected tensile failure gradually becomes the main factor affecting the formation of the explosion crater. In **Figure 6A**, the volume of the crater increased from 338.63 cm^3 without pressure to 440.64 cm^3 with a pressure of 20 MPa. It indicates that the blasting fragmentation range increases with increasing confining pressure. In **Figures 6B,C**, the average fragmentation (x_{50}) of blasting decreases gradually, indicating that the fragmentation is more uniform with increasing confining pressure.

2) Blasting test results and analysis under the condition that the direction of the confining pressure loading was perpendicular to the direction of the hole-to-heart line

Figure 7 shows the shape of the double-hole simultaneous initiation crater under unidirectional confining pressure when the confining pressure loading direction was perpendicular to the direction of the hole-to-hole line. The crater was smaller without the confining pressure, and the length of the crater in the direction of the hole-to-heart line was slightly longer than that in the other direction. However, the application of unidirectional confining pressure in the direction perpendicular to the hole-to-hole line did not cause much change in the crater length in the

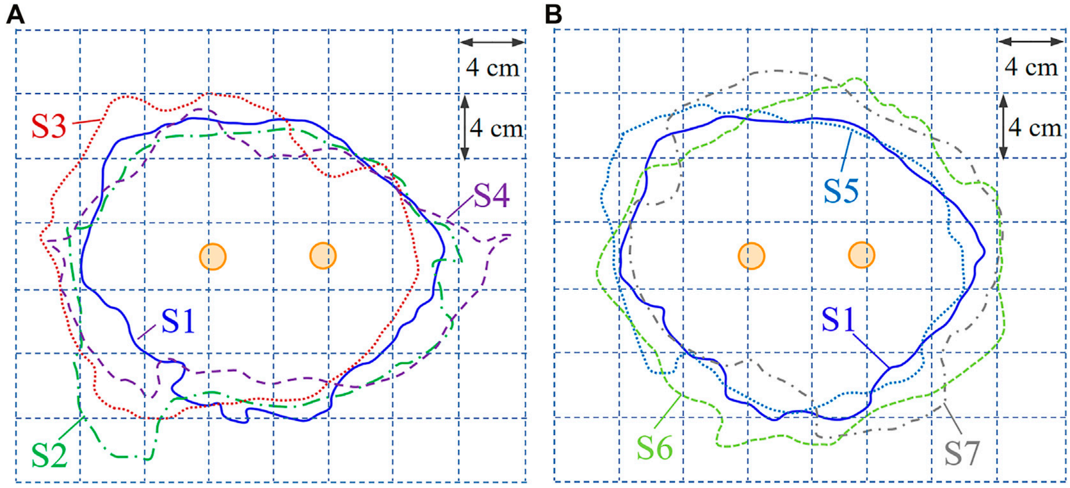

FIGURE 9 | (A) Crater surface outline of S1, S2, S3, and S4. **(B)** Crater surface outline of S1, S5, S6, and S7. Comparison of crater contour under different pressure directions.

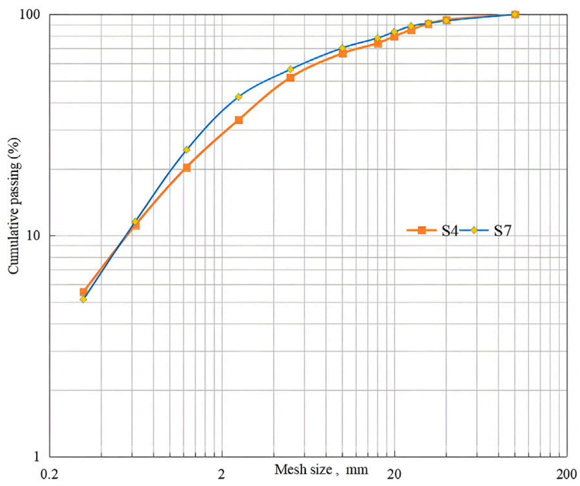

FIGURE 10 | Blasting fragmentation distribution under two loading 20 MPa pressure schemes.

direction of the hole-to-hole line; however, the crater length increased in the direction perpendicular to the hole-to-hole line, that is, the pressurization direction, especially in the middle of the hole-to-hole line. This was because the stress in the middle of the hole increased due to the confining pressure applied in the direction perpendicular to the line connecting the hole to the heart, which further promoted the blasting rupture in the middle of the hole. In **Figure 8**, with the increase of unidirectional pressure, the volume of the crater increases, in which the volume of the crater is 628.32 cm^3 under 20 MPa loading stress.

3) Comparing the effects of the crater under different pressurization directions

Figures 9, **10** show the comparison of the shapes of double-hole craters under different pressurization directions. The shape of the crater (S4 and S7) was obviously different when the direction of pressurization (S4) was different from that of the hole-to-heart line (S7). When the pressure direction was consistent with the direction of the hole-to-heart line, the crater length in the pressure direction was obviously larger than that in the other pressure scheme. In contrast, the crater length perpendicular to the pressure direction was smaller than that in the other pressure scheme. **Figure 11** shows the distribution diagram of blasting fragmentation of two schemes. The distribution of blasting fragmentation was more uniform than that of the other pressurization schemes when the pressurization direction was consistent with the direction of the hole-to-heart line, and its average fragmentation (x_{50}) was also smaller than that of the other scheme. When the pressure direction was parallel to the hole-to-hole line direction, the blasting fragmentation was found to be better than when the pressure direction was perpendicular to the hole-to-hole line direction.

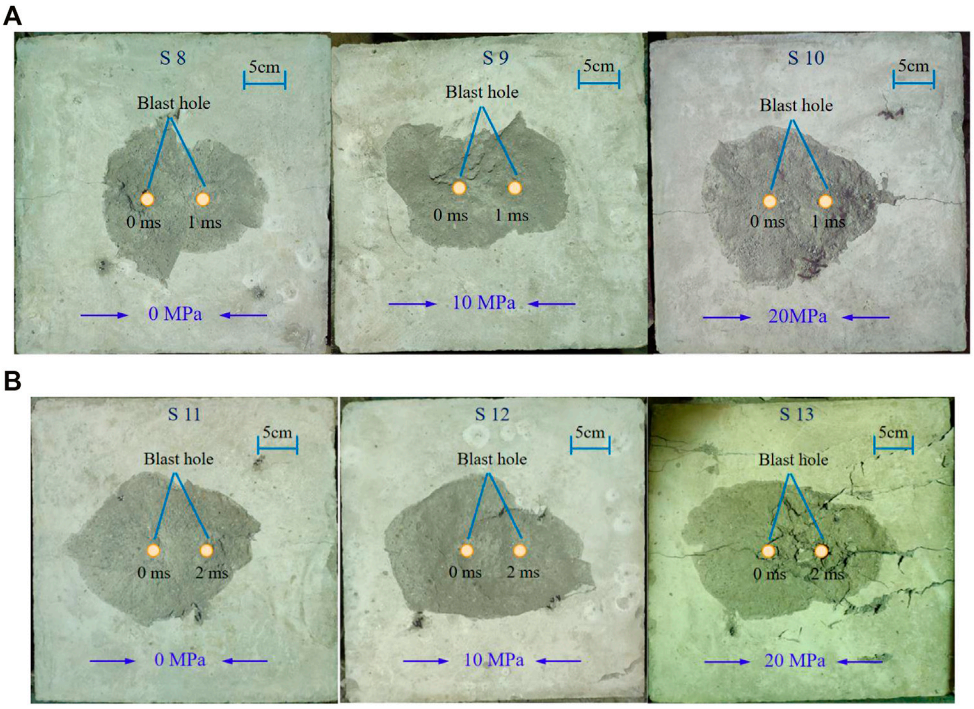

FIGURE 11 | Crater shape of double-hole short-delay initiation blasting under confining pressure loading. **(A)** 1 ms delay between holes. **(B)** 2 ms delay between holes.

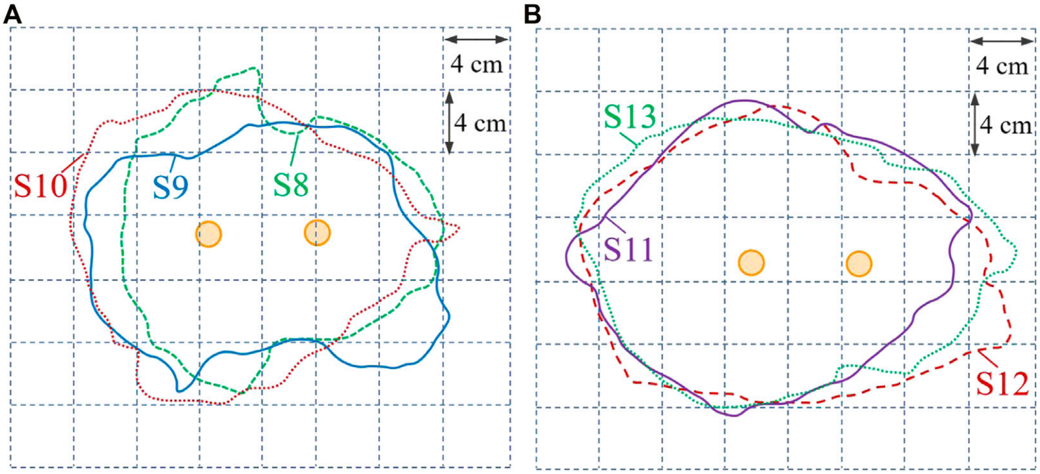

FIGURE 12 | Crater contour comparison of delay blasting. **(A)** Crater surface outline of S8, S9, and S10. **(B)** Crater surface outline of S11, S12, and S13.

Test Results and Analysis of Double-Hole Short-Delay Blasting Under Confining Pressure Loading

Figure 11 shows the shape of a double-hole short-delay initiation crater under confining pressure loading. When no confining pressure was applied, in S8 and S11, the crater under double-hole short-delay initiation was found to be similar to V-shape. The first blasting hole formed a larger crater, the second blasting hole took the first crater as the free surface for lateral blasting, and the width of the crater on one side of the second blasting hole was smaller in S8, S10, and S12 indicating the influence of delayed initiation, and two adjacent holes failed to form a common crater. However, after applying the confining pressure, the craters of adjacent holes were obviously more uniform and reasonable than those without confining pressure, and the widths of craters at two holes were closer. In addition, the rupture range of S13 blasting is larger than that of S11 without confining pressure due to the confining pressure applied along the direction of the core line of the hole. This showed that under short-delay initiation, double-hole blasting could make good use of confining pressure to form a suitable crater. **Figures 12, 13** show the variation in the crater volume with confining pressure under 1 and 2 ms initiation. It can be concluded that with the increase of unidirectional confining pressure and delay time, the crater volume also increases.

Figure 14 shows the fragmentation distribution of 2 ms initiation under different confining pressures. **Figure 14B** shows that the average fragmentation x_{50} after confining pressure loading was smaller than that without confining pressure, and the average fragmentation gradually decreased with an increase in the confining pressure, which was consistent with the research results of Chenhui et al., (2016), indicating that the application of confining pressure under short-delay initiation could effectively improve the fragmentation.

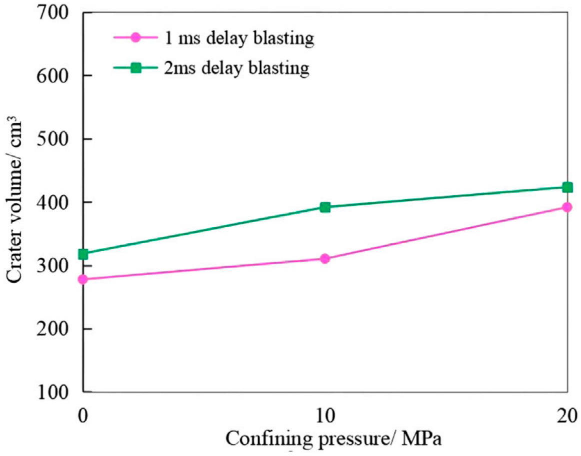

FIGURE 13 | Crater volume of delayed initiation blasting under confining pressure.

DISCUSSION

1) Boundary of the experimental model

The boundary of the test block was covered with a 20-mm-thick rubber plate to absorb the stress wave at the boundary. Because of its energy absorption and buffering characteristics, it is often used to reduce the impact of dynamic loads in tests. The 20-mm-thick steel plate is set outside the rubber plate to induce uniform boundary stress and reduce the influence of blasting effect on the boundary (Henrych and Major, 1979).

2) Formation mechanism and time of new free surface in delayed blasting

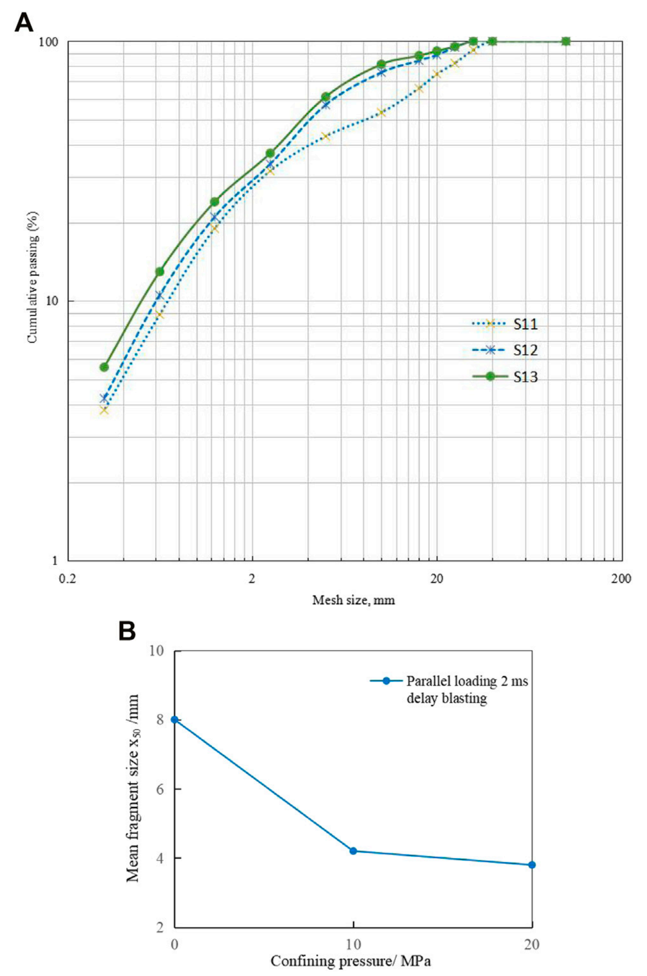

FIGURE 14 | Comparison of blasting fragmentation distribution under 2 ms delay. **(A)** Blasting fragmentation 274 distribution. **(B)** Average block size.

Figure 15A shows that when two electronic detonators were detonated at the same time, the stress wave loading time was much shorter than the gas pressure. At the same time, the explosive gas did not leak out from the front crater. Therefore, the explosive gases caused by adjacent blasting were gathered through cracks, thus pushing the fractured rocks to form a common crater. If the delay is longer than the new free surface formation time, as shown in **Figure 15B**, the post-detonated blast hole would have two free surfaces, the free surface and the free surface generated by the previous blast hole. The rock fracture process of double-hole blasting with delayed initiation would be completely separated, making it unable to form the same crater (Qiu et al., 2018).

However, there is still no consensus on the determination of the formation time of the new free surface. The formation time of a new free surface includes three different stages: the first stage is the time required for the explosive stress wave to propagate to the free surface and return to the explosive, and the second stage is the time required for the crack to propagate to the free surface (Henrych and Major, 1979). The third stage is the time required for the crack to continue to expand and form a new free surface with a certain crack width. Therefore, the formation time of the new free surface is as follows:

$$t = \frac{W}{C_p} + \frac{L_f}{C_f} + \frac{S}{V_S}, \tag{1}$$

where W is the minimum burden, C_P is the p-wave velocity of the sample (m/s), L_f is the crack length (m), $L_f \approx 1.4W$, c_f is the average speed of crack expansion, S is the crack width, V_S is the initial velocity of crushed rock (normally 10 mm), and V_S is the fly-out speed of broken rock (normally 15–25 m/s).

In the experiment of double-hole delay blasting, the formation time of new free surface after the first hole blasting is calculated according to **Equation 1** as 558–858 us. Similar results were reported by Chi et al. (2019). The crater of double-hole delay blasting is larger than that of delay blasting, which is consistent with the experimental crater.

3) Fragment Loss

Previous studies showed that smaller fragments consume a lot of energy, which was very important for evaluating the crushing

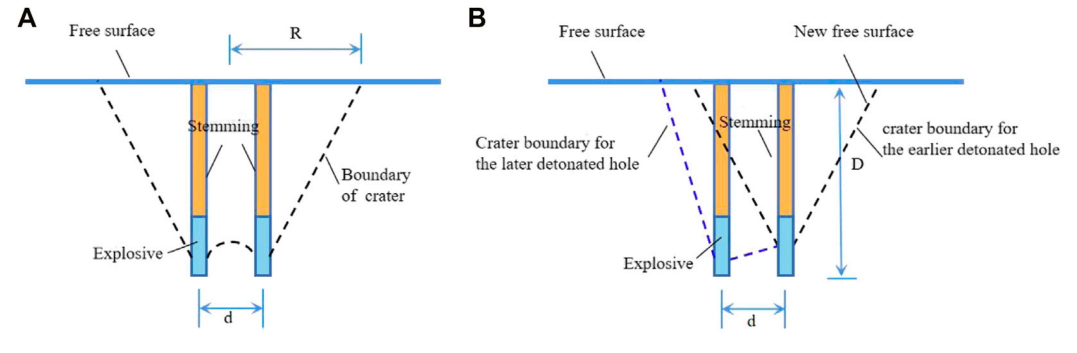

FIGURE 15 | (A) Simultaneous initiation of multiple blast holes. **(B)** Multiple blast holes with delayed initiation (Qiu et al., 2018).

results. Each test block was wrapped in a cuboid of 50 × 50 × 40 cm^3 by a steel grid embedded with a thick sponge to reduce the fragment loss of blasting test blocks. Under the same charge and boundary test conditions, a collision may occur between the blasting fragments and the collecting steel grid, which may exist in each explosion. Hence, the impact on the crushing results of each explosion was almost the same. Before the experiment, the hole was blocked with stemming, and the detonator fragments were removed when collecting fragments. The stemming and the removed detonator fragments had the same influence on the explosive crushing results.

CONCLUSION

1) Static stress significantly affected the shape of the crater. The experimental results of double-hole blasting with two kinds of lateral stress showed that the shape of the crater was extended along the loading direction, and the loading direction became the dominant direction of crack propagation. The blasting experiments with different initiation delay times showed that the loading direction became the dominant direction of radial crack propagation and was not affected by the initiation delay.
2) With the increase of unidirectional confining pressure, the volume of the double-hole blasting crater in different loading directions generally increases. The blasting surface loaded with static stress in the vertical borehole direction is rounder than that loaded with static stress in the horizontal direction. In addition, the volume of the blasting crater loaded with static stress in the vertical borehole direction is larger than that loaded with static stress in the horizontal direction.
3) Static stress and delay time significantly affected the crushing effect of the blasting test block. The experimental results showed that the greater the loading stress is, the better the crushing effect is. The longer the delay time is, the better the crushing effect is. In deep geological engineering, a blasting scheme matching with the *in situ* stress could be designed to achieve a better rock blasting and crushing effect.

DATA AVAILABILITY STATEMENT

The original contributions presented in the study are included in the article/Supplementary Material, further inquiries can be directed to the corresponding author.

AUTHOR CONTRIBUTIONS

HC and XQ: investigation, software, and writing—original draft; XS: project administration and supervision; HC and JZ: writing—review and editing; XH and DL: investigation. All authors have read and agreed to the published version of the manuscript.

FUNDING

This research was funded by the National Natural Science Foundation Project of China, under grant numbers 51874350 and 52004329 and Accurate Delay Rock Breaking Mechanism and Key Technology Innovation Team, under grant number 2020D14043.

REFERENCES

Bangbiao Wu, B., Chen, R., and Xia, K. (2015). Dynamic Tensile Failure of Rocks under Static Pre-tension. *Int. J. Rock Mech. Mining Sci.* 80, 12–18. doi:10.1016/j.ijrmms.2015.09.003

Chenhui, W., Wancheng, Z., Yu, B., and Leilei, N. (2016). Numerical Simulation on Cutting Seam Cartridge Blasting under Different *In-Situ* Stress Conditions. *Explos. Shock Waves* 02. doi:10.11883/1001-1455(2016)02-0161-09

Chi, L. Y., Zhang, Z.-X., Aalberg, A., and Li, C. C. (2019). Experimental Investigation of Blast-Induced Fractures in Rock Cylinders. *Rock Mech. Rock Eng.* 52, 2569–2584. doi:10.1007/s00603-019-01749-0

Fan, X., Wang, M., and Shi, C. (2009). Study on Effects of Initial Stress on Stress Wave Propagation and Block Movement Law. *Chin. J. Rock Mech. Eng.* 28, 442–443.

Han, H., Fukuda, D., Liu, H., Salmi, E. F., Sellers, E., Liu, T., et al. (2020). Combined Finite-Discrete Element Modelling of Rock Fracture and Fragmentation Induced by Contour Blasting during Tunnelling with High Horizontal *In-Situ* Stress. *Int. J. Rock Mech. Mining Sci.* 127, 104214. doi:10.1016/j.ijrmms.2020.104214

He, C., and Yang, J. (2019). Experimental and Numerical Investigations of Dynamic Failure Process in Rock under Blast Loading. *Tunnelling Underground Space Tech.* 83, 552–564. doi:10.1016/j.tust.2018.08.047

He, C., Yang, J., and Yu, Q. (2018). Laboratory Study on the Dynamic Response of Rock under Blast Loading with Active Confining Pressure. *Int. J. Rock Mech. Mining Sci.* 102, 101–108. doi:10.1016/j.ijrmms.2018.01.011

Henrych, J., and Major, R. (1979). *The Dynamics of Explosion and its Use*. Amsterdam: Elsevier.

Huo, X., Shi, X., Qiu, X., Chen, H., Zhou, J., Zhang, S., et al. (2021). Study on Rock Damage Mechanism for Lateral Blasting under High *In Situ* Stresses. *Appl. Sci.* 11, 4992. doi:10.3390/app11114992

Jayasinghe, L. B., Shang, J., Zhao, Z., and Goh, A. T. C. (2019). Numerical Investigation into the Blasting-Induced Damage Characteristics of Rocks Considering the Role of *In-Situ* Stresses and Discontinuity Persistence. *Comput. Geotechnics* 116, 103207. doi:10.1016/j.compgeo.2019.103207

Kutter, H. K., and Fairhurst, C. (1971). "On the Fracture Process in Blasting," in *International Journal of Rock Mechanics and Mining Sciences & Geomechanics Abstracts* (Elsevier), 8, 181–202. doi:10.1016/0148-9062(71)90018-0*Int. J. Rock Mech. Mining Sci. Geomechanics Abstr.*

Lei, Z., and Jiang, X. (2019). Numerical Analysis of Impact of Shot Hole Spacing on Crack Growth in Rock. *Chin. J. High Press. Phys.* 33, 044103. doi:10.11858/gywlxb.20180683

Li, E., Yang, F., Ren, M., Zhang, X., Zhou, J., and Khandelwal, M. (2021). Prediction of Blasting Mean Fragment Size Using Support Vector Regression Combined with Five Optimization Algorithms. *J. Rock Mech. Geotechnical Eng.* 13, 1380–1397. doi:10.1016/j.jrmge.2021.07.013

Peng, J., Zhang, F., Du, C., and Yang, X. (2020). Effects of Confining Pressure on Crater Blasting in Rock-like Materials under Electric Explosion Load. *Int. J. Impact Eng.* 139, 103534. doi:10.1016/j.ijimpeng.2020.103534

Qiu, J., Li, X., Li, D., Zhao, Y., Hu, C., and Liang, L. (2021). Physical Model Test on the Deformation Behavior of an Underground Tunnel under Blasting Disturbance. *Rock Mech. Rock Eng.* 54, 91–108. doi:10.1007/s00603-020-02249-2

Qiu, X., Shi, X., Gou, Y., Zhou, J., Chen, H., and Huo, X. (2018). Short-delay Blasting with Single Free Surface: Results of Experimental Tests. *Tunnelling Underground Space Tech.* 74, 119–130. doi:10.1016/j.tust.2018.01.014

Wang, S.-m., Liu, Y.-s., Du, K., and Zhou, J. (2019). Dynamic Failure Properties of sandstone under Radial Gradient Stress and Cyclical Impact Loading. *Front. Earth Sci.* 7, 251. doi:10.3389/feart.2019.00251

Xiao, S.-Y., Su, L.-J., Jiang, Y.-J., and Liu, Z.-X. (2019). Numerical Analysis of Hard Rock Blasting Unloading Effects in High *In Situ* Stress fields. *Bull. Eng. Geol. Environ.* 78, 867–875. doi:10.1007/s10064-017-1067-7

Xiao, Z., Zhang, Z., and Li, D. (1996). *The Influence of Initial Stress Field on Blasting*, 21. Xuzhou, China: Mei Tan Hsueh Pao J. China Coal Soc.

Yan, P., Zhou, W., Lu, W., Chen, M., and Zhou, C. (2016). Simulation of Bench Blasting Considering Fragmentation Size Distribution. *Int. J. Impact Eng.* 90, 132–145. doi:10.1016/j.ijimpeng.2015.11.015

Yang, L.-Y., and Ding, C.-X. (2018). Fracture Mechanism Due to Blast-Imposed Loading under High Static Stress Conditions. *Int. J. Rock Mech. Mining Sci.* 107, 150–158. doi:10.1016/j.ijrmms.2018.04.039

Yang, L., Yang, A., Chen, S., Fang, S., Huang, C., and Xie, H. (2021). Model Experimental Study on the Effects of *In Situ* Stresses on Pre-splitting Blasting Damage and Strain Development. *Int. J. Rock Mech. Mining Sci.* 138, 104587. doi:10.1016/j.ijrmms.2020.104587

Yang, R., Ding, C., Li, Y., Yang, L., and Zhao, Y. (2019). Crack Propagation Behavior in Slit Charge Blasting under High Static Stress Conditions. *Int. J. Rock Mech. Mining Sci.* 119, 117–123. doi:10.1016/j.ijrmms.2019.05.002

Yilmaz, O., and Unlu, T. (2013). Three Dimensional Numerical Rock Damage Analysis under Blasting Load. *Tunnelling Underground Space Tech.* 38, 266–278. doi:10.1016/j.tust.2013.07.007

Zhang, F., Peng, J., Qiu, Z., Chen, Q., Li, Y., and Liu, J. (2017). Rock-like Brittle Material Fragmentation under Coupled Static Stress and Spherical Charge Explosion. *Eng. Geology.* 220, 266–273. doi:10.1016/j.enggeo.2017.02.016

Zhang, Y., Ma, J., Sun, D., Zhang, L., and Chen, Y. (2020). AE Characteristics of Rockburst Tendency for Granite Influenced by Water under Uniaxial Loading. *Front. Earth Sci.* 8, 55. doi:10.3389/feart.2020.00055

Zhang, Z.-X., Qiao, Y., Chi, L. Y., and Hou, D.-F. (2021). Experimental Study of Rock Fragmentation under Different Stemming Conditions in Model Blasting. *Int. J. Rock Mech. Mining Sci.* 143, 104797. doi:10.1016/j.ijrmms.2021.104797

Zhao, G., Wang, D., Gao, B., and Wang, S. (2017). Modifying Rock Burst Criteria Based on Observations in a Division Tunnel. *Eng. Geology.* 216, 153–160. doi:10.1016/j.enggeo.2016.11.014

Zhu, W. C., Gai, D., Wei, C. H., and Li, S. G. (2016). High-pressure Air Blasting Experiments on concrete and Implications for Enhanced Coal Gas Drainage. *J. Nat. Gas Sci. Eng.* 36, 1253–1263. doi:10.1016/j.jngse.2016.03.047

Conflict of Interest: Author DL was employed by the company China Nonferrous Metal Mining Group Co., Ltd.

The remaining authors declare that the research was conducted in the absence of any commercial or financial relationships that could be construed as a potential conflict of interest.

frontiers in Earth Science

ORIGINAL RESEARCH
published: 10 February 2022
doi: 10.3389/feart.2021.794783

Structural Evolution and Motion Characteristics of a Hard Roof During Thickening Coal Seam Mining

Xiangyang Zhang, Xiangyang Zhao and Lei Luo*

School of Mining Engineering, Anhui University of Science and Technology, Huainan, China

This study combined theoretical analysis, physical simulation, and numerical simulation to discuss the influences of the structural evolution and motion characteristics of a hard roof during thickening coal seam mining on working face pressure. Results showed that during the mining of the thickening coal seam with a hard roof, the settlement curve of low-level strata was a stepwise wave slope, and the settlement curve of high-level strata shifted from a “V-shaped” distribution pattern to a parabola under the full mining of the coal seam. When the mining thickness was relatively small, the mining space expanded with the increase in mining thickness due to the “masonry beam” structure formed by the low-level, sub-critical overlying strata. The low-level critical strata formed a “composite cantilever beam” structure with a hard immediate roof after advancing into the caving zone. After complete recovery, the overlying strata were in a steady-movement state, and the plastic failure zone of the overlying strata of the thickening coal seam presented obvious distribution characteristics of longitudinal and transverse partitions. This study provides theoretical reference for coal seam mining under similar geological conditions.

Keywords: hard roof, thickening coal seam, overlying strata structure, motion characteristics, physical simulation, numerical simulation

Edited by:
Kun Du,
Central South University, China

Reviewed by:
Jian Cui,
Tianjin University, China
Jinwang Zhang,
China University of Mining and Technology, China

****Correspondence:***
Xiangyang Zhao
673908201@qq.com

Specialty section:
This article was submitted to Geohazards and Georisks, a section of the journal Frontiers in Earth Science

Received: *14 October 2021*
Accepted: *31 December 2021*
Published: *10 February 2022*

Citation:
Zhang X, Zhao X and Luo L (2022) Structural Evolution and Motion Characteristics of a Hard Roof During Thickening Coal Seam Mining. Front. Earth Sci. 9:794783. doi: 10.3389/feart.2021.794783

INTRODUCTION

Decades-long production practices have shown that the caving height of overlying strata in a goaf increases, and the sphere of influence of the overlying strata on the working face pressure expands as the disposal mining thickness increases in fully mechanized caving mining of thick coal seams. Meanwhile, a main roof with a hinged balance structure at low-level positions of the fully mechanized mining face might change into an immediate roof. Studying the structural morphology and motion type of overlying strata in the stope is the basis of analyzing the behavior law of working face pressure.

In this regard, a lot of studies have been carried worldwide. Generally, deformation, fracture propagation, and energy release are highly associated with mining-induced stress evolution (Gao et al., 2021). After mining, the state of stress equilibrium is disturbed by an opening formed due to underground extraction of part of the coal seam (Wang et al., 2018a), resulting in the change of overburden structure above the coal seam. Zhang (Zhang and Wang, 1998) pointed out that there is a stable “masonry beam” above the stope and a “semi-arch” structure below the “masonry beam.” The combination of the two forms the basic form of overburden structure of a fully mechanized caving face. The cantilever beam is formed by the rupture of low-level critical strata in a fully mechanized caving face, whereas the masonry beam is formed in high-level critical strata (Huang et al., 2020; Kong et al., 2020; Li et al., 2018). The higher the mining height, the closer the subcritical stratum is to the coal seam, and the easier it is to move as a “cantilever beam” (He et al., 2020; Ju et al., 2011; Li et al., 2017; Liang et al., 2017; Wang et al., 2014; Xu and Ju, 2011; Yan et al., 2011; Yu and Yan, 2015; Yang et al., 2020; Zhang et al., 2021). Li (Li et al., 2014) constructed a strata rupture model of periodic roof weighting on a fully mechanized sub-level caving face with a large mining height and found that the support has to bear only the acting force of the inferior cantilever structure during normal recovery stages. With the decrease of bottom coal thickness, the stress concentration around roadways and coalfaces decreased rapidly and then tended to be stable (Li et al., 2018; Zhu et al., 2016). The failure scopes of the coal seam and top coal on the working face present a nonlinear proportional correlation with mining thickness (Wen et al., 2019; Xie and Wang, 2010). Yan (Yan, 2009) showed that the scope of "deformation pressure strata" expands with the increase in coal seam thickness during the exploitation of super high seams, thus increasing the external loads on the support. Due to the controlling effect of critical overlying strata, the development height of water conductive fissures presents stepwise sudden changes with mining thickness rather than continuous approximate linear variations (Feng et al., 2011; Miao et al., 2011; Wang et al., 2019). Wang (Wang et al., 2018b) established the critical conditions for the loss of stability of coal walls by constructing a vertical mechanical model to analyze the influencing mechanism of mining thickness. Through a physical simulation test, Fan (Fan and Shen, 2019) found that the superior immediate roof in the overlying strata is a "simply supported beam" when the mining thickness is 30 m, and the overburden pressure is shared by the caving gangues in the goaf, resulting in a weaker strata pressure behavior compared with that when the mining thickness is 17 m.

Scholars have focused on mining analysis by using several mining thickness values in the same mining area or the mean coal seam thickness, but they ignored the overlying strata structural difference and mine pressure characteristics caused by continuous variations in coal seam thickness under a specific condition. This disregard leads to a serious judgment error in certain cases. To address this issue, this study analyzed the settlement characteristics of overlying strata and the evolutionary laws of critical strata during the mining of a thickening coal seam with a hard roof by combining similarity and numerical simulations on the basis of critical strata theory of strata control. The research results can provide theoretical reference for coal seam mining under similar geological conditions.

PROJECT OVERVIEW

The 4,321 fully mechanized caving face in Sangshuping Coal Mine in Hancheng City was selected as the research object. The 3# coal seam is undergoing exploitation. On the working face, the 3# coal seam is 6.08–28.41 m away from the 2# coal seam above (14.47 m on the average). The working face has a simple coal seam structure with a rare dirt band. The immediate roof is generally occupied by siltstone and medium sandstone with hard lithology and an average thickness of 9.83 m. It is covered by 2# and 1# coal seams. The roof of 1# coal seam is composed of medium sandstone and fine sandstone and has an average thickness of 10.38 m. According to evaluations of the critical overlying strata on the working face (Xu and Qian, 2000; Qian et al., 2003), the 3# coal seam has two sub-critical overlying strata made of 8.0 m thick fine sandstone and 10.38 m thick medium sandstone. A comprehensive histogram of the strata is shown in **Figure 1**.

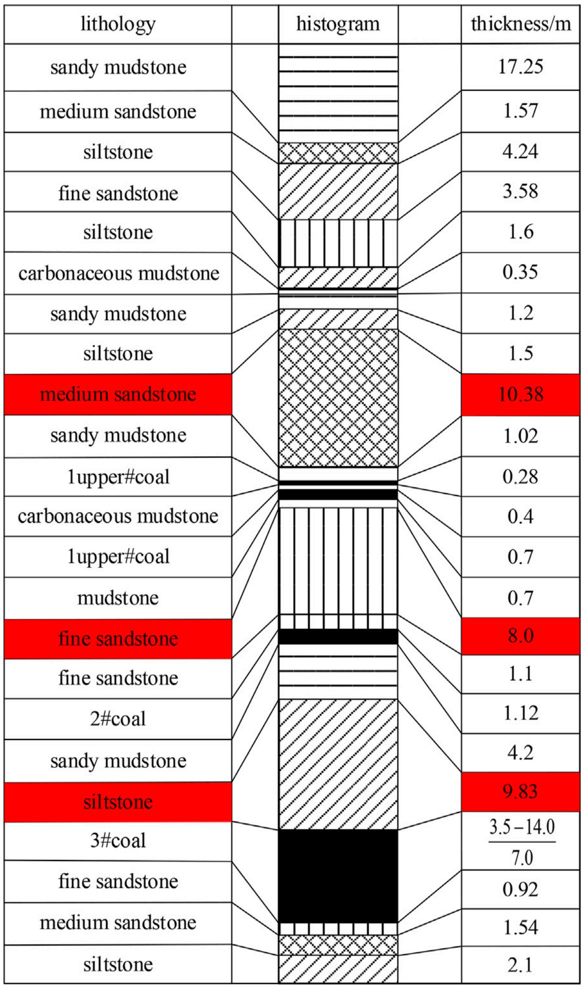

lithology	thickness/m
sandy mudstone	17.25
medium sandstone	1.57
siltstone	4.24
fine sandstone	3.58
siltstone	1.6
carbonaceous mudstone	0.35
sandy mudstone	1.2
siltstone	1.5
medium sandstone	10.38
sandy mudstone	1.02
1upper#coal	0.28
carbonaceous mudstone	0.4
1upper#coal	0.7
mudstone	0.7
fine sandstone	8.0
fine sandstone	1.1
2#coal	1.12
sandy mudstone	4.2
siltstone	9.83
3#coal	$\frac{3.5-14.0}{7.0}$
fine sandstone	0.92
medium sandstone	1.54
siltstone	2.1

FIGURE 1 | Comprehensive histogram of rock strata.

In Sangshuping Coal Mine, the 3# coal seam is soft and clamped between the upper and lower hard and thick sandstones, thus forming a composite structure of "hard–soft–hard strata." Functioning as two pieces of "washboards," the hard sandstone strata exert a strong squeezing effect on the coal seam under the action of tectonic stress. Slip surfaces are formed in the hard–soft interfaces due to differences in coal petrography, mechanical strength, and elastoplasticity, and they further develop to sliding surfaces. In the "hard–soft–hard strata" structure, the coal seam produces plastic flows that "creep" from the high-pressure zone to the low-pressure zone. Macroscopically, coal seam thickness and structure change to release stress and maintain stress balance.

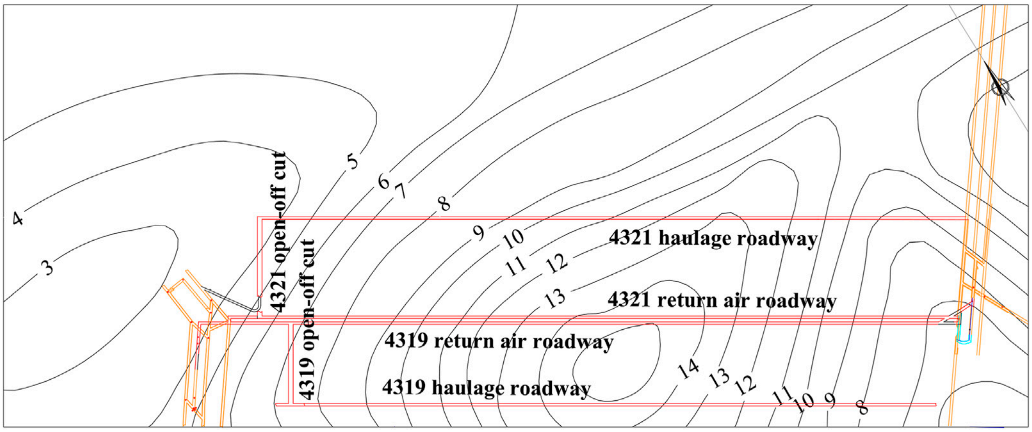

FIGURE 2 | Contour line of coal seam thickness on the 4,321 working face.

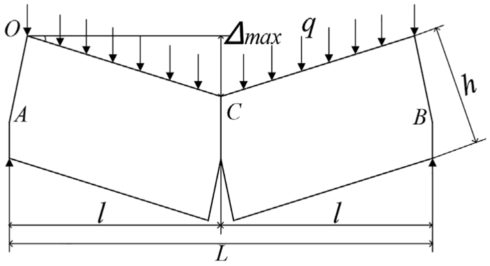

FIGURE 3 | Rotary deformation buckling model of critical blocks.

The 3# coal seam is 3.5–14 m thick, with an average of 7.0 m. After advancing from the open–off cut by 500 m, the coal seam thickness increases gradually from 3 m to 14 m. The contour line of the 3# coal seam's thickness on the working face is shown in **Figure 2**.

PHYSICAL SIMULATION OF THE MINING OF A THICKENING COAL SEAM WITH A HARD ROOF

Mining Thickness Conditions Formed by the "Cantilever Beam" Structure in the Critical Strata

During the mining of a thickening coal seam with a hard roof, the structural morphology and motion characteristics of the hard immediate roof and sub-critical strata change with coal seam thickness. When the sub-critical strata are at a low level, the available gyrating mass of blocks in the sub-critical strata is higher than the ultimate value, and the masonry beam structure loses stability, thus developing into a cantilever or simply supported beam. In this section, the effects of coal seam thickness on the structure of the sub-critical strata are analyzed by combining the judgment results of the critical strata.

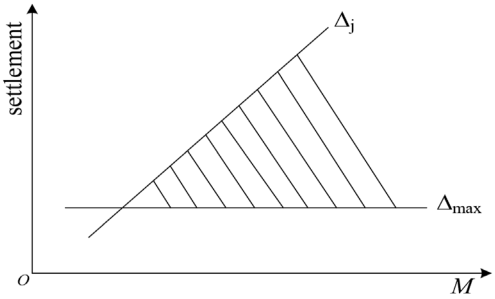

FIGURE 4 | Discrimination diagram of the structural morphology of the critical strata.

The rotary deformation buckling model of critical blocks is shown in **Figure 3**. Δ_{max} is the ultimate rotary mass that is necessary for rupture blocks in the critical strata to form a stable "masonry beam" structure by hinge joints. Δ_{max} varies in strata that have different thicknesses, strengths, and levels. It is an eigenvalue and attribute value of roof strata under a specific mining condition.

$$\Delta_{\max} = h - \sqrt{\frac{2ql^2}{\sigma_c}} \tag{1}$$

where h is the thickness of the masonry block, q is the uniformly distributed load of the rock beam, l is the length of the masonry block, and σ_c is the extrusion strength of the block at the corner.

The spatial displacement between the immediate roof after collapse and the critical strata is Δ_j.

$$\Delta_j = M + (1 - K_P)\sum h_i \tag{2}$$

where M is the mining thickness of the coal seam (m), K_P is the caving crack-expansion coefficient of the immediate roof, and $\sum h_i$ is the sum thickness of rock strata below the critical strata (m).

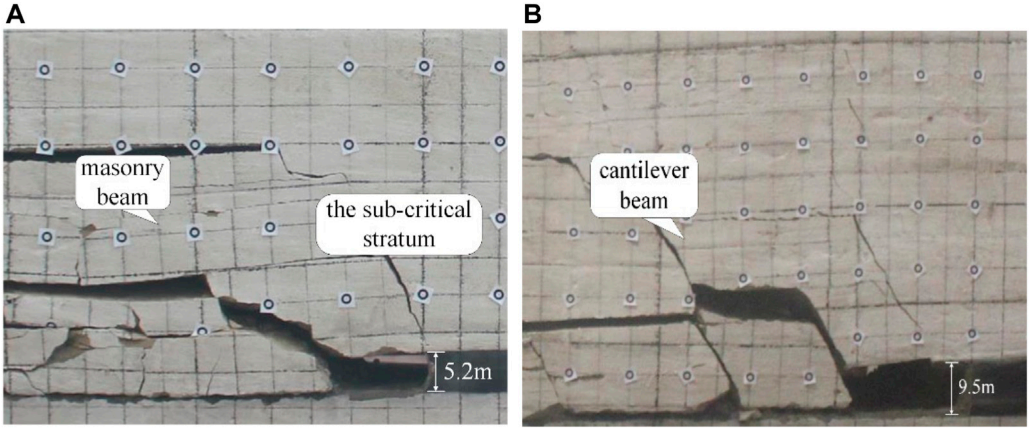

Mining thickness of 5.2 m

Mining thickness of 9.5 m

FIGURE 5 | Morphology test results of critical overlying strata during thickening coal seam mining under different mining thicknesses. **(A)** Mining thickness of 5.2 m; **(B)** Mining thickness of 9.5 m.

The mining thickness condition for forming the "cantilever beam" structure of the low-level critical strata is

$$M + (1 - K_{\mathrm{P}}) \sum h_{\mathrm{i}} > h - \sqrt{\frac{2ql^2}{\sigma_{\mathrm{c}}}} \tag{3}$$

Δ_{j} is a value that changes with the mining thickness of the coal seam (M) and the thickness of the immediate roof ($\sum h_{\mathrm{i}}$). It increases with the increase in M, thereby increasing the possibility of $\Delta_{\mathrm{j}}>\Delta_{\max}$ significantly. As a result, the longitudinal and transverse scopes of movement of the surrounding rocks on the working face are increased.

Figure 4 indicates that with the increase in M, $\Delta_{\mathrm{j}}>\Delta_{\max}$ is proven after entering the shadow when the "masonry beam" structure of the sub-critical strata loses its stability and becomes part of the immediate roof. It is presented as a "cantilever beam" structure.

A physical simulation test was designed to compare the structural differences of the critical overlying strata during thickening coal seam mining under the same overlying conditions and to verify the above-mentioned discriminant formula. The results are shown in **Figure 5**. When the mining thickness was 5.2 m, sub-critical stratum 1 formed a "masonry beam" structure. When the mining thickness was 9.5 m, it formed a "cantilever beam" structure, and the "masonry beam" structure shifted toward the high-level strata.

Displacement and Settlement Laws of Overlying Strata in the Stope

A laboratory 2D physical simulation test was performed to discuss the settlement deformation laws of the overlying strata and the evolutionary features of the structure during thickening coal seam mining. The process wherein the thickening coal seam mining advanced from 3 m to 10 m was simulated. According to the actual situation of the project site, excavate 5 m every 4 h, maintain the simulated mining height of 2.3 m, and the caving height increases with the increase of coal thickness. In the physical simulation test, the geometric similarity ratio, volume–weight similarity ratio, time similarity ratio, and stress similarity ratio were 1:100, 1:1.6, 1:10, and 1:160, respectively. The Poisson's ratio was equal to that of the prototype. The thickness values of different strata were designed as those in **Figure 1**. In the test, the aggregate was fine sand, and the cement used was made of lime and gypsum. The ratio is shown in **Table 1**.

The initial state of physical model is shown in **Figure 6A** and the test model design is shown in **Figure 6B**. Vertical displacement monitoring lines I, II, III, IV, and V were designed in the test, and they corresponded to hard immediate roof, sub-critical stratum 1 and its subsequent stratum, and sub-critical stratum 2 and its subsequent stratum, respectively.

The siltstone immediate roof corresponding to Line I developed the primary rupture when the working face advanced by 90 m. At this moment, the maximum settlement of the rock stratum was 5.037 m. As the working face advanced, the rock stratum entered the periodic rupture stage, and the primary periodical rupture distance was 10 m. The relevant settlement curve was a wave slope as the coal seam mining advanced forward. According to the analysis, the settlement curve was determined by the thick and hard characteristics of the immediate roof. Moreover, the settlement curve declined in a stepwise manner as the coal seam mining advanced gradually.

With the advancing of the working face, the settlement volumes of Lines II and III close to the working face became significantly higher than those at other positions in the goaf. Influenced by the hard roof, the settlement curve close to the working face had a large slope. With the increase in mining thickness of the coal seam, the settlement curve after the periodic rupture of rock strata presented a stepwise wave slope.

Lines IV and V presented an approximately symmetric "V-shaped" distribution pattern after the primary rupture of rock strata. The "V-shaped" distribution pattern after periodic

TABLE 1 | Proportion and dosage of similar materials in the test model.

Seque-nce	Lithology	Thickness/m	Total weight/kg	Ratio	Weight/kg		
				Sand: lime: gypsum	Sand	Lime	Gypsum
1	siltstone	20	270	7:0.8:0.2	236.25	27	6.75
2	medium sandstone	1.54	20.79	7:0.7:0.3	18.191	1.819	0.780
3	fine sandstone	0.92	12.42	7:0.6:0.4	10.868	0.932	0.621
4	3#coal and siltstone	17.6–24.6	332.1	7:0.8:0.2	290.588	33.21	8.303
5	sandy mudstone	2.5–9.5	37.8	8:0.7:0.3	33.6	2.94	1.26
6	2#coal	1.12	15.12	9:0.8:0.2	13.608	1.210	0.302
7	fine sandstone	9.1	122.85	7:0.6:0.4	107.494	9.214	6.143
8	1upper#coal	2.08	28.08	9:0.8:0.2	25.272	2.246	0.562
9	sandy mudstone	1.02	13.77	8:0.7:0.3	12.24	1.071	0.459
10	medium sandstone	10.38	140.13	7:0.7:0.3	122.614	12.261	5.255
11	siltstone	1.5	20.25	7:0.8:0.2	17.719	2.025	0.506
12	sandy mudstone	1.55	20.925	8:0.7:0.3	18.6	1.628	0.698
13	siltstone	1.6	21.6	7:0.8:0.2	18.9	2.16	0.54
14	fine sandstone	3.58	48.33	7:0.6:0.4	42.289	3.625	2.417
15	siltstone	4.24	57.24	7:0.8:0.2	50.085	5.724	1.431
16	medium sandstone	1.57	21.195	7:0.7:0.3	18.546	1.855	0.795
17	sandy mudstone	40	540	8:0.7:0.3	480	42	18

The initial state of physical model

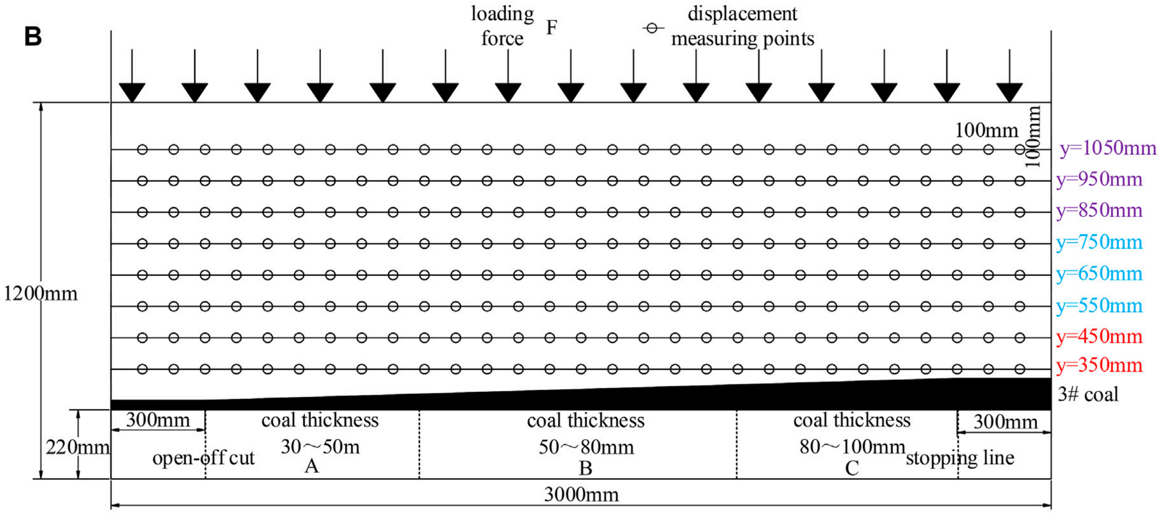

Test model design

FIGURE 6 | Model of physical simulation test. **(A)** The initial state of physical model; **(B)** Test model design.

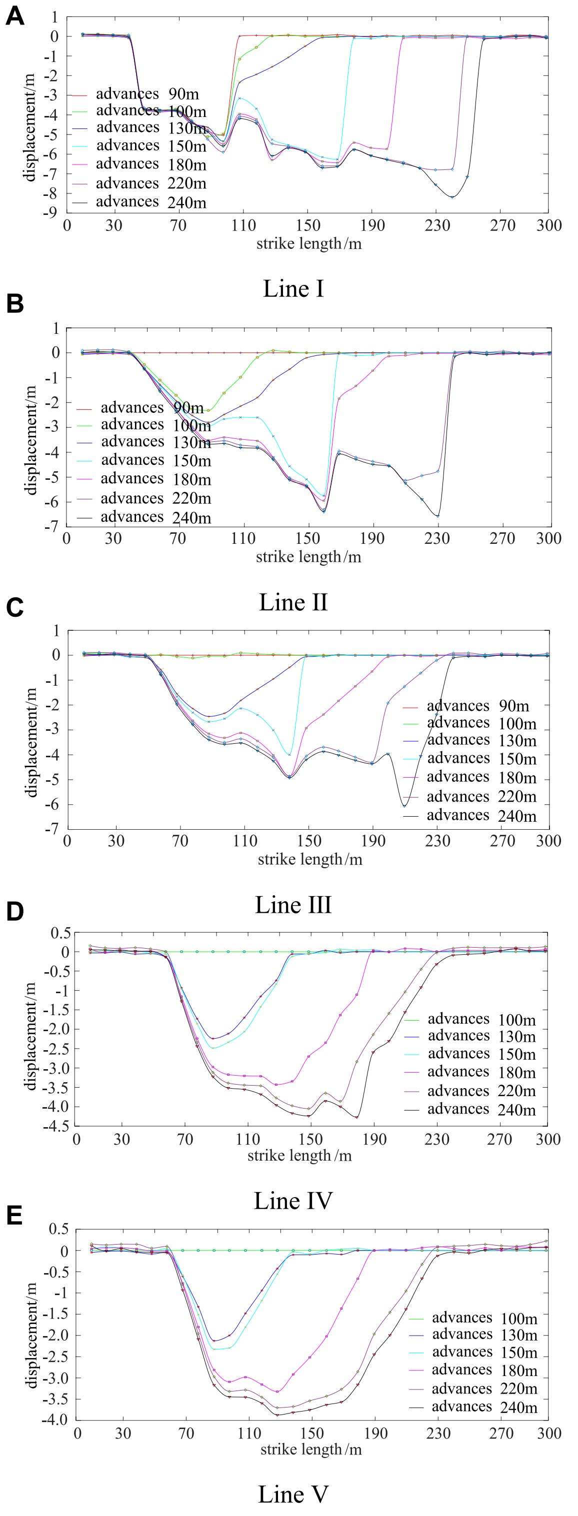

FIGURE 7 | Variations in the settlement curves of overlying strata in the recovery process. **(A)** Line I; **(B)** Line II; **(C)** Line III; **(D)** Line IV; **(E)** Line V.

weighting was gradually changed into a parabola pattern. As the working face advanced continuously, the parabola pattern of the settlement curve expanded continuously. The displacement at the maximum settlement point increased continuously, but the slope at the coal wall declined gradually.

The maximum settlement volume of Line I was 1.24 times that of Line II, 1.35 times that of Line III, 1.91 times that of Line IV, and 2.1 times that of Line V. The maximum settlement volumes of the five monitoring lines indicate that the sub-critical stratum 1 of Line II and the sub-critical stratum 2 of Line IV could control the settlement deformation of overlying strata locally.

The maximum settlement volumes of the five lines were at 240, 230, 210, 179, and 128 m of the strike positions of the coal seam. These values indicate that the maximum settlement volumes approached the working face from the upper strata to the bottom overlying strata. This result differs significantly from the simulation results on uniform-thickness coal seam mining, that is, the maximum settlement volumes of overlying strata are all located in the center of the goaf.

Structural Evolution of Critical Overlying Strata in the Stope

In accordance with the failure deformation laws of overlying strata in the physical simulation test, a structural evolution model of critical overlying strata during the mining of the thickening coal seam with a hard roof was constructed (**Figure 7**, **Figure 8**). In the early mining stage, a cantilever structure was formed due to the collapse of the hard and thick immediate roof. Sub-critical stratum 1 reached the maximum suspension step pitch and ruptured to form a three-hinged arc “masonry beam” balance structure (**Figure 8A**). As the working face advanced, the strata structure of the cantilever beam below the masonry beam developed periodic sliding buckling at the coal wall. With the subsequent increase in coal seam thickness, the bed-separated fissures between the cantilever beam structure and the masonry beam structure expanded further. The available rotary deformation volume of the masonry beam blocks increased, placing the masonry beam in the critical buckling state (**Figure 8B**). With the increase in mining thickness, the available rotary volume of the masonry beam blocks formed by sub-critical stratum 1 exceeded the ultimate value, resulting in rotary deformation buckling of the low-level masonry beam structure. The masonry beam structure formed a composite cantilever beam with the immediate roof beneath and the upper supporting stratum (**Figure 8C**). With the continuous advancement of the working face, the composite cantilever beam structure developed periodic ruptures and slid at the coal wall. Meanwhile, the masonry beam structure was formed at a high level, and the “small structures” at the rear positions of the coal wall were changed. New forms of composite strata structure and motion state were developed (**Figure 8D**).

NUMERICAL SIMULATION

Construction of a Numerical Simulation Model

The coal seams, roof, and floor in the model were designed based on the deposition characteristics of coal seams on the 4,321 working face and mining technological conditions. The 3D numerical simulation model is shown in **Figure 9**. In this model, the lengths in the x and y directions were 900 and 570

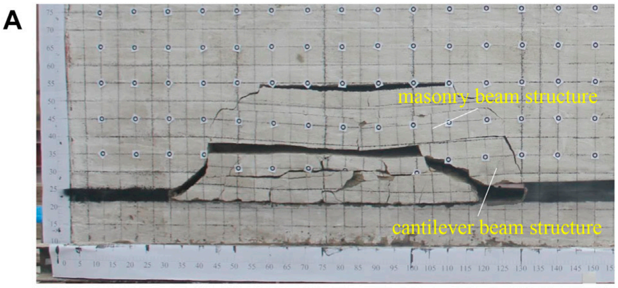

Sub-critical stratum 1 presents a “masonry beam” structure

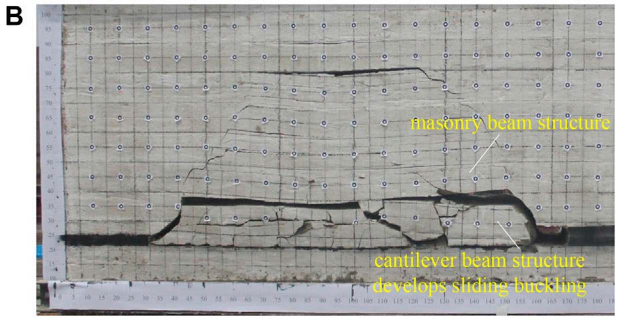

“Cantilever beam” structure of the hard immediate roof develops sliding buckling

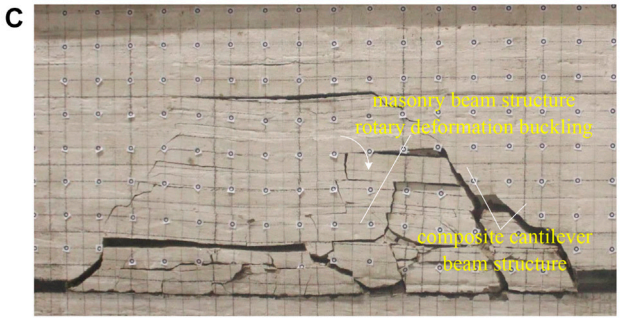

“Masonry beam” structure of sub-critical stratum 1 shows rotary deformation buckling

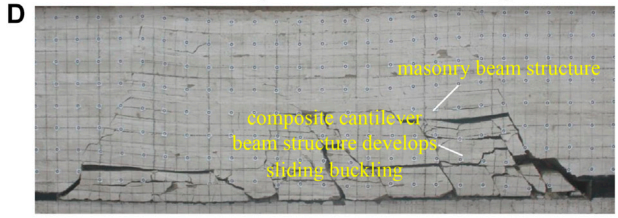

“Composite cantilever beam” structure develops sliding buckling

FIGURE 8 | Structural evolution model of the critical strata. **(A)** Sub-critical stratum 1 presents a “masonry beam”; **(B)** “Cantilever beam” structure of the hard immediate roof develops sliding buckling; **(C)** “Masonry beam” structure of sub-critical stratum 1 shows rotary deformation buckling; **(D)** “Composite cantilever beam” structure develops sliding buckling.

m, respectively, and the height in the *z* direction was 200 m. Normal constraints were applied at the sides and bottom to restrict horizontal and vertical movements. The stress boundary was used at the top. However, equivalent compensation loads of 4.7 MPa on the strata were not simulated. The corresponding physical and mechanical parameters for the numerical simulation are shown in **Table 2**.

The advancing length of the thickening coal seam was 300 m, and the width of the working face was 170 m. The 200 m boundary pillars were retained at two ends of the advancing direction (*x* direction) and surface length direction (*y* direction) to analyze evolution laws of the plastic zone of the surrounding rocks caused by the mining of thickening coal seams with a hard roof and to eliminate the boundary effects. The coal seam was excavated at 200 m away from the boundaries of the model, and it entered into the thickening coal seam zone ($x = 400–700$ m) after advancing by 200 m ($x = 200–400$ m).

Analysis of Numerical Simulation Results

The internal stress in overlying strata is redistributed after the mining of thickening coal seams. Rock strata rupture when the stress over the rock strata is greater than the rock strength, which further influences the transmission, release, and redistribution of stresses and lithological changes. The numerical simulation results during thickening coal seam mining are shown in **Figure 10**. Influenced by the supports of the coal pillars, areas of strong tensile stress concentration occurred in the open–off cut in the goaf and the upper inclined rock strata at the coal walls. The plastic failure zone developed the most, and a plastic failure distribution pattern of “high at two ends and low in the middle” was formed preliminarily. Influenced by the increasing mining thickness of the thickening coal seam, the tensile failure zone of the roof expanded continuously toward the high places.

At the end of recovery, the plastic failure zone of the overlying strata of the thickening coal seam had obvious characteristics of longitudinal and transverse partitions after achieving the steady-movement state. Longitudinally, the low-level strata area of the thickening coal seam developed tensile failure because of the two-way tensile stresses, showed the development of fractures and separation layer, and collapsed. On this basis, this area was determined to be the caving zone. The stresses over the roof strata at middle-level and high-level positions exceeded the yield or shear strength. Shear plastic failure played the dominant role. Hence, the development height of the strata state in this area was defined as the upper limit of the fissure zone. The stress state in these strata areas was still in the elastic deformation stage, and these areas were defined as the bending settlement belt. Transversely, the roof tensile and shear plastic failure zone in the thick coal seams was significantly larger than that in the thin coal seams. Shear failure was the major mode in the coal mass in front of the boundary pillars and above the rock strata. The plastic zones at the two sides of the stope were higher than those above the stope. The plastic zone close to the open–off cut was relatively higher than that at the coal walls of the working face.

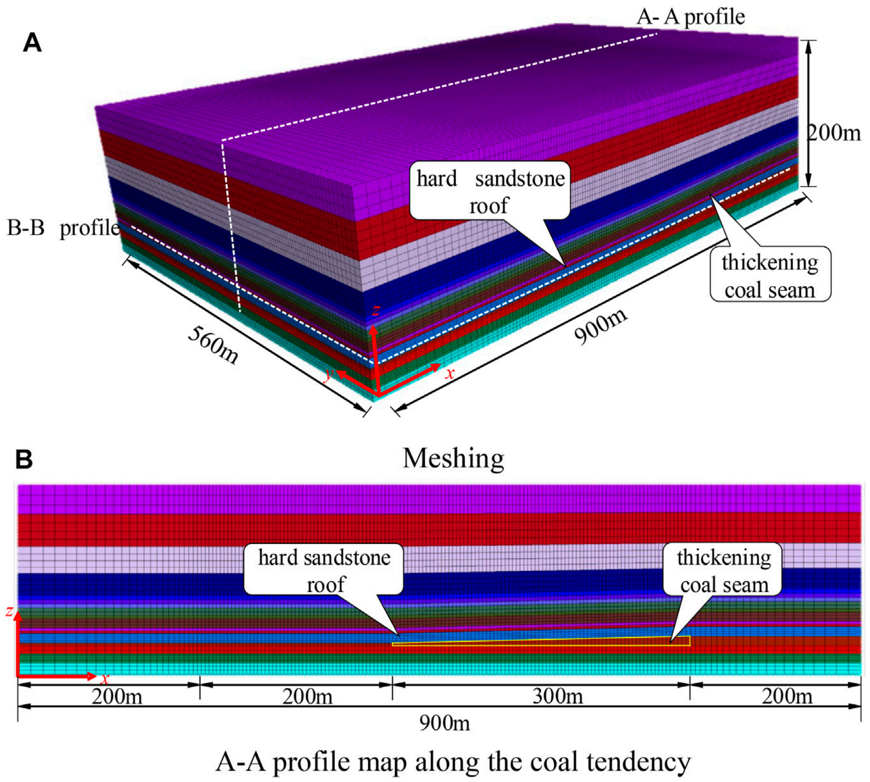

FIGURE 9 | Numerical calculation mesh model. **(A)** Meshing; **(B)** A-A profile map along the coal tendency.

TABLE 2 | Physical and mechanical parameters.

Lithology	Density/kg·m^{-3}	Elastic modulus/Gpa	Poisson's ratio	Tensile strength/Mpa	Cohesion/Mpa	Internal friction angle/°
siltstone	2,620	26.7	0.2	3.3	6.34	37.33
medium sandstone	2,690	35.5	0.18	5.5	7.47	38.48
fine sandstone	2,640	35.9	0.19	8.5	7.68	38.7
3#coal	1,400	5.31	0.33	1.32	1.25	32
sandy mudstone	2,650	19.47	0.22	2.5	5.75	36.43
2#coal	1,400	5.31	0.33	1.32	1.25	32
1upper#coal	1,400	5.31	0.33	1.32	1.25	32

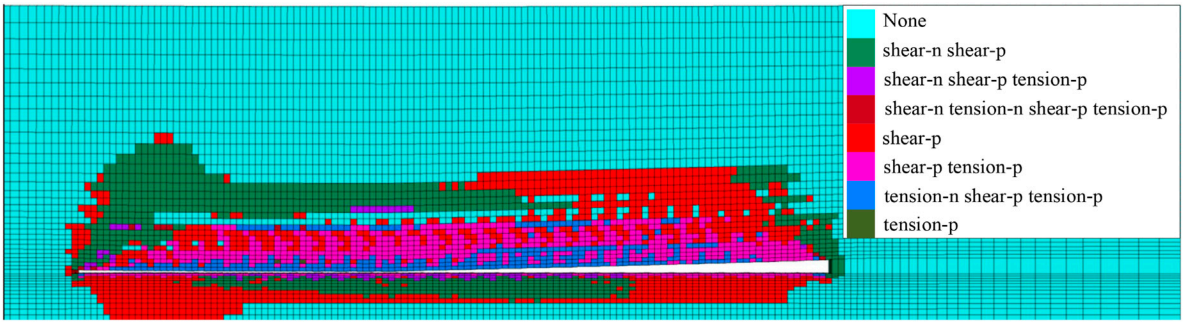

FIGURE 10 | Evolutionary laws of plastic zones during thickening coal seam mining.

A

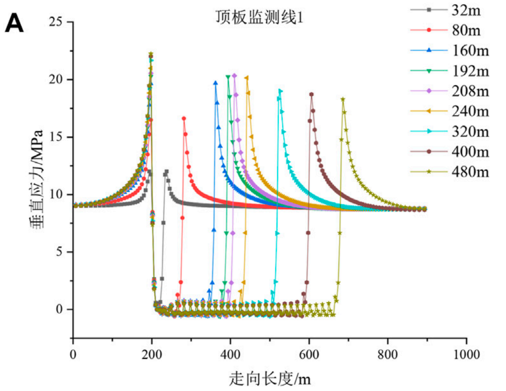

Roof monitoring line 1
(5m above the coal seam)

B

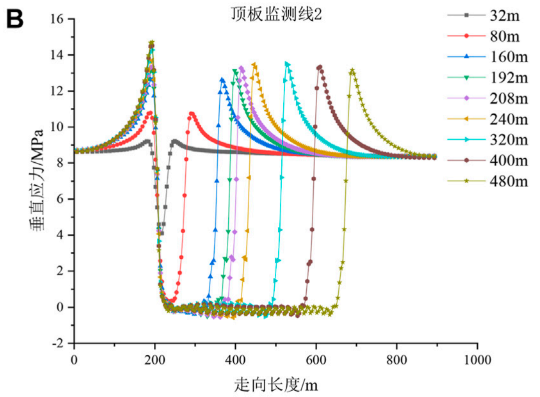

Roof monitoring line 2
(19m above the coal seam)

C

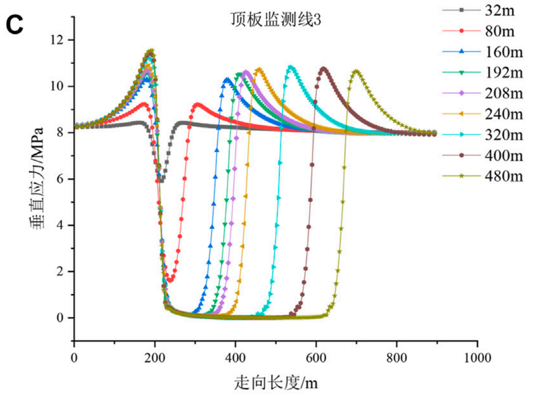

Roof monitoring line 3
(33m above the coal seam)

FIGURE 11 | Variation of vertical stress curve during working face advancement. **(A)** Roof monitoring line 1 (5m above the coal seam); **(B)** Roof monitoring line 2 (19 m above the coal seam); **(C)** Roof monitoring line 3 (33 m above the coal seam).

Figure 11 is the vertical stress variation curve of the roof in different layers with coal seam excavation, in which roof 1, roof 2, and roof 3 are 5, 19, and 33 m away from the coal seam respectively, and the layers correspond to thick and hard direct roof, sub key layer 1, and sub key layer 2 respectively.

In the area with no change in coal thickness (within the excavation range of 0–200 m), during the simulated coal seam excavation, the peak value of advance bearing pressure of roof 1 is 20.26 MPa and the stress concentration factor is 2.31. The peak value of advance bearing pressure of roof 2 is 13.14 MPa and the stress concentration factor is 1.57. The peak value of advance bearing pressure of roof 3 is 10.53 MPa and the stress concentration factor is 1.31. In the 3–10 m unequal thickness coal seam area (within the excavation range of 200–500 m), during the simulated coal seam excavation, the peak advance bearing pressure of roof 1 is 20.33 MPa and the stress concentration factor is 2.32. The peak value of advance bearing pressure of roof 2 is 13.52 MPa and the stress concentration factor is 1.61. The peak value of advance bearing pressure of roof 3 is 10.82 MPa and the stress concentration factor is 1.35. It shows that different distances from the coal seam have a significant impact on the stress distribution of the roof. The closer to the coal seam, the more significant the stress concentration effect caused by the excavation of the coal seam.

In the mining area of unequal thickness coal seam, the thickness of coal seam increases continuously. Under the action of "cushion" of top coal, the stress distribution in the front arch foot and arch of stress arch evolves, the peak value of advance bearing pressure gradually decreases, and the peak position gradually goes deep into the coal body.

CONCLUSION

Through the analysis of the roof structure of a hard roof during thickening coal seam mining, the physical simulation test and numerical simulation calculation are carried out. The structural evolution and motion characteristics of roof structure are studied, and the following conclusions are drawn:

1) The mining thickness conditions for structural changes in low-level critical strata during the mining of thickening coal seams with a hard roof were deduced and verified through a simulation test.
2) The settlement curve of low-level strata presented a stepwise wave slope. The settlement curve of the high-level strata changed from a "V" pattern into a parabola pattern with the full mining of the coal seam. From top to bottom, the position of the maximum settlement volume of the overlying strata approached the working face. We conclude that sub-critical strata have local control over the settlement of overlying strata.

3) With the increase in mining thickness, the available rotary volume of "masonry beam" blocks in the low-level critical strata increased continuously, and the masonry structure lost its stability gradually, entering into the caving zone. The "masonry beam" structure formed a "composite cantilever beam" structure with the hard immediate roof beneath.
4) A numerical model was established by combining practical geological conditions to simulate thickening coal seam mining. After the overlying strata achieved movement stability, the plastic failure zone presented obvious characteristics of longitudinal and transverse partitions.

DATA AVAILABILITY STATEMENT

The original contributions presented in the study are included in the article/supplementary material, and further inquiries can be directed to the corresponding author.

AUTHOR CONTRIBUTIONS

XZhang and LL designed experiments. XZhao and LL carried out the experiments. XZhang and XZhao analyzed the experimental results. XZhao and LL wrote the manuscript.

FUNDING

This work was conducted with support from the National Natural Science Funded Projects (award no. 52074007) and Anhui Province Natural Science Funded Projects (award no. 2008085ME142).

ACKNOWLEDGMENTS

We thank Hancheng Mining Group and Anhui University of Science and Technology for giving us access to the mine, data, and physical resources necessary to complete this work.

REFERENCES

Fan, K. s., and Shen, B. h. (2019). Research on Mining Thickness Effect of Underground Mine Pressure Behavior by Fully–Mechanized Caving Mining in Extra Thick Coal Seams. *Coal Sci. Tech.* 47 (3), 239–243. doi:10.13199/j.cnki.cst.2019.03.036

Feng, S. j., Sun, S. g., Lv, Y. g., and Lv, J. (2011). Research on the Height of Water Flowing Fractured Zone of Fully Mechanized Caving Mining in Extra-thick Coal Seam. *Proced. Eng.* 26, 466–471. doi:10.1016/j.proeng.2011.11.2193

Gao, M., Xie, J., Gao, Y., Wang, W., Li, C., Yang, B., et al. (2021). Mechanical Behavior of Coal under Different Mining Rates: A Case Study from Laboratory Experiments to Field Testing. *Int. J. Mining Sci. Tech.* 31, 825–841. doi:10.1016/j.ijmst.2021.06.007

He, F. l., Li, X. b., He, W. r., Zhao, Y. Q., Xu, Z., and Li, Q. S. (2020). The Key Stratum Structure Morphology of Longwall Mechanized Top Coal Caving Mining in Extra-thick Coal Seams: a Typical Case Study. *Adv. Civil Eng.* 2020, 1–13. Article ID 7916729, 13 pages. doi:10.1155/2020/7916729

Huang, Q. x., Zhou, J. l., and Cao, J. (2020). Key Stratum Structure and Support Working Resistance of Longwall Face with Large Mining Height in the Shallow Coal Seams, china. *Adv. Civil Eng.*, 2020. Article ID 8834403, 14 pages. 1–14 doi:10.1155/2020/8834403

Ju, J. f., Xu, J. l., and Wang, Q. x. (2011). Cantilever Structure Moving Type of Key Strata and its Influence on Ground Pressure in Large Mining Height Workface. *J. China Coal Soc.* 36 (12), 2115–2120. doi:10.13225/j.cnki.jccs.2011.12.028

Kong, D., Lou, Y., Zheng, S., and Pu, S. (2020). The Characteristics of Roof Breaking and the Law of Ground Pressure Behavior in Fully Mechanized Top-Coal Caving Face with Large Mining Height. *Geotech Geol. Eng.* 39, 285–297. doi:10.1007/s10706-020-01492-2

Li, H. m., Jiang, D. j., and Li, D. y. (2014). Analysis of Ground Pressure and Roof Movement in Fully-Mechanized Top Coal Caving with Large Mining Height in Ultra-thick Seam. *J. China Coal Soc.* 39 (10), 1956–1960. doi:10.13225/j.cnki.jccs.2013.1366

Li, M., Zhang, J.-x., Huang, Y.-l., and Gao, R. (2017). Measurement and Numerical Analysis of Influence of Key Stratum Breakage on Mine Pressure in Top-Coal Caving Face with Super Great Mining Height. *J. Cent. South. Univ.* 24 (8), 1881–1888. doi:10.1007/s11771-017-3595-5

Li, Z.-l., He, X.-q., Dou, L.-m., Song, D.-z., and Wang, G.-f. (2018). Numerical Investigation of Load Shedding and Rockburst Reduction Effects of Top-Coal Caving Mining in Thick Coal Seams. *Int. J. Rock Mech. Mining Sci.* 110, 266–278. doi:10.1016/j.ijrmms.2018.08.005

Liang, Y. p., Li, B., Yuan, Y., et al. (2017). Moving Type of Key Strata and its Influence on Ground Pressure in Fully Mechanized Mining Face with Large Mining Height. *J. China Coal Soc.* 42 (06), 1380–1391. doi:10.13225/j.cnki.jccs.2016.1320

Miao, X., Cui, X., Wang, J. a., and Xu, J. (2011). The Height of Fractured Water-Conducting Zone in Undermined Rock Strata. *Eng. Geology.* 120, 32–39. doi:10.1016/j.enggeo.2011.03.009

Qian, M. g., Miao, X. x., Xu, J. l., and Mao, X. b. (2003). *"Study of Key Strata Theory in Ground Control*," Xuzhou. China University of Mining and Technology Press, 16–18.

Wang, J. l., Yuan, Y., Tu, S. h., and Li, B. (2014). Roof Structure Characteristics in Fully Mechanized Coalface with Large Mining Height and Reasonable Loading of Support. *J. Mining Saf. Eng.* 31 (4), 512–518. doi:10.13545/j.issn1673-3363.2014.04.003

Wang, X., Wen, Z. j., Jiang, Y. j., and Huang, H. (2018a). Experimental Study on Mechanical and Acoustic Emission Characteristics of Rock-like Material under Non-uniformly Distributed Loads. *Rock Mech. Rock Eng.* 51 (03), 729–745. doi:10.1007/s00603-017-1363-3

Wang, H. w., Wu, Y. p., Xie, P. s., Luo, S. h., Liu, K. z., and Liu, M. f. (2018b). Coal Rib Stability Effect of Mining-Thickness with Large Mining Height of Working Face in Steeply Inclined Seams. *J. Mining Saf. Eng.* 35 (1), 64–70. doi:10.13545/j.cnki.jmse.2018.01.009

Wang, X. z., Xu, J. l., Han, H. k., Ju, J. f., and Xing, Y. t. (2019). Stepped Development Characteristic of Water Flowing Fracture Height with Variation of Mining Thickness. *J. China Coal Soc.* 44 (12), 3740–3749.

Wen, J., Li, H., Jiang, F., Yu, Z., Ma, H., and Yang, X. (2019). Rock Burst Risk Evaluation Based on Equivalent Surrounding Rock Strength. *Int. J. Mining Sci. Tech.* 29 (4), 571–576. doi:10.1016/j.ijmst.2019.06.005

Xu, J. I, and Qian, M. g. (2000). Method to Distinguish Key Strata in Overburden. *J. China Univ. Mining Tech.* 29 (05), 463–467.

Xie, G. x., and Wang, L. (2010). Thickness Effects of Fracture Characteristics of Coal Seam and Surrounding Rocks in Fully Mechanized Top-Coal Caving Face. *J. China Coal Soc.* 35 (02), 177–181. doi:10.13225/j.cnki.jccs.2010.02.010

Xu, J. l., and Ju, J. f. (2011). Structural Morphology of Key Strata and its Influence on Strata Behavior in Fully–Mechanized Face with Super Great Mining Height. ". *Chin. J. Rock Mech. Eng.* 30 (08), 1547–1556.

Yan, S. h. (2009). Theory Study on the Load on Support of Long wall with Top Coal Caving with Great Mining Height in Extra Thick Coal Seam. *J. China Coal Soc.* 34 (05), 590–593.

Yan, S. h., Yin, X. w., Xu, H. j., Li, B., Yan, S. H., YIn, X. W., et al. (2011). Roof Structure of Short Cantilever-Articulated Rock Beam and Calculation of

Support Resistance in Full-Mechanized Face with Large Mining Height. *J. China Coal Soc.* 36 (11), 1816–1820. doi:10.13225/j.cnki.jccs.2011.11.022

Yang, D., Zhang, Y., Chen, Z., and Chen, Z. h. (2020). Analysis on Catastrophe Theory during First Weighting Sliding Instability and Support Crushing of Main Roof with Large Mining Height in Shallow Coal Seam. *Appl. Sci.* 10 (16), 5408. doi:10.3390/app10165408

Yu, L., and Yan, S. h. (2015). Study on Roof Movement Form and Mine Strata Pressure Law of Fully-Mechanized Top Coal Caving Mining in Ultra Thick Seam. *Coal Sci. Tech.* 43 (08), 40–44+59. doi:10.13225/j.cnki.jccs.2011.11.022

Zhang, B. s., Yang, Z. p., Ji, C. x., Guo, Z., and Li, H. Y. (2021). Research on the Influence of the Key Stratum Position on the Support Working Resistance during Large Mining Height Top-Coal Caving Mining. *Adv. Civil Eng.* 2021, 1–9. Article ID 6690280, 9 pages. doi:10.1155/2021/6690280

Zhang, D. l., and Wang, Y. h. (1998). Analysis of Strata Structure in Fully Mechanized Sub Level Caving Faces. *Xuzhou: J. China Univ. Mining Tech.* 04, 340–343.

Zhu, G. a., Dou, L. m., Li, Z. l., Cai, W., Kong, Y., and Li, J. (2016). Mining-induced Stress Changes and Rock Burst Control in a Variable-Thickness Coal Seam. *Arabian J. Geosciences* 9 (5), 365. doi:10.1007/s12517-016-2356-3

Conflict of Interest: The authors declare that the research was conducted in the absence of any commercial or financial relationships that could be construed as a potential conflict of interest.

frontiers in Earth Science

ORIGINAL RESEARCH
published: 15 February 2022
doi: 10.3389/feart.2021.808535

Geomechanical Modeling and Inversion Analysis of the *in-situ* Stress Field in Deep Marine Shale Formations: A Case Study of the Longmaxi Formation, Dingshan Area, China

Qinjie Liu[1,2], Qiang Fu[1,2]*, Ke Yang[1,2,3], Quanchao Wei[4], Huihu Liu[5] and Haibo Wu[5]

[1]State Key Laboratory of Mining Response and Disaster Prevention and Control in Deep Coal Mines, Anhui University of Science and Technology, Huainan, China, [2]School of Mining Engineering, Anhui University of Science and Technology, Huainan, China, [3]Institute of Energy, Hefei Comprehensive National Science Center, Hefei, China, [4]Sinopec Exploration Company, Chengdu, China, [5]Department of Earth and Environment, Anhui University of Science and Technology, Huainan, China

Edited by:
Yilin Gui,
Queensland University of Technology,
Australia

Reviewed by:
Tianshou Ma,
Southwest Petroleum University,
China
Yiquan Li,
Nanjing University, China

***Correspondence:**
Qiang Fu
fqymc@aust.edu.cn

Specialty section:
This article was submitted to Geohazards and Georisks, a section of the journal Frontiers in Earth Science

Received: *03 November 2021*
Accepted: *27 December 2021*
Published: *15 February 2022*

Citation:
Liu Q, Fu Q, Yang K, Wei Q, Liu H and Wu H (2022) Geomechanical Modeling and Inversion Analysis of the in-situ *Stress Field in Deep Marine Shale Formations: A Case Study of the Longmaxi Formation, Dingshan Area, China.*
Front. Earth Sci. 9:808535.
doi: 10.3389/feart.2021.808535

Based on the comprehensive analysis of wellbore characteristics in a deep shale gas field, the *in-situ* stress state of the shale reservoir was assessed in this study for the Longmaxi formation in the Dingshan area, Southwestern China. The data obtained from hydraulic fracturing, drilling-induced fractures, and *in-situ* core testing were used to determine the magnitude and direction of the maximum principal horizontal stress in five wells. Besides, hydraulic fracturing and cross-multipole array acoustic logging (XMAC) were employed to determine the vertical variation of the *in-situ* stress. Based on the logging interpretation and mechanical test results, the spatial distribution of rock mechanical parameters in the Dingshan area was assessed by the amplitude variation versus offset (AVO) seismic inversion. A 3D heterogeneous mechanical inversion model was realized *via* the ANSYS and CATIA3D finite element software packages, providing the area *in-situ* stress field simulation. The depth, fault strike, and position change effects on the main stress, horizontal stress difference, and horizontal stress difference coefficient were numerically simulated. The results show that the maximum principal stress azimuth was mainly concentrated in the NE20°-NE80° sector. Moreover, the development zone of natural fractures was related to the area with the highest principal stress differences. The maximum principal stress variation in the study area was mainly in the compressive range from −135 to −45 MPa, gradually increasing from east to west and south to north. The stress type mainly depended on the depth, fault strike, and rock mechanical parameters, while the stress difference and stress difference coefficient near the fault structure were relatively small. This study's findings are considered instrumental in improving the borehole stability, determining the casing setting point, and optimizing the well location in deep shale reservoirs with similar geological conditions.

Keywords: shale formation, hydraulic fracturing, *in-situ* stress field, geomechanical model, inversion analysis

INTRODUCTION

The rapid progress of horizontal staged fracturing and similar technologies provided breakthrough solutions for the global commercial development of shale gas. In particular, it became an important field of natural gas exploration and development in China, which self-generation and self-contained shale reservoirs have low porosity, ultra-low permeability, and relatively developed natural fractures (Wang et al., 2019). Since most of them have to be hydraulically fractured before economic development (Jang et al., 2015), shale gas production requires shale fracturing by the most effective methods, thus deriving many fracturing stimulation theories to create a complex fracture network (Kim and Lee, 2015). The development of a fracture system directly affects the exploitation efficiency of the shale gas reservoir and determines its quality and output (Ren and Lau, 2019). The assessments of hydraulic fracture expansion and designs of fracturing and perforation schemes are based on the main parameters of the *in-situ* stress field in the shale formation. The accuracy of formation rock stress state measurement and the authenticity of the adopted *in-situ* stress prediction model directly control the hydraulic fracturing efficiency. Therefore, the study of the *in-situ* stress field of shale reservoirs is crucial for shale gas exploration and development.

The rock stress in the formation is mainly formed by gravity and tectonic stresses induced by drilling, slotting, and coring (Li et al., 2019). The geomechanical model is established in the early stage of the oil and gas field development, which can address various problems encountered in the life cycle of oil and gas reservoir development. These problems may occur in the following stages: 1) in the exploration and evaluation stages of the reservoir to be developed, such as the evaluation of fault sealing (or leakage) potential (Ciftci et al., 2013), wellbore stability (He et al., 2015; Liu et al., 2019), and the potential location of oil-gas migration and accumulation (Zeng et al., 2010); 2) in the formal development stage of the reservoir, such as the determination of the best well trajectory (Zhang et al., 2015), casing set point and mud specific gravity, as well as prediction of anisotropic permeability of the fractured reservoir (Dubey et al., 2020); 3) in the whole subsequent production stage of the reservoir, which requires to select the best completion method, such as hydraulic fracturing or repetitive hydraulic fracturing (Chen et al., 2018), and stress sensitivity evaluation of the reservoir and fracture (Han et al., 2021); 4) in the secondary and tertiary oil recovery stages of reservoir development and process optimization, including water injection and steam injection (Sun et al., 2018).

After nearly a century of development, the reservoir stress state can be determined by various means. At present, the research techniques for determining *in-situ* stress of oil and gas reservoirs and mines are mainly divided into five categories (Ljunggren et al., 2003): 1) well trajectory analysis methods (Zhao et al., 2015), 2) core test methods (Nian et al., 2016), 3) calculation methods based on logging data (Han et al., 2018), 4) methods of actual measurement of underground *in-situ* stresses (Fu et al., 2021) and 5) simulation methods, including physical and numerical ones (Bai et al., 2018). In the study (Hashimoto and Matsu'Ura, 2006; Lü et al., 2017), the stress field simulation was performed using a simple three-dimensional geological model, whereas the geological unit was regarded as homogeneous and had constant mechanical parameters. However, such an assumption was often inconsistent with actual geological conditions, which deteriorates the accuracy of such stress field simulations.

In this paper, the geological conditions of the study area are assessed, and the rock mechanics parameters are experimentally determined. The single-well *in-situ* stress data of the study area are measured using the acoustic emission, drilling-induced fractures, and well deviation statistics. They are monitored, adjusted, and analyzed to obtain the *in-situ* stress distribution characteristics and their variation with depth. Based on the logging interpretation and rock mechanics test results, the spatial distribution of mechanical parameters is obtained by the amplitude variation versus offset (AVO) inversion. The maximum and minimum principal stress distribution characteristics, horizontal stress difference, and horizontal stress difference coefficient are predicted *via* the numerical simulation using a commercial finite element CATIA software package.

GEOLOGICAL BACKGROUND

Location and Structure

The case study is the shale formation in the Dingshan area, located in the Qijiang District of Chongqing, Southwest China, about 150 km away from Jiaoshiba Block of Fuling shale gas field. **Figure 1** shows the location of the Dingshan area and the cross-section through Dingshan wells (Liu et al., 2017a; Hu et al., 2019). The NE-trending structural belt of the Lintanchang-Dingshan in Southeast Sichuan belongs to the complex basin margin structure. The structural characteristics of this area are as follows. It straddles four structural units: East Sichuan high and steep fault-fold area, South Sichuan low and steep fold area, North Guizhou thrust belt, and South Sichuan cover coat detachment zone. The sedimentary cap has experienced multi-stage tectonic movements. Like other blocks in the Sichuan Basin, it underwent six major tectonic cycles in geological history, including Yangtze, Caledonian Hercynian, Indosinian, Yanshan, and Himalayan (Liu et al., 2021). Most of the above structural units have fold and fault structures, i.e., trough-like folds composed of high and steep anticline belts and the fault belt in NE and NNE directions. The structural style is anticline wide and gentle, syncline compact, parallel arrangement in rows and belts. Most faults are reverse ones with large dip angles ranging from 60 to 85°.

Stratigraphy

The main strata developed from bottom to top in the Dingshan area are Sinian of Proterozoic, Permian of Early

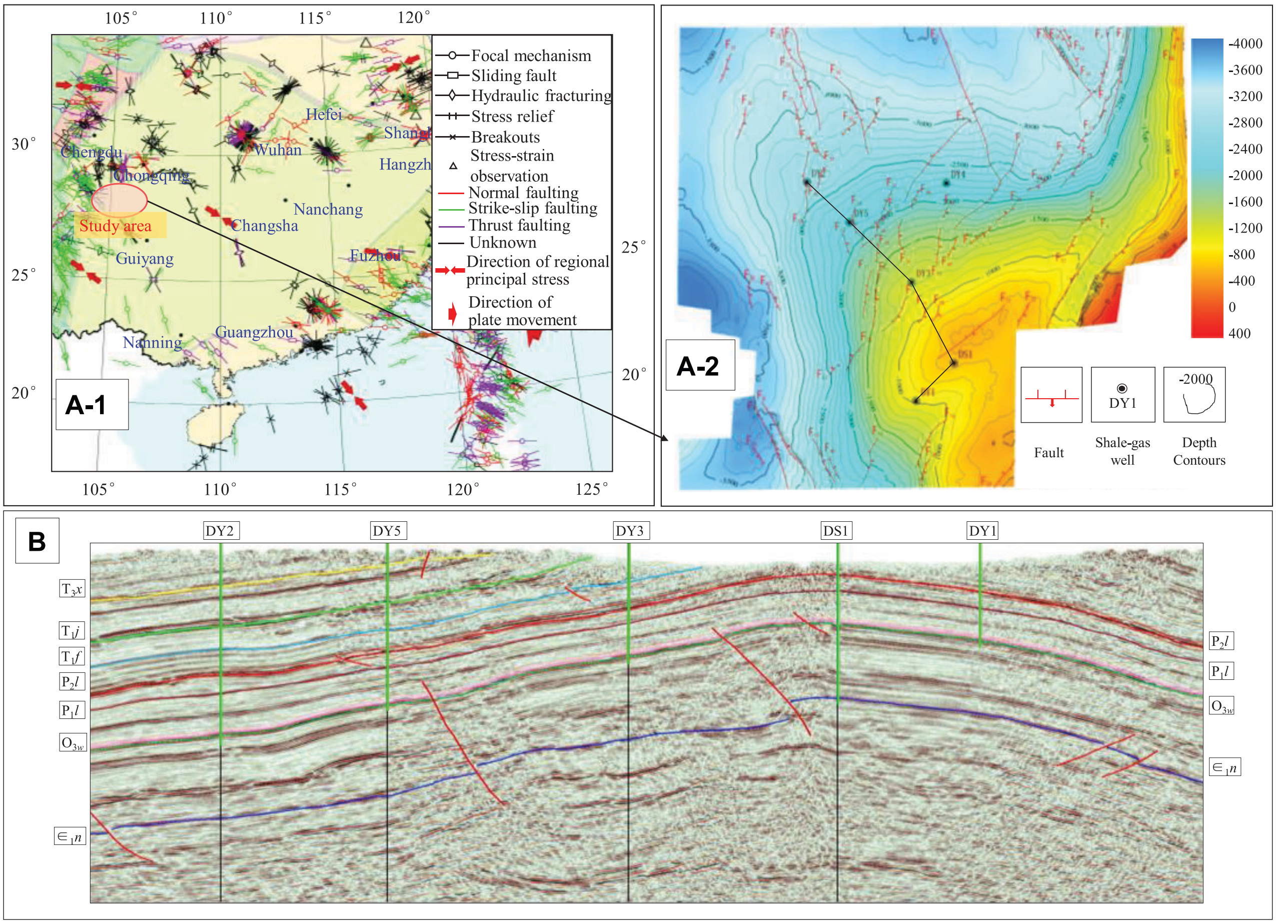

FIGURE 1 | [(A), 1,2] Location of the Dingshan area and **(B)** Cross-section through the Dingshan area (Liu et al., 2017b; Hu et al., 2019) (The crustal stress data were provided by the China Earthquake Data Center).

Paleozoic, and Late Paleozoic and Mesozoic (Liu et al., 2013). The strata in the study area are well developed, and the sedimentary basement is an epimetamorphic rock of the Banxi group of pre-Sinian. Triassic strata are exposed on the area surface, while Devonian, Carboniferous, and Cenozoic strata are absent. Carbonaceous and sandy shales dominate the lower part of the Longmaxi formation, and the upper part is interbedded with calcareous shale and thin argillaceous limestone. According to the field thickness measurement, the high-quality shale section of the Longmaxi formation is stably developed, with a thickness of 28.9–35 m, as shown in **Figure 2**.

Natural Fractures

The development orientation of fractures is closely related to *in-situ* stress, which is an important factor in controlling the distribution of natural and hydraulic-induced fractures in reservoirs. The paleotectonic stress field controls natural fractures' formation, distribution, and development. The modern stress field controls the current occurrence state and effectiveness (opening and connectivity) of underground natural fractures, fracture forms, and extension directions of artificial fractures.

Core observation shows that the Longmaxi formation in the Dingshan area mainly features shear fractures, followed by tensile fractures, torsional fractures, interlayer fractures, and a small number of artificially induced fractures, as shown in **Figure 3**. High-angle shear fractures (**Figures 3A–E**) and vertical fractures (**Figure 3B**) are mainly developed, characterized by large extension length and straight fracture surface, and are mostly filled with calcite. The shale is rich in brittle index minerals; it undergoes the ductile shear fracture under local or regional tectonic stresses, forming high-angle tensile or Mode I fractures (also referred to as an opening mode, with tensile stresses normal to the crack plane) and shear or Mode II fractures (i.e., a sliding mode, with shear stresses acting parallel to the crack plane and perpendicular to the crack front), which are related to faults and folds, respectively. Tensile fractures are frequently referred to as joints, where no appreciable slip or shear is observed. The tensile fractures generally have small extension length and uneven fracture

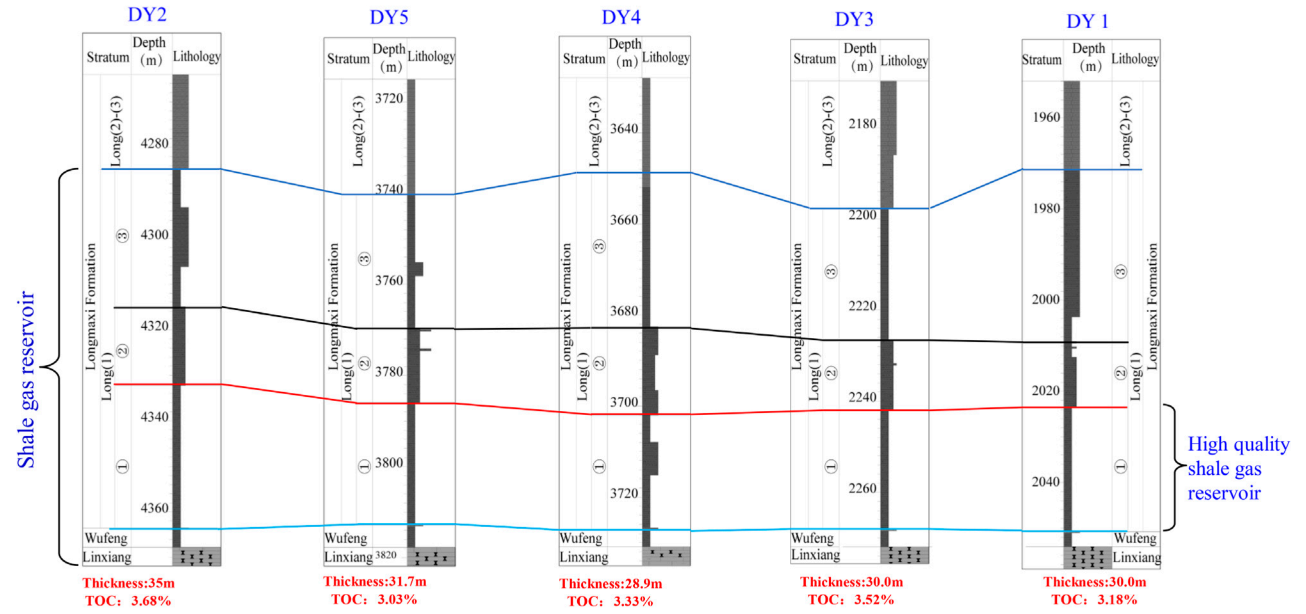

FIGURE 2 | Distribution of shale gas intervals in the Longmaxi formation of Dingshan area.

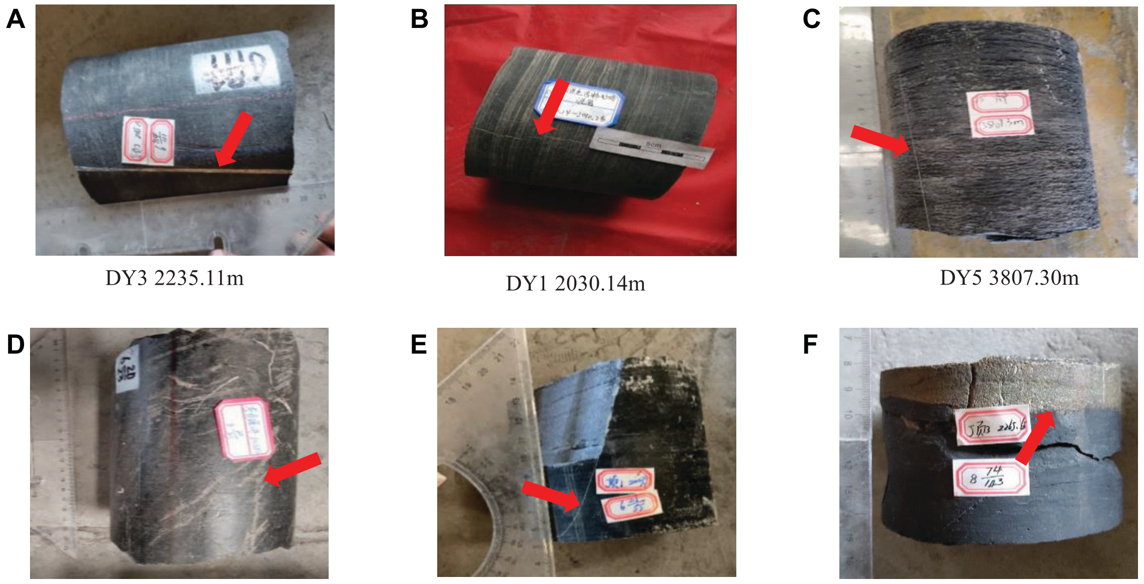

DY3 2235.11m

DY1 2030.14m

DY5 3807.30m

DY1 3013.82m

DY1 2003.91m

DY3 2265.65m

FIGURE 3 | Characteristics of shale core fracture in the Longmaxi formation of Dingshan area. **(A)** DY3 2235.11 m. **(B)** DY1 2030.14 m. **(D)** DY1 3013.82 m. **(E)** DY1 2003.91 m. **(F)** DY3 2265.25 m.

surface, being mostly filled with calcite (**Figure 3D**). Besides, a small number of tearing mode or Mode III fractures (i.e., a tearing mode with shear stresses acting parallel to the crack plane and parallel to the crack front) are observed. In organic-rich shale, the interlayer fractures (**Figure 3F**) are usually filled with calcite, pyrite, and organic matter. The occurrence of slip fractures is the same as that of rock stratum, with small dip angles, large trend variations, uneven fracture surfaces, and visible scratches. The induced fractures are artificial fractures caused by an imbalance between heavy mud and *in-situ* stresses, drilling tool loads, and torsion during drilling.

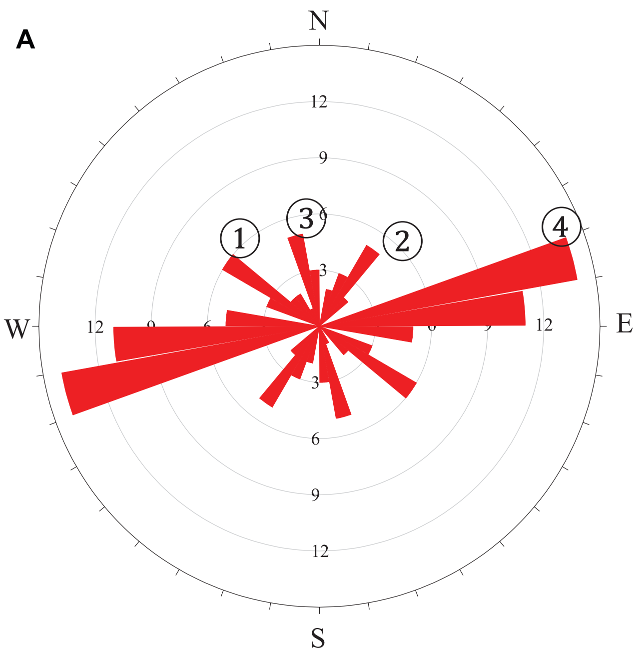

Rose diagram of shear fracture strike

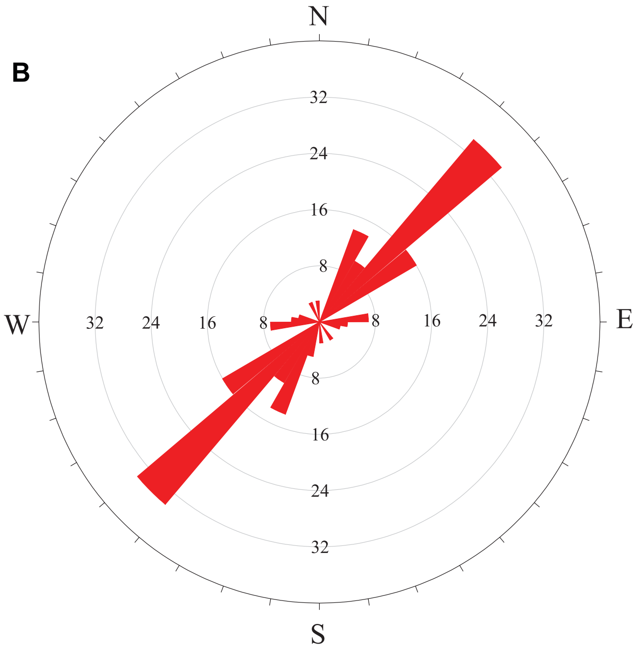

Rose diagram of tensile fracture strike

FIGURE 4 | Rose diagram of fracture trend in shale gas well in the Dingshan area. **(A)** Rose diagram of shear fracture strike. **(B)** Rose diagram of tensile fracture strike.

The filling of fractures after their formation is a long-term process. According to the filling degree of minerals in fractures, they can be subdivided into full-filled, half-filled, and unfilled fractures. The filling degree of fractures becomes gradually weak, and so does the sealing of fractures. Core observation shows that about 60% of the fractures in the whole area are full-filled, 20% are half-filled, and 20% are unfilled. The core data analysis of five deep wells (namely Dingye 1–5, hereinafter abbreviated as DY1, DY2, DY3, DY4, and DY5) shows that the fracture filling materials include calcite, pyrite, organic matter, etc. The half-filled and filled fractures are mainly filled with calcite, accounting for about 68%, followed by the mixed filling of calcite and pyrite, accounting for 20%. The ratios of pyrite and organic matter filling are relatively small. Organic matter filling allows the respective fractures to play an important role in oil-gas migration and transportation in the reservoir space.

The core observation results combined with imaging logging interpretation data show that (**Figure 4**) there are mainly four groups of structural fracture development orientations, among which the NEE (80 ± 10) fractures are the most developed, followed by the NWW (305° ± 5°). The NNE (30° ± 5°) and NNW (350° ± 5°) fractures are relatively poorly developed. According to the intersecting relationship of core fractures and the analysis of the characteristics of fillings, NWW (305° ± 5°) and NNW (350° ± 5°) fractures are of the same stage, which can be matched as plane “X” type conjugate shear fractures. The fractures of NNE (30° ± 5°) and NEE (80° ± 10°) can be matched as another stage of plane “X” type conjugate shear fractures.

SAMPLES AND TESTING

The engineering rock mechanics was used to study the mechanical characteristics and failure types of rock, which was also essential for the stress field distribution analysis. It was necessary to prepare test specimens meeting the respective standards to determine their mechanical parameters adequately. The rock samples were acquired from DY1, DY2, DY3, DY4, and DY5 wells in the Longmaxi formation of the Dingshan area (three samples per well) and processed into cylindrical specimens with a diameter of 25 mm and a height of 50 mm. Their end face’s parallelism was controlled within 0.01 mm. The testing procedure complied with the GB/T 23561.7-2009 Part 7 and GB/T 23561.8-2009 Part 8: Methods for Determining the Uniaxial Compressive Strength and Deformation Parameters of Coal and Rock, which implied the stress

TABLE 1 | The uniaxial compression test results for the Longmaxi formation shale of the Dingshan area, China.

Sample	Depth/m	*R*/MPa	*E*/GPa	*μ*
DY1 well	1,974	69.4	35.4	0.22
DY3 well	2,175	75.3	25.5	0.24
DY4 well	3,588	80.6	32.5	0.18
DY5 well	3,773	82.3	42.1	0.27
DY2 well	4,363	90.1	40.4	0.26

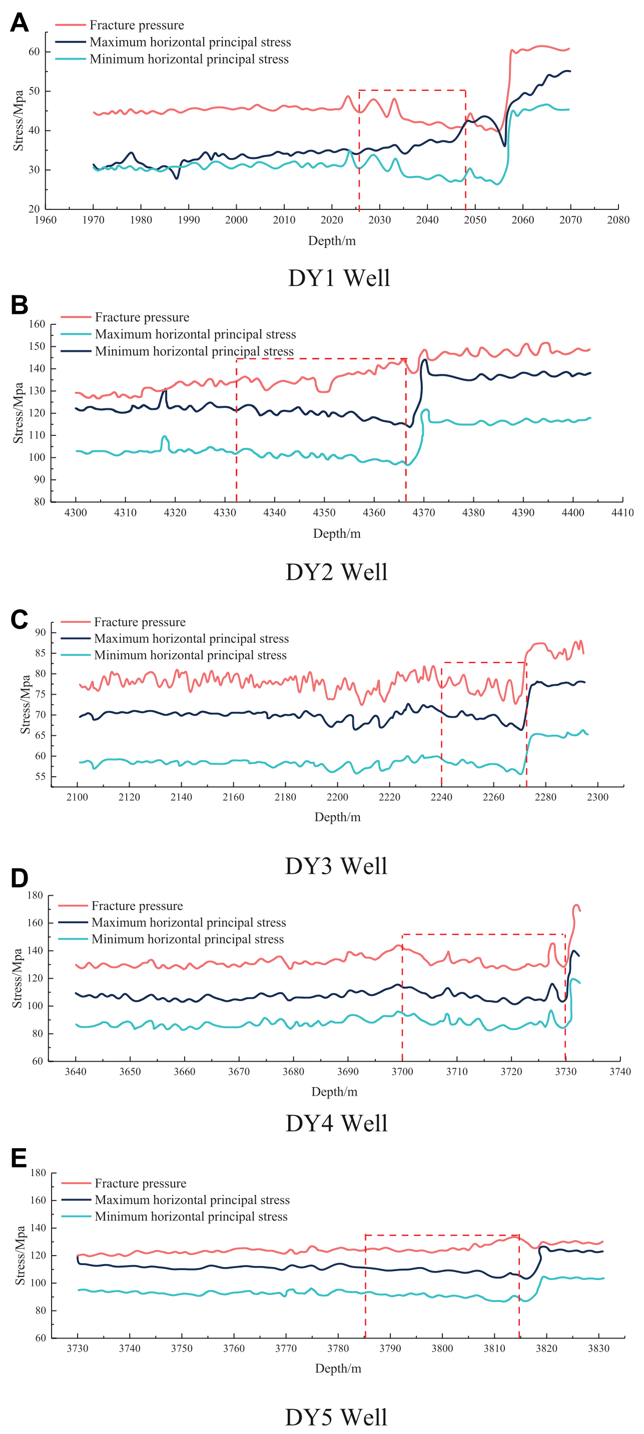

FIGURE 5 | Stress profile of shale gas well of the Longmaxi formation in Dingshan area (based on logging interpretation results). **(A)** DY1 Well. **(B)** DY2 Well. **(C)** DY3 Well. **(D)** DY4 Well. **(E)** DY5 Well.

loading rate of 0.5–1.0 MPa/s and the displacement-measuring device accuracy of 0.001 mm. A WDW-100E microcomputer-controlled electronic universal testing machine loading system was employed in the tests. The maximum axial load range of the WDW–100E testing machine was 100 kN, and the accuracy was ±0.5%. A computer-aided high-precision test control was performed, with online monitoring and recording of the loads and displacements. The uniaxial compression tests were carried out on specimens with different bedding angles. The displacement-controlled loading mode was adopted, with a 0.12 mm/min loading rate.

The uniaxial compression test results are listed in **Table 1**. As observed, the average uniaxial compressive strength values of DY1, DY2, DY3, DY4, and DY5 specimens were 69.4, 90.12, 75.3, 80.6, and 82.3 MPa, respectively.

Herein, R, E, and μ are rock's compressive strength, the Young (elastic) modulus, and Poisson's ratio, respectively.

TEST RESULTS ON THE *IN-SITU* STRESS IN THE HORIZONTAL DIRECTION

When an object is subjected to an external force, a force opposing the external force is produced in its interior to keep balance, which is called the internal force. The *in-situ* stress is the internal stress existing in the crust rock mass, which is the force per unit area inside the medium caused by the vertical and horizontal movements of the crust and other factors. The *in-situ* stress state is described by the stress tensor, which includes three orthogonal principal stresses, and each principal stress has a direction and size (Rajabi et al., 2016). Only four components usually describe the *in-situ* stress tensor: the minimum horizontal stress magnitude, the maximum horizontal stress magnitude, the vertical stress magnitude, and the maximum horizontal stress direction (Bell, 1996; Yin et al., 2020). This paper mainly focuses on shale formation (namely the Longmaxi formation in China). Compared with the length and width in the horizontal direction of the study area, the distance changes little in the vertical direction. Therefore, we did not focus on the change of vertical stress of each well.

Longitudinal Profile of Horizontal Stress and Stress Difference

The *In-Situ* Stress Profile Based on the Logging Analysis

The stress difference distribution in five wells (DY1–DY5) of the Dingshan Block was obtained and analyzed in detail based on the logging interpretation results. The results show that the stress difference in the DY3 sidetracking horizontal well was 5 MPa. Those in DY1, DY2, DY4, and DY5 were 9, 8, 8, and 10 MPa, respectively, while the stress difference in the general bedding of deep wells was usually higher. As shown in **Figure 5**, the fracture pressure gradient significantly exceeded the maximum horizontal stress gradient and the minimum principal horizontal stress (PHS) gradient.

Vertical Variation Characteristics of *In-Situ* Stress Based on Fracturing Curve Reading

According to the fracture closure pressure data of each well (borehole) in the study area, the relationship between fracture

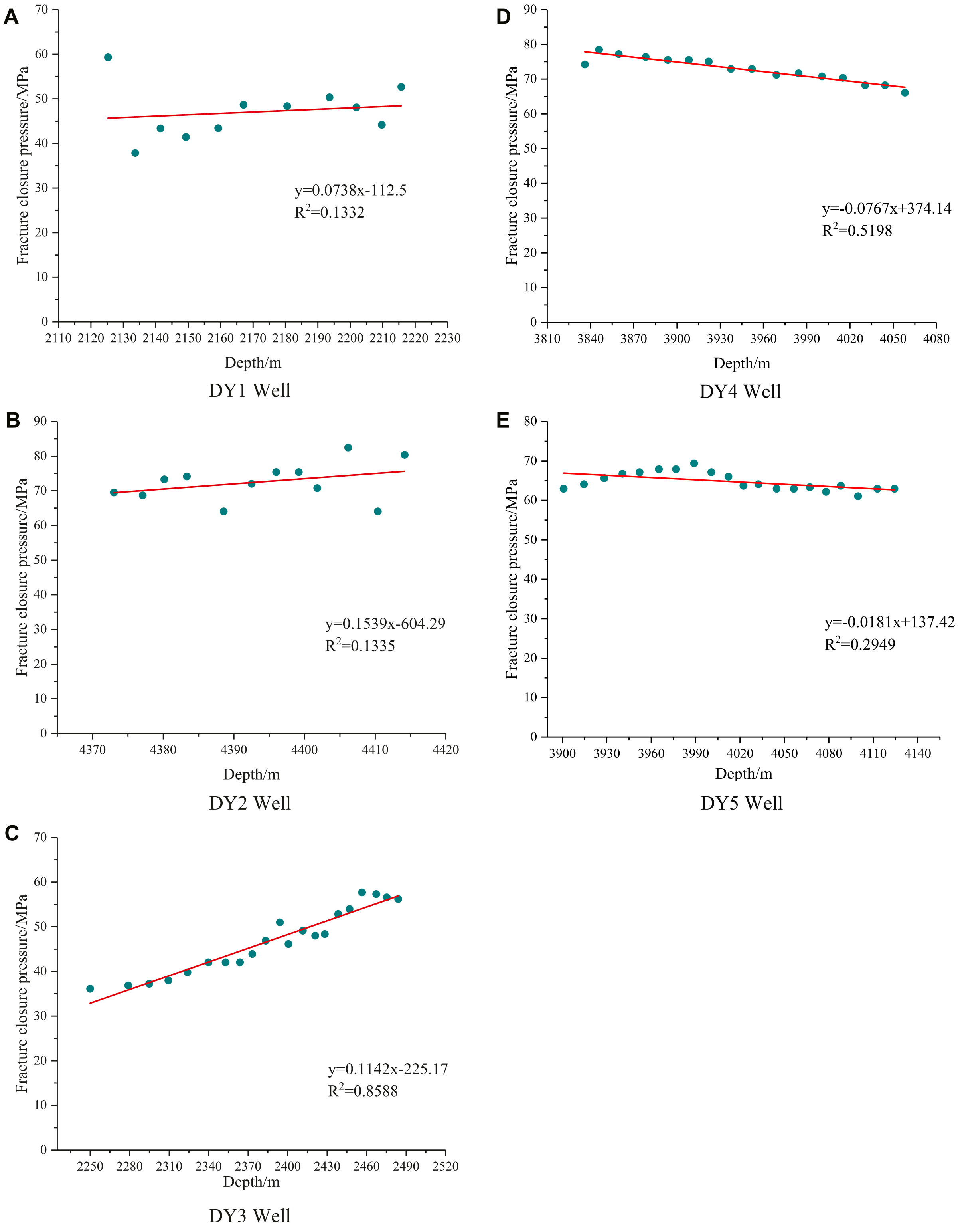

FIGURE 6 | Relationship between fracture closure pressure and depth in Dingshan area. **(A)** DY1 Well. **(B)** DY2 Well. **(C)** DY3 Well. **(D)** DY4 Well. **(E)** DY5 Well.

closure pressure and depth was obtained and plotted, as shown in **Figure 6**. As observed, there is a certain correlation between the fracture closure pressure and depth. The fracture closure pressure in DY2 and DY3 specimens increased with depth. However, fracture closure pressure in DY2 fluctuated with a poor correlation with depth. The DY4 and DY5 fracture closure

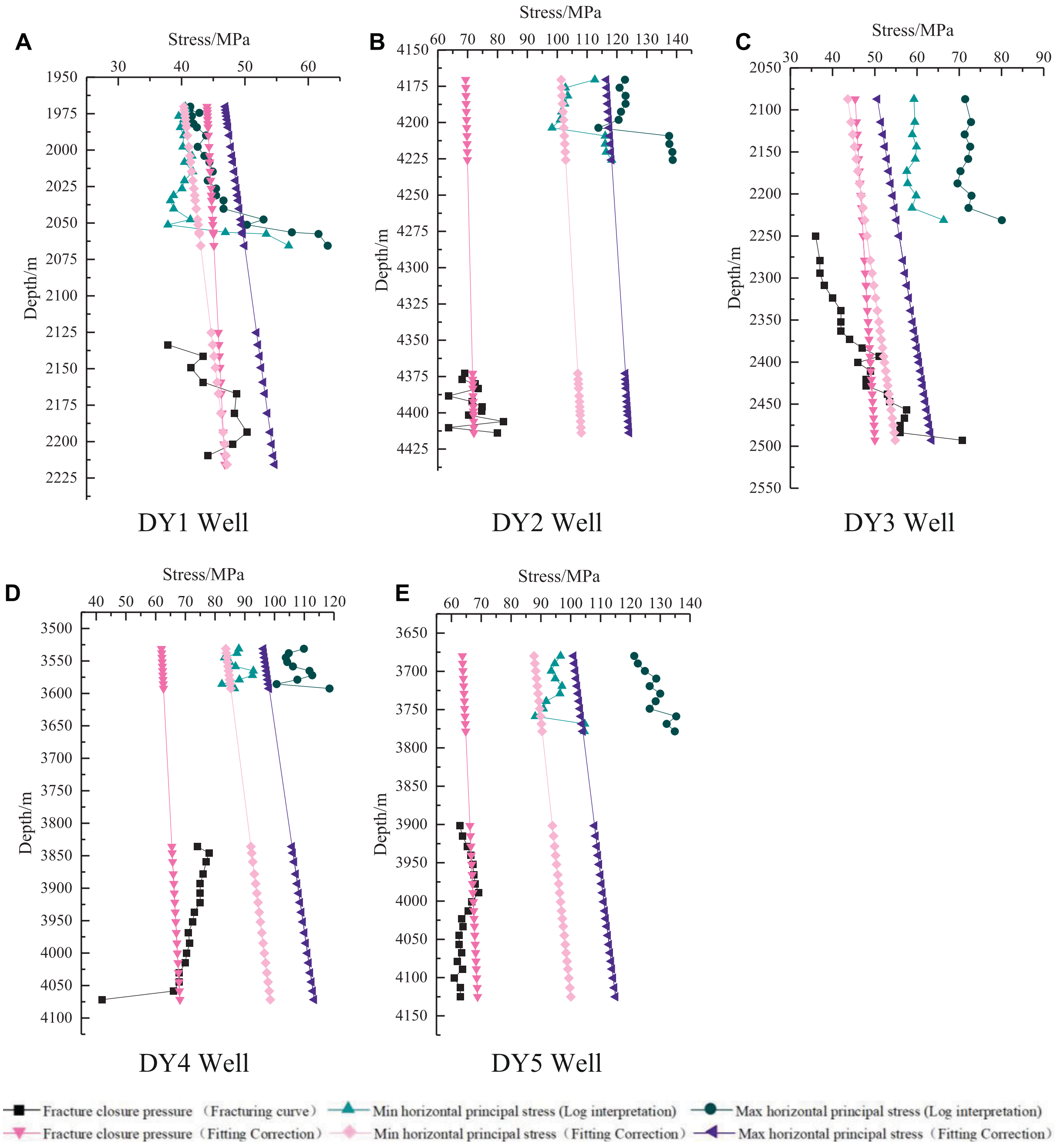

FIGURE 7 | Stress vertical section of Dingshan area. **(A)** DY1 Well. **(B)** DY2 Well. **(C)** DY3 Well. **(D)** DY4 Well. **(E)** DY5 Well.

pressures decreased with depth, exhibiting a pronounced downward trend.

According to the above results on fracture closure pressure, the maximum and minimum principal horizontal stress (PHS) values and the logging interpretation data were fitted to re-compile the vertical profile of the *in-situ* stress, as shown in **Figure** 7. It can be seen in **Figure** 7 that the fracture closure pressure obtained by logging interpretation differed from the horizontal minimum stress. The principal stress obtained from logging interpretation exceeded the corrected principal stress of well testing. However, the principal stresses obtained by different acquisition techniques increased with depth.

The Magnitude and Direction Distributions of the Horizontal *In-Situ* Stress

The Magnitude Distribution Characteristics of the *In-Situ* Stress

The magnitude and direction on the horizontal *in-situ* stress in the Dingshan area were based on fracturing curve data,

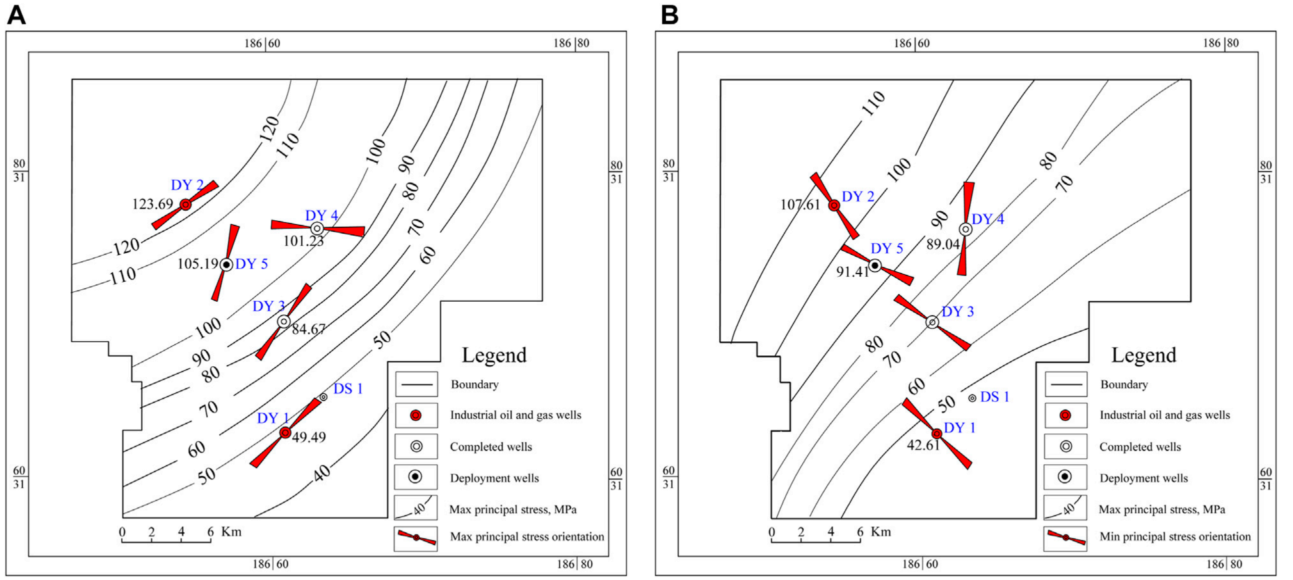

Magnitude and direction characteristics of maximum horizontal principal stress

Magnitude and direction characteristics of minimum horizontal principal stress

FIGURE 8 | Magnitude and direction distribution of horizontal principal stress in the Longmaxi formation. **(A)** Magnitude and direction characteristics of maximum horizontal principal stress. **(B)** Magnitude and direction characteristics of minimum horizontal principal stress.

minimum PHS data, and operation data obtained from well testing. The data on maximum and minimum PHS values in the study area were imported into AutoCAD. The preliminary contour maps of the maximum and minimum PHS values in the study area of the Longmaxi formation were drawn, as shown in **Figure 8**. As observed, the maximum PHS distribution in the Dingshan area decreased from the northwest (NW) direction to the southeast (SE) one. The maximum and minimum PHS values around DY4, DY5, and DY2 wells were relatively high, forming high-stress areas, while those near DY1 and DY3 wells were relatively low, corresponding to low-stress areas. The above maximum and minimum parameters decreased gradually from northwest to southeast, and the *in-situ* stress magnitudes dramatically dropped between DY3 and DY4 wells.

Among the five deep shale gas wells under study, the largest principal stress was observed in the DY2 well, and its minimum PHS was 107.61 MPa. The minimum PHS values were lower in relatively developed fractures. The fractures did not develop at higher compressive stresses, and the minimum PHS gradient was higher.

Azimuth Plane Distribution Characteristics of the *In-Situ* Stress

The preliminary orientation diagrams of maximum and minimum PHS in the Dingshan-Dongxi area were constructed, as shown in **Figure 8**. According to **Figure 8A**, the maximum PHS directions of DY2 well fell into the (NE-SW, NE40°) sector. The above directions changed from DY5 to DY4 wells from NW-SW to approximately E-W. DY3 and DY1 wells exhibited similar orientation changes. The maximum PHS direction of the DY1 well coincided with NEE-SW (~NE40°). As shown in **Figure 8B**, the minimum PHS directions of DY2 and DY5 wells fell into the NW-SW sector, while those of DY3, DY2, and DY1 fluctuated from north to west. The minimum PHS direction of DY4 was approximately from south to north, slightly fluctuating between NW and NE directions.

MODEL AND NUMERICAL SIMULATION

The stress field of the Longmaxi formation in the Dingshan area was simulated via the finite element method (FEM) and the ANSYS software. The stress field simulation required the following steps: 1) determining the structural elements (such as faults, anticlines, and synclines) and strata geometry (e.g., elevation, thickness, etc.); 2) determining the spatial distribution of mechanical parameters (such as Poisson's ratio and the Young modulus) of the rocks at different positions; 3) determining the load state and related boundary conditions of the geological body.

Geomechanical Model

Mechanical Parameters

Nuclear magnetic resonance and XMAC logging techniques were used to determine the mechanical parameters (the Young modulus, Poisson's ratio, etc.), brittleness index, and rock element weight fraction in the profile. For various lithologies, the rock mechanical parameters may vary with formations. The AVO synchronous inversion of prestack seismic data can yield multiple-reservoir elastic parameters, making it possible to calculate the brittleness index *via* dynamic elastic parameters. Therefore, the AVO

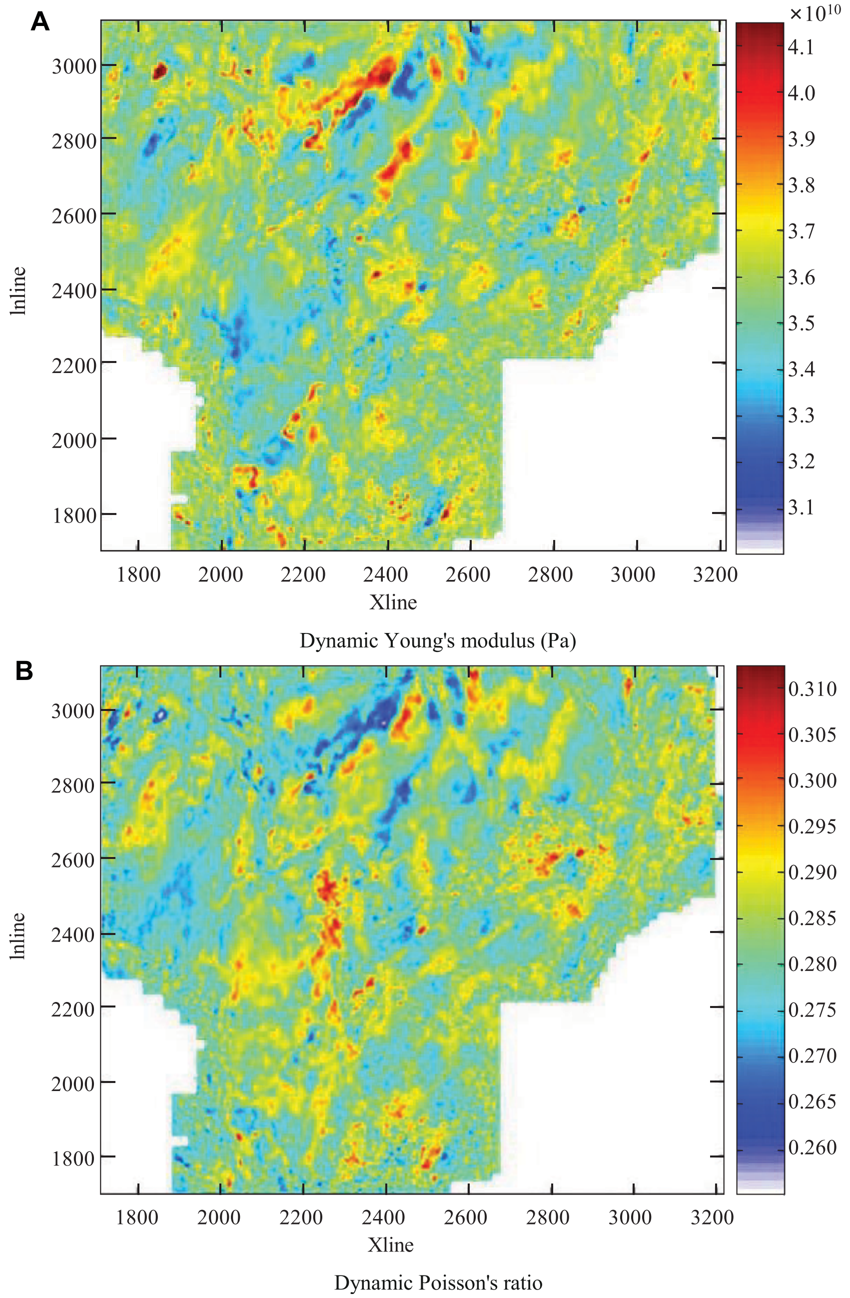

FIGURE 9 | Slicing of dynamic Young's modulus and Poisson's ratio along strata of the Longmaxi formation in Dingshan area. **(A)** Dynamic Young's modulus (Pa). **(B)** Dynamic Poisson's ratio.

synchronous inversion can directly obtain dynamic elastic parameters (Liu et al., 2018). Compression and shear wave velocity and density logging data are the basic data for calculating dynamic elastic parameters. These logging data are vital for establishing the initial inversion model and constraining inversion results. Using the low-frequency components of logging curves in the Dingshan area, the initial 3D inversion model of the study area was constructed. Using the wide-azimuth angle gathers extraction to get the input data, the horizon mean slices of dynamic Young moduli and Poisson's ratios of the Longmaxi formation in the Dingshan area were obtained by the AVO inversion, as shown in **Figure 9**.

The Young moduli of the fault zone were usually smaller by 15–35% than those of the normal strata in the Dingshan area (Liu et al., 2017a; Yong et al., 2018; Zhong et al., 2019). Such mechanical parameters as the Young moduli and Poisson's ratios vary with fault size: the larger the fault length, the

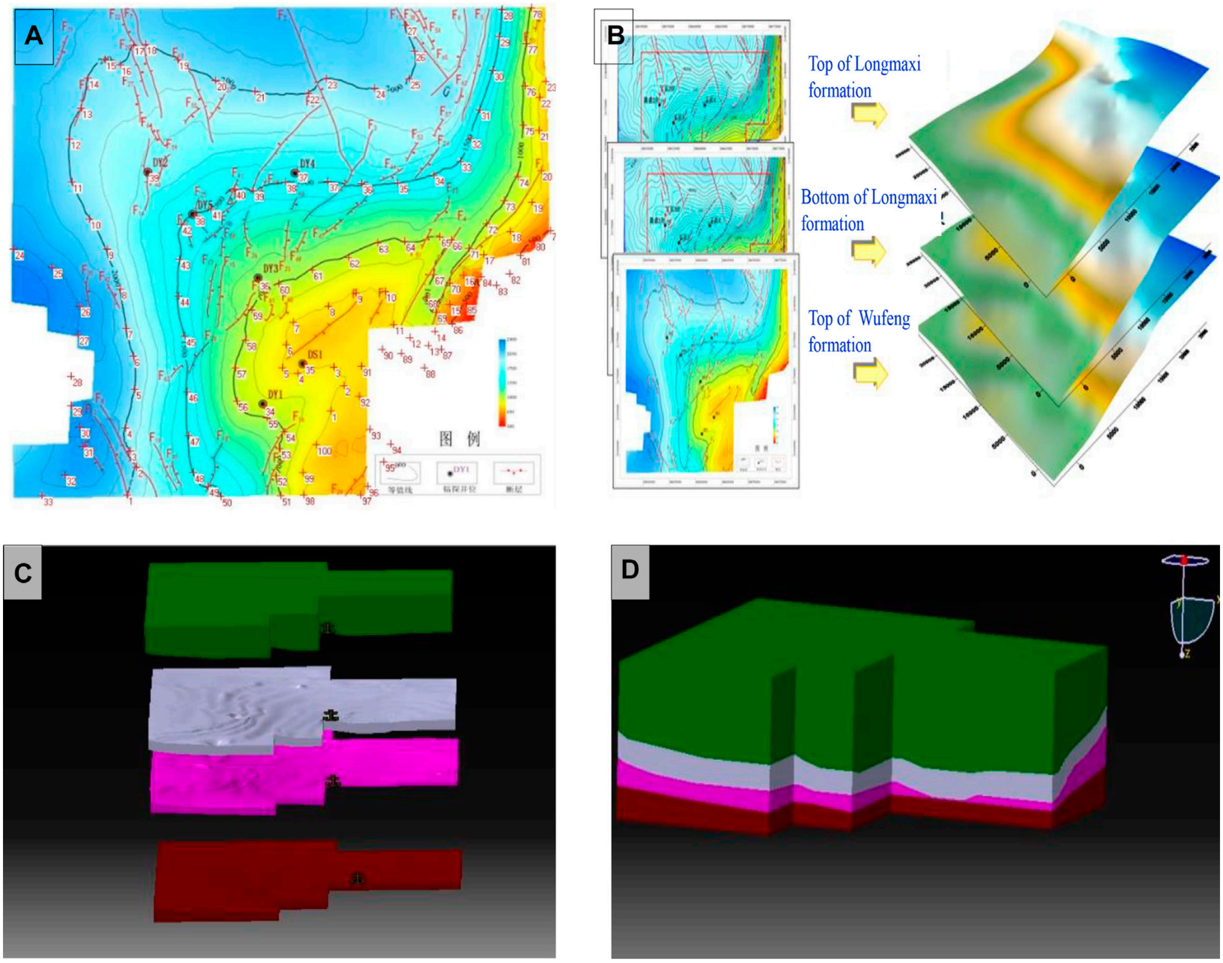

FIGURE 10 | Modeling process of numerical simulation. **(A)** Construction information extraction point distribution map. **(B)** Fitting surface of each layer interface. **(C)** Development map of rock geological body. **(D)** 3D geological model of Longmaxi formation shale in Dingshan area.

greater the fault drop; the larger the Young modulus of the rock, the smaller is its Poisson's ratio and vice versa.

Geological Model and Finite Element Mesh

The steps to establish the geological model of the Dingshan area were as follows:

(1) The CAD software was used to extract the position information on the contour lines of each layer in the geological structure map to obtain the structural features at different positions.
(2) According to the geological information on several layers in the study area, the surfer software was used for surface fitting to obtain the surface related to the actual stratum distribution characteristics.
(3) The Catia 3D modeling software is used to simulate the closure and filling of the research object, and then the initial geological model of the Dingshan area was established.
(4) The initial geological model of the Dingshan area was imported into the ANSYS finite element simulation software.

As shown in **Figure 10**, to reduce the computational complexity and improve the computational accuracy, the geological model was meshed by quadrilateral elements and then subdivided into a series of nodes and elements. According to the characteristics of element types in the finite element software, the Solid 45 elements were used for meshing the shale reservoir as the most suitable for layered structure element division. More precise element division could produce more accurate results, but the computational complexity would also be increased. Therefore, the target strata and fault zones were subdivided into several quadrilateral grid elements with side lengths of 3–10 m. The surrounding rock was simulated with a coarse grid with a side length of 10–300 m. The study area around the borehole was split into fine grids, and the area far away from the study area was subdivided into coarse grids. The FEM model contained 1,124,643 elements and 188,632 nodes. Each of these nodes was assigned different mechanical properties, according to the results depicted in **Figure 10**, which turned the initially homogeneous model into a heterogeneous one. In the computations, tensile and

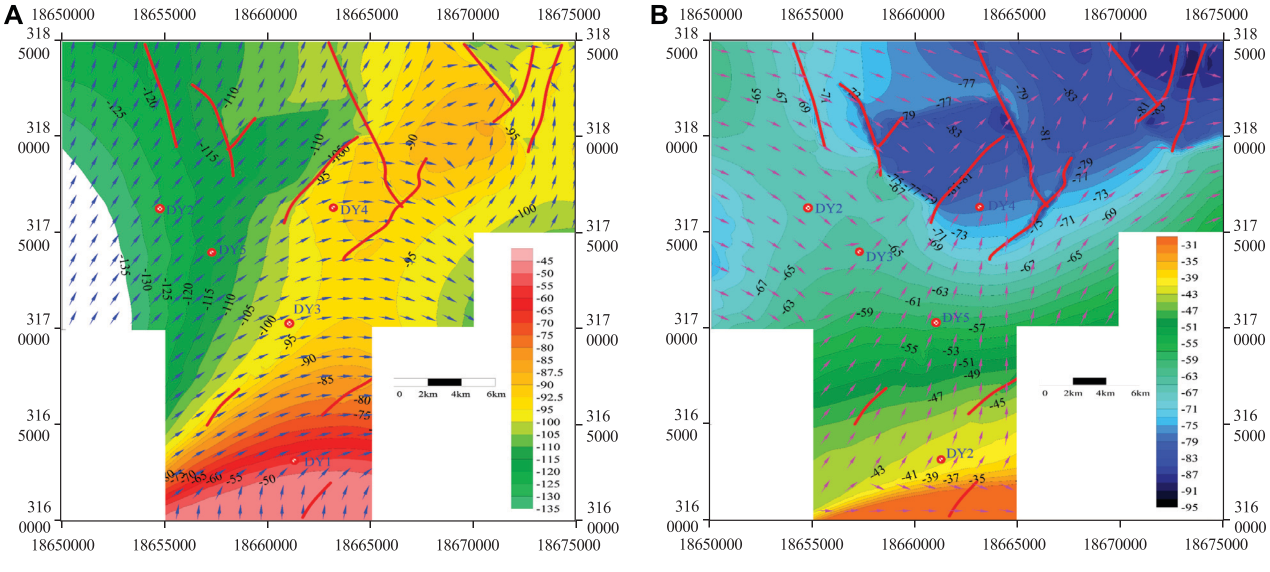

Maximum horizontal principal stress and its azimuth distribution in the Longmaxi formation

Minimum horizontal principal stress and its azimuth distribution in the Longmaxi formation

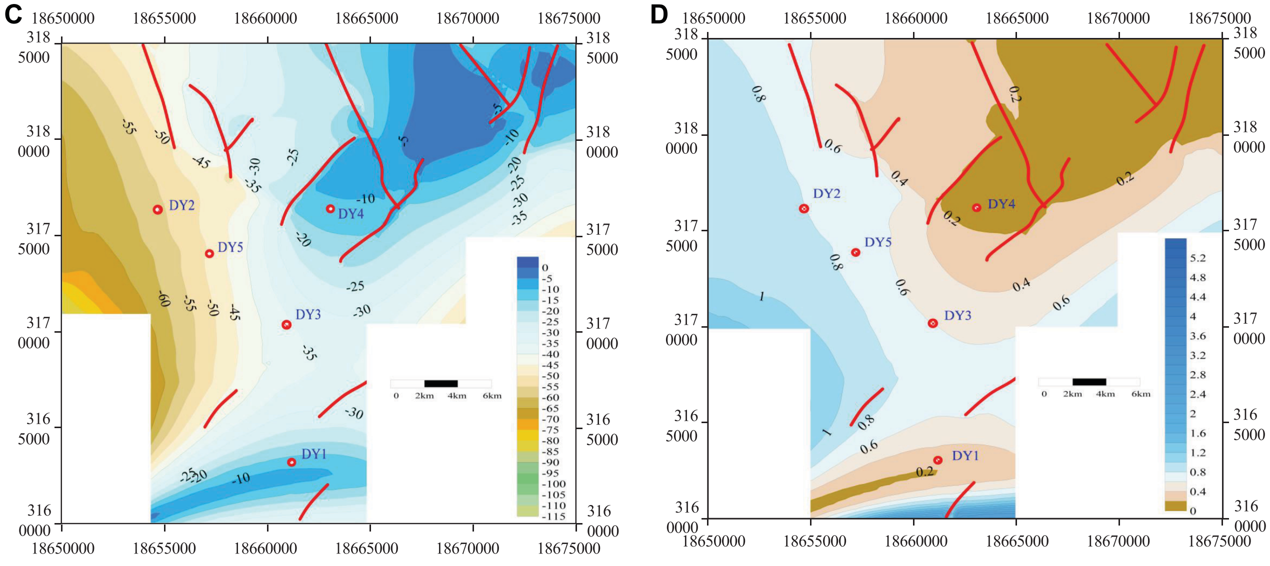

Distribution of stress difference in the Longmaxi formation

Distribution of stress difference coefficient in the Longmaxi formation

FIGURE 11 | Stress field of shale gas reservoir of the Longmaxi formation in Dingshan area. **(A)** Maximum horizontal principal stress and its azimuth distribution in the Longmaxi formation. **(B)** Minimum horizontal principal stress and its azimuth distribution in the Longmaxi formation. **(C)** Distribution of stress difference in the Longmaxi formation. **(D)** Distribution of stress difference coefficient in the Longmaxi formation.

compressive stresses had positive and negative values, respectively.

RESULTS AND DISCUSSION

In the fractured reservoir, the propagation direction of hydraulic fractures was closely related to the stress state, fracture extension, and the development of natural fractures. Various stress parameters, horizontal stress difference Δσ, and horizontal stress difference coefficient (Kh) were the main factors controlling the propagation of hydraulic fractures along the maximum principal stress direction (Liu et al., 2017b).

As seen in **Figures 11A,B**, the maximum and minimum principal stresses had similar distribution patterns. In contrast, gravity and plate boundary stress played a major part in the Dingshan area. **Figure 11A** shows the distribution diagram of the maximum PHS and azimuth contour of shale gas reservoirs in the Longmaxi formation of the Dingshan area. As observed, the variation range of the maximum principal stress in the study area

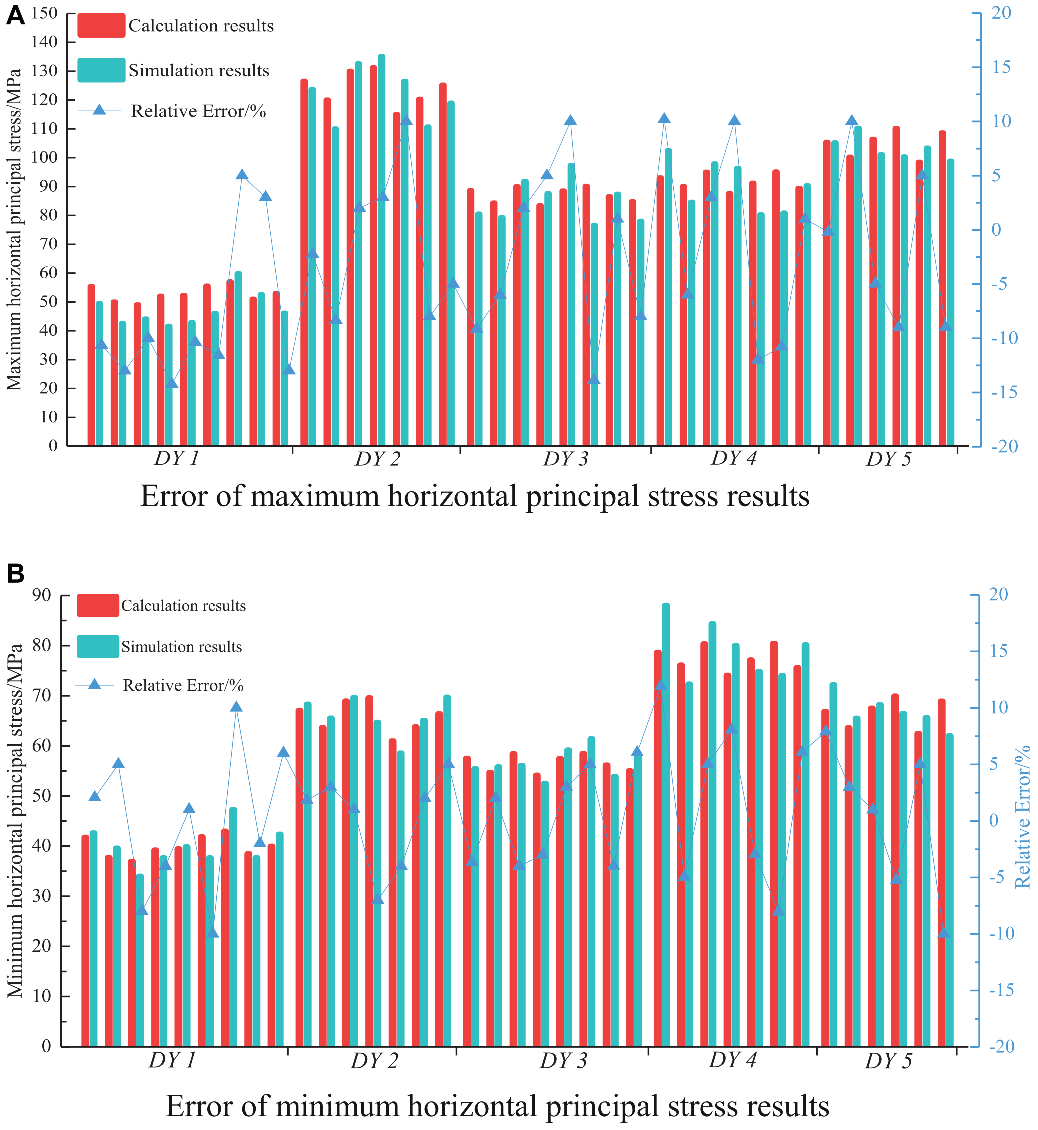

FIGURE 12 | Comparison of horizontal principal stress results based on simulation and calculation. **(A)** Error of maximum horizontal principal stress results. **(B)** Error of minimum horizontal principal stress results.

ranged from −135 to −45 MPa, which implied the prevailing compressive stress state. The increasing trends from east to west and south to north were observed, strongly correlated with the strata buried depth of strata but could not be described by simple linear relationships. Due to the large fault structure segmentation of the near NEE trending, the stress field in the study area was characterized by obvious zoning. The existence of fault structures greatly affected the maximum principal stress: its variation gradient was the highest near the fault zone, especially in the areas with fault structure turns or intersection of multiple faults. Meanwhile, since the internal rocks of the fractured structure were partially broken, the relevant mechanical parameters were slightly lower, the maximum principal stress value in the fracture structure was reduced correspondingly. The larger fracture structure scales corresponded to the larger decline of the maximum principal stress.

As shown in **Figure 11A**, the azimuth of the maximum PHS of the Longmaxi formation in the Dingshan area mainly ranged between NE20° and NE80° directions, which was consistent with the stress azimuth of the far-field area on the whole. However, there were also some differences: the orientation of the maximum principal stress in the study area was approximately parallel to the strike of the main fault zone, while that in the local area was normal to the fault structure. The fault zone significantly affected the maximum principal stress distribution. The principal stress orientation exhibited refraction and deflection near the fault structure, especially at large fault scales and in multiple fault structures' intersections.

The minimum PHS and its orientation distribution in the shale gas reservoir of the Longmaxi formation in the Dingshan area are shown in **Figure 11B**. As observed, the minimum PHS mainly ranged between −95 and −35 MPa, featuring the prevailing compressive stress state. The minimum PHS in the study area increased from south to north and from east to west, with an obvious depth correlation. However, in terms of the specific values, the minimum PHS value variation pattern strongly differed from the maximum principal stress. In the area under study, due to the high degree of rock breaking near the fault structure and the low ability to bear the shear load, the difference between the maximum and minimum principal stresses and the coefficient of stress difference were relatively small, as shown in **Figures 11C,D**. The fractured structure had a stronger effect on the distribution of the minimum principal stress than on the maximum one, showing a higher variation gradient and local zoning characteristics.

As shown in **Figure 11B**, the orientation distribution of the minimum PHS of the shale gas reservoir in the Dingshan area was more complex. The variation range was wider than that of the maximum principal stress. In particular, the orientation of the minimum principal stress near several main faults in the north and northeast directions of the study area changed greatly, indicating that the orientation of the minimum PHS was also affected by faults.

The reliability of the simulation results was verified by comparing the calculation results on the *in-situ* stresses of DY1, DY2, DY3, DY4, and DY5. As shown in **Figure 12**, the maximum relative error between the maximum and minimum PHS values did not exceed 15%, while the relative error of the local position did not exceed 10%. Therefore, the method of heterogeneous geomechanical modeling proposed in this paper accurately predicted the 3D *in-situ* stress field.

CONCLUSION

1) The fracture extension directions of the Longmaxi formation in the Dingshan structure were mainly NWW, NE, approx. SN, and NNW, and the fracture development was relatively poor. The seismic interpretation results show that the structural pattern of the Longmaxi formation was high in the east and low in the west, mainly developing NE-SW, NNW-SSE fault systems and a small number of near-SN fault systems, mainly reverse faults. The implies that the area was mainly affected by tectonic compression and consistent with the *in-situ* stress distribution.

2) The maximum PHS in the study area varied within the range from 63.0 to 127.0 MPa, and the minimum PHS ranged from 48.0 to 109.0 MPa. The maximum and minimum PHS directions coincided with NE-SW and NW-SE lines, respectively. The northwest part of the study area was higher than the southeast one, and the PHS magnitude variation was directional. The maximum PHS and minimum PHS exhibited a certain correlation with the strata depth. The maximum PHS direction in the study area slightly deviated from the NE-SW direction to the near-EW direction. The minimum PHS direction coincided with the NW-SE line. The respective directions of DY3, DY2, and DY1 wells exhibited a systematic deviation from the north to the west, while that of the DY4 well deflected from the north to the east.

DATA AVAILABILITY STATEMENT

The data used for supporting the conclusion of this article are available from the corresponding authors upon request.

AUTHOR CONTRIBUTIONS

All authors contributed to this paper. QL prepared and edited the manuscript. QL and QF substantially contributed to the data analysis and revised the article. KY, QW, HL, and HW reviewed the manuscript and processed the investigation during the research process.

FUNDING

This study was supported by the Institute of Energy, Hefei Comprehensive National Science Center under Grant No.19KZS203, the Science and Technology Research Project of the Exploration Branch of Sinopec Group (35450003-19-zc0613-0002), the Natural Science Foundation of Anhui Province(1708085ME133), Chinese Excellent Young Talents Support Program Project in Universities (gxyq-ZD2019025), Graduate Innovation Fund Project of Anhui University of Science and Technology of China (2020CX1002).

REFERENCES

Bai, X., Zhang, D.-m., Wang, H., Li, S.-j., and Rao, Z. (2018). A Novel *In Situ* Stress Measurement Method Based on Acoustic Emission Kaiser Effect: a Theoretical and Experimental Study. *R. Soc. Open Sci.* 5, 181263. doi:10.1098/rsos.181263

Bell, J. S. (1996). Petro Geoscience 2. *In Situ* Stresses in Sedimentary Rocks (Part 2): Applications of Stress Measurements. *Geosci. Can.* 23, 135–153.

Chen, X., Wang, R., Huang, W., Jiang, Y., and Yin, C. (2018). Clustering-based Stress Inversion from Focal Mechanisms in Microseismic Monitoring of Hydrofracturing. *Geophys. J. Int.* 215, 1887–1899. doi:10.1093/gji/ggy388

Ciftci, N. B. (2013). *In-situ* Stress Field and Mechanics of Fault Reactivation in the Gediz Graben, Western Turkey. *J. Geodynamics* 65, 136–147. doi:10.1016/j.jog.2012.03.006

Dubey, V., Abedi, S., and Noshadravan, A. (2021). A Multiscale Modeling of Damage Accumulation and Permeability Variation in Shale Rocks under Mechanical Loading. *J. Pet. Sci. Eng.* 198, 108123. doi:10.1016/j.petrol.2020.108123

Fu, Q., Liu, Q.-j., and Yang, K. (2021). Optimization Inversion Analysis of a Geo-Stress Field in a Deep Mine Area: a Case Study. *Arab J. Geosci.* 14, 1–11. doi:10.1007/s12517-021-06880-3

Han, D., Wang, H., Wang, C., Yuan, W., Zhang, J., Lin, W., et al. (2021). Differential Characterization of Stress Sensitivity and its Main Control Mechanism in Deep Pore-Fracture Clastic Reservoirs. *Sci. Rep.* 11, 7374. doi:10.1038/s41598-021-86444-3

Han, H. X., Yin, S., and Aadnoy, B. S. (2018). Impact of Elliptical Boreholes on *In Situ* Stress Estimation from Leak-Off Test Data. *Pet. Sci.* 15, 794–800. doi:10.1007/s12182-018-0248-8

Hashimoto, C., and Matsu'Ura, M. (2006). 3-D Simulation of Tectonic Loading at Convergent Plate Boundary Zones: Internal Stress fields in Northeast Japan. *Pure Appl. Geophys.* 163, 1803–1817. doi:10.1007/s00024-006-0098-y

He, S., Wang, W., Zhou, J., Huang, Z., and Tang, M. (2015). A Model for Analysis of Wellbore Stability Considering the Effects of Weak Bedding Planes. *J. Nat. Gas Sci. Eng.* 27, 1050–1062. doi:10.1016/j.jngse.2015.09.053

Hu, W. G., Li, F. G., Fan, C. H., and Zhou, Z. Z. (2019). Prediction and Evaluation of marine Deep Shale Gas Reservoirs in Sichuan Basin: a Case Study of Dingshan Area. *Nat. gas exploration Dev.* 42, 66–77. doi:10.12055/gaskk.issn.1673-3177.2019.03.008

Jang, H., Lee, J., and Lee, J. (2015). Effect of Fracture Design Parameters on the Well Performance in a Hydraulically Fractured Shale Gas Reservoir. *Energy Exploration & Exploitation* 33, 157–168. doi:10.1260/0144-5987.33.2.157

Kim, T. H., and Lee, K. S. (2015). Pressure-transient Characteristics of Hydraulically Fractured Horizontal wells in Shale-Gas Reservoirs with Natural- and Rejuvenated-Fracture Networks. *J. Can. Pet. Tech.* 54, 245–258. doi:10.2118/176027-PA

Li, Y., Fu, S., Qiao, L., Liu, Z., and Zhang, Y. (2019). Development of Twin Temperature Compensation and High-Level Biaxial Pressurization Calibration Techniques for CSIRO *In-Situ* Stress Measurement in Depth. *Rock Mech. Rock Eng.* 52, 1115–1131. doi:10.1007/s00603-018-1618-7

Liu, H., Cui, S., Meng, Y., Zhao, X., and Han, X. (2019). Influence of Relation between Stress Field and Bedding Space on Wellbore Stability in Shale Formation. *Arab J. Geosci.* 12, 629. doi:10.1007/s12517-019-4727-z

Liu, J., Ding, W., Wang, R., YinYang, S. H., Yang, H., and Gu, Y. (2017a). Simulation of Paleotectonic Stress fields and Quantitative Prediction of Multi-Period Fractures in Shale Reservoirs: A Case Study of the Niutitang Formation in the Lower Cambrian in the Cen'gong Block, South China. *Mar. Pet. Geology.* 84, 289–310. doi:10.1016/j.marpetgeo.2017.04.004

Liu, J., Ding, W., Yang, H., Wang, R., Yin, S., Li, A., et al. (2017b). 3D Geomechanical Modeling and Numerical Simulation of *In-Situ* Stress fields in Shale Reservoirs: A Case Study of the Lower Cambrian Niutitang Formation in the Cen'gong Block, South China. *Tectonophysics* 712-713, 663–683. doi:10.1016/j.tecto.2017.06.030

Liu, J., He, Z.-l., Liu, X.-w., Huo, Z.-z., and Guo, P. (2019). Using Frequency-dependent AVO Inversion to Predict the "sweet Spots" of Shale Gas Reservoirs. *Mar. Pet. Geology.* 102, 283–291. doi:10.1016/j.marpetgeo.2018.12.039

Liu, S., Ma, W., Jansa, L., Huang, W., Zeng, X., and Zhang, C. (2013). Characteristics of the Shale Gas Reservoir Rocks in the Lower Silurian Longmaxi Formation, East Sichuan Basin, China. *Energy Exploration & Exploitation* 31, 187–219. doi:10.1260/0144-5987.31.2.187

Liu, S., Yang, Y., Deng, B., Zhong, Y., Wen, L., Sun, W., et al. (2021). Tectonic Evolution of the Sichuan basin, Southwest China. *Earth-Science Rev.* 213, 103470. doi:10.1016/j.earscirev.2020.103470

Ljunggren, C., Chang, Y., Janson, T., and Christiansson, R. (2003). An Overview of Rock Stress Measurement Methods. *Int. J. Rock Mech. Mining Sci.* 40, 975–989. doi:10.1016/j.ijrmms.2003.07.003

Lü, J., Zhou, W., Xie, R., Shan, Y., Zhang, C., and Xu, H. (2017). Three-dimensional *In Situ* Stress-Field Simulations of Shale Gas Formations: A Case Study of the 5th Member of the Xujiahe Formation in the Xinchang Gas Field, West Sichuan Depression. *Acta Geologica Sinica - English Edition* 91, 617–629. doi:10.1111/1755-6724.13121

Nian, T., Wang, G., Xiao, C., Zhou, L., Sun, Y., and Song, H. (2016). Determination of *In-Situ* Stress Orientation and Subsurface Fracture Analysis from Image-Core Integration: an Example from Ultra-deep Tight sandstone (BSJQK Formation) in the Kelasu Belt, Tarim Basin. *J. Pet. Sci. Eng.* 147, 495–503. doi:10.1016/j.petrol.2016.09.020

Rajabi, M., Tingay, M., and Heidbach, O. (2016). The Present-Day State of Tectonic Stress in the Darling Basin, Australia: Implications for Exploration and Production. *Mar. Pet. Geology.* 77, 776–790. doi:10.1016/j.marpetgeo.2016.07.021

Ren, W., and Lau, H. C. (2020). Analytical Modeling and Probabilistic Evaluation of Gas Production from a Hydraulically Fractured Shale Reservoir Using a Quad-Linear Flow Model. *J. Pet. Sci. Eng.* 184, 106516. doi:10.1016/j.petrol.2019.106516

Sun, F., Yao, Y., Li, X., Li, G., Miao, Y., Han, S., et al. (2018). Flow Simulation of the Mixture System of Supercritical CO2 & Superheated Steam in Toe-point Injection Horizontal Wellbores. *J. Pet. Sci. Eng.* 163, 199–210. doi:10.1016/j.petrol.2017.12.085

Wang, R., Hu, Z., Long, S., Liu, G., Zhao, J., Dong, L., et al. (2019). Differential Characteristics of the Upper Ordovician-Lower Silurian Wufeng-Longmaxi Shale Reservoir and its Implications for Exploration and Development of Shale Gas In/around the Sichuan Basin. *Acta Geologica Sinica - English Edition* 93, 520–535. doi:10.1111/1755-6724.13875

Yin, Z., Chen, W., Hao, H., Chang, J., Zhao, G., Chen, Z., et al. (2020). Dynamic Compressive Test of Gas-Containing Coal Using a Modified Split Hopkinson Pressure Bar System. *Rock Mech. Rock Eng.* 53, 815–829. doi:10.1007/s00603-019-01955-w

Yong, T., Fan, Y., Lv, Q. Q., Tang, W. J., and Wang, H. K. (2018). Analysis of the Tectonic Stress Field of SE Sichuan and its Impact on the Preservation of Shale Gas in Lower Silurian Longmaxi Formation of the Dingshan Region, China. *J. Geol. Soc. India* 92, 92–100. doi:10.1007/s12594-018-0957-z

Zeng, L., Wang, H., Gong, L., and Liu, B. (2010). Impacts of the Tectonic Stress Field on Natural Gas Migration and Accumulation: A Case Study of the Kuqa Depression in the Tarim Basin, China. *Mar. Pet. Geology.* 27, 1616–1627. doi:10.1016/j.marpetgeo.2010.04.010

Zhang, G. Z., Chen, J. J., Chen, H. Z., Ma, Z. G., and Yin, X. Y. (2015). Prediction for *In-Situ* Formation Stress of Shale Based on Rock Physics Equivalent Model. *Chin. J. Geophysics- Chin. Edition* 58, 2112–2122. doi:10.6038/cjg20150625

Zhao, X. G., Wang, J., Qin, X. H., Cai, M., Su, R., He, J. G., et al. (2015). *In-situ* Stress Measurements and Regional Stress Field Assessment in the Xinjiang Candidate Area for China's HLW Disposal. *Eng. Geology.* 197, 42–56. doi:10.1016/j.enggeo.2015.08.015

Zhong, C., Qin, Q., Fan, C., and Hu, D. (2019). Geochemical Characteristics of Shale Gas and its Response to thermal Maturity (Ro) in the Longmaxi Formation, Dingshan Area, Southeast Sichuan. *Pet. Sci. Tech.* 37, 1270–1278. doi:10.1080/10916466.2018.1558241

Conflict of Interest: Author QW was employed by the company Sinopec Exploration Company.

The remaining authors declare that the research was conducted in the absence of any commercial or financial relationships that could be construed as a potential conflict of interest.

frontiers
in Earth Science

ORIGINAL RESEARCH
published: 01 March 2022
doi: 10.3389/feart.2022.843191

Mining-Induced Stress and Ground Pressure Behavior Characteristics in Mining a Thick Coal Seam With Hard Roofs

Zhijie Zhu[1,2]*, Yunlong Wu[1] and Zhuang Liang[3]

[1]School of Mining, Liaoning Technical University, Fuxin, China, [2]State Key Laboratory of Coal Mining and Clean Utilization, Beijing, China, [3]Research Centre, Ministry of Emergency Management, Beijing, China

The hard roof of coal mines has the characteristics of high hardness, good integrity, and large layer thickness, which leads to many ground control problems. To reveal the influence of a hard roof structure on the stress performance and coal pillar stability during mining operations, the 8,104 and 8,105 working faces in the Tongxin coal mine were considered as the research object to analyze the stress behavior during the working face advance. Numerical simulation software FLAC^{3D} was used to establish the numerical model of the longwall face under hard roof conditions. The stress distribution laws and coal pillar stability under different roof strengths were analyzed so as to explain the impacts of the hard roof on the stress distribution at the working face. The results show that during the second face proceeding, the influence zone of the front abutment pressure under hard roof conditions is 6 m wider than that under soft roof conditions, and the bearing stress at the working face is 10.4 MPa higher. At the mining position, the plastic zone of the pillar under hard roof conditions is 11 m wider than that under soft roof conditions, and the peak vertical stress is 5.13 MPa higher than that under soft roof conditions. At 25 m ahead of the working face, the plastic zone of the pillar under hard roof conditions is 6 m wider than that under soft roof conditions, and the peak vertical stress is 24.84 MPa higher than that under soft roof conditions. Additional overburden pressure produced by the uncaved hard roof increased pillar stress and plastic zones. Therefore, the hard roof is the main cause of strong ground pressure behavior in the Tongxin coal mine. Aiming at the strong mine pressure behavior, it is suggested to adopt the pre-splitting technology to reduce the influence of the hard roof on mine pressure.

Keywords: hard roof, longwall face, coal pillar stability, mining stress, pillar stress

Edited by:
Zhiqiang Yin,
Anhui University of Science and Technology, China

Reviewed by:
Hongchao Zhao,
Xinjiang University, China
Bangyou Jiang,
Shandong University of Science and Technology, China
Wu Cai,
China University of Mining and Technology, China

***Correspondence:**
Zhijie Zhu
zhuzhijie@lntu.edu.cn

Specialty section:
This article was submitted to Geohazards and Georisks, a section of the journal Frontiers in Earth Science

Received: *25 December 2021*
Accepted: *25 January 2022*
Published: *01 March 2022*

Citation:
Zhu Z, Wu Y and Liang Z (2022) Mining-Induced Stress and Ground Pressure Behavior Characteristics in Mining a Thick Coal Seam With Hard Roofs.
Front. Earth Sci. 10:843191.
doi: 10.3389/feart.2022.843191

1 INTRODUCTION

In coal mining, hard and difficult-to-collapse roofs refer to thick, stable, and hard rock layers such as sandstone, conglomerate, or limestone that occur above the coal seam or directly on the thin layer and have the characteristics of high strength, undeveloped joints and fissures, and large thickness. The hard roof structure is frequently encountered in many mining areas. In China, the quantity of coal seams with hard overlying strata accounts for about one third of the total reserves and are distributed in over than 50% of the mining districts (Yang et al., 2019). Datong coalfield is a most typical area characterized by hard roof strata in China (Liu et al., 2021). During mining of the coal seam with hard roofs, it is difficult to effectively predict and overcome the accompanied problems such as roadway serious deformation, abnormal mine pressure, and engineering disasters. Existing theories of mine pressure and ground control cannot provide scientific guidance on dealing with these problems (Rajwa et al., 2020; Yang 2010; Zhang et al., 2021). Therefore, it is necessary to intensively study the instability mechanism when mining the coal seam with hard roofs and deeply understand the rules of ground pressure performance in hard-roof coal mining.

Wang et al., (2020) pointed out that the overlying strata will break and subside when mining the coal face in hard roof circumstances and believed the interaction among the broken rocks in the roof will produce a dynamic balance structure. Zonglong et al., (2006) presented the evolution model of hard roof breaking and elaborated the breaking mechanism of the hard roof. Mahini et al., (2013) developed a model of hard roof failure and learned the energy change during hard roof fracturing. Qin et al., (2019) calculated the collapse span of hard overlying rocks and explored the mechanism of hard roof caving. Taking the 8,939 working faces of the Xinzhouyao mine as the research site, Zhang et al., (2018) uncovered that when a hard roof breaks, a large amount of energy that is not beyond the critical value will be released by the broken rocks, leading to the coal and rock masses in an unstable state. Ardehjani et al., (2020) investigated the behavior of steep layers during the roof caving process in the gob space using numerical modeling. Bai and Tu (2016) used field observations and numerical simulation methods to investigate failure of a large span longwall drift under water-rich roofs. Das (2000) studied the splitting and caving characteristics of the strata's rocks and established the development of a roof–rock classification system to calculate the powered support capacity. Hosseini et al., (2014) calculated the periodic roof weighting interval in longwall mining using the finite element method. Ju et al., (2021) investigated the bedding adhesion strength on the stratified rock–roof fracture at the longwall coal mining face using physical and numerical methods. Juárez-Ferreras et al., (2008) proposed a new empirical formula to determine the roof pressure that the props must support, which fits longwall workings in Castile–Leon coalfields. Kang et al., (2018) created a large-scale physical model and a numerical model to study the roof failure mechanism, abutment pressure distribution, and collapsed roof pattern during longwall face retreat mining. Liu et al., (2017) studied the influence of the varying immediate roof thickness on the lower strong roof strata movement and failure pattern in longwall coal mining with a large mining height by field tests. Mohammadi et al., (2021) and Murmu and Budi (2021) presented a hybrid probabilistically qualitative–quantitative model to evaluate cavability of the immediate roof and to estimate the main caving span in longwall mining. Ning et al., (2017) investigated the mining-induced fracturing and the roof movement under the double-layer hard and thick roof *via* microseismic (MS) monitoring. Xu et al., (2015) investigated the fracturing and caving process of key strata in overburden strata and the distribution law of abutment stress over key strata and immediate roof and analyzed the effect of the rupture of key strata on abutment stress in the coal rib. Most researchers mainly focused on the structure of hard overburden, the length of roof caving, and the characteristics of overburden movement when studying the stress distribution and evolution in hard roof mines. Few efforts are made on the influence of hard roof strata on the stress behavior at the working face.

A total of 8,104 and 8,105 working faces in the Tongxin coal mine were selected as the study site in this work. The FLAC^{3D} numerical model is established to simulate the progression of the working face under different roof conditions. The influence of the stratified hard roof on the mining stress at the working face is analyzed. The influence of hard overlying rocks on the coal pillar stability was also surveyed by investigating the elastic–plastic zone and stress distribution in the coal pillar.

2 MINING CONDITIONS

The coal seam with a thickness of 15.3 m and a dip angle of 1–3° is buried at 448 m at Tongxin coal mine underground. The thickness changes a little on the whole. The roof is mainly sandstone with a steady occurrence. The roof is considered as a hard roof from the perspective of mechanical properties. The 8,104 working face is 207 m along the dip and 1932 m along the strike. A 45-m-wide pillar is reserved between the 8,104 and 8,105 working faces. The layout of the two working faces is shown in **Figure 1**. The working face adopts the comprehensive mechanized top coal caving mining methods. The mining height is 3.9 m, and the coal caving thickness is 11.59 m. Roof and floor strata distributions of three to five coal seams are shown in **Table 1**. There are three hard roofs above three to five coal seams. The section of the return air tunnel is a rectangular section, and the section size is width × height = 5,000 mm × 3,700 mm. The section of the transport roadway is a rectangular section, and the section size is width × height = 5,600 mm × 3,400 mm. The roadway adopts the joint support method of the anchor bolt, anchor cable, steel belt, and metal mesh. The spacing and row spacing of anchor bolts are 0.8 × 0.8 m, while cables are 1.6 × 1.6 m. The length of the anchor bolt and cable are 2.5 and 8.3 m.

The ground pressure behavior of fully mechanized caving face mining with the hard roof has the following characteristics:

1) The main roof first caving interval was about 130.8 m, and the periodic caving interval was about 18.3 m. Due to the large inclination length of the working face and the thickness of the top coal, the pressure of the working face was relatively large, which can reach more than 14,000 kN, and the pressure in the middle of the working face was bigger.
2) Strong ground pressure behavior occurred during the main roof weighting. The strength of weighting is high with long duration time. The safety valve is opened frequently, and the maximum retraction speed of the movable column of the support is 300 mm/h. The depth of the coal wall of the working face can reach more than 1,000 mm.

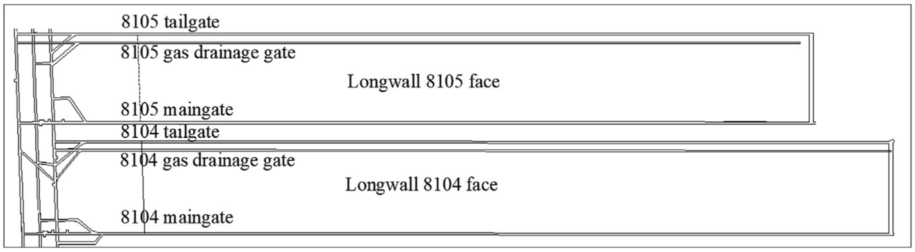

FIGURE 1 | Location map of working faces.

TABLE 1 | Roof and floor strata distribution of 3-5 coal seams.

Number	Strata name	Depth/ m	Thickness/ m	Uniaxial compressive strength/ MPa	Number	Strata name	Depth/ m	Thickness/ m	Uniaxial compressive strength/ MPa
1	Carbonaceous mudstone	460.15	6.30	7.36	23	Siltstone	313.75	3.75	55.73
2	Fine-grained sandstone	453.85	5.85	71.53	24	Mudstone	310	2.40	41.35
3	3–5 coal	448	15.30	15.94	25	Coarse-grained sandstone	307.6	6.75	43.87
4	**Coarse-grained sandstone**	**432.7**	**13.35**	**43.87**	26	Sandy mudstone	300.85	3.00	41.35
5	Siltstone	419.35	7.05	55.73	27	Siltstone	297.85	10.65	55.73
6	Coarse-grained sandstone	412.3	3.15	43.87	28	Medium-grained sandstone	287.2	1.95	56.73
7	Siltstone	409.15	4.35	55.73	29	Fine-grained sandstone	285.25	8.55	71.53
8	Sandy mudstone	404.8	5.55	41.35	30	Siltstone	276.7	17.25	55.73
9	Siltstone	399.25	1.95	55.73	31	Sandy mudstone	259.45	2.25	41.35
10	Fine-grained sandstone	397.3	1.65	71.53	32	Siltstone	257.2	3.15	55.73
11	Siltstone	395.65	2.25	55.73	33	Medium-grained sandstone	254.05	4.65	56.73
12	**Coarse-grained sandstone**	**393.4**	**14.85**	**43.87**	34	Sandy mudstone	249.4	4.80	41.35
13	Siltstone	378.55	4.35	55.73	35	Medium-grained sandstone	244.6	2.25	56.73
14	Coarse-grained sandstone	374.2	3.90	43.87	36	Sandy mudstone	242.35	1.95	41.35
15	Siltstone	370.3	4.95	55.73	37	Medium-grained sandstone	240.4	2.85	56.73
16	Mudstone	365.35	9.60	43.23	38	Sandy mudstone	237.55	17.25	41.35
17	Coarse-grained sandstone	355.75	1.80	43.87	39	Siltstone	220.3	13.95	55.73
18	Mudstone	353.95	3.15	41.35	40	Medium-grained sandstone	206.35	1.95	56.73
19	**Coarse-grained sandstone**	**350.8**	**11.85**	**43.87**	41	Fine-grained sandstone	204.4	5.55	71.53
20	Sandy mudstone	338.95	7.05	41.35	42	Siltstone	198.85	6.30	55.73
21	Coarse-grained sandstone	331.9	2.55	43.87	43	Coarse-grained sandstone	192.55	11.25	43.87
22	Sandy mudstone	329.35	15.60	41.35	44	Siltstone	181.3	19.05	55.73

The bold lines are hard roofs.

3) Under the combined action of the advance pressure of the working face and the roof pressure of the adjacent goaf, the pressure of the gob roadway is relatively large. The roof of the roadway is sinking, the floor is heaving, and the two sides are seriously deformed. The concrete spray layer on the roadway surface cracks and falls (**Figure 2**). The maximum vertical and horizontal convergences were 1.1 and 0.8 m, especially the pillar side is more serious. The steel strip of the roof is deformed in some areas, and the anchor rod is pulled off.

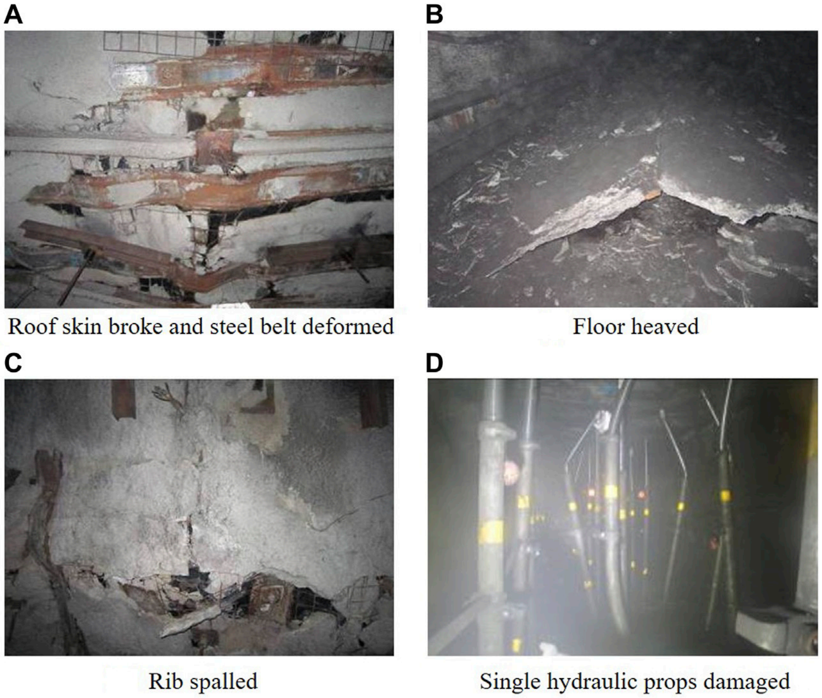

FIGURE 2 | Support damage and roadway floor heave.

TABLE 2 | Mechanical parameters of the strain-softening model.

Shear strain	Cohesion (MPa)	Internal friction angle (°)
0.000	C	Φ
0.005	C	Φ
0.010	C/2	Φ-2.5
0.050	C/5	Φ-5

C is initial cohesion, Φ is initial internal friction angle.

TABLE 3 | Estimated stress and strain of goaf materials according to Salamon's theoretical calculation.

Strain	Stress (MPa)
0	0
0.01	0.66
0.02	1.41
0.03	2.28
0.04	3.3
0.05	4.5
0.06	5.96
0.07	7.74
0.08	9.98
0.09	12.9
0.10	16.8
0.11	22.3
0.12	30.8
0.13	45.3
0.14	76
0.15	185

3 ESTABLISHMENT OF THE NUMERICAL MODEL

3.1 Selection of Constitutive Models

1) Strain-softening model for coal and rock simulation

After the stress peaks, the strength of the rock drops rapidly to a lower level as the deformation continues to increase, a phenomenon known as "strain softening". The strain-softening model believes that the properties of rock materials change with the plasticity. After plastic yielding begins, the cohesion, internal friction angle, and dilatancy angle of the rock will all attenuate with the plastic strain constantly. In the numerical simulation calculation, the strain-softening model can truly reflect the failure of the surrounding rock. Thus, this model is extensively applied in the fields of rock mechanics, geotechnical, and mining engineering. The softening parameters are shown in **Table 2**, and the internal friction angle and the cohesion of the coal and rock change with shear strain.

2) Double-yield model for goaf simulation

The gangue collapsed in the goaf is in a loose state at first and is gradually compacted under the action of its own gravity and overlying rock pressure as the working face advances. The strength and modulus of the rock mass in

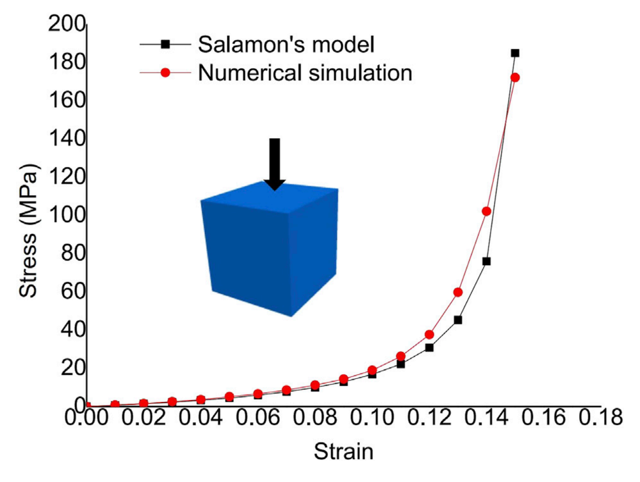

FIGURE 3 | Stress–strain curve comparison between Salamon theoretical analysis and numerical simulation.

the caving zone increase gradually during the gradual compaction process, but it is impossible to reach its original state. This progressively compacted property can be simulated using the double-yield model in FLAC3D. The double-yield constitutive model proposed by Salamon (Salamon 1990) is widely used to analyze the mechanical properties of goaf materials. The formulae are shown below:

$$\sigma = \frac{E_0 \varepsilon}{1 - \varepsilon / \varepsilon_m}, \tag{1}$$

$$\varepsilon_m = \frac{b-1}{b}, \tag{2}$$

$$b = \frac{h_{cav} + h_m}{h_{cav}}, \tag{3}$$

$$E_0 = \frac{10.39 \sigma_c^{1.042}}{b^{7.7}}. \tag{4}$$

In the equations, ε_m is the maximum strain, E_0 is the initial modulus, b is the bulking factor, hm is the height of the caving zone, h_{cav} is the mining height, and σ_c is the virgin vertical stress. According to the field data of the working face with a mining height of 15.3 m collected by the EH4 magnetotelluric imaging system, it is estimated that the caving height of the goaf is 80 m (Wu et al. 2019). Therefore, the maximum strain and bulking factor of the collapsed rock are calculated to be 0.15 and 1.16 by **Eqs 2**, **3**, respectively. **Eq. 1** is utilized to quantify the goaf displacement for making a comparison with the simulation results. **Table 3** tabulates the stress and strain of goaf materials calculated by Salamon's equations.

In order to obtain the relevant parameters of the double-yield model of the goaf in the Tongxin coal mine, a single cubic model of 1 × 1 m×1 m is established. The parameters of the model are assigned by trial and error until the stress–strain curves match each other, as shown in **Figure 3**. The two curves are in good agreement, confirming the applicability of the double-yield constitutive model in FLAC3D for goaf simulation. The mechanical parameters of the double-yield model determined that the bulk modulus was 8.6 GPa, shear modulus was 6.3 GPa, density was 2000 kg/m^3, cohesion was 0.1 MPa, internal friction angle was 5°, and dilation angle was 6°.

3.2 Model Setup and Mining Process

By taking the 8,104 and 8,105 working faces in the Tongxin coal mine as the engineering background, numerical simulation software FLAC^{3D} is used to establish a model with a size of 400 × 645 × 324.3 m (length × width × height), and the number of the model

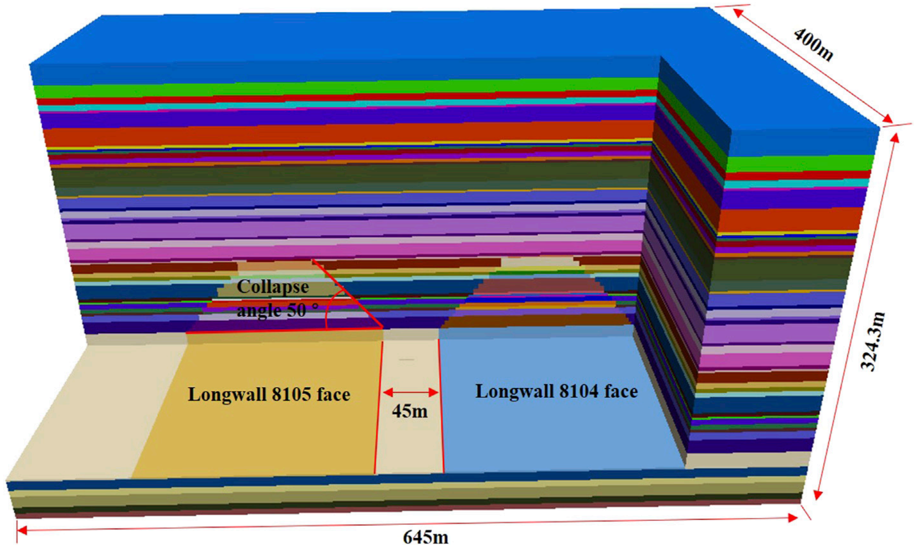

FIGURE 4 | Model stereogram.

TABLE 4 | Mechanical parameters of rock mass in each layer of the model.

Lithology	Density (kg.m-3)	Bulk modulus (GPa)	Shear modulus (GPa)	Internal friction angle (°)	Cohesion (MPa)	Tensile strength (MPa)
Coal	1,373	3.25	1.50	29.9	8.00	1.33
Siltstone	2,532	15.96	10.04	34.6	26.00	4.85
Fine sandstone	2,560	15.98	11.49	34.1	19.80	8.60
Medium sandstone	2,650	17.70	9.80	37.0	17.45	7.10
Grit sandstone	2,383	13.20	10.90	35.7	21.30	6.20
Sandy mudstone	2,570	11.25	7.75	31.3	14.20	4.40
Mudstone	2,747	4.30	2.40	24.0	7.20	2.50
Carbonaceous mudstone	2,728	3.10	1.20	28.0	5.30	2.00

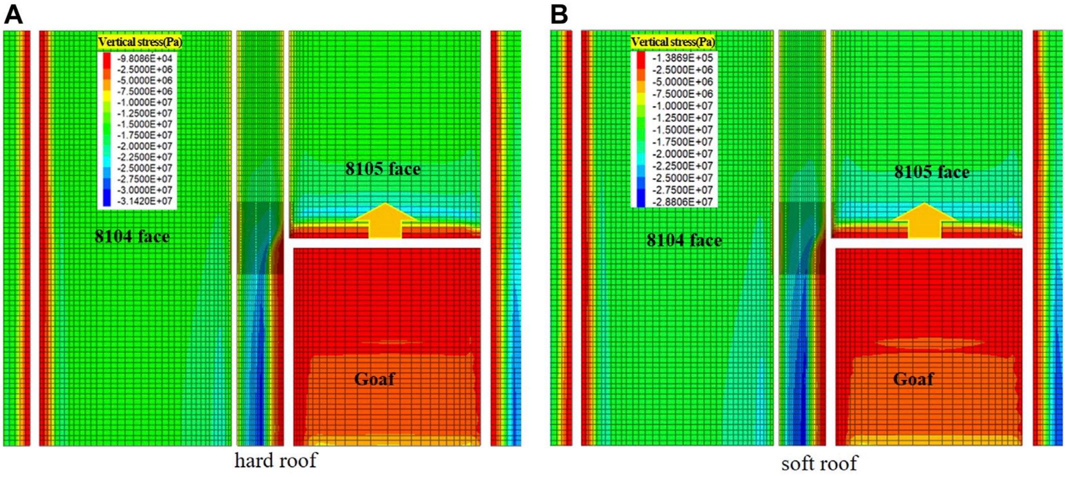

FIGURE 5 | Vertical stress distribution after primary mining under different roof strength conditions.

elements is 758,400 (**Figure 4**). Physical and mechanical parameters are described in **Table 4**. The four sides and the bottom of the model are constrained by displacement. A gradient stress of 15–24.73 MPa is applied in the advancing direction of the working face, and a gradient stress of 12.5–20.6 MPa is applied in the vertical direction of the model.

To accurately investigate the stress distribution in the coal pillar, a 65 × 65 × 65 m grid densification area is established in the middle of the model. Based on the research of Galvin (Galvin 2016), the caving angle of the hard and soft roof is set at 50° and 80°, respectively. In the numerical model of the weak roof, the strength is reduced to 25% of the hard roof. The 8,105 working face is first excavated. After it is completed, mining the 8,104 working face begins. According to the onsite situations in the mine, the 8,104 and 8,105 working faces advance 20 m every step in the numerical model.

4 NUMERICAL SIMULATION RESULTS

4.1 Influence of the Roof Strength on Mining Stress Distribution

1) Mining stress distribution at the working face during the first face advance.

The overhanging state of the roof above the working face varies with different overlying rock strengths. In hard roof conditions, as the working face proceeds, the overhanging area of the roof increases. The working face will bear more abutment pressure, and the roof is not easy to collapse, resulting in strong mining stress. In view of this, the mining stress distribution at the working face is analyzed based on numerical simulation and comparison with the mining process with soft roofs.

Figure 5 shows the mining stress distributions during mining the 8,105 working face in hard and soft roof conditions, respectively. The stress concentration area in front of the working face presents a symmetrical stripe-shape distribution. In hard roof conditions, the influence zone of the front abutment pressure is up to 80 m, the peak stress reaches 26.4 MPa, and the stress concentration factor is 1.84. In soft roof conditions, the influence zone of front abutment pressure is 74 m, the peak stress is 22 MPa, and the stress concentration factor is 1.53.

It can be seen that the roof strength has an obvious influence on the stress concentration area and stress peak value at the mining face. The influence zone of the front abutment pressure is 6 m wider, and the stress peak value is 4.4 MPa higher in hard roof conditions than that in soft roof conditions. The hard

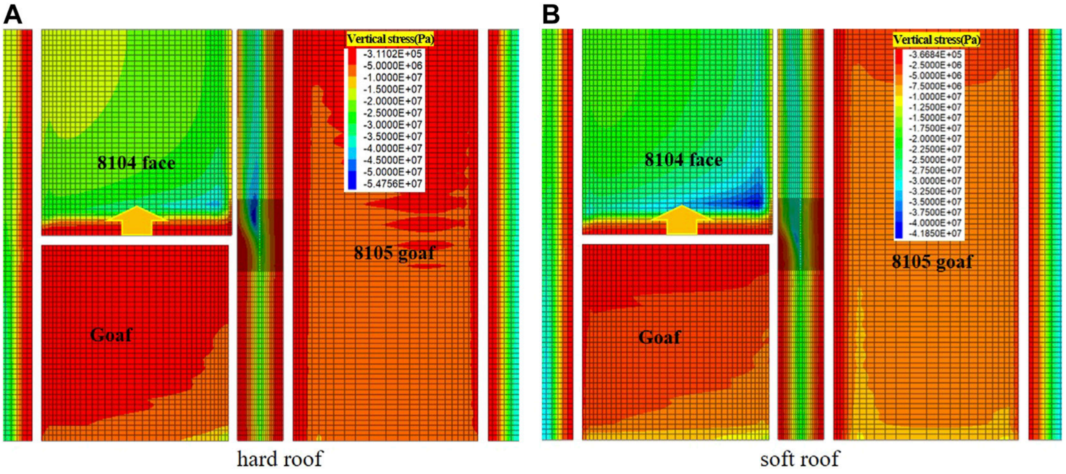

FIGURE 6 | Vertical stress distribution after secondary mining under different roof strength conditions.

overlying strata are more difficult to collapse in the mining process than soft ones and can generate a larger area affected by the higher abutment pressure. Hence, more intense mining stress is produced at the working face during mining the coal seam with a hard roof.

2) Mining stress distribution at the working face during the second face advance.

The stress distributions during mining the 8,104 working face with different roof strengths are compared. In the second mining process, the zone ahead of the working face is affected by two driving disturbances, that is, the influences of the lateral abutment pressure of the adjacent goaf and the front abutment pressure of the working face. The stress will be concentrated in the area close to the goaf, forming a triangular stress concentration zone.

Figure 6 shows the stress distributions in the second excavation under different roof conditions. For hard roof circumstances, the influence range of front abutment stress reaches 97 m, the peak stress increases to 55.4 MPa, and the stress concentration factor gets to 3.85. In the other condition, the influence range of front abutment stress is 91 m, the peak stress is 45 MPa, and the stress concentration factor is 3.13.

It can be seen that the roof strength has a significant impact on the stress concentration zone and stress peak value at the working face. The influence zone of the front abutment pressure is 6 m wider, and the stress peak value is 10.4 MPa higher than a soft overburden. The data indicate that there is greater abutment pressure in front of the working face because the overhanging length of the roof is larger under hard roof conditions. In terms of mining stress, the mining stress at the working face is higher under the condition of a hard overburden, which is more harmful to the safety of the working face.

4.2 Influence of a Hard Roof on Coal Pillar Stability

1) Influence of the roof strength on coal pillar stability in the first face advance

Figure 7 shows the coal pillar after one mining under different roof strengths. It can be seen that the 45-m-wide coal pillar is not completely yielded after the first panel extracted despite different roof conditions. The stability of the coal pillar with different roof strengths has little difference at this time. The width of the plastic zone in the coal pillar under hard roof conditions is the same as that under soft roof conditions. The elastic zone width (14 m) occupies 31.1% of the pillar width (45 m). Due to the influence of the mined-out space, the area of the coal pillar approaching the goaf is destroyed, but the yield zone fails to penetrate through the pillar which is still in a stable state.

The peak stress in the coal pillar with a hard roof is 30.83 MPa which is 4.92 MPa higher than that with a soft roof (25.91 MPa). It is clearly seen from **Figure 8** that the stress exhibits a unimodal-shape distribution due to the effect of the lateral abutment pressure in the goaf. The stress is concentrated in the area close to the solid coal. The lower stress area nearby the goaf indicates that the coal pillar at this region has yielded. The positions bearing the largest stress are basically the same under different roof strengths, but the peak stressed place is much closer to the solid coal under hard roof conditions, and the stress in the coal pillar is also greater.

2) Influence of the roof strength on coal pillar stability in the second face advance

Figure 9 shows the coal pillar after secondary mining under different roof strengths. The plastic zone in the coal pillar is enlarged due to the effects of the two goafs. It can be seen that

Elastoplastic Regional Correlation of the Coal Pillar:

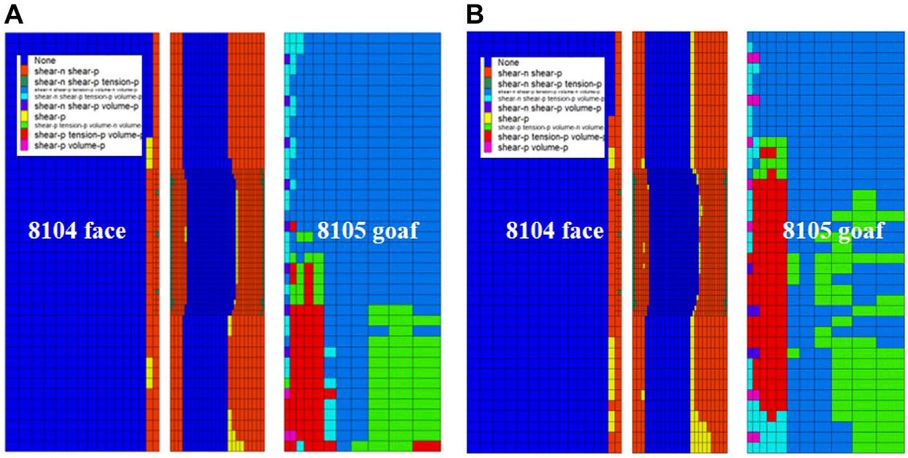

Elastoplastic zone of coal pillar under the condition of hard roof

Elastoplastic zone of coal pillar under the condition of soft roof

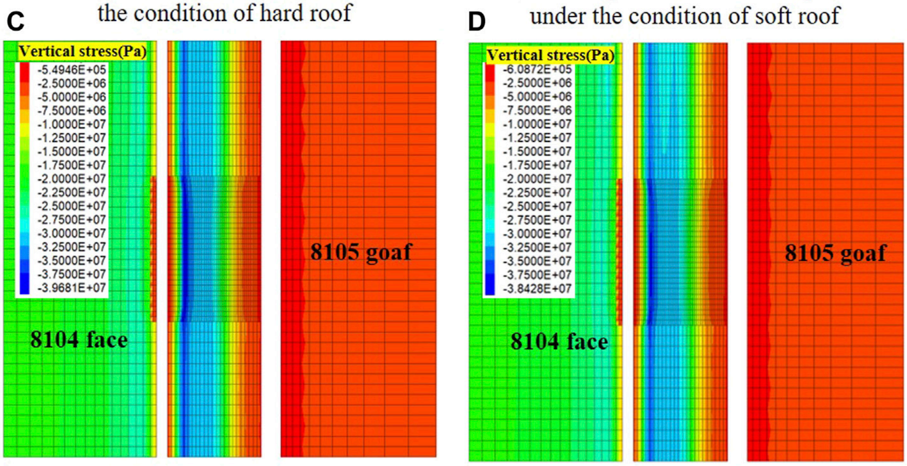

Vertical stress of coal pillar under the condition of hard roof

Vertical stress of coal pillar under the condition of soft roof

FIGURE 7 | Coal pillar stress and damage after first mining under different roof strength conditions.

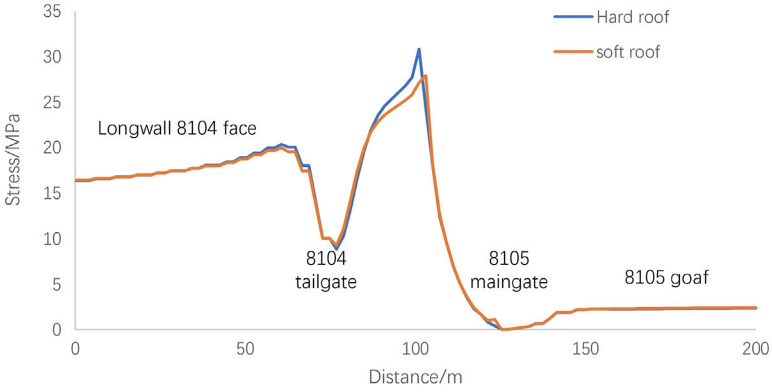

FIGURE 8 | Vertical stress curves in the pillar after the first face was excavated.

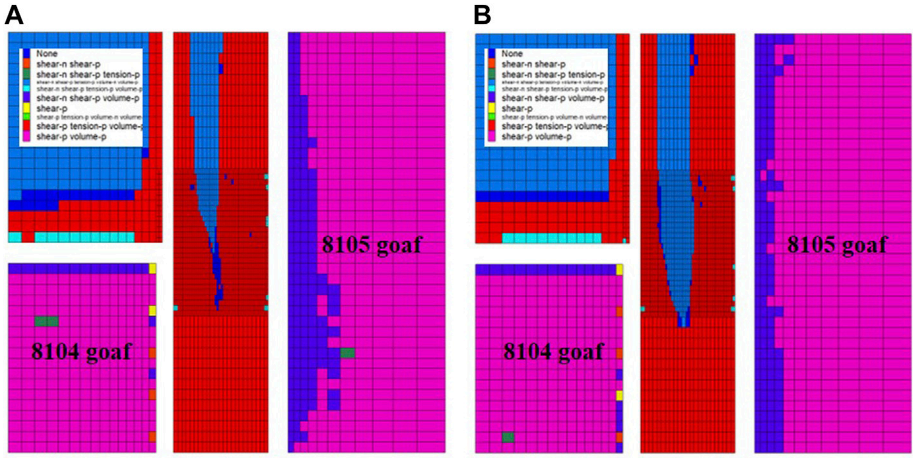

Elastoplastic zone of coal pillar under the condition of hard roof

Elastoplastic zone of coal pillar under the condition of soft roof

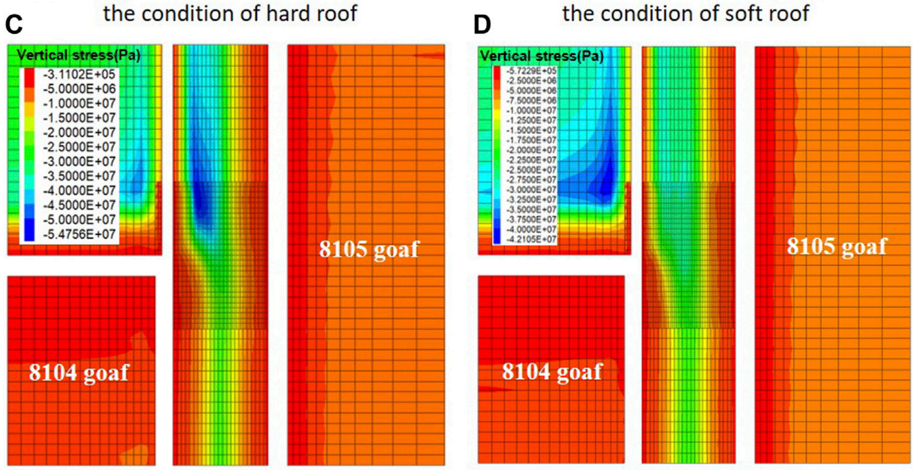

Vertical stress of coal pillar under the condition of hard roof

Vertical stress of coal pillar under the condition of soft roof

FIGURE 9 | Coal pillar stress and damage after secondary mining under different roof strength conditions.

① At 80 m behind the working face, despite different roof strengths, the 45-m-wide coal pillar is yielded in the whole width, and the coal pillar is completely destabilized owing to the influence of the two goafs.

② At the working face, the elastic zone in the pillar is 5 m, accounting for 11.1% of the total pillar width in hard roof circumstances, while the elastic zone width is 16 m, which is 35.5% of the pillar width in soft roof circumstances. Thereby, hard overlying rocks are unfavorable to the stability of working faces and mining roadways.

③ At 25 m ahead of the working face, the elastic zone width is 11 m, accounting for 24.4% of the pillar width. Regarding the soft roof, the elastic zone is 15 m, that is, 33.3% of the pillar width. The failure zone under hard roof conditions is 4 m wider than that under soft roof conditions. By comparison, the plastic failure zone in the hard roof coal pillar is bigger; the coal pillar is easier to lose stability, the roof is more prone to collapse, and the roadway is easily deformed.

④ At 80 m in front of the working face, for mining with a hard roof structure, the elastic zone width (12 m) is 26.6% of the pillar width. Considering mining the coal seam beneath the soft rock strata, the elastic zone width is 15 m and accounts for 33.3% of the pillar width. The plastic zone width in the first mining situation is 3 m larger than that in the second situation. The comparison shows that the stability of the coal pillar with a hard roof is worse than that with a soft roof, and the roadway is easier to fail.

Comparison of the Stress Distribution Diagram of the Coal Pillar (**Figures 9**, **10**):

① In spite of different roof conditions, the stress has little difference at two monitoring points, namely, 80 m behind the working face and the working face position. The peak stress in the coal pillar under hard roof conditions is 21.9 MPa and that under the other situation is 21.67 MPa. The stress values are quite similar and relatively small, implying that the coal pillar is in a complete yield state.

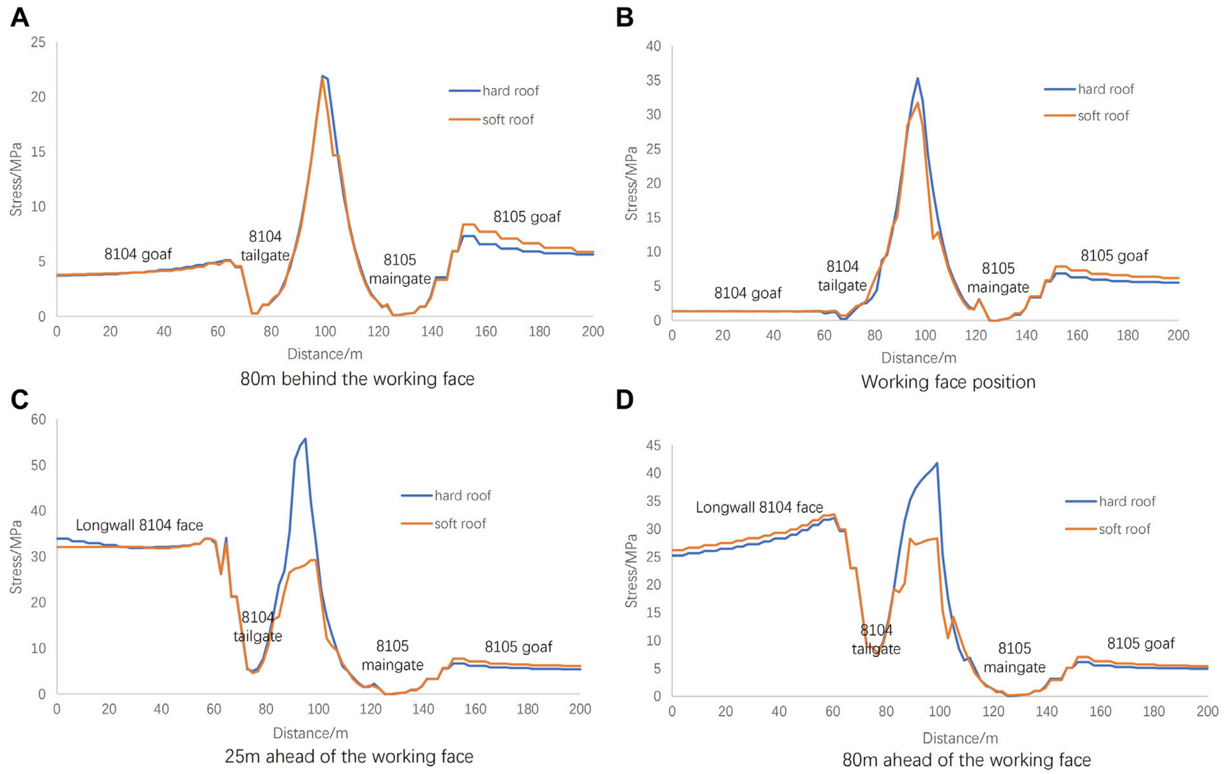

FIGURE 10 | Vertical stress distribution curve of the coal pillar at different positions.

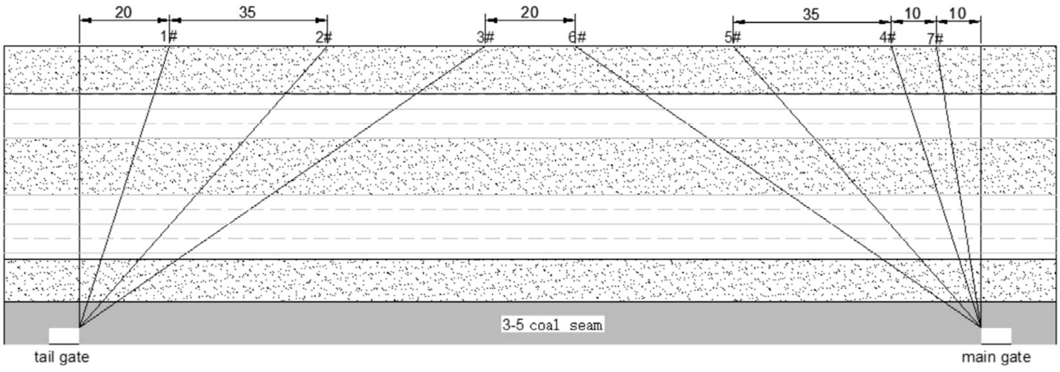

FIGURE 11 | Layout parameters of roof pre-split blasting technology.

② At the face position, the peak stress in the coal pillar with hard overlying strata is 35.27 MPa, which is 5.13 MPa higher than that with soft overlying strata (30.14 MPa). This suggests that the coal pillar is in a relatively low stress state but still in a yield condition, and the coal pillar has a poor load-bearing capacity. The overburden load will impose on the face supports. As a result, the face supports bear more loads, and the working face encounters more mining stress when extracting a coal seam with a hard roof, leading to face support damage and further influencing the stability and safety of the mining roadway and working face.

③ At 25 m in front of the working face, the maximum stress is loaded on the coal pillar. At this position, the difference in peak stress in the coal pillar under different roof strengths is the largest. The peak stress under hard roof conditions (55.76 MPa) is 24.84 MPa higher than that under soft roof circumstances (30.92 MPa). The stress state here manifests that in hard-rock coal mining, the peak stress in front of the working face acts upon the coal pillar, leading to the pillar bearing a greater stress. Hence, the coal pillar is more prone to lose stability, making the working face bear more front abutment pressure.

④ At 80 m ahead of the working face, the peak stress in the coal pillar having a hard roof is 41.77 MPa. It is 13.19 MPa higher than the peak stress in the coal pillar having a soft roof (i.e., 28.58 MPa). This shows that under hard roof conditions, the loads in the coal pillar are larger, and the pillar is easier to fail, and the roadway is more likely to deform.

3) The action mechanism of the hard roof on the working face and pillar system

With the mining of the working face, the roof strata gradually collapsed, and the pressure of the overlying strata was transferred to the coal pillars and the coal body at the goaf boundary. For the mining of extra-thick coal seams, the cantilever beam structure with a height of 80 m is formed because the range of the caving zone is as high as 80 m. For the hard roof, because it is not easy to collapse, the gangue in the goaf cannot support the cantilever beam structure. Moreover, the high-strength roof creates a larger cantilever structure on the horizontal scale. Therefore, most of the overburden pressure acts on the coal walls around the working face and pillars. If the coal pillar does not have sufficient strength, the damage of the cantilever beam structure will occur on the coal body or the coal pillar, further increasing the deformation and damage of the coal pillar. If the coal pillar has high strength, the damage of the cantilever beam structure will occur at the edge of the gob and will not increase the stress of the coal pillar.

5 DISCUSSION

1) Hard roof treatments.

In view of the influence of the hard roof on the working face and coal pillar, the roof pre-split blasting technology can be used to weaken the hard roof. The pre-splitting technology of the hard roof of the working face can destroy the complete overburden structure so that the hard roof can collapse in time and release the stress and energy and reduce damage to the working face due to dynamic load effects. At the same time, in view of the cantilever beam structure formed above the coal pillar, the goaf roof cutting technology is adopted to improve the stress state of the coal pillar and reduce the mine pressure behavior in the adjacent gob roadway. The layout parameters of presplit blasting are shown in **Figure 11**.

2) Limitations of the numerical model.

After the working face is mined, the roof stratum and surrounding rock have plastic failure, and the continuous medium is transformed into a discontinuous medium. The roof of the coal seam forms caving blocks as mining. This article simplifies the roof strata and simulates the gangue in the caving zone with a double-yield constitutive model, which is simplified according to the rock characteristics of the goaf. The surrounding rock of the working face and roadway forms a discontinuous fracture structure. The analysis in this article is based on the continuous medium, and there is a certain error with the actual situation. In the future, the continuous–discontinuous method will be used to study the stability of the coal pillar.

6 CONCLUSION

1) Mining stress evolution rules under different roof strengths are analyzed. It is found that the difference in the mining stress distribution is bigger in the second face mining. The area affected by the front abutment pressure under hard roof conditions is 6 m wider than that under soft roof conditions, and the bearing stress at the working face is 10.4 MPa higher as well.

2) At the mining position, the plastic zone of the pillar under hard roof conditions is 11 m wider than that under soft roof conditions, and the peak vertical stress is 5.13 MPa higher than that under soft roof conditions. At 25 m ahead of the working face, the plastic zone of the pillar under hard roof conditions is 6 m wider than that under soft roof conditions, and the peak vertical stress is 24.84 MPa higher than that under soft roof conditions. The working face beneath the hard overburden is disturbed by greater mining stress, and the roadway is more likely to deform and fail.

3) Concerning strong mine pressure during the working face advance, in view of hard overlying rocks, it is recommended to adopt pre-cracking techniques to reduce the influence of the roof on the appearance of strong mine pressure.

DATA AVAILABILITY STATEMENT

The original contributions presented in the study are included in the article/supplementary material, further inquiries can be directed to the corresponding author.

AUTHOR CONTRIBUTIONS

ZZ contributed to the conception of the study. YW contributed significantly to analysis and manuscript preparation. ZL contributed model analysis.

FUNDING

This work was supported by the State Key Laboratory of Coal Mining and Clean Utilization (2021-CMCU-KF016) and the Basic Scientific Research Projects of Universities in Liaoning Province (LJKZ0343).

ACKNOWLEDGMENTS

The assistance and guidance of the steering group members are gratefully acknowledged.

REFERENCES

Ardehjani, E. A., Ataei, M., and Rafiee, R. (2020). 'Estimation of First and Periodic Roof Weighting Effect Interval in Mechanized Longwall Mining Using Numerical Modeling. *Int. J. Geomechanics* 20, 1–13. doi:10.1061/(asce)gm.1943-5622.0001532

Bai, Q.-S., and Tu, S.-H. (2016). Failure Analysis of a Large Span Longwall Drift under Water-Rich Roofs and its Control Techniques. *Eng. Fail. Anal.* 67, 15–32. doi:10.1016/j.engfailanal.2016.05.028

Das, S. K. (2000). Observations and Classification of Roof Strata Behaviour over Longwall Coal Mining Panels in India. *Int. J. Rock Mech. Mining Sci.* 37, 585–597. doi:10.1016/s1365-1609(99)00123-9

Galvin, J. M. (2016). *Ground Engineering-Principles and Practices for Underground Coal Mining*. Springer.

Hosseini, N., Goshtasbi, K., Oraee-Mirzamani, B., and Gholinejad, M. (2014). Calculation of Periodic Roof Weighting Interval in Longwall Mining Using Finite Element Method. *Arab J. Geosci.* 7, 1951–1956. doi:10.1007/s12517-013-0859-8

Ju, M., Wang, D., Shi, J., Li, J., Yao, Q., and Xing, L. (2021). 'Physical and Numerical Investigations of Bedding Adhesion Strength on Stratified Rock Roof Fracture with Longwall Coal Mining. *Geomechanics Geophys. Geo-Energy Geo-Resources* 7, 1–31. doi:10.1007/s40948-020-00209-2

Juárez-Ferreras, R., González-Nicieza, C., Menéndez-Díaz, A., Álvarez-Vigil, A. E., and Álvarez-Fernández, M. I. (2008). Measurement and Analysis of the Roof Pressure on Hydraulic Props in Longwall. *Int. J. Coal Geology.* 75, 49–62. doi:10.1016/j.coal.2008.01.007

Kang, H., Lou, J., Gao, F., Yang, J., and Li, J. (2018). A Physical and Numerical Investigation of Sudden Massive Roof Collapse during Longwall Coal Retreat Mining. *Int. J. Coal Geology.* 188, 25–36. doi:10.1016/j.coal.2018.01.013

Liu, C., Li, H., Mitri, H., Jiang, D., Li, H., and Feng, J. (2017). Voussoir Beam Model for Lower strong Roof Strata Movement in Longwall Mining - Case Study. *J. Rock Mech. Geotechnical Eng.* 9, 1171–1176. doi:10.1016/j.jrmge.2017.07.002

Liu, J., Li, C., Shi, Y., and Zhang, Y. (2021). Stability Analysis and Fracture Patterns of Hard Main Roof in Longwall Top Coal Caving with Large Mining Height. *Shock and Vibration* 2021, 9930221. doi:10.1155/2021/9930221

Mahini, M. R., Moharrami, H., and Cocchetti, G. (2013). A Dissipated Energy Maximization Approach to Elastic-Perfectly Plastic Analysis of Planar Frames. *Arch. Mech.* 65, 171–194.

Mohammadi, S., Ataei, M., Kakaie, R., Mirzaghorbanali, A., and Aziz, N. (2021). A Probabilistic Model to Determine Main Caving Span by Evaluating Cavability of Immediate Roof Strata in Longwall Mining. *Geotech Geol. Eng.* 39, 2221–2237. doi:10.1007/s10706-020-01620-y

Murmu, S., and Budi, G. (2021). A Probability-Based Risk Assessment of Roof Strata Weighting in Longwall Panels. *Arabian J. Geosciences* 14, 1–16. doi:10.1007/s12517-021-06637-y

Ning, J., Wang, J., Jiang, L., Jiang, N., Liu, X., and Jiang, J. (2017). Fracture Analysis of Double-Layer Hard and Thick Roof and the Controlling Effect on Strata Behavior: A Case Study. *Eng. Fail. Anal.* 81, 117–134. doi:10.1016/j.engfailanal.2017.07.029

Qin, S., Li, Y., and Sun, L. (2019). 'Stability Evaluation of Karst Cave Roof under Pile in Karst Areas Based on the Interval Non-probabilistic Reliability Method. *Hydrogeology Eng. Geology.* 46, 81–88. doi:10.16030/j.cnki.issn.1000-3665.2019.05.11

Rajwa, S., Janoszek, T., and Prusek, S. (2020). 'Model Tests of the Effect of Active Roof Support on the Working Stability of a Longwall. *Comput. Geotechnics* 118, 103302. doi:10.1016/j.compgeo.2019.103302

Salamon, M. D. G. (1990). "Mechanism of Caving in Longwall Coal Mining," in *Rock Mechanics Contributions and Challenges: Proceedings of the 31st US Symposium* (Golden, Colorado: Publ Rotterdam, 161–168.

Wang, H., Chen, X., Zhou, Y., Xia, B., Wang, J., Zhao, S., et al. (2020). A Method Based on Elastic Mechanics for Judging Compound Hard Roof and its Application. *Shock and Vibration* 2020, 8867259. doi:10.1155/2020/8867259

Wu, W.-D., Bai, J.-B., Wang, X.-Y., Zhu, Z.-J., and Yan, S. (2019). Field Investigation of Fractures Evolution in Overlying Strata Caused by Extraction of the Jurassic and Carboniferous Coal Seams and its Application: Case Study. *International Journal of Coal Geology* 208, 12–23. doi:10.1016/j.coal.2019.04.002

Xu, T., Yang, T.-h., Chen, C.-f., Liu, H.-l., and Yu, Q.-l. (2015). Mining Induced Strata Movement and Roof Behavior in Underground Coal Mine. *Geomech. Geophys. Geo-energ. Geo-resour.* 1, 79–89. doi:10.1007/s40948-015-0010-2

Yang, S., Wang, J., Li, X., Ning, J., and Qiu, P. (2019). *In Situ* investigations into Mining-Induced Hard Main Roof Fracture in Longwall Mining: A Case Study. *Eng. Fail. Anal.* 106, 104188. doi:10.1016/j.engfailanal.2019.104188

Yang, Z. L. (2010). Stability of Nearly Horizontal Roof Strata in Shallow Seam Longwall Mining. *Int. J. Rock Mech. Mining Sci.* 47, 672–677. doi:10.1016/j.ijrmms.2010.03.001

Zhang, H., Cao, Y., Zhu, F., and Shao, L. (2018). 'Precursor Discrimination and Mechanism of Rock Burst in the Island Workface with Hard Roof. *Coal Geology. Exploration* 46, 118–123. doi:10.3969/j.issn.1001-1986.2018.02.018

Zhang, J., Zhang, Y., Du, W., Wang, H., and Serati, M. (2021). An Analytical Approach to Estimate the Mechanical State of Roof Strata in Underground Longwall Mining. *Geomechanics Eng.* 27, 55–62. doi:10.12989/gae.2021.27.1.055

Zonglong, M. U., Linming, D. O. U., Zhang, G., Zhang, S., Zhihua, L. I., and Zhang, J. (2006). Study of Prevention Methods of Rock Burst Disaster Caused by Hard Rock Roof. *J. China Univ. Mining Technology. Nat. Sci.* 35, 737–741. doi:10.1093/carcin/bgm010

Conflict of Interest: The authors declare that the research was conducted in the absence of any commercial or financial relationships that could be construed as a potential conflict of interest.

frontiers in Earth Science

ORIGINAL RESEARCH
published: 28 March 2022
doi: 10.3389/feart.2022.797358

Characteristics of Microseismic Waveforms Induced by Underground Destress Blasting: Comparison With Those Induced by Ground Blasting and Coal Mining

***Jiliang Kan*[1,2], *Linming Dou*[1,2]*, *Jiazhuo Li*[3], *Xuwei Li*[1,2], *Jinzheng Bai*[1,2] and *Mengqi Wang*[4]**

[1]Key Laboratory of Deep Coal Resource Mining, Ministry of Education, China University of Mining and Technology, Xuzhou, China, [2]School of Mines, China University of Mining and Technology, Xuzhou, China, [3]School of Energy Resources and Safety, Anhui University of Science and Technology, Huainan, China, [4]Zienkiewicz Centre for Computational Engineering, College of Engineering, Swansea University, Swansea, United Kingdom

Some industrial activities in mines, such as underground coal mining, destress blasting for preventing rockburst, and ground blasting for mining, can cause microseismic occurrence. The microseismic waveform contains abundant information on the hypocenter and propagation path, which is valuable to study the microseismic mechanism and propagation. Therefore, this study adopts the multifractal detrended fluctuation analysis (MF-DFA) and the Hilbert–Huang transform (HHT) method to study the nonlinear and time–frequency–energy characteristics of different types of microseismic waveforms. The microseismic waveform induced by mining and destress blasting has a higher dominant frequency (above 100 Hz) and shorter duration (less than 0.5 s) than ground blasting-induced microseismic waveforms (dominant frequency below 25 Hz and duration more than 3 s). Furthermore, for destress blasting-induced microseismic waveforms, the waveform is characterized by rich spectrum, complex energy attenuation, developed coda wave, and clear multifractal characteristics, which indicate that the waveform is more complex and variable. The complex underground geological environment and the superposition effect of blasting stress and mining stress are the main reasons. Moreover, the propagation distance and source energy of microseismic waveforms also greatly affect waveform characteristics. The results show that the waveform information of destress blasting-induced microseismic waveforms can describe the release process of blasting stress and mining stress. Based on this, a blasting efficiency index B_e was proposed to evaluate the effect of pressure relief, and the classification system was developed. Then, the evaluation index was successfully applied to 63 rounds of destress blasting in the Yutian coal mine. The research results can provide a certain reference for some work such as the identification of different microseismic, rock dynamic failure process analysis, and evaluation of the destress blasting effect.

Keywords: induced microseismic, microseismic waveform, multifractal characteristics, time–frequency–energy characteristics, blasting efficiency index

Edited by:
Yilin Gui,
Queensland University of Technology,
Australia

Reviewed by:
Zhenlei Li,
University of Science and Technology
Beijing, China
Longjun Dong,
Central South University, China

****Correspondence:***
Linming Dou
lmdou@126.com

Specialty section:
This article was submitted to
Geohazards and Georisks,
a section of the journal
Frontiers in Earth Science

Received: *18 October 2021*
Accepted: *07 March 2022*
Published: *28 March 2022*

Citation:
Kan J, Dou L, Li J, Li X, Bai J and
Wang M (2022) Characteristics of
Microseismic Waveforms Induced by
Underground Destress Blasting:
Comparison With Those Induced by
Ground Blasting and Coal Mining.
Front. Earth Sci. 10:797358.
doi: 10.3389/feart.2022.797358

INTRODUCTION

Microseismic emission during the rock failure process is a common phenomenon in mines around the world. The elastic vibration wave will be produced in the failure process of rocks under external disturbance (such as blasting, drilling, hydraulic fracturing, and mining), which will propagate in the rock and be recorded by microseismic sensors. In general, most induced microseismic events with small magnitude are unfelt and nondestructive. However, more and more engineering practices have shown that microseismic events with large magnitude occur in mines due to coal mining, fracture of the hard roof, or destress blasting. These large-magnitude microseismic events may cause the destruction of underground structures or even induce the dynamic disaster of rockburst and casualties (Li et al., 2007; Dou et al., 2018; Yin et al., 2020; Cai et al., 2021). For example, in August 2007, a magnitude 3.9 seismic event induced by the coal pillar burst occurred in the Utah coal mine, resulting in casualties (Dreger et al., 2008; Pechmann et al., 2008). Microseismic events induced by hydraulic fracturing for the development of gas and geothermal resources or the massive rupture of underground rock strata are also pervasive in mining countries around the world (Bao and David, 2016; Brudzinski and Kozłowska, 2019; Tan et al., 2020). Destress blasting for preventing rockburst in coal mines also induces large-magnitude microseismic events, which may cause damage to roadway and equipment (Konicek and Waclawik, 2018; Drover and Villaescusa, 2019). Research studies on induced microseismic events have been carried out fruitfully in recent decades. For example, Zhu et al. (2016), He et al. (2017), Cai et al. (2019), and Wojtecki et al. (2021) predicted rockburst based on mining-induced microseismic event parameters (source energy, frequency, and location) in coal mines. They found that the occurrence of a microseismic event is highly correlated with the coal and rock failure processes, and microseismic data can provide valuable information for the prediction of rockburst. Moreover, the microseismic waveform induced by destress blasting was also used to evaluate pressure-relief effects, which can guide the parameter design of destress blasting (Wojtecki and Konicek, 2016; Wen et al., 2020). Therefore, it is essential to study induced microseismic waveforms deeply, which can improve the understanding of the destruction process of large-magnitude microseismic events or the utilization of microseismic data for some useful work.

Microseismic signals can be regarded as the response of rock medium to the dynamic disturbance at the microseismic source, which means it contains rich information of the hypocenter and propagation medium property. Different types of induced microseismic waveforms have different focal mechanisms and propagation characteristics due to different induced factors and propagation medium properties. Amplitude, frequency, and duration are the three basic parameters of microseismic waveforms, which have been concerned by many researchers. In the past few decades, the fast Fourier transform (FFT), short-time Fourier transform (STFT), and wavelet analysis theory have been successively used to study the time–frequency characteristics of natural earthquakes or induced microseismic waveforms (Stockwell et al., 1996; Chen et al., 2002; Mucciarelli et al., 2004; Salajegheh and Heidari 2005; Yin et al., 2018). However, the aforementioned methods have limitations in the analysis of nonlinear and non-stationary waveforms. To overcome this weakness, some new analysis methods, such as the Wigner–Ville distribution, Hilbert–Huang transform, and machine learning, have been developed for analyzing the microseismic waveforms and obtained many encouraging results (Huang et al., 1998; Li and Zheng, 2007; Reynen and Audet, 2017; Shang et al., 2017; Dong et al., 2020). Fan et al. (2017) and Danqing Song et al. (2020) investigated the time–frequency characteristics of the earthquake waveforms and the seismic failure mechanism using the HHT method. Liu and Gao (2020) and Ma et al. (2021) used the HHT method to study tunnel blasting vibration signals. Guangdong Song et al. (2020) used convolutional neural networks and the Stockwell transform to identify microseismic and blasting signals. Dong et al. (2015, 2016) established discriminators for mine seismic events and blasts using the Fisher classifier, naive Bayesian classifier, and logistic regression. In addition, as a powerful tool to describe nonlinear and unstable signals, multifractal analysis has been widely used to study microseismic signals generated during rock fracture. Qiu et al. (2020) and Li et al. (2020b) obtained rock failure signals at different loading stages in the laboratory and analyzed the nonlinear characteristics of signals by multifractal theory. Li et al. (2017, 2021) analyzed the multifractal characteristics of mining and blasting signals and then proposed a discriminant model to distinguish the microseismic events induced by coal mining and blasting. Li et al. (2020a) combined HHT and multifractal methods to analyze the waveform characteristics of three types of induced microseismic waveforms (natural earthquakes, microseismic induced by hydraulic fracturing, and mining activities). Based on the results mentioned before, a foundation for the understanding of the focal mechanism, assessment of seismic damage effects, and identification of different microseismic events was constructed.

Compared to natural earthquakes, due to the diversity of production operations (coal mining, destress measures, and ground blasting) and complex underground geological conditions in coal mines (roadway, gob, geological structure, joint, etc.), the induced microseismic in coal mines is more complex in the focal mechanism and propagation process. However, research on induced microseismic events in coal mines has just been unfolding. At present, there is little literature that makes systematic research on waveform characteristics of induced microseismic and analysis of the influencing factors. Therefore, by taking the Yutian coal mine, Xinjiang province, China, as an example, this study investigated waveform characteristics (time–frequency, attenuation, and nonlinear characteristics) of some typical induced microseismic in coal mines (microseismic induced by coal mining, ground blasting, and destress blasting) through multifractal and HHT methods. Furthermore, the internal relations among waveform characteristics with focal mechanisms, microseismic source energy, and propagation

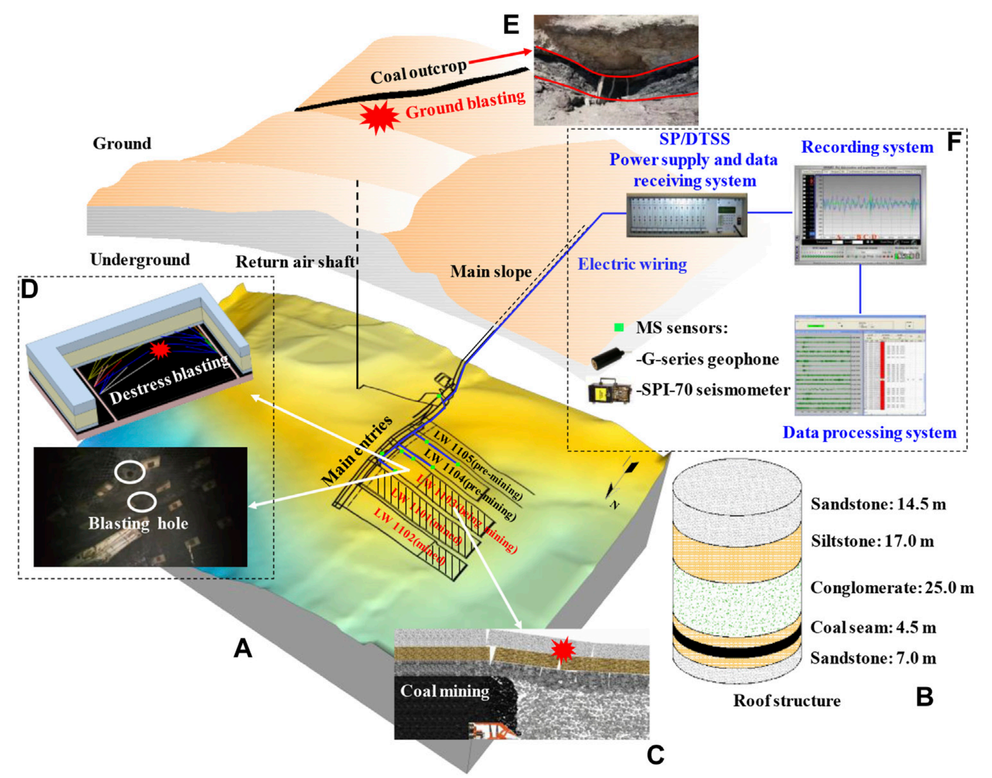

FIGURE 1 | Related information of 3-3# coal seam in the Yutian coal mine. **(A)** 3–3# coal mine floor and layout of longwall panel; **(B)** roof structure; **(C)** coal mining and roof breakage; **(D)** destress blasting in the roof; **(E)** ground blasting in coal outcrop; and **(F)** microseismic monitoring system.

distance were also discussed. Finally, a blasting efficiency index B_e was proposed to evaluate the effect of pressure relief, and the classification system was developed. This research is meaningful for further revealing the failure mechanism of microseismic waveforms, distinguishing different types of microseismic events, and evaluating pressure-relief effects of destress blasting.

DATA PREPARATION AND PREPROCESSING

Data Acquisition and Selection

The induced microseismic waveforms were collected in the Yutian coal mine, which locates in the middle west of the Kerjian mining area of Xinjiang province, China. In this coal mine, the coal seam 3-3# with 400–600 m depth and 4.5 m height was mainly mined. By October 2019, longwall panel (LW) 1103 is being mined, LW 1101 and 1102 have been mined, and LW 1104 and 1105 are planned to be mined later (see **Figure 1A**). There are multiple thick and hard sandstone above the 3-3# coal seam (see **Figure 1B**). In coal mines, the microseismic signal can be divided into two types according to the source; the first is generated by human production operations, such as blasting for mining and destress measures. The second is induced by mining activities, such as coal-rock failure, strata caving, and fault slip. However, influenced by the propagation medium and environment, the microseismic signal with the same type of source may also show great differences. At this time, the microseismic signals need to be further divided. In this research, three types of induced microseismic waveforms were divided as follows. First, coal and rock mass are destroyed accompanied by the release of accumulated elastic energy during coal mining. At this time, microseismic events are generated and propagated. This type of microseismic event can be named as the mining-induced microseismic event (see **Figure 1C**). Moreover, LW 1103 suffers from a severe rockburst risk under the thick and hard conglomerate roof during mining, and underground destress blasting was implemented to prevent rockburst. Blasting in rocks will cause elastic vibration of rock around the blasting location, which propagates outward in the form of elastic waves. This type of microseismic event belongs to destress blasting-induced microseismic (see **Figure 1D**). In addition, there are multiple layers of the shallow coal seam in the Kerjian mining area, and coal seam outcrops are distributed in the Yutian coal mine. It is easy to cause spontaneous combustion in coal seam outcrops, resulting in environmental pollution, resource waste, and threats to personnel safety. Therefore, blasting in coal mine outcrops areas was carried out to remove the coal and avoid its spontaneous combustion (see **Figure 1E**). Similarly, ground blasting will also produce seismic waves, which are received by underground microseismic sensors and can be recorded as ground blasting-induced microseismic waveforms.

Since July 2015, a microseismic monitoring system "ARAMIS M/E" has been installed in the Yutian coal mine.

TABLE 1 | Information of induced microseismic events.

Number	Microseismic event type	Source energy/J
1	Ground blasting-induced microseismic (GB-M-1)	1.1×10^6
2	Ground blasting-induced microseismic (GB-M-2)	8.6×10^5
3	Mining-induced microseismic (M-M-1)	7.5×10^6
4	Mining-induced microseismic (M-M-2)	7.2×10^6
5	Destress blasting-induced microseismic (DB-M-1)	1.5×10^7
6	Destress blasting-induced microseismic (DB-M-2)	1.7×10^7
7	Destress blasting-induced microseismic (DB-M-3)	2.9×10^7
8	Destress blasting-induced microseismic (DB-M-4)	3.9×10^7

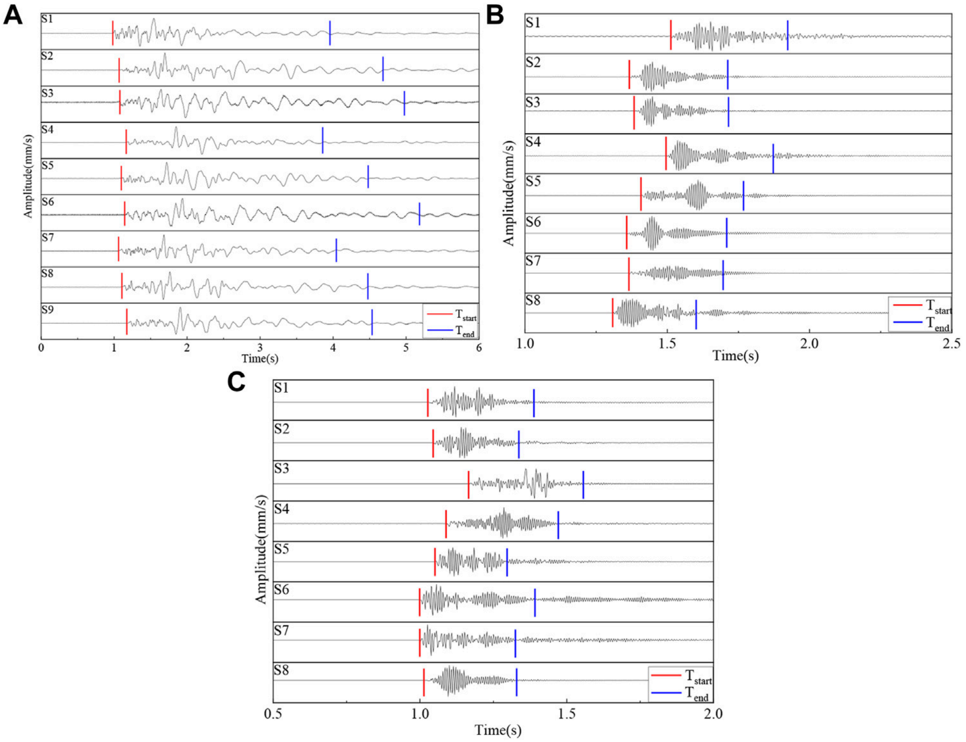

FIGURE 2 | Waveforms of different types of induced microseismic waveforms. **(A)** Ground blasting-induced microseismic (GB-M-1); **(B)** mining-induced microseismic (M-M-1); and **(C)** destress blasting-induced microseismic (DB-M-1).

This system includes underground microseismic sensors (G-series geophone and SPI-70 seismometer) and the ground analysis system (power supply and data receiving system, recording system, and data processing system). The underground hardware allows for automatic triggering and recording of various induced microseismic events. The piece of software enables data processing to obtain source location and energy calculation information of microseismic events (see **Figure 1F**). For destress blasting or ground blasting, the blasting operator will inform the technicians who operated the monitoring system information about the blasting position, time, and type in advance. Then, the corresponding microseismic event will be marked and saved. The waveform received by each microseismic sensor can be recorded and exported. The following study focuses on the microseismic waveform characteristics of different types of induced microseismic waveforms (microseismic induced by coal mining, ground blasting, and destress blasting). Two ground blasting-induced microseismic events (GB-M-1 and GB-M-1), two mining-induced microseismic events (M-M-1 and M-M-2), and four destress blasting-induced microseismic events (DB-M-1, DB-M-2, DB-M-3, and DB-M-4) were selected as research objects. The information of eight induced microseismic events is shown in **Table 1**.

Figure 2 shows the waveforms of some typical induced microseismic events in **Table 1**. For all the induced microseismic waveforms, the arrival time of the P wave can be accurately picked. However, limited by the coal mine

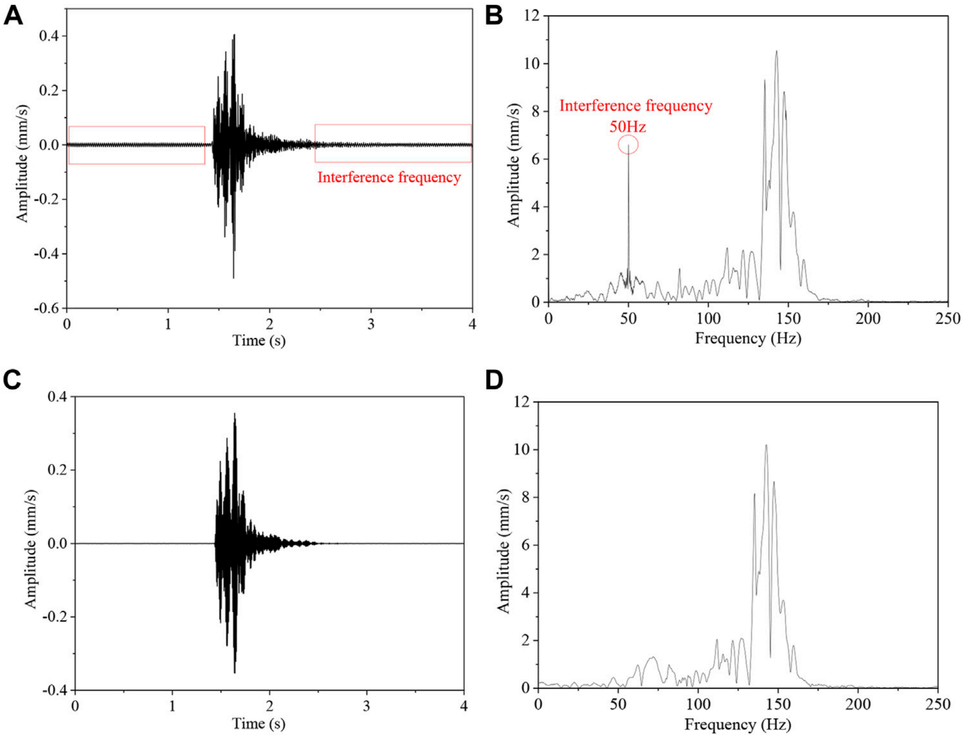

FIGURE 3 | Waveform and frequency spectrum of original and de-noising waveform. **(A)** Original waveform; **(B)** frequency spectrum of the original waveform; **(C)** de-noising waveform; and **(D)** frequency spectrum of the de-noising waveform.

conditions, both the source rupture scale and the distance between the microseismic sensors and the source are relatively small, resulting in a small-time difference in the arrival of P and S waves to microseismic sensors. Therefore, the exact arrival time pickup of the S wave is a challenging task. The duration of the ground blasting-induced microseismic waveform is generally 3–4 s, which is far longer than that of mining and destress blasting-induced microseismic waveforms (less than 0.5 s). The waveform appearance of the ground blasting-induced microseismic is more clear, simple, and regular. Existing research studies show that microseismic waveforms are related to the magnitude, propagation distance, propagation medium, and sensor property. Due to the existence of underground roadway, gob, and fault structures, the propagation path of microseismic in the underground is more complicated. Moreover, the distance between the source of microseismic induced by mining and destress blasting and the sensor is relatively small (generally 30–500 m), which leads to the microseismic wave being greatly affected by the propagation medium and path. However, the distance between the source of ground blasting-induced microseismic and the sensor is relatively far (more than 1000 m), and the rock structure and properties along the propagation path are more stable and uniform. Therefore, in terms of the propagation medium and path, the microseismic waveforms induced by mining and destress blasting are usually more complicated.

Data Preprocessing

In general, there are lots of machines used for production activities in underground roadways, including the shearer, transport machine, drilling machine, and microseismic monitoring system. These machines are usually powered by alternating current or AC/DC transformers. During the operation of the microseismic monitoring system, it is inevitable to be interfered by the power frequency of the aforementioned machines, which leads to the distortion of microseismic signals. For instance, a waveform recorded by one of the sensors in the microseismic induced by underground destress blasting is shown in **Figure 3A**. There are noise signals with fixed amplitude in the original waveform. FFT was performed on the original signal. The result shows that there is an interference signal with a frequency of 50 Hz (**Figure 3B**). Therefore, the noise signals in the microseismic waveforms need to be filtered out before the formal analysis. This study used the complete EEMD with adaptive noise (CEEMDAN) and the wavelet packet threshold de-noising method to de-noise. The signal de-noising steps are as follows (Wang et al., 2021; Zhao et al., 2021). The method first uses the CEEMDAN method to decompose the original signal and obtain the finite number of modal components. Then, the correlation coefficient between the modal component and the original signal is calculated. Next, the modal components with high correlation are retained, and the modal components with low correlation are removed. The retained modal components are reconstructed to obtain a new signal. Finally, the wavelet packet threshold method was used to perform noise reduction on the reconstructed signal. The waveform and frequency spectrum of the de-noised signal by the aforementioned method are shown in **Figures 3C,D**, respectively. The results show the interference signals have been removed, and the main characteristics of the original signal are retained.

TIME–FREQUENCY–ENERGY AND MULTIFRACTAL CHARACTERISTICS OF WAVEFORMS

Hilbert–Huang Transform Theory

The microseismic signals are typically nonlinear and non-stationary random signals, which have the characteristics of instantaneousness and fast mutation, so it is particularly important to analyze the local characteristics of the microseismic signal. HHT is a time–frequency local analytical method suitable for nonlinear and unstable signals. The HHT method first uses EMD to decompose a complex signal into finite inherent mode functions (IMF), and then performs the Hilbert transform on the decomposed IMF components to obtain the time–frequency distribution. The calculation steps of the EMD and Hilbert transform algorithm are as follows (Huang et al., 1998; Peng et al., 2005; Li et al., 2016).

All the maximum and minimum points of signal time–velocity curve X(t) are found first, and then, the upper and lower envelopments of the original sequence are fitted using the cubic spline function. Second, a new sequence h_1(t) can be created by subtracting the mean of the upper and lower envelopments m_1(t) from X(t):

$$h_1(t) = X(t) - m_1(t). \tag{1}$$

The IMF must meet the following two conditions: first, the extreme point of the signal is equal to the number of zero-crossing points or at most one difference, and second, the average value between the upper and lower envelopes defined by the local extreme points is zero. If h_1(t) satisfies the aforementioned two conditions, then h_1(t) is an IMF. Otherwise, repeat the screening process k times until the h_{1k}(t) becomes a certain IMF:

$$h_{1k}(t) = h_{1(k-1)}(t) - m_{1k}(t). \tag{2}$$

The first eigenmode function component $c1$ is obtained, which represents the highest frequency of the data sequence X(t).

A new data sequence r_1(t) can be constructed by subtracting $c1$ from X(t):

$$r_1(t) = X(t) - c_1(t). \tag{3}$$

r_1(t) has performed the aforementioned decomposition to obtain the second eigenmode function component $c2$, and this process is repeated until the last data sequence r_n cannot be decomposed. At this time, r_n represents the trend of the data sequence X(t).

Multiple IMF components are obtained by EMD decomposition of signal X(t), and each IMF component is subjected to the Hilbert transform:

$$H[c(t)] = \frac{1}{\pi} PV \sum_{-\infty}^{+\infty} \frac{c(t')}{t-t'} dt', \tag{4}$$

where PV denotes the Cauchy principal value and then constructs the analytical signal Z(t):

$$Z(t) = a(t)e^{j\phi(t)}, \tag{5}$$

$$a(t) = \sqrt{c^2(t) + H^2[c(t)]}, \tag{6}$$

$$\phi(t) = \arctan\frac{H[c(t)]}{c(t)}. \tag{7}$$

The instantaneous frequency is defined as follows:

$$\omega(t) = \frac{d\phi(t)}{dt}. \tag{8}$$

The Hilbert spectrum can be calculated as follows:

$$H(\omega, t) = Re\sum_{i=1}^{n} a_i(t)e^{j\int \omega_i(t)dt}. \tag{9}$$

The Hilbert marginal energy spectrum E(ω) and Hilbert instantaneous energy spectrum IE(t) can be obtained by integrating the square of H (ω, t) in the time and frequency domain, respectively.

$$E(\omega) = \int_0^t H^2(\omega, t)dt, \tag{10}$$

$$IE(t) = \int_{\omega} H^2(\omega, t)dt. \tag{11}$$

Multifractal Detrended Fluctuation Analysis Method

Fractal theory, first proposed by Mandelbrot, is an effective tool to describe unstable and complex signals. Fractal establishes the relationship between the local-scale characteristics and global characteristics of signals. Multifractal analysis has been applied to study the nonlinear characteristics of natural earthquakes and induced microseismic signals. However, the current multifractal analysis based on the partition function method is not enough to highlight the local singularity feature of non-stationary signals. Kantelhardt et al. (2002) proposed the MF-DFA method, which can effectively analyze the multifractal property of non-stationary signals. Xu et al. (2011) and Fu et al. (2020) introduced the MF-DFA method into the analysis of blasting signal and rock failure signals. This research used the MF-DFA method to analyze the nonlinear characteristics of different types of induced microseismic signals.

The induced microseismic signals are one-dimensional time series. For a nonlinear and non-stationary microseismic signal x_k with length N, the steps of the MF-DFA method are as follows (Telesca et al., 2004):

1) Removing the mean value of x_k and constructing a sum sequence.

$$y_i = \sum_{k=1}^{i} (x_k - \bar{x}), i = 1, \cdots, N, \tag{12}$$

$$\bar{x} = \frac{1}{N} \sum_{k=1}^{N} x_k. \tag{13}$$

2) Dividing $y(i)$ into N_s non-overlapping segments with length s. Because the signal data length N is usually not a multiple of s, the remainder segment of data is unusable. Therefore, the same division is performed for the reverse sequence of the signal, and the $2N_s$ segment is obtained.
3) Using the least square method to local trends on each subinterval v (v = 1, ..., $2N_s$). Then, the variance of each segment is calculated after removing the fluctuation trend.

$$F^2(v, s) = \frac{1}{s} \sum_{i=1}^{s} \{y[(v-1)s + i] - y_v(i)\}^2, v = 1, \cdots, N_s, \tag{14}$$

$$F^2(v, s) = \frac{1}{s} \sum_{i=1}^{s} \{y[N - (v - N_s)s + i] - y_v(i)\}^2, v = N_s + 1, \cdots, 2N_s. \tag{15}$$

4) Calculating the average value of fluctuation function with q-order.

$$F(q, s) = \left\{ \frac{1}{2N_s} \sum_{v=1}^{2N_s} [F^2(v, s)]^{\frac{q}{2}} \right\}^{\frac{1}{q}}. \tag{16}$$

5) If the microseismic signal x_k has self-similar characteristics, there is an exponential relationship between F (q, s) and s.

$$F(q, s) \propto s^{h(q)}, \tag{17}$$

where $h(q)$ is the generalized Hurst exponent. If the microseismic signal x_k is a multifractal time series, $h(q)$ will change with q.

6) The multifractal scaling exponent $\tau(q)$ can be calculated based on $h(q)$.

$$\tau(q) = qh(q) - 1. \tag{18}$$

Two parameters describing multifractals can be obtained by the Legendre transformation.

$$\alpha = h(q) + qh'(q), \tag{19}$$

$$f(\alpha) = q[\alpha - h(q)] + 1. \tag{20}$$

Multifractal spectral width $\Delta\alpha$ ($\Delta\alpha = \alpha_{\max} - \alpha_{\min}$) can describe the unevenness degree of microseismic waveforms. The greater the value, the more severe is the fluctuation of the microseismic waveform. Otherwise, the microseismic waveform fluctuates stably. $\Delta f(\alpha) = f(\alpha_{\max}) - f(\alpha_{\min})$ represents the ratio of large and small peaks in the microseismic waveform. When $\Delta f(\alpha) < 0$, the large amplitude occupies a higher proportion, and when $\Delta f(\alpha) > 0$, the proportion of small amplitude is higher.

To prove microseismic waveforms can be studied using the MF-DFA method, one of the waveforms in the GB-M-1 microseismic event was analyzed. The MF-DFA results of the microseismic waveform are shown in **Figure 4**. The q-order fluctuation function $F(q, s)$ has a power-law relationship with time scale s, which indicates that the time series of the microseismic waveform has scale invariance in a certain scale or has fractal characteristics. Moreover, the q-order Hurst exponent is a decreasing function, that is, $h(q)$ varies with q. The curve of the q-order mass exponent shows a concave shape, and the relationship between $\tau(q)$ and q is nonlinear. Therefore, the time series of the microseismic waveform not only has scale invariance but also has multifractal characteristics. In the multifractal spectrum, the opening width of the curve represents the degree of inhomogeneity of the microseismic waveform, and the curve shape (left hook and right hook) can reflect the proportion of small and large amplitude.

Time–Frequency–Energy and Multifractal Characteristics of Microseismic Waveforms

For any induced microseismic, the vibration intensity decreases with the increase of the propagation distance, and its effect on the near-field area is the objective for researchers. In addition, the influence of the underground complex environment (roadway, gob, geological structure, and joint) on vibration propagation should be avoided as far as possible. Therefore, the waveforms received from microseismic sensors close to the source in each induced microseismic event are selected in **Table 1**. The Hilbert spectrum and multifractal spectrum of the selected waveforms were obtained using HHT and MF-DFA methods. **Figure 5** shows the original waveform 1), Hilbert spectrum 2), marginal energy spectrum 3), instantaneous energy spectrum 4), and multifractal spectrum 5) of different induced microseismic waveforms.

First, the frequency characteristic of different types of the induced microseismic waveforms was analyzed. The frequency distribution range of the ground blasting-induced microseismic waveform is 0–25 Hz, and the dominant frequency of the GB-M-1 and GB-M-2 waveform is 3 Hz. However, the dominant frequency of mining-induced microseismic waveform (M-M-1 and M-M-2) is 131 and 131.5 Hz, respectively, while those of destress blast-induced microseismic waveform (DB-M-1, DB-M-2, DB-M-3, and DB-M-4) is 126.5 Hz, 121 Hz, 128 Hz, and 43 Hz, respectively. For the DB-M-4 waveform, the first dominant frequency is 43 Hz, but the high-frequency components account for a large proportion, and the second dominant frequency is 133 Hz. Therefore, the dominant frequency of mining and destress blasting-induced microseismic waveform is much higher than that of the ground blasting-induced microseismic waveform. Moreover, the dominant frequency difference between the mining and destress blasting- induced microseismic waveform is small, but there are great differences in the marginal energy spectrum. The frequency band of the mining-induced microseismic waveform is narrow, ranging from 120 to 160 Hz, which accounts for almost all the signal energy. The marginal energy spectrum is relatively concentrated and follows the unimodal distribution. However, the frequency band of destress blasting-induced microseismic waveforms is relatively wide, ranging from 1 to 160 Hz. Compared with mining-induced microseismic waveform, the proportion of low-frequency components increases significantly, and multiple

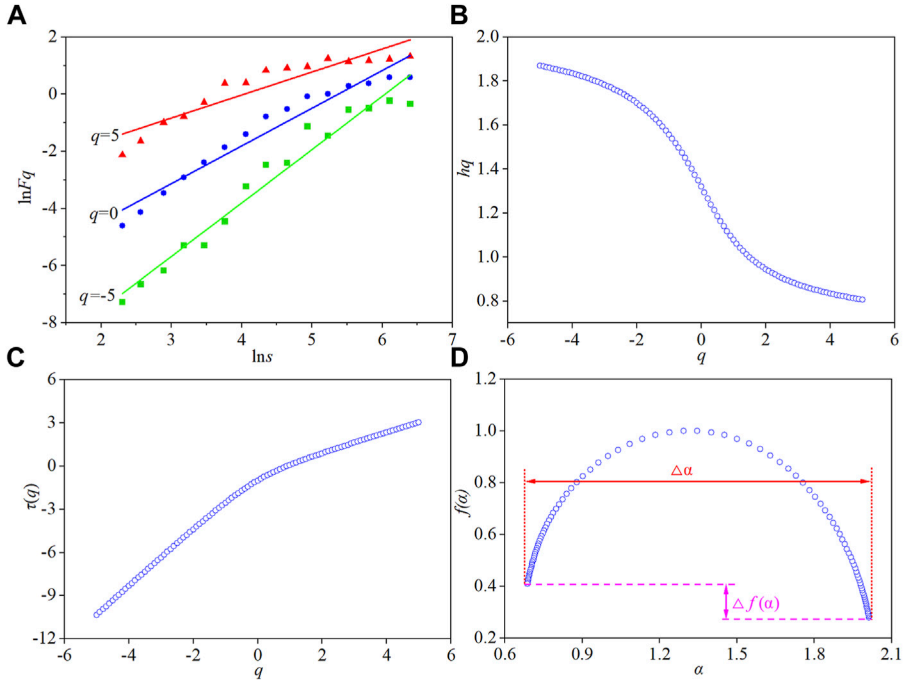

FIGURE 4 | MF-DFA results of the microseismic waveform. **(A)** Relationship between ln *s* and ln F*q*; **(B)** q-order Hurst exponent; **(C)** q-order mass exponent; and **(D)** multifractal spectrum.

peaks appear in the marginal energy spectrum. There is even no absolute dominant frequency in the DB-M-2 waveform. The aforementioned results indicate that the three types of induced microseismic waveforms are significantly different in frequency characteristics. Generally speaking, the frequency characteristic of the destress blasting-induced microseismic waveform is more complex than the other two types of induced microseismic waveforms.

From the instantaneous energy spectrum of the ground blasting-induced microseismic waveform, it can be seen that there is a relatively small energy peak before the energy reaches the maximum. The instantaneous energy gradually attenuates and stabilizes after reaching the maximum, and the coda is not developed. The results suggest that the rise and fall process of the instantaneous energy of ground blasting-induced microseismic waveforms is relatively regular. However, for the instantaneous energy spectrum of mining and destress blasting-induced microseismic waveforms, the energy generally rises to the maximum instantly without large fluctuation. The instantaneous energy attenuation is complicated after the peak, and there are multiple energy peaks and relatively developed coda. In particular, the microseismic waveform induced by underground destress blasting is more prominent in the complexity of the instantaneous energy spectrum.

As can be seen from **Figure 5V**, the multifractal spectrum of ground blasting-induced microseismic waveform is in approximately symmetrical distribution, while that of mining and destress blasting-induced microseismic waveform shows a slightly left hook shape and a significant left hook shape, respectively. The multifractal parameters of Δα and Δ*f(α)* of all the selected waveforms are calculated and listed in **Table 2**. We can see that the parameter Δα of destress blasting-induced microseismic waveforms is higher than that of ground blasting and mining-induced microseismic waveforms. In particular, the waveform amplitude of some microseismic induced by mining is very close to that induced by underground destress blasting, but there is a large difference in parameter Δα. For example, the amplitude of M-M-1, M-M-2, DB-M-3, and DB-M-4 waveform is close to 30 mm/s, but the parameters Δα of M-M-1 and M-M-2 waveforms is only about 1.0, while the parameter Δα of DB-M-3 and DB-M-4 waveforms is 1.8863 and 2.1846, respectively. According to the physical meaning of Δα discussed before, the relative fluctuation of microseismic waveform induced by underground destress blasting is more violent, and the multifractal characteristic is more prominent. However, for the waveform of mining-induced microseismic, because the waveform fluctuation is not violent, the multifractal feature is not evident even though its amplitude is large, which indicated the waveform amplitude attenuation is relatively regular. Moreover, the parameters Δ*f*(α) of the ground blasting-induced microseismic waveforms are close to 0, indicating that the proportion of small and large peaks in the waveform is approximately equal, that is, the waveform is relatively stable. For the waveform of microseismic induced by mining and destress blasting, the parameter Δ*f*(α) of the waveform is less than 0, indicating the large peak accounts for a larger proportion. The Δ*f*(α) of microseismic waveforms induced by underground

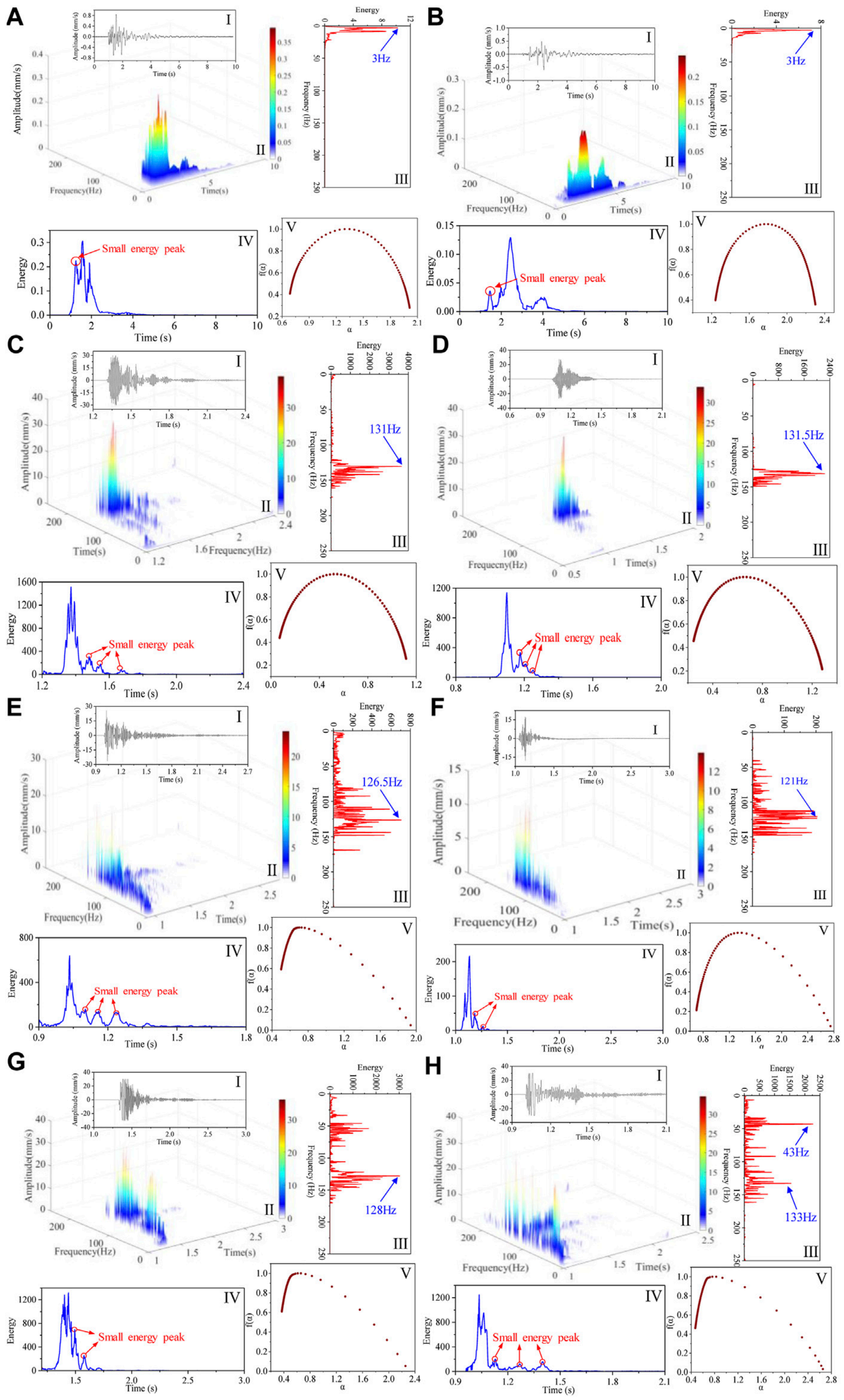

FIGURE 5 | Hilbert spectrum and multifractal spectra *f(α)-α* of different induced microseismic waveforms **(A)** GB-M-1; **(B)** GB-M-2; **(C)** M-M-1; **(D)** M-M-2; **(E)** DB-M-1; **(F)** DB-M-2; **(G)** DB-M-3; and **(H)** DB-M-4.

destress blasting is much smaller than that induced by mining, which further proves that its relative fluctuation is more violent.

By comparing and analyzing the Hilbert spectrum and multifractal spectrum of three types of induced microseismic waveforms, there is a large difference in frequency, energy

TABLE 2 | Multifractal parameters of Δα and Δ*f*(α).

Waveform	Δα	Δ*f*(α)
GB-M-1	1.3254	−0.1292
GB-M-2	1.0599	−0.0336
M-M-1	1.0449	−0.1825
M-M-2	1.0344	−0.2398
DB-M-1	1.4366	−0.5448
DB-M-2	2.0495	−0.1621
DB-M-3	1.8863	−0.5573
DB-M-4	2.1846	−0.4287

attenuation, and multifractal characteristics. In particular, the magnitude, propagation distance, and medium of microseismic induced by mining and destress blasting are very close, but both the Hilbert spectrum and multifractal spectrum are quite different. Generally speaking, the microseismic waveforms induced by underground destress blasting are more complex and variable. All induced microseismic events in the coal mine are elastic waves caused by rock deformation and fracture under external disturbance. Therefore, the external disturbance characteristics are the decisive factors affecting the waveform characteristics. For ground blasting, most explosion energy is consumed to destroy the coal and rock, and small partial energy is released in the form of seismic waves and received by underground microseismic sensors, that is, ground blasting-induced microseismic. During coal mining, rock deformation and failure under the mining stress will induce microseismic. As shown in **Figure 6**, ground blasting-induced microseismic is caused by the blasting stress, while mining-induced microseismic is caused by the mining stress, and both of them are caused by the single external stress. However, for destress blasting-induced microseismic, the cavity and crack are formed near the blasting hole in the rock under the blasting stress. Then, the elastic energy accumulated in the rock will be released on the free surface of the cavity and crack. Therefore, the microseismic is caused by the coupling action of blasting stress and mining stress.

Different types of external disturbances have different action mechanisms on the rock, which leads to different microseismic source rupture types. The superposition of the elastic waves induced by the blasting stress and mining stress lead to a complex source rupture type, which means that the destress blasting-induced microseismic waveforms are complex and variable. The complexity of waveform features is mainly manifested by rich frequency spectrum, violent energy fluctuation, and clear multifractal features. The Hilbert spectrum of microseismic waveforms induced by underground destress blasting is further analyzed; we can see that the low-frequency components are concentrated in the early stage of the vibration and significantly decrease in the post-stage. According to the action process of destress blasting on the rock, the blasting stress is first released to destroy the rock and attenuation rapidly, and then, the mining stress begins to be released. Combined with the frequency distribution of the other two types of induced microseismic waveforms, it can be concluded that the low-frequency components are mainly induced by the blasting stress, while the high-frequency components are mainly induced by the instantaneous release of mining stress.

Effects of Propagation Distance and Magnitude on Waveform Characteristics

Existing research studies show that waveform characteristics are not only related to the source rupture type and mechanism but also the magnitude and propagation distance, so it is necessary to study the effects of propagation distance and magnitude on waveform characteristics.

Two mining-induced microseismic events (M-M-1 and M-M-2) and two destress blasting-induced microseismic events (DB-M-2 and DB-M-4) were selected to discuss the variation in maximum instantaneous energy and dominant frequency of waveforms with the propagation distance, as shown in **Figure 7**. We can see that the maximum instantaneous energy of all induced microseismic events decreases nonlinearly with the

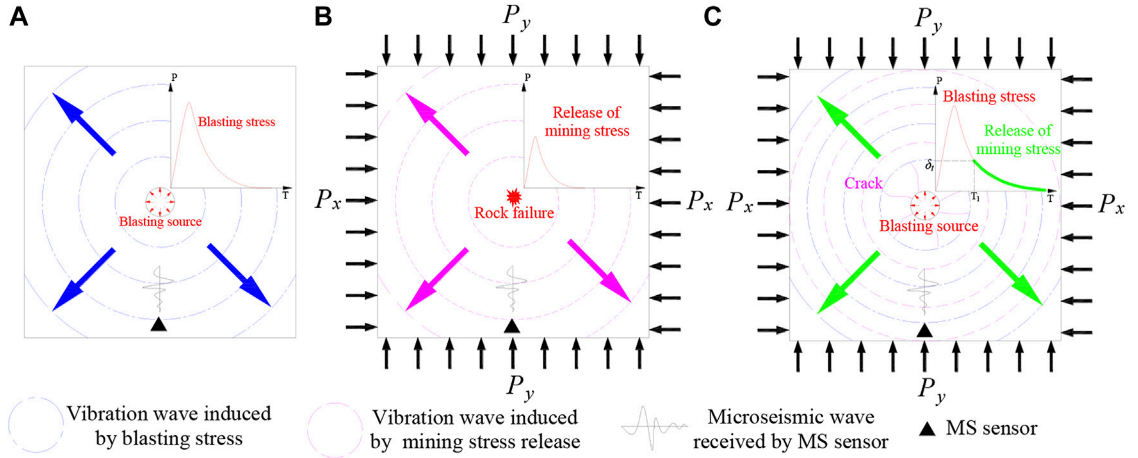

FIGURE 6 | External disturbance characteristics of different types of induced microseismic waveforms. **(A)** Ground blasting-induced microseismic; **(B)** mining-induced microseismic; and **(C)** destress blasting-induced microseismic.

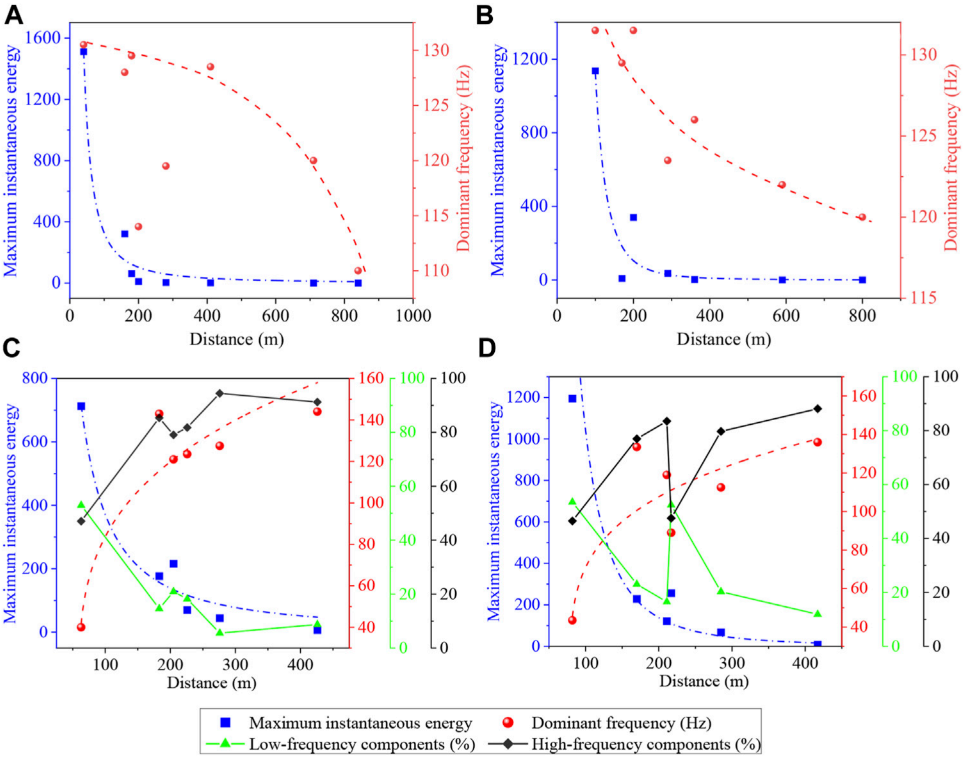

FIGURE 7 | Maximum instantaneous energy, frequency, and propagation distance. **(A)** M-M-1; **(B)** M-M-2; **(C)** DB-M-2; and **(D)** DB-M-4.

increase of propagation distance. However, the relationship between the dominant frequency and propagation distance of the two types of induced microseismic waveforms shows an opposite law. With the increase in the propagation distance, the dominant frequency of mining-induced microseismic waveforms decreases, while that of destress blasting-induced microseismic waveforms increases. Moreover, according to the previous analysis, the frequency spectrum of destress blasting-induced microseismic waveforms is rich and complex, and there is even no absolute dominant frequency. Therefore, it is not enough to study the waveform spectrum only by discussing the variation of the dominant frequency. To further study the energy distribution of each frequency band in the waveform, frequency is relatively divided into the low-frequency band (0–100 Hz) and high-frequency band (101–200 Hz). The relationship between the energy ratio of the two frequency bands with the propagation distance is shown in **Figures 7C,D**. The proportion of the low-frequency band of waveforms decreases gradually, while that of the high-frequency band increases. Actually, for the waveforms recorded by microseismic sensors near the source, the blasting stress is much higher than the mining stress. At this time, the vibration caused by blasting is also stronger than that induced by the mining stress. Therefore, blasting vibration characteristics are dominant in the waveform, resulting in the higher energy proportion of the low-frequency band in the waveform. However, with the increase of the distance between the microseismic senor and the blast source, the blasting stress first attenuates, and blasting vibration weakens. When the mining stress release effect is greater than the blasting stress, the vibration induced by the mining stress will play a dominant role in the waveform, resulting in a decrease in the energy proportion of the low-frequency band, while a relative increase in that of the high-frequency band.

To study the influence of source energy on waveform frequency distribution, the dominant frequency and low-frequency components of the two destress blasting-induced microseismic waveforms are compared and analyzed, as shown in **Figure 8**. According to **Table 1**, the source energy of the DB-M-4 microseismic event is higher than that of DB-M-2. Generally speaking, the dominant frequencies of DB-M-4 microseismic waveforms are lower than those of DB-M-2, while the proportion of low-frequency components in DB-M-4 microseismic waveform is higher. The results show that with the increase of source energy, the dominant frequency of waveform decreases, and the proportion of low-frequency components increases, which means that the frequency components of waveforms become more abundant. Due to the increase of source energy, the rock damage degree and scope are larger, resulting in more energy in the rock being released. The superposition effect of vibration induced by blasting stress and mining stress is more complex, and the frequency distribution of the waveform is more complex. The aforementioned results show that the waveform characteristics are correlated with the release process of mining stress. For example, the low-frequency components of waveforms can reflect the blasting stress strength, while the high-frequency components can reflect the

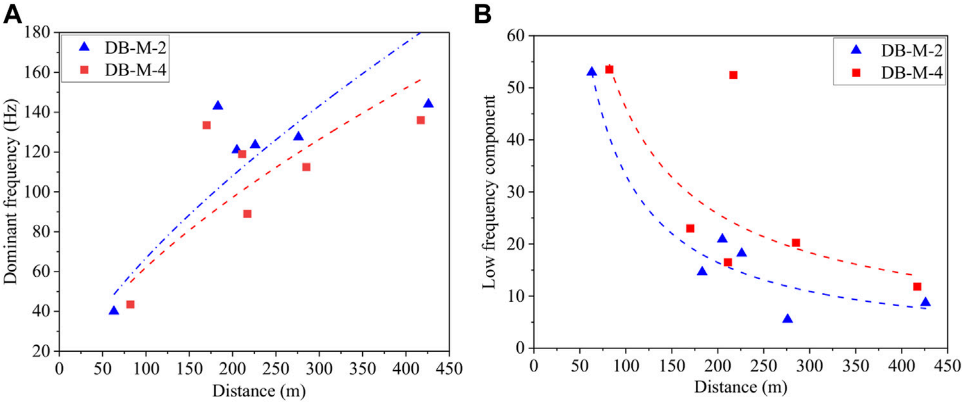

FIGURE 8 | Comparison of frequency distribution of DB-M-2 and DB-M-4 microseismic. **(A)** Dominant frequency; **(B)** low-frequency components.

mining stress release effect, which can provide a reference for the evaluation of the destress blasting effect for preventing rockburst.

DISCUSSION

The underground destress blasting technology is an important method to prevent rockburst. The evaluation of the pressure relief effect is necessary for mine safety production and destress blasting parameter design. The aforementioned results verify that the waveform information of destress blasting-induced microseismic can reflect the release process of blasting stress and mining stress. Therefore, the microseismic source energy consists of explosion energy and rock strain energy, and the amount of energy released by the mining stress can be used to evaluate the effect of pressure relief. Based on the aforementioned analysis, a blasting efficiency index B_e was proposed to evaluate the effect of pressure relief, and the classification system was developed. The calculation formula of the B_e index is as follows:

$$B_e = \frac{logE_s - logE_p}{logP_e}, \tag{21}$$

where E_s is the destress blasting-induced microseismic source energy calculated using the microseismic system, E_p is the seismic energy converted from the explosive chemical energy, and P_e is the explosive charge.

The parameter of E_p can be calculated by **Eq. 22**.

$$E_p = E_{pi} \times P_e \times k_s, \tag{22}$$

where E_{pi} is the theoretical chemical energy per kilogram of explosive, and the value of emulsified explosive is 3,200 kJ/kg in this research; k_s is blasting seismic energy conversion coefficient.

For the blasting seismic energy conversion coefficient k_s, many researchers have studied its value by theoretical analysis, blasting experiments, and empirical methods. However, their results are not unanimous because there are great differences in the properties of explosives and propagation media, the types of microseismic sensor, and energy calculation methods. For example, Sanchidrián et al. (2007) collected 10 production blasts in two ground quarries and analyzed that the seismic energy was 1–3% of the total energy of explosives. Zhang and Guo (1984) found that the blasting seismic energy conversion coefficient of underground mine blasting ranges from 0.00183% to 0.203% using statistical analysis methods. For blasting-induced microseismic events received using the ARAMIS A/E microseismic monitoring system in coal mines, the empirical value of this coefficient is generally 0.01%. In this study, the seismic energy conversion coefficient of blasting was determined using the statistical analysis of 63 destress blasting-induced microseismic data of the Yutian coal mine, which includes the correlation analysis of independent variables, dispersion analysis, and error elimination. As shown in **Figure 9**, the logarithmic transformation was performed for microseismic source energy and explosive charge, and a linear dependence between the transformed microseismic source energy (log E_s) and transformed explosive charge (log P_e) was obtained. The standard deviation of the transformed microseismic source energy (log E_s) is 0.70. Data located under the straight line

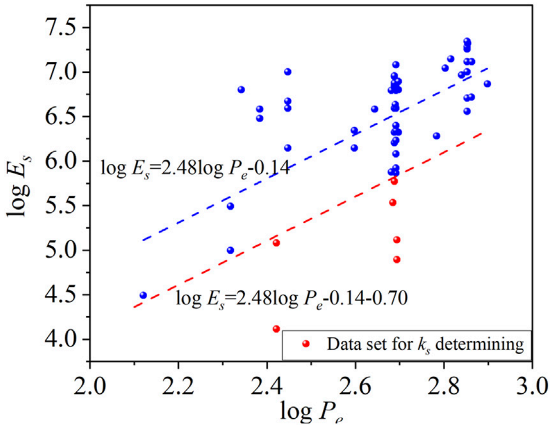

FIGURE 9 | Relationship between microseismic source energy and explosive charge.

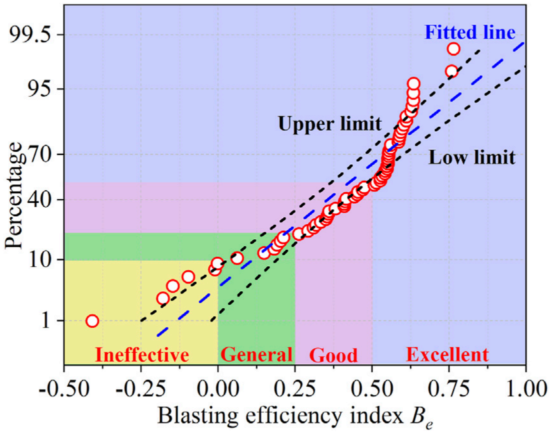

FIGURE 10 | Normal probability distribution of the blasting efficiency index B_e.

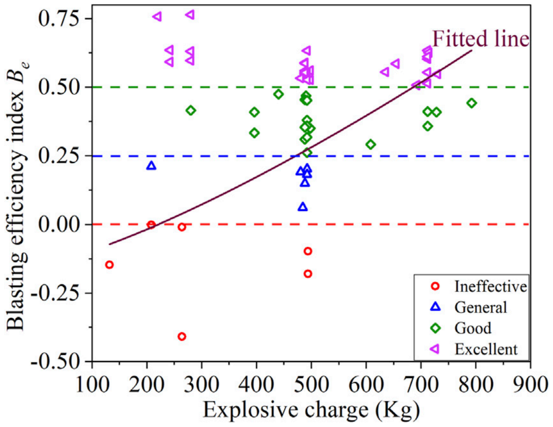

FIGURE 11 | Relationship between the blasting efficiency index and explosive charge.

TABLE 3 | Classification system for the evaluation of B_e.

Blasting efficiency index (B_e)	Effect of pressure relief	Percentage (%)
$B_e \le 0$	Ineffective	9.5
$0 < B_e \le 0.25$	General	9.5
$0.25 < B_e \le 0.50$	Good	30
$B_e > 0.50$	Excellent	51

parallel to the regression line and shifted by the standard deviation were then selected. It is assumed that the microseismic source energy of the selected data is only converted from the explosive energy; in other words, the accumulated strain energy in the rock mass is not released in destress blasting. The average k_s of the selected dataset was calculated to be 0.015%. Therefore, the blasting seismic energy conversion coefficient k_s in this research is 0.015%.

According to **Eqs 21**, **22**, the blasting efficiency index B_e for 63 rounds of destress blasting was calculated. The normal probability distribution of the blasting efficiency index (B_e) is shown in **Figure 10**, and a classification system was developed to evaluate B_e based on the distribution probabilities of B_e, as shown in **Table 3**. In this classification system, the critical values of blasting efficiency indexes are 0, 0.25, and 0.50, respectively, and the four classification systems are ineffective ($B_e \le 0$), general ($0 < B_e \le 0.25$), good ($0.25 < B_e \le 0.50$), and excellent ($B_e > 0.50$), respectively. Among the 63 rounds of destress blasting, the effect of pressure relief varied from ineffective to excellent, with 51% being excellent and approximately 30% good, while both the ineffective and general are 9.5%. The results show that destress blasting in the Yutian coal mine has achieved good results, which can play a beneficial role in the control of rockburst disasters. Moreover, the relationship between the blasting efficiency index (B_e) and explosive charge (P_e) is shown in **Figure 11**. With the increase of explosive charge, the blasting efficiency index presents an upward trend, indicating that destress blasting with a large explosive charge is more likely to obtain a better pressure relief effect.

CONCLUSION

By analyzing time–frequency, energy attenuation, and the multifractal spectrum of different types of induced microseismic waveforms, the main conclusions are as follows.

1) Generally, the ground blasting-induced microseismic waveforms have a longer duration (more than 3 s) than the other two types of induced microseismic waveforms (both less than 0.5 s). Both the dominant frequency and band range of microseismic waveforms induced by mining and destress blasting are much higher than those of ground blasting-induced microseismic waveforms. Moreover, there is a large number of low-frequency components distributed in the microseismic waveform induced by destress blasting, which is more abundant in the frequency spectrum than mining-induced microseismic waveforms. The ground blasting-induced microseismic waveforms have regular energy attenuation and undeveloped coda waves. However, for mining and destress blasting-induced microseismic, there are multiple energy peaks in the energy attenuation process and relatively developed coda waves in waveforms. With the increase in the propagation distance, both the dominant frequency and the proportion of high-frequency components of destress blasting-induced microseismic waveforms show a nonlinear upward trend, while those of the mining-induced microseismic waveform are opposite. For destress blasting-induced microseismic waveforms, with the increase of source energy, the dominant frequency decreases, and the proportion of low-frequency components increases.
2) All the induced microseismic waveforms show clear multifractal characteristics. The multifractal parameters Δα

and $\Delta f(\alpha)$ of three types of induced microseismic waveforms indicate that ground blasting-induced microseismic waveform fluctuations are relatively stable; the mining-induced microseismic waveforms have a moderate fluctuation, while the destress blasting-induced microseismic waveforms are more violent. The results further prove that destress blasting-induced microseismic waveforms are more complex and changeable.

3) The destress blasting-induced microseismic is induced by the coupling effect of blasting stress and mining stress. The superposition of the elastic waves leads to complex source rupture types. Moreover, the complex underground geological environment also greatly affects the propagation of microseismic waveforms. Therefore, destress blasting-induced microseismic waveforms are clearly different from the other two kinds of microseismic waveforms, which are manifested as rich frequency, complex energy attenuation, and clear multifractal characteristics.
4) A blasting efficiency index B_e was proposed to evaluate the effect of pressure relief, and the classification system was developed. For 63 rounds of destress blasting in the Yutian coal mine, the effect of pressure relief varied from ineffective to excellent, with 51% being excellent and approximately 30% good, while both the ineffective and general are 9.5%. Moreover, a large explosive charge is more likely to obtain a better pressure relief effect.

DATA AVAILABILITY STATEMENT

The original contributions presented in the study are included in the article/Supplementary Material, further inquiries can be directed to the corresponding authors.

AUTHOR CONTRIBUTIONS

Conceptualization: JK, LD, and XL; methodology: JK, and JL; formal analysis and investigation: JK, JB, and MW; validation: JL and JB; writing—review and editing: JK, LD, JL, XL, JB, and MW.

FUNDING

We gratefully acknowledge the financial support for this work provided by the Postgraduate Research and Practice Innovation Program of Jiangsu Province (Grant No. KYCX21_2378), the National Natural Science Foundation of China (Grant No. 51874292, 51804303), and the Natural Science Foundation of Jiangsu Province, China (Grant No. BK20180643).

ACKNOWLEDGMENTS

The authors thank the members of the Yutian coal mine for their support during the fieldwork.

REFERENCES

Bao, X., and Eaton, D. W. (2016). Fault Activation by Hydraulic Fracturing in Western Canada. *Science* 354, 1406–1409. doi:10.1126/science.aag2583

Brudzinski, M. R., and Kozłowska, M. (2019). Seismicity Induced by Hydraulic Fracturing and Wastewater Disposal in the Appalachian Basin, USA: a Review. *Acta Geophys.* 67, 351–364. doi:10.1007/s11600-019-00249-7

Cai, W., Dou, L., Si, G., Cao, A., Gong, S., Wang, G., et al. (2019). A New Seismic-Based Strain Energy Methodology for Coal Burst Forecasting in Underground Coal Mines. *Int. J. Rock Mech. Mining Sci.* 123, 104086. doi:10.1016/j.ijrmms.2019.104086

Cai, W., Dou, L., Si, G., and Hu, Y. (2021). Fault-Induced Coal Burst Mechanism under Mining-Induced Static and Dynamic Stresses. *Engineering* 7, 687–700. doi:10.1016/j.eng.2020.03.017

Chen, J., Wald, D. J., and Helmberger, V. D. (2002). Source Description of the 1999 Hector Mine, California, Earthquake, Part I: Wavelet Domain Inversion Theory and Resolution Analysis. *Bull. Seismol. Soc. Am.* 92, 1192–1207.

Song, D., Liu, X., Huang, J., and Zhang, J. (2020). Energy-based Analysis of Seismic Failure Mechanism of a Rock Slope with Discontinuities Using Hilbert-Huang Transform and Marginal Spectrum in the Time-Frequency Domain. *Landslides* 18, 105–123. doi:10.1007/s10346-020-01491-7

Dong, L., Wesseloo, J., Potvin, Y., and Li, X. (2015). Discrimination of Mine Seismic Events and Blasts Using the Fisher Classifier, Naive Bayesian Classifier and Logistic Regression. *Rock Mech. Rock Eng.* 49, 183–211. doi:10.1007/s00603-015-0733-y

Dong, L.-J., Wesseloo, J., Potvin, Y., and Li, X.-B. (2016). Discriminant Models of Blasts and Seismic Events in Mine Seismology. *Int. J. Rock Mech. Mining Sci.* 86, 282–291. doi:10.1016/j.ijrmms.2016.04.021

Dong, L.-j., Tang, Z., Li, X.-b., Chen, Y.-c., and Xue, J.-c. (2020). Discrimination of Mining Microseismic Events and Blasts Using Convolutional Neural Networks and Original Waveform. *J. Cent. South. Univ.* 27, 3078–3089. doi:10.1007/s11771-020-4530-8

Dou, L., Cai, W., Cao, A., and Guo, W. (2018). Comprehensive Early Warning of Rock Burst Utilizing Microseismic Multi-Parameter Indices. *Int. J. Mining Sci. Technol.* 28, 767–774. doi:10.1016/j.ijmst.2018.08.007

Dreger, D. S., Ford, S. R., and Walter, W. R. (2008). Source Analysis of the Crandall Canyon, Utah, Mine Collapse. *Science* 321, 217. doi:10.1126/science.1157392

Drover, C., and Villaescusa, E. (2019). A Comparison of Seismic Response to Conventional and Face Destress Blasting during Deep Tunnel Development. *J. Rock Mech. Geotech. Eng.* 11, 965–978. doi:10.1016/j.jrmge.2019.07.002

Fan, G., Zhang, L.-M., Zhang, J.-J., and Yang, C.-W. (2017). Time-frequency Analysis of Instantaneous Seismic Safety of Bedding Rock Slopes. *Soil Dyn. Earthquake Eng.* 94, 92–101. doi:10.1016/j.soildyn.2017.01.008

Fu, X. Q., Yang, R. S., Cui, X. Q., Liu, X., Liu, J. F., and Lei, Z. (2020). Multi-fractal Detrended Fluctuation Analysis of the Blasting Vibration Signal in a Frozen Shaft. *J. Vib. Shock* 39, 51–58. doi:10.13465/j.cnki.jvs.2020.06.008

He, J., Dou, L., Gong, S., Li, J., and Ma, Z. (2017). Rock Burst Assessment and Prediction by Dynamic and Static Stress Analysis Based on Micro-seismic Monitoring. *Int. J. Rock Mech. Mining Sci.* 93, 46–53. doi:10.1016/j.ijrmms.2017.01.005

Huang, N. E., Shen, Z., Long, S. R., Wu, M. C., Shih, H. H., Zheng, Q., et al. (1998). The Empirical Mode Decomposition and the Hilbert Spectrum for Nonlinear and Non-stationary Time Series Analysis. *Proc. R. Soc. Lond. A.* 454, 903–995. doi:10.1098/rspa.1998.0193

Kantelhardt, J. W., Zschiegner, S. A., Koscielny-Bunde, E., Havlin, S., Bunde, A., and Stanley, H. E. (2002). Multifractal Detrended Fluctuation Analysis of Nonstationary Time Series. *Physica A: Stat. Mech. its Appl.* 316, 87–114. doi:10.1016/s0378-4371(02)01383-3

Konicek, P., and Waclawik, P. (2018). Stress Changes and Seismicity Monitoring of Hard Coal Longwall Mining in High Rockburst Risk Areas. *Tunnelling Underground Space Technol.* 81, 237–251. doi:10.1016/j.tust.2018.07.019

Li, Y., and Zheng, X. (2007). Wigner-Ville Distribution and its Application in Seismic Attenuation Estimation. *Appl. Geophys.* 4, 245–254. doi:10.1007/s11770-007-0034-7

Li, T., Cai, M. F., and Cai, M. (2007). A Review of Mining-Induced Seismicity in China. *Int. J. Rock Mech. Mining Sci.* 44, 1149–1171. doi:10.1016/j.ijrmms.2007.06.002

Li, X., Li, Z., Wang, E., Feng, J., Chen, L., Li, N., et al. (2016). Extraction of Microseismic Waveforms Characteristics Prior to Rock Burst Using Hilbert-Huang Transform. *Measurement* 91, 101–113. doi:10.1016/j.measurement.2016.05.045

Li, B., Li, N., Wang, E., Li, X., Niu, Y., and Zhang, X. (2017). Characteristics of Coal Mining Microseismic and Blasting Signals at Qianqiu Coal Mine. *Environ. Earth Sci.* 76, 722. doi:10.1007/s12665-017-7070-2

Li, N., Li, B., Chen, D., Wang, E., Tan, Y., Qian, J., et al. (2020a). Waveform Characteristics of Earthquakes Induced by Hydraulic Fracturing and Mining Activities: Comparison with Those of Natural Earthquakes. *Nat. Resour. Res.* 29, 3653–3674. doi:10.1007/s11053-020-09699-z

Li, N., Zhang, Z., Khan, M., Zhang, S., Liu, X., and Li, S. (2020b). Research on Anisotropic Characteristics of Rock and Intelligent Recognition of Precursory Signal. *Adv. Civil Eng.* 2020, 1–11. doi:10.1155/2020/3147203

Li, B., Wang, E., Li, Z., Niu, Y., Li, N., and Li, X. (2021). Discrimination of Different Blasting and Mine Microseismic Waveforms Using FFT, SPWVD and Multifractal Method. *Environ. Earth Sci.* 80, 36. doi:10.1007/s12665-020-09330-7

Liu, J.-c., and Gao, W.-x. (2020). Vibration Signal Analysis of Water Seal Blasting Based on Wavelet Threshold Denoising and HHT Transformation. *Adv. Civil Eng.* 2020, 1–14. doi:10.1155/2020/4381480

Ma, C.-y., Wu, L., Sun, M., and Yuan, Q. (2021). Time-Frequency Analysis and Application of a Vibration Signal of Tunnel Excavation Blasting Based on CEEMD-MPE-HT. *Shock and Vib.* 2021, 1–10. doi:10.1155/2021/6672942

Mucciarelli, M., Masi, A., Gallipoli, M. R., Harabaglia, P., Vona, M., and Ponzo, F. (2004). Analysis of RC Building Dynamic Response and Soil-Building Resonance Based on Data Recorded during a Damaging Earthquake (Molise, Italy, 2002). *Bull. Seismol. Soc. Am.* 94, 1943–1953. doi:10.1785/012003186

Pechmann, J. C., Arabasz, W. J., Pankow, K. L., Burlacu, R., and McCarter, M. K. (2008). Seismological Report on the 6 August 2007 Crandall Canyon Mine Collapse in Utah. *Seismol. Res. Lett.* 79, 620–636. doi:10.1785/gssrl.79.5.620

Peng, Z. K., Tse, P. W., and Chu, F. L. (2005). An Improved Hilbert-Huang Transform and its Application in Vibration Signal Analysis. *J. Sound Vib.* 286, 187–205. doi:10.1016/j.jsv.2004.10.005

Qiu, L., Song, D., He, X., Wang, E., Li, Z., Yin, S., et al. (2020). Multifractal of Electromagnetic Waveform and Spectrum about Coal Rock Samples Subjected to Uniaxial Compression. *Fractals* 28, 2050061. doi:10.1142/s0218348x20500619

Reynen, A., and Audet, P. (2017). Supervised Machine Learning on a Network Scale: Application to Seismic Event Classification and Detection. *Geophys. J. Int.* 210, 1394–1409. doi:10.1093/gji/ggx238

Salajegheh, E., and Heidari, A. (2005). Time History Dynamic Analysis of Structures Using Filter banks and Wavelet Transforms. *Comput. Struct.* 83, 53–68. doi:10.1016/j.compstruc.2004.08.008

Sanchidrián, J. A., Segarra, P., and López, L. M. (2007). Energy Components in Rock Blasting. *Int. J. Rock Mech. Mining Sci.* 44, 130–147. doi:10.1016/j.ijrmms.2006.05.002

Shang, X., Li, X., Morales-Esteban, A., and Chen, G. (2017). Improving Microseismic Event and Quarry Blast Classification Using Artificial Neural Networks Based on Principal Component Analysis. *Soil Dyn. Earthquake Eng.* 99, 142–149. doi:10.1016/j.soildyn.2017.05.008

Song, G., Cheng, J., and Grattan, K. T. V. (2020). Recognition of Microseismic and Blasting Signals in Mines Based on Convolutional Neural Network and Stockwell Transform. *IEEE Access* 8, 45523–45530. doi:10.1109/access.2020.2978392

Stockwell, R. G., Mansinha, L., and Lowe, R. P. (1996). Localization of the Complex Spectrum: the S Transform. *IEEE Trans. Signal. Process.* 44, 998–1001. doi:10.1109/78.492555

Tan, Y., Hu, J., Zhang, H., Chen, Y., Qian, J., Wang, Q., et al. (2020). Hydraulic Fracturing Induced Seismicity in the Southern Sichuan Basin Due to Fluid Diffusion Inferred from Seismic and Injection Data Analysis. *Geophys. Res. Lett.* 47, e2019GL084885. doi:10.1029/2019gl084885

Telesca, L., Colangelo, G., Lapenna, V., and Macchiato, M. (2004). Fluctuation Dynamics in Geoelectrical Data: an Investigation by Using Multifractal Detrended Fluctuation Analysis. *Phys. Lett. A* 332398, 404. doi:10.1016/j.physleta.2004.10.011

Wang, H. L., Zhao, Y., Wang, H. J., Peng, C. Y., and Tong, X. (2021). De-noising Method of Tunnel Blasting Signal Based on CEEMDAN Decomposition-Wavelet Packet Analysis. *Explosion Shock Waves* 41, 125–137. doi:10.11883/bzycj-2020-0123

Wen, Y. Y., Guo, Z. G., Cao, A. Y., Wang, S. W., Bai, X. X., and Jiang, S. Q. (2020). Analysis of Prssure Relief Effect of Roof Deep Hole Blasting Parameters Based on Micro-seismic Data Evaluation. *Coal Sci. Technol.* 48 (6), 57–63. doi:10.13199/j.cnki.cst.2020.06.006

Wojtecki, Ł., and Konicek, P. (2016). Estimation of Active Rockburst Prevention Effectiveness during Longwall Mining under Disadvantageous Geological and Mining Conditions. *J. Sustain. Mining* 15, 1–7. doi:10.1016/j.jsm.2016.04.003

Wojtecki, Ł., Kurzeja, J., and Knopik, M. (2021). The Influence of Mining Factors on Seismic Activity during Longwall Mining of a Coal Seam. *Int. J. Mining Sci. Technol.* 31, 429–437. doi:10.1016/j.ijmst.2021.01.010

Xu, F. L., Wang, E. Y., Song, D. Z., Song, X. Y., and Wei, M. Y. (2011). Long-range Correlation and Multifractal Distribution of Acoustic Emission of Coal-Rock. *Rock Soil Mech.* 32, 2111–2116. doi:10.16285/j.rsm.2011.07.028

Yin, Z.-q., Hu, Z.-x., Wei, Z.-d., Zhao, G.-m., Hai-feng, M., Zhang, Z., et al. (2018). Assessment of Blasting-Induced Ground Vibration in an Open-Pit Mine under Different Rock Properties. *Adv. Civil Eng.* 2018, 1–10. doi:10.1155/2018/4603687

Yin, Z., Chen, W., Hao, H., Chang, J., Zhao, G., Chen, Z., et al. (2020). Dynamic Compressive Test of Gas-Containing Coal Using a Modified Split Hopkinson Pressure Bar System. *Rock Mech. Rock Eng.* 53, 815–829. doi:10.1007/s00603-019-01955-w

Zhang, S., and Guo, J. (1984). Calculation and Application of Energy Conversion Coefficient of Explosion Seismic. *Chin. J. Geophys.* 27, 537–547.

Zhao, Y., Shan, R. L., and Wang, H. L. (2021). Research on Vibration Effect of Tunnel Blasting Based on an Improved Hilbert-Huang Transform. *Environ. Earth Sci.* 80, 206. doi:10.1007/s12665-021-09506-9

Zhu, G.-a., Dou, L.-m., Cai, W., Li, Z.-l., Zhang, M., Kong, Y., et al. (2016). Case Study of Passive Seismic Velocity Tomography in Rock Burst Hazard Assessment during Underground Coal Entry Excavation. *Rock Mech. Rock Eng.* 49, 4945–4955. doi:10.1007/s00603-016-1026-9

Conflict of Interest: The authors declare that the research was conducted in the absence of any commercial or financial relationships that could be construed as a potential conflict of interest.

frontiers in Earth Science

ORIGINAL RESEARCH
published: 31 March 2022
doi: 10.3389/feart.2022.861847

Fractal Characteristics and Energy Dissipation of Granite After High-Temperature Treatment Based on SHPB Experiment

Lei Liu[1,2], *Yuan Wang*[1] *and Huaming An*[3]*

[1]*Faculty of Land Resources Engineering, Kunming University of Science and Technology, Kunming, China,* [2]*Key Laboratory for Development and Utilization of Sino German Blue Mine and Special Underground Space in Yunnan Province, Kunming University of Science and Technology, Kunming, China,* [3]*Faculty of Public Security and Emergency Management, Kunming University of Science and Technology, Kunming, China*

In deep mining and high-concentration nuclear waste storage engineering, the surrounding rocks may be subjected to the combined action of high-temperature fire and impact load. In this study, the fracture morphology and the energy dissipation of granite following high-temperature treatment at 25–800°C were analyzed using the split Hopkinson pressure bar (SHPB) device. The fracture characteristics and the dynamic mechanical properties of granite were determined. The energy dissipation of granite specimens affected by high temperatures in the SHPB experiment was also analyzed. When the temperature of the impact rate was less than 200°C, the fragmentation degree, transmitted energy, and dissipated energy of granite increased with an increase in temperature. When the temperature was higher than 200°C, the change law was opposite. A strong linear correlation existed among the fragmentation, fractal dimension, and energy consumption density of granite at different impact rates after high-temperature treatment. Moreover, a strong quadratic correlation existed between the damage factors and temperature. When the temperature was less than 200°C, the damage factor decreased with the increase in temperature. When the temperature was higher than 200°C, the change law was opposite, which corresponded with the influence law of temperature on dynamic compressive strength. Scanning electron microscopy and X-ray diffraction analyses were conducted to study the fracture modes and mineral composition changes in the granites. A quantitative relationship existed between macro- and meso-properties. The results could provide theoretical basis for the design of underground engineering structures, post-disaster assessment, and rehabilitation activities.

Keywords: high temperature, granite, energy dissipation, fractal dimension, SHPB

Edited by:
Zhiqiang Yin,
Anhui University of Science and Technology, China

Reviewed by:
Zhaozhao Chang,
Zhejiang University of Technology, China
Chongchong Qi,
Central South University, China
Yang Liu,
Anhui Jianzhu University, China

****Correspondence:***
Huaming An
huaming.an@kust.edu.cn

Specialty section:
This article was submitted to Geohazards and Georisks, a section of the journal Frontiers in Earth Science

Received: *25 January 2022*
Accepted: *28 February 2022*
Published: *31 March 2022*

Citation:
Liu L, Wang Y and An H (2022) Fractal Characteristics and Energy Dissipation of Granite After High-Temperature Treatment Based on SHPB Experiment.
Front. Earth Sci. 10:861847.
doi: 10.3389/feart.2022.861847

INTRODUCTION

During deep mining and deep underground engineering constructions, deep surrounding rocks inevitably encounter "three high and one disturbance" environments (Xie, 2019). Moreover, drilling and blasting, large-scale mechanical vibration, and other engineering activities produce dynamic impact loads. High temperatures and dynamic disturbances affect the stability of deep surrounding rocks (Sasmito et al., 2015; Yuan et al., 2011), thereby posing huge threat to the safety of deep resource exploration and deep underground engineering construction personnel (Qi et al., 2021). By studying the internal energy variation characteristics of the rock material affected by high temperature under impact load, the dynamic mechanical properties of rock materials affected by high temperature can be comprehensively analyzed. This provides a theoretical basis for the structural design and safety evaluation of the surrounding rock during deep resource exploration and deep underground engineering construction (Li et al., 2021).

In terms of statics, the change rule of rock properties after high-temperature treatment was studied using conventional uniaxial compression tests and non-destructive monitoring (Bandini and Berry, 2012; Brotóns et al., 2013; Liu and Xu, 2015; Wang et al., 2013). With the increase in temperature, the strength, elastic modulus, and p-wave velocity of the rock all exhibited a decreasing trend. In engineering practice, the stability of the surrounding rock is typically associated with the dynamic impact load. With the development and application of split Hopkinson pressure bar (SHPB) technology, researchers have conducted relevant studies on the mechanical properties of rocks at normal and high temperatures (Yin et al., 2016b; Imani et al., 2017; Malik et al., 2018; Yin et al., 2019). Mishra et al. (2018) studied the dynamic mechanical responses of three types of magmatic rocks using a small-diameter SHPB device. They revealed that the strain rate effect was evident and proposed a correlation equation for the granite dynamic growth factor. Liu and Xu (2014) studied the mechanical properties of granite at high temperatures using an SHPB test system and found that there is a critical temperature that causes structural changes and mechanical deterioration in the granite. Through dynamic compression experiments, Yin et al. (2011) found that temperature promoted the evaporation of water inside the rock, decomposition of mineral particles, and reduction of internal bonding force, resulting in sandstone fragments tending to be fine-grained after dynamic impact with an increase in temperature. Rock damage always accompanies energy conversion and consumption. The dynamic impact failure of rocks is a process of energy input, absorption, and release (Xu and Shi, 2013). Yin et al. (2016a) studied the energy consumption law of the dynamic impact compression tests of coal and rock under high temperatures. They found that the reflected energy increased with increasing temperature, whereas the transmitted energy and absorbed energy exhibited opposite trends. Zhang and Jing (2018) analyzed the energy dissipation of sandstone after dynamic impact under high and low temperatures and found that the change in incident energy and absorbed energy was divided at −5 and 400°C. It increased with increasing temperature before the cutoff point and, thereafter, decreased with increasing temperature. Some researchers have linked the dissipated energy to the degree of breakage. They found that the specific energy absorption increased linearly with the incident energy and exhibited an exponential relationship with average fragmentation (Hong et al., 2009). Wu et al. (2019, 2020) analyzed the dynamic failure modes and the impact fragmentation of phyllites with different bedding angles considering the incident energy, energy absorption, and wave propagation characteristics. Ji et al. (2020) explored the fractal characteristics of the dynamic impact breakage of granite and sandstone using an SHPB test system. They found that the fractal dimension could quantitatively analyze crushing energy consumption and fragmentation.

In recent years, comparative studies on the energy absorption value, fractal dimension, and fracture morphology have been sufficient. However, there are few reports on the energy evolution law of rock materials affected by temperature during dynamic impact compression and considering the fractal dimension from the perspective of fracture conditions. The formation of granite iron, copper, gold, and tin ores is closely related (He, 1994). Therefore, granite was selected as the research object in this study. Dynamic impact compression tests were conducted on granite specimens treated at room temperature (25°C) and high temperatures (200°C, 400 °C, 600°C, and 800°C). A standard circular hole screen was used to screen and count the granite broken test blocks after the dynamic impact compression. The variations in the peak stress, fracture morphology, and energy dissipation of granite specimens with temperature grade were studied.

EXPERIMENTS

Preparation and High-Temperature Treatment of Granite Samples

Granite samples were obtained from the Kafang tin mine in Honghe Hani and Yi Autonomous Prefecture, Yunnan Province, China. According to the International Society for Rock Mechanics (ISRM) standard (Zhou et al., 2012), granite was processed into a cylindrical sample with a diameter of 50 mm and an aspect ratio of 0.5. A KRX-17B box-type resistance furnace was used to treat granite samples at high temperatures. The heating rate was set at 2°C/min. After heating to the target temperature, the temperature was maintained constant for 2 h. After heating, the sample was cooled to room temperature (25°C) in a furnace chamber before removal. To prevent the reaction between the rock samples and water vapor in the air following the high-temperature treatment, the samples were stored in a Tester WGLL-230BE electric blast-drying oven. The granite specimen after high-temperature treatment is shown in **Figure 1**. Evidently, with an increase in the heating temperature, the surface color of the granite specimens gradually deepened. When the heating temperature exceeded 400°C, thermal cracks appeared on the surface of granite specimens.

SHPB Testing System

Figure 2 shows the schematic of a 50 mm diameter SHPB test system used in this study. The system includes a dynamic loading part (nitrogen tank, gas gun, and spindle punch), rod part (incident bar and transmission bar), and data acquisition part (infrared speed measuring, single recording device, and data-processing device). The incident, transmission, and impact bars were all ^{40}Cr high-strength alloy steels. The density was 7.81 g/cm^3. The lengths of the incident rod and transmission rod were 2 m. The longitudinal wave velocity was 5,100 m/s. The elastic modulus was 210 GPa. The strain gauge was pasted on 1/2 of the rod.

During the SHPB experiment, the sample was placed between the incident and transmission bars, and the bullet was discharged at a certain speed. A stress wave was thus formed in the incident

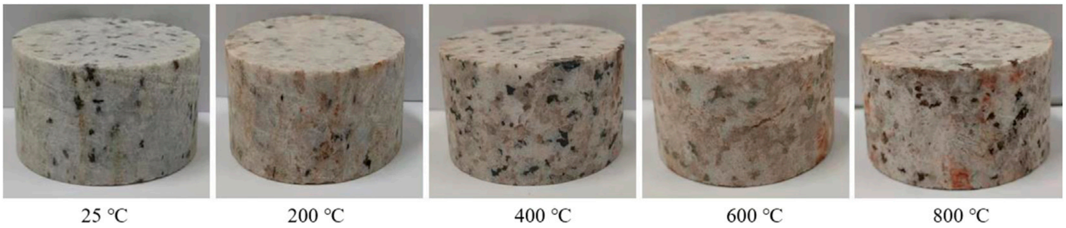

FIGURE 1 | Granite specimen after high-temperature treatment.

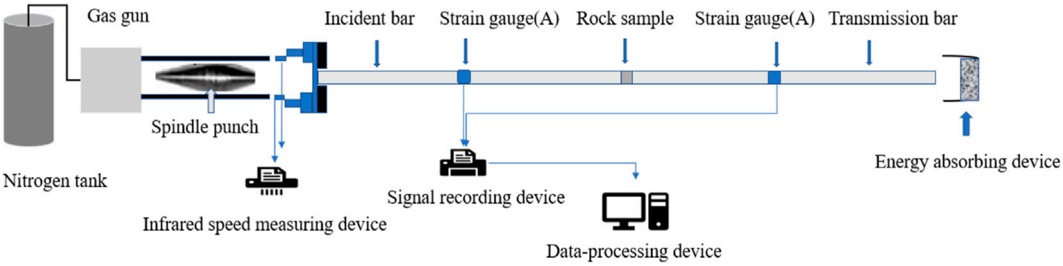

FIGURE 2 | Schematic of the split Hopkinson pressure bar device.

bar after impacting the incident bar. The incident waves were then propagated forward in the incident bar. When transmitted to the interface between the incident rod and the sample, a part of the incident wave was reflected back to the incident rod as a reflected wave, owing to the wave impedance difference between the rod and the sample. The other part was transmitted through the sample into the transmission rod as a transmission wave. Based on the one-dimensional stress assumption and stress uniformity assumption (Hu et al., 2015), the following method was described by Wang (2005). By substituting the signal collected by the strain gauge in **Eq. 1**, the stress $\sigma(t)$, strain $\varepsilon(t)$, and strain rate $\dot{\varepsilon}(t)$ of the specimen can be obtained as follows:

$$\left.\begin{aligned}\sigma(t) &= \frac{EA}{2A_s}\left[\varepsilon_i(t) + \varepsilon_r(t) + \varepsilon_t(t)\right]\\ \dot{\varepsilon}(t) &= \frac{C}{l_s}\left[\varepsilon_i(t) - \varepsilon_r(t) - \varepsilon_t(t)\right]\\ \varepsilon(t) &= \frac{C}{l_s}\int_0^t \left[\varepsilon_i(t) - \varepsilon_r(t) - \varepsilon_t(t)\right]dt\end{aligned}\right\}, \tag{1}$$

where $\varepsilon_i(t)$, $\varepsilon_r(t)$, and $\varepsilon_t(t)$ are the incident, reflected, and transmitted strains on the bar, respectively; A, E, and C represent the cross-sectional area, elastic modulus, and longitudinal wave velocity of the pressure rod, respectively.

Experimental Scheme

In this experiment, the granite specimens were heated and naturally cooled at room temperature (25°C) and high temperatures at different temperature levels (200°C, 400°C, 600°C, and 800°C). The specimens were then subjected to the dynamic impact compression experiments at different impact velocities (8.5 m/s, 11.5 m/s, and 13.5 m/s). The standard circular hole screens with different diameters (0.3, 0.5, 1, 2.5, 5, 10, 15, 20, and 25 mm) were used to screen the granite fragments following the experiment. A total of three-independent experiments were conducted for each working condition. Statistically significant data were selected for statistical analysis.

To ensure the validity of the experimental data, the stress balance must be ensured at both ends of the rock sample before the dynamic impact compression test. Typical waveforms at both ends of the sample are shown in **Figure 3A**. **Figure 3B** shows that the overlapping waveforms of the incident and reflection stresses have a high degree of coincidence with those of the transmission stress, which can guarantee the stress balance state in the dynamic impact process and the validity of the test data results.

SHPB Dynamic Stress–Strain Curve

The dynamic stress–strain curves of the granite specimens affected by different temperatures at different impact rates are shown in **Figure 4**.

As shown in **Figure 4**, the dynamic stress–strain curves of granite can be roughly divided into three stages: elasticity, yield, and failure. The initial stage of the curve was approximately a straight line, indicating that granite had a strong linear elastic relationship during the initial stage of dynamic impact compression. The slope of the curve at this stage can be approximated as the initial elastic modulus of rock. The stress–strain curve at the same impact rate initially moved up slightly and then moved sharply to the lower right along with the position of the ascending curve of the temperature grade. The initial elastic modulus and peak stress of the rock first increased

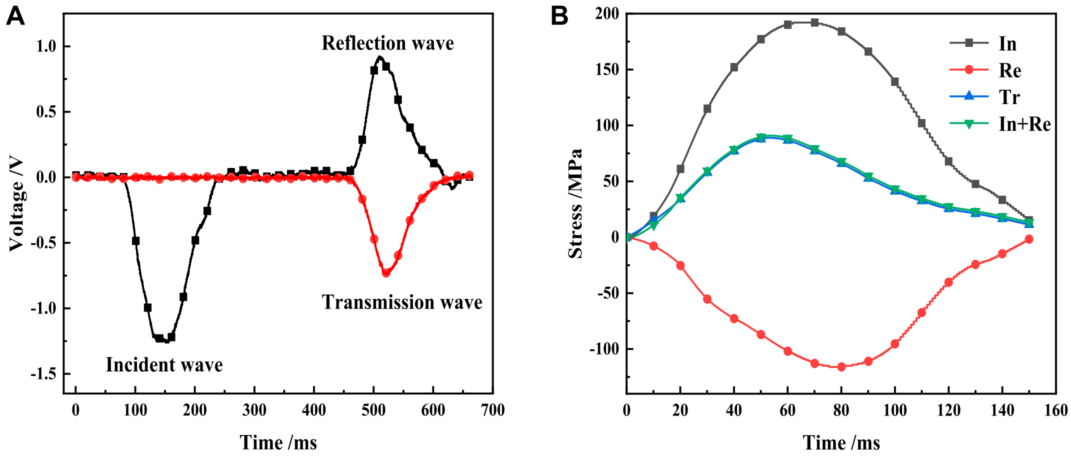

FIGURE 3 | Typical waveforms at both ends of the sample.

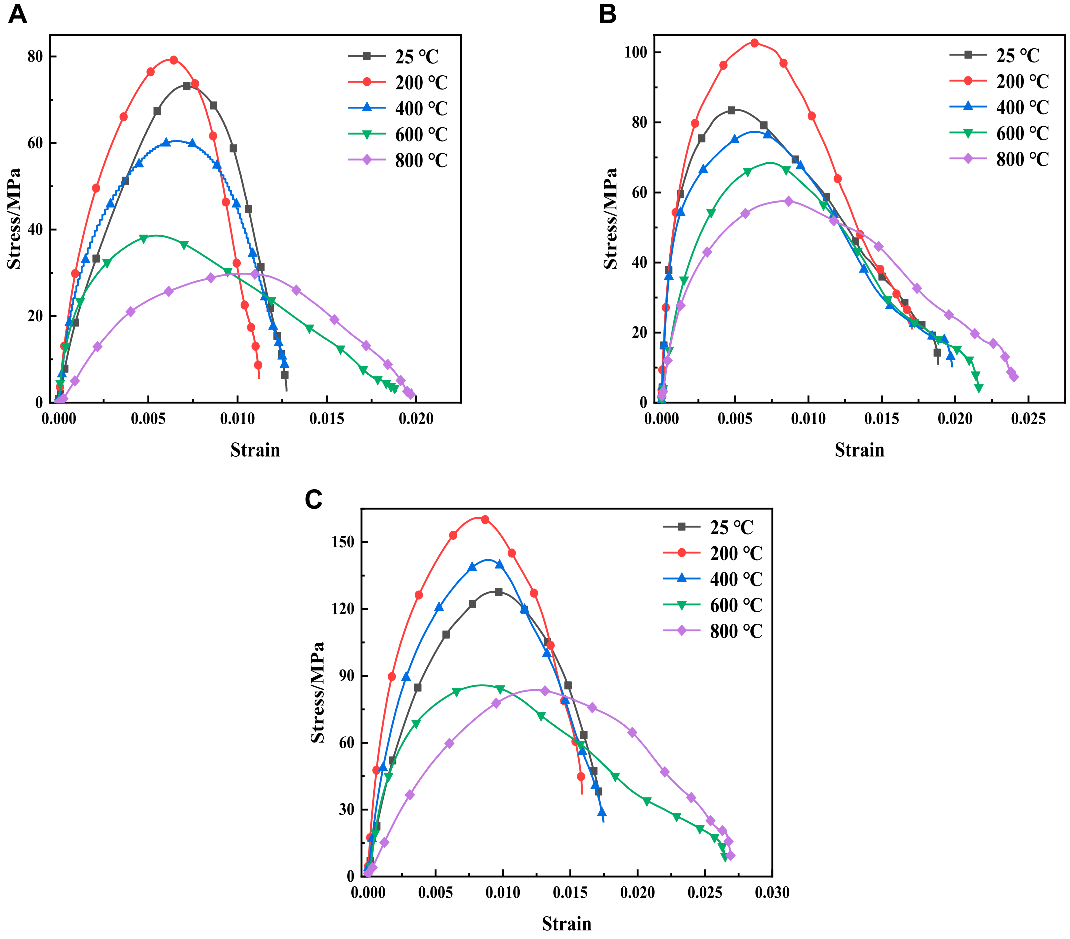

FIGURE 4 | Dynamic stress–strain curves of granite specimens affected by different temperatures at different impact velocities of **(A)** 8.5 m/s, **(B)** 11.5 m/s, and **(C)** 13.5 m/s.

TABLE 1 | Energy dissipation of granite under different working conditions.

Temperature (°C)	Impact velocity (m/s)	Incident energy W_I/J	Reflected energy W_R/J	Transmission energy W_T/J	Dissipation energy W_S/J	SEA J/cm^3
25	8.5	54.57	19.15	12.73	22.69	0.462
	11.5	108.94	41.72	19.36	47.86	0.976
	13.5	154.69	55.52	30.07	69.10	1.408
200	8.5	55.75	14.65	16.35	24.75	0.504
	11.5	114.71	36.91	25.95	51.85	1.057
	13.5	150.54	40.37	36.80	73.37	1.496
400	8.5	53.22	18.10	12.45	22.67	0.462
	11.5	111.88	48.25	18.49	45.14	0.920
	13.5	162.27	60.10	39.14	63.03	1.285
600	8.5	53.94	25.11	8.24	20.59	0.420
	11.5	113.65	59.27	11.26	43.12	0.879
	13.5	161.46	77.91	31.75	51.80	1.056
800	8.5	54.42	31.99	3.86	18.57	0.379
	11.5	112.27	67.58	8.03	36.66	0.747
	13.5	157.35	89.58	25.29	42.48	0.866

and then decreased. They reached the maximum at 200°C. The curve moved down significantly at 400°C than at normal temperature and 200°C, indicating that there is a threshold temperature for the deterioration of rock mechanical properties between 200 and 400°C. At 25–800°C, the curve gradually moved to the lower right. Thus, the continuous increase in rock failure strain indicates that the ductility of the rock was enhanced by high temperature, and it transitioned from brittleness to plasticity. With an increase in the strain rate at the same temperature level, the peak stress and elastic modulus of the rock have different degrees of buoyancy, which is an evident strain rate effect.

RESULTS AND DISCUSSION

Energy Dissipation

The development of fractures in rocks is the result of energy absorption (Xia et al., 2006; Zhao et al., 2019). **Eq. 2** was used to calculate the incident, reflected, transmitted, and dissipated energies during the dynamic impact compression tests of granite, as presented in **Table 1**.

$$\left.\begin{aligned} W_I &= ACE\int_0^t \varepsilon_i^2(t)d(t) \\ W_R &= ACE\int_0^t \varepsilon_r^2(t)d(t) \\ W_T &= ACE\int_0^t \varepsilon_t^2(t)d(t) \end{aligned}\right\}, \tag{2}$$

where W_I represents the incident energy; W_R represents the reflected energy; and W_T represents the transmitted energy; $\varepsilon_i(t)$, $\varepsilon_r(t)$, and $\varepsilon_t(t)$ are the incident, reflected, and transmitted strains on the bar, respectively; and A, E, and C represent the cross-sectional area, elastic modulus, and longitudinal wave velocity of the pressure rod, respectively.

The relationship among the incident, reflected, and transmitted energies under different working conditions is shown in **Figure 5**. At the same temperature, the energy levels of the incident, reflected, and transmitted energies increased with an increase in the impact rate. The growth rate was also positively correlated with the impact rate, exhibiting an evident strain rate effect. This conforms to the relevant laws of kinetic energy theorem (Shu et al., 2019). The influence of temperature was primarily reflected in the evolution of reflected and transmitted energies. With an increase in temperature, the transmission energy first increased and reached a maximum value at 200°C. When the temperature level exceeded 400°C, the transmitted energy gradually decreased with an increase in temperature; however, the effect on reflected energy was the opposite.

The influence of reflected or transmitted energy on granite specimens cannot be directly characterized by the influence of temperature on granite specimens during the crushing process. Xia et al. (2006) introduced the concept of crushing energy (**Eq. 3**) to characterize the energy dissipation during granite destruction.

$$W_S = W_I - [W_R + W_T], \tag{3}$$

where W_S represents the dissipated energy, W_I represents the incident energy, W_R represents the reflected energy, and W_T represents the transmitted energy.

Compared with other dissipated energies (such as heat energy), previous studies (Zhang and Jing, 2018; Shu et al., 2019) have considered dissipated energy as the main energy causing the propagation of crack and breakage of rock materials during the dynamic impact. In this case, the dissipated energy can be approximated as broken energy. The statistics of crushing energy under different working conditions are shown in **Figure 6**. **Figure 6** shows that the dissipated energy has an evident strain rate effect and temperature effect on the failure process of the granite specimen. Dissipated energy increases with an increase in the strain rate and becomes a quadratic parabola with an increase in temperature. The overall evolution law of the crushing energy of granite during the dynamic impact was consistent compared to the dynamic compressive strength

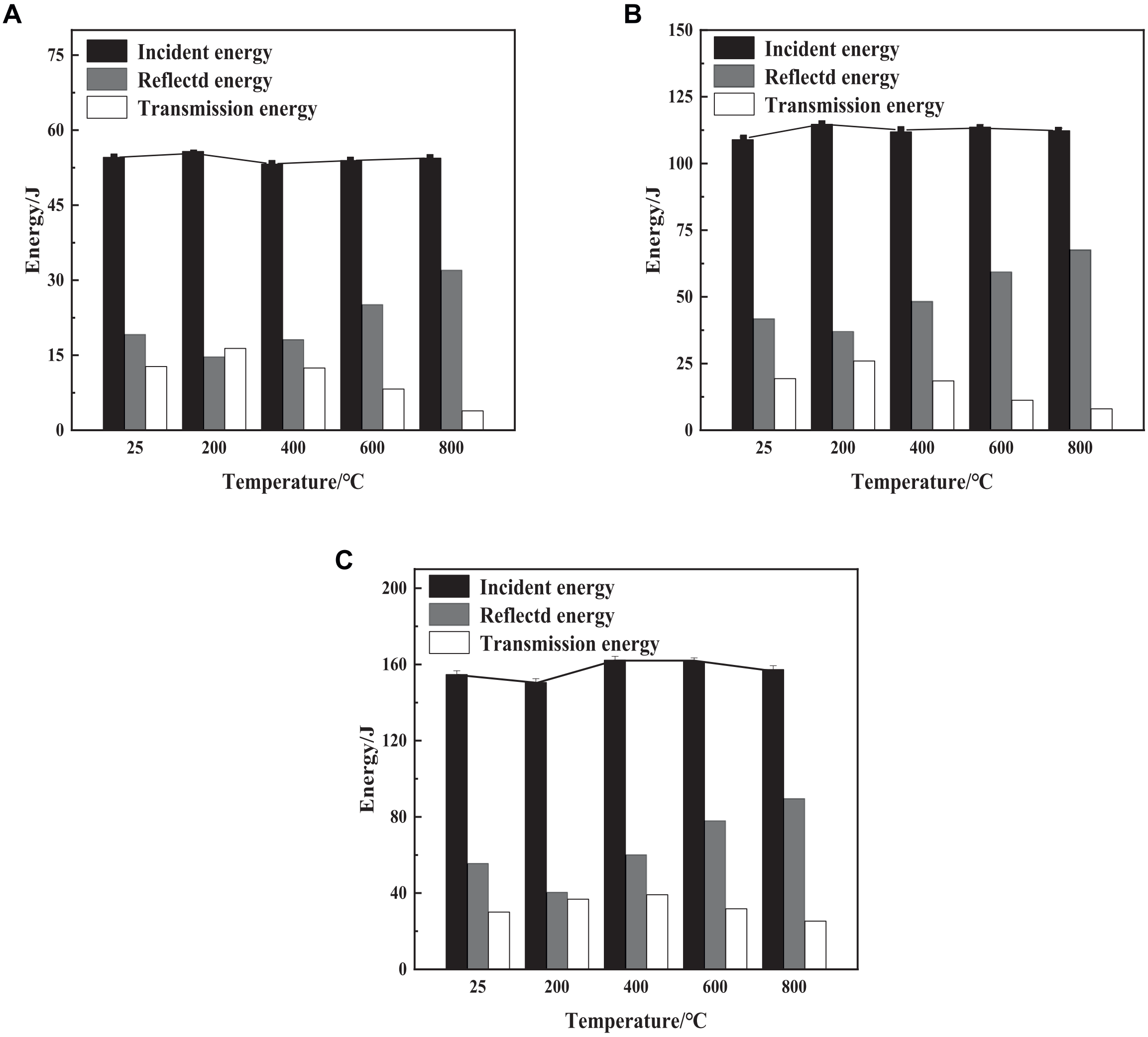

FIGURE 5 | Relationship curves of reflected and transmitted energies with incident energy at impact velocities of **(A)** 8.5 m/s, **(B)** 11.5 m/s, and **(C)** 13.5 m/s.

under different working conditions. This can also explain the strain rate and temperature effects on the dynamic compressive strength of granite from the perspective of energy dissipation.

Shape Features

The fracture morphology of the granite after high-temperature treatment is shown in **Figure 7**. The failure modes of the granite specimens exhibit obvious temperature and strain rate effects (**Figure 7**). With an increase in temperature and impact rate grades, both showed a trend of deepening crushing degree, increasing granular fragments, and gradually decreasing particles after crushing. Thus, it was concluded that the temperature and the impact rate influence the final failure mode of the granite specimen by affecting the energy dissipation during the impact. Under the same impact rate, the granite specimen gradually developed from splitting failure mode with a less fracture surface to compression failure mode, with an increase in temperature and strain rate grade.

The distribution of rock fragmentation reflects the overall effect on it under the combined influence of temperature and impact load (Xu and Liu, 2012). A standard circular hole screen was used to screen-crushed granite specimens. Statistical analysis was conducted to obtain the distribution of broken lumpiness in granite specimens at different impact rates and temperature levels. The method introduced by Xu and Liu (2012) was implemented to calculate the average fragmentation, dm, of the granite specimens using **the**following equation (**Figure 8**):

$$d_m = \sum (r_i d_i) \Big/ \sum r_i, \tag{4}$$

where d_i is the average size of residual screen fragments (0.15, 0.4, 0.75, 1.75, 3.75, 7.5, 12.5, 17.5, 22.5, and 37.5 mm) and r_i is the percentage of residual screen fragments in the total mass of fragments.

It can be seen from **Figure 8** that the average fragmentation of granite ranges from 7.22 to 34.27 mm. At the same impact velocity, and

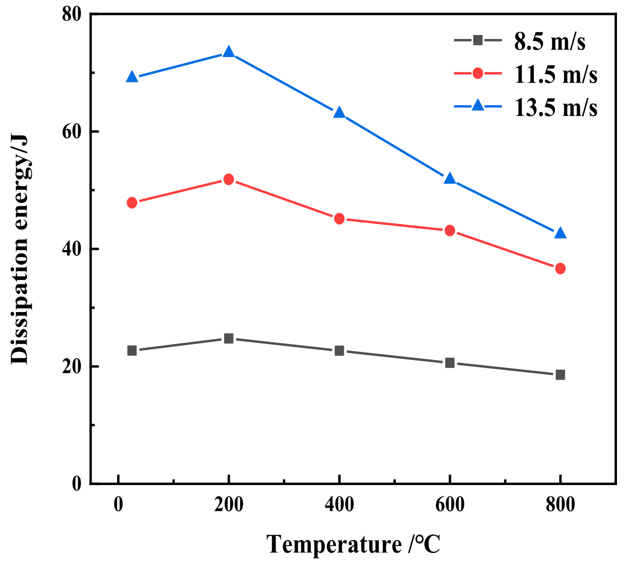

FIGURE 6 | Variations in dissipated energy under different working conditions.

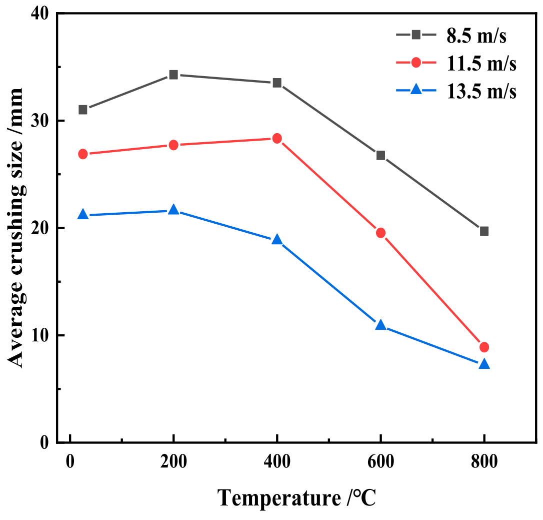

FIGURE 8 | Average fragment size distribution of granite.

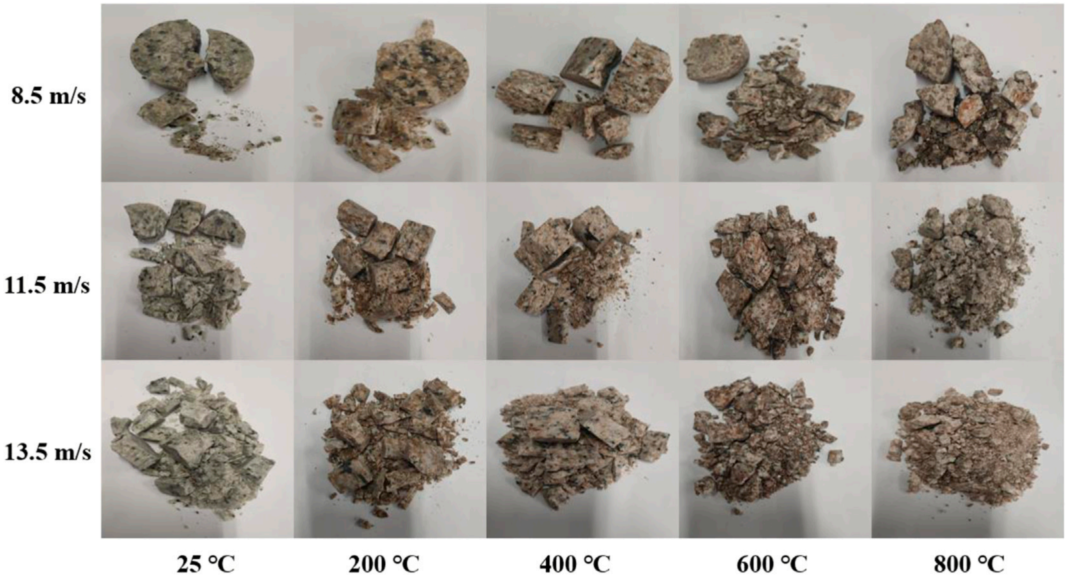

FIGURE 7 | Failure modes of granite under different temperatures and impact velocities.

an increasing temperature grade, the average fragmentation degree of granite increases gradually and reaches a maximum value between 200 and 400°C. When the heating temperature exceeded 400°C, the average fragmentation of granite began to decrease, reaching a minimum value at 800°C. This indicates that there exists a threshold temperature that affects the variation in the average fragmentation size of granite. In our experiments for the present study, the threshold temperature ranged between 200 and 400°C. Under the same heating temperature grade, the average fragmentation of granite showed a gradually increasing trend with an increase in the impact rate grade.

According to the fractal dimension, D_b of the mass–frequency relationship of the screening test, and the calculation formula can be expressed as follows (Xu and Liu, 2012):

$$lg\left(M_{x_0}/M_T\right) = (3 - D_b)lg\left(\frac{x_0}{x_m}\right), \tag{5}$$

where M_{x_0} and M_T are the cumulative mass of the material under the sieve and the total mass of fragments, respectively; x_0 and x_m represent the size of the broken fragments and maximum size of the fragments, respectively.

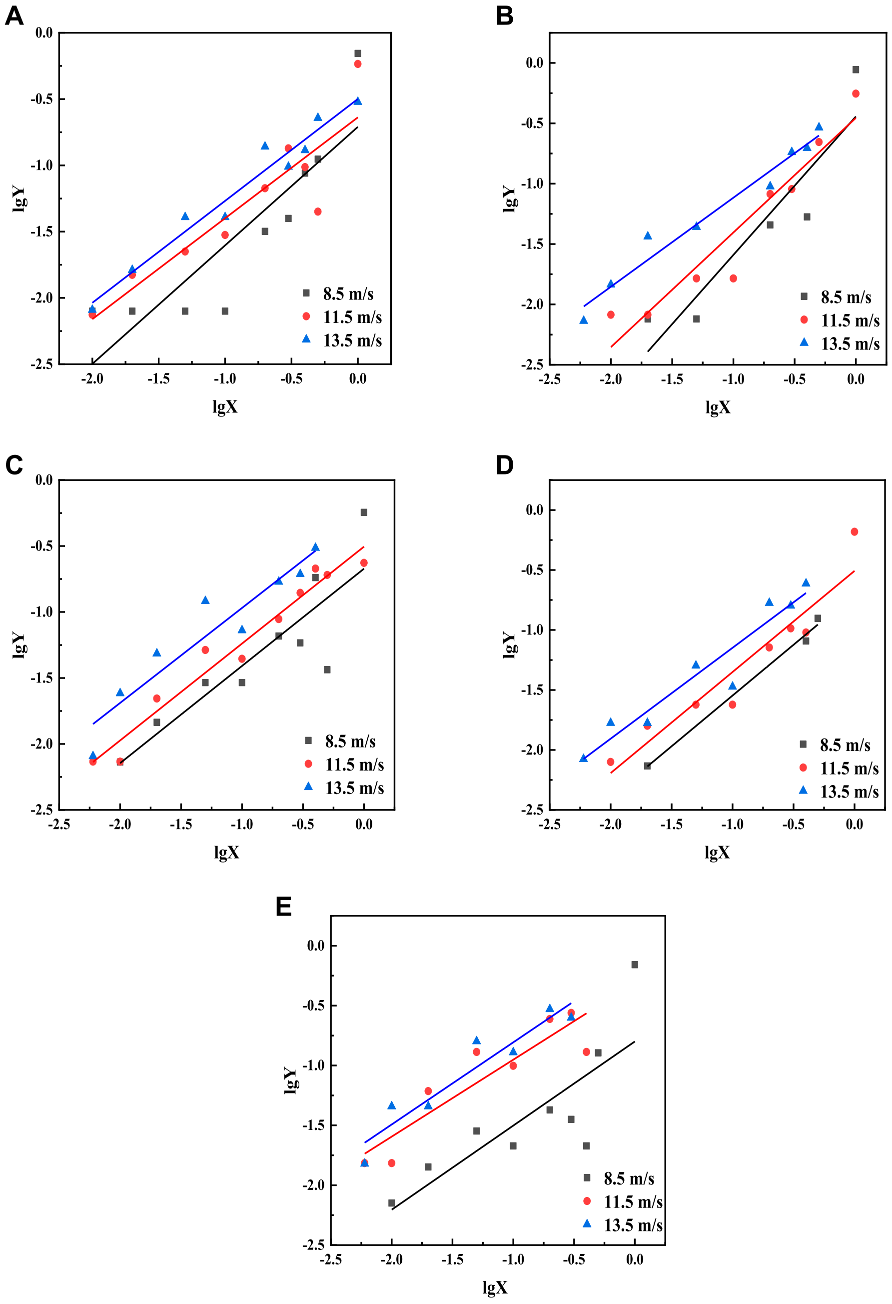

FIGURE 9 | lgY–lgX curves: **(A)** 25°C, **(B)** 200°C, **(C)** 400°C, **(D)** 600°C, and **(E)** 800°C.

The fractal dimension D_b of granite fragmentary lumpiness can be obtained by linearly fitting $M_{x_0}/M_T = Y$, $x_0/x_m = X$ on the data points in the lgY–lgX-type logarithmic coordinate system. The logarithmic coordinate curve for the calculation of the dynamic impact fractal dimension of granite after high-temperature treatment is shown in **Figure 9**. The statistical results for the fractal dimension are listed in **Table 2**.

It can be observed from **Table 2** that the fitting line has a good correlation. With an improvement in the impact rate grade, the correlation of the fitting increases continuously. In the dynamic compression test, the fractal dimension of the granite fluctuated between 2.0138 and 2.3640. The fractal dimension is not only related to the strain rate but also to the properties of the rock itself (Ji et al., 2020). Under the condition of a constant impact load, the change in fractal dimension with temperature is opposite to the peak stress change in the dynamic impact of granite. The smaller the peak stress of granite, the more severe the degree of breakage, and the larger the fractal dimension. The change in the fractal dimension indirectly reflects the influence of temperature and impact load coupling on the mechanical properties of granite (Xu and Liu, 2012).

TABLE 2 | Fractal dimensions and fitting degrees at different temperatures.

Temperature/°C	8.5 m/s		11.5 m/s		13.5 m/s	
	Fractal dimension	Fitting degree	Fractal dimension	Fitting degree	Fractal dimension	Fitting degree
25	2.1061	0.7715	2.1829	0.8246	2.2332	0.9604
200	2.0138	0.8575	2.0908	0.9143	2.1528	0.9672
400	2.1536	0.9897	2.2060	0.9038	2.2417	0.9203
600	2.2030	0.7680	2.2655	0.9572	2.2799	0.8793
800	2.2975	0.6542	2.3372	0.8449	2.3640	0.8825

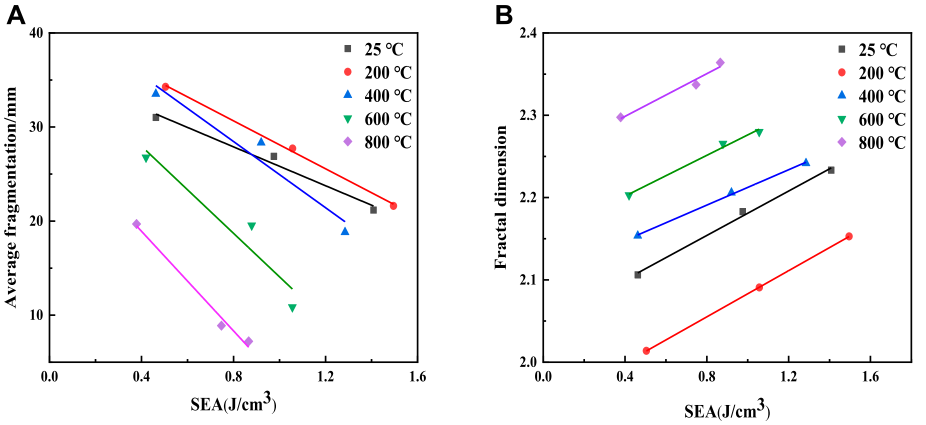

FIGURE 10 | Relationship of **(A)** average fragmentation and **(B)** fractal dimensions with energy consumption density.

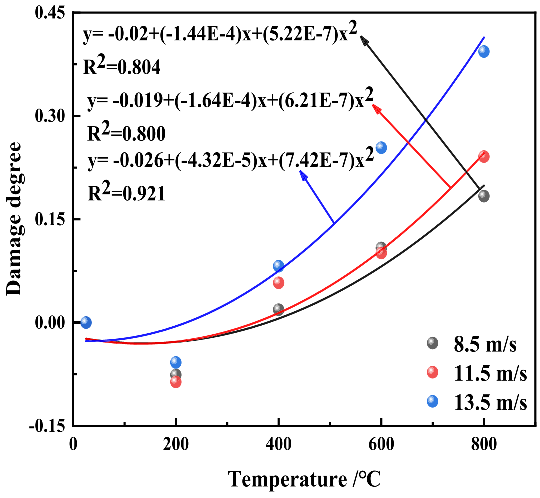

FIGURE 11 | Temperature damage degrees in different working conditions.

Relationship Between Fractal Characteristics and Energy Dissipation

To explore the quantitative relationship between the macro- and micro-characteristics of granite after high-temperature treatment, this study established the relationship between the fractal dimension theory and the associated characterization indexes in the energy dissipation theory. **Figure 10** shows the relationship among average fragmentation, fractal dimension, and energy consumption density.

As shown in **Figure 10**, under the same temperature grade, the average fragmentation of granite decreases linearly with an increase in the energy consumption density. The fractal dimension increased linearly with energy consumption density. The smaller the mean fragmentation, the larger is the fractal dimension. This indicates that the crushing degree of granite was higher during the dynamic impact process. Rock failure is the process of the development, expansion, and coalescence of microfractures in the rock, which is the result of internal damage due to macroscopic failure. The development and propagation of microfractures require energy absorption. As energy consumption density increased, so did the energy absorbed by granite per unit volume during dynamic impact compression and the energy used for rock damage and fracture; this led to the development and expansion of microcracks in the rock. Consequently, the degree of breakage became more intense, the number of new cracks and fracture surfaces, output of small particle size fragments, and the fractal dimension increased, while the average fragmentation size decreased.

Degree of Damage Analysis

The failure process of the rock under a given impact load and temperature is caused by the damage to breakage (Yu et al.,

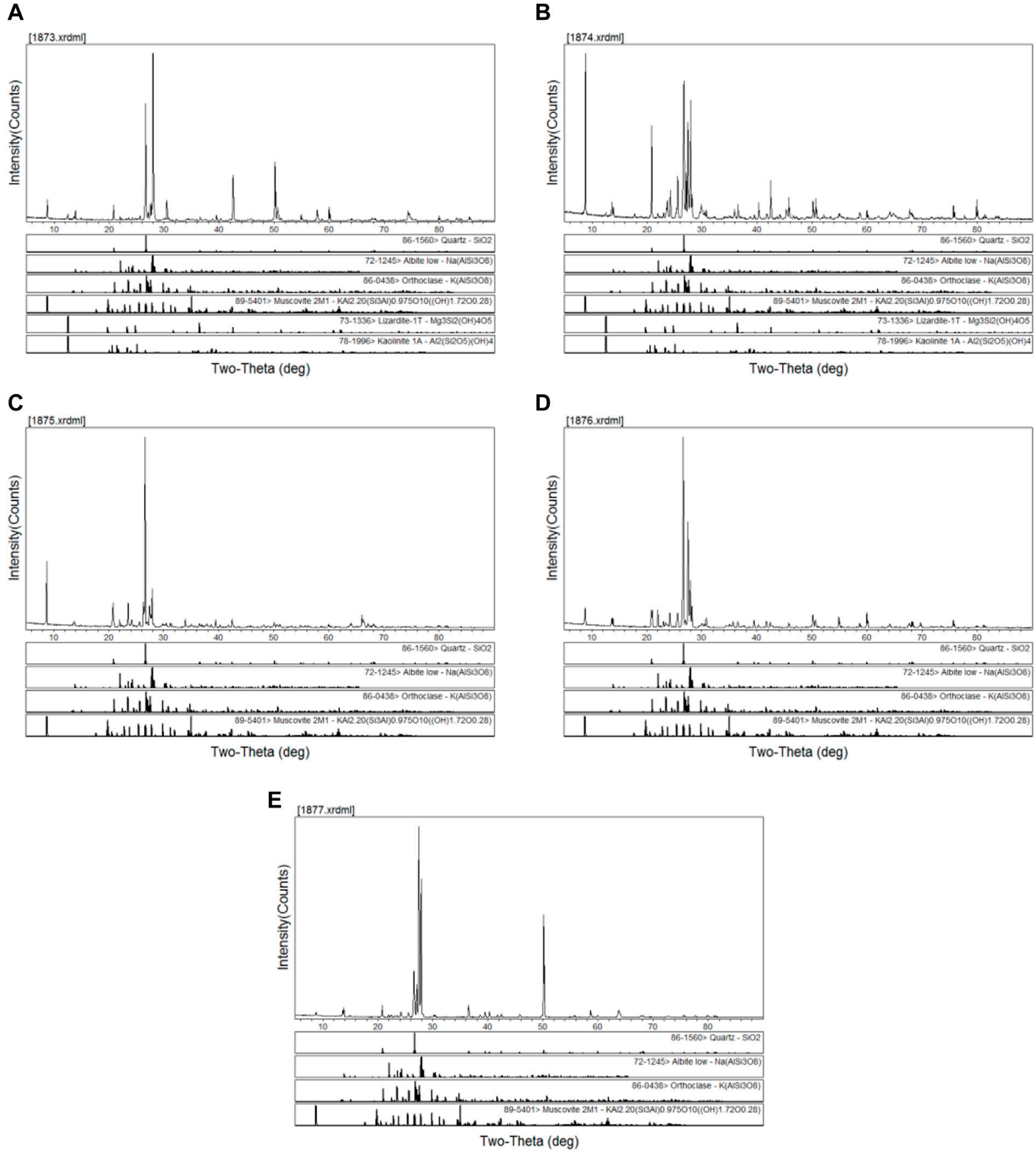

FIGURE 12 | X-ray diffraction phase analysis of granite at different temperatures: **(A)** 25°C, **(B)** 200°C, **(C)** 400°C, **(D)** 600°C, and **(E)** 800°C.

2020). The calculation of the degree of rock damage in this process forms the basis for constructing a dynamic constitutive equation of rock materials under different working conditions. So far, some studies have discussed the measurement and calculation methods for the rock damage degree from the perspective of non-destructive testing and damage testing. Non-destructive testing is mainly carried out through CT scanning of the damaged rock specimens (Wang et al., 2018), measurement of longitudinal wave velocity (Zuo et al., 2017), and other tests in a manner such that the test objects are not damaged. In contrast, the damage testing method mainly involves destructive mechanical experiments on the tested specimen; this method characterizes the damage degree of rock materials using data obtained from experiments

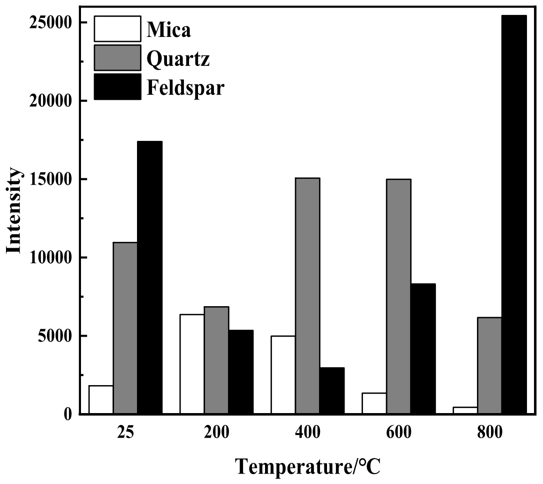

FIGURE 13 | Diffraction intensity of main mineral components of granite at different temperatures.

involving dynamic elastic modulus (Xu et al., 2020), dynamic compressive strength (Guo et al., 2017), energy dissipation (Zhao et al., 2019), breakage of the test specimen (Zhai, 2015), and development and expansion mode of cracks in the failure process (Li et al., 2020). Owing to the limitation of the experimental conditions, this study only considered the degree of damage from the perspective of the energy absorption value.

Based on the strain equivalence principle (He et al., 2018), **Eq. 6** was used to characterize the temperature damage from the perspective of energy dissipation:

$$D_{T(W)} = \frac{W_T - W_0}{1 - W_0}, \tag{6}$$

where $D_{T(W)}$ represents the damage factor, W_0 represents the dissipated energy at 25°C, and W_T represents the corresponding temperature dissipated energy.

It can be observed from **Figure 11** that $D_{T(W)}$ of different temperature grades presents a quadratic non-linear correlation under the same impact velocity. When the heating temperature ranges from 25 to 200°C, $D_{T(W)} < 0$. This reflects the strengthening effect of temperature on the dynamic mechanical properties of granite. When the heating temperature level exceeds 200°C, $D_{T(W)}$ shows an increasing trend with an increase in the heating temperature level. The results indicate that temperature degrades the dynamic mechanical properties of granite over time, which is consistent with the effect of temperature on the dynamic compressive strength. However, with the increase in impact velocity in the test, the energy used for crushing the rock increased, and the coupled effect of impact velocity and temperature aggravated the internal damage of the rock.

Analysis of Granite Facies Characteristics

X-ray diffraction (XRD) experiments were performed on granite at room temperature and high temperature to analyze the changes in the physical phase characteristics of granite before and after high-temperature treatment. The XRD patterns of granite at various temperatures are shown in **Figure 12**.

As shown in **Figure 12**, the mineral composition and primary components of granite tend to change at different temperature grades. The variation in the diffraction intensities of the main components is shown in **Figure 13**.

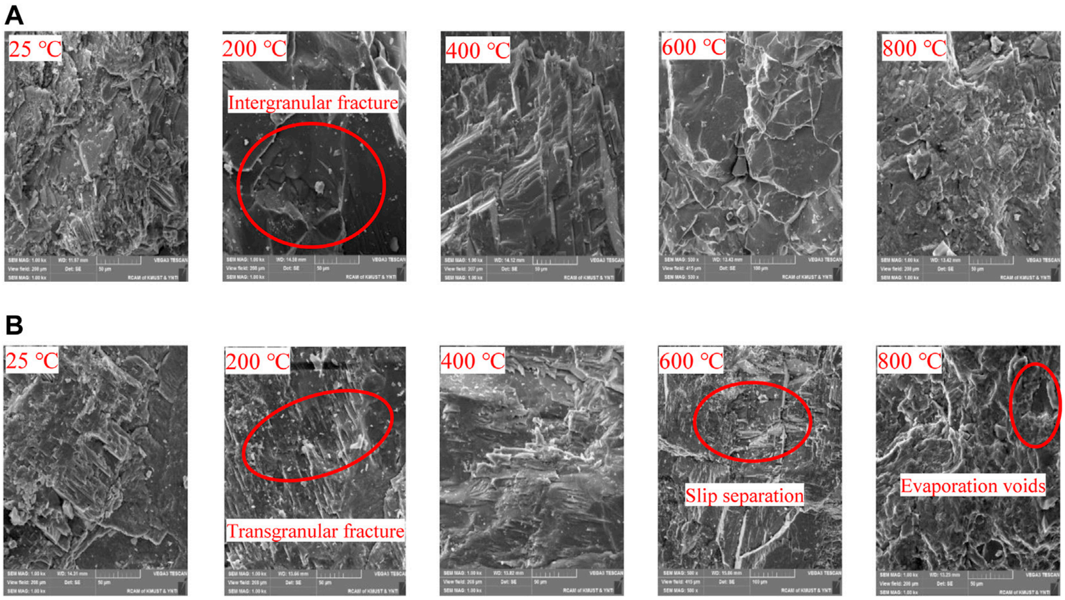

FIGURE 14 | Scanning electron microscopy image of granite at different conditions: **(A)** impact velocity of 11.5 m/s and **(B)** impact velocity of 13.5 m/s.

As shown in **Figure 13**, the primary mineral components of granite at normal temperatures are mica, quartz, feldspar, and small amounts of silicate minerals. When the heating temperature was 200°C, the diffraction intensity of mica increased to 6,354 counts, which continued to decrease with an increase in the heating temperature. When the heating temperature was 800°C, the diffraction intensity was 432 counts. With an increase in the heating temperature, the diffraction intensity of feldspar first decreased and then increased. When the heating temperature was 400°C, the diffraction intensity reached a minimum of 2,958 counts. Overall, the diffraction intensity of quartz was correlated with the change in mineral compositions, and the minimum diffraction intensity was observed at 800°C.

When the heating temperature was 200°C, the main mineral components in granite at normal temperature were the same. However, the effect of temperature on the diffraction intensity varied significantly; that is, the diffraction intensity of mica was greater than that of the other main mineral components, which exhibited similar diffraction intensities. Meanwhile, the grain was not structurally damaged, and the rock compressive strength improved significantly. When the temperature rose to 400°C, the diffraction intensity of quartz increased due to the effect of high temperature on the main mineral composition and decomposition reaction of silicate minerals. Between 400 and 600°C, α-quartz becomes β-modification. Subsequently, the crystal expanded and led to the formation of small cracks inside the rock, thereby weakening the cementation force between grains and decreasing the compressive strength of granite; this result is consistent with the apparent morphology of the granite specimen after the high-temperature treatment (**Figure 1**). When the temperature reaches 800°C, feldspar changes from a crystalline state to an amorphous state (Jia et al., 2021). Thus, after the high-temperature treatment, the granite strength decreases, failure strain increases, and the diffraction intensity fluctuates significantly compared to that in the normal temperature state. A change in the crystal structures of feldspar and quartz deteriorated the mechanical properties of the granite specimens. Meanwhile, decreasing the diffraction intensity of mica promotes the brittle–plastic transformation of granite specimens to a certain extent, which is consistent with the results of macroscopic mechanical experiments.

Analysis of Fracture Morphology After Dynamic Impact

A tungsten wire scanning electron microscope (SEM) was used to observe the fracture morphology of granite specimens after impact compression failure at 25–800°C, and study the influence of the impact rate and temperature on the fracture failure form of granite. The fracture morphologies are shown in **Figure 14**.

Figure 14 shows that under dynamic impact compression conditions, the fracture morphology of granite presents different failure forms under different working conditions (temperature grade and impact rate). At a constant temperature, intergranular fractures tend to be dominant when the impact rate is 11.5 m/s. With an increase in the impact rate, transgranular fractures increase to 200°C, as shown in **Figure 14**. When the temperature is 400°C, fine cracks appear on the rock. When the temperature rises to 600–800°C, plastic failure characteristics are observed (Liang et al., 2015; Tao et al., 2019).

A low shock rate, low incident energy, and the formation of a crack that extends along the crystal boundary lead to an intergranular fracture. Meanwhile, the impact velocity increases, leading to a rise in the incident energy and dynamic impact load time; in a short period of time, the internal atomic bonds in the crystal with low energy consumption cannot be damaged to produce a transgranular fracture. Although the internal mineral composition and granite microstructure are significantly correlated at high temperatures (such as between 25 and 400°C), the fracture morphology of the rock gives priority to brittle fracture, does not exhibit ductile fracture characteristics, and demonstrates a neat rock fracture morphology; meanwhile, the irregular fracture of quartz and feldspar led to a line shaped transgranular (conchoidal) fracture morphology, with a step cleavage plane fracture. During 600–800°C, the fracture morphology changed from a strip structure to a coarse block structure. The high temperature changed the rock's internal structure, the sliding and separation phenomenon indicates the brittle-to-plastic transformation of granite, which was consistent with the macro mechanical characteristics.

CONCLUSION

In this study, the granite subjected to high-temperature treatment was taken as the research object. The fragmentation morphology and the energy dissipation of the rock after normal (25°C) and high-temperature treatments (200°C, 400°C, 600°C, and 800°C) were studied using the SHPB device, while the fragmentation characteristics and dynamic mechanical properties of granite were elucidated. The crushing characteristics and the energy dissipation law of granite specimens affected by high temperatures in the SHPB experiment were also studied, while the temperature damage under different impact velocities was discussed with regard to energy dissipation. The main conclusions of this study are as follows:

1) Temperature and the strain rate affect the dynamic mechanical properties of granite and the energy dissipation during the failure process, which are closely related to the threshold value of the heating temperature grade. In the experiments conducted in this study, the threshold temperature is 200°C. Below 200°C, the transmitted energy first increases, and then decreases with an increase in the temperature grade; meanwhile, the transmitted energy exhibits an opposite change trend.

2) With an increase in the temperature grade, the failure mode of the rock changes from splitting failure to compression failure; the impact rate of ascension, which increases the energy density, tends to decrease the broken blocks of granite. Meanwhile, the fractal dimension increases with a rise in the energy consumption and density. Moreover, strain rate effects, broken blocks, changes in the fractal dimension, and the influence of temperature on rock mechanical characteristics are closely related; thus, these characteristics can reflect both the rock crushing processes to some extent.
3) From the perspective of energydissipation characterization of the rock damage degree, a quadratic non-linear relationship is observed with temperature. When the heating temperature range is 25–200°C, $D_{T(W)} < 0$; this reflects the effect of temperature on the rock's mechanical properties of the reinforcement. Meanwhile, the damage degree increased with a rise in the temperature, which is consistent with the influence law of temperature on the dynamic compressive strength.
4) High temperatures affect the compositional characteristics of granite and change its mechanical properties. A decrease in the muscovite content and the transformation of quartz and feldspar crystals led to the gradual deterioration of the mechanical behavior of granite. At a same temperature level, it is observed that the higher the impact velocity, the higher is the proportion of transgranular fractures. With an increase in the heating temperature, the fracture morphology becomes more complex and ductile fracture failure characteristics are observed, thus indicating that the rock underwent a brittle-to-plastic transformation under the influence of high temperature.

DATA AVAILABILITY STATEMENT

The original contributions presented in the study are included in the article/Supplementary Material, further inquiries can be directed to the corresponding author.

AUTHOR CONTRIBUTIONS

Conceptualization: HA and LL; methodology: HA and LL; formal analysis: HA and LL; investigation: YW; writing—original draft preparation: HA and YW; and funding acquisition: LL. All authors read and agreed to the published version of the manuscript.

FUNDING

This research was funded by the National Natural Science Foundation of China (grant Nos.11862010 and 51964023).

REFERENCES

Bandini, A., and Berry, P. (2012). Influence of Marble's Texture on its Mechanical Behavior. *Rock Mech. Rock Eng.* 46 (4), 785–799. doi:10.1007/s00603-012-0315-1

Brotóns, V., Tomás, R., Ivorra, S., and Alarcón, J. C. (2013). Temperature Influence on the Physical and Mechanical Properties of a Porous Rock: San Julian's Calcarenite. *Eng. Geol.* 167, 117–127. doi:10.1016/j.enggeo.2013.10.012

Ge, Z., and Sun, Q. (2018). Acoustic Emission (AE) Characteristics of Granite after Heating and Cooling Cycles. *Eng. Fracture Mech.* 200, 418–429. doi:10.1016/j.engfracmech.2018.08.011

Guo, H., Guo, W., Zhai, Y., and Su, Y. (2017). Experimental and Modeling Investigation on the Dynamic Response of Granite after High-Temperature Treatment under Different Pressures. *Const. Build. Mater.* 155, 427–440. doi:10.1016/j.conbuildmat.2017.08.090

He, A. L., Wang, Z. L., and Bi, C. C. (2018). Study on Thermal Damage Characteristics and Mechanism of Huashan Granite. *Hydro-Science and Engineering* 01, 95–101. doi:10.16198/j.cnki.1009-640X.2018.01.014

He, J. F. (1994). Resource Distribution and Geological Genesis of marble and Granite in Some Places, Prefectures and Counties in Yunnan Province. *Yunnan Building Mater.* 000 (03), 4–7.

Hong, L., Zhou, Z.-l., Yin, T.-b., Liao, G.-y., and Ye, Z.-y. (2009). Energy Consumption in Rock Fragmentation at Intermediate Strain Rate. *J. Cent. South. Univ. Technol.* 16 (4), 677–682. doi:10.1007/s11771-009-0112-5

Hu, S. S., Wang, L. L., Song, L., and Zhang, L. (2015). Review of the Development of Hopkinson Pressure Bar Technology in China. *Explos. Shock Waves* 34 (06), 641–657. doi:10.11883/1001-1455(2014)06-0641-17

Imani, M., Nejati, H. R., and Goshtasbi, K. (2017). Dynamic Response and Failure Mechanism of Brazilian Disk Specimens at High Strain Rate. *Soil Dyn. Earthquake Eng.* 100, 261–269. doi:10.1016/j.soildyn.2017.06.007

Ji, J. J., Li, H. T., Wu, F. M., and Yao, Q. (2020). Fractal Characteristics of Rock Fracture under Impact Loading. *Shock Vib.* 39 (13), 176–183. doi:10.13465/j.cnki.jvs.2020.13.026

Jia, P., Yang, Q. J., Liu, D. Q., Wang, S. H., and Zhao, Y. (2021). Physical and Mechanical Properties and Micro-fracture Characteristics of High Temperature Granite after Water Cooling. *Rock Soil Mech.* 42 (06), 1568–1578. doi:10.16285/j.rsm.2020.1383

Li, D. Y., Hu, C. W., and Zhu, Q. Q. (2020). Experimental Study on Mechanical Properties and Failure Law of Precast Fractured Granite under Dynamic and Static Combined Loading. *Chin. J. Rock Mech. Eng.* 39 (06), 1081–1093. doi:10.13722/j.cnki.jrme.2019.1089

Li, G., Sun, Y., and Qi, C. (2021). Machine Learning-Based Constitutive Models for Cement-Grouted Coal Specimens under Shearing. *Int. J. Mining Sci. Techn.* 31, 813–823. doi:10.1016/j.ijmst.2021.08.005

Liang, C. Y., Wu, S. R., and Li, X. (2015). Study on fine-microscopic Characteristics of Granite Fracture under Uniaxial Compression in the Range of Medium and Low Strain Rates. *Chin. J. Rock Mech. Eng.* 34 (S1), 2977–2986. doi:10.13722/j.cnki.jrme.2014.0701

Liu, S., and Xu, J. Y. (2014). Study on the Effect of High Temperature on the Dynamic Compression Mechanical Properties of Granite. *Vibration Shock* 33 (04), 195–198. doi:10.13465/j.cnki.jvs.2014.04.034

Liu, S., and Xu, J. (2015). An Experimental Study on the Physico-Mechanical Properties of Two post-high-temperature Rocks. *Eng. Geol.* 185, 63–70. doi:10.1016/j.enggeo.2014.11.013

Malik, A., Chakraborty, T., and Rao, K. S. (2018). Strain Rate Effect on the Mechanical Behavior of basalt: Observations from Static and Dynamic Tests. *Thin-Walled Struct.* 126, 127–137. doi:10.1016/j.tws.2017.10.014

Mishra, S., Chakraborty, T., Matsagar, V., Loukus, J., and Bekkala, B. (2018). High Strain-Rate Characterization of Deccan Trap Rocks Using SHPB Device. *J. Mater. Civ. Eng.* 30 (5), 04018059. doi:10.1061/(asce)mt.1943-5533.0002229

Qi, C. C., Yang, X. Y., Li, G. C., Chen, Q. S., and Sun, Y. T. (2021). Summary and prospect of the Application of New Generation Artificial Intelligence in Mine Filling. *J. Coal* 46 (02), 688–700. doi:10.13225/j.cnki.jccs.xr20.1704

Sasmito, A. P., Kurnia, J. C., Birgersson, E., and Mujumdar, A. S. (2015). Computational Evaluation of thermal Management Strategies in an Underground Mine. *Appl. Therm. Eng.* 90, 1144–1150. doi:10.1016/j.applthermaleng.2015.01.062

Shu, R.-h., Yin, T.-b., Li, X.-b., Yin, Z.-q., and Tang, L.-z. (2019). Effect of thermal Treatment on Energy Dissipation of Granite under Cyclic Impact Loading. *Trans. Nonferrous Met. Soc. China* 29 (2), 385–396. doi:10.1016/s1003-6326(19)64948-4

Tao, M., Wang, J., Li, Z. W., Hong, Z. X., Wang, Y. Q., and Zhao, R. (2019). Fine-microscopic Experimental Study on Fracture Surface of Granite Layer under Impact Loading. *J. Rock Mech. Eng.* 38 (11), 2172–2181. doi:10.13722/j.cnki.jrme.2019.0185

Wang, X.-Q., Schubnel, A., Fortin, J., Guéguen, Y., and Ge, H.-K. (2013). Physical Properties and Brittle Strength of Thermally Cracked Granite under Confinement. *J. Geophys. Res. Solid Earth* 118 (12), 6099–6112. doi:10.1002/2013jb010340

Wang, Y., Hou, Z. Q., and Hu, Y. Z. (2018). *In Situ* X-ray Micro-CT for Investigation of Damage Evolution in Black Shale under Uniaxial Compression. *Environ. Earth Sci.* 77 (20), 1–12. doi:10.1007/s12665-018-7904-6

Wang, L. l. (2005). *Stress Wave Foundation [M]*. Beijing: National Defense Industry Press, 52–60.

Wu, R. J., Li, H. B., Li, X. F., Yue, H. Z., Yu, C., and Xia, X. (2019). Study on Compressive Mechanical Properties of Layered Phyllite under Different Impact Loads. *J. Rock Mech. Eng.* (S2), 3304–3312. doi:10.13722/j.cnki.jrme.2018.1084

Wu, R. J., Li, H. B., Li, X. F., Yu, C., Xia, X., and Liu, L. W. (2020). Energy Consumption and Fragmentation Characteristics of Layered Rock under Impact Loading. *J. Coal* 45 (03), 1053–1060. doi:10.13225/j.cnki.jccs.2019.0266

Xia, C. J., Xie, H. P., Ju, Y., and Zhou, H. W. (2006). Experimental Study on Energy Dissipation of Porous Rock under Impact Loading. *Eng. Mech.* 23 (09), 1–5. doi:10.3969/j.issn.1000-4750.2006.09.001

Xie, H. P. (2019). Research Progress of Deep Rock Mass Mechanics and Mining Theory. *J. Coal* 44 (05), 1283–1305. doi:10.13225/j.cnki.jccs.2019.6038

Xu, J. Y., and Liu, S. (2012). Analysis of Fractal Characteristics of marble Fragments in Impact Loading Test. *Rock Soil Mech.* 33 (11), 3225–3229. doi:10.16285/j.rsm.2012.11.005

Xu, J. Y., and Shi, L. (2013). Analysis of Energy Consumption Law of Rock Deformation and Failure Process under High Temperature in SHPB Test. *J. Rock Mech. Eng.* 32 (S2), 3109–3115.

Xu, J., Kang, Y., Wang, Z., Wang, X., Zeng, D., and Su, D. (2020). Dynamic Mechanical Behavior of Granite under the Effects of Strain Rate and Temperature. *Int. J. Geomech.* 20 (2), 04019177. doi:10.1061/(asce)gm.1943-5622.0001583

Yin, T. B., Li, X. B., Wang, B., Yin, Z. Q., and Jin, J. F. (2011). Study on Mechanical Properties of sandstone under Dynamic Compression after High Temperature. *J. Geotechn. Eng.* 33 (05), 777–784.

Yin, T.-b., Peng, K., Wang, L., Wang, P., Yin, X.-y., and Zhang, Y.-l. (2016a). Study on Impact Damage and Energy Dissipation of Coal Rock Exposed to High Temperatures. *Shock Vib.* 2016, 1–10. doi:10.1155/2016/5121932

Yin, T.-b., Shu, R.-h., Li, X.-b., Wang, P., and Liu, X.-l. (2016b). Comparison of Mechanical Properties in High Temperature and thermal Treatment Granite. *Trans. Nonferrous Met. Soc. China* 26 (7), 1926–1937. doi:10.1016/s1003-6326(16)64311-x

Yin, Z., Chen, W., Hao, H., Chang, J., Zhao, G., Chen, Z., et al. (2019). Dynamic Compressive Test of Gas-Containing Coal Using a Modified Split Hopkinson Pressure Bar System. *Rock Mech. Rock Eng.* 53, 815–829. doi:10.1007/s00603-019-01955-w

Yu, L., Peng, H. W., Li, G. W., Zhang, Y., Han, Z. H., and Zhu, H. Z. (2020). Experimental Study on Granite under High Temperature-Water Cooling Cycle. *Rock Soil Mech.* 42 (04), 1025–1035. doi:10.16285/j.rsm.2020.1154

Yuan, L., Xue, J. H., Liu, Q. S., and Liu, B. (2011). Surrounding Rock Control Theory and Support Technology of Deep Rock Roadway in Coal Mine. *J. China Coal Soc.* 36 (04), 535–543. doi:10.13225/j.cnki.jccs.2011.04.014

Zhai, Y. (2015). Space Wave Equation Considering Damage-Induced Weakening and Strain Rate Dependency of Rock. *Teh. Vjesn.* 22 (4), 1035–1042. doi:10.17559/tv-20150406112756

Zhang, R. R., and Jing, L. W. (2018). Analysis of the Relationship between Crushing Degree and Energy Dissipation of Deep sandstone after the Action of High and Low Temperature in SHPB Test. *J. Coal* 43 (07), 1884–1892. doi:10.13225/j.cnki.jccs.2017.1493

Zhao, Z., Ma, W., Fu, X., and Yuan, J. (2019). Energy Theory and Application of Rocks. *Arab J. Geosci.* 12 (15), 1–26. doi:10.1007/s12517-019-4617-4

Zhou, Y. X., Xia, K., Li, X. B., Li, H. B., Ma, G. W., Zhao, J., et al. (2012). Suggested Methods for Determining the Dynamic Strength Parameters and Mode-I Fracture Toughness of Rock Materials. *Int. J. Rock Mech. Min.* 49, 105–112. doi:10.1007/978-3-319-07713-0_3

Zuo, J.-P., Wang, J.-T., Sun, Y.-J., Chen, Y., Jiang, G.-H., and Li, Y.-H. (2017). Effects of thermal Treatment on Fracture Characteristics of Granite from Beishan, a Possible High-Level Radioactive Waste Disposal Site in China. *Eng. Fracture Mech.* 182, 425–437. doi:10.1016/j.engfracmech.2017.04.043

Conflict of Interest: The authors declare that the research was conducted in the absence of any commercial or financial relationships that could be construed as a potential conflict of interest.

frontiers | Frontiers in Earth Science

ORIGINAL RESEARCH
published: 25 April 2022
doi: 10.3389/feart.2022.870595

Study on the Influence of Rock Clip Production and Empty Hole Volume Effect of Upward Blind Shaft Blasting

Yonghui Huang[1], **Bo Sun**[2†], **Zhiyu Zhang**[2,3]*, **Jiale Meng**[2] **and Hua Zeng**[2]

[1]Faculty of Electric Power Engineering, Kunming University of Science and Technology, Kunming, China, [2]Faculty of Land Resources Engineering, Kunming University of Science and Technology, Kunming, China, [3]Yunnan Key Laboratory of Sino-German Blue Mining and Utilization of Special Underground Space, Kunming University of Science and Technology, Kunming, China

Cutting blasting is the principal construction method for roadway and shaft excavation, but the studies on the damage mechanism of cutting blasting affected by the volume effect of empty holes under high ground stress are not insufficient. During cutting blasting, different damage zones are formed. In this paper, combined with the rock damage criterion and RHT constitutive function, the ranges of these damage zones are determined. The smooth particle hydrodynamics method is used to study the influence of high *in-situ* stress on rock blasting damage from the perspective of the number of empty holes and the production coefficient of rock clamp. The accuracy of the determined damage zone range is verified by supplemented field tests. The research results show that in the process of rock clamp production, the propagation of blasting stress wave is inhibited, especially the tensile stress wave which is more obviously inhibited. The empty holes reduce the inhibitory effect of rock clamp production. With the increase in the production coefficient of rock clip, the blasting damage radius is reduced by 39.7%, 35.1%, 30.5%, 26.7%, and 22.9% compared with the theoretical value, respectively, while its influence on the radius of crushing zone is small. The three-dimensional scanning results were used to inverse calculate the production coefficient of the rock clip. The fitting degree between the numerical simulation and the field test scanning results is about 94.5%, which proves the accuracy of the RHT constitutive parameters and the reliability of the determination range. The mathematical relationship between the production coefficient K_r for rock clip and the relative height H of the wellhead and the area S_c of the cross-section cavity is fitted based on the data of several upward cutting blasting field tests.

Keywords: numerical simulation, rock damage, cutting blasting, RHT constitutive model, high *in-situ* stress, clamp production

Edited by:
Kun Du,
Central South University, China

Reviewed by:
Fuqiong Huang,
China Earthquake Networks Center, China
Xiaolei Wang,
North China University of Science and Technology, China
Shuxin Liu,
Inner Mongolia University of Science and Technology, China

***Correspondence:**
Zhiyu Zhang
11301052@kust.edu.cn

†These authors share first authorship

Specialty section:
This article was submitted to Geohazards and Georisks, a section of the journal Frontiers in Earth Science

Received: 07 February 2022
Accepted: 24 March 2022
Published: 25 April 2022

Citation:
Huang Y, Sun B, Zhang Z, Meng J and Zeng H (2022) Study on the Influence of Rock Clip Production and Empty Hole Volume Effect of Upward Blind Shaft Blasting.
Front. Earth Sci. 10:870595.
doi: 10.3389/feart.2022.870595

INTRODUCTION

At present, in the excavation process of mines, roadways, and shafts, the drilling and blasting method is mainly adopted. With the continuous excavation, the mine and roadway projects are constantly developing deep underground, and the influence of high *in-situ* stress on construction becomes more significant. The blasting construction under high *in-situ* stress is mainly affected by the coupling effect of explosion load and *in-situ* stress field. Therefore, under the condition of ensuring the blasting effect, controlling the damage range of rock mass becomes a further concern (Li et al., 2011; Yao-Ji, Xiao-Shuang, and Wang 2014; Fan et al., 2017; Xie et al., 2018).

For the blasting parameters in cut blasting, a lot of studies have been carried out (Cai et al., 2004; Cheng et al., 2020; K. ; Gao et al., 2021; X.S. ; Li et al., 2021; Man et al., 2018; D.Q. ; Yang, Wang, et al., 2020; H. ; Zhang et al., 2021; X.Y. ; Zhang et al., 2020), but most of them are based on shallow burial depth and only consider blasting load conditions. With the deepening of research, Kaiser, Zou, and Lang (1990) proposed a method taking into account initial stress unloading and stress field, and summarized the determination method for excavation damage area of the tunnel. Besides, L. Xie, Lu, Jiang, et al. (2017); L.X. Xie, Lu, Zhang, et al. (2017) used a numerical simulation method to study the influence of *in-situ* stress and rock damage inoculation mechanism in the process of deep tunnel cutting blasting and proposed a simplified method for determining blasting load (NDIL). In addition, Q. Li et al. (2016); Q.Y. Li et al. (2018) established the stress state equation of rock mass in the cutting area according to the influence of cutting rock breaking under different stress fields and carried out visual analysis by numerical simulation. The introduction effect of the initial stress field on crack growth and the tensile stress concentration effect of the empty hole was studied. Furthermore, by establishing a damage model under the coupling effect of blasting load and dynamic unloading, and combining the fracture mechanics and rock damage failure criterion, Xiao et al. (2018) calculated the rock stress distribution and fracture characteristics under high *in-situ* stress conditions. Moreover, Li et al. (2010) introduced the damage variable D into the elastic-plastic constitutive model of FLAC^{3D} numerical software. Through the parameter of rock effective stress, cross-analysis of field blasting vibration monitoring and numerical simulation was performed, and the critical damage vibration velocity was obtained as the safety criterion of blasting damage. Additionally, Wei et al. (2016) established a mechanical model for rock blasting damage and carried out numerical simulation analysis on the crack evolution of slotted cartridge blasting under different *in-situ* stress conditions. Through these methods, the controlled factors of the crack propagation direction of slotted cartridge under blasting were obtained. What's more, by using the improved SHPB test, (Z.Q. Yin et al., 2020; Z.Q. Yin et al., 2018; Z.Q. Yin et al., 2014; Z.-q. Yin et al., 2012) and analyzed the fracture mechanical properties of coal seam with gas under coupling load, analyzed the damage of coal seam by observing the changes of stress, strain, and energy dissipation, which provides a theoretical basis for the design of deep mining support with gas. Differently, D. Yang et al. (2014) used the finite difference method to study the damage distribution of the rock surrounding the tunnel under the combined action of blasting load and dynamic unloading of *in-situ* stress and analyzed the influence of damage range from lateral pressure coefficient, unloading rate and mechanical properties of the rock mass. Further, based on the theory of cylindrical cartridge blasting funnel, Jun and Qihu (2007) established a criterion of collapse blasting standard funnel under high *in-situ* stress and proposed the calculation formula for roadway collapse blasting parameters. According to the SPH-FEM coupling method, J. Yang, Wu, et al., 2020; J. Yang, Sun, et al., 2020) studied the influence of *in-situ* stress field on seismic wave energy in rock blasting fragmentation areas and outside the fragmentation area. It is concluded that the *in-situ* stress field has an inhibitory effect on blasting fragmentation and affects the propagation of blasting seismic waves. Du, Li, Tao, et al. (2020), Du et al. (2021), Du, Li, Yang, et al. (2020) obtained the conclusion that the fatigue failure of rocks within the biaxial stress boundary is related to the peak level of fatigue load, the magnitude of intermediate principal stress and lithology through biaxial compression test and biaxial fatigue test on the fracture characteristics of marble and sandstone. The rock-breaking efficiency under fatigue load is higher, but it is also easier to induce severe hard rockburst disasters. Apart from the above studies, through numerical simulation, X.J. Yang et al. (2020) studied the influence of *in-situ* stress on roadway deformation, and obtained that directional blasting can play a role of pressure relief by changing the structure of surrounding rock and control the deformation of the roadway. Further, J. Gao et al. (2020) analyzed the blasting effects of different blasting delays and charge hole diameters under high *in-situ* stress conditions and obtained the evolution law of crack propagation in cutting blasting under *in-situ* stress and different lateral pressure coefficients. S. Wang et al. (2021), S.F. Wang et al. (2019) studied rock machinability by using the rock crushing test under true triaxial loading. The rock machinability was analyzed by the biaxial confining pressure, uniaxial cutting force, and the penetration depth under the initial fracture and complete fracture of the specimen, and a series of measures to improve the machinability were proposed, which provided suitable conditions for mechanized mining in hard rock. To sum up, the researches on cutting blasting under high *in-situ* stress are relatively limited, and most of the models used in

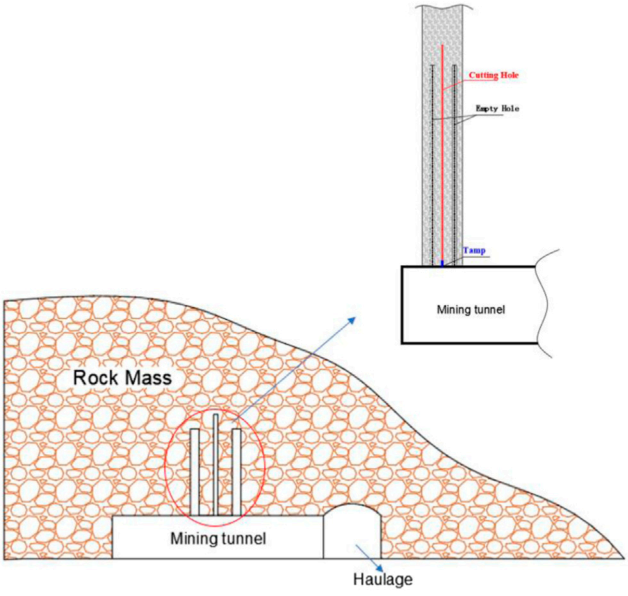

FIGURE 1 | Site construction conditions.

numerical simulation adopted RHT damage constitutive model. However, there is a lack of in-depth study on the rock damage partition of this constitutive model in numerical simulation, thus it is necessary to establish the blasting damage partition in RHT constitutive model.

At present, the Dahongshan Iron Mine in Yunnan requires a large amount of blind shaft construction, and the construction mainly adopts the one-time deep hole blasting well completion technology of upward blind shaft, of which the key point is the cutting blasting, and the general situation of field construction is shown in **Figure 1**.

Therefore, in this paper, the cutting effect of different hole layout methods is explored and using the smooth particle hydrodynamics method, the calculation formula of rock damage partition in RHT constitutive is proposed based on the RHT damage constitutive model and rock damage variable partition. By applying stress to simulate the rock clamp production in cutting blasting, and supplemented field tests, the feasibility of RHT damage partition and simulation clamp production is verified. Through the three-dimensional scanning of the cavity area, the production coefficient of the rock clamp is inversely deduced, and the mathematical relationship between the production coefficient of the rock clamp and the relative height of the wellhead and the section cavity area is fitted, which provides theoretical guidance for the analysis of the fracture zone and the design of blasting parameters in deep cutting blasting.

RHT DAMAGE DETERMINATION RANGE AND CONSTITUTIVE PARAMETERS

RHT Damage Determination Range

In the numerical simulation, the RHT damage constitutive proposed by Riedel, Hiermaier, and Thoma in 1997 is selected. The relationship between the elastic limit strain, material failure strength, residual strength, and hydrostatic pressure is described by introducing the elastic limit surface, failure strength surface, and residual strength surface (Riedel, Kawai, and Kondo 2009).

The damage factor D in the RHT constitutive model is defined as:

$$D = \sum\left(\Delta\varepsilon_p / \varepsilon_p^f\right) \tag{1}$$

Which:

$$\Delta\varepsilon_p = \varepsilon_p^f - \varepsilon_p \tag{2}$$

$$\varepsilon_p^f = \begin{cases} D_1\left(p^* - (1-D)p_t^*\right)^{D_2} & p^* \geq (1-D)p_t^* + \left(\varepsilon_p^m / D_1\right)^{1/D_2} \\ \varepsilon_m^p & (1-D)p_t^* + \left(\varepsilon_p^m / D_1\right)^{1/D_2} > p^* \end{cases} \tag{3}$$

where, $\Delta\varepsilon_p$ is the equivalent plastic strain increment; $\varepsilon_p{}^f$ is the final failure equivalent plastic strain; $\varepsilon_p{}^m$ is the minimum equivalent plastic strain when the material is damaged; D_1 and D_2 are the initial damage parameter and the complete damage parameter, respectively.

For p^*, $p_t{}^*$ in materials, **Eqs 4**, **5** are usually used:

$$p^* = \frac{p}{f_c} \tag{4}$$

$$p_t^* = \frac{F_r Q_2 f_s^* f_t^*}{3\left(Q_1 f_t^* - Q_2 f_s^*\right)} \tag{5}$$

where, p is the pressure on the material, MPa; f_c is the uniaxial compressive strength of rock, MPa; F_r is a dynamic strain rate increment factor; Q_0 is the initial meridian ratio parameter; f_s^* and f_t^* are shear-compression strength ratio and tensile-compression strength ratio, respectively; B represents the Rode angle parameters.

The increment factor of dynamic strain rate is related to the material strain rate and shear strength, and the expression is:

$$F_r = \begin{cases} F_r^c & 3p^* \geq F_r^c \\ F_r^c - \left(3p^* - F_r^c\right)\left(F_r^t - F_r^c\right)/F_r^c + F_t^c f_t^* & F_r^c > 3p^* > -F_r^t f_t^* \\ F_r^t & -F_r^t f_t^* > 3p^* \end{cases} \tag{6}$$

The elastic limit surface in RHT constitutive should be set by the elastic limit surface equation and the 'cap function' of the elastic limit stress overflow of the constraint material under high hydrostatic pressure. The elastic limit surface equation is:

$$\sigma_{el}^*\left(p, \theta, \dot{\varepsilon}\right) = \sigma_y^* \cdot F_e \cdot F_c\left(p^*\right) \tag{7}$$

Where F_e is the elastic scaling function, and the expression is:

$$F_e = \begin{cases} g_c^* \\ g_c^* - \left(3p^* - F_r^c g_c^*\right)\left(g_t^* - g_c^*\right)/F_r^c g_c^* + F_r^t g_t^* f_t^* \\ g_t^* \end{cases}$$

$$\begin{gathered} 3p^* \geq F_r^c g_c^* \\ F_r^c g_c^* \geq 3p^* \geq -F_r^t g_t^* f_t^* \\ -F_r^t g_t^* f_t^* \leq 3p^* \end{gathered} \tag{8}$$

where, F_c is the cap function, which is introduced to reduce the volume expansion caused by shear stress and limit the elastic limit stress of materials under high hydrostatic pressure. The expression is:

$$F_c = \begin{cases} 1 & p^* \geq p_c^* \\ \sqrt{1 - \left(\dfrac{p^* - p_u^*}{p_c^* - p_u^*}\right)^2} & p_c^* > p^* > p_u^* \\ 0 & p_u^* \geq p^* \end{cases} \tag{9}$$

Qin et al. (2021) studied the damage failure behavior of rock materials according to the existing research results of rock damage variable D and the damage failure criterion of rock materials. The damage value corresponding to the peak strength of rock materials is regarded as the rock critical damage parameter D_{cr}, and the material failure is mainly caused by the plastic deformation of materials. Therefore, the relationship between the rock plastic strain and rock critical damage parameter can be expressed by **Eq. 10**:

$$D_{cr} = \frac{\varepsilon_p}{\varepsilon_{\max}} \tag{10}$$

TABLE 1 | RHT constitutive parameters.

Parameter	Value	Parameter	Value
Mass density R_o (kg/m^3)	2,887	Relative tensile strength f_t*	0.044
Compressive strength f_c/MPa	98.300	Relative shear strength f_s*	0.022
Lode angle dependence factor Q_0	0.681	Lode angle dependence factor B	0.011
Initial damage value D_1	0.04	Complete damage value D_2	1
Elastic shear modulus G/GPa	2.150	Compressive yield surface parameter g_c*	0.530
Compaction pressure p_{comp}/MPa	600	Tensile yield surface parameter g_t*	0.700
Compressive strain rate dependence exponent β_c	0.001	Tensile strain rate dependence exponent β_t	0.017
Tensile strength f_t/MPa	4.330	Crush pressure p_{el}/MPa	65.500

In order to establish the mathematical relationship between the critical damage parameters of rock in the RHT constitutive model and the parameters in the model, the RHT constitutive function is sorted out according to **Eq. 10**. Therefore, the plastic strain and ultimate strain in **Eq. 10** can be sorted as:

$$\varepsilon_p = \frac{p - f_c \cdot R_3\left(\frac{\pi}{6}\right) \cdot F_r \cdot g_c^*}{3G\zeta} \tag{11}$$

$$\varepsilon_{max} = D_1\left[p^* - (1 - D_{cr})\frac{F_r Q_2 f_s^* f_t^*}{3\left(Q_1 f_t^* - Q_2 f_s^*\right)}\right] \tag{12}$$

The rock damage and fragmentation thresholds D_{cr} and D_{cf} are evaluated by the stress p_{el} at the beginning of rock crushing and the stress p_{comp} at rock compaction, respectively. Therefore, **Eqs 11**, **12** can be transformed into:

$$Rock\ Damage = \begin{cases} \varepsilon_{p,damage} = \dfrac{p_{el} - f_c R_3\left(\dfrac{\pi}{6}\right) F_r g_c^*}{3G\zeta} \\ \varepsilon_{\max,damage} = D_1\left[\dfrac{p_{el}}{f_c} - (1 - D_{cr})\dfrac{F_r Q_2 f_s^* f_t^*}{3\left(Q_1 f_t^* - Q_2 f_s^*\right)}\right] \end{cases} \tag{13}$$

$$Rock\ crack = \begin{cases} \varepsilon_{p,frag} = \dfrac{p_{comp} - f_c R_3\left(\dfrac{\pi}{6}\right) F_r g_c^*}{3G\zeta} \\ \varepsilon_{\max,frag} = D_1\left[\dfrac{p_{comp}}{f_c} - \left(1 - D_{cf}\right)\dfrac{F_r Q_2 f_s^* f_t^*}{3\left(Q_1 f_t^* - Q_2 f_s^*\right)}\right] \end{cases} \tag{14}$$

RHT Constitutive Parameters

The lithology of the tested rock is sodium metamorphosed lava, and the parameters of its RHT constitutive model can be obtained by related mechanical tests and theoretical calculations, as shown in **Table 1**.

By substituting the determined RHT constitutive parameters of sodium metamorphosed lava into **Eqs 13**, **14**, the obtained critical damage parameter $D_{cr} = 0.11$ and the rock fragmentation threshold $D_{cf} = 0.51$, which are used as the criteria for rock damage and fragmentation in subsequent numerical simulations.

In this cutting blasting, the initial rock damage D_1, explosive quantity Q, and initial propagation frequency f_0 are regarded as constant, thus there is a certain relationship between rock damage D and blasting center distance r:

TABLE 2 | Damage subarea of rock under blasting load.

Blasting Partition	Rock damage D	Blasting Center Distance r/m
Fragmentation zone	$0.510 < D \le 1$	$r_c < 0.690$
Zoning threshold	$D_{cf} = 0.510$	0.690
Damage zone	$0.110 < D < 0.510$	$0.690 < r_d < 1.310$
Zoning threshold	$D_{cr} = 0.110$	1.310
Vibration zone	$D < 0.110$	$r_o > 1.310$

$$\frac{d^2D}{dr^2} = \frac{4a^2\left(5a_2r^2 - a_1Q^{1/3}\right)}{f_0^2\left(a_1Q^{1/3} + a_2r^2\right)^5} \tag{15}$$

Order $\frac{d^2D}{dr^2}$ to 0, the relationship between explosive center distance r and charge Q can be obtained when the damage change rate is maximum, and the relationship is shown in **Eq. 16**:

$$r = \sqrt{\frac{a_1Q^{1/3}}{5a_2}} \tag{16}$$

Combining **Eqs 15**, **16**, the relationship curve between the detonation center distance r and damage variable D can be obtained:

$$r = \sqrt[4]{\frac{1}{36a_1^2 f_0^1 (D - D_0)}} \tag{17}$$

where, the attenuation coefficients a_1 and a_2, blasting initial frequency f_0 can refer to previous research, and the blasting data fit that $a_1 = 7.8 \times 10^{-3}$, $a_2 = 9.5 \times 10^{-4}$, $f_0 = 47$ Hz. Therefore, combined with the previously determined critical rock damage threshold D_{cr} and rock fragmentation threshold D_{cf}, the blasting damage zones in cut blasting are obtained (**Table 2**):

In the table: r_c, r_d, r_o are the critical blast center distance of fragmentation zone, critical blast center distance of damage zone, and critical blast center distance of original rock vibration zone respectively, in m.

Explosives Constitution

Explosives use the ANN-2 viscous ammonium nitrate explosive provided by mines, and the explosive parameters are shown in **Table 3**. The explosives used in the numerical simulation are implemented by keyword *

TABLE 3 | ANN-2 Viscous ammonium nitrate explosive parameters.

Density/Kg/m^3	Detonation velocity/m/s	C-J Pressure/GPa	Ferocity/mm	Blasting force/ml	JWL state equation Parameters				
					A/GPa	*B*/GPa	R_1	R_2	ω
1,200	2,800	6.500	18	280	326	5.800	5.800	1.560	0.570

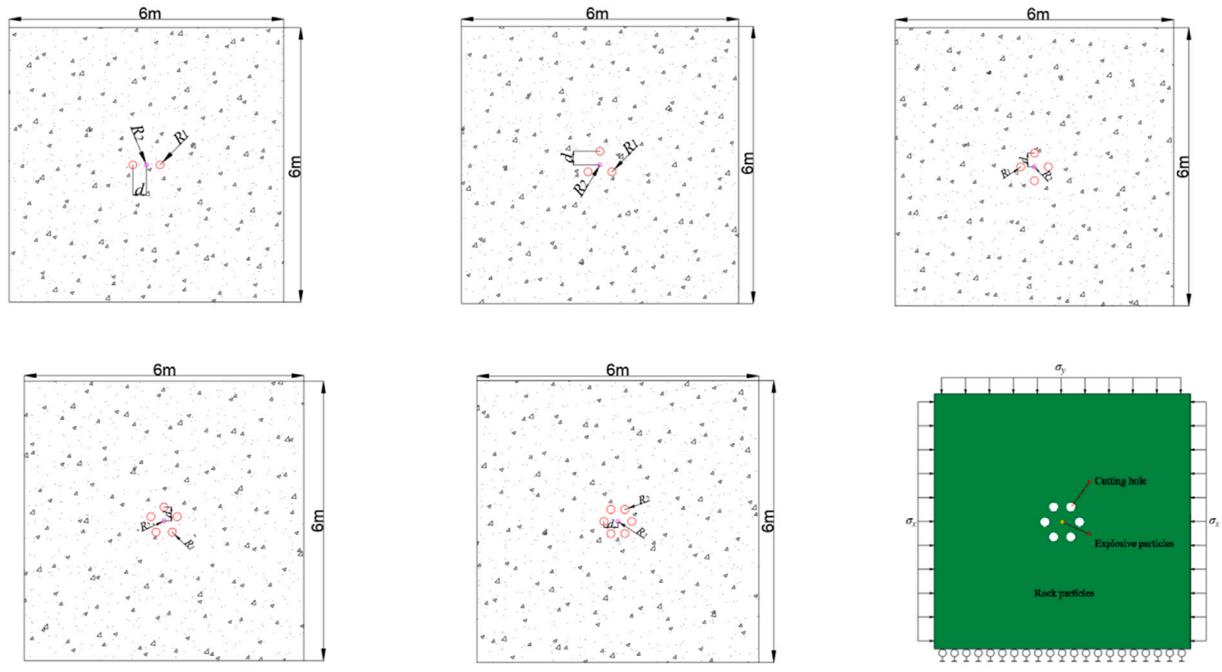

FIGURE 2 | (A–E) Geometric model and **(F)** numerical model.

MAT_HIGH_EXPLOSIVE_BURN. JWL equation of state to introduce the description of volume, pressure, and energy variation characteristics of explosive production during the explosion. The expression equation is as follows **Eq. 18**:

$$P = A\left(1 - \frac{\omega}{R_1 V}\right)e^{-R_1 V} + B\left(1 - \frac{\omega}{R_2 V}\right)e^{-R_2 V} + \frac{\omega E_0}{V} \tag{18}$$

The parameters of the explosive and JWL state equation can be determined by fitting experimental data, as shown in **Table 3**.

NUMERICAL SIMULATION PROCESS ANALYSIS FOR ROCK CLAMP FABRICATION

Numerical Model

The upward cutting blasting test project of Yunnan Dahongshan Iron Mine is taken as the research object in this paper. The test is expected to form a blind shaft of 2 m × 2 m through a well completion blasting, and the upward cutting blasting test is the preparatory work for the well completion blasting, of which the purpose is to select the best cutting hole arrangement method. Herein, the quasi-three-dimensional model with unit thickness is selected to explore the blasting effect. In order to eliminate the boundary effect, the model size is set as 6 m × 6 m × 0.01 m. The drilling equipment provided by the mine isa D421 car and T150 drilling rig, which carries a 50 mm drilling bit, 152 mm, and 203 mm expanding bit. Therefore, in the numerical simulation, the empty hole radius R_1 = 0.1 m, the charging hole radius R_2 = 0.05 m, and the hole spacing d = 0.35 m. The LS-DYNA finite element software is used in the numerical model, and the SPH method is used to replace the finite element to smooth particles. Fixed constraints are applied at the bottom of the model, and compressive stresses are applied in the other three directions to simulate the rock clamp production. The cutting geometry model with a different number of holes is shown in **Figures 2A–E**, and the numerical model of cut blasting with a scheme (e) as an example is shown in **Figure 2F**.

Numerical Simulation Process Analysis

In order to study the influence of the empty hole compensation effect on the cutting blasting effect for rock clip production, numerical simulations were carried out on the above schemes.

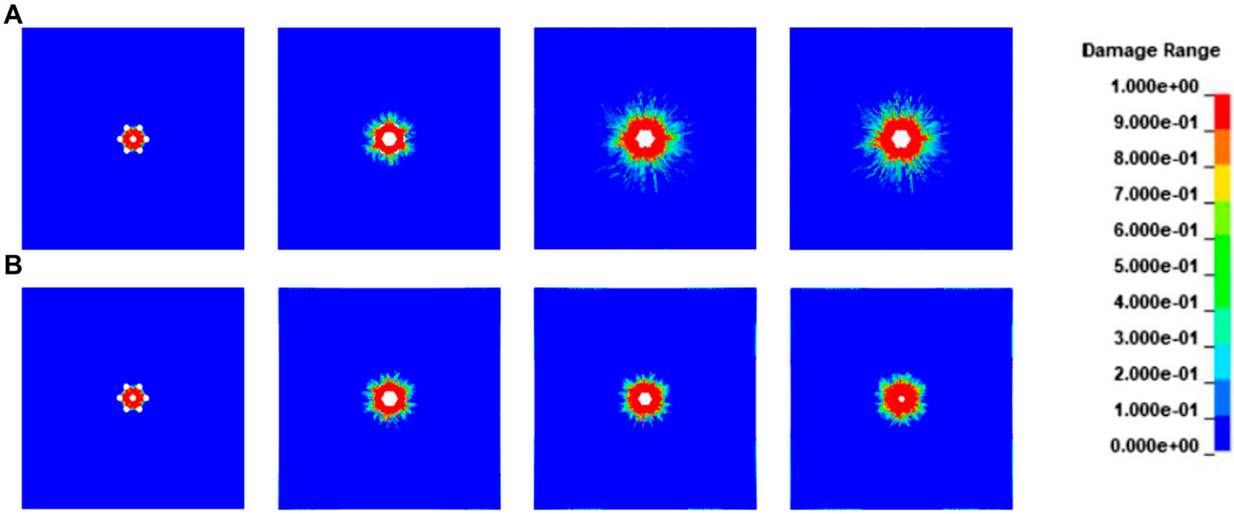

FIGURE 3 | Numerical Simulation Process: **(A)** No *in-situ* stress condition; **(B)** K_r = 1.0.

The coefficient K_r for different rock clip production was simulated by changing the applied stress, and the simulation results were analyzed by the post-processing software LS-Prepost.

It can be seen from **Figure 3A** that when the *in-situ* stress is not considered, under the action of explosion stress wave and the stress introduction of the empty hole, the rock fragmentation is first concentrated in the rock between the empty hole and the charge hole. **Figure 3B** is the blasting effect of rock clip with 1.0. The fragmentation of rock between the empty hole is slightly delayed, and the empty hole plays a certain role in hindering the propagation of explosion stress wave, thus the pressure on the rock outside the empty hole is reduced. The range of rock fracture is smaller than that of the space hole. However, due to the introduction effect of the empty hole on the blasting stress wave, the range of rock damage at the center of the empty hole and the charge hole is wider. The main tensile cracks are more obviously concentrated outside the empty hole, and the number of empty holes is more. The formation and development of micro-splitting cracks outside the rock damage area under the action of blasting gas are more significant. Therefore, it can be speculated that the introduction effect of the empty hole on the blasting stress wave is beneficial to the formation and development of rock cracks after blasting, and the compensation effect of the empty hole can improve the cavity-forming effect and the rock damage range. However, after applying the rock clamping stress, the damage range of the rock is significantly reduced. The influence of the compressive stress on the outer side of the empty hole inhibits the initiation and propagation of tensile cracks under blasting. Therefore, no obvious main cracks are formed, thus the blasting generated explosive gas reduces the efficiency of rock splitting, and only short cracks are formed around the empty hole wall.

ANALYSIS OF BLASTING EFFECT FOR DIFFERENT ROCK CLIP PRODUCTION

Numerical Analysis for Clamping Action

To explore the influence of rock clip production on the cutting blasting effect and damage range of rock, the cavity area S_c and rock damage range S_d were delineated according to the previously determined damage zoning variables.

It can be seen from the amplification of the blasting effect position that with the increase of the production coefficient of the rock clip, the inhibitory effect of compressive stress on the formation of the main tensile crack outside the empty hole gradually increases, and the crack initiation phenomenon outside the rock crushing zone gradually disappears, and the crack propagation phenomenon in the direction of the empty hole diameter significantly disappears. When the production coefficient of the rock clip is 2.0, only very small damage is initiated outside the rock crushing zone, and no crack is formed. The damage range of rock near the empty hole is significantly reduced under the influence of compressive stress. The mechanism of the inhibition for the propagation of stress wave by the rock outside the empty hole is analyzed under the coupling effect of the attenuation of blast stress wave and the production of rock clip. The energy reaching here cannot break the rock or cause large damage. Through the coordinate output of the area near the blasting and the area delineation, the statistics of the cutting blasting area carried out by scheme (e) are shown in **Figure 4**.

Figures 5A–D show the variation trends of the cavity area S_c, rock damage range S_d and stress of rock outside the hole after each cutting blasting under different production forces of rock clip. It can be found that with the increase of hole number, S_c and S_d show an increasing trend. The main reasons are the compensation effect and stress concentration effect provided

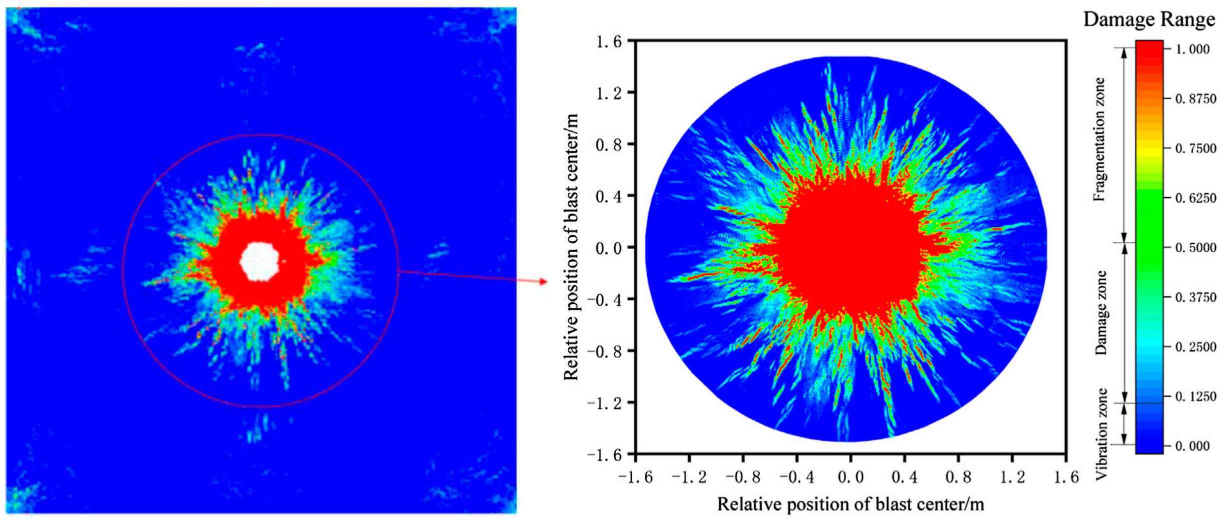

FIGURE 4 | Calibration of blasting damage area.

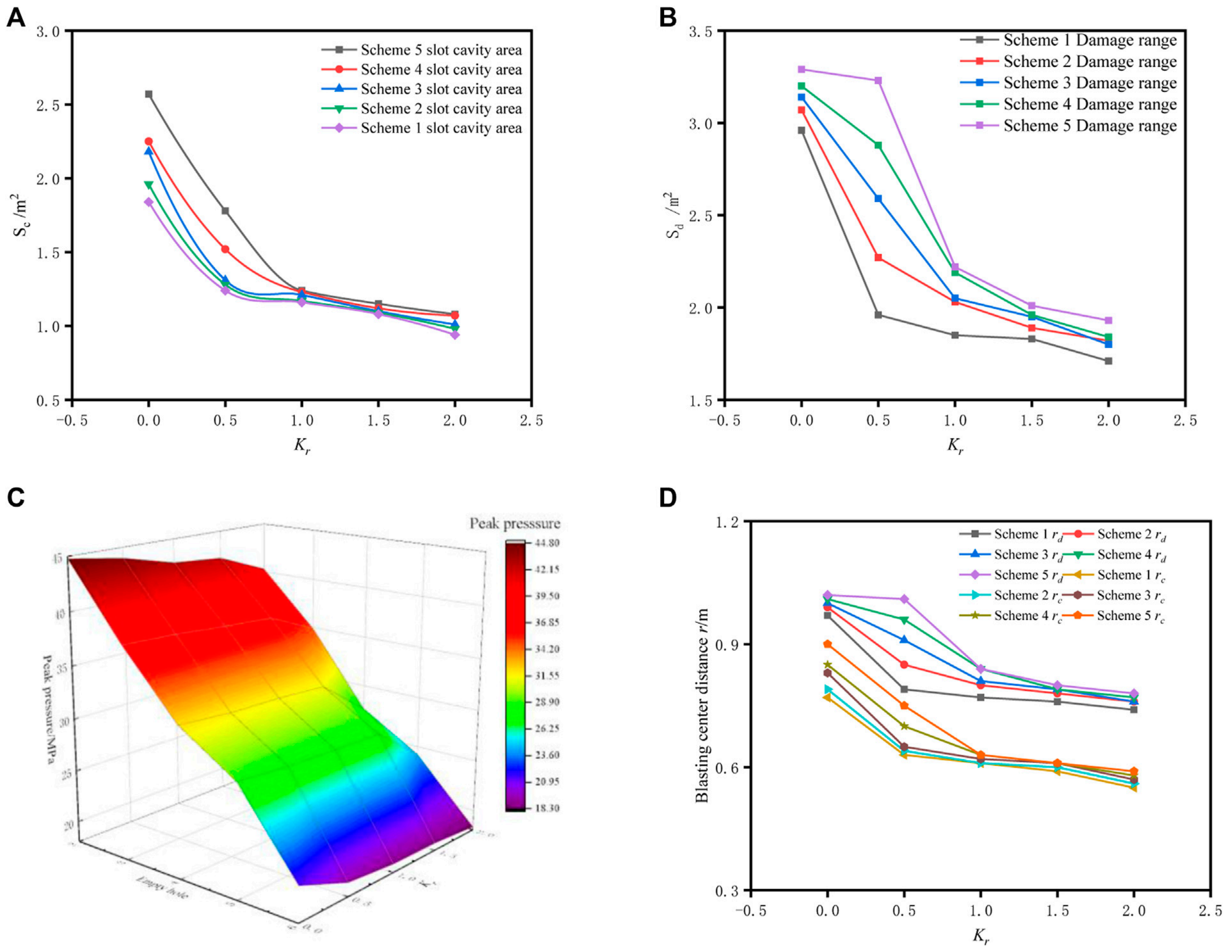

FIGURE 5 | Numerical simulation blasting effect curve: **(A)** Slot cavity curve; **(B)** Damage area curve; **(C)** Peak pressure curve; **(D)** Blasting center distance curve.

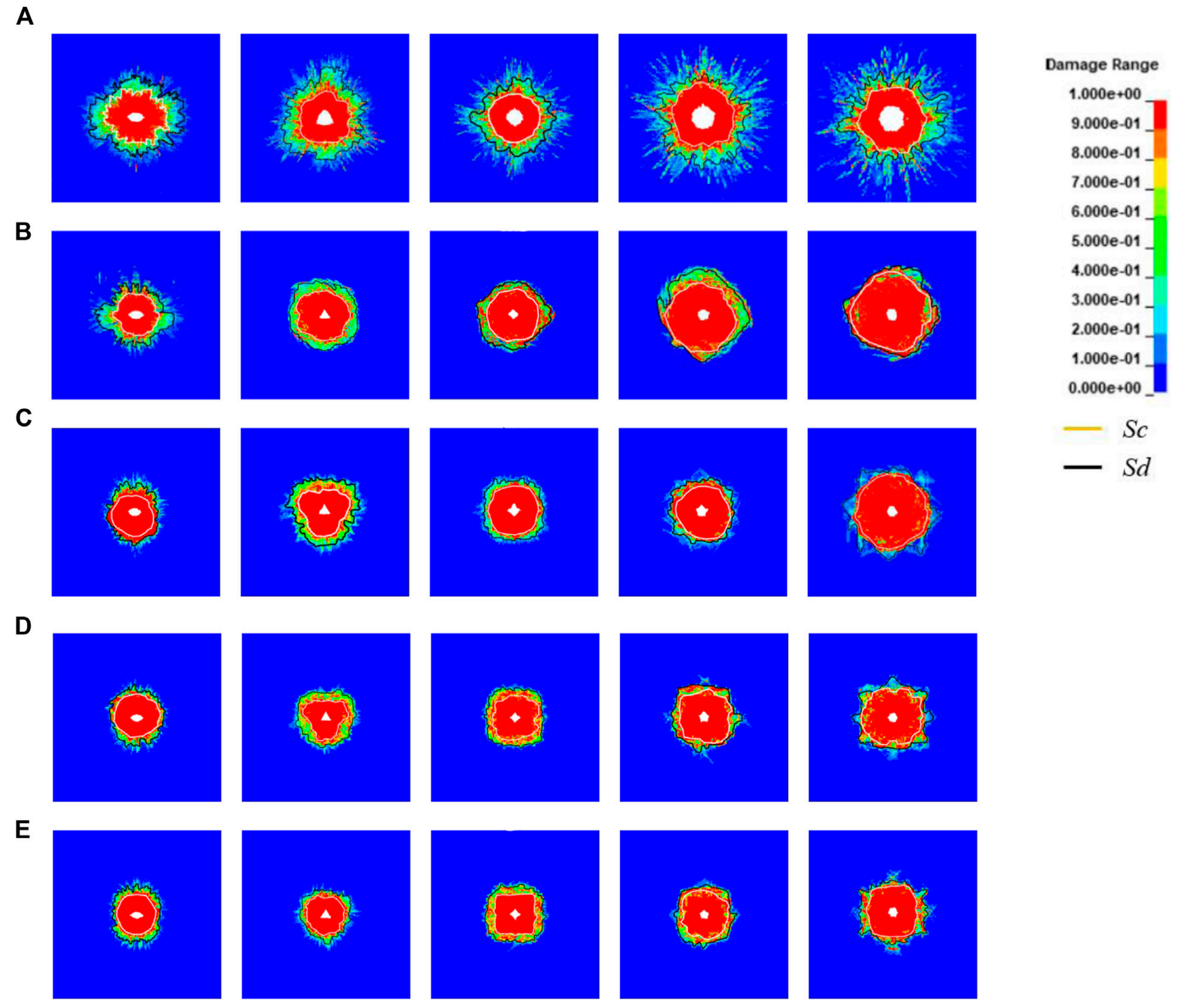

FIGURE 6 | Numerical simulation of cutting blasting with different rock clamping coefficients: **(A)** $K_r = 0$, **(B)** $K_r = 0.5$, **(C)** $K_r = 1.0$, **(D)** $K_r = 1.5$, and **(E)** $K_r = 2.0$.

by holes, which enhance the blasting failure effect and improve the crushing effect of cavity rock. After applying the stress conditions, S_c and S_d show a decreasing change with the increase of the coefficient K_r of rock clip production.

As can be seen from **Figures 5C, D**, due to the inhibitory effect of rock clip force on blasting stress wave and the dispersion and coupling effect of empty holes on blasting stress wave, the pressure P on the outer side of the empty hole and the blasting center distance r show a nonlinear downward trend, with the increase of empty hole number and the production coefficient of rock clip. When the production coefficient of rock clips are between 0 and 1, the influence of blasting changes greatly, but the overall change is small. It can be speculated that the rock clamping force mainly affects the range of rock damage zone by inhibiting the initiation and propagation of blasting cracks, but it has little inhibitory effect on the blasting effect of the rock crushing zone. Combined with the data in **Figures 5D**, **6**, it can be seen that the greater the number of empty holes, the less the blasting inhibitory effect of rock clamp production, and the inhibitory effect is most significant in the direction of the connection between the empty holes and charge holes.

The study of the influence law of rock clamp production on cutting blasting provides a theoretical reference for the determination of cutting blasting test parameters under deep ground pressure. According to the data in **Figure 5D**, the relationship curve between the radius of crushing zone r_c and the coefficient K_r of rock clamp production (later called r_c-K_r curve) is obtained, and the r_c-K_r curve is:

$$r_c = 0.35K_r^{-0.12} \tag{19}$$

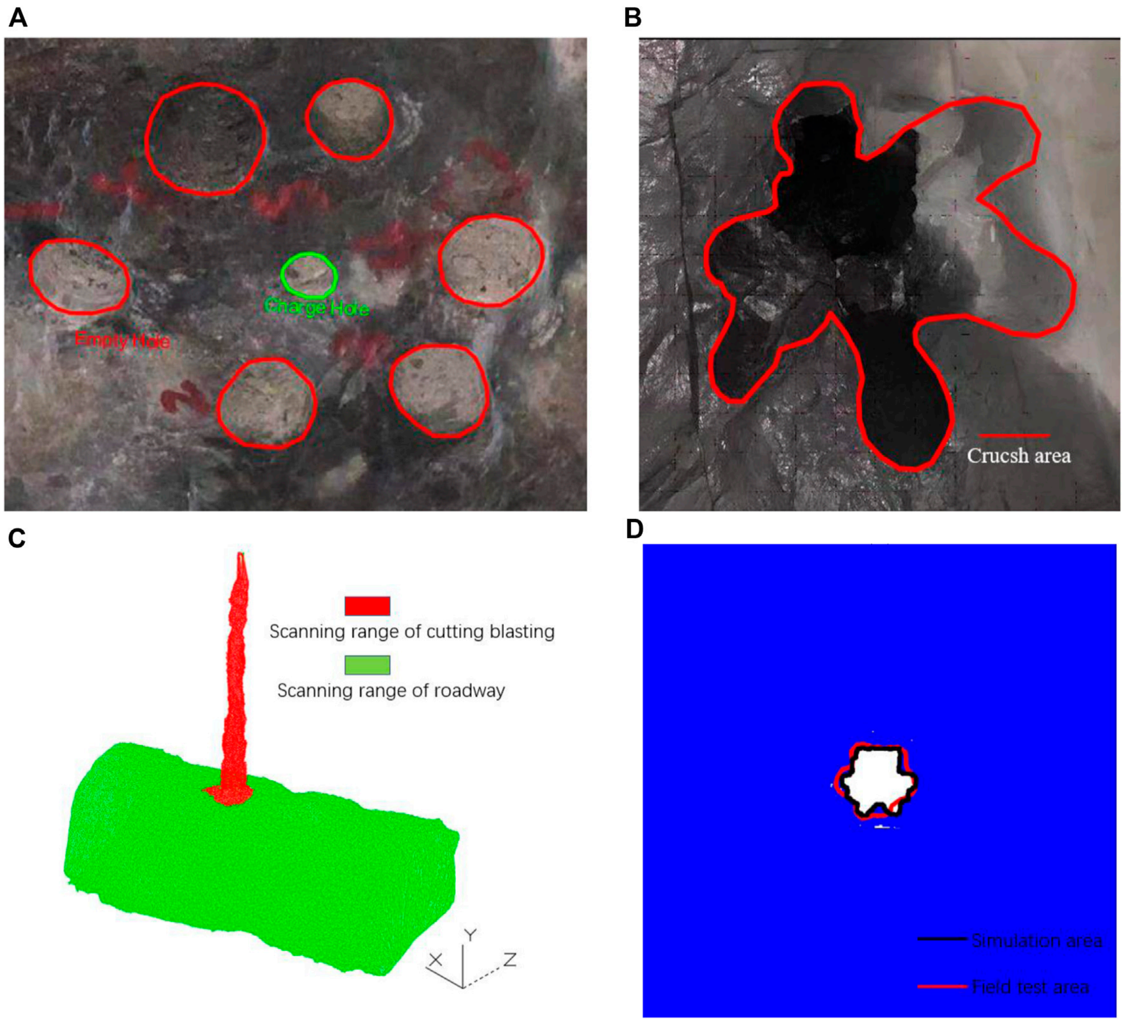

FIGURE 7 | 1#Field test results and verification:**(A)** Blasthole construction drawing; **(B)** Cutting blasting effect; **(C)** scanning results; **(D)** Numerical simulation and field scanning comparison.

In the field test of cut blasting, the determination method of rock fracture zone radius is:

$$r_{frag} = r_e\left(\frac{K_r p_r}{\sigma^{\theta}}\right)^{1/a} \tag{20}$$

Tang, Zhou, and Liao (2015) established a reliable rock damage zoning for underground engineering construction blasting, and the damage variable of the fracture zone is:

$$D = D_1 + 1\Big/\left[\left(a_1 Q^{1/3} + a_2 r^2\right)^2 f_0^2\right] \tag{21}$$

Therefore, the rock fragmentation damage value D_{frag} can be obtained by the **Eqs. 20, 21**:

$$D_{frag} = D_1 + 1\Big/\left[f_0^2\left(a_1 Q^{1/3} + 0.12 a_2\left(\sigma_\theta r_c^\alpha / r_2^\alpha\right)^{-0.24}\right)\right] \tag{22}$$

Preliminary Verification by Field Test

The field test adopts the six-hole cutting form for construction. The DL421 trolley is used to cooperate with the T150 drilling rig, and the error of the drilling operation is controlled within the allowable range. The data are provided by the mine geological exploration department. The buried depth of the test area is about 640 m, and the horizontal *in-situ* stress is about 18.4 MPa, thus the production coefficient of the rock clamp is about 1.01. It can be observed that from the orifice to the bottom of the cavity, the increase of rock clamp production leads to a decrease of the cavity area. **Figure 7A–C** are the field blasting effect diagram.

Figure 7D shows the comparison of the scanning area and the simulation area of the cutting wellhead section, and their values are 0.441 and 0.435 m^2, respectively, with a fitting degree of 98.6%. According to the three-dimensional scanning results, the radius of the crushing zone is counted,

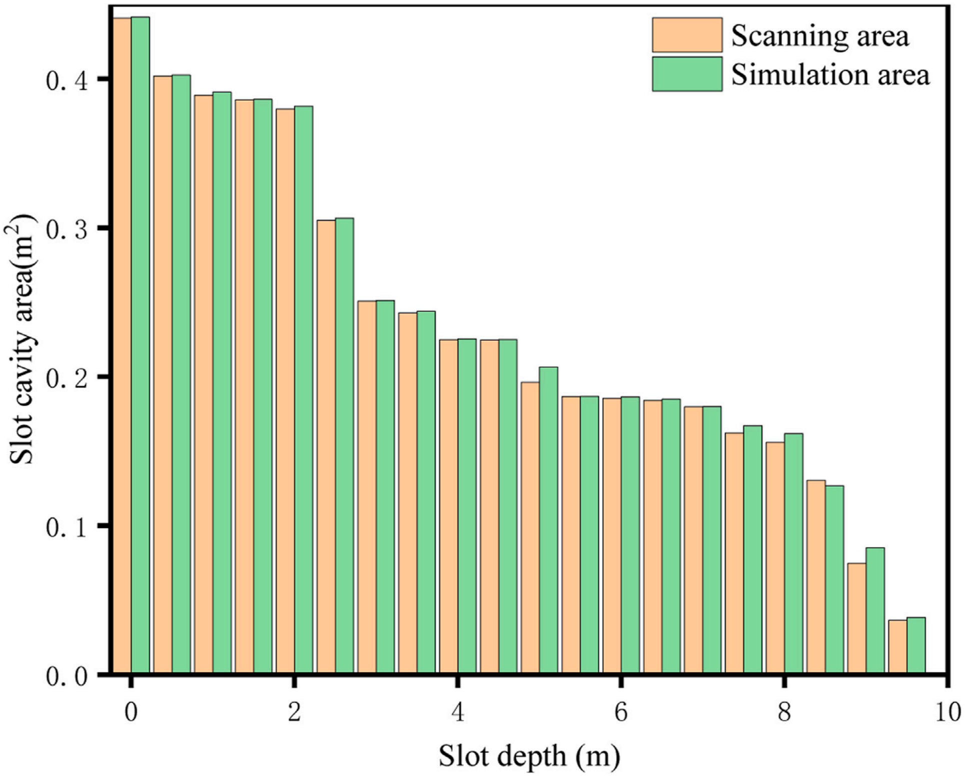

FIGURE 8 | Reliability comparison between numerical simulation effect and field scanning result.

and the production coefficient for the rock clip is inversely deduced in combination with **Eq. 22**, to carry out a numerical simulation on the cutting section at different depths. The area comparison at different depths is shown in **Figure 8**, and the overall fitting degree is 94.5%, which proves the reliability of the numerical simulation inversion method and the feasibility of the RHT fracture criterion.

ESTABLISHMENT OF INFLUENCE PREDICTION CURVE FOR ROCK CLIP PRODUCTION

Several groups of upward cutting blasting tests are carried out, and the cavity area after blasting is scanned by three-dimensional laser scanning. The cavity area under different depths in the test is simulated by the numerical simulation inversion method. The drilling construction in the upward cutting blasting site and the effect of the wellhead section after blasting are shown in **Figure 9**.

It can be observed from the blasting effect that the rock between the charge hole and the 6 # empty hole has not penetrated due to the long distance of the 6 # empty hole in the second group of 15 m. The cavity formation at the wellhead of the cutting blasting test in other groups is satisfying, and the expected blasting effect is achieved. Then, a three-dimensional laser scanner was used to scan the cut blasting cavity. Due to the large depth of the cavity in the test and the limitation of the scanning instrument, the cut blasting cavity of 15 and 20 m was scanned every 1 m, and then the area of the section cavity was inversely calculated by numerical simulation. The inversed numerical results were compared with the field three-dimensional scanning results, as shown in **Figure 10**.

When the wellhead relative height is in the range of 0–0.5 m, the charge hole in this section is mainly filled with mud, and the numerical inversion is mainly based on the application of blasting load. Therefore, the Numerical backstepping analysis will be carried out from the wellhead relative height of 1 m. The production coefficient statistics of rock clips are carried out by combining the follow-up numerical simulation inversion data with the previous inversion data, and the variation law between S_c-K_r-H is analyzed. **Eqs. 23**, **24** show the mathematical relationship between the coefficient K_r for rock clip production and the relative height of the wellhead H and the cavity area S_c of the cut blasting section respectively. The variation law is shown in **Figure 11**.

$$K_r = -2.48e^{-H/18.56} + 3.48 \tag{23}$$

$$S_c = 1.17e^{-K_r/1.15} - 0.06 \tag{24}$$

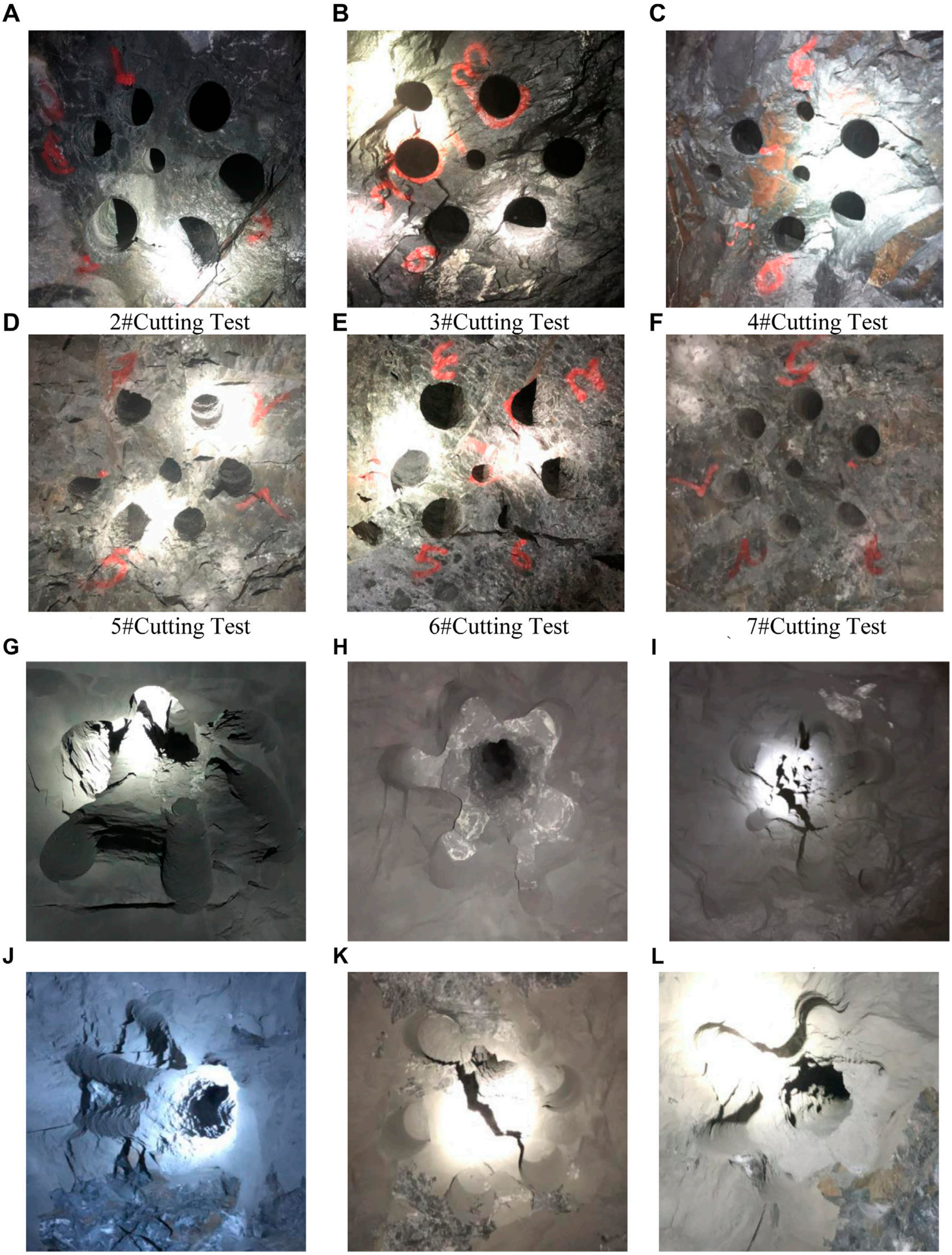

FIGURE 9 | (A)10 m Cutting drilling **(B)**~**(C)**15 m Cutting drilling **(D–F)**20 m Cutting drilling **(G–L)** 1–6#Test blasting effect.

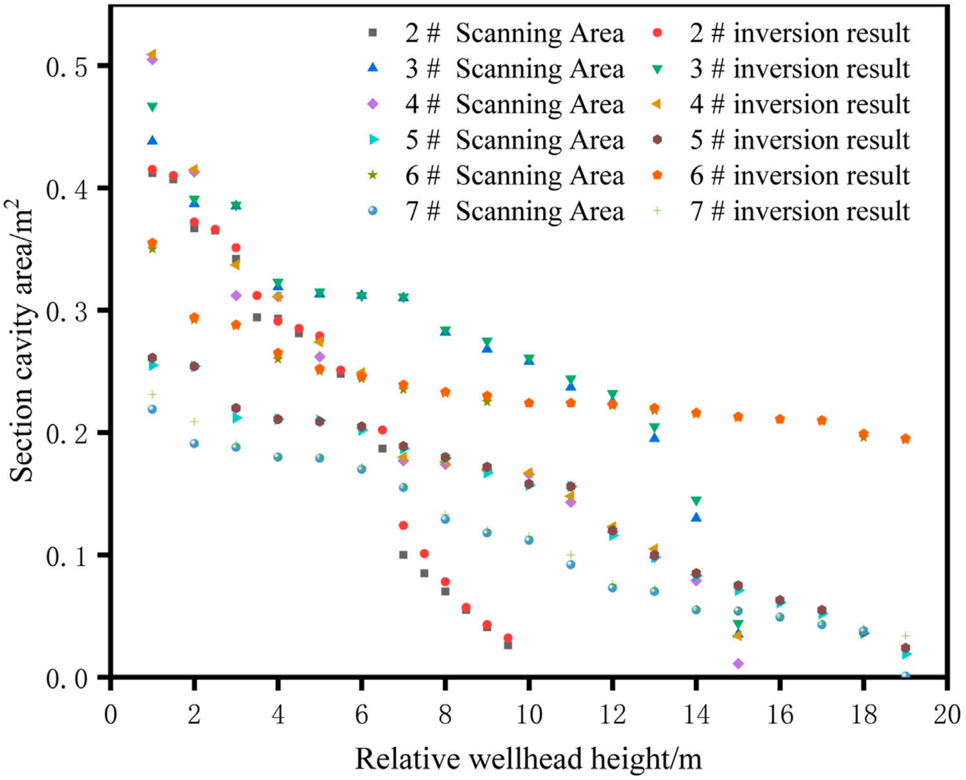

FIGURE 10 | Comparison of field scanning results and numerical inversion results.

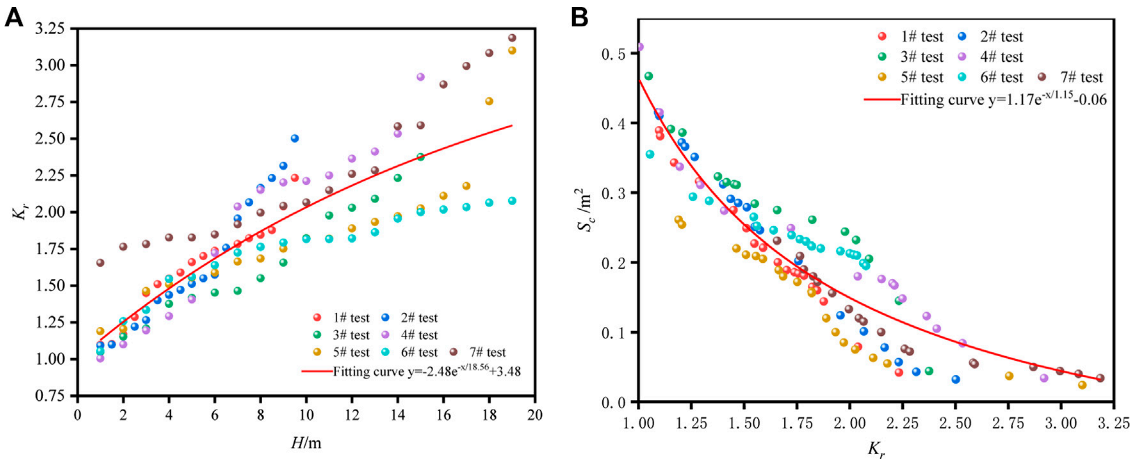

FIGURE 11 | (A) K_r-H optimal curve **(B)**S_c-K_r optimal curve.

CONCLUSION

In this paper, aiming at the lack of research on blasting damage partition of RHT damage constitutive in numerical simulation, the rock clip production in cutting blasting was simulated, and the cutting mode and rock clip coefficient of a different number of empty holes were numerically studied. The following conclusions are obtained:

1) Based on the rock critical damage threshold equation, the blasting rock breaking strain mechanism, and the RHT constitutive embedded function, the blasting damage

zoning range in numerical simulation is deduced. According to the filed test, the mechanical parameters of variable sodium lava are obtained, and the range of different damage zones in numerical simulation is determined.

2) The rock damage area caused by blasting attenuates to a certain extent after applying the rock clip, and the initiation and propagation of tensile cracks are also inhibited. The larger the coefficient of rock clip, the more obvious the suppression effect of the blasting tensile effect. Compared with the splitting effect, the blasting crushing area is less affected. The empty holes provide a certain compensation space for cutting blasting, and the stress concentration of empty holes enhances the blasting effect. The empty holes also reduce the inhibitory effect of rock clip production on blasting damage. The rock damage area is mainly concentrated in the direction of the maximum principal stress, and the tensile failure is mainly near the empty hole. With the increase of rock clip production, the tensile stress decreases, indicating that rock clip production mainly affects the range of rock damage by inhibiting the propagation of tensile stress.
3) According to the comparative analysis of field test results and numerical simulation results, the fitting degree of numerical simulation is high. Therefore, it is proved that the stress application method and the constitutive parameters of RHT have certain accuracy. The production coefficient of rock clip at different depths is inversely calculated by using the three-dimensional laser scanning results. The data showed that the fitting degree of comparison is 94.5%, indicating that the divided RHT damage zoning determination range has certain reliability. Combined with multiple sets of test field scanning data, the blasting effect of the cut section is inversely calculated, and the mathematical relationship between the production coefficient K_r of rock clip and the relative height of wellhead H and the section cavity area S_c is fitted, which provides theoretical guidance for the design of cutting blasting and one-time well completion blasting parameters under the condition of high *in-situ* stress.

DATA AVAILABILITY STATEMENT

The original contributions presented in the study are included in the article/Supplementary Material, further inquiries can be directed to the corresponding author.

AUTHOR CONTRIBUTIONS

Conceptualization, methodology, software, validation, formal analysis, writing-original draft, writing-review and editing: BS; Investigation, data curation: JM, HZ; Supervision, software: YH; Funding acquisition, project administration Resources, investigation: ZZ.

FUNDING

This research is supported by financial grants from the National Natural Science Foundation of China (52064025, 52164009, 52164010). The authors are very grateful to the financial contribution and convey their appreciation to the organization for supporting this basic research.

REFERENCES

Cai, M., Kaiser, P. K., Tasaka, Y., Maejima, T., Morioka, H., and Minami, M. (2004). Generalized Crack Initiation and Crack Damage Stress Thresholds of Brittle Rock Masses Near Underground Excavations. *Int. J. Rock Mech. Mining Sci.* 41 (5), 833–847. doi:10.1016/j.ijrmms.2004.02.001

Cheng, B., Wang, H. B., Zong, Q., Xu, Y., Wang, M. X., Zheng, Q. Q., et al. (20202020). A Study on Cut Blasting with Large Diameter Charges in Hard Rock Roadways. *Adv. Civil Eng.* doi:10.1155/2020/8873412

Du, K., Li, X., Tao, M., and Wang, S. (2020). Experimental Study on Acoustic Emission (AE) Characteristics and Crack Classification during Rock Fracture in Several Basic Lab Tests. *Int. J. Rock Mech. Mining Sci.* 133. doi:10.1016/j.ijrmms.2020.104411

Du, K., Li, X., Wang, S., Tao, M., Li, G., and Wang, S. (2021). Compression-shear Failure Properties and Acoustic Emission (AE) Characteristics of Rocks in Variable Angle Shear and Direct Shear Tests. *Measurement* 183. doi:10.1016/j.measurement.2021.109814

Du, K., LiLi, X.-f., YangYang, C.-z., Zhou, J., Chen, S.-j., and Manoj, K. (2020). Experimental Investigations on Mechanical Performance of Rocks under Fatigue Loads and Biaxial Confinements. *J. Cent. South. Univ.* 27 (10), 2985–2998. doi:10.1007/s11771-020-4523-7

Fan, Y., Lu, W., Zhou, Y., Zhao, C., and Peng, Y. (2017). Evolution Mechanism of Damage Zone in Surrounding Rock Mass during Excavation of Deep Tunnels under High Geostress Condition. *J. Eng. Geology.* 25 (2), 308–316.

Gao, J., Xie, S. Z., Zhang, X. T., Wang, H. L., Gao, W. L., and Zhou, H. M. (2020). Study on the 2D Optimization Simulation of Complex Five-Hole Cutting Blasting under Different Lateral Pressure Coefficients. *Complexity* 2020. doi:10.1155/2020/4639518

Gao, K., Huang, P., Liu, Z. G., Liu, J., Wang, F., and Shu, C. M. (2021). Pressure Relief by Blasting Roof Cutting in Close Seam Group Mining under Thick Sandstone to Enhance Gas Extraction for Mining Safety. *Processes* 9 (4). doi:10.3390/pr9040603

Jun, D. A. I., and Qian, Q. (2007). Break Blasting Parameters for Driving a Roadway in Rock with High Residual Stress. *Explosion and Shock Waves* 27 (3), 272–277.

Kaiser, P. K., Zou, D., and Lang, P. A. (1990). Stress Determination by Back-Analysis of Excavation-Induced Stress Changes ? a Case Study. *Rock Mech. Rock Engng* 23 (3), 185–200. doi:10.1007/bf01022953

Li, Q., Huang, W., Wu, Z., Kong, D., and Liu, K. (2016). Theoretical Study and Numerical Simulation on Rock Failure Process in Cutting by Parallel Hole under Different Ground Stress Conditions. *J. Saf. Sci. Tech.* 12 (11), 57–62.

Li, Q.-y., Liu, K., Li, X.-b., Wang, Z.-w., and Weng, L. (2018). Cutting Parameter Optimization for One-step Shaft Excavation Technique Based on Parallel Cutting Method. *Trans. Nonferrous Met. Soc. China* 28 (7), 1413–1423. doi:10.1016/s1003-6326(18)64780-6

Li, X., Chen, J., Li, Y., and Dai, Y. (2010). Study of Criterion and Damage Zone Induced by Excavation Blasting of Underground Power-House of Xiluodu Hydropower Station. *Chin. J. Rock Mech. Eng.* 29 (10), 2042–2049.

Li, X., Yao, J., and Gong, F. (2011). Dynamic Problems in Deep Exploitation of Hard Rock Metal Mines. *Chin. J. Nonferrous Met.* 21 (10), 2551–2563. doi:10.1016/s1003-6326(11)60720-6

Li, X. S., Peng, K., Peng, J., and Hou, D. (2021). Effect of thermal Damage on Mechanical Behavior of a fine-grained sandstone. *Arabian J. Geosciences* 14 (13). doi:10.1007/s12517-021-07607-0

Man, K., Liu, X. L., Wang, J., and Wang, X. Y. (20182018). Blasting Energy Analysis of the Different Cutting Methods. *Shock and Vibration*, 13. doi:10.1155/2018/9419018

Qin, Q., Li, K., Li, M., and Liu, B. (2021). Study on Damage Failure Criterion and Failure Behavior of Non-homogeneous Rock Materials. *Chin. J. Rock Mech. Eng.* 40 (9), 1812–1825.

Riedel, W., Kawai, N., and Kondo, K.-i. (2009). Numerical Assessment for Impact Strength Measurements in concrete Materials. *Int. J. Impact Eng.* 36 (2), 283–293. doi:10.1016/j.ijimpeng.2007.12.012

Tang, H., Zhou, Y., and Liao, Y. (2015). Damage Zone of Surrounding Rock of Underground Engineering under Construction Blasting. *J. Vibration Shock* 34 (23), 202–206.

Wang, S., Sun, L., Li, X., Wang, S., Du, K., Xiang, L., et al. (2021). Experimental Investigation of Cuttability Improvement for Hard Rock Fragmentation Using Conical Cutter. *Int. J. Geomechanics* 21 (2). doi:10.1061/(asce)gm.1943-5622.0001899

Wang, S. F., Li, X. B., Yao, J. R., Gong, F. Q., Li, X., Du, K., et al. (2019). Experimental Investigation of Rock Breakage by a Conical Pick and its Application to Non-explosive Mechanized Mining in Deep Hard Rock. *Int. J. Rock Mech. Mining Sci.* 122. doi:10.1016/j.ijrmms.2019.104063

Wei, C., Zhu, W., Yu, B., and Niu, L. (2016). Numerical Simulation on Cutting Seam Cartridge Blasting under Different In-Situ Stress Conditions. *Explosion and Shock Waves* 36 (2), 161–169.

Xiao, S., Jiang, Y., Liu, Z., and Su, L. (2018). Hard Rock Blasting Energy Distribution and Fragmentation Characteristics under High Earth Stress. *J. Vibration Shock* 37 (15), 143–149.

Xie, L., Lu, W., Jiang, Q., Zhang, Q., Wang, G., Chen, M., et al. (2017). Damage Evolution Mechanism of Deep Rock Mass in Process of Cut Blasting. *J. Cent. South Univ. Sci. Tech.* 48 (5), 1252–1260.

Xie, L.-T., Yan, P., Lu, W.-B., Chen, M., and Wang, G.-H. (2018). Effects of Strain Energy Adjustment: A Case Study of Rock Failure Modes during Deep Tunnel Excavation with Different Methods. *KSCE J. Civ Eng.* 22 (10), 4143–4154. doi:10.1007/s12205-018-0424-9

Xie, L. X., Lu, W. B., Zhang, Q. B., Jiang, Q. H., Chen, M., and Zhao, J. (2017). Analysis of Damage Mechanisms and Optimization of Cut Blasting Design under High In-Situ Stresses. *Tunnelling Underground Space Tech.* 66, 19–33. doi:10.1016/j.tust.2017.03.009

Yang, D., Li, H., Xia, X., and Luo, C. (2014). Study of Blasting-Induced Dynamic Damage of Tunnel Surrounding Rocks under High In-Situ Stress. *Rock Soil Mech.* 35 (4), 1110.

Yang, D. Q., Wang, X. G., Wang, Y. J., An, H. M., and Lei, Z. (20202020). Experiment and Analysis of Wedge Cutting Angle on Cutting Effect. *Adv. Civil Eng.* doi:10.1155/2020/5126790

Yang, J., Sun, W., Yao, C., and Zhang, X. (2020). Mechanism of Rock Fragmentation by Multi-Hole Blasting in Highly-Stressed Rock Masses. *Explosion and Shock Waves* 40 (7).

Yang, J., Wu, Z., Yao, C., Jiang, S., and Jiang, Q. (2020). Influences of In-Situ Stress on Blast-Induced Rock Fracture and Seismic Waves. *J. Vibration Shock* 39 (13), 64.

Yang, X. J., Liu, C. K., Sun, H. L., Yue, S. L., Ji, Y. G., Zhang, X. Y., et al. (2020). Researchonthe Deformation Mechanism and Directional Blasting Roof Cutting Control Measures of a Deep Buried High-Stress Roadway. *Shock and Vibration*. doi:10.1155/2020/6742504

Yao-Ji, L. I., Xiao-Shuang, L. I., and Wang, M. L. (2014). Progress of Research on Mining Technology for Transition from Open-Pit to Underground Mine of Gently Inclined,thin and Medium Thick Phosphate Rocks. *Ind. Minerals Process.*

Yin, Z.-q., Li, X.-b., Jin, J.-f., He, X.-q., and Du, K. (2012). Failure Characteristics of High Stress Rock Induced by Impact Disturbance under Confining Pressure Unloading. *Trans. Nonferrous Met. Soc. China* 22 (1), 175–184. doi:10.1016/s1003-6326(11)61158-8

Yin, Z., Chen, W., Hao, H., Chang, J., Zhao, G., Chen, Z., et al. (2020). Dynamic Compressive Test of Gas-Containing Coal Using a Modified Split Hopkinson Pressure Bar System. *Rock Mech. Rock Eng.* 53 (2), 815–829. doi:10.1007/s00603-019-01955-w

Yin, Z. Q., Hu, Z. X., Wei, Z. D., Zhao, G. M., Ma, H. F., Zhuo, Z., et al. (20182018). Assessment of Blasting-Induced Ground Vibration in an Open-Pit Mine under Different Rock Properties. *Adv. Civil Eng.* doi:10.1155/2018/4603687

Yin, Z. Q., Ma, H. F., Ma, H. F., Hu, Z. X., and Zou, Y. (2014). Effect of Static - Dynamic Coupling Loading on Fracture Toughness and Failure Characteristics in Marble. *Jestr* 7 (2), 169–174. doi:10.25103/jestr.072.25

Zhang, H., Li, T. C., Du, Y. T., Zhu, Q. W., and Zhang, X. T. (2021). Theoretical and Numerical Investigation of Deep-Hole Cut Blasting Based on Cavity Cutting and Fragment Throwing. *Tunnelling Underground Space Tech.* 111, 18. doi:10.1016/j.tust.2021.103854

Zhang, X. Y., Hu, J. Z., Xue, H. J., Mao, W. B., Gao, Y. B., Yang, J., et al. (2020). Innovative Approach Based on Roof Cutting by Energy-Gathering Blasting for Protecting Roadways in Coal Mines. *Tunnelling Underground Space Tech.* 99. doi:10.1016/j.tust.2020.103387

Conflict of Interest: The authors declare that the research was conducted in the absence of any commercial or financial relationships that could be construed as a potential conflict of interest.

frontiers | Frontiers in Earth Science

ORIGINAL RESEARCH
published: 27 April 2022
doi: 10.3389/feart.2022.886221

Deformation and Failure Characteristics and Control Technology of Surrounding Rocks in Deep High-Horizontal Stress Rock Roadways in the Wanbei Mining Area

Denghong Chen[1]*, *Yongqiang Yuan*[2] *and Li Ma*[1,2]*

[1]*School of Mining Engineering, Anhui University of Science and Technology, Huainan, China,* [2]*Wanbei Coal-Electricity Group Co., Ltd, Suzhou, China*

Edited by:
Yilin Gui,
Queensland University of Technology,
Australia

Reviewed by:
Bowen Wu,
China University of Mining and
Technology, China
Xiangyu Wang,
China University of Mining and
Technology, China

***Correspondence:**
Denghong Chen
dhchen@aust.edu.cn
Li Ma
348306585@qq.com

Specialty section:
This article was submitted to
Geohazards and Georisks,
a section of the journal
Frontiers in Earth Science

Received: *28 February 2022*
Accepted: *17 March 2022*
Published: *27 April 2022*

Citation:
Chen D, Yuan Y and Ma L (2022)
Deformation and Failure
Characteristics and Control
Technology of Surrounding Rocks in
Deep High-Horizontal Stress Rock
Roadways in the Wanbei Mining Area.
Front. Earth Sci. 10:886221.
doi: 10.3389/feart.2022.886221

Taking the engineering conditions of the Zhujixi coal mine and Hengyuan coal mine in the Wanbei mining area as the background, based on the investigation of the deformation and failure status of the surrounding rock of the two mines, the deformation and failure characteristics of the surrounding rock of the deep rock roadway in the Wanbei mining area are systematically studied by using the comprehensive research methods of the surrounding rock mechanical parameter test, *in situ* stress measurements, and numerical simulation. The results show that the measured value of the intermediate principal stress is slightly less than the theoretical value, which is obviously affected by the tectonic stress. The lateral pressure coefficients of the two mines calculated according to the theory are between 1.06 and 1.24 and 1.18 and 1.24, respectively. The simulation shows that when the lateral pressure is higher than 1.5, the arrangement of drilling holes with a depth of 5–10 m and a diameter of 200–300 mm can effectively transfer the stress concentration, proposed using Φ22 L = 2800 mm anchor rods, row spacing 800 × 800 mm, specification Φ 22. For the anchor cable with a length of L = 6,300 mm, the row spacing between anchor cables is 1,600 ± 100 mm, and the coordinated support technology of the reinforcement support and grouting is added. The technology can fully mobilize the deep stable rock stratum when it is applied from the slope change point of 11 coal belt roadways in the east wing of the Zhujixi coal mine to the machine head chamber of 11 coal belt roadways in the west wing, and the field application is good.

Keywords: deep high-horizontal stress, side pressure coefficient, stability of roadway surrounding rocks, coordinated control technology, pressure relief and reinforcement

INTRODUCTION

With the development of the world economy, the mineral resources in the shallow part of the earth are gradually exhausted, and the resource development continues to move toward the deep part of the earth. At the same time, the human demand for survival and development and the exploration of the unknown world also continue to expand the underground activity space. In terms of resource mining, the mining depth of nonferrous metal mines is more than 4,350 m, and the geothermal mining depth is more than 3,000 m. As the main fossil energy resource endowed by nature, the mining depth of coal has reached 1,500 m. In the future, the mining of deep resources will become the norm (Xie et al., 2015; Xie et al., 2021a). The stress level of the surrounding rock of the shallow roadway is low, the stress concentration caused by excavation is low, and the deformation and fracture range of the surrounding rock is small. It can be effectively controlled by the conventional support. In contrast, the surrounding rock of the deep roadway is in the special stress environment of "three high and one disturbance," and is often subject to complex geological tectonic movement, forming obvious regional and directional high-horizontal stress. The surrounding rock of the roadway shows significant non-linear soft rock mechanical characteristics, serious fragmentation and expansion, and poor support and maintenance effects (Hou et al., 2021a; Xie et al., 2021b; Zhang, 2020). The horizontal stress of a deep roadway will be several times larger than that in the shallow roadway, resulting in a more complex mechanical environment. Especially, without considering the influence of the high-horizontal stress direction, mining design and excavation will often cause sudden convergence deformation and collapse damage of the surrounding rock of the development roadway and working face, roof subsidence, and serious floor heave. It will even lead to dynamic failure such as rockburst (Zhu, 2018; Zhao et al., 2021).

Theoretical and engineering practice research has shown that under the current support level, blindly increasing the support strength and support density cannot better control the large deformation of the roadway surrounding rock (Ma et al., 2015). The research shows that the surrounding rock of underground engineering is usually subjected to the coupling action of compressive stress and shear stress (Du et al., 2021); according to the variation trend of acoustic emission blow count and acoustic emission energy characteristic parameters, the rock fracture process shows obvious piecewise variation characteristics and has a significant growth cycle (Du et al., 2020). In deep mines, due to the sudden fracture of the hard roof in the mining process, the roadway may also be subjected to dynamic load (Yin et al., 2020); the increase of axial preloading stress is helpful to improve the crack growth rate and reduce the dynamic crack initiation toughness (Yin et al., 2014). Through the numerical calculation and on-site teaching and research on the rock mass excavation process of the underground powerhouse of the Xiaolangdi water control project, Zhu Weishen and others believe that the support structure has a significant effect on fixing the loose and broken rock mass of the surrounding rock and preventing its collapse and falling off (Zhu et al., 2006). Through the analysis and research on the measured data of roadway surrounding rock deformation in Huainan, Pingdingshan, and other mining areas, Yang Chao and others believe that increasing the support resistance is mainly to curb the expansion of the roadway surrounding rock fracture area (Yang et al., 2000). The subsidence of roadway roofs has little correlation with the support strength provided by the existing support equipment. Increasing the high continuous support resistance can prevent the caving of the loose surrounding rock (Fan et al., 2003). Hou Chaojiong put forward the basic theory and technical framework of surrounding rock control in the deep roadway, which takes the strengthening of the surrounding rock as the core and the active stress intervention and grouting modification as the support (Hou et al., 2021b). According to Wang Weijun's research, high stress will lead to continuous deformation of the roadway surrounding rock dominated by plastic deformation (Wang et al., 2016). Meng Qingbin found that the supporting stress field of the bolt and anchor cable improves the disturbed stress field of the surrounding rock after roadway excavation, inhibits the generation of the tensile stress zone, reduces the shear stress zone, and limits the tensile and shear failure of coal and rock mass (Meng et al., 2017).

To sum up, the original rock stress value of the deep roadway is much greater than the strength of the surrounding rock, and the original rock stress is the main influencing factor of large deformation, failure, and instability of the surrounding rock of the roadway. At present, there are few in-depth studies on the deformation and failure characteristics and control technology of surrounding rocks in deep high-horizontal stress rock roadways. The interaction principle between such roadway supports and surrounding rocks needs to be clarified. Targeted prevention and control countermeasures such as optimization of layout orientation, pressure relief in high-stress areas of the surrounding rock, and asymmetric support in low-stress areas are difficult to put forward. In this work, the influence of deep high-horizontal stress on the deformation and failure characteristics of the rock roadway surrounding rock is studied by means of field tests and numerical calculations.

ENGINEERING BACKGROUND

The Hengyuan coal mine and Zhujixi coal mine in the Wanbei mining area have successively entered deep mining. The Zhujixi coal mine is located in the north of the Huainan coalfield and in the west section of the Zhuji—Tangji anticline. The occurrence form of coal seams in the mine is generally an axial NW syncline structure, which is controlled by regional large faults. The mine is located in the footwall of North–South reverse faults, and there are large tensile faults in the north of the northern reverse fault group. The rock layer near the Hengyuan coal mine is a monoclinic structure with an inclination of 3–20°, and the overall geological conditions are relatively simple. The normal fault DF56 may be exposed in the later stage of tunneling. According to different roadway types, the two mines have used a variety of support methods, including the bolt mesh shotcrete support, the bolt mesh cable support, the bolt cable coupling support, bolt meshes, the cable shotcrete grouting support, and other support forms, but have not achieved good support results. In order to study the deformation and failure characteristics of the surrounding rock of the deep high-horizontal stress rock roadway in the Wanbei mining area, rock coring and *in situ* stress tests were

FIGURE 1 | Compressive failure process of the rock.

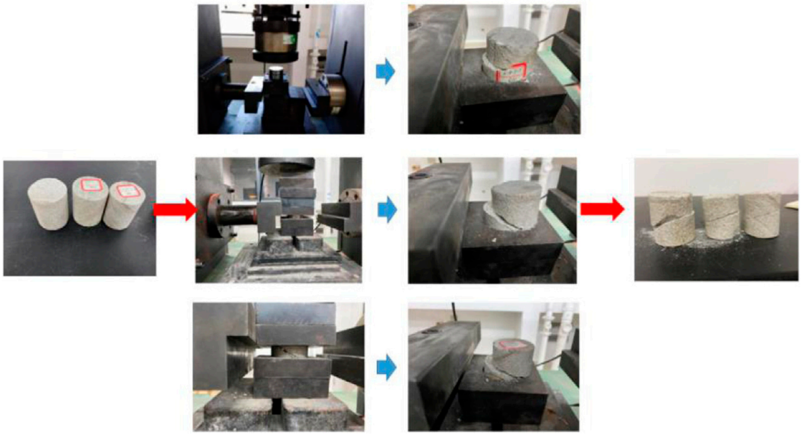

FIGURE 2 | Flow chart of the rock shear test.

carried out in the above two mines in order to carry out the subsequent geomechanical evaluation of the deep roadway.

GEOMECHANICAL ASSESSMENT OF DEEP ROADWAYS

Testing of Mechanical Parameters Around Surrounding Rocks

In order to provide corresponding parameters for the subsequent *in situ* stress test and numerical simulation, the author took two holes in the roof and floor, respectively, at two positions with an interval of about 20 m in the 11 coal track roadway on the West Wing of the Zhujixi mine and the 940 m return air auxiliary crosscut of the Hengyuan coal mine and processed the core to obtain standard samples according to the relevant national test standards. Using the RMT-150 rock mechanics testing machine, the tensile strength and compressive strength of the sample are tested at the loading speed of 0.1 KN/s, and the basic mechanical parameters of the rock body are obtained. The flow of the surrounding rock mechanical parameter test of the two mines is shown in **Figures 1**, **2**.

Through the overall analysis of the mechanical parameters of the cores taken from the two mines, it is obtained that the top and bottom slates of the 11 coal track roadway in the West Wing of the Zhujixi mine are mainly sandstone–mudstone, in which the tensile strength of the mudstone is low, ranging from 0.8 to 1.7 MPa, the compressive strength is about 20.1 MPa, and the tensile strength of some sandy mudstones is 4.79 MPa. The maximum compressive strength of the sandstone is 109.5 MPa, with high strength; Sandstone cohesion c = 12.58 MPa, and internal friction angle φ = 38.51°. The results show that the lithology of the roof of the Hengyuan mine and the 940 return air auxiliary crosscut is mainly mudstone and the lithology of the floor is mainly sandstone. The tensile strength of mudstone is low, ranging from 1.661 to 4.442 MPa, and the compressive strength is 28.27–49.65 MPa. The highest compressive strength of the sandstone is 73.695 MPa, followed by the strength; Sandstone cohesion c = 5.765 MPa, and internal friction angle φ = 23.17°. Based on the above analysis, it is found that the mechanical properties of the surrounding rock of the Hengyuan return air auxiliary crosscut roadway are better than those of the Zhujixi 11 coal roadway.

Test of *in situ* Stress

In order to ensure the stability of underground rock mass engineering, various factors affecting the engineering stability

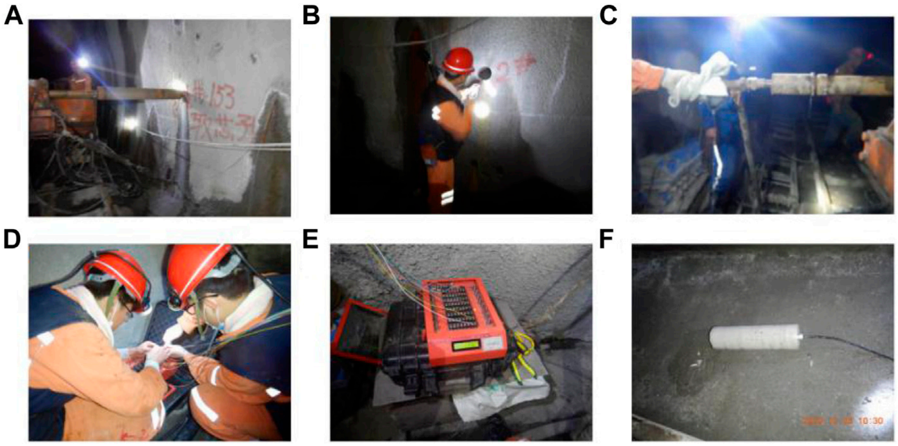

FIGURE 3 | Flow chart of the rock shear test. **(A)** Adjust the orientation of the drilling rig. **(B)** Start drilling test holes. **(C)** Install the hollow enclosure. **(D)** Relieve the stress of hollow inclusion. **(E)** Collect strain gauge data. **(F)** Core pulling.

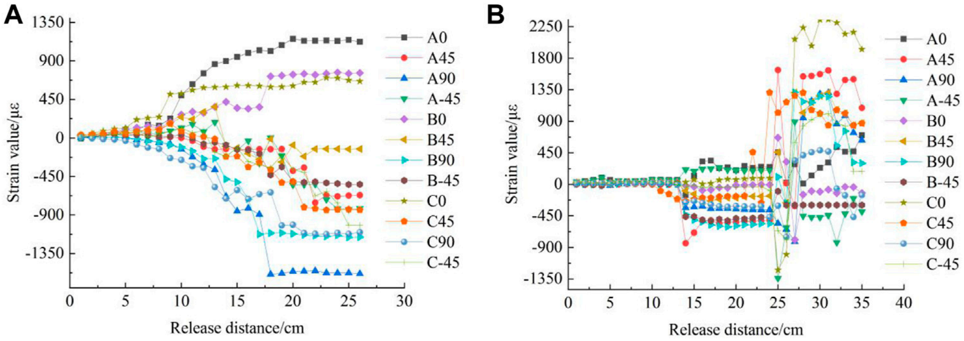

FIGURE 4 | Stress relief process curve. **(A)** Survey points of the 11 coal track roadway in the West Wing of the Zhujixi mine. **(B)** Shengyuan mine–940 return air auxiliary crosscut measuring point.

must be fully investigated and studied. Among many influencing factors, the *in situ* stress state of rock mass is one of the important factors. For mine roadway engineering, only by mastering the *in situ* stress conditions of specific engineering areas can we reasonably determine the roadway direction, optimal section shape, size, excavation steps, support forms, and support parameters.

In order to obtain the *in situ* stress distribution of the Hengyuan coal mine and Zhujixi coal mine, the *in situ* measurement of *in situ* stress was carried out by using the stress relief method. The field measurement process is shown in **Figure 3**. In this measurement, a hollow inclusion stress meter is used to measure the two sides of the 11 coal track roadway on the West Wing of Zhujixi mine and the 940 m return air auxiliary crosscut of the Hengyuan coal mine at an interval of about 20 m. The measured data are stress-relieved. Some stress relief process curves are shown in **Figure 4**, and then the magnitude and direction of *in situ* stress at the measured position are deduced by professional software.

As can be seen from **Figure 4**, the stress relief process of hollow inclusion carried out by two mining coring drill heads can be roughly divided into three stages: there is no disturbance relief influence area, and the strain curve is basically in a state of little change. This process is mainly because the coring bit has not been pushed to the position of the strain gauge. In the stress elastic release area, at this time, the strain value of each strain gauge increases rapidly with the increase of release distance, indicating that the coring bit is rapidly passing near the hollow inclusion stress gauge where the strain gauge is located and stripping it from the complete rock. Due to the removal of the core boundary constraint around the stress gauge, the hollow inclusion stress gauge will rebound and expand properly with the core. In the strain stability zone, the strain value of each strain gauge tends to be flat and fluctuates up and down in a small range, marking the end of the stress relief process.

It can also be seen from **Figure 4** that the lifting distance of the two mines in the non-lifting disturbance-affected area is the same, both between 0 and 12 cm, while the lifting range of the stress

TABLE 1 | Rock mechanical parameters selected in *in situ* stress calculations.

Measuring point	Name	Group A strain rosette	Group B strain rosette	Group C strain rosette	Average
Hengyuan mine	E/GPa	27.26	25.05	21.21	24.51
	μ	0.355	0.313	0.324	0.331
Zhujixi mine	E/GPa	49.82	41.51	33.95	41.76
	μ	0.188	0.166	0.354	0.236

elastic release area of the Zhujixi mine is 7 cm less than that of the Hengyuan mine, the strain stability area of the Zhujixi mine starts from 18 cm, and the strain stability area of the Hengyuan mine starts from 25 cm. This shows that the difference of the *in-situ* stress field between the two mines is obvious.

The *in situ* stress measurement by the hollow inclusion stress meter method is to calculate the stress through the strain value in the stress relief process of the rock mass to be measured around the stress meter and combined with the elastic mechanical parameters reflecting the stress–strain relationship of the rock mass. Therefore, the determination of rock elastic parameters at the measuring point is particularly important. **Table 1** shows the rock mechanics parameters selected in the *in situ* stress calculation of the two mines.

By comprehensively analyzing all the data in the above progress process and using Mathcad calculation software for calculations and processing, the *in situ* stress distribution state of the 11 coal track roadway in the West Wing of the Zhujixi mine is obtained. It is found that the maximum principal stress at the location of the roadway is between 25.6 and 29.9 MPa, and the azimuth of the maximum principal stress is mainly distributed in NE192° and NE94.5°、NE98.3, and the inclination angle is mainly less than 30°. The intermediate principal stress is between 22.3 and 23.6 MPa. The minimum principal stress is mainly distributed between 16.3 and 18.4 MPa, the azimuth is approximately orthogonal to the azimuth of the maximum principal stress, and the inclination is relatively small, showing a near-horizontal distribution. At 25 Kn/m^3, the overburden pressure calculated by the average unit weight is 24.05 MPa, the measured value of the intermediate principal stress is slightly less than the theoretical calculation value, which is obviously affected by the tectonic stress, and the lateral pressure coefficient calculated according to the theory is between 1.06 and 1.24.

The *in situ* stress distribution state of the Hengyuan mine with the 940 return air auxiliary crosscut is obtained. It is found that the maximum principal stress at the location of the roadway is between 27.91 and 29.18 MPa, the azimuth of the maximum principal stress is mainly distributed in NE109.9°–NE129.21°, the inclination angle is mainly less than 45°, and the intermediate principal stress is between 17.6 and 19.9 MPa. The minimum principal stress is mainly distributed between 11.4 and 13.3 MPa; at 25 Kn/m^3, the overburden pressure calculated by the average unit weight is 23.5 MPa, the measured value of the intermediate principal stress is slightly less than the theoretical calculation value, which is obviously affected by the tectonic stress, and the lateral pressure coefficient calculated according to the theory is between 1.18 and 1.24.

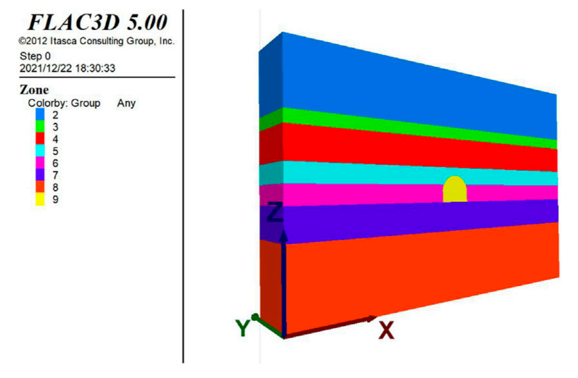

FIGURE 5 | Numerical simulation model.

SIMULATION AND OPTIMIZATION OF THE SURROUNDING ROCK CONTROL SCHEME OF THE DEEP HIGH-HORIZONTAL STRESS ROADWAY

Model Establishment

In this analysis, FLAC3D finite difference software is used to simulate the roadway deformation, and the modeling is based on the design size of the 11 coal track roadway in the West Wing of the Zhujixi mine, and the model size is 60 m × 10 m × 40 m. The buried depth of the roadway is 940 m, the vertical stress is 23.5 MPa, and the mechanical model adopts the Mohr–Coulomb criterion. After the model is established, the horizontal displacement constraint is applied to the boundaries on both sides, the vertical displacement constraint is applied to the bottom, the lateral displacement constraint is applied to the front and rear surfaces, and the stress boundary is applied to the top surface. The model is shown in **Figure 5**.

Simulation Scheme Design

According to the theory of mine pressure behavior and deep rock stratum control and combined with the main problems of the roadway support at present, 15 simulation schemes are orthogonally designed according to different lateral pressure coefficients, support parameters, and roof and floor lithology

TABLE 2 | Numerical simulation scheme of the roadway surrounding rock.

Scheme	Lateral pressure coefficient	Roof: Fine sandstone, floor: Mudstone Support parameters
1	1.5	Row spacing between anchor bolts 700 mm × 700 mm; 19 full face supports
2		Row spacing between anchor bolts 700 mm × 700 mm; 19 full face supports; row spacing between anchor cables 700 mm × 700 mm; 5 full face supports
3		Row spacing between anchor bolts 800 mm × 800 mm; 15 full face supports; row spacing between anchor cables 1600 mm × 1600 mm; 5 full face supports
4		Row spacing between anchor bolts 700 mm × 700 mm; 13 full face supports and 4 base plates; row spacing between anchor cables 1400 mm × 1400 mm; 5 full face supports
5	1.25	Row spacing between anchor bolts 700 mm × 700 mm; 19 full face supports
6		Row spacing between anchor bolts 700 mm × 700 mm; 19 full face suppors; row spacing between anchor cables 700 mm × 700 mm; 5 full face supports
7		Row spacing between anchor bolts 800 mm × 800 mm; 15 full face supports; row spacing between anchor cables 1600 mm × 1600 mm; 5 full face supports
8		Row spacing between anchor bolts 700 mm × 700 mm; 13 full face supports and 4 base plates; row spacing between anchor cables 1400 mm × 1400 mm; 5 full face supports
Scheme	**Lateral pressure coefficient**	**Roof: fine sandstone, floor: siltstone Support parameters**
9	1.5	Row spacing between anchor bolts 700 mm × 700 mm; 19 full face supports
10		Row spacing between anchor bolts 700 mm × 700 mm; 19 full face supports; row spacing between anchor cables 700 mm × 700 mm; 5 full face supports
11		Row spacing between anchor bolts 800 mm × 800 mm; 15 full face supports; row spacing between anchor cables 1600 mm × 1600 mm; 5 full face supports
12		Row spacing between anchor bolts 700 mm × 700 mm; 13 full face supports and 4 base plates; row spacing between anchor cables 1400 mm × 1400 mm; 5 full face supports
Scheme	**Lateral pressure oefficient**	**Roof: fine sandstone, floor: mudstone**
Support parameters		Row spacing between anchor bolts 700 mm × 700 mm; 13 full face supports and 4 base plates; row spacing between anchor cables 1400 mm × 1400 mm; 5 full face supports
Borehole pressure relief parameters		
13	1.5	Drilling length: 6m; row spacing between drilling holes: 1500 mm × 600 mm
14		Drilling length: 12 m; row spacing between drill holes; 1500 mm × 600 mm
15		Drilling length: 3M; row spacing between drilling holes: 1500 mm × 600 mm

(mudstone, siltstone, and fine sandstone), including high-strength bolt φ22 × 2,800 mm and anchor cable φ φ22 × 6,300 mm as shown in **Table 2**.

Numerical Simulation Results

In order to understand the distribution of roadway stress, the failure of the plastic zone, and the change of support stress under different simulation schemes, various simulation results are comprehensively analyzed.

Comparing the simulation results of schemes 1–4, as shown in **Figure 6**, it can be seen from the cloud diagram of ZZ stress distribution that there is no special stress concentration as in scheme 3. The distribution position of the maximum-horizontal stress extends from the roadway side foot to the middle of the left and right sides of the roadway, and the maximum value reaches 10.248 MPa; the vertical stress is mainly tensile at the top and bottom of the roadway, with the maximum value of 1.7837 MPa, while the stress on the roadway side is 23.627 MPa. It can be found that the tensile force on the top of scheme 4 is 0.327 MPa lower than that in scheme 3, and the pressure on the two sides basically does not increase. At the same time, the maximum stress on the anchor cable is 0.30359 MPa, which is also lower than that in scheme 3. However, the plastic zone of the roadway shoulder is expanded to 2.6 m, which is 0.4 m less than that of scheme 3, and the plastic zone of the side is expanded by 2.6 m as in scheme 3. Schemes 1 to 4 are the comparison results of various supports under the vertical stress with the lateral pressure coefficient of 1.5 times. It can be clearly found that the support mode of scheme 4 is more conducive to the stability of the roadway surrounding rock and less damage to the anchor cable.

Comparing the simulation results of schemes 5 to 8, as shown in **Figure 7**, it can be seen from the cloud diagram of XX stress distribution that there is no stress expansion like scheme 7, with the maximum tensile value of 4.4498 MPa and the maximum compressive value of 4.4281 MPa; the distribution position of the position with the maximum-horizontal stress is similar to the first three schemes, and the maximum value is 0.51719 MPa; the vertical stress is mainly tensile at the top and bottom of the roadway, with the maximum value of 1.8082 MPa, while the stress at the roadway side is 23.627 MPa. At the same time, the maximum stress of the anchor cable is 0.30372 MPa, which is also increased to a certain extent compared with scheme 3. However, the position of the plastic zone at the roadway shoulder is expanded to 2.8 m, which is increased by 0.2 m compared with scheme 3, and the plastic zone at the side is expanded by 2.6 m as in scheme 3. Schemes 5 to 8 are the comparison results of various supports under the vertical

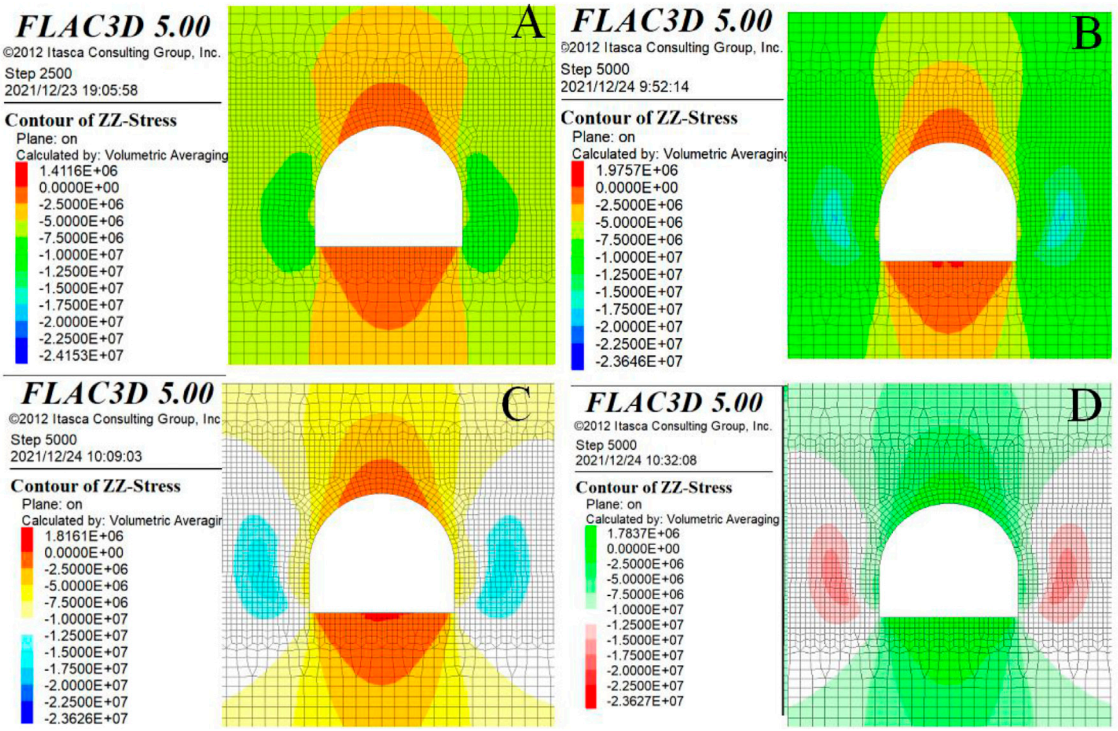

FIGURE 6 | Cloud diagram of ZZ stress distribution. **(A)** Option 1. **(B)** Option 2. **(C)** Option 3. **(D)** Option 4.

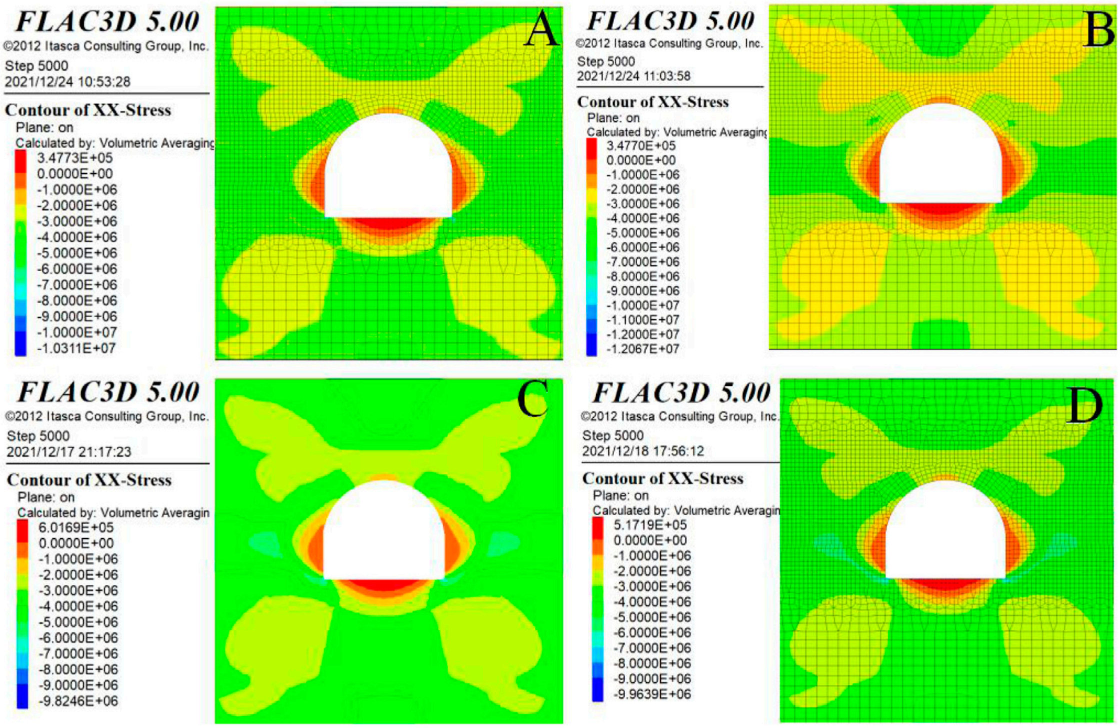

FIGURE 7 | Cloud diagram of ZZ stress distribution. **(A)** Option 5. **(B)** Option 6. **(C)** Option 7. **(D)** Option 8.

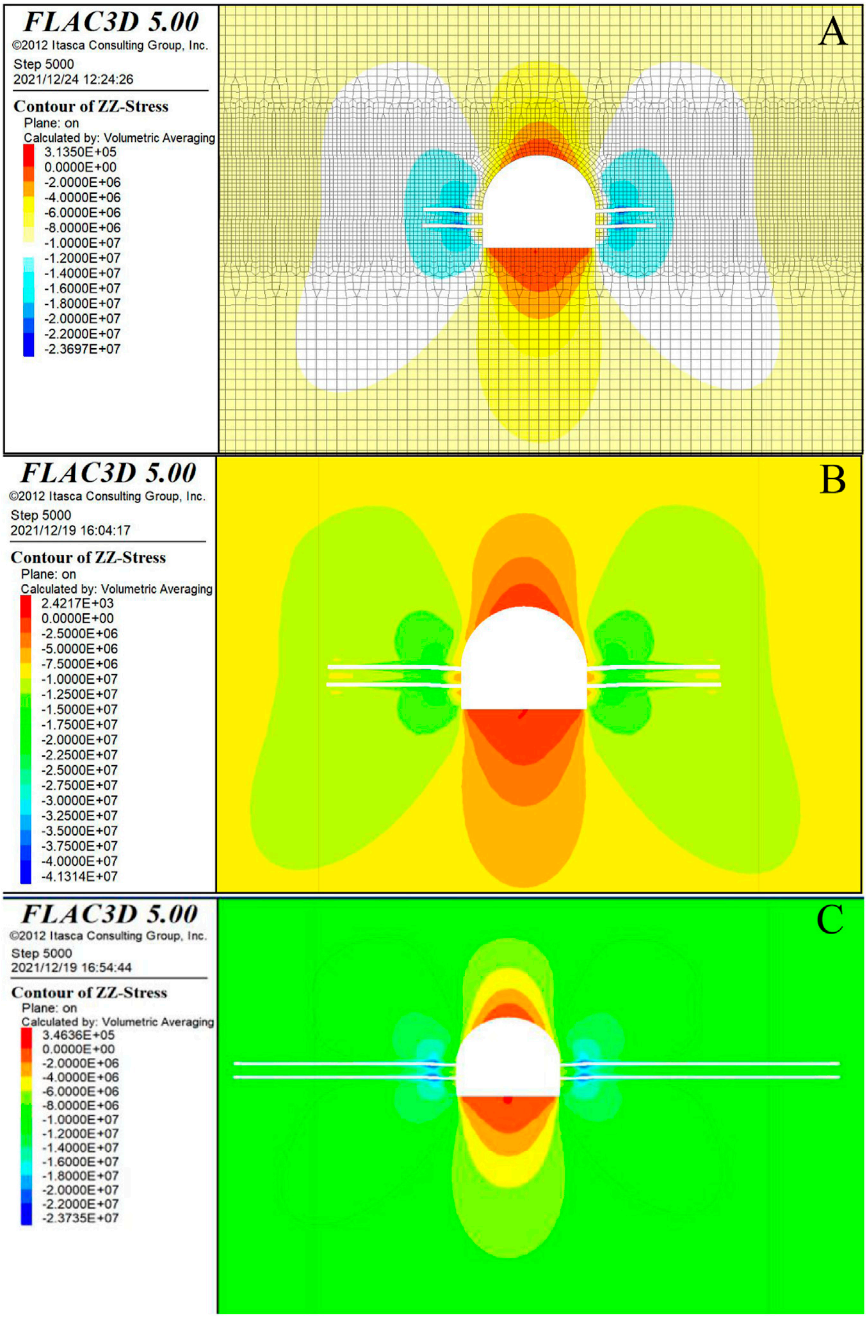

FIGURE 8 | Borehole pressure relief ZZ stress distribution nephogram. **(A)** Option 13. **(B)** Option 14. **(C)** Option 15.

stress with the lateral pressure coefficient of 1.25 times. It can be clearly found that the support mode of scheme 7 is more conducive to the stability of the roadway surrounding rock and less damage to anchor cables. Schemes 9 to 12 are under the vertical stress with the lateral pressure coefficient of 1.5 times, and the comparison results of various supports after the lithology of the surrounding rock are changed; it can be clearly found that the support mode of scheme 12 is more conducive to the stability of the roadway surrounding rock.

A certain number of boreholes are drilled in the surrounding rock of the roadway in the high-stress area. Under the action of stress, the borehole wall is collapsed, a certain crushing area is formed around the borehole, and the failure areas of adjacent boreholes are connected to form a large-scale failure zone. The high-stress roadway realizes pressure relief by arranging boreholes: the boreholes are crushed, releasing energy and transferring the stress peak to the deep, which reduces the stress concentration of the coal seam and improves the stress

FIGURE 9 | Field investigation on the deformation status of the 11 coal belt roadway.

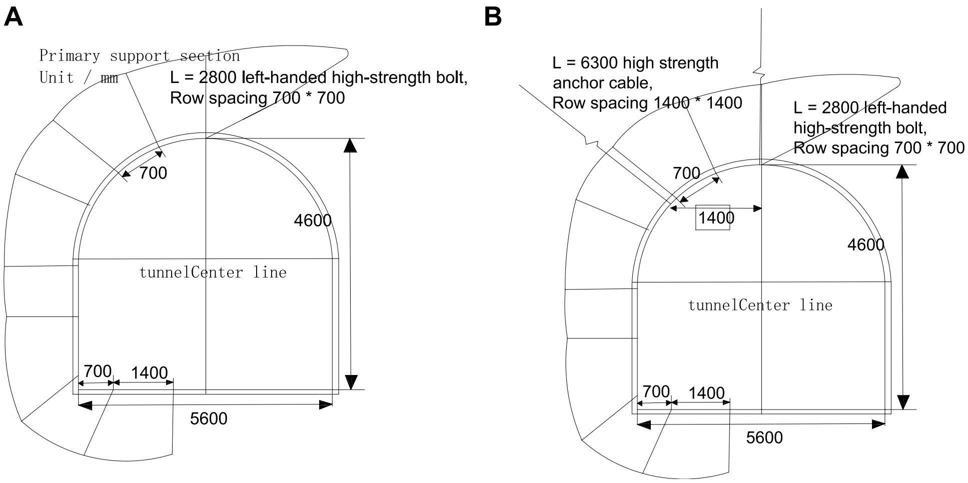

FIGURE 10 | Support section. **(A)** Permanent support. **(B)** Reinforcement support.

environment of the roadway. Drilling changes the physical and mechanical bearing characteristics, reduces the brittleness of the coal seam and the ability of the coal seam to store elastic properties, and thus reduces the possibility of local stress concentration in the surrounding rock of the roadway. **Figure 8** shows the simulation results of different borehole pressure relief parameters.

From the simulation results, it can be seen that the stress in the vertical direction of the roadway decreases in the vault and floor of the roadway, and the stress around the two sides of the borehole decreases slightly. There is still a slight stress concentration at the corner points such as the arch waist and the foot of the sidewall. The stress concentration zone is transferred around the borehole. The maximum stress value of scheme 13 is 22.5 MPa, that of scheme 14 is 23.735 MPa, and that of scheme 15 is 23.697 MPa. In the actual pressure relief construction, due to the different working faces, different material properties, and the requirements of drilling technology and construction efficiency, it is reasonable to arrange the drilling depth of 5–10 m, which depends on the specific stope conditions.

Through comparison, it is found that the simulated support parameter is the row spacing between bolts of 700 mm × 700 mm, 13 full section supports, 4 base plates, and a 1,400 mm row spacing between anchor cables compared with other schemes; the simulation effect of the scheme of 1,400 mm and 5 full face supports is more obvious; and the damage of the anchor cable is less. When the above support parameters are used to simulate after changing the roof and floor rock properties, the plastic zone of the roadway side is expanded to 1.2 m and the plastic zone of the floor is expanded to 1.8 m. It can be clearly found that this support method is more conducive to the stability of the surrounding rock of the roadway floor. In the actual pressure relief construction, due to the different working faces, different material properties, and the requirements of drilling technology and construction efficiency, when the lateral pressure is higher than 1.5, the drilling depth is 5–10 m and the hole diameter is 200–300 mm, which can effectively transfer the stress concentration, depending on the specific stope conditions. Coordinated control technology of the deep high-horizontal stress roadway is required.

FIGURE 11 | Support effect of the 11 coal belt roadway in the west-east wing of Zhuji.

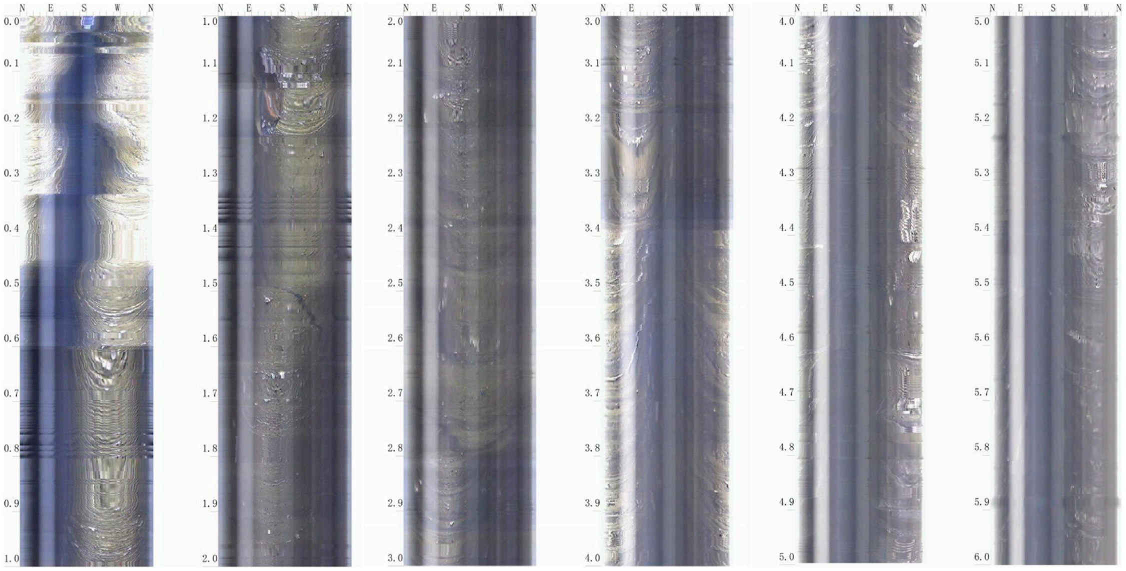

FIGURE 12 | Peeping through 0–6 m boreholes in the 11 coal belt roadway in the west-east wing of Zhuji.

COORDINATED CONTROL TECHNOLOGY OF THE DEEP HIGH-HORIZONTAL STRESS ROADWAY

After on-site investigation, it is found that from the slope change point of the No. 11 coal belt roadway in the West Wing of Zhuji to the machine head chamber of the No. 11 coal belt roadway in the West Wing of Zhuji, it is compressed and deformed, squeezing the belt conveyor in the roadway and restricting safety production. The deformation of the on-site investigation roadway is shown in **Figure 9**.

Then, under the results of numerical simulation, the coordinated control is carried out from the slope change point of the 11 coal belt roadway in the east wing to the head chamber of the 11 coal belt roadway in the West Wing of the Zhujixi coal mine. The anchor mesh shotcrete cable support is adopted for permanent support Φ 22, L = 2,800 mm left-hand non-longitudinal reinforcement high-strength deformed steel bolts, with a row spacing of 800 × 800 mm. 1 × 19 strand high-strength anchor cables with specification Φ 22 are used. The length is L = 6,300 mm, the exposed length is 150–250 mm, and the row spacing between anchor cables is 1,600 ± 100 mm. The reinforced support anchor bolt and anchor cable are alternately arranged in the whole cross-section between the transverse and longitudinal middle of the original primary support anchor bolt, and the rows between adjacent anchor bolts and anchor cables are 800 × 800 mm. Grouting is also carried out for the machine head chamber and belt roadway of the 11 coal belt roadway. The diameter of the grouting pipe is 20 mm, and the grouting material is a single liquid cement slurry. The supporting section is shown in **Figure 10**.

After adopting the coordinated control technology of the deep high-horizontal stress roadway, the field investigation on the support of the East Wing 11 coal belt roadway is carried out, and it can be seen that the support effect is remarkable, as shown in **Figure 11**.

In order to further verify the roadway support effect, a borehole peeping camera is used to peep at the roadway after support, as shown in **Figure 12**. From the results, it can be seen that there is no obvious separation in the deep part of the roadway.

CONCLUSION

(1) Through the test, the mechanical parameters of the deep rock roadway surrounding rock in the Zhujixi coal mine and Hengyuan coal mine are obtained. Among them, the top and bottom slates of the 11 coal track roadway in the West Wing of the Zhujixi mine are mainly sandstone–mudstone. The tensile strength of mudstone is low, ranging from 0.8 to 1.7 mpa, and the compressive strength is about 20.1 mpa. The maximum compressive strength of sandstone is 109.5 mpa, the cohesion of sandstone C = 12.58 mpa, and the internal friction angle $\varphi = 38.51^{\circ}$. The roof lithology of the Hengyuan mine and the 940 return air auxiliary crosscut is mainly mudstone, and the floor lithology is mainly sandstone. The tensile strength of mudstone is low, ranging from 1.6 to 4.4 mpa, and the compressive strength is 28.27–49.65 mp. The compressive strength of sandstone is up to 73.6 mpa, the cohesion of sandstone C = 5.7 mpa, and the internal friction angle $\varphi = 23.17^{\circ}$.

(2) Through the test, the *in situ* stress occurrence characteristics of the typical deep rock roadway in the Zhujixi coal mine and Hengyuan coal mine are obtained. The maximum principal stress at the location of the 11 coal track roadway on the West Wing of the Zhujixi mine is 25.6–29.9 mpa, the middle principal stress is 22.3–23.6 mpa, and the minimum principal stress is mainly distributed between 16.3 and 18.4 mpa. The maximum principal stress at the location of the Hengyuan mine and the 940 return air auxiliary crosscut is 27.9–29.1 mpa, the middle principal stress is 17.6–19.9 mpa, and the minimum principal stress is mainly distributed between 11.4 and 13.3 mpa. The measured value of the intermediate principal stress is slightly less than the theoretical calculation value, which is obviously affected by the tectonic stress. The lateral pressure coefficients of the two mines calculated according to the theory are between 1.06 and 1.24 and between 1.18 and 1.24, respectively.

(3) The optimization scheme of the coordinated control technology is obtained by numerical simulation. Through comparison, it is found that the simulated support parameter is the row spacing between bolts of 700 mm × 700 mm, 13 full section supports, 4 base plates, and a 1400 mm row spacing between anchor cables × 1400 mm, and it can be clearly found that this support method is more conducive to the stability of the roadway floor surrounding rock. In the actual pressure relief construction, due to the different working faces, different material properties, and the requirements of drilling technology and construction efficiency, when the lateral pressure is higher than 1.5, the drilling depth is 5–10 m and the hole diameter is 200–300 mm, which can effectively transfer the stress concentration, depending on the specific stope conditions.

(4) The coordinated control technology is implemented from the slope change point of the 11 coal belt roadway in the east wing of the Zhujixi coal mine to the machine head chamber of the 11 coal belt roadway in the west wing. In the 11 coal belt roadway in the east wing of the Zhujixi coal mine, which is one of the places where the technology is implemented, it is found that the technology can fully mobilize the deep stable rock stratum by using the borehole peeping technology and on-site actual monitoring.

DATA AVAILABILITY STATEMENT

The original contributions presented in the study are included in the article/supplementary material; further inquiries can be directed to the corresponding author.

AUTHOR CONTRIBUTIONS

All authors contributed to this work. DC prepared and edited the manuscript. DC and YY substantially contributed to the data analysis and revised the article. DC, YY, and LM reviewed the manuscript and processed the investigation during the research process.

FUNDING

The project was supported by the National Natural Science Foundation of China (51974008); the University Synergy Program of Anhui Province(GXXT-2020-008),the graduate innovation fund project of Anhui University of Technology (2021CX2012); and the National Key R&D Plan (2019YFC1904300).

REFERENCES

Du, K., Li, X., Tao, M., and Wang, S., (2020).Experimental Study on Acoustic Emission (AE) Characteristics and Crack Classification during Rock Fracture in Several Basic Lab Tests. *Int. J. Rock Mech. Mining Sci.*, 133:104411. doi:10.1016/j.ijrmms.2020.104411

Du, K., Li, X., Wang, S., Tao, M., Li, G., and Wang, S.,(2021) .Compression-shear Failure Properties and Acoustic Emission (AE) Characteristics of Rocks in Variable Angle Shear and Direct Shear Tests. *Measurement*, 183:109814. doi:10.1016/j.measurement.2021.109814

Fan, K. G., Zhai, D. Y., Jiang, J. Q., and Jiang, J. Q. (2003). *The Shape of Plastic Area and Fracture Ring of Thin Layer Weakness Structure in Roadsides*, 4, 6–8. 1003-5923,04-0006-03.

Hou, C. J., Wang, X. Y., and Bai, J. (2021a). Basic Theory and Technology Study of Stability Control for Surrounding Rock in Deep Roadway. *J. china Univ. mining Technol.* 50 (01), 1–12.

Hou, C, J., Wang, X, Y., Bai, J, B., Meng, N, K., and Wu, W, D. (2021b). Research on Basic Theory and Technology of Surrounding Rock Stability Control of Deep Roadway. *J. China Univ. mining Technol.* 50, 1–12. doi:10.13247/j.cnki.jcumt.001242

Ma, N. J., Zhao, X. D., Zhao, Z. Q., Li, J., and Guo, X. F. (2015). Stability Analysis and Control Technology of Mine Roadway Roof in Deep Mining. *J. China Coal Soc.* 40, 2287–2295. doi:10.13225/j.Cnki.jccs.6011

Meng, Q. B., Han, L. J., Zhang, F. G., Zhang, J., Nin, J. W., and Wen, S. Y. (2017). Coupling Support Effect on High-Stress Deep Soft Rock Roadway and its Application. *Rock Soil Mech.* 38 (05), 1424–1435+1444. doi:10.16285/j.rsm.2017.05.025

Wang, W. J., Yuan, C., Yu, W. J., Wu, H., Peng, W. Q., Peng, G., et al. (2016). Stability Control Method of Surrounding Rock in Deep Roadway with Large Deformation. *Jour-nal China Coal Soc.* 41 (12), 2921–2931. doi:10.13225/j.cnki.jccs.1115

Xie, H, P., Gao, F., and Ju, Y. (2015). Research and Development of Rock Mechanics in Deep. *J. rock Mech. Eng.* 34, 2161–2178. doi:10.13722/j.cnki.jrme.1369

Xie, H, P., Li, C, B., Gao, M, Z., Zhang, R., Gao, F., and Zhu, J, B. (2021a). Conception and Preliminary Exploration of Deep *In-Situ* Rock Mechanics in Coal Journal. *J. rock Mech. Eng.* 40, 217–232. doi:10.13722/j.cnki.jrme.0317

Xie, H, P., Ren, S, H., Xie, Y, C., and Jiao, X, M. (2021b). Development Opportunities of Coal Industry under the Goal of Carbon Neutralization. *J. coal.* 46, 2197–2211. doi:10.13225/j.cnki.jccs.0973

Yang, C., Lu, S. L., and Jiang, Y. D. (2000). Controlling Effects of Support Resistance on Roadway Deformation under Different Rock Conditions. *J. China Univ. Mining Tech.* 29, 170–173. DIO:1000-1964,02-0170-04.

Yin, Z. Q., Ma, H. F., Ma, H. F., Hu, Z. X., and Zou, Y. Effect of Static - Dynamic Coupling Loading on Fracture Toughness and Failure Characteristics in Marble. *J. Eng. Sci. Technol. Rev.*, 2014, 7(2): 169–174. doi:10.25103/jestr.072.25

Yin, Z., Chen, W., Hao, H., Chang, J., Zhao, G., Chen, Z., et al.,(2020). Dynamic Compressive Test of Gas-Containing Coal Using a Modified Split Hopkinson Pressure Bar System, *Rock Mech. Rock Eng.*, 53(2): 815–829. doi:10.1007/s00603-019-01955-w

Zhang, Y, H. (2020). *Study on Deep* In-Situ *Stress Measurement Method Considering Non-linear Elasticity of Rock Mass*. Beijing: Beijing University of science and technology. doi:10.26945/d.cnki.gbjku.000098

Zhao, X., Wang, J., Qin, X. H., and Chen, Q. C.,(2021).*In-situ* Stress Measurements at Depth and Engineering Application at China's Underground Research Laboratory Site for High-Level Radioactive Waste Disposal. *J. Cent. South Univ. (Science Technology)*.52,2634–2645. doi:10.11817/j.issn.1672-7207.08.011

Zhu, L.,(2018).*Study on Deformation Mechanism of Surrounding Rock in Different Directions under High Horizontal Stress*. doi:10.27275/d.cnki.gsdku.001239

Zhu, W. S., Liu, J. H., and Yang, F. Y. (2006). Numerical Analysis of Supporting Effect of Underground Caverns Surrounding Rockmass of Xiaolangdi Key Water Control Project. *Rock Soil Mech.* 07, 1087–1091. doi:10.16285/j.rsm.07.013

Conflict of Interest: LM and YY were employed by Wanbei Coal-Electricity Group Co., Ltd.

The remaining author declares that the research was conducted in the absence of any commercial or financial relationships that could be construed as a potential conflict of interest.

frontiers | Frontiers in Earth Science

ORIGINAL RESEARCH
published: 09 May 2022
doi: 10.3389/feart.2022.886309

Experimental Study on Work of Adsorption Gas Expansion After Coal and Gas Outburst Excitation

Yi Zhao[1,2]* *and XinGang Niu*[1,2,3,4]*

[1]State Key Laboratory of the Gas Disaster Detecting Preventing and Emergency Controlling, China Coal Technology and Engineering Group Chongqing Research Institute, Chongqing, China, [2]Gas Research Branch, China Coal Technology and Engineering Group Chongqing Research Institute, Chongqing, China, [3]State Key Laboratory of Mining Response and Disaster Prevention and Control in Deep Coal Mines, Anhui University of Science and Technology, Huainan, China, [4]School of Safety Science and Engineering, Anhui University of Science and Technology, Huainan, China

Coal and gas outburst is an extremely complex dynamic phenomenon of mine gas, which is mainly manifested in a very short time. A large amount of coal and rock are thrown out from the coal body to the mining space and accompanied by a large volume of high-pressure gas. In the process of coal and gas outburst, the internal energy consumption of gas is composed of two parts: one is used to throw out broken coal and rock mass, and the other is used to pulverize broken coal. In this article, from the perspective of energy dissipation, the experiment of broken coal ejection with different coal particle sizes, different adsorption gas, and pressure is studied. The characteristics of coal ejection are studied and analyzed, and the proportion of adsorbed gas participating in the outburst work is quantitatively analyzed. The results show that after outburst excitation, residual gas will continue to desorb and work on outburst until the power is insufficient to throw coal body; compared with air, CO_2 gas has a stronger ability to work on the outburst, and the outburst coal is thrown far away, and the pulverization effect is stronger. Through the energy analysis in the process of outburst, the results show that when the particle size of the coal sample is consistent, the greater the outburst pressure is, the larger the desorption amount of the adsorbed gas is, and the larger the volume involved in the outburst work is. When the test gas is consistent with the outburst pressure, the gas desorption amount of the small-size coal sample is more, the desorption gas has a stronger ability to work on the outburst, and the proportion of participating in outburst work is higher. The crushing degree of coal plays an important role in the expansion and release of gas internal energy.

Keywords: coal and gas outburst, gas expansion energy, energy dissipation, expansion energy of adsorbed gas, crushing energy

Edited by:
Kun Du,
Central South University, China

Reviewed by:
Hao Wu,
China University of Mining and Technology, China
Xiaobo Zhang,
Nanchang University, China
Liang Cui,
Lakehead University, Canada

***Correspondence:**
Yi Zhao
374202367@qq.com
XinGang Niu
xingang202012@163.com

Specialty section:
This article was submitted to Geohazards and Georisks, a section of the journal Frontiers in Earth Science

Received: *28 February 2022*
Accepted: *24 March 2022*
Published: *09 May 2022*

Citation:
Zhao Y and Niu X (2022) Experimental Study on Work of Adsorption Gas Expansion After Coal and Gas Outburst Excitation. Front. Earth Sci. 10:886309. doi: 10.3389/feart.2022.886309

1 INTRODUCTION

Coal and gas outburst is an extremely complex dynamic phenomenon in the process of underground mining in coal mines. It is mainly manifested in a short period of time. A large amount of coal and rock are thrown out to the mining space, and a large volume of high-pressure gas is sprayed out. The formation of coal and rock-gas flow with high-speed movement can directly strike and bury the workers, casualties, or equipment, and facilities near the underground, which poses a great threat to the safe production of coal mines. Frequent coal and gas outburst accidents have caused a large number of casualties.

Domestic and foreign scholars define the causes, conditions, and the whole process of coal and gas outburst as the coal and gas outburst mechanism (Dong, 2015). It has been reported that some experts have made abundant research results in highlighting the mechanisms. Beamish et al. (Basil and Beamish, 1998; Jin et al., 2018) believed that gas played an important role in the occurrence of coal and gas outbursts. Paterson (1986) analyzed the gas flow and stress distribution of two-dimensional coal seam, and considered that coal and gas outburst was structural instability under high gas pressure gradient; Noack and Li et al. (Klaus, 1998; Li et al., 2018) considered that ground stress played a leading role in the occurrence of outburst. Sato and Fujii (1989) studied the location of coal and gas outbursts in detail, and considered that the geological structure had obvious influence on the outburst. Cao et al. (2001) studied the influence of reverse faults in geological structures on the outburst. The results show that the coal seam in the lower wall of the reverse fault experienced more tectonic deformation than that in the upper wall. The area with high gas content almost always appears in the lower wall, and outburst is more likely to occur in these areas. Dmytro Rudakov (Dmytro and Valeriy, 2019) believed that the release of large amounts of gas in coal seam was caused by the decomposition of coal organic matter with unstable thermodynamics, and based on this, a one-dimensional mathematical model of gas flow in the outburst excitation stage was established. With the continuous improvement and enrichment of the outburst mechanism, people have gradually formed a unified understanding that coal and gas outburst is caused by the combined effect of ground stress, coal seam gas pressure, and coal's physical and mechanical properties (Norbert, 1997; Alexeev et al., 2004; Jacek, 2014; Du et al., 2020a; Yin et al., 2020). At the same time, the gas internal energy has gradually become a hot topic for many scholars. Wang et al. (2017a) carried out outburst simulation experiments with different strength briquettes and created the gas containing conditions of "the same free gas content and different adsorbed gas content" by using different adsorption characteristics of gas. The influence of adsorbed gas content on outbursts was discussed. Valliappan S (Valliappan and Wohua, 1999) believed that the gas energy released from the gas desorbed from the coal matrix to the pores was the main reason for the outburst energy; Baohai Y (Yu et al., 2015) studied the gas expansion energy in the outburst process, and the results show that the gas expansion energy is the key source of outburst energy; Peng S J et al. (Peng et al., 2012; Zhi-qiang et al., 2012; Du et al., 2020b; Wu et al., 2021a) also verified the above point of view through many experiments and proved that gas expansion energy is the main energy of throwing and crushing coal; with the continuous research and breakthrough of scholars, gas expansion energy has also begun to be used to evaluate the risk of outburst. Yang D (Yang et al., 2018) and Xu L (Xu and Jiang, 2017) studied the initial desorption characteristics of gas through experiments, indicating that the initial expansion energy of released gas can reflect the risk of outbursts. At the same time, Zhao et al. (Wang et al., 2012; Yin et al., 2014; Zhou and Wang, 2016; Zhao et al., 2017; Du et al., 2020c; Wu et al., 2021b) research results show that gas expansion can also be used to evaluate the damage of coal and rock mass during the development of coal and gas outburst.

In summary, the rich research results of many scholars in the field effectively promote the development of coal and gas outburst mechanisms, and provide theoretical guidance for the application of engineering research. However, there are few studies on the role of adsorbed gas in the process of outburst, especially the quantitative analysis of adsorbed gas work in the process of outburst. In this article, based on the existing results, combined with the mechanical impact crushing test of broken coal and the sudden unloading throw test of broken coal containing gas, the above problems are analyzed and studied. The purpose is to provide the basis for quantitative analysis of the energy of adsorbed gas participating in outbursts and lay the foundation for an in-depth understanding of the energy dissipation law of outbursts.

2 ENERGY CONVERSION IN COAL AND GAS OUTBURST

Coal and gas outburst is a process of energy accumulation and release. Mining disturbance breaks the original stress balance state and makes the load on the coal body in the mining area begin to transfer to the adjacent coal body. The adjacent coal body is subjected to strength failure, strain softening, and flow deformation due to the increase of pressure. In this process, a large amount of deformation energy is gathered, and a stress concentration area is formed. At the same time, due to the stress concentration, the compression of coal pore cracks is caused so that the gas pressure in the coal seam is also increased, and the potential of gas expansion work is also increased. Finally, a limit stress balance and high gas gradient area are formed in the coal wall in front of the work. The mechanical failure conditions are created for prominent subsequent excitation. The deformation and failure of the coal body developed to a critical condition, or under the action of external disturbance load, the coal body was destroyed and unstable. The stored elastic energy in the coal and rock mass quickly released and acted on the coal and rock mass so that the original fracture of the unloading coal body expanded and produced new fractures. At the same time, with the penetration of the fractures, the coal body gradually destroyed, and finally formed broken coal or pulverized coal. The expansion of primary fractures, the generation of new fractures, and the fragmentation of coal have created favorable conditions for the release of gas, which promotes rapid desorption of adsorbed gas to free gas and participates in the outburst and the formation of coal–gas–solid two-phase flow with broken coal. After the outburst excitation, the broken coal will be thrown out by the rapid expansion of gas, and the broken coal will be further pulverized in the process of throwing until gas expansion cannot be enough to throw the broken coal and terminate the outburst.

In the process of outburst energy release and dissipation, the proportion of friction heat, sound, vibration, and other energy

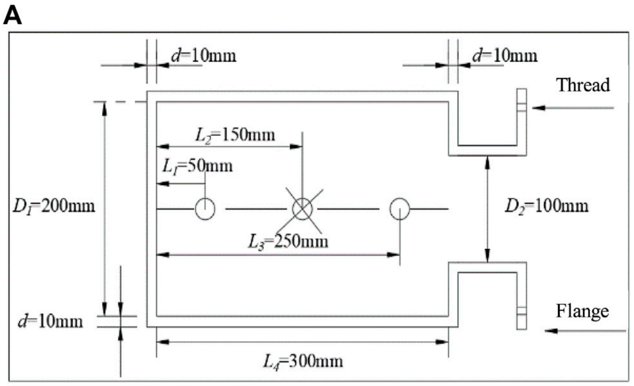

Main parameters of sealing cavity

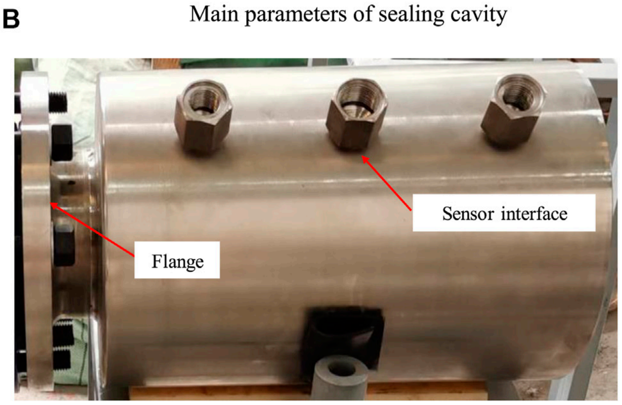

Solid diagram of sealing cavity

FIGURE 1 | High pressure sealing cavity.

consumed by outburst coal impacting roadway walls, support, and other obstacles is small. For the convenience of research, it can be ignored (Wen, 2003; Wang et al., 2015), and the energy dissipation in the process of outburst can be expressed as (Hu and Wen, 2013)

$$W_1 + W_2 = A_1 + A_2, \tag{1}$$

where W_1 is the elastic potential energy of coal and rock mass in the outburst range; W_2 is the gas internal energy of coal and rock mass in the outburst range; $A_1$is the fracture energy of coal and rock mass; and A_2 is the throwing power of coal and rock mass.

Combined with the dynamic phenomenon of coal and gas outburst and the above analysis, the energy in the process of the outburst comes from the release of elastic energy of coal body and internal energy of the gas, mainly acting on the crushing and throwing of coal body, and part of the energy is dissipated in the friction heat, sound, and vibration caused by the outburst coal body impacting the roadway wall, support, and other obstacles. Previous research results show that the elastic energy caused by ground stress in the process of outburst is first consumed, and after the ground stress destroys the coal body, the elastic energy of the coal body has been consumed (Jiang and Yu, 1996). The physical simulation experiment carried out in the laboratory also found that after the outburst excitation, the coal body in the outburst area was quickly released and destroyed, and the stress of the coal body near the outburst area decreased rapidly, almost simultaneously to zero (Jin, 2017). Therefore, it can be considered that after outburst excitation, the development of outburst is a process in which high-pressure gas flow quickly throws out a broken coal body. The energy of the thrown out broken coal body and pulverized broken coal body comes from gas expansion energy, and the gas expansion energy comes from the rapid analysis of free gas and adsorbed gas. At this stage, **Eq 1** can be rewritten as

$$W_f + W_a = A_1 + A_2, \tag{2}$$

where W_f is the energy of free gas expansion participating in the work, J; $W\alpha$ is the adsorption gas expansion involved in work energy, J; A_1 is the energy consumed by gas-pulverized coal crushing, J; A_2 is the gas that throws out the energy consumed by broken coal, J.

In the process of the outburst, the throwing power of gas to the coal sample is the kinetic energy when the coal sample is sprayed out of the hole, but the speed of throwing coal is different for different outbursts and different times of the same outburst. It is difficult to monitor in the field and test. Therefore, according to the equivalent distance and potential energy of the coal sample, the equivalent distance can be expressed as

$$S_P = \frac{1}{B}\int x\mathrm{d}M, \tag{3}$$

where S_p is the equivalent distance, m; B is the outburst strength, kg; and dM is the mass of the thrown coal sample within the range x to dx of the outburst exit, kg; the coal and gas outburst is regarded as near-horizontal ejection (Hu and Wen, 2013), and the relationship between the equivalent distance Sp and the ejection velocity of the coal sample can be obtained by using the flat ejection formula:

$$S_P = v\sqrt{{}^{\mathrm{h}}\!/_{g}}, \tag{4}$$

where h is the coal seam thickness, m, and g is the acceleration of gravity, m/s^2.

Then the work of gas throwing out the outburst coal sample is

$$A_1 = \frac{1}{2}Bv^2 = \frac{BgS_P^2}{2h}. \tag{5}$$

According to Wang et al. (Jin), the crushing work can be expressed as

$$A_2 = 550.8\frac{f}{\rho}\left(\frac{1}{d} - \frac{1}{D}\right), \tag{6}$$

where f is the consistent coefficient of coal; ρ is the density of coal, kg/m^3; D is the average particle size of coal before crushing, m; and d is the average particle size of coal after crushing, m.

Coal has strong adsorption of gas, so there are a large amount of adsorbed gas in the coal seam. There is a significant difference between the process of gas expansion and the conventional gas

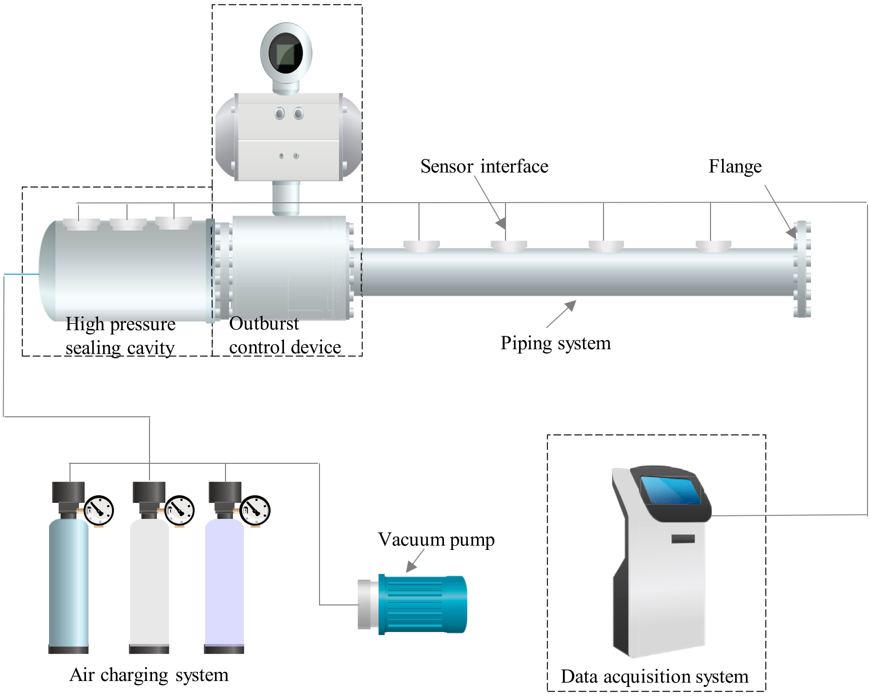

FIGURE 2 | Visualized coal and gas outburst simulation system.

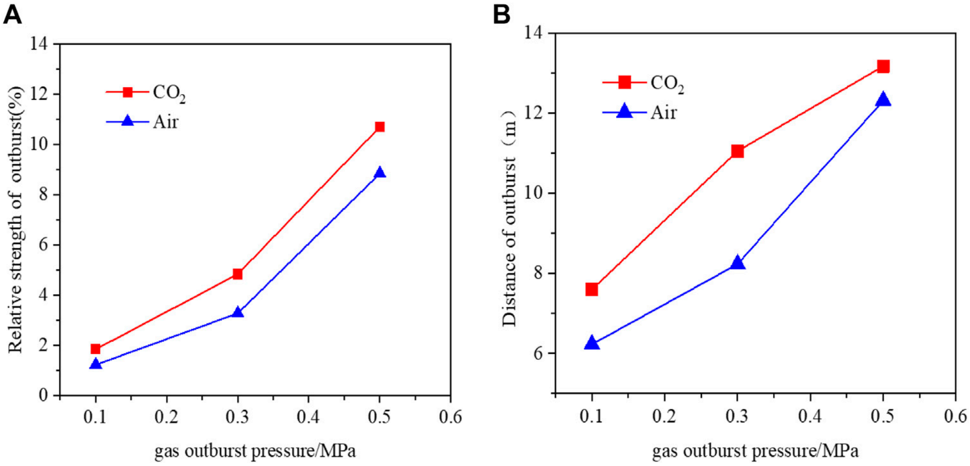

FIGURE 3 | Relationship between outburst pressure and outburst relative strength, and outburst distance.

expansion when coal and gas outburst occurs. At the same time, the adsorbed gas in the coal body will continue to desorb and participate in the outburst work. Therefore, the amount of gas in the outburst work is between the amount of free gas and the total amount of gas. In the process of outburst, on the one hand, the free gas expansion at the moment of pressure relief works on the outburst, and on the other hand, the adsorbed gas is desorbed continuously, and the power source is continuously supplemented and involved in the outburst work, which makes it difficult to accurately analyze the adsorbed gas internal energy in the process of outburst. Therefore, it is necessary to calculate the gas internal energy from another point of view. If the loss of other energy in the outburst process is ignored, the whole outburst process is regarded as an adiabatic process. Assuming that the gas expansion energy in the outburst process fully affects the ejection and crushing of the outburst coal body, the amount of adsorbed gas participating in the work can be expressed as follows:

TABLE 1 | Test parameters.

Test gas (MPa)	Particle size of coal sample (mm)	Gas pressure	Coal filling amount (kg)
CO_2	0.5	3–10	9.81
Air	0.5	3–10	9.61
CO_2	0.3	3–10	9.71
Air	0.3	3–10	9.76
CO_2	0.1	3–10	9.72
Air	0.1	3–10	9.74
CO_2	0.3	1–3	8.71
CO_2	0.3	0.5–1	8.41

$$W_a = A_1 + A_2 - W_f. \tag{7}$$

Formula for calculating expansion energy of free gas:

$$W_f = \frac{P_1 V_1}{n-1}\left[\left(\frac{P_0}{P_1}\right)^{\frac{n-1}{n}} - 1\right], \tag{8}$$

where V_1 is the free gas volume involved in the outburst work, m^3/t; P_1 is the gas pressure of working face after coal thrown out, MPa; P_0 is the coal seam gas pressure before the outburst, MPa; and n is the process index; for isothermal process, $n = 1$, adiabatic process, $n = 1.31$, and for variable process, $n = 1–1.31$.

3 TEST SCHEME

The test equipment adopts the self-developed visual simulation experiment system of the dynamic effect of coal and gas outburst to carry out the simulation experiment of gas-containing coal ejection. The test system is mainly composed of a high-pressure sealing chamber, inflatable system, outburst control device, pipeline system, and data acquisition system. The length of the high-pressure sealing cavity is 30 cm, and the inner diameter is 10 cm. The gas-filled/vacuum-pumping dual-purpose interface is opened at its tail, and the three-way conical valve is used for sealing, so as to realize the conversion of the gas-filled and vacuum-pumping interface during the test. There are three uniformly distributed sensor interfaces at the top of the cavity, which can be used to monitor the temperature, pressure, and gas concentration in the cavity, as shown in **Figure 1**. During the test, the protruding cavity was connected with the protruding control device by flange and fixed on the ground through the support. The outburst control device is controlled by a pneumatic electromagnetic ball valve. The designed pressure strength is 1.5 MPa. During the test, the gas pressure in the valve reaches 0.6 MPa, and pressure is maintained. When the pressure relief is needed, the instantaneous exposure of the outburst port is realized through the power switch. The material of the pipeline system is the transparent acrylic pipe, the length of each pipe is 1 m, and the inner diameter is 10 cm. During the test, the flange connection is used between the pipes and the control device of the outburst port, and the bracket is fixed on the ground. There are four uniformly distributed sensor interfaces above the pipeline with corresponding plugs. The pneumatic system is mainly composed of high-pressure cylinders and vacuum pumps. After the completion of coal sample filling and sensor layout, the high-pressure sealing cavity is vacuumed and inflated. By filling gas into the high-pressure sealing tube step by step, the gas pressure in the high-pressure sealing cavity is monitored by means of a data acquisition system and pressure sensors on the high-pressure sealing cavity so that it can reach the adsorption equilibrium and meet the pressure requirements of the experimental design. The data acquisition system mainly includes a computer, a data acquisition card, supporting sensors, a high-speed camera, and a transmitter. During the test, the parameters such as gas pressure, gas concentration, and temperature in the simulated roadway and sealing chamber can be automatically monitored and collected by the system, the overall structure of the test system is shown in **Figure 2**.

The coal sample used in this experiment is the M8 coal seam in the Fengchun Coal Mine of Chongqing. The average thickness of the M8 coal seam is 1.61 m, the original gas content is 25.87 m^3/t, and the measured maximum gas pressure is 3.8 MPa, which is the coal and gas outburst coal seam. In order to systematically study the working ability of adsorbed gas in the process of coal and gas outburst, two different gases and three different particle sizes of coal samples were designed in this experiment. The sudden unloading simulation test of broken coal containing gas under three different pressure (absolute pressure) conditions was carried out. The parameters of the test scheme are shown in **Table 1**.

4 TEST RESULTS AND ANALYSIS

4.1 Test Results

In order to fully reflect the results of simulation tests, the outburst strength, that is, the total mass of outburst coal, the

TABLE 2 | Outburst strength and throw distance.

Gas pressure (MPa)	Test gas	Particle size of coal sample (mm)	Coal filling amount (kg)	Coal outburst quantity (kg)	Relative outburst strength (%)	Throw distance (m)
0.5	CO_2	3–10	9.81	1.05	10.70	13.17
0.5	Air	3–10	9.61	0.85	8.84	12.31
0.3	CO_2	3–10	9.71	0.47	4.84	11.05
0.3	Air	3–10	9.76	0.32	3.28	8.23
0.1	CO_2	3–10	9.72	0.22	2.26	7.60
0.1	Air	3–10	9.74	0.12	1.23	6.38
0.3	CO_2	1–3	8.71	1.47	16.87	8.72
0.3	CO_2	0.5–1	8.41	1.83	21.76	7.83

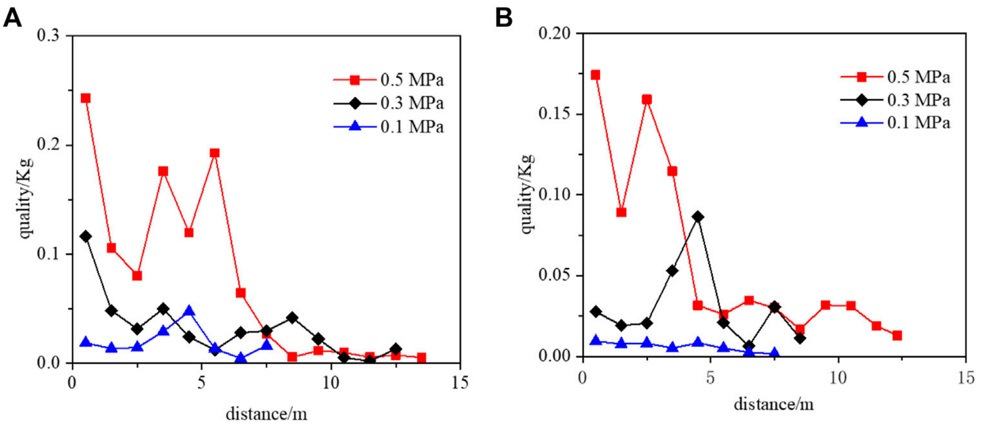

CO$_2$/3~10 mm

Air/3~10 mm

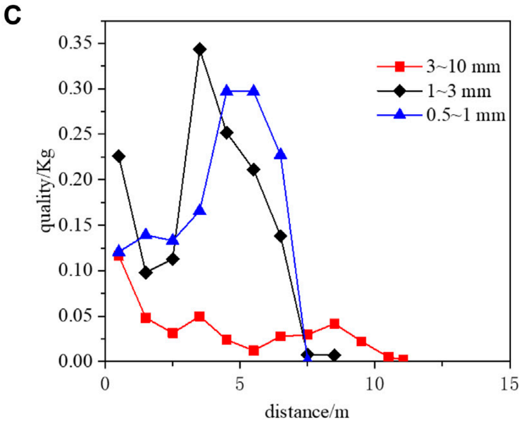

0.3 MPa/CO$_2$

FIGURE 4 | Quality distribution of outburst coal.

TABLE 3 | Statistical results of particle size of outburst coal.

Test condition	**Statistical results of coal samples with different particle sizes (kg)**					
	>3	**1–3**	**0.5–1**	**0.25–0.5**	**0.1–0.25**	**<0.1**
0.5 MPa/CO$_2$/3–10 mm	0.8910	0.0858	0.0259	0.0145	0.0205	0.0109
0.5 MPa/air/3–10 mm	0.7245	0.0754	0.0188	0.0105	0.0166	0.0065
0.3 MPa/CO$_2$/3–10 mm	0.4098	0.0364	0.0102	0.0056	0.0102	0.0027
0.3 MPa/air/3–10 mm	0.2692	0.0245	0.0079	0.0049	0.0080	0.0023
0.1 MPa/CO$_2$/3–10 mm	0.1853	0.0248	0.0046	0.0028	0.0047	0.0015
0.1 MPa/air/3–10 mm	0.0939	0.0252	0.0013	0.0007	0.0013	0.0006
0.3 MPa/CO$_2$/1~3 mm	—	1.3564	0.0597	0.0186	0.0207	0.0165
0.3 MPa/CO$_2$/0.5~1 mm	—	—	1.2929	0.1161	0.0391	0.0189

mass distribution of outburst coal, and the average particle size of outburst coal, are counted. These three physical quantities are also important indexes for calculating the energy dissipation of outbursts. The quality of outburst coal powder was counted according to 1m, and the particle size was screened according to 3, 1, 0.5, 0.25, and 0.1 mm.

4.1.1 Outburst Strength and Distance

The ratio of outburst coal quality to total coal filling is defined as the outburst relative strength (Jin, 2017). It can be seen from **Table 2** and **Figure 3** that with the increase of outburst gas pressure, the relative strength of outburst also increases, almost linearly increasing, and the maximum throw distance also increases with the increase of pressure. When

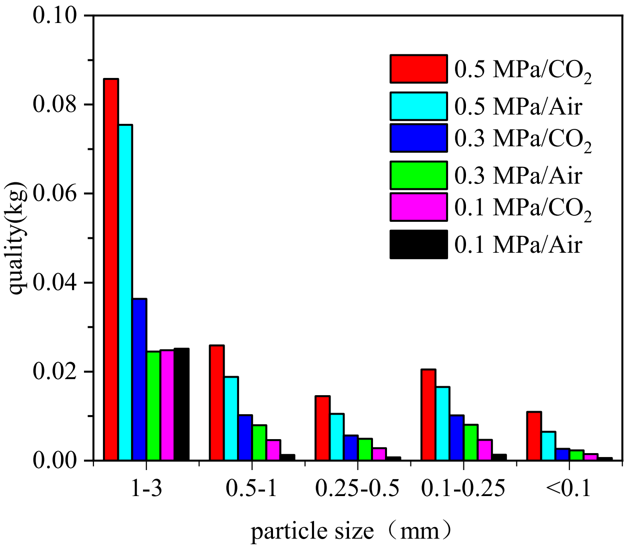

FIGURE 5 | Particle size distribution of outburst coal with particle size less than 3 mm (initial particle sizes are 3–10 mm).

the air pressure and the initial particle size of the coal sample are the same, the ability of CO_2 to work for outburst coal is stronger than that of air, and more pulverized coal is thrown out, and the throw distance is farther. From the above experimental results, we can know that the greater the outburst pressure, the more the energy released by gas expansion, the stronger the ability to work on coal, and the more the amount of coal thrown out; the larger the initial kinetic energy of the thrown coal is, the farther the distance of the thrown coal migration is. When the pressure is the same as the particle size of the coal sample, the ability of CO_2 gas to work for outburst coal is better than that of air, indicating that the gas with strong adsorption has stronger ability to work. When an outburst occurs, the outburst strength is greater.

4.1.2 Quality Distribution Characteristics of Outburst Coal

It can be seen from **Figure 4** that the gas type, outburst gas pressure, and coal sample particle size all affect the quality distribution of outburst coal. Although the quality distribution of outburst coal has a certain degree of fluctuation, the overall quality distribution law is basically consistent with the quality distribution law of typical coal and gas outburst. There are more outburst coal samples near the outburst mouth. With the increase in distance, the quality of outburst coal generally shows a decreasing trend. It can also be seen from **Figures 4A and B** that when the outburst pressure is large, the initial kinetic energy obtained by the outburst coal body is larger, and the thrown distance is farther. When the gas pressure is small, the outburst coal is mainly distributed near the outburst mouth due to the small initial kinetic energy.

It can be seen from **Figure 4C** that under the same pressure condition, the coal sample with a larger particle size was thrown farther, while the coal sample with a smaller particle size was thrown closer to the outburst port, but the quality of outburst coal was relatively large. The main reason for this phenomenon is that although the large-size coal sample obtains a large initial kinetic energy at the outburst moment, its adsorption is relatively weak, the gas adsorption is small, and the residual gas in the cavity after the outburst is relatively small, resulting in the fact that the residual gas is not enough to be thrown out of the coal body.

4.1.3 Particle Size Distribution Characteristics of Outburst Coal

From the statistical results of **Table 3**, we can know that there are coal samples with particle size less than the initial particle sizes in each group of experimental outburst coal. It shows that in the process of coal and gas outburst driven by gas, gas not only has a throwing effect on outburst coal but also has a certain powdering effect on outburst coal in the process of outburst. In the thrown coal, the diameter of pulverized coal after crushing is counted as the particle size below the initial particle size. The initial particle

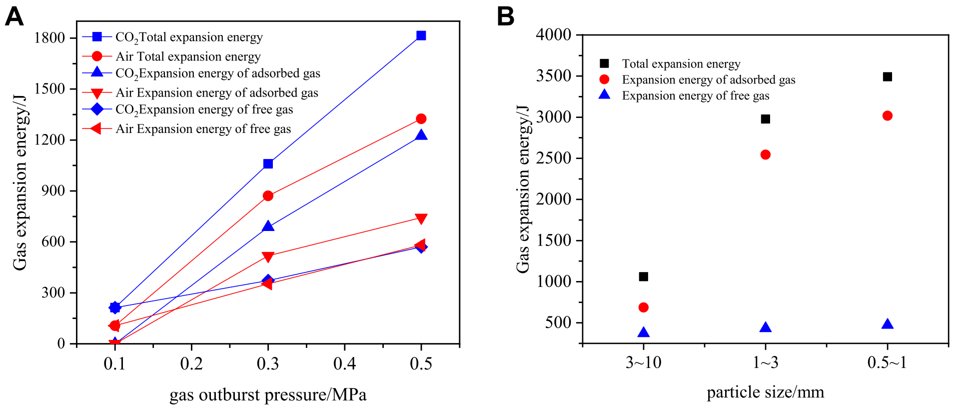

FIGURE 6 | Effect of pressure and particle size on gas expansion energy. **(A)** Effect of outburst pressure on gas expansion energy. **(B)** Effect of particle size on gas expansion energy.

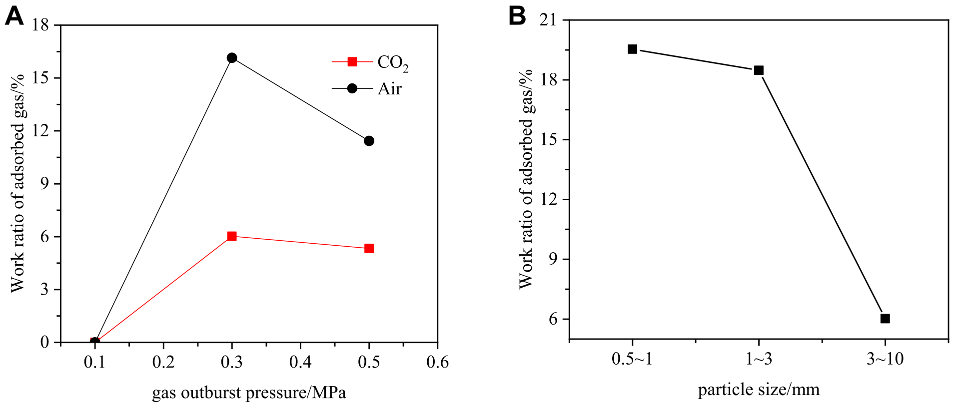

FIGURE 7 | Relationship between work ratio of adsorbed gas and outburst pressure, and coal particle size.

TABLE 4 | Energy calculation results.

Test condition	W_a(J)	W_f(J)	A_2 (J0)	A_1(J)
0.5 MPa/CO$_2$/3–10 mm	1244.54	570.62	930.68	884.48
0.5 MPa/air/3–10 mm	743.10	581.63	655.72	669.01
0.3 MPa/CO$_2$/3–10 mm	687.51	372.50	347.50	712..51
0.3 MPa/air/3–10 mm	581.50	352.51	230.16	640.86
0.1 MPa/CO$_2$/3–10 mm	—	212.91	114.20	98.71
0.1 MPa/air/3–10 mm	—	106.77	36.58	70.19
0.3 MPa/CO$_2$/1~3 mm	2544.97	432.30	1175.88	1801.39
0.3 MPa/CO$_2$/0.5~1 mm	3018.69	472.68	1434.44	2056.93

size of the data in **Figure 5** is 3–10 mm, and the diameter of outstanding pulverized coal is counted as 1–3 mm and below. In addition, it can be seen from **Figure 5** that with the decrease of gas pressure, the pulverization effect of gas on outburst coal decreases. Due to the strong adsorption of CO$_2$, the amount of desorption expansion and work gas is larger than that of air when outbursts occurs. Therefore, when the pressure and initial particle size are the same, the pulverization effect of CO$_2$ on outburst coal is stronger than that of air.

4.2 Energy Analysis During Outburst Occurrence

Combining **Formulas (5)** ~ (6), the throwing power and crushing power of coal samples under different test conditions are calculated. The expansion energy of free gas and adsorbed gas are calculated from **Formula (7)** to **(8)**. The calculation results are shown in **Table 4**.

It can be seen from **Table 4** and **Figure 6A** that with the increase of outburst pressure, the crushing effect and ejection effect of test gas on outburst coal are enhanced, and the amount of adsorbed gas participating in work is also increasing. When the outburst pressure is small (0.1 MPa), the ejection effect and crushing effect of CO$_2$ and air on coal are relatively small, and the sum of ejection work and crushing work is less than that of free gas internal energy, so it is considered that the adsorbed gas does not participate in outburst work under this condition. When the particle size is consistent with the outburst pressure, the crushing and ejection work of CO$_2$ gas for outburst coal is greater than that of air, and the amount of adsorbed gas participating in the work is larger. In addition, compared with the experimental results under the condition of 0.3 MPa/CO$_2$, it is found that the fragmentation degree of coal samples also affects the release of gas internal energy. When the fragmentation degree of coal samples is small, that is, the particle size is small, the gas expansion energy is larger, and the crushing work and ejection work of coal samples are also increased accordingly, as shown in **Figure 6B**. The reason for this phenomenon, on the one hand, is that because the coal sample with a smaller particle size has a larger specific surface area, stronger adsorption capacity for CO$_2$ gas, and larger gas internal energy is stored in the coal body; on the other hand, when the pressure is suddenly unloaded, the smaller particle size coal samples with a more obvious crushing degree are conducive to the rapid desorption of adsorbed gas and participate in the prominent work. Therefore, the degree of coal fragmentation plays an important role in the release of gas internal energy in coal. The higher the degree of coal fragmentation is, the more conducive it is to the rapid release of gas internal energy and works on the outburst.

4.3 Work Proportion Analysis of Adsorption Gas

The gas in the coal seam mainly exists in the adsorbed state, and its content can generally reach 80–90%. At present, the research on the influence of adsorbed gas on outbursts is not deep enough. In the process of outbursts, on the one hand, the instantaneous expansion and release of free gas can work on outbursts. On the other hand, the process of rapid desorption of adsorbed gas to continuously supplement free gas and participate in the work of outburst is relatively complex, resulting in the current consensus on how much adsorbed gas is desorbed and how much is involved in the work of outburst (Wang et al., 2017b), and the existing research results believe that the slow escape of gas on the outburst work efficiency is low, or even not work, only when the coal is seriously damaged will quickly desorb participate in the outburst work (Wen, 2003). Therefore, the desorption of adsorbed gas in the

TABLE 5 | Calculation results of work ratio of adsorbed gas.

Test condition	Desorption volume (m^3)	Work volume of adsorbed gas (m^3)	Proportion of desorption (%)	Proportion of adsorption amount (%)
0.5 MPa/CO_2 3–10 mm	0.1251	0.0083	6.63	5.33
0.5 MPa/air 3–10 mm	0.0329	0.0051	15.50	11.43
0.3 MPa/CO_2 3–10 mm	0.0777	0.0071	9.14	6.02
0.3 MPa/air 3–10 mm	0.0228	0.0056	24.56	16.14
0.3 MPa/CO_2 1~3 mm	0.087	0.0263	30.23	18.48
0.3 MPa/CO_2 0.5~1 mm	0.0923	0.0312	33.80	19.54

process of coal and gas outburst will experience the whole process of rapid desorption, slow desorption, and stop desorption. Although some of the residual adsorbed gas is slowly desorbed into free gas, this part of adsorbed gas is not fully involved in work. It is necessary to know the adsorption capacity of coal samples with different particle sizes under different gas pressures and the volume of adsorbed gas participating in the work. The gas adsorption capacity per unit mass of coal can be expressed as

$$Q = \frac{abp}{1+bp} \times \frac{1}{1+0.31M} \times \frac{100-A-M}{100}, \tag{9}$$

where Q is the coal of unit mass adsorbing gas volume, m^3, at gas pressure p, m^3; a is the maximum surface adsorption of coal per unit mass, m^3/kg; b is the adsorption coefficient; A is the ash in coal, %; and M is the moisture in coal, %.

Using the formula of gas expansion energy (8), the volume of the adsorbed gas work is inversely solved, and the volume ratio of adsorbed gas participating in the outburst is calculated by combining **Formula (9)**. The calculation results are shown in **Table 5**.

It can be seen from **Table 5** that the proportion of gases involved in the outburst work in the desorption amount of adsorbed gas is between 6.63 and 33.80%, and the volume of adsorbed gas involved in the outburst work accounts for 5.33–19.54% of the total adsorption amount.As **Figure 7A** shows, when the particle size of the test gas is consistent with the coal sample, the greater the outburst pressure, the desorption amount of the adsorbed gas is relatively large, and the volume of the work involved in the outburst is also larger. The proportion of the work volume to the total adsorption amount has a certain fluctuation. When the pressure is 0.1 MPa, there is no adsorbed gas to participate in the outburst work, and the proportion of 0.3 MPa is relatively higher than 0.5 MPa. It shows that when the gas pressure is low, due to the pressure drop in the cavity being too fast, the power of adsorption gas desorption is not enough to work on the outburst. When the outburst pressure is relatively large, the pressure in the outburst chamber drops instantly, but the speed of absorbing gas to supplement the power is relatively fast. Therefore, this part of the gas will participate in the outburst work. However, with the continuous decline of the pressure, the subsequent supplement power is no longer sufficient to work on the outburst, resulting in the loss of this part of the gas. When the pressure drop of 0.5 MPa is larger than that of 0.3 MPa, the desorption amount of gas is more, and the continuous desorption time is longer. When the pressure drops to a certain critical value from 0.1 to 0.3 MPa, the subsequent desorbed gas no longer participates in the outburst work, resulting in more adsorbed gas not participating in the outburst work, so the proportion of adsorbed gas participating in the outburst work is less than 0.3 MPa. When the test gas is consistent with the outburst pressure (**Figure 7B**), the adsorbed gas desorbed from the coal sample with a smaller particle size is larger than that of the coal sample with a larger particle size, and the adsorbed gas volume participating in the work is also higher, indicating that the smaller the particle size, the more conducive to the rapid desorption of adsorbed gas in coal and participating in the work of outburst.

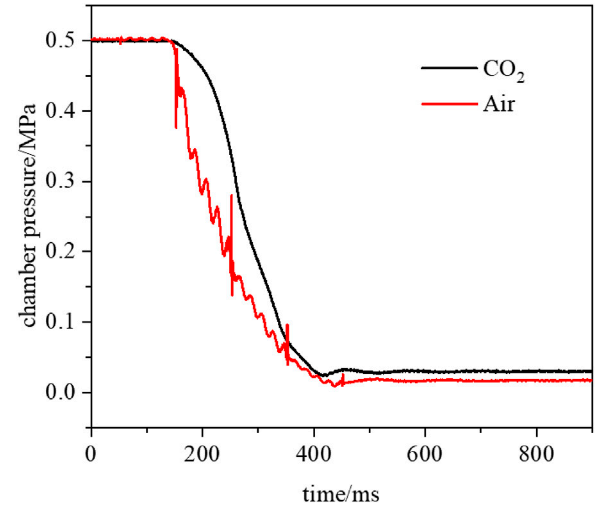

FIGURE 8 | Pressure changes in the protruding cavity.

When the particle size of the coal sample corresponds to the outburst pressure, although the work ability of air on outburst coal is less than that of carbon dioxide gas, and the adsorption and desorption amount is also less than that of carbon dioxide gas, the proportion of work involved in desorption volume is relatively high. Combined with the change of air pressure in the outburst chamber (**Figure 8**), this phenomenon can be explained under the experimental conditions as follows: when the outburst is excited, the free gas in the chamber is released instantly and works on the outburst, resulting in the decrease of air pressure in the outburst chamber, but the adsorbed gas will continue to be desorbed as a supplemental power source for the outburst until it is not enough to throw out the broken coal, so the gas pressure will not decrease linearly, and **Figure 8** shows that the rate of pressure drop of carbon dioxide gas is significantly lower than that of air. Although the adsorption capacity of carbon dioxide gas is large, it will continue to desorb relatively more gas, but when the pressure drops to a certain extent, the power of residual gas is no longer enough to work on the outstanding gas, which leads to the subsequent slow desorption of the gas to do “no work.” Therefore, although the adsorption capacity, desorption capacity, and workability of carbon dioxide gas are greater than those of air, the proportion of gas volume participating in work is lower than that of air.

5 CONCLUSION

(1) The mass distribution characteristics and particle size distribution characteristics of pulverized coal after outburst show that the ability of CO_2 gas for the outburst work is greater than that of air. When the test gas is CO_2, the throw distance of outburst coal is farther, and the pulverized effect of outburst coal is stronger than that of air.
(2) The test results of coal samples with different particle sizes show that the degree of coal fragmentation affects the release of gas internal energy to a large extent. The higher the degree of coal fragmentation, the more conducive it is to the rapid release of gas internal energy and participation in the outburst work. The larger the pressure is, the larger the desorption amount of adsorbed gas is, and the larger the volume of work is.
(3) The larger the pressure of outburst gas is, the larger the desorption amount of adsorbed gas is, and the larger the volume of the outburst work is. The desorption amount of adsorbed gas in coal samples with small particle sizes is greater than that in coal samples with large particle sizes, and the ability to work in outburst coal is stronger. The volume proportion of adsorbed gas participating in work is also higher; that is, the degree of coal crushing plays an important role in the expansion and release of gas.

DATA AVAILABILITY STATEMENT

The raw data supporting the conclusion of this article will be made available by the authors, without undue reservation.

AUTHOR CONTRIBUTIONS

I would like to thank XN for his guidance and help in the process of experimentation and thesis writing.

FUNDING

This work was financially supported by the Technological Innovation and Entrepreneurship Fund Special Project of Tiandi Technology Co., Ltd. (2021-2-TD-ZD008) and the State Key Laboratory Open Fund Project (SKLMRDPC20KF01).

REFERENCES

Alexeev, A. D., Revva, V. N., Alyshev, N. A., and Zhitlyonok, D. M. (2004). True Triaxial Loading Apparatus and its Application to Coal Outburst Prediction. *Int. J. Coal Geology.* 58, 245–250. doi:10.1016/j.coal.2003.09.007

Basil, B., and Beamish, P. (1998). Instantaneous Outbursts in Underground Coal Mines: An Overview and Association with Coal Type. *Int. J. coal Geology.* 35 (1-4), 27

Cao, Y., He, D., and David, C. (2001). Coal and Gas Outbursts in Footwalls of Reverse Faults. *Int. J. coal Geology.* 48 (1-2), 47–63. doi:10.1016/s0166-5162(01)00037-4

Dmytro, R., and Valeriy, S. (2019). A Mathematical Model of Gas Flow during Coal Outburst Initiation. *Int. J. Mining Sci. Technol.* 29 (5), 791–796. doi:10.1016/j.ijmst.2019.02.002

Dong, K. (2015) *Failure and Outburst Mechanism of Coal and Gas Microelement [Dissertation]*. Xi'An, China: Xi'an University of Science and Technology.

Du, K., Li, X. F., Yang, C. Z., Zhou, J., Chen, S. J., and Manoj, K. (2020). Experimental Investigations on Mechanical Performance of Rocks under Fatigue Loads and Biaxial Confinements [J]. *J. Cent. south Univ.* (27), 2985–2998. doi:10.1007/s11771-020-4523-7

Du, K., Li, X., Tao, M., and Wang, S. (2020). Experimental Study on Acoustic Emission (AE) Characteristics and Crack Classification during Rock Fracture in Several Basic Lab Tests. *Int. J. Rock Mech. Mining Sci.* 133, 104411. doi:10.1016/j.ijrmms.2020.104411

Du, K., Yang, C., Su, R., Tao, M., and Wang, S. (2020). Failure Properties of Cubic Granite, marble, and sandstone Specimens under True Triaxial Stress. *Int. J. Rock Mech. Mining Sci.* 130, 104309. doi:10.1016/j.ijrmms.2020.104309

Hu, Q., and Wen, G. (2013). *Mechanical Mechanism of Coal and Gas Outburst*. Beijing, China: Beijing Science Press.

Jacek, S. (2014). A Comparison of the Influence of Adsorbed Gases on Gas Stresses Leading to Coal and Gas Outburst. *Fuel* 114 (1), 288

Jiang, C., and Yu, Q. (1996). Research on the Law of Energy Dissipation in the Process of Coal and Gas Outburst. *Coal J.* (02), 173

Jin, K. (2017). *Research on the Formation Mechanism and Disaster-Causing Characteristics of High-Pressure Pulverized Coal-Gas Two-phase Flow in the Process of Coal and Gas Outburst [Dissertation]*. Xuzhou, China: China University of Mining and Technology.

Jin, K., Cheng, Y., Ren, T., Zhao, W., Tu, Q., Dong, J., et al. (2018). Experimental Investigation on the Formation and Transport Mechanism of Outburst Coal-Gas Flow: Implications for the Role of Gas Desorption in the Development Stage of Outburst. *Int. J. Coal Geology.* 194, 45–58. doi:10.1016/j.coal.2018.05.012

Klaus, N. (1998). Control of Gas Emissions in Underground Coal Mines. *Int. J. Coal Geology.* 35 (1), 57–82.

Li, W., Campos-Vargas, C., Marzahn, P., and Sanchez-Azofeifa, A. (2018). On the Estimation of Tree Mortality and Liana Infestation Using a Deep Self-Encoding Network. *Int. J. Appl. Earth Observation Geoinformation* 73, 1–13. doi:10.1016/j.jag.2018.05.025

Norbert, S. (1997). “Laboratory Study of the Phenomenon of Methane and Coal Outburst,” in *International Journal of Rock Mechanics and Mining Sciences* (Oxford, England, 55.

Paterson, L. (1986). A Model for Outbursts in Coal. *Int. J. Rock Mech. Mining Sci. Geomechanics Abstr.* 23 (4), 327–332. doi:10.1016/0148-9062(86)90644-3

Peng, S. J., Xu, J., Yang, H. W., and Liu, D. (2012). Experimental Study on the Influence Mechanism of Gas Seepage on Coal and Gas Outburst Disaster. *Saf. Sci.* 50 (4), 816–821. doi:10.1016/j.ssci.2011.08.027

Sato, K., and Fujii, Y. (1989). *Source Mechanism of a Large Scale Gas Outburst at Sunagawa Coal Mine in Japan*. 129(3-4). 325–343. doi:10.1007/978-3-0348-9270-4_5

Valliappan, S., and Wohua, Z. (1999). Role of Gas Energy during Coal Outbursts. *Int. J. Numer. Meth. Engng.* 44 (7), 875–895. doi:10.1002/(sici)1097-0207(19990310)44:7<875::aid-nme527>3.0.co;2-g

Wang, G., Wu, M., Wang, H, Huang, Q., and Yang, Z. (2015). Sensitivity Analysis of Influencing Factors of Coal and Gas Outburst Based on Energy Balance Model. *J. rock Mech. Eng.* (02), 238–248.

Wang, H., Zhang, B., Yuan, L., Li, Q., Li, S., Xue, J., et al. (2017). Influence of Adsorbed Gas Content on Coal and Gas Outburst and Energy Analysis. *J. rock Mech. Eng.* (10), 2449–2456.

Wang, H., Zhang, B., Yuan, L., Li, Qingchuan., Li, Shucai., Xue, Junhua., et al. (2017). Influence of Adsorbed Gas Content on Coal and Gas Outburst and Energy Analysis. *J. rock Mech. Eng.* (10), 2449–2456.

Wang, K., Zhou, A., Zhang, J., and Zhang, P. (2012). Real-time Numerical Simulations and Experimental Research for the Propagation Characteristics of Shock Waves and Gas Flow during Coal and Gas Outburst. *Saf. Sci.* 50 (4), 835–841. doi:10.1016/j.ssci.2011.08.024

Wen, G. (2003). *Research on Coal and Gas Outburst Energy*. Chongqing, China: Mining safety and environmental protection, 1–3.06

Wu, Hao., Ma, Dan., Spearing, A. J. S., and Zhao, Guoyan. (2021). Fracture Phenomena and Mechanisms of Brittle Rock with Different Numbers of Openings under Uniaxial Loading. *Geomechanics Eng.* 25 (6), 481–493. doi:10.12989/gae.2021.25.6.481

Wu, H., Dai, B., Cheng, L., Lu, R., Zhao, G., and Liang, W. (2021). Experimental Study of Dynamic Mechanical Response and Energy Dissipation of Rock Having a Circular Opening under Impact Loading. *Mining, Metall. Exploration* 38 (2), 1111–1124. doi:10.1007/s42461-021-00405-y

Xu, L., and Jiang, C. (2017). Initial Desorption Characterization of Methane and Carbon Dioxide in Coal and its Influence on Coal and Gas Outburst Risk. *Fuel* 203, 700–706. doi:10.1016/j.fuel.2017.05.001

Yang, D., Chen, Y., Tang, J., Li, X., Jiang, C., Wang, C., et al. (2018). Experimental Research into the Relationship between Initial Gas Release and Coal-Gas Outbursts. *J. Nat. Gas Sci. Eng.* 50, 157–165. doi:10.1016/j.jngse.2017.12.015

Yin, Z., Chen, W., Hao, H., Chang, J., Zhao, G., Chen, Z., et al. (2020). Dynamic Compressive Test of Gas-Containing Coal Using a Modified Split Hopkinson Pressure Bar System. *Rock Mech. Rock Eng.* 53 (2), 815–829. doi:10.1007/s00603-019-01955-w

Yin, Z. Q., Ma, H. F., Ma, H. F., Hu, Z. X., and Zou, Y. (2014). Effect of Static - Dynamic Coupling Loading on Fracture Toughness and Failure Characteristics in Marble. *Jestr* 7 (2), 169–174. doi:10.25103/jestr.072.25

Yu, B., Su, C., and Wang, D. (2015). Study of the Features of Outburst Caused by Rock Cross-Cut Coal Uncovering and the Law of Gas Dilatation Energy Release. *Int. J. Mining Sci. Technol.* 25 (3), 453–458. doi:10.1016/j.ijmst.2015.03.020

Zhao, W., Cheng, Y., Guo, P., Jin, K., Tu, Q., and Wang, H. (2017). An Analysis of the Gas-Solid Plug Flow Formation: New Insights into the Coal Failure Process during Coal and Gas Outbursts. *Powder Technol.* 305, 39–47. doi:10.1016/j.powtec.2016.09.047

Zhi-qiang, Y., Li, X., Jin, J., Xian-qun, H., and du, K. (2012). Failure Characteristics of High Stress Rock Induced by Impact Disturbance under Confining Pressure. *unloadingTransactions Nonferrous Met. Soc. China* 22 (1), 175–184. doi:10.1016/S1003-6326(11)61158-8

Zhou, A., and Wang, K. (2016). Airflow Stabilization in Airways Induced by Gas Flows Following an Outburst. *J. Nat. Gas Sci. Eng.* 35, 720–725. doi:10.1016/j.jngse.2016.09.021

Conflict of Interest: The authors declare that the research was conducted in the absence of any commercial or financial relationships that could be construed as a potential conflict of interest.

frontiers | Frontiers in Earth Science

ORIGINAL RESEARCH
published: 10 May 2022
doi: 10.3389/feart.2022.885681

Stress Distribution Law of Full-Length Anchorage Bolt in Rectangular Roadway

Dongdong Pang[1,2], Kai He[3]*, Yatao Xu[3], Jucai Chang[1], Xingang Niu[4,5] and Chuanming Li[1]

[1]State Key Laboratory of Mining Response and Disaster Prevention and Control in Deep Coal Mines, Anhui University of Science and Technology, Huainan, China, [2]Coal Mine Safety Mining Equipment Innovation Center of Anhui Province, Anhui University of Science and Technology, Huainan, China, [3]School of Civil Engineering and Transportation, South China University of Technology, Guangzhou, China, [4]State Key Laboratory of the Gas Disaster Detecting Preventing and Emergency Controlling, China Coal Technology and Engineering Group Chongqing Research Institute, Chongqing, China, [5]Gas Research Branch, China Coal Technology and Engineering Group Chongqing Research Institute, Chongqing, China

To study the evolution law of axial force and shear stress of a full-length anchorage bolt in a rectangular roadway during roadway driving and working face mining, based on the stress analysis of the bolt, considering the elastic parameters and geometric size of the bolt, the effect of a bearing plate on surrounding rock, roadway cross-section shape, roadway deformation degree, and roadway elastic parameters, elastic mechanics and mathematical analysis methods were used to establish the mechanical model describing the interaction between the bolt and surrounding rock, and the mechanical formulas for calculating the axial force and shear stress of the bolt were derived. Taking the mining roadway of 1,131(1) working face in the Zhujidong coal mine of the Huainan mining area as the engineering background, the axial force and shear stress of the bolt in the middle of the roof and side of the rectangular roadway with the advance of driving face and working face were analyzed. The mechanical model and theoretical analysis results are verified by installing force measuring bolts with the same mechanical properties as the field and observing the real axial force distribution of the bolts.

Keywords: rectangular roadway, full-length anchorage, force measuring bolt, neutral point, stress distribution

Edited by:
Kun Du,
Central South University, China

Reviewed by:
Jianbiao Bai,
China University of Mining and Technology, China
Lei Fan,
Hunan University of Science and Engineering, China

***Correspondence:**
Kai He
e-2718@foxmail.com

Specialty section:
This article was submitted to Geohazards and Georisks, a section of the journal Frontiers in Earth Science

Received: *28 February 2022*
Accepted: *11 April 2022*
Published: *10 May 2022*

Citation:
Pang D, He K, Xu Y, Chang J, Niu X and Li C (2022) Stress Distribution Law of Full-Length Anchorage Bolt in Rectangular Roadway. Front. Earth Sci. 10:885681. doi: 10.3389/feart.2022.885681

1 INTRODUCTION

The rectangular roadway has been widely used in coal mining roadways because of its advantages of fast driving speed and convenient construction. A rectangular roadway with bolts and cable support has become the most important design scheme for the coal mining roadway. With the continuous increase of coal mining depth, the support strength of mining roadways continues to improve. The full-length anchoring bolt can not only provide the surface force but also effectively prevent the deformation of the shallow surrounding rock of the roadway, which has become a powerful measure to improve the support strength. However, because of the complexity of the surrounding rock stress distribution of a rectangular roadway, the stress of its full-length anchoring bolt is obviously different from that of regular section roadways such as circular, oval, and straight wall semicircular arch, which has attracted the attention of many coal mine engineers and technicians (Lv et al., 2018; Mei et al., 2020).

Many scholars at home and abroad have carried out significant research on the mechanical properties of full-length anchoring bolts through theoretical analysis, numerical simulation, laboratory tests, or field tests. Wang et al. established the dynamic response model of full-length anchorage bolts. Based on structural dynamics and the explosion spherical wave theory, they calculated and analyzed the variation characteristics and distribution law of axial stress and shear stress of bolts with time under a blasting dynamic load (Wang et al., 2018; Zou and Zhang, 2021). Wang et al. systematically studied the mechanical characteristics of the full-length anchorage bolt under different working conditions, developed the anchor algorithm, carried out numerical tests, and analyzed the effects of continuous deformation magnitude, crack parameters, and confining pressure-drawing conditions on the distribution of the axial force and shear stress of the full-length anchoring bolt. Li et al., based on the deformation of the surrounding rock, established the bolt-surrounding rock interaction model, and deduced the analytical expressions of the distribution of axial force and shear stress along the bolt body during the normal support process and critical failure of the bolt (Wu et al., 2018; Zhao et al., 2020). Chang et al. proposed a simplified method to analyze the interaction between full-length anchoring bolts and rock mass in circular roadways under hydrostatic stress field. In this process, the relative motion between the rock mass and bolt is determined by considering the interfacial shear stiffness. In addition, the elastic elongation of the bolt is also considered. The rock bolt interaction is simulated in the initial and final states (Cheng et al., 2015; Chang et al., 2019). Zhou et al. proposed a numerical model based on the double exponential curve shear slip-model of the anchorage interface and the linear strengthened elastoplastic constitutive model of the bolt, and verified the model through the pull-out test (Cui et al., 2021). Chen et al. established an analytical model to study the load transfer characteristics of the full-length anchoring bolt and verified the theoretical model by the field pull-out test. It is found that the axial load of the bolt attenuates from the loading end to the free end, which is independent of the pull-out load (Chen et al., 2020). Zou et al. proposed a dynamic bond-slip model to describe the dynamic evolution characteristics of the bond strength of the bolt rock interface, and deduced the analytical solutions of the shear stress distribution, load-displacement relationship, and relative displacement of the bolt considering the free end slip (Jin-feng and Peng-hao, 2019). Aghchai et al. studied the interaction between the full-length anchoring bolt and slurry and the surrounding rock in the pull-out test, considered different stages such as complete bonding and partial anchoring, and analyzed and obtained the load-displacement curve of the anchor head (Aghchai et al., 2020). Liu et al. considered the combined action of axial force and shear force of the bolt, and proposed an improved prediction method for the shear strength contribution of full-length anchoring bolts (Liu and Li, 2020). Liu et al. established the analytical model of the interaction between the bolt and surrounding rock, deduced the control differential equation of load transfer, obtained the stress distribution of the anchor body, and proposed the calculation method of the bolt considering the shear damage of the anchorage interface based on the finite element method (Liu et al., 2017; Lyu et al., 2018). Liu and Li analyzed the load distribution and deformation characteristics of the deflection section of the full-length anchoring bolt, and established the structural mechanics model. Based on the force method equation and deformation coordination relationship, the analysis method of the influence of axial force and shear force at the intersection of the bolt and joint surface on the stability of the rock slope is established, and the influence of bolt inclination on the joint surface is discussed (Liu and Li, 2017; Li and Liu, 2019). There are many similar research results, such as those achieved by Liu et al., (2017) and Sun et al. (2021). Although the existing studies have carried out detailed research on the mechanical properties of full-length anchoring bolts and have achieved rich research results, the existing research methods seldom consider the influence of the roadway section shape and roadway surrounding rock deformation characteristics on the full-length anchoring bolt. This leads to many conclusions which cannot be directly applied to production practice.

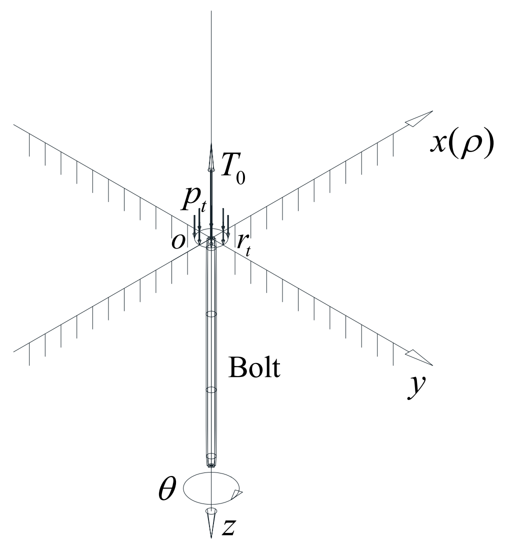

FIGURE 1 | Stress diagram of the bolt and surrounding rock.

To sum up, this study refers to the existing research results, fully considers the section shape of the mining roadway and the deformation of the surrounding rock of the mining roadway, establishes and solves the mechanical model of the bolt through the stress analysis of the bolt, and deduces the mechanical formula for calculating the axial force and shear stress of the bolt. Based on the engineering background of 1,131(1) working face of the Zhujidong coal mine in the Huainan mining area, the variation law of axial force and shear stress of full-length anchoring bolts in the middle of the roof and side of a rectangular roadway with the advance of the driving face is analyzed. The change of axial force of full-length anchoring bolts during roadway driving is observed by the force measuring bolt, which verifies the correctness of theoretical analyses. It provides a theoretical basis for bolt support design.

2 BOLT MECHANICS MODEL

It is assumed that the surrounding rock is an isotropic elastomer without considering the influence of an anchoring agent. At the same time, it is assumed that the bolt is a one-dimensional

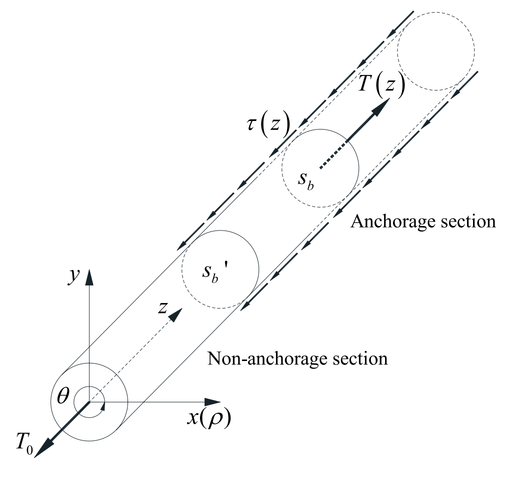

FIGURE 2 | Bolt stress diagram.

elastomer without considering the transverse deformation of the bolt. It is assumed that the stress and displacement of the bolt are continuous at the anchorage surface. The coordinate system is established as shown in **Figure 1**, and mechanical model is obtained for calculating the axial force and shear stress of the bolt by analyzing the stress of the bolt and deformation of the surrounding rock.

In **Figure 1**, T_0 shows the working resistance of the bolt; p_t indicates the action load of the bearing plate on the surrounding rock; and r_t represents the equivalent circle radius of the bearing plate. **Figure 1** also shows the rectangular coordinate system *x*-*y* and the cylindrical coordinate system $\rho - \theta$ used to establish the model and their corresponding relationships.

2.1 Stress Analysis of the Bolt

The stress of the bolt is shown in **Figure 2**. $T(z)$ shows the axial force of the bolt; $\tau(z)$ shows the shear stress on the surface of the bolt body; $S_b^{'}$ represents the interface between the anchorage section and the non-anchorage section; and S_b shows the arbitrary section in the anchorage section. The axial force $T(z)$ of the bolt is constant in the non-anchorage section and its value is the same as the working resistance T_0. In the anchorage section, it is an unknown function about z. The shear stress $\tau(z)$ is 0 in the non-anchorage section and an unknown function about z in the anchorage section.

The bolt body from the end of the anchor to the section S_b is taken as the research object. In the cylindrical coordinate system, the direction of shear stress in **Figure 2** is negative. According to the balance condition of the force system, the relationship between the axial force $T(z)$ and shear stress of $\tau(z)$ can be obtained as follows:

$$T(z) = T_0 + 2\pi r_b \int_0^z \tau(z)\mathrm{d}z. \tag{1}$$

In **Eq. 1**, r_b represents the radius of the bolt. The elastic modulus of the bolt is much larger than that of the surrounding rock and the cross-section of the bolt is much smaller than that of the roadway. Therefore, it can be assumed that the normal stress $\sigma(z)$ on the cross-section of the bolt is evenly distributed. Then, the relationship between the axial force $T(z)$ and normal stress $\sigma(z)$ is

$$T(z) = \pi \cdot (r_b)^2 \cdot \sigma(z). \tag{2}$$

According to the field observation data and the design requirements of the bolt support, the bolts are in the elastic state during roadway driving. Therefore, the relationship between the axial normal stress $\sigma(z)$ and the axial strain $\varepsilon(z)$ of the bolt is

$$\sigma(z) = E \cdot \varepsilon(z). \tag{3}$$

In **Eq. 3**, E represents the elastic modulus of the bolt. Substituting **Eq. 3** into **Eq. 2**, we can get

$$T(z) = \pi E \cdot (r_b)^2 \cdot \varepsilon(z). \tag{4}$$

By substituting **Eq. 4** into **Eq. 1**, the relationship between the bolt surface shear stress $\tau(z)$ and the bolt axial strain $\varepsilon(z)$ is

$$2\pi r_b \cdot \int_0^z \tau(z)\mathrm{d}z - \pi E \cdot (r_b)^2 \cdot \varepsilon(z) + T_0 = 0. \tag{5}$$

The shear stress and strain of the surrounding rock at the anchorage surface are the same as the shear stress and axial strain of the bolt. Then, the shear stress and strain of the surrounding rock at the anchorage surface can be substituted into **Eq. 5**. By solving **Eq. 5**, the expressions of axial force and shear stress of the bolt are derived.

2.2 Effect Analysis of the Bearing Plate on Surrounding Rock

Assuming that the extrusion force of the bearing plate on the surrounding rock is uniformly distributed and there is no shear load on the surrounding rock, the force of the bearing plate on the surrounding rock is shown in **Figure 3**:

In **Figure 3**, the calculation method of p_t and r_t are as follows:

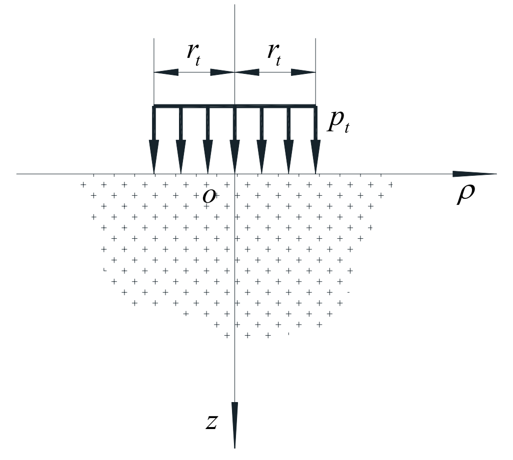

FIGURE 3 | Force of the bearing plate on the rock wall.

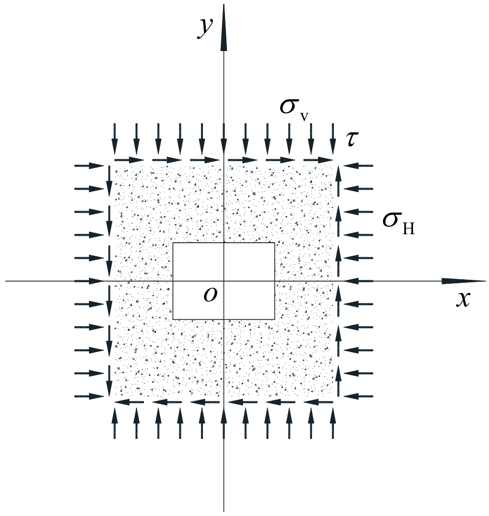

FIGURE 4 | Stress diagram of the rectangular roadway.

$$r_t = \sqrt{\frac{S_t}{\pi}},\quad p_t = \frac{T_0}{S_t}. \tag{6}$$

In **Eq. 6**, S_t represents the area of the bearing plate. When the Love displacement function is taken in the form as shown in **Eq. 7**, the exact solution of the mechanical problem shown in **Figure 3** can be obtained.

$$\Phi_r = \int_0^z (\phi_0 + z\cdot\phi_3)\mathrm{d}z \tag{7}$$

In **Eq. 7**, ϕ_0 and ϕ_3 are displacement functions, and the expression is

$$\begin{cases} \phi_0 = (1-2\nu)p_t r_t \cdot \displaystyle\int_0^{+\infty} \frac{J_1(r_t\lambda)\cdot J_0(\rho\lambda)\cdot e^{-\lambda z}}{\lambda^2}\mathrm{d}\lambda, \\ \phi_3 = -p_t r_t \cdot \displaystyle\int_0^{+\infty} \frac{J_1(r_t\lambda)\cdot J_0(\rho\lambda)\cdot e^{-\lambda z}}{\lambda}\mathrm{d}\lambda. \end{cases} \tag{8}$$

In **Eq. 8**, J_0 () and J_1 () represent the first kind of Bessel functions of order 0 and order 1; ν represents Poisson's ratio of the surrounding rock; e represents the base of the natural logarithm; and λ represents the integral variable.

By substituting the Love displacement function **Eq. 7** into **Eq. 9**, the displacement distribution law of the surrounding rock when it is squeezed by the bearing plate can be obtained.

$$\begin{cases} u_\rho = \dfrac{1}{2G}\cdot\dfrac{\partial^2\Phi}{\partial\rho\partial z} \\ u_\theta = 0 \\ u_z = \dfrac{\nu-1}{G}\cdot\nabla^2\Phi + \dfrac{1}{2G}\cdot\dfrac{\partial^2\Phi}{\partial z^2} \end{cases} \tag{9}$$

In **Eq. 9**, Φ represents the Love displacement function and G represents the shear modulus of the surrounding rock. By substituting the displacement component of the surrounding rock obtained from **Eq. 9** into the geometric equation, the strain tensor of the surrounding rock under the bearing plate extrusion can be obtained, and then the stress tensor of the surrounding rock can be obtained by Hooke's law.

2.3 Deformation Analysis of the Surrounding Rock of Rectangular Roadways

Assuming that the stress distribution of roadway surrounding rock is a plane strain problem, the proposed complex function method is used to solve the strain distribution law of rectangular roadways (Muskhelishvili and Noordhoff, 1953; Feng et al., 2014; Tran Manh et al., 2015; Shen et al., 2017; Chang et al., 2020). The stress of a rectangular roadway is shown in **Figure 4**.

The stress distribution of the surrounding rock of a rectangular roadway can be characterized by two complex functions $\varphi(\xi)$ and $\psi(\xi)$. The form of complex functions $\varphi(\xi)$ and $\psi(\xi)$ are

$$\begin{cases} \varphi(\xi) = \dfrac{\sigma_V + \sigma_H}{4}\cdot\omega(\xi) + \varphi_0(\xi), \\ \psi(\xi) = \sqrt{(\sigma_V - \sigma_H)^2 + 4\tau^2}\cdot\dfrac{e^{2i\alpha}\omega(\xi)}{4} + \psi_0(\xi). \end{cases} \tag{10}$$

In **Eq. 10**, the function $\omega(\xi)$ represents the conformal mapping function from the outer domain of the rectangular roadway to the unit circle on the complex plane, and the solution method is shown in the literature (Nazem et al., 2015; Yuan et al., 2018; Baddoo and Crowdy, 2019; Badreddine et al., 2019; He et al., 2022). Analytic functions $\varphi_0(\xi)$ and $\psi_0(\xi)$ satisfy Cauchy–Riemann conditions. The values of variables ξ and α are as follows:

$$\begin{cases} \xi = \eta e^{i\beta}, \\ \alpha = \arctan\left(\dfrac{\sigma_V - \sigma_H + \sqrt{(\sigma_V - \sigma_H)^2 + 4\tau^2}}{2\tau}\right). \end{cases} \tag{11}$$

In **Eq. 11**, η and β represent the coordinate components of the curvilinear coordinate system determined by the conformal mapping function $\omega(\xi)$. The surrounding rock stress of the rectangular roadway is

$$\begin{cases} \sigma_\eta^r + \sigma_\beta^r = 4\mathrm{Re}\left(\dfrac{\varphi'(\xi)}{\omega'(\xi)}\right), \\ \sigma_\eta^r - \sigma_\beta^r + 2i\tau_{\eta\beta}^r = \dfrac{2\xi^2}{\eta^2}\cdot\left[\dfrac{\overline{\omega(\xi)}}{\overline{\omega'(\xi)}}\cdot\left(\dfrac{\varphi'(\xi)}{\omega'(\xi)}\right)' + \dfrac{\overline{\psi'(\xi)}}{\overline{\omega'(\xi)}}\right]. \end{cases} \tag{12}$$

In **Eq. 12**, σ_η, σ_β, and $\tau_{\eta\beta}$ represent the stress components in the curvilinear coordinate system. According to the method in the reference (He et al., 2022), the stress tensor in the rectangular coordinate system can be obtained. Then, the strain tensor of the surrounding rock can be obtained from the stress tensor.

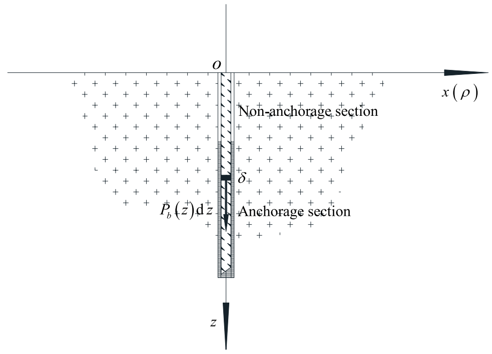

FIGURE 5 | Schematic diagram of $P_b\,(z)$ acting on the surrounding rock.

2.4 Effect Analysis of the Bolt on Surrounding Rock

The load function $P_b\,(z)$ is used to equivalent the effect of the bolt on the surrounding rock. The load function is distributed along the axial direction of the bolt. It is an unknown function of variable z in the anchorage section and 0 in the non-anchorage section. The effect of the load on the surrounding rock is the same as that of the bolt on surrounding rock. The force of the load on the surrounding rock is shown in **Figure 5**.

Take microelements on the bolt for analysis. At this time, the surrounding rock $z = \delta$ is under the action of the concentrated load $P_b\,(z)\mathrm{d}z$, and when the Love displacement function is in the form shown in **Eq. 13**, the stress distribution law of the surrounding rock under the concentrated load $P_b\,(z)\mathrm{d}z$ can be obtained by the following equation.

$$\Phi = P_b\,(\delta)\mathrm{d}\delta \cdot F\left(z, \rho, \delta\right). \tag{13}$$

In **Eq. 13**, the function $F\,(z, r, \delta)$ is a known function and satisfies the following equation:

$$\begin{aligned} 8\pi \cdot (1-\nu) \cdot F\left(z,\rho,\delta\right) = R_1 + R_2 \cdot \left(8\nu - 8\nu^2 - 1\right) \\ + (4 - 8\nu)\,(z - \nu z - \nu\delta) \\ \cdot \log\left(R_2 + z + \delta\right) - \frac{2\delta z}{R_2}. \end{aligned} \tag{14}$$

In **Eq. 14**, R_1 and R_2 are

$$\begin{cases} R_1 = \sqrt{\rho^2 + (z-\delta)^2}, \\ R_2 = \sqrt{\rho^2 + (z+\delta)^2}. \end{cases} \tag{15}$$

Integrate **Eq. 13** on the bolt body to obtain the Love displacement function:

$$\Phi_b = \int_0^L P_b\,(\delta) \cdot F\left(z,\rho,\delta\right)\mathrm{d}\delta. \tag{16}$$

Through **Eq. 16**, the effect of the distribution load $P_b\,(z)$ on the surrounding rock can be obtained, that is, the effect of the bolt on the surrounding rock. Substituting **Eq. 16** into **Eq. 9** can obtain the displacement component of the surrounding rock under the action of the bolt, and then obtain the stress and strain tensor of the surrounding rock under the action of the bolt as follows:

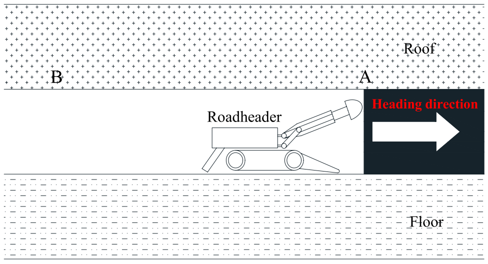

FIGURE 6 | Schematic diagram of the driving roadway.

$$\begin{cases} \sigma_{ij}^b = \int_0^L P_b\,(\delta) \cdot \sigma_{ij}^0 \mathrm{d}\delta, \\ \varepsilon_{ij}^b = \int_0^L P_b\,(\delta) \cdot \varepsilon_{ij}^0 \mathrm{d}\delta. \end{cases} \tag{17}$$

In **Eq. 17**, the sum of tensors σ_{ij}^0 and ε_{ij}^0 is a known quantity, which is only related to the function $F\,(z, r, \delta)$.

2.5 Calculation Formula of Axial Force and Shear Stress of Bolt

According to the uniqueness theorem of solution in elasticity, there is only one exact solution satisfying the corresponding boundary conditions. The contact surface between the bolt and the surrounding rock can be regarded as a boundary condition. When the surrounding rock is taken as the research object, it has two boundaries. The first is the free surface of the surrounding rock and the second is the contact surface between the bolt and the surrounding rock, that is, the anchorage surface. When the two boundary conditions are consistent, the stress-strain state in the surrounding rock is unique and determined. The boundary condition of the surrounding rock at the free surface is not affected by the bolt. When the anchorage surface does not slide, the stress and strain are continuous on the anchorage surface. The stress and strain on the anchorage surface meet both the mechanical equation of the surrounding rock and the mechanical equation of the bolt. Therefore, the stress and strain of the surrounding rock at the anchorage surface can be substituted into the mechanical equation of the bolt, and the functional equation with the distributed load function $P_b\,(\iota)$ as the unknown function can be obtained. The solution of the unknown function $P_b\,(\iota)$ can be obtained by solving this equation. The calculation formulas of the axial force and shear stress of the bolt can be obtained by substituting the obtained function $P_b\,(\iota)$ into the relevant formulas.

Substituting the values of stress and strain at the anchorage surface into **Eq. 5**, we can get

$$2\pi r_b \cdot \int_0^z \tau_{rz}^m\Big|_{r=r_b}\mathrm{d}z - \pi E \cdot (r_b)^2 \cdot \varepsilon_z^m\Big|_{r=r_b} + T_0 = 0. \tag{18}$$

TABLE 1 | Bolt support parameters.

Parameter	Roof (mm)	Sides (mm)
Bolt diameter × bolt length	22 × 2800mm	22 × 2500mm
Anchorage length	2,800	2,500
Row spacing between anchor bolts	750 × 800mm	700 × 800mm

In **Eq. 18**, τ_{rz}^m and ε_z^m are

$$\begin{cases} \tau_{rz}^m = \tau_{rz}^r + \tau_{rz}^t + \tau_{rz}^b, \\ \varepsilon_z^m = \varepsilon_z^r + \varepsilon_z^t + \varepsilon_z^b. \end{cases} \tag{19}$$

Substitute **Eq. 17** into **Eq. 18** and simplify it to obtain

$$\int_0^L P_b(\delta) \cdot K(z, \delta) \mathrm{d}\delta = f(z) \tag{20}$$

Eq. 20 is the first kind of Fredholm integral equation (Mesgarani and Azari, 2019; Khan et al., 2020), in which the function $K(z, \delta)$ is called the kernel of the integral equation and the function $f(z)$ is called the free term of the integral equation. The kernel function and free term are known functions and their expressions are

$$\begin{cases} K(z, \delta) = \int_0^z \tau_{rz}^0\big|_{r=r_b} \mathrm{d}z - \dfrac{Er_b}{2} \cdot \varepsilon_z^0\big|_{r=r_b}, \\ f(z) = \dfrac{Er_b}{2} \cdot \left(\varepsilon_z^r + \varepsilon_z^t\right)\big|_{r=r_b} - \dfrac{T_0}{2\pi r_b} - \int_0^z \left(\tau_{rz}^r + \tau_{rz}^t\right)\big|_{r=r_b} \mathrm{d}z. \end{cases} \tag{21}$$

According to the relevant theory of integral equation, the outgoing load function $P_b(z)$ can be solved from **Eq. 20**. Substituting the load function obtained from the solution into **Eq. 19** and then substituting the second equation of **Eq. 19** into **Eq. 4**, the expression of the bolt axial force can be obtained

$$T(z) = \pi E \cdot (r_b)^2 \cdot \left[\left[\int_0^L P_b(\delta) \varepsilon_z^0 \mathrm{d}\delta + \varepsilon_z^t + \varepsilon_z^r\right]\right]\Big|_{r=r_b}. \tag{22}$$

Substituting **Eq. 22** into **Eq. 1**, and then differentiating and sorting **Eq. 1**, the expression of the surface shear stress $\tau(z)$ can be obtained by

$$\tau(z) = \frac{Er_b}{2} \cdot \left\{\int_0^L P_b(\delta) \cdot \frac{\mathrm{d}\varepsilon_z^0}{\mathrm{d}z} \cdot \mathrm{d}\delta + \frac{\mathrm{d}}{\mathrm{d}z}\left(\varepsilon_z^t + \varepsilon_z^r\right)\right\}\Big|_{r=r_b}. \tag{23}$$

By substituting the stress variables of the surrounding rock under different engineering conditions into **Eq. 18**, the distribution curves of the bolt axial force and shear stress under the corresponding engineering conditions can be obtained.

2.6 Effect of the Driving Face and Working Face

The schematic diagram of a driving roadway is shown in **Figure 6**. When the roadheader cuts out the complete roadway section, some bolts are installed immediately to support the roadway, and its position is shown at point A of **Figure 6**. At this time, the surrounding rock is supported by the front coal wall without deformation or the deformation is very small, which can be ignored compared with the deformation of the surrounding rock in the later stage. When it is far away from the coal wall, as shown at point B, the bolt is affected by the deformation of the surrounding rock and the axial force of the bolt changes (Chang et al., 2021).

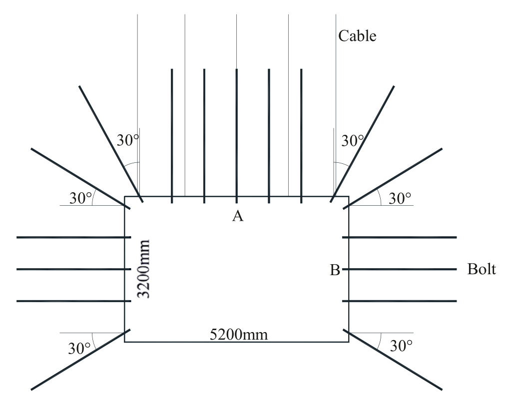

FIGURE 7 | Schematic diagram of the roadway support scheme.

L_{AB} is used to indicate the influence range of the driving face. It is assumed that at point A, the surrounding rock is not deformed, and at point B, the surrounding rock reaches a stable state. The creep of the surrounding rock and other factors are not considered in this study. According to the numerical simulation results and on-site roadway deformation observation data, the exponential function is used to describe the strain of the surrounding rock between point A and point B.

$$\varepsilon_{ij}^s = \varepsilon_{ij}^r\left(1 - e^{-\frac{a_1}{L_{AB}} l}\right). \tag{24}$$

In **Eq. 24**, the parameter a_1 reflects the severity of the surrounding rock deformation within the influence range of the driving face; l represents the distance between the bolt and the working face; ε_{ij}^r represents the strain tensor of the surrounding rock when it is not affected by the driving face; and ε_{ij}^s represents the strain tensor of the surrounding rock within the influence range of the driving face. By substituting ε_{ij}^s into **Eqs 21**, **22**, **23**, the distribution laws of the axial force and shear stress of bolts with different anchor lengths in a rectangular roadway during roadway driving can be obtained. Reference Chang et al. (2020) gives the stress distribution law of the roadway surrounding rock during working face mining. Under the influence of mining stress of the working face, the vertical stress of the roadway can be expressed as

$$\sigma_{\mathrm{V}}(1) = \mathrm{H}(1_s - 1) \cdot \frac{k_{\mathrm{s}} \cdot \sigma_{\mathrm{V}}^0}{e^{a_2 \cdot 1_{\mathrm{s}}} - 1} \cdot \left(e^{a_2 \cdot 1} - 1\right) + H(1 - 1_s) \cdot \sigma_{\mathrm{V}}^0 \cdot \left[(k_{\mathrm{s}} - 1) \cdot e^{b_2 \cdot (1_{\mathrm{s}} - 1)} + 1\right]. \tag{25}$$

In **Eq. 25**, function H( ) represents the Heaviside step function; l represents the distance from the working face; σ_{V}^0 represents the

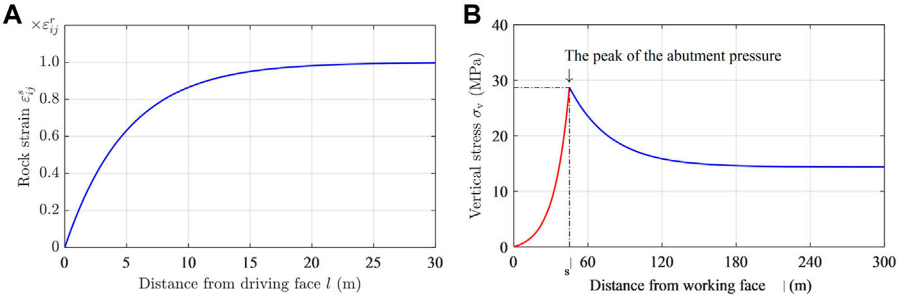

FIGURE 8 | Influence of mining stress: **(A)** variation curve of the surrounding rock strain with an advance of the driving face; and **(B)** the abutment pressure curve.

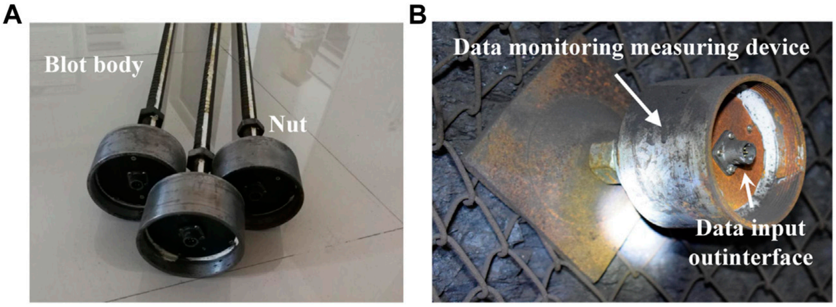

FIGURE 9 | Force measuring bolt: **(A)** force measuring bolt in the laboratory; and **(B)** force measuring bolt installed on site.

TABLE 2 | Location of measuring points.

Position	Point 1 (m)	Point 2 (m)	Point 3 (m)	Point 4 (m)	Point 5 (m)	Point 6 (m)
Roof bolt	0.00	0.52	1.04	1.56	2.08	2.60
Side bolt	0.00	0.46	0.92	1.38	1.84	2.30

vertical pressure of the original rock; k_s represents the vertical stress concentration coefficient at the peak of the abutment pressure; l_s represents the peak position of the abutment pressure; and coefficients a_2 and b_2 are used to describe the change severity of the abutment pressure curve. We can obtain the horizontal stress σ_H and shear stress τ through the pressure measurement coefficient λ and shear stress coefficient η. Similar to the influence of the driving face on the bolt, we can obtain the stress distribution of the bolt under the influence of the working face through **Eq. 25**.

3 ENGINEERING ANALYSIS

Based on the engineering background of 1,131(1) working face of the Zhujidong coal mine in the Huainan mining area, the distribution law of the axial force and shear stress of full-length anchoring bolts in a rectangular roadway during driving is studied. The mining roadway of 1,131(1) working face has a width of 5.2 m and a height of 3.2 m, which is supported by the bolt and a cable. The bolt support parameters are shown in **Table 1** and the roadway section and support structure are shown in **Figure 7**.

The roof and floor of 1,131(1) working face are mudstone, which is similar to the mechanical properties of a coal seam and can be combined. Through the measurement test of rock mechanical parameters, the shear modulus G of the surrounding rock is 1.72 GPa and Poisson's ratio v is 0.21. According to the tensile test results of a bolt, the elastic modulus E of the bolt is 203 GPa. According to the *in-situ* stress test results, the vertical pressure of the roadway σ_V is 14.35 MPa, the horizontal pressure σ_H is 13.38 MPa, and the shear stress τ is 0. Through the fitting and analysis of the field surrounding rock deformation data, L_{AB} is taken as 20 m and parameter a_1 is 3. The variation curve of the surrounding rock strain within the influence range of the driving face with the advance of the working face is shown in **Figure 8A**. According to Chang et al. (2020), let $k_s = 1.9$, $a_2 = 0.1$, and $b_2 = 0.03$. Substitute the aforementioned parameters into **Eq. 25** to obtain the abutment pressure curve, as shown in **Figure 8B**.

Taking bolts A and B in the middle of the roof and side as examples, the evolution law of the axial force and shear stress of full-length anchoring bolts during driving roadway is studied. To verify the theoretical analysis results, during roadway driving, some force measuring bolts with the same mechanical parameters and geometric dimensions as the on-site bolts are used to replace bolts A and B to observe the axial force distribution of bolts. The force measuring bolt is shown in **Figure 9A** and the force measuring bolt installed on site is shown in **Figure 9B**.

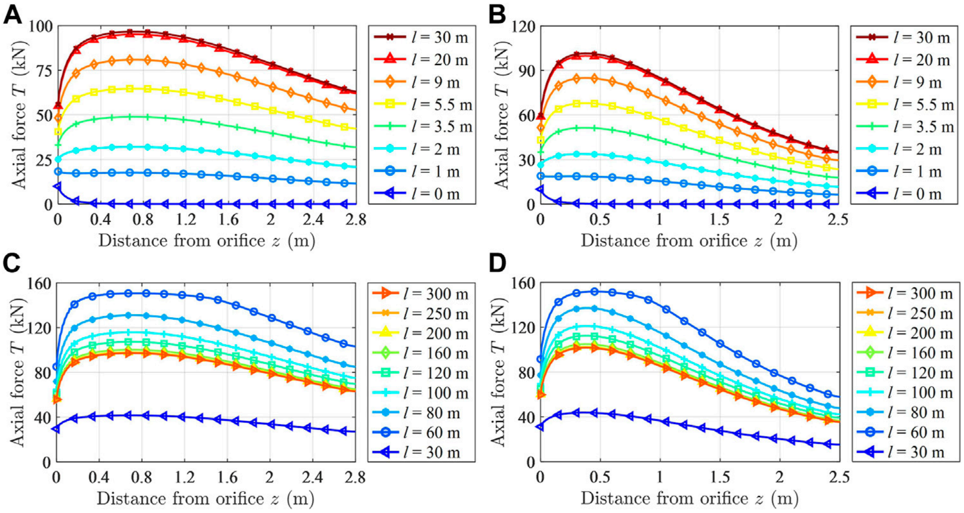

FIGURE 10 | Distribution law of the axial force of the bolt with the bolt body: **(A)** Variation law of the axial force of bolt A with the advance of the driving face; **(B)** Variation law of the axial force of bolt B with the advance of the driving face; **(C)** Variation law of the axial force of bolt A with the advance of the working face; and **(D)** variation law of the axial force of bolt B with the advance of the working face.

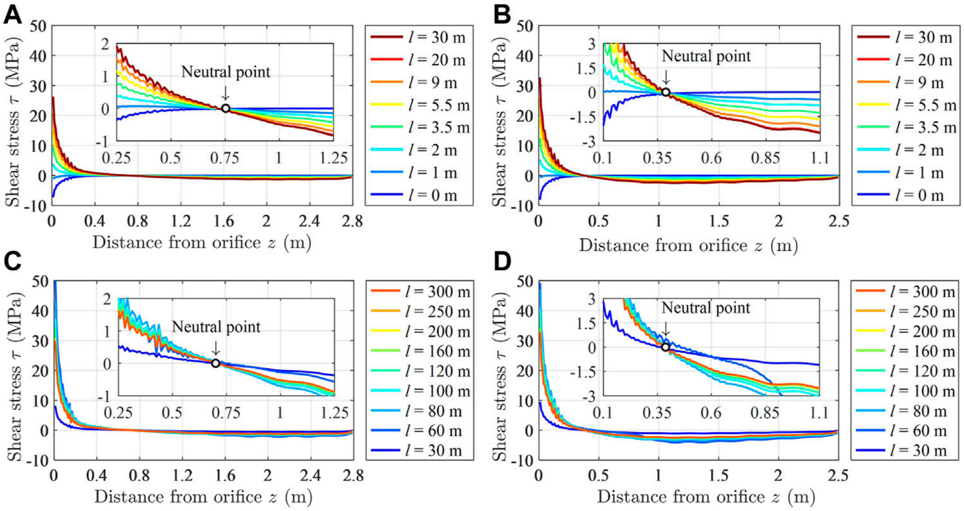

FIGURE 11 | Distribution law of the shear stress of the bolt with the bolt body: **(A)** Variation law of the shear stress of bolt A with the advance of the driving face; **(B)** Variation law of the shear stress of bolt B with the advance of the driving face; **(C)** the variation law of the shear stress of bolt A with the advance of the working face; and **(D)** variation law of the shear stress of bolt B with the advance of the working face.

Six groups of axial force-monitoring points are arranged on each force measuring bolt and the distance between each group of axial force-monitoring points and the bearing plate is shown in **Table 2**.

3.1 Distribution Law of Axial Force of Full-Length Anchoring Bolts in a Rectangular Roadway

By substituting the relevant data into the bolt mechanical model, the variation curve of the axial force of a full-length anchoring bolt in a rectangular roadway during roadway driving and working face mining can be obtained. The variation curve of the axial force of the bolts A and B with the advance of driving face and working face is shown in **Figure 10**.

It can be seen from **Figure 10** that for the full-length anchoring bolt in the middle of the roof and side of the rectangular roadway, the distribution law of its axial force along the bolt body direction is roughly the same. With the advance of the driving face, the axial force rapidly evolves from a monotonous decreasing trend to the change law of first increasing and then decreasing. But with the advance of the working face, the axial force increases first and then decreases. The axial force change of the bolt in the middle of the

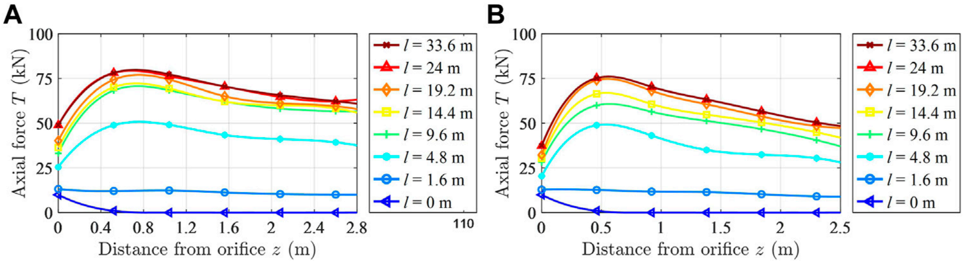

FIGURE 12 | Variation curve of the axial force of a force measuring bolt: **(A)** Force measuring anchor bolt A in the middle of the roof and **(B)** force measuring anchor bolt B in the middle of the side.

roof is gentler than that in the middle of the side. The maximum axial force point of the bolt quickly stabilizes at the neutral point from the orifice position with the advance of the driving face. The neutral point of the bolt in the middle of the roof is 0.75 m away from the orifice, and the neutral point of the bolt in the middle of the side is 0.40 m away from the orifice. The neutral point of the bolt on the roadway side is closer to the roadway surface. The working resistance of the bolt shows a monotonous increasing trend with the advance of the driving face and the working face.

3.2 Shear Stress Distribution Law of a Full-Length Bolt in a Rectangular Roadway

According to **Eq. 23**, the distribution curve of the shear stress of the bolt body can be obtained. The evolution curve of the shear stress of the bolt body with the advance of the driving face and the working face is shown in **Figure 11**. In **Figure 11**, the sub coordinate system is a local magnification of the main coordinate system.

It can be seen from **Figure 11** that the evolution law of the shear stress in the middle of the roof and the bolt in the middle of the side is the same with the advance of the driving face and the working face. When there is no neutral point in the bolt, that is, when the bolt is installed in the surrounding rock, the shear stress of the bolt shows a monotonous increasing trend. When there is a neutral point in the bolt, that is, when the bolt is far away from the driving face, the shear stress of the bolt shows a monotonous decreasing trend. The variation range of the shear stress of the bolt in the middle of the side is greater than that of the bolt in the middle of the roof. The shear stress curve of the bolt intersects at one point, that is, the neutral point of the bolt, which indicates that the neutral point position of the bolt does not change during roadway driving and working face mining.

Comparing **Figures 10**, **11**, it can be seen that when the shear stress of the bolt is less than 0, the axial force of the bolt decreases. When the shear stress of the bolt is greater than 0, the axial force of the bolt increases. On both sides of the neutral point of the bolt, the sign of the shear stress of the bolt is different, which is consistent with the neutral point theory.

3.3 Observation Results of Force Measuring Bolt

The mining roadway of 1,131(1) working face is driving for 4.8 m every day. After installing the force measuring bolt, it is observed twice on the first day and once every day, after that, for a total of 7 days. The observed data are shown in **Figure 12**.

It can be seen from **Figure 12** that the axial force distribution law of the bolt measured by the force measuring bolt is basically consistent with the axial force distribution law obtained by theoretical calculations. When the force measuring bolt is installed into the surrounding rock, the axial force of the bolt shows a monotonous decreasing trend. When it is far from the driving face, the axial force of the bolt increases first and then decreases. The maximum value is reached at the neutral point of the bolt. The neutral point of the roof force measuring bolt is between 0.52 and 1.04 m. The neutral point of the side force measuring bolt is about 0.46 m, which is consistent with the theoretical calculation results. The variation range of the axial force of the force measuring bolt in the middle of the roadway side is greater than that of the force measuring bolt in the middle of the roof. The working resistance of the force measuring bolt in the middle of the roadway side is less than that of the force measuring bolt in the middle of the roof, which is consistent with the theoretical calculation results. The correctness of the theoretical calculation results can be verified from the observation data of the force measuring bolt.

4 CONCLUSION

To study the evolution law of the axial force and shear stress of full-length anchoring bolts in a rectangular roadway during roadway driving and working face mining, considering the deformation of the surrounding rock, the mechanical model of the bolt is established and solved through the stress analysis of the bolt. Then, the mechanical formulas for calculating the axial force and the shear stress of the bolt are deduced. Taking the mining roadway of 1,131(1) working face in the Zhujidong coal mine as the engineering background, the evolution law of the axial force and the shear stress of the full-length anchoring bolt in the middle of the roof and the side of the rectangular roadway with the advance of the driving and the working face are analyzed. The theoretical analysis results are verified by the observation data of the force measuring bolt. The axial force distribution law of the bolt in the middle of the roof and the bolt in the middle of the roadway side is the same. When the bolt is installed, the axial force of the bolt decreases monotonically along the direction of the bolt. The axial force of the bolt first increases and then decreases along the direction of the bolt, and the maximum value appears at the neutral point. The neutral point position remains unchanged. The distribution law of the shear stress of the bolt body in the middle of roof and side is the same. The shear stress of the bolt shows a monotonous increasing trend along the direction of the bolt. At different distances from the driving face or the working face, the shear stress of the bolt converges at the neutral point. The variation range of the shear stress of the bolt body in the middle of the roadway is greater than that of the bolt in the middle of the roof.

DATA AVAILABILITY STATEMENT

The original contributions presented in the study are included in the article/Supplementary Material; further inquiries can be directed to the corresponding author.

AUTHOR CONTRIBUTIONS

DP wrote the main manuscript text. KH and YX established and solved the theoretical mode. JC designed the experiments. XN and CL collected field test data. All authors reviewed the manuscript.

FUNDING

This work was supported by the National Natural Science Foundation of China (nos. 51774009, 52174103, and 52174105); Key Research and Development Projects in Anhui Province (No. 202004a07020045), and the Natural Science Foundation of Anhui Provincial Natural Science Foundation (No. 2008085ME147).

REFERENCES

Aghchai, M. H., Maarefvand, P., and Salari Rad, H. (2020). Analytically Determining Bond Shear Strength of Fully Grouted Rock Bolt Based on Pullout Test Results. *Period. Polytech. Civ. Eng.* 64 (1), 212–222. doi:10.3311/PPci.15195

Baddoo, P. J., and Crowdy, D. G. (2019). Periodic Schwarz-Christoffel Mappings with Multiple Boundaries Per Period. *Proc. R. Soc. A* 475 (2228), 20190225. doi:10.1098/rspa.2019.0225

Badreddine, M., DeLillo, T. K., and Sahraei, S. (2019). A Comparison of Some Numerical Conformal Mapping Methods for Simply and Multiply Connected Domains[J]. *Discrete Continuous Dyn. Syst. - Ser. B* 24 (1), 5. doi:10.3934/dcdsb.2018100

Chang, C.-Y., Chang, E.-C., and Huang, C.-W. (2019). *In Situ* Diagnosis of Industrial Motors by Using Vision-Based Smart Sensing Technology. *Sensors* 19, 5340. doi:10.3390/s19245340

Chang, J., He, K., Pang, D., Li, D., Li, C., and Sun, B. (2021). Influence of Anchorage Length and Pretension on the Working Resistance of Rock Bolt Based on its Tensile Characteristics. *Int. J. Coal Sci. Technol.* 8 (6), 1384–1399. doi:10.1007/s40789-021-00459-9

Chang, J., He, K., Yin, Z., Li, W., Li, S., and Pang, D. (2020). Study on the Instability Characteristics and Bolt Support in Deep Mining Roadways Based on the Surrounding Rock Stability Index: Example of Pansan Coal Mine. *Adv. Civ. Eng.* 2020, 1–16. doi:10.1155/2020/8855335

Chen, J., He, F., and Zhang, S. (2020). A Study of the Load Transfer Behavior of Fully Grouted Rock Bolts with Analytical Modelling. *Int. J. Min. Sci. Technol.* 30 (1), 105–109. ISSN 2095-2686. doi:10.1016/j.ijmst.2019.12.010

Cheng, L., Zhang, Y., Ji, M., Cui, M., Zhang, K., and Zhang, M. (2015). Theoretical Calculation and Analysis on the Composite Rock-Bolt Bearing Structure in Burst-Prone Ground. *Math. Problems Eng.* 2015, 1–6. Article ID 434567. doi:10.1155/2015/434567

Cui, L., Sheng, Q., Dong, Y., Ruan, B., and Xu, D.-D. (2021). A Quantitative Analysis of the Effect of End Plate of Fully-Grouted Bolts on the Global Stability of Tunnel. *Tunn. Undergr. Space Technol.* 114, 104010–202110. ISSN 0886-7798. doi:10.1016/j.tust.2021.104010

Feng, Q., Jiang, B.-S., Zhang, Q., and Wang, L.-P. (2014). Analytical Elasto-Plastic Solution for Stress and Deformation of Surrounding Rock in Cold Region Tunnels. *Cold Regions Sci. Technol.* 108, 59–68. doi:10.1016/j.coldregions.2014.08.001

He, K., Chang, J., Pang, D., Sun, B., Yin, Z., and Li, D. (2022). Iterative Algorithm for the Conformal Mapping Function from the Exterior of a Roadway to the Interior of a Unit Circle. *Arch. Appl. Mech.* 92, 971–991. doi:10.1007/s00419-021-02087-w

Jin-feng, Z., and Peng-hao, Z. (2019). Analytical Model of Fully Grouted Bolts in Pull-Out Tests and *In Situ* Rock Masses. *Int. J. Rock Mech. Min. Sci.* 113, 278–294. ISSN 1365-1609,. doi:10.1016/j.ijrmms.2018.11.015

Khan, F., Arshad, T., Ghaffar, A., Sooppy Nisar, K., and Kumar, D. (2020). Numerical Solutions of 2D Fredholm Integral Equation of First Kind by Discretization Technique. *AIMS Math.* 5 (3), 2295–2306. doi:10.3934/math.2020152

Li, Y., and Liu, C. (2019). Experimental Study on the Shear Behavior of Fully Grouted Bolts. *Constr. Build. Mater.* 223, 1123–1134. ISSN 0950-0618. doi:10.1016/j.conbuildmat.2019.06.207

Liu, C. H., and Li, Y. Z. (2017). Analytical Study of the Mechanical Behavior of Fully Grouted Bolts in Bedding Rock Slopes. *Rock Mech. Rock Eng.* 50 (9), 2413–2423. doi:10.1007/s00603-017-1244-9

Liu, C., and Li, Y. (2020). Predicting the Shear Resistance Contribution of Passive Full-Length Anchoring Bolts to Jointed Rock[J]. *Int. J. Geomechanics* 20 (2), 1–11. doi:10.1061/(asce)gm.1943-5622.0001581

Liu, G., Xiao, M., Chen, J., and Zhou, H. (2017). Study on Mechanical Characteristics of Fully Grouted Rock Bolts for Underground Caverns under Seismic Loads[J]. *Math. Problems Eng.* 2017, 12. doi:10.1155/2017/1657369

Lv, Z., Qin, Q., Jiang, B., Luan, Y., and Yu, H. (2018). Comparative Study on the Mechanical Mechanism of Confined Concrete Supporting Arches in Underground Engineering. *PLoS ONE* 13 (2), e0191935. doi:10.1371/journal.pone.0191935

Lyu, X., Zhao, Z., Ma, Q., Wang, X., and Gao, X. (2018). 2D Semimodel of Full-Section Anchorage in Thick Soft Rock Roadway. *Shock Vib.* 2018, 1–15. doi:10.1155/2018/9853853

Mei, Y., Li, W., Yang, N., Wang, G., Li, T., and Sun, L. (2020). Failure Mechanism and Optimization of Arch-Bolt Composite Support for Underground Mining Tunnel. *Adv. Civ. Eng.* 2020, 18. doi:10.1155/2020/5809385

Mesgarani, H., and Azari, Y. (2019). Numerical Investigation of Fredholm Integral Equation of the First Kind with Noisy Data. *Math. Sci.* 13, 267–278. doi:10.1007/s40096-019-00296-7

Muskhelishvili, N. I. (1953).. Editor P. Noordhoff. 4th edition (Holland: Groningen).*Some Basic Problems of the Mathematical Theory of Elasticity[M*

Nazem, A., Hossaini, M., Rahami, H., and Bolghonabadi, R. (2015). Optimization of Conformal Mapping Functions Used in Developing Closed-form Solutions for Underground Structures with Conventional Cross Sections[J]. *Int. J. Min. Geo-Engineering* 49 (1), 93–102. doi:10.22059/ijmge.2015.54633

Shen, W., Wang, X., Bai, J., Li, W., and Yu, Y. (2017). Rock Stress Around Noncircular Tunnel: A New Simple Mathematical Method. *Adv. Appl. Math. Mech.* 9 (6), 1330–1346. doi:10.4208/aamm.2016.m1530

Sun, Z., Zhang, D., Fang, Q., Liu, D., and Dui, G. (2021). Displacement Process Analysis of Deep Tunnels with Grouted Rockbolts Considering Bolt Installation Time and Bolt Length. *Comput. Geotechnics* 140, 104437–202137. ISSN 0266-352X. doi:10.1016/j.compgeo.2021.104437

Tran Manh, H., Sulem, J., and Subrin, D. (2015). A Closed-form Solution for Tunnels with Arbitrary Cross Section Excavated in Elastic Anisotropic Ground. *Rock Mech. Rock Eng.* 48, 277–288. doi:10.1007/s00603-013-0542-0

Wang, W., Song, Q., Xu, C., and Gong, H. (2018). Mechanical Behaviour of Fully Grouted GFRP Rock Bolts under the Joint Action of Pre-tension Load and Blast Dynamic Load. *Tunn. Undergr. Space Technol.* 73, 82–91. ISSN 0886-7798. doi:10.1016/j.tust.2017.12.007

Wu, C., Chen, X., Hong, Y., Xu, R., and Yu, D. (2018). Experimental Investigation of the Tensile Behavior of Rock with Fully Grouted Bolts by the Direct Tensile Test. *Rock Mech. Rock Eng.* 51, 351–357. doi:10.1007/s00603-017-1307-y

Yuan, M., Peng, H., and Lei, Y. (2018). Applied Symmetrical Principle to Solve Schwarz-Christoffel Parameter Problem[J]. *Proc. Jangjeon Math. Soc.* 21 (4), 599–616. doi:10.17777/pjms2017.28.4.599

Zhao, C., Li, Y., Liu, G., Chen, D., and Meng, X. (2020). Research on the Stress Distribution Law of Fully Anchored Bolt and Analysis of Influencing Factors under the Condition of Surrounding Rock Deformation. *Adv. Civ. Eng.* 2020, 14. Article ID 8818375. doi:10.1155/2020/8818375

Zou, J., and Zhang, P. (2021). A Semi-analytical Model of Full-Length Anchoring Bolts in Jointed Rock Masses. *Appl. Math. Model.* 98, 266–286. ISSN 0307-904X. doi:10.1016/j.apm.2021.05.012

Conflict of Interest: The authors declare that the research was conducted in the absence of any commercial or financial relationships that could be construed as a potential conflict of interest.

frontiers | Frontiers in Earth Science

ORIGINAL RESEARCH
published: 19 May 2022
doi: 10.3389/feart.2022.884633

Identification of Rock Properties of Rock Wall Cut by Roadheader Based on PSO-VMD-LSSVM

Pengfei Qi, Jucai Chang, Xiao Chen*, Tuo Wang and Mengyun Wu

School of Mining Engineering, Anhui University of Science and Technology, Huainan, China

The problem of low digging efficiency and mining imbalance due to outdated digging technology and low degree of equipment intelligence has long existed in coal mine roadway excavation work. Lithology identification is the key to the intelligence of roadheading equipment. Accurate lithology identification significantly affects the automatic control of roadheader cutting conditions. Completing the identification of lithology in the process of rock wall cutting by a roadheader involved the following steps: building a tunneling experiment platform, making four rock specimens with different lithologies, completing the tunneling simulation experiments on four lithologies, obtaining current sensor data of four lithologies cutting, and finally proposing an intelligent lithology identification method of PSO-VMD-LSSVM. The research results show that the particle swarm algorithm (PSO) optimized the variational modal decomposition (VMD) with minimum envelope information entropy as the fitness function can realize the adaptive decomposition of the current signal of truncated motors. The signal reconstruction can increase the signal-to-noise ratio of the current signal by selecting the eigenmodal components according to the energy density and correlation coefficient criterion. The multi-scale fuzzy entropy is used as the eigenvector of the reconstructed current signal as the fuzzy entropy of different lithology cut-off motor currents has better differentiation at different scales. The least-squares support vector machine (LSSVM) is used to classify the feature vectors processed by custom decomposition parameter VMD and gives a recognition rate of 87.5%. The recognition rate increases to 97.5% for the feature vectors processed by PSO-VMD. The particle swarm algorithm optimizes the noise reduction *via* VMD to effectively improve the lithology recognition rate. The research results can provide a methodological reference for rock property recognition during rock cutting by a roadheading machine.

Keywords: particle swarm optimization, variational modal decomposition, minimum envelope entropy, multi-scale fuzzy entropy, least square support vector machine, identify rock properties

Edited by:
Kun Du,
Central South University, China

Reviewed by:
Hao Zhang,
Henan Agricultural University, China
Yong Ren,
Changshu Institute of Technology, China
Mingquan Qiu,
Guizhou Minzu University, China
Bo Wu,
China University of Mining and Technology, China

***Correspondence:**
Xiao Chen
chenxiao8ban@163.com

Specialty section:
This article was submitted to Geohazards and Georisks, a section of the journal Frontiers in Earth Science

Received: *26 February 2022*
Accepted: *11 April 2022*
Published: *19 May 2022*

Citation:
Qi P, Chang J, Chen X, Wang T and Wu M (2022) Identification of Rock Properties of Rock Wall Cut by Roadheader Based on PSO-VMD-LSSVM. Front. Earth Sci. 10:884633. doi: 10.3389/feart.2022.884633

INTRODUCTION

Coal mining mainly involves underground mining, and several underground roadways are required to ensure continuous and efficient coal production. As the key technology of coal mine roadway, rapid roadway digging is directly related to the economy and safety of coal mine production, an important guarantee for high and stable coal production. Yin studied the damage characteristics of rocks, mainly based on semi-rock or whole rock, under the action of dynamic and static coupling to improve the safety of deep mining (Yin et al., 2019). Methods to avoid the overlying rock layers being affected by mining to prevent accidents were studied by analyzing mining techniques and the mechanical properties of rocks (Du et al., 2020a). Extensive research has been conducted to minimize the impact of mining and ensure the safety and efficiency of coal production (Yin et al., 2012). However, reducing the impact of mining using roadway boring machines must be studied to minimize blasting vibrations and ensure a high degree of safety even with continuous rapid digging. Roadheader excavation has gradually become the main method of roadway mining, but safe and efficient roadheading technology is still in the exploration stage. In the process of excavation, cut-off rock wall properties change drastically. However, the roadheader driver cannot promptly adjust the cut-off speed, cantilever swing speed, and other conditions according to the cut-off lithology because of limited vision due to excessive coal and rock dust. These limitations lead to unstable output of cutting motor, excessive wear of cut-off teeth, abnormal collapse of working face, thus significantly impacting mining, accelerating the damage and aging of the digging equipment, and affecting the safety of digging the working face. Therefore, if the rock properties can be identified in the excavation, the efficiency of excavation can be improved, the service life of the excavator can be prolonged, the safety of excavation can be guaranteed, and the impact on the working face can be reduced.

The problem of rock identification has been extensively studied since it was introduced in the 1960s (Li and Ouyang, 2017; Yang et al., 2020). There are two main methods classified according to the means used: direct detection and indirect detection. The direct detection methods are as follows: 1. The natural ray method (Wang S. et al., 2021) uses the ray intensity remaining after the ray penetrates the coal seam and determines the thickness of the top and bottom coal seams according to the attenuation law to achieve the purpose of identifying lithology. However, this method is difficult to operate and has a small adaptation range (K., H, Sampath et al., 2019); 2. The radar detection method (Wang et al., 2016) determines the top coal thickness based on the characteristics of the speed, phase, propagation time of the reflected electromagnetic wave and the frequency of the emitted wave. This method is applicable only if large differences exist in the coal and rock properties as the recognition rate is low if the coal and rock properties are similar. 3. Infrared detection method (Zhang et al., 2022) uses a highly sensitive infrared temperature sensor to measure the temperature difference change of the truncated part. The lithology is identified after applying algorithm classification and artificial ray detection methods (Zhang et al., 2017). In addition to these methods, there are terahertz spectroscopy methods (Wang et al., 2018). Direct detection methods are susceptible to environmental, terrain, and working conditions due to direct contact with different lithologies. These methods are also limited by low tolerance, small application range, minimal feature extraction effects, and low recognition accuracy.

Indirect electric parametric detection is an indirect detection method. It uses image detection (Gao et al., 2021; Wang and Zhang, 2020; Wang X. et al., 2021) and was used in the early 20th century in the United Kingdom and the United States. It has re-emerged now due to the development of artificial intelligence and lithology recognition methods. Different lithology pictures are analyzed using modern image detection techniques to identify the lithology. However, the method is susceptible to working surface dust, light, and other conditions. Rocks exhibit certain electrical properties such as cutting force (Dai, 2020), current (He et al., 2020), and working voltage (Wang et al., 2018). The acceleration sensor (Zhang et al., 2020) and acoustic emission sensor (Du et al., 2020b) also show different readings. These properties can form the basis for distinguishing different lithologies. This method has the advantages of strong anti-interference ability, wide application range, clear feature extraction, and fast recognition. Moreover, current acquisition requires only the placement of the current sensor at the truncation motor, which is easy to perform with little modification to the machine. In this paper, the current signal is processed and used to identify rock lithology.

A simulated excavation experiment platform is built to simulate the cutting process and obtain the current sensor data of the excavator working on different lithologies to realize the identification of rock properties while cutting rock walls to improve the excavation efficiency. The current data are firstly decomposed by adaptive variational modal decomposition and the components are reconstructed according to the energy density and correlation coefficient criterion, Next, the multi-scale fuzzy entropy is used as the current signal feature vector. Finally, the least-squares support vector machine (LSSVM) is used to classify the features to achieve the purpose of identifying different lithologies.

RESEARCH ON LITHOLOGY IDENTIFICATION METHODS

Variational Modal Decomposition

Variational modal decomposition (VMD) is a nonlinear signal processing method that determines the center frequency and bandwidth of each component by iteratively searching the variational model in the optimal solution to achieve the effective separation of each signal component. VMD can highlight the local characteristics of the data.

The constrained variational model constructed by the VMD algorithm is (Dragomiretskiy and Zosso, 2013):

$$\begin{cases} \min\limits_{\{u_k\},\{\omega_k\}} \left\{ \sum\limits_k \left\| d_t \left[\left(\delta(t) + \frac{j}{\pi t} \right) \cdot u_k(t) \right] e^{-j\omega_k t} \right\|_2^2 \right. \\ s.t. \sum\limits_k u_k = f \end{cases} \tag{1}$$

Where u_k is the component of each mode, ω_k is the central frequency of each mode component, $\delta(t)$ is the pulse function, and k is the number of modes obtained by decomposition.

To solve the variational problem, the model is converted into an unconstrained variational solution by introducing Lagrange multipliers λ and multiplicative factors α, where the extended Lagrange operator equation is:

$$L\left(\{u_k\},\{\omega_k\},\lambda\right) = \alpha \sum_k \left\| \partial_t \left[\left(\delta(t) + \frac{j}{\pi t} \right) \cdot u_k(t) \right] e^{-j\omega_k t} \right\|_2^2 + \left\| f(t) - \sum_k u_k(t) \right\|_2^2 + \left\langle \lambda(t), f(t) - \sum_k u_k(t) \right\rangle \tag{2}$$

Then the multiplier alternating direction method is used to search for the extended Lagrangian expression, and the updated equation for each modal component u_k, central frequency ω_k, and Lagrangian operator is:

$$\hat{u}_k^{n+1}(\omega) = \frac{\hat{f}(\omega) - \sum_{i \neq k} \hat{u}(\omega) + \frac{\lambda(\omega)}{2}}{1 + 2\alpha(\omega - \omega_k)^2} \tag{3}$$

$$\omega_k^{n+1} = \frac{\int_0^\infty \omega |\hat{u}_k(\omega)|^2 d\omega}{\int_0^\infty |\hat{u}_k(\omega)|^2 d\omega} \tag{4}$$

$$\hat{\lambda}^{n+1}(\omega) = \hat{\lambda}(\omega) + \tau \left(\hat{f}(\omega) - \sum_{k=1}^{K} \hat{u}^{n+1}(\omega) \right) \tag{5}$$

If the following equation, with $e > 0$, is satisfied for a given discriminant accuracy, then VMD can be achieved.

$$\sum_k \left\| \hat{u}_{k,n+1} - \hat{u}_{k,n} \right\|_2^2 \Big/ \left\| \hat{u}_{k,n} \right\|_2^2 < e \tag{6}$$

Combined with the above VMD decomposition process, there are four main parameters: decomposition mode number k, penalty factor α, noise tolerance τ, and convergence error e. Among them, the decomposition mode number k and penalty factor α significantly influence the decomposition performance; the decomposition signal will be incomplete if the value of k is too small, while too large a value will lead to over-decomposition and modal mixing. α will be large when the bandwidth of decomposition mode is small, and the bandwidth of decomposition mode will be small if α is too large. Therefore, the key to determining the decomposition modes is to determine the decomposition mode number k and penalty factor α correctly.

Particle Swarm Algorithm Optimized Variational Modal Decomposition

The particle swarm algorithm (Kennedy and Eberhart, 1995; Eberhart and Kennedy, 2002) is a population-based evolutionary algorithm. The core idea of the algorithm is that each feasible solution is considered a "particle" and all solutions are scales of particles, each of which has an adaptation value determined by the fitness function. Each particle also has a velocity that determines its position and direction. These particles are updated iteratively in the solution space following the optimal particle value *gbest* and the individual extreme value *pbest*, and finally converge to the optimal solution. The velocity and position update is performed as follows:

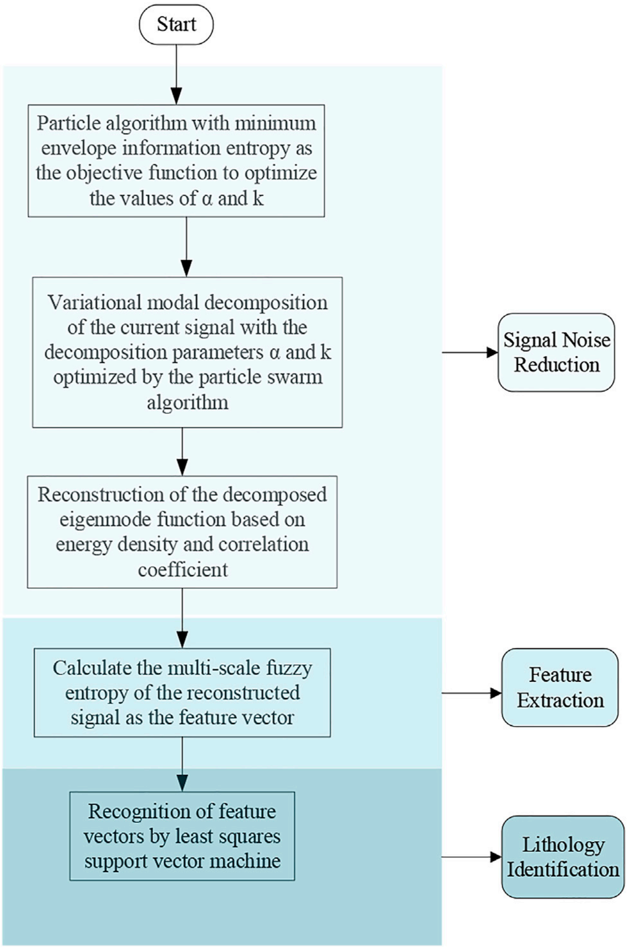

FIGURE 1 | Flow chart of PSO-VMD-LSSVM algorithm.

$$v_{id}(t+1) = \lambda v_{id}(t) + \kappa_1 r_1 \left(pbest(t) - x_{id}(t) \right) + \kappa_2 r_2 \left(gbest(t) - x_{id}(t) \right) \tag{7}$$

$$x_{id}(t+1) = x_{id}(t) + \alpha v_{id}(t) \tag{8}$$

where d is the dimension of the particle; λ is the inertia weight, κ_1 and κ_2 are the learning factors, usually chosen between [0, 2], r_1 and r_2 are random values, and α is the constraint factor, which controls the weight of the velocity. The position change and velocity change should be constrained according to the actual situation so that they do not exceed the boundary values.

The number of decomposition modes k and the penalty factor α for VMD decomposition can be determined quickly using the particle swarm algorithm; however, this optimization process requires an objective function to qualify the optimization. The information entropy can well reflect the sparsity of the

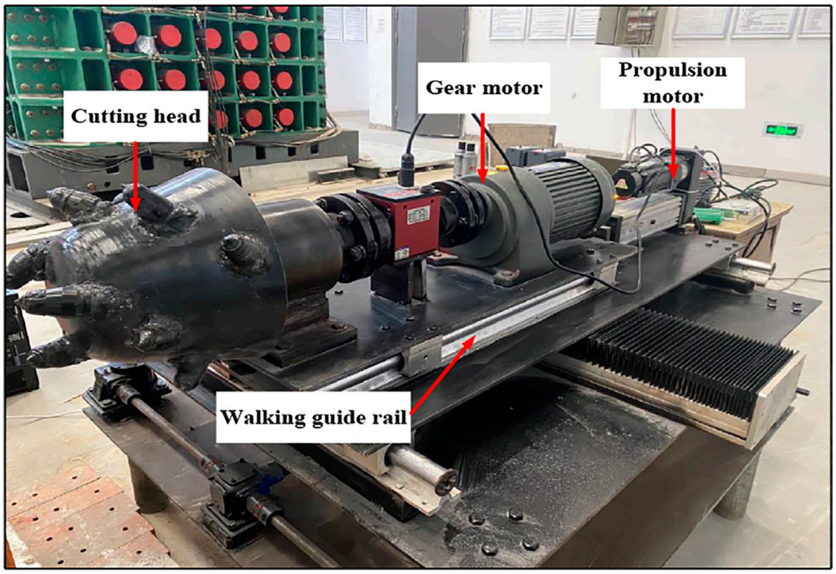

FIGURE 2 | Diagram of the tunneling experiment platform.

decomposition signal, and the magnitude of its value can reflect the uniformity of the probability distribution. The most uncertain distribution will have the largest entropy value. Information entropy is based on this concept. The envelope signal obtained after applying the demodulation operation on the signal gets processed into a series of probability distributions p_i, and the entropy value calculated from it reflects the sparsity of the original signal. After the noise reduction process, the more the information contained, the smaller the minimum envelope information entropy is. In this paper, the minimum envelope information entropy is used as the fitness function of the PSO algorithm.

$$p_i = \frac{a_i}{\sum_{i=1}^{N} a_i}, i = 1, 2, \ldots\ldots, N \tag{9}$$

a_i is the envelope amplitude of the i th point of the modal signal after VMD decomposition, N is the length of the modal signal after VMD decomposition, and p_i is the normalized envelope of the modal signal.

$$IMFF_{EE}(k) = -\sum_{j=1}^{N} p_i \log_2 (p_j) \tag{10}$$

$IMFF_{EE}(k)$ is the entropy of the envelope information of the k modal signals.

$$MEE = \min\{IMFF_{EE}(1), \ldots\ldots, IMFF_{EE}(k)\} \tag{11}$$

The minimum value of envelope information entropy of k modal signals is chosen as the minimum envelope information entropy, which is the adaptation function MEE. When the adaptation function reaches the minimum value, i.e., the minimum envelope information entropy reaches the minimum, the best decomposition modal number k and penalty factor α are determined to achieve adaptive decomposition.

FIGURE 3 | Four similar simulated specimens.

Signal Reconstruction

When decomposing the current signal using PSO-optimized VMD, the sampling rate may be insufficient, and spurious intrinsic mode function (IMF) components may occur. This problem is addressed by combining energy density and correlation coefficient to reconstruct the components of the current signal truncated from different lithology acquisitions. The steps are as follows.

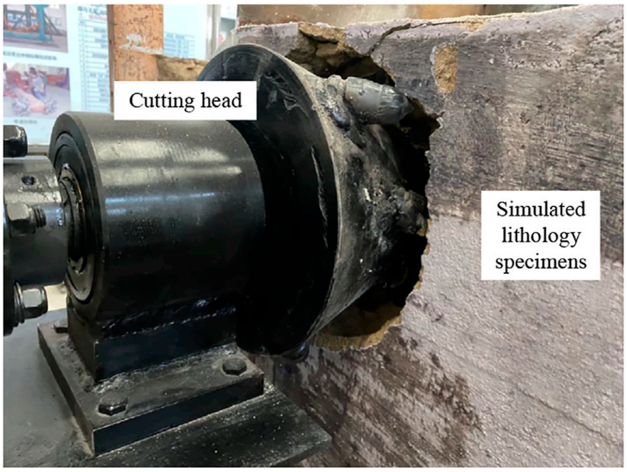

FIGURE 4 | Diagram of tunneling simulation experiment.

1) Perform energy analysis on the four components obtained and calculate the energy density of each IMF:

$$E_k = \frac{1}{K}\int |C_k(t)|^2 dt = \frac{1}{K}\sum_{d=1}^{K}[x_k(d)]^2 \tag{12}$$

where E_k is the energy density of the k^{th} energy mode, k is the length of the IMF, and $x_k(d)$ is the amplitude of the k^{th} IMF component.

2) Analysis of the correlation between the IMF component and the cutting current signal.

$$R_k = \frac{E[(C_k - \mu_k)(y - \mu)]}{\sigma_k \sigma} \tag{13}$$

R_k denotes the mathematical expectation, μ_k is the mean of the IMF components, μ is the mean of the original signal y, σ_k is the standard deviation of the IMF components, and σ is the standard deviation of the original current signal.

The average energy of the IMF components of the intercepted current signals of the four lithologies multiplied by the correlation coefficient. The three IMF components with the largest product are selected and superimposed to reconstruct the simulated current signals of the four lithologies.

Feature Extraction

The relevant features, such as the input for recognition, need to be extracted from the reconstructed current signal. Multi-scale fuzzy entropy is based on fuzzy entropy with the addition of scale factors. The fuzzy entropy value of the same time series under different scale factors, which can effectively overcome the defects of single-scale fuzzy entropy value, is used to measure the possible abrupt changes of time series to effectively measure the

TABLE 1 | Four types of ratios and rock mechanical properties.

Lithology	Sand to Glue Ratio	Water to Paste Ratio	Density/(g/Cm^3)	Compressive Strength/MPa	Modulus of Elasticity/MPa
Lithology1	4:1	3:7	1.731	3.101	560.084
Lithology2	5:1	7:3	1.823	2.445	451.744
Lithology3	6:1	6:4	1.957	1.965	345.873
Lithology4	7:1	5:5	1.623	1.132	265.463

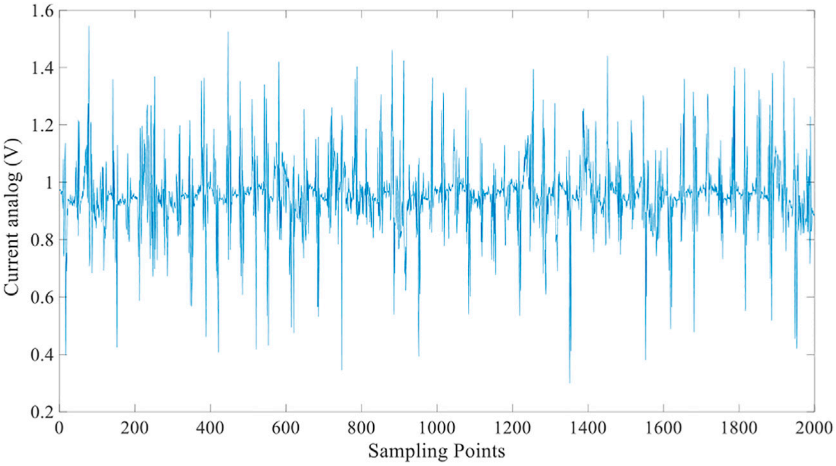

FIGURE 5 | Cut-off lithology 1 cut-off motor current sampling graph.

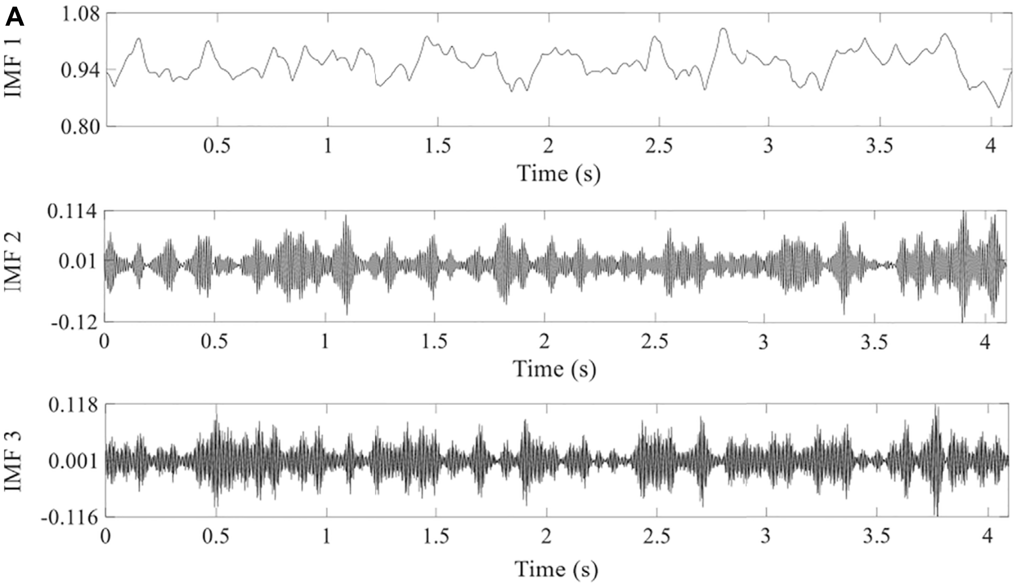

IMFS obtained by truncating the lithology 1 motor current signal by VMD processing with custom parameters

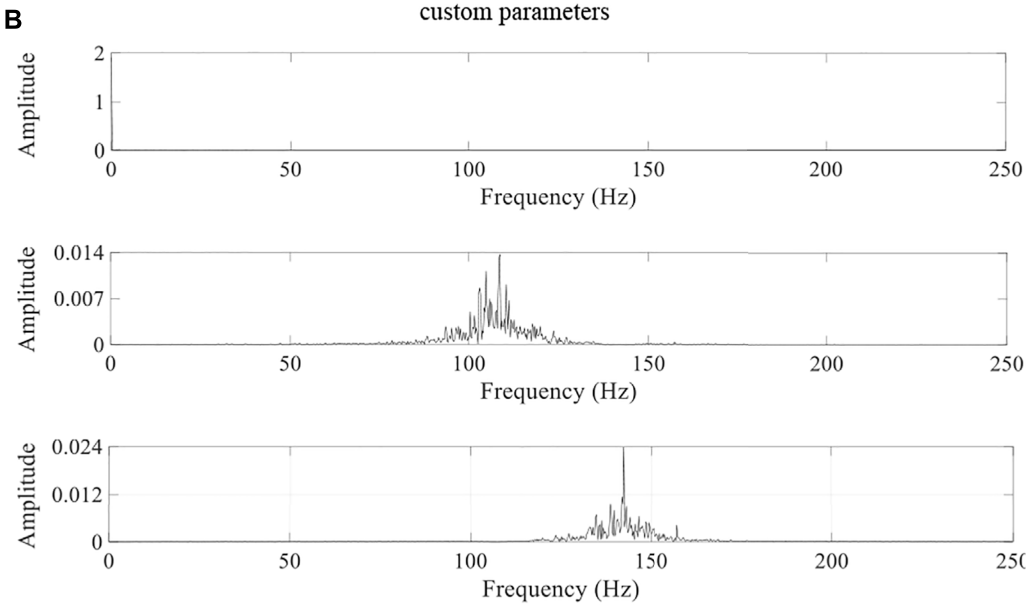

Spectrogram obtained by truncating the lithology 1 motor current signal by VMD processing with custom parameters

FIGURE 6 | VMD with custom parameters to process the truncated lithology 1 motor current signal graph. **(A)** IMFs obtained by truncating the lithology 1 motor current signal by VMD processing with custom parameters **(B)** Spectrogram obtained by truncating the lithology 1 motor current signal by VMD processing with custom parameters.

nonlinearity and complexity changes of the current signal. The algorithm description of multi-scale fuzzy entropy is:

1) Construct a new coarse-grained vector $y_j(\tau)$ for the reconstructed current signal $X_i = \{x_1, x_2, \ldots, x_n\}$, where N denotes the sequence length

$$y_j(\tau) = \frac{1}{\tau} \sum_{i=(j-1)\tau+1}^{j\tau} x_i, \ 1 \le j \le \frac{N}{\tau} \tag{14}$$

Where $\tau = 1, 2, \ldots, n$ denotes the scale factor. When $\tau = 1$, $\{y_1(1), y_2(1), \cdots, y_n(1)\} = X_i$ is the original time series.

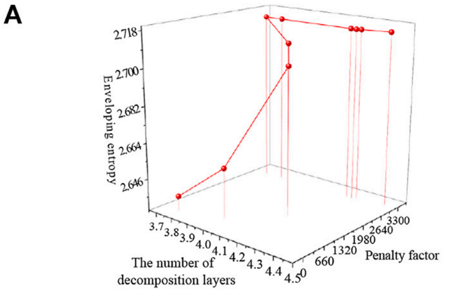

Lithology 1 Lithology 1 current decomposition parameters corresponding to envelope entropy iterative diagram

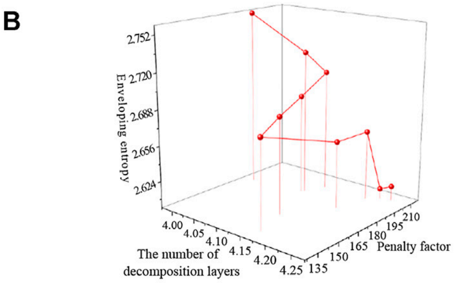

Lithology 2 Lithology 1 current decomposition parameters corresponding to envelope entropy iterative diagram

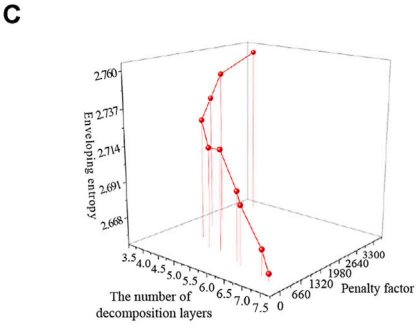

Lithology 3 Lithology 1 current decomposition parameters corresponding to envelope entropy iterative diagram

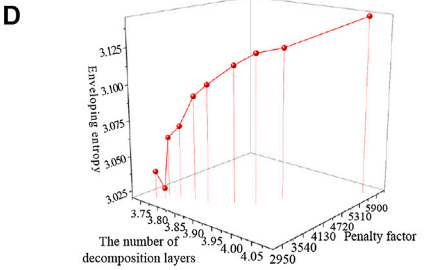

Lithology 4 Lithology 1 current decomposition parameters corresponding to envelope entropy iterative diagram

FIGURE 7 | Truncation current decomposition parameters corresponding to the iterative process of envelope entropy. **(A)** Lithology 1 Lithology 1 current decomposition parameters corresponding to envelope entropy iterative diagram **(B)** Lithology 2 Lithology 1 current decomposition parameters corresponding to envelope entropy iterative diagram **(C)** Lithology 3 Lithology 1 current decomposition parameters corresponding to envelope entropy iterative diagram **(D)** Lithology 4 Lithology 1 current decomposition parameters corresponding to envelope entropy iterative diagram.

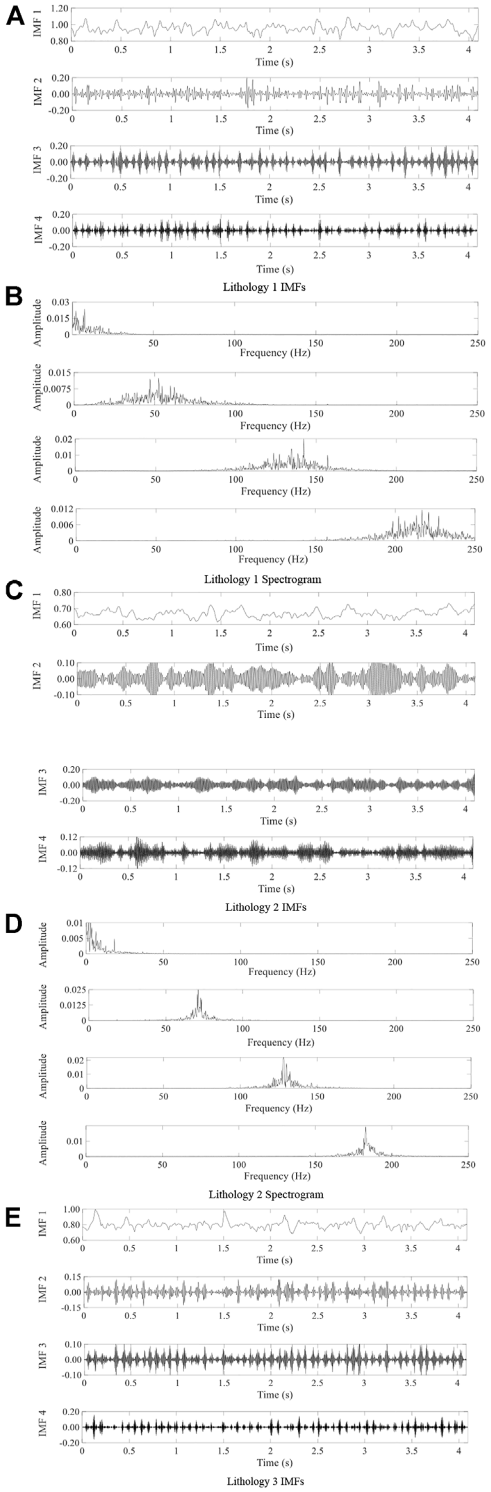

FIGURE 8 | Results of truncated motor current signal decomposition of PSO-VMD for four lithologies. **(A)** Lithology 1 IMFs **(B)** Lithology 1 Spectrogram **(C)** Lithology 2 IMFs **(D)** Lithology 2 Spectrogram **(E)** Lithology 3 IMFs **(F)** Lithology 3 Spectrogram **(G)** Lithology 4 IMFs **(H)** Lithology 4 Spectrogram.

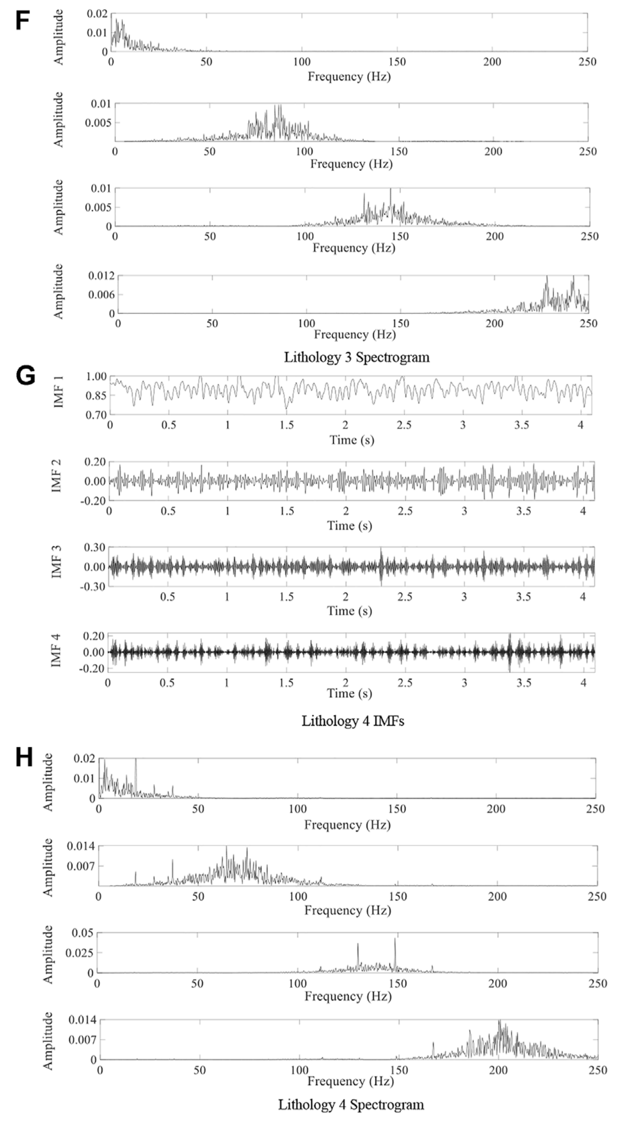

FIGURE 8 | *(Continued).*

2) Fuzzy entropy solutions of all time series $y_j(\tau)$ are converted into the corresponding scale factor function.

Rockiness Identification

The LSSVM is an improvement of the support vector machine, using equations instead of inequality constraints, and applying the linear least-squares criterion to the optimization of the loss function to improve the convergence efficiency, with the following process (Fu et al., 2021):

1) The training data set $\{(x_1, y_1), (x_2, y_2), \cdots, (x_n, y_n)\}$ in which x_i is the i^{th} input sample and y_i is the output variable, and the kernel function mapping is used to construct the regression function in the high-dimensional space as follows:

$$y(x) = \omega \cdot \varphi(x) + b \tag{15}$$

where ω is the weight vector and $\varphi(x)$ is the normal vector and b is the intercept of the hyperplane in the high-dimensional space.

2) According to the structural risk minimization criterion, ω and b must be optimized. The optimization equations are:

$$\begin{cases} \min J(\omega, \zeta) = \frac{1}{2}\|\omega\|^2 + \frac{\gamma}{2}\sum_{i=1}^{n}\xi_i^2 \\ s.t. y_i = \omega^T \cdot \varphi(x_i) + b + \xi_i \end{cases} \tag{16}$$

Where γ is the regularization parameter and ξ_i is the relaxation variable.

3) Construction of Lagrangian function

$$L(\omega, b, \xi, \alpha) = \frac{1}{2}\|\omega\|^2 + \frac{\gamma}{2}\sum_{i=1}^{n}\xi_i^2 - \sum_{i=1}^{n}\alpha_i\left(\omega \cdot \varphi(x_i) + b - y_i + \xi_i\right) \tag{17}$$

Here α_i is the Lagrangian multiplier corresponding to x_i.

4) Find the partial differential for ω, b, ξ, α, get the optimal value, and establish the regression function

$$y(x) = \sum_{i=1}^{n}\alpha_i K(x, x_i) + b \tag{18}$$

where $K(x_i, x_j)$ is the kernel function.

In lithology identification with LSSVM, the choice of kernel function significantly influences the identification performance of LSSVM. It is known from the literature that the prediction accuracy of radial basis kernel function is higher (Jiang et al., 2016); hence, the radial basis kernel function is chosen as the kernel function of LSSVM in this paper.

$$K\left(x_i, x_j\right) = \exp\left(-\frac{\left\|x_i, x_j\right\|^2}{2\sigma^2}\right) \tag{19}$$

Where σ is the kernel width.

The flow chart of PSO-VMD-LSSVM based lithology identification method is shown in **Figure 1**.

CUT-OFF MOTOR CURRENT SIGNAL ACQUISITION

Experimental Platform for Simulating Roadheading

As shown in **Figure 2**, the roadheading experimental platform, mainly comprising the propulsion system, the cutting system, and the signal acquisition system, was built to obtain the current sensor data of the roadheader under different lithology cutting work. The propulsion system comprises a 0.75 kW servo motor as the cutting propulsion motor and two slide rails as the walking guide. The cutting system uses a 1.5 kW, 60:1 reduction ratio gear motor with a frequency converter to control the cutting drilling

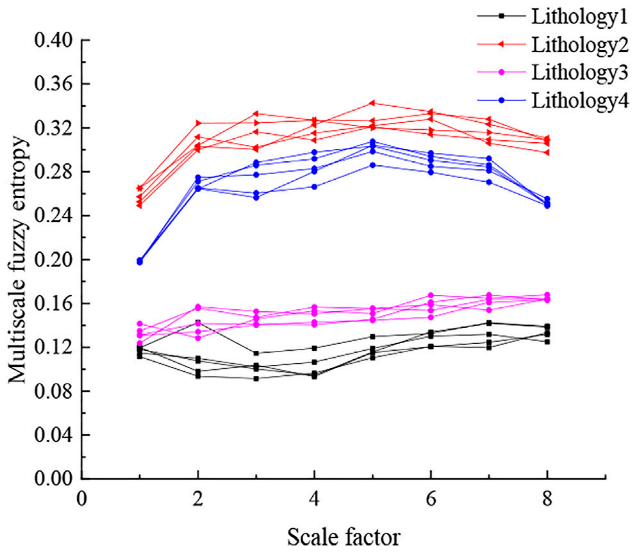

FIGURE 9 | Fuzzy entropy values of the four current reconstruction signals with scale factor.

speed. A cutting head of the roadheader with equal proportional reduction is used as the cutting tool for cutting different rock properties. The signal acquisition system uses 1.4 J LT series three-phase AC sensor; the output is analog with a range: 0 ~ 5 V and response time is under 1 ms. LabJack T7-PRO data acquisition card, used to collect the analog output of the current sensor, is connected to the upper computer; the upper computer processes and analyzes the collected current data.

Lithology Specimen Production

When studying the damage process, the damage of rocks is related to the force and the different rock properties (Du et al., 2020c), and the difference of compressive strength, density, and elastic modulus of similar materials can be used as a basis for different lithologies (Liu et al., 2020). In this paper, four specimen blocks with four different lithologies were prepared with four different ratios to realize the identification of lithology in the process of cutting off rocks wall using a roadheader. We selected quartz sand as the aggregate, cement and gypsum as the cementing material, and borax as an additive, collectively in four ratios (Shi et al., 2015). After weighing, mixing, compacting, resting, and air-drying, four similar simulated specimens with different lithologies were prepared as shown in **Figure 3**; the ratios of the four lithologies and rock mechanical properties are shown in **Table 1**.

As seen from **Table 1**, the mastic sand ratio plays a major role in controlling the uniaxial compressive strength and elastic modulus of similar materials; these quantities decrease significantly with the increase of the mastic sand ratio. The density, compressive strength, and elastic modulus of similar materials made with the selected four ratios are uniformly large and different. Thus, the simulated specimens can represent four kinds of lithologies.

TABLE 2 | Truncated motor current signal IMF component average energy density table.

E	IMF1	IMF2	IMF3	IMF4
Lithology 1	0.4573	0.0049	0.0073	0.0048
Lithology 2	0.4567	0.0043	0.0066	0.0042
Lithology 3	0.5938	0.0011	0.0017	9.8963
Lithology 4	0.6069	0.0035	0.0036	0.0023

TABLE 3 | Truncated motor current signal IMF component correlation coefficient table.

R	IMF1	IMF2	IMF3	IMF4
Lithology 1	0.4985	0.5756	0.6318	0.5078
Lithology 2	0.4903	0.5629	0.6186	0.5004
Lithology 3	0.5231	0.5020	0.5497	0.4022
Lithology 4	0.3656	0.5333	0.5910	0.5134

Digging Simulation Experiment

After the four pieces of specimens were left to air-dry and stabilize, the tunneling simulation experiment was carried out for the four specimen blocks with different lithologies by controlling the reducer motor parameters; the cutting head was rotated at a speed of 10 r/min and the propulsion motor at a propulsion speed of 0.5 m/min, as shown in **Figure 4**.

As shown in **Figure 4**, the four roadheader cut-off motor currents were obtained by conducting the tunneling simulation experiments on the four simulated rock specimens of different lithologies, using 2048 sampling points. The results of the cut-off motor current sampling for cut-off lithology 1 are shown in **Figure 5**.

EXPERIMENTAL RESULTS AND DISCUSSION

To verify the effectiveness of adaptive modal decomposition, the current signal of the truncated motor on lithology 1 working steadily for 4s, is first subjected to variable modal decomposition with custom decomposition parameters. The input parameters are chosen as follows: decomposition modal number $k = 3$, penalty factor under $\alpha = 3000$, noise tolerance $\tau = 0$ and convergence error $e = 10^{-7}$, to obtain the decomposition results shown in **Figure 6**.

As seen in **Figure 6**, using VMD with custom decomposition parameters will lead to no decomposition results at frequencies 0–70 Hz, incomplete signal decomposition, modal mixing at 114–138 Hz as the main frequency separation is not complete because the signal mainly contains the frequency signal and is not completely decomposed. Therefore, the particle swarm algorithm with the minimum envelope information entropy as the fitness function is used to optimize the selection of the parameters of the variational modal decomposition. The parameters of the particle swarm algorithm are initialized to the following values: dimension of particles, $d = 2$; r $\lambda = 0.8$; learning factors κ_1 and κ_2 are 1 and 2, respectively; number of iterations = 15; particle population size = 30. The selection of VMD parameters is optimized, and the penalty factors of the four lithologies and the number of decomposition layers

TABLE 4 | Signal-to-noise ratio comparison before and after signal reconstruction.

Current Signal	Lithology 1 Current Signal	Lithology 2 Current Signal	Lithology 3 Current Signal	Lithology 4 Current Signal
Signal-to-noise ratio before reconstruction	20.1807	4.7738	20.5560	16.9654
Signal-to-noise ratio after reconstruction	25.0162	8.6162	22.6319	19.4205

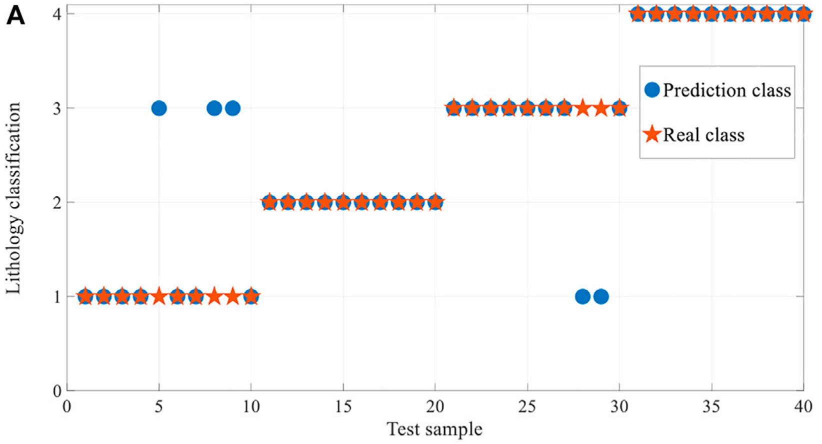

LSSVM results for rockiness classification of current signals processed by VMD with custom parameters

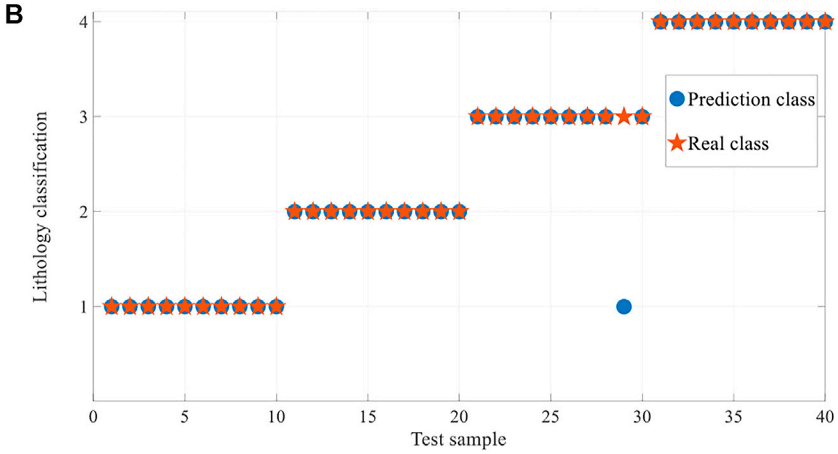

LSSVM results for lithology classification of current signals processed by PSO-VMD

FIGURE 10 | LSSVM recognition result graph. **(A)** LSSVM results for rockiness classification of current signals processed by VMD with custom parameters **(B)** LSSVM results for lithology classification of current signals processed by PSO-VMD.

corresponding to the envelope entropy part of the selection point iteration curve are shown in **Figure 7**.

As seen in **Figure 7**, using PSO to optimize the VMD parameter selection first uses the envelope entropy as the objective function to randomly select the decomposition modal number k and penalty factor α as the initial positions of the particles, and then calculates the envelope entropy value corresponding to each particle position. Next, the optimization function continuously compares the envelope entropy values and selects the minimum value of the envelope entropy for each update and determines the parameters k and α at this minimum position as the local extremes. Finally, the global minimum as the final decomposition modal number k and penalty factor α are selected. The lithologies of the four truncated motor current simulation signals are determined by the particle swarm algorithm as the best decomposition parameters with different penalty factors, wit the number of decomposition layers set to 4. Under these parameters, the fitness function of the particle swarm algorithm, i.e., the envelope entropy, reaches the minimum.

The variable modal decomposition of the cutter motor current signal after the particle swarm algorithm optimizes the value of the excavator under the four different lithologies is shown in **Figure 8**.

As seen from the above figure, the PSO-VMD determines the optimal decomposition parameters modal number k and penalty factor α. The VMD decomposition of the truncated currents of the four lithologies achieves an adaptive and completely non-recursive decomposition, effectively separating each modal component of the four current signals and overcoming the problems of endpoint effects and modal component mixing, with a good decomposition effect.

The results of calculating the average energy density and correlation coefficient for the decomposed current signal eigenmode function are shown in **Tables 2**, **3**.

The average energy of the IMF components of the current signals of the four lithologies are correspondingly multiplied by the average energy. The three IMF components with the largest product are superimposed to reconstruct the current analog signals of the four lithologies. The signal-to-noise ratio before and after signal reconstruction is shown in **Table 4**.

The PSO-VMD reconstructs the eigenmodes based on the correlation coefficient and energy density to reduce the noise of the original truncated current signal (Liang et al., 2021).

After noise reduction of the current signal, multi-scale fuzzy entropy is calculated, with the scale factor set to 8 and the similarity tolerance limit of 0.15. Fifty sets of 8-scale fuzzy entropy are taken for each of the current signals truncated on the four lithologies to obtain a total of 200 sets of 8-scale fuzzy entropy. Part of the 8-scale fuzzy entropy is shown in **Figure 9**.

As seen from **Figure 9**, the fuzzy entropy values of lithology 1 and lithology 3 overlap when the scale factor is 2. When the scale factors are 3, 4, and 5, the scale factors of lithology 2 and lithology 4 do not differ much. Finally, when the scale factors are 5, 6 and 7, the scale factors of lithology 1 and lithology 3 are closer, but they do not overlap. In general, the multi-scale fuzzy entropy of each lithology is distinguishable and can be used as a feature vector for identifying these four lithologies.

Forty sets of 50 sets of multiscale fuzzy entropy for each lithology were randomly selected as the training set and 10 sets as the test set. Finally, the four lithologies are classified using a least squares support vector machine with kernel function as the radial basis function. Considering the regularization parameter γ as 3.1 and the kernel width σ as 10, the lithology was identified using LSSVM for the eigenvectors of the current signal with VMD of custom parameters; the recognition rate was 87.%. Further, the lithology was identified for the current signal optimized using PSO-VMD, and the final recognition rate was 97.5%. The recognition results are shown in **Figure 10**.

As seen from **Figure 10**, using LSSVM to identify the lithology of the current signal processed by VMD with custom decomposition parameters, three of the ten test groups of lithology 1 failed to identify lithology 1 as lithology 3, and two of the test groups of lithology 3 identified lithology 3 as lithology 1, possibly due to the inconspicuous difference between the features of lithology 1 and 3 by multi-scale fuzzy entropy. While identifying the PSO-VMD processed current signals using LSSVM, only lithology 3 was identified as lithology 1 in one test group; the identification effect was better, and the recognition rate was improved by 10% relative to the custom parameter processed VMD.

In this study, we first obtained the eigenmode function by PSO-VMD, and then obtained the reconstructed current signal by summing the eigenmode function with energy density and correlation coefficient criterion. Multi-scale fuzzy entropy was used as the feature vector, and finally, the LSSVM was used to identify different lithologies. Further improvement of the recognition efficiency could be realized by applying other methods to improve the signal-to-noise ratio before and after noise reduction, or feature vectors with better differentiation between different lithologies.

CONCLUSION

Aiming to resolve the lithology identification problem of cut-off rock walls during excavation, we obtained current sensor data by building an excavation experiment platform and proposed an intelligent lithology identification method of PSO-VMD-LSSVM. The following conclusions are mainly obtained.

1) The particle swarm algorithm using the minimum envelope information entropy as the fitness function can optimize the parameter selection of the variational modal function of the current signal, ensuring that the parameters of the VMD can be selected adaptively.
2) The energy density and correlation coefficient criteria are used to reconstruct the modal components of the current signal after the VMD to increase the signal-to-noise ratio of the current signal.
3) Multi-scale fuzzy entropy is used as a feature vector for truncating the reconstructed current signal of different lithologies. It can be used as a feature vector for recognition because it has better differentiation for different lithologies under different scale factors.
4) The lithology classification by the LSSVM is performed for the VMD with custom decomposition parameters and the PSO-VMD; the recognition results are 87.5 and 97.5%, respectively. Thus, the PSO-VMD can improve the recognition rate of the LSSVM.

DATA AVAILABILITY STATEMENT

The original contributions presented in the study are included in the article/Supplementary Material, further inquiries can be directed to the corresponding author.

AUTHOR CONTRIBUTIONS

PQ: Conceptualization, Methodology, Software, Data curation, Validation, Writing-original draft. JC: Writing-review and editing, Funding acquisition. XC: Supervision, Writing-review and editing, Funding acquisition. TW: Writing-review and editing. XZ: Writing-review. MW: Data curation.

FUNDING

This work was supported by the National Natural Science Foundation of China (Grant No.52174105), Collaborative

Innovation Project of Anhui University(GXXT-2019-029), University-level key projects of Anhui University of science and technology (xjzd2020-14), the Key Projects of Natural Science Research in Anhui Universities (KJ2021A0426).

REFERENCES

Dai, B. (2020). *Coal-rock Identification Method Based on Load Data Fusion of Shearer Rocker Axle*. China: Liaoning Technical University. doi:10.27210/d.cnki.glnju.2020.000032

Dragomiretskiy, K., and Zosso, D. (2013). Variational Mode Decomposition. *IEEE Transactions Signal. Processing* 62 (3), 531–544.

Du, K., Li, X.-f., Yang, C.-z., Zhou, J., Chen, S.-j., and Manoj, K. (2020a). Experimental Investigations on Mechanical Performance of Rocks under Fatigue Loads and Biaxial Confinements. *J. Cent. South. Univ.* 27 (10), 2985–2998. doi:10.1007/s11771-020-4523-7

Du, K., Li, X., Tao, M., and Wang, S. (2020b). Experimental Study on Acoustic Emission (AE) Characteristics and Crack Classification during Rock Fracture in Several Basic Lab Tests. *Int. J. Rock Mech. Mining Sci.* 133, 104411. doi:10.1016/j.ijrmms.2020.104411

Du, K., Yang, C., Su, R., Tao, M., and Wang, S. (2020c). Failure Properties of Cubic Granite, marble, and sandstone Specimens under True Triaxial Stress. *Int. J. Rock Mech. Mining Sci.* 130, 104309. doi:10.1016/j.ijrmms.2020.104309

Eberhart, R., and Kennedy, J. (2002). "A New Optimizer Using Particle Swarm Theory," in Mhs95 Sixth International Symposium on Micro Machine & Human Science, Nagoya, Japan, 4-6 Oct. 1995 (IEEE).

Fu, L., Li, P., and G ao, L. (2021). Improved LSSVM Algorithm Considering Sample Outliers. *Chin. J. Scientific Instrument* 42 (06), 179–190. doi:10.19650/j.cnki.cjsi.J2107724

Gao, F., Yin, X., Liu, Q., Huang, X., Bo, Y., Zhang, T., et al. (2021). Coal-rock Image Recognition Method for Mining and Heading Face Based on Spatial Pyramid Pooling Structure. *J. China Coal Soc.* 46 (12), 4088–4102. doi:10.13225/j.cnki.jccs.2021.0624

He, Y., Tian, M., Song, J., Feng, J., and Dong, Z. (2020). Rock Hardness Identification Based on Cutting Motor Current of Roadheader. *Saf. Coal Mines* 138 (12), 159–162. doi:10.13347/j.cnki.mkaq.2020.12.032

Jiang, Y., Yang, X., He, F., Chen, L., and He, Z. (2016). Super-short-time Wind Power Forecasting Based on EEMD-IGSA-LSSVM[J]. *J. Hunan University(Natural Sciences)* 43 (10), 70–78. doi:10.16339/j.cnki.hdxbzkb.2016.10.009

Kennedy, J., and Eberhart, R. (1995). "Particle Swarm Optimization," in Icnn95-international Conference on Neural Networks, Perth, WA, Australia, 27 Nov.-1 Dec. 1995 (IEEE).

Li, L., and Ouyang, C. (2017). Research on Coal-Rock Interface Recognition Based on Ultrasonic Phased Array. *J. China Univ. Mining Tech.* 46 (03), 485–492. doi:10.13247/j.cnki.jcumt.000668

Liang, Y., Tiegen, L., Kun, L., Junfeng, J., and Yafan, L. (2021). Optimized Gas Detection Method Based on Variational Mode-Decomposition Algorithm. *Chin. J. Lasers* 48 (7), 0706003–706011. doi:10.3788/CJL202148.0706003

Liu, Y., Zhou, W., Guo, B., Ma, Q., and Xiao, H. (2020). Study on Similar Materials in Similar Simulation Test. *Chin. J. Rock Mech. Eng.* 39 (S1), 2795–2803. doi:10.13722/j.cnki.jrme.2019.0885

Sampath, K. H. S. M., Perera, M. S. A., Li, D., Ranjith, P. G., and Matthai, S. K. (2019). Characterization of Dynamic Mechanical Alterations of Supercritical Co2-Interacted Coal through Gamma-ray Attenuation, Ultrasonic and X-ray Computed Tomography Techniques - Sciencedirect. *J. Pet. Sci. Eng.* 174, 268–280. doi:10.1016/j.petrol.2018.11.044

Shi, X., Liu, B., and Xiao, J. (2015). A Method for Determining the Ration of Similar Materials with Cement and Plaster as Bonding Agents. *Rock Soil Mech.* 36 (05), 1357–1362. doi:10.16285/j.rsm.2015.05.017

Wang, C., and Zhang, Q. (2020). Coal Rock Image Feature Extraction and Recognition Method Based on LBP and GLCM. *Saf. Coal Mines* 51 (04), 129–132. doi:10.13347/j.cnki.mkaq.2020.04.028

Wang, H., and Zhang, Q. (2018). Dynamic Identification of Coal-Rock Interface Based on Adaptive Weight Optimization and Multi-Sensor Information Fusion. *Inf. Fusion* 51, 114–128. doi:10.1016/j.inffus.2018.09.007

Wang, S., Wang, S., and Liu, W. (2021a). The Measurement Model and Error Analysis for Shearer Cutting Height. *Chin. J. Sci. Instrument* 42 (04), 140–149. doi:10.19650/j.cnki.cjsi.J2107324

Wang, X., Ding, E., Hu, K., and &Zhao, R. (2016). Effects of Coal-Rock Scattering Characteristics on the GPR Detection of Coal-Rock Interface. *J. China Univ. Mining Tech.* 45 (01), 34–41. doi:10.13247/j.cnki.jcumt.000455

Wang, X., Gao, F., Chen, J., He, P., and Jing, Z. (2021b). Generative Adversarial Networks Based Sample Generation of Coal and Rock Images. *J. China Coal Soc.* 46 (09), 3066–3078. doi:10.13225/j.cnki.jccs.2020.1718

Wang, X., Zhao, D., and Ding, E. (2018). Coal-rock Identification Method Based on Terahertz Spectroscopy Technology. *Coal Mining Tech.* (01), 13–17+91. doi:10.13532/j.cnki.cn11-3677/td.2018.01.004

Yang, J., Zhang, Q., Wang, C., Chang, B., Wang, X., Ge, S., et al. (2020). Status and Development of Robotization Research on Roadheader for Coal Mines. *J. China Coal Soc.* (08), 2995–3005. doi:10.13225/j.cnki.jccs.2019.1452

Yin, Z., Chen, W., Hao, H., Chang, J., Zhao, G., Chen, Z., et al. (2019). Dynamic Compressive Test of Gas-Containing Coal Using a Modified Split Hopkinson Pressure Bar System. *Rock Mech. Rock Eng.* 53, 815–829. doi:10.1007/s00603-019-01955-w

Yin, Z. Q., Xi-Bing, L. I., Jin, J. F., Xian-Qun, H. E., and Kun, D. U. (2012). Failure Characteristics of High Stress Rock Induced by Impact Disturbance under Confining Pressure Unloading. *Chin. J. Mech. Eng.* 22, 175–184.

Zhang, J., Han, X., and Cheng, D. (2022). Improving Coal/gangue Recognition Efficiency Based on Liquid Intervention with Infrared Imager at Low Emissivity. *Measurement* 189, 110445. doi:10.1016/j.measurement.2021.110445

Zhang, Q., Liu, Z., and Qiu, J. (2017). Design of Cutting Vibration Signal Acquisition and Recognition System for a New Type of Shearer. *Colliery Mech. Electr. Tech.* (06), 1–4+8. doi:10.16545/j.cnki.cmet.2017.06.001

Zhang, Q., Sun, S., Zhang, K., Zhang, X., and Guo, T. (2020). Coal and Rock Interface Identification Based on Active Infrared Excitation. *J. China Coal Soc.* (09), 3363–3370. doi:10.13225/j.cnki.jccs.2019.0748

Conflict of Interest: The authors declare that the research was conducted in the absence of any commercial or financial relationships that could be construed as a potential conflict of interest.

frontiers | Frontiers in Earth Science

ORIGINAL RESEARCH
published: 23 May 2022
doi: 10.3389/feart.2022.903773

Composition and Characteristics of Rock Vibration Generated in Blasting Excavation of Deep Tunnels

Jianhua Yang[1,2,3], *Jinshan Sun*[1,2]*, *Yongsheng Jia*[1,2], *Yingkang Yao*[1,2], *Weipeng Zhang*[3] *and Tiejun Tao*[4]

[1]State Key Laboratory of Precision Blasting, Jianghan University, Wuhan, China, [2]Hubei Key Laboratory of Blasting Engineering, Jianghan University, Wuhan, China, [3]School of Infrastructure Engineering, Nanchang University, Nanchang, China, [4]School of Civil Engineering, Guizhou University, Guiyang, China

During blasting excavation in deep rock masses, the *in situ* stress initially exerted on blast-created free surfaces is rapidly released along with rock cracking by blasting. The rapid stress release can initiate seismic waves transmitting through the medium. In addition to explosion loading, the rapid stress release occurring on blast-created free surfaces is another excitation source of the rock vibration generated in blasting excavation of deep rock masses. In this paper, a theoretical model of seismic wave radiation from a circular blasting excavation in a deep rock mass is first developed to study the frequency differences between explosion seismic waves and stress release-induced seismic waves. Based on this, variational mode decomposition (VMD) is then introduced to separate explosion seismic waves and stress release-induced seismic waves from coupled vibration signals in the frequency domain. By utilizing the VMD separation, the composition and the amplitude and frequency characteristics of the rock vibration monitored in an actual deep tunnel blasting are investigated. The theoretical analysis and field investigation show that the vibration frequency of stress release-induced seismic waves is significantly lower than that of explosion seismic waves. Due to the existence of stress release-induced seismic waves with lower frequency, the coupled vibration amplitude is increased and vibration frequency is reduced. The monitored rock vibration in the near field is dominated by explosion seismic waves. However, in the far field, stress release-induced seismic waves become the major component due to their lower frequency and slower attenuation with distance. Extra care should be taken for the stress release-induced seismic waves in the far field. The stress release-induced seismic waves can be effectively reduced through shortening blast-created free surface sizes and increasing blasthole lengths moderately.

Keywords: deep tunnel, blasting excavation, in situ stress release, rock vibration, variational mode decomposition

Edited by:
Zhiqiang Yin,
Anhui University of Science and Technology, China

Reviewed by:
Gongda Lu,
Sichuan University, China
Lehua Wang,
China Three Gorges University, China
Xiuzhi Shi,
Central State University, United States

Correspondence:
Jinshan Sun
sunjinshan@jhun.edu.cn

Specialty section:
This article was submitted to Geohazards and Georisks, a section of the journal Frontiers in Earth Science

Received: 24 March 2022
Accepted: 02 May 2022
Published: 23 May 2022

Citation:
Yang J, Sun J, Jia Y, Yao Y, Zhang W and Tao T (2022) Composition and Characteristics of Rock Vibration Generated in Blasting Excavation of Deep Tunnels. Front. Earth Sci. 10:903773. doi: 10.3389/feart.2022.903773

INTRODUCTION

In mining, hydropower and transportation industries, the excavation of deep tunnels is becoming common. Mponeng gold mine in South Africa, which is the deepest mine in the world, has extended down to a depth exceeding 4,350 m (Nex and Kinnaird, 2019). At present in China, there are about 47 coal mines and 32 metal mines excavated at depths between 1,000 and 2,000 m below the ground surface (Xie et al., 2019). The maximum depth of the diversion tunnels in the Jinping-II hydropower station reaches 2,525 m (Fan et al., 2021). Bayu tunnel on the Sichuan-Tibet railway is constructed underground with a maximum depth of 2,080 m (He et al., 2021; Ma and Liu, 2022). With regard to mining and construction at a great depth, the greatest challenge to engineering safety is that the rock mass is subjected to high *in situ* stress. At a depth greater than 2,000 m below the surface, the *in situ* stress caused by gravity alone can reach a level comparable to the rock mass compressive strength. According to the *in situ* stress measurements in South African gold mines, the maximum principal stress at a depth from 1,000 to 3,400 m ranges between 80 and 146 MP (Ogasawara et al., 2014). High *in situ* stress is the decisive force that causes severe rock damage and hazards in deep mining and construction, such as spalling, v-shaped notches, rockbursts and mine earthquakes (Siren et al., 2015; Xie et al., 2017; Yin et al., 2020; Du et al., 2021; Feng et al., 2021; Kaiser and Moss, 2021; Si et al., 2021; Yang et al., 2021).

When cavities are excavated underground in highly stressed rock masses, some of strain energy stored in the rock masses is released. Theoretical and experimental studies have demonstrated that the speed of the stress or strain energy release has an important effect on the subsequent rock responses (Carter and Booker, 1990; He et al., 2015; Yang J. H. et al., 2018; Li M. et al., 2020; Xu et al., 2020). (Miklowitz, 1978), (Carter and Booker, 1990), (Yang J. H. et al., 2018) and Xu et al. (2020) deemed that the transient release of the stress that was initially exerted on an elastic medium would initiate stress waves transmitting through the medium. Such stress fluctuations are unobvious or even not generated when a slower stress release occurs. For the current mining and construction in deep rock masses, drilling and blasting is still the main method for rock fragmentation and removal (Huo et al., 2021; Chen et al., 2022). During rock fragmentation by blasting, free surfaces are created almost instantaneously and meanwhile the *in situ* stress initially exerted on these faces is rapidly released. According to the observations by using high-speed photography, this process occurs over a period of several milliseconds or even less, depending on rock and explosive properties, confined conditions and blasthole layouts (He and Yang, 2018; Ding et al., 2021).

Related studies have shown that the rapid *in situ* stress release occurring during explosion or blasting could induce stress waves or seismic waves, leading to vibration in nearby structures (Toksöz and Kehrer, 1972; Carter and Booker, 1990; Lu et al., 2012; Yang et al., 2022). This phenomenon was first noticed in underground nuclear explosions. In underground nuclear explosion tests, horizontally polarized shear waves (SH and Love waves) were often observed along with P, SV and Rayleigh waves (Toksöz et al., 1965). Theoretically, in a horizontally layered, homogeneous and isotropic medium that is not pre-stressed, an explosive source with radial symmetry should not generate any SH and Love waves. Through numerous studies, it was found that in a pre-stressed rock medium, the rapid stress release along with explosion-induced rock fracture was responsible for the generation of the horizontal shear waves (Toksöz and Kehrer, 1972). (Press and Archambeau, 1962) studied the radiation pattern of the seismic waves due to an induced rupture in a stressed medium. His studies reveal that all the stress conditions give symmetric quadrupole radiation patterns. (Toksöz and Kehrer, 1972). researched the vibration magnitude of the seismic waves resulted from the release of tectonic strain energy during underground nuclear explosions. Their results show that the strain energy related vibration component of the surface waves can exceed the component due to the explosion itself in some cases.

In mining and construction blasts, the seismic waves and structural vibration due to *in situ* stress release also receive attention in recent years as the excavation depth and the *in situ* stress level increase. In surveying the rock vibration induced by blasting excavation of deep hydraulic tunnels, (Lu et al., 2012), and (Yang J. et al., 2018) observed that the vibration amplitude was higher than that expected when high *in situ* stress was present. Through numerical studies, they further concluded that if the *in situ* stress reached a level higher than 50 MPa, the rapid release of *in situ* stress could generate comparable vibration velocity to that caused by blast loading (Lu et al., 2012; Cao et al., 2016; Li C. et al., 2020) found that the vibration amplitude of the stress release-induced seismic waves also depended on stress release rates and paths. A non-linear stress release over a shorter period produces a greater vibration velocity. After summarizing these influencing factors, (Lu et al., 2017), developed a semi-empirical formula for predicting the peak particle velocity (PPV) of the stress release-induced seismic waves. In addition, Tao et al. (2013), Zhu et al. (2014), Li M. et al. (2020), and Tao et al. (2021) studied the rock damage responses under the disturbance of rapid *in situ* stress release. These studies also demonstrate that in mining and construction blasts under high *in situ* stress conditions, the rapid stress release occurring on blast-created free surfaces is an important dynamic disturbance that cannot be ignored.

It is seen that during blasting excavation in highly stressed rock masses, the monitored rock vibration includes not only seismic waves caused by explosion, but also seismic waves induced by rapid release of *in situ* stress. However, there is no obvious demarcation point between these two types of waves in the time domain because the *in situ* stress release on the excavation boundaries occurs along with rock fragmentation by blasting. This brings a great trouble to study the respective vibration component from the field monitoring data. Because of this, the above studies with respect to the stress release-induced seismic waves were conducted mainly by using numerical modeling methods, in which blast loading and stress release can be performed separately. There are few researches reported on the vibration composition analysis based on an effective separation of explosion seismic waves and stress release-induced seismic waves from monitored vibration signals. Recently, a novel variational method, called variational mode decomposition (VMD), was proposed in the field of tone detection, tone separation and noise robustness for decomposing a signal into different modes of unknown but separate spectral bands (Dragomiretskiy and Zosso, 2014). In comparison to existing decomposition models, like the empirical mode decomposition (EMD), the VMD model is theoretically well

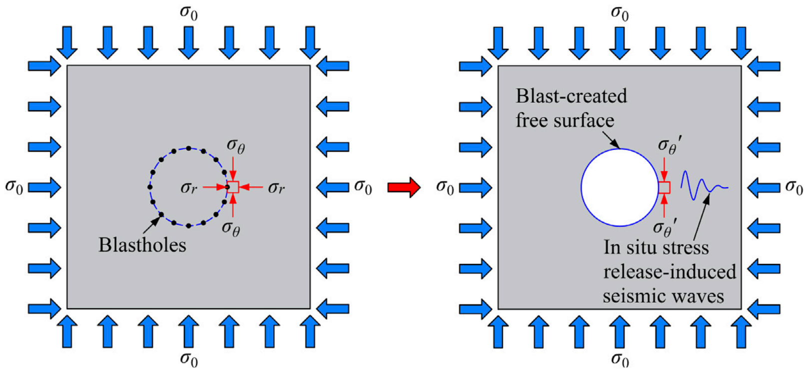

FIGURE 1 | Diagram of the rapid *in situ* stress release occurring on blast-created free surfaces.

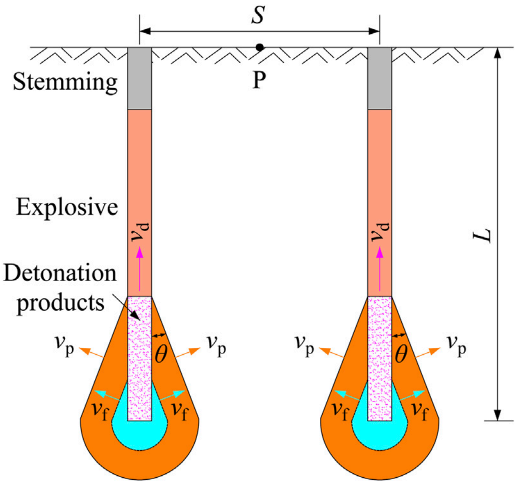

FIGURE 2 | Diagram of the mach cone formation around blastholes.

founded and still easy to understand. Furthermore, this model determines the relevant bands adaptively and estimates the corresponding modes concurrently, thereby properly balancing the errors between them. Due to these advantages, the VMD algorithm has been successfully applied to the identification and separation of rock fracturing microseismic signals form blasting vibration signals (Zhang et al., 2018).

In this study, a mathematical physics model of seismic wave radiation from a circular blasting excavation in a deep rock mass is first developed to analyse the frequency differences between explosion seismic waves and stress release-induced seismic waves. Then the VMD method is utilized to separate explosion seismic waves and stress release-induced seismic waves from the monitored vibration signals in the blasting excavation of the experimental tunnels in China Jinping Underground Laboratory (CJPL). The applicability of the VMD method in the separation is verified by a numerical test. Based on the separated results of the field monitoring data, the composition of the monitored vibration, and the PPV attenuation and frequency characteristics of the respective vibration are investigated.

THEORETICAL ANALYSIS OF ROCK VIBRATION INDUCED BY RAPID IN SITU STRESS RELEASE

In Situ Stress Release Process on Blast-Created Free Surfaces

In tunnel blasting, a row of blastholes are often detonated at the same time. The interactions of explosion-induced stress waves from adjacent blastholes encourage rock cracks to grow preferentially along the connecting line between the adjacent blastholes. The highly cracked zone between the adjacent blastholes becomes a preferential path for detonation gases to escape due to the weakest resistance. The high gas pressure causes the cracks to further extend in the direction of the connecting line. When the cracks between the adjacent blastholes are completely connected, a new free surface is created. It should be noted that in actual rock blasts, particularly in cut hole blasting and caving hole blasting, the shape of blast-created free surfaces are complicated because blast-induced cracks radiate around blastholes and interact with each other. To facilitate theoretical analysis, it is considered that the new free surface is generated along the center line of the blastholes in the same row, as shown in **Figure 1**. During the formation of the new free surface, the *in situ* stress initially exerted on this surface is rapidly released along with the blast-induced rock cracking. Therefore, the period of the *in situ* stress release occurring on blast-created free surfaces approximates the duration of the crack propagation through the zone between adjacent blastholes.

Cylindrical charges with detonation initiation at the bottom are commonly used in tunnel blasting. After the explosive at the blasthole bottom is detonated, detonation waves spread upwards at a limited velocity to fire the explosives at other locations. Affected by the propagation of the detonation waves, the dominant wave radiation in the near field of the blastholes is in the form of cone-shaped Mach waves, as shown in **Figure 2**. The Mach cone is described by the Mach number $M = v_d/v_p$ and Mach angle $\theta = \arcsin(1/M)$, where v_d is the velocity of detonation and v_p is the velocity of wave propagation in the rock medium. It is assumed that the blastholes in the same row are detonated

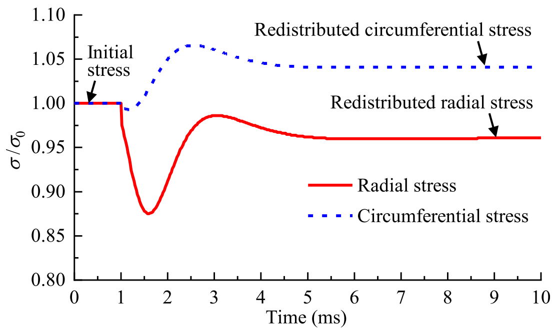

FIGURE 3 | Stress waves induced by the rapid *in situ* stress release in a circular excavation (Yang J. H. et al., 2018).

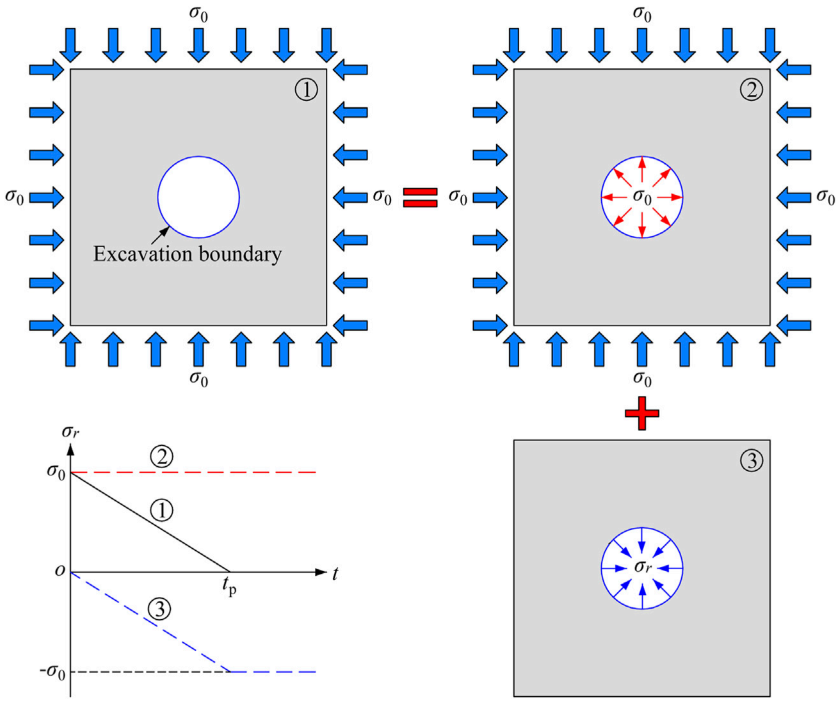

FIGURE 4 | Equivalent model of a circular excavation under a hydrostatic *in situ* stress field.

precisely at the same time and generate the same Mach waves. When the Mach wave fronts reach the midpoint P of the connecting line, the zone between the adjacent blastholes is entirely covered by the Mach waves. Then the rock mass between the adjacent blastholes is fully cracked by the Mach waves and a new free surface is created. According to the propagation path of the Mach waves, when the cracks between the adjacent blastholes are completely connected, the length of the longest crack d is (Blair, 2010):

$$d = \frac{L}{M} + \frac{S\sqrt{M^2 - 1}}{2M} \tag{1}$$

where L is the blasthole length, and S is the space between the adjacent blastholes.

It is assumed that the blast-induced cracks grow at a constant velocity v_f. Then the duration for the crack penetration between the adjacent blastholes, i.e., the period of the *in situ* stress release occurring on blast-created free surfaces can be estimated by t_p:

$$t_p = \frac{d}{v_f} = \frac{L}{M v_f} + \frac{S\sqrt{M^2 - 1}}{2M v_f} \tag{2}$$

The full-face blasting excavation of deep tunnels normally uses short blastholes with a length ranging from 1.5 to 5.0 m and a space varying from 0.5 to 1.5 m. The velocity of detonation v_d = 5,500 m/s, the rock P-wave velocity v_p = 4,000 m/s, and the stable crack propagation velocity $v_f = 0.25 v_p$ = 1,000 m/s are considered in this study. Then it is estimated from **Eq. 2** that the period of the *in situ* stress release on blast-created free surfaces is in the range of 1.3–4.2 ms with respect to the short-hole blasting in deep tunnels. For the rock mass with a Young's modulus E = 10–100 GPa, if the initial stress reaches a level of 20–50 MPa, the strain rate due to the rapid stress release over the period of 10^0–10^1 ms can attain 10^{-1}–10^1 s^{-1}. According to the classification standard of statics and dynamics (Aydan, 2017), this is a dynamic mechanical process in which the inertial force cannot be ignored. The studies of Carter and Booker (1990), Zhu et al. (2014), Yang J. H. et al. (2018) and Tao et al. (2021) also demonstrate that the rapid *in situ* stress release in a circular excavation generates stress fluctuations transmitting through the medium, as presented in

Figure 3. The stress fluctuations give rise to higher circumferential stress and lower radial stress than the final static stress values in a transient time. This causes greater deviatoric stress and thus produces a larger compression-shear damage zone around the excavation under high *in situ* stress conditions. Beyond the damage zone, the stress waves continue to spread outward as elastic seismic waves, thereby inducing vibration in the surrounding rock mass.

Theoretical Solution Procedure

The PPV characteristics of the rock vibration induced by the rapid *in situ* stress release have been reported in some literature (Cao et al., 2016; Lu et al., 2017). However, the frequency content of the stress release-induced seismic waves receives much less attention. This section focuses on investigating the frequency differences between explosion seismic waves and stress release-induced seismic waves so as to provide a basis for the following VMD separation between them. The investigation is based on the theoretical solution of the seismic wave radiation from a circular excavation reported by Carter and Booker (1990). To facilitate the theoretical solution, a hydrostatic *in situ* stress condition is considered. The rock medium is considered to be homogeneous, isotropic and linear elastic. Under these assumptions, the creation of a deep circular cavity by the removal of the stressed rock mass is mechanically equivalent to the application of a traction on the excavation boundary (Carter and Booker, 1990), as shown in **Figure 4**. The traction load starts from zero and then increases to the initial *in situ* stress σ_0 over the short period t_p. The impulsive traction load will induce stress waves to transmit through the rock medium. It is assumed that the explosion pressure and *in situ* stress are uniform along the blasthole axis. Then the circular excavation can be simplified as a plane strain problem. The motion of applying an impulsive traction load on a circular inner boundary under the condition of plane strain is governed by the equation:

$$\frac{\partial^2 u}{\partial r^2} + \frac{\partial}{\partial r}\left(\frac{u}{r}\right) = \frac{1}{v_p^2}\frac{\partial^2 u}{\partial t^2} \tag{3}$$

where u is the radial displacement, r is the distance to the center, t is time, and v_p is the velocity at which P-waves pass through the rock medium. The quantity v_p is given by:

$$v_p = \sqrt{\frac{\lambda + 2G}{\rho}} \tag{4}$$

where λ and G are Lame constants, and ρ is the rock density.

The initial condition of the motion **Eq. 3** is:

$$u(r,0) = \frac{\partial u(r,0)}{\partial t} = 0, \quad (r \geq a) \tag{5}$$

where a is the radius of the circular excavation.

The boundary condition of the motion **Eq. 3** is the traction load on the inner boundary. It is determined by the path of the rapid *in situ* stress release occurring on blast-created free surfaces. Unfortunately, the stress release path has not been clearly figured out as the blast-induced crack initiation and growth is complicated. Since the cracks are assumed to spread at a constant velocity, therefore, a linear stress release path, in which the initial *in situ* stress is reduced from σ_0 to zero at a constant rate over the period t_p, is adopted in the theoretical solution. Under the action of *in situ* stress, it is conventionalized that the compressive stress is in positive and the tensile stress is in negative. Then the boundary condition is expressed as:

$$\sigma_r(a,t) = \begin{cases} -\dfrac{t}{t_p}\sigma_0, & (0 \leq t \leq t_p) \\ -\sigma_0, & (t > t_p) \end{cases} \tag{6}$$

where σ_r is the radial stress.

In order to obtain the complete solution to this problem, it is convenient to take a Laplace transform of the governing **Eq. 3** as follows (Carter and Booker, 1990):

$$r^2\frac{\partial^2 \bar{u}}{\partial r^2} + r\frac{\partial \bar{u}}{\partial r} - \left[1 + \left(\frac{sr}{v_p}\right)^2\right]\bar{u} = 0 \tag{7}$$

where the superior bar denotes a Laplace transform, and s is the Laplace transform parameter.

Taking Laplace transforms of the initial and boundary conditions and applying them to **Eq. 7** yield (Miklowitz, 1978):

$$\bar{u}(r,s) = \frac{\sigma_0}{t_p}\cdot\frac{f(s)K_1(sr/v_p)}{(2G/a)K_1(sa/v_p) + (\lambda + 2G)(s/v_p)K'_1(sa/v_p)} \tag{8}$$

with,

$$f(s) = \left(e^{-t_p s} - 1\right)/s^2 \tag{9}$$

where K_1 is the second kind of the modified Bessel functions.

The vibrational waveform at any position is usually represented by the particle velocity history $v(r, t)$. According to the velocity-displacement relationship $v(r,t) = \partial u(r,t)/\partial t$, the Laplace transform of $v(r, t)$ can be obtained by:

$$\begin{aligned}\bar{v}(r,s) &= s\bar{u}(r,s) \\ &= \frac{\sigma_0}{t_p}\cdot\frac{sf(s)K_1(sr/v_p)}{(2G/a)K_1(sa/v_p) + (\lambda + 2G)(s/v_p)K'_1(sa/v_p)}\end{aligned} \tag{10}$$

Eq. 10 gives the solution to the Laplace transform of the velocity history $v(r, t)$ in terms of the modified Bessel function and its derivative. In order to recover the actual velocity history, **Eq. 10** needs to be inverted. This can be achieved efficiently by using the numerical contour integration developed by Talbot (1979). The core of this algorithm is to construct a trapezoidal integration along a special contour, and then the results are obtained through resorting to the residue theorem. Details of the numerical inversion are given in the literature of Talbot (1979) and Cao et al. (2016).

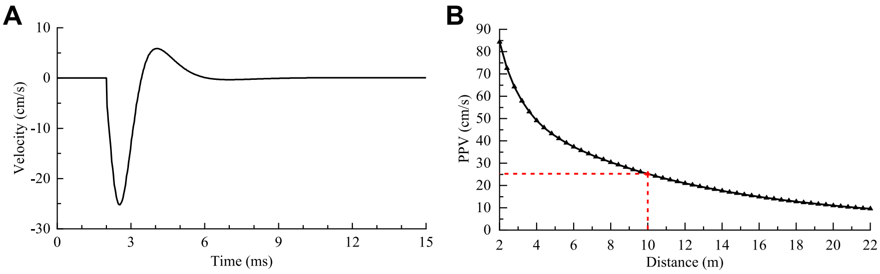

FIGURE 5 | Velocity history and PPV of the rock vibration induced by rapid *in situ* stress release. **(A)** Velocity history at $r = 5a$, **(B)** PPV variation with distance.

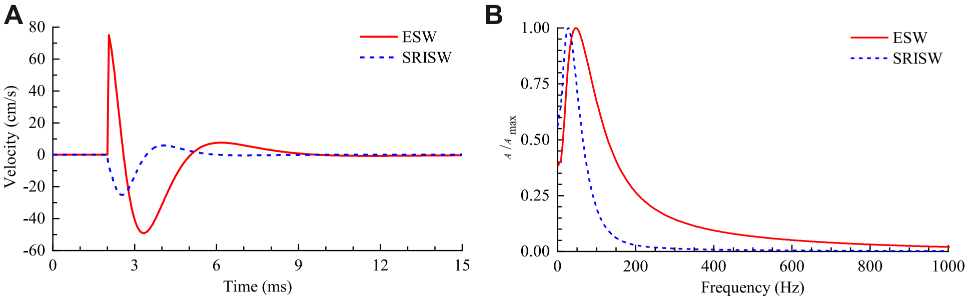

FIGURE 6 | Comparisons of the explosion seismic wave (ESW) and the stress release-induced seismic wave (SRISW). **(A)** Velocity histories at $r = 5a$, **(B)** Normalized amplitude-frequency spectra of the velocity histories.

Rock Vibration Induced by Rapid in Situ Stress Release

In the theoretical solution to the rock vibration induced by rapid *in situ* stress release, the following parameters are considered: $E = 50$ GPa, $v_{\mathrm{p}} = 4{,}000$ m/s, $\sigma_0 = 30$ MPa, $t_{\mathrm{p}} = 2.0$ ms, and $a = 2.0$ m. **Figure 5** presents the typical particle velocity history observed at the distance $r = 5a = 10$ m and the PPV variation with distance obtained from the theoretical solution. The peak vibration velocity due to the rapid *in situ* stress release reaches 84 cm/s on the excavation boundary at $r = a = 2$ m. With an increase in the distance, the PPV gradually decreases due to geometric spreading and damping attenuation. At the distance $r = 5a = 10$ m, the PPV is still as high as 25 cm/s. It exceeds the allowable PPV limit stipulated in the Chinese standard for hydraulic tunnels under blasting vibration, in which the PPV less than 15 cm/s is allowed. Therefore, the rock vibration caused by rapid *in situ* stress release cannot be ignored with regard to blasting excavation of deep tunnels under high *in situ* stress conditions.

The *in situ* stress release occurring on blast-created free surfaces proceeds along with explosive detonation. The explosion load is another important source of the rock vibration caused by blasting excavation in highly stressed rock masses. The explosion seismic wave radiation from a circular excavation can also be solved theoretically through the above procedure provided that the explosion load is equivalently applied to the excavation boundary. This problem has been studied by Yang J. H. et al. (2018) when investigating the dynamic stress change and rock damage during blasting excavation in a deep circular tunnel. The velocity history of the explosion-induced rock vibration can be obtained by simply replacing **Eqs 9**, **10** with the following formulas:

$$f(s) = \left(t_{\mathrm{d}}e^{-t_{\mathrm{r}}s} - t_{\mathrm{r}}e^{-t_{\mathrm{d}}s} - t_{\mathrm{d}} + t_{\mathrm{r}}\right)/s^2 \tag{11}$$

$$\bar{v}(r,s) = \frac{P_{\mathrm{e}}}{t_{\mathrm{r}}(t_{\mathrm{d}} - t_{\mathrm{r}})} \cdot \frac{s f(s) K_1(sr/v_{\mathrm{p}})}{(2G/a)K_1(sa/v_{\mathrm{p}}) + (\lambda + 2G)(s/v_{\mathrm{p}})K'_1(sa/v_{\mathrm{p}})} \tag{12}$$

where P_{e} denotes the peak pressure of the equivalent explosion load on the excavation boundary, and t_{r} and t_{d} are the rise time and duration of the explosion load. According to the research of Yang J. H. et al. (2018), $P_{\mathrm{e}} = 100$ MPa, $t_{\mathrm{r}} = 0.1$ ms, and $t_{\mathrm{d}} = 0.9$ ms are considered in this theoretical study.

Figure 6A shows the velocity histories of the explosion-induced rock vibration and the stress release-induced rock vibration at $r = 5a = 10$ m. At this distance, the PPV of the explosion seismic wave is much higher than that of the stress release-induced seismic wave, and the explosion seismic wave dominates the rock vibration at this position. Taking Fourier transforms of the velocity histories gives the amplitude-frequency spectra of these two types of waves, as shown in **Figure 6B**. For facility of comparison, the normalized amplitude, i.e., the ratio of the current amplitude to its maximum value is presented on the coordinate. For the explosion seismic wave, the vibration frequency is mainly distributed in the band 0–1,000 Hz. In

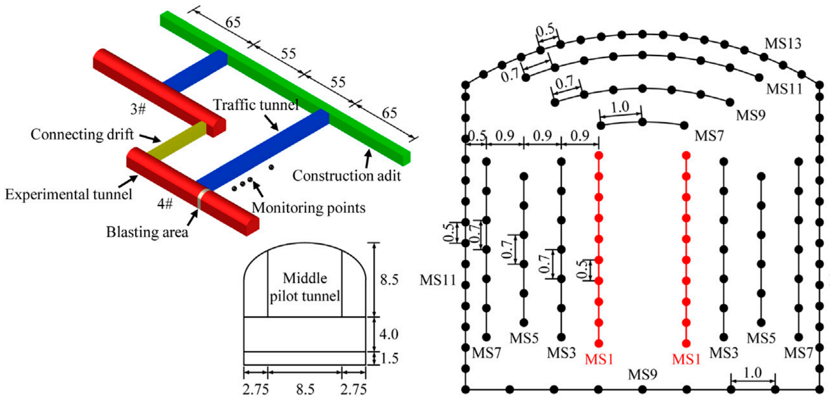

FIGURE 7 | Blasting design of the pilot tunnel and the arrangement of the vibration monitoring.

comparison, the frequency distribution of the stress release-induced seismic wave is narrower, mainly lying within 0–400 Hz. The mean or center frequency f_m normally serves as a characteristic frequency of the average spectral measure. The mean frequencies are 240 Hz and 91 Hz, respectively, for the explosion seismic wave and the stress release-induced seismic wave. In summary, the frequency of the stress release-induced rock vibration is significantly lower than that of the explosion-induced rock vibration at the same position. This is simply because the vibration frequency depends on loading or unloading rates, and the period of the *in situ* stress release is much longer than the rise time of the explosion load. The difference in the frequency content makes it possible to use the VMD method to separate explosion seismic waves and stress release-induced seismic waves from monitored rock vibration.

FIELD INVESTIGATION OF ROCK VIBRATION COMPOSITION FOR BLASTING EXCAVATION OF A DEEP TUNNEL

The above theoretical analysis demonstrates that during blasting excavation under high *in situ* stress conditions, the rapid stress release occurring on blast-created free surfaces can indeed generate non-negligible rock vibration. It also shows that the stress release-induced rock vibration is significantly different from the explosion-induced rock vibration in frequency content. In this section, the rock vibration composition and characteristics for blasting excavation in highly stressed rock masses are further analyzed by using field monitoring data. As mentioned earlier, the field data analysis relies on an effective separation of explosion seismic waves and stress release-induced seismic waves from the monitored vibration. In the present study, the VMD method is introduced in an attempt to achieve this separation. The VMD is a signal processing method based on the frequency domain, and hence the above frequency content analysis can provide a theoretical basis for the following VMD separation.

Site Description

The field rock vibration monitoring was carried out during the blasting excavation of the experimental tunnels in China Jinping Underground Laboratory (CJPL). CJPL is located in Jinping Mountain in Sichuan Province, China. It is the deepest underground laboratory currently in operation in the world. By utilizing the construction adit as the entrance, four groups of experimental tunnels and traffic tunnels and two connecting drifts are excavated for this underground laboratory, as shown in **Figure 7**. The excavation size of each experimental tunnel is 130 m long, 14 m wide and 14 m high. The drilling and blasting method is used in the excavation of the experimental tunnels. In order to minimize the adverse effects of blasting, the blasting excavation of the experimental tunnels is divided into three horizontal layers. Each layer has a height of 8.5 m, 4.0 m and 1.5 m, respectively.

In the upper layer, a horizontal pilot tunnel measuring 8.5 m wide and 8.5 m high is first created in the middle prior to the two sides. The blasthole arrangement and detonation network for the pilot tunnel excavation are shown in **Figure 7**. The blastholes in an excavation cycle are detonated sequentially in seven delays with time intervals of 50–200 ms. Short holes with a length of 3.5 m and a diameter of 50 mm are used in the pilot tunnel blasting. The space between the adjacent blastholes in the same delay varies from 0.5 to 1.0 m. The tunnels and drifts in CJPL are excavated at depths greater than 2000 m, and the maximum excavation depth is 2,375 m. The *in situ* stress tests in the experimental tunnels show that the maximum principal stress reaches 50–70 MPa. For the pilot tunnel that is first excavated, it is a typical case of rock blasting excavation under high *in situ* stress. Therefore, in this case, the rapid *in situ* stress release occurring on blast-created free surfaces is likely to be an important excitation source to induce rock vibration.

Vibration Monitoring and Rock Vibration

During the blasting excavation of the pilot tunnel in No. Four experimental tunnel, four vibration sensors are installed inside the surrounding rock mass of the traffic tunnel to monitor the

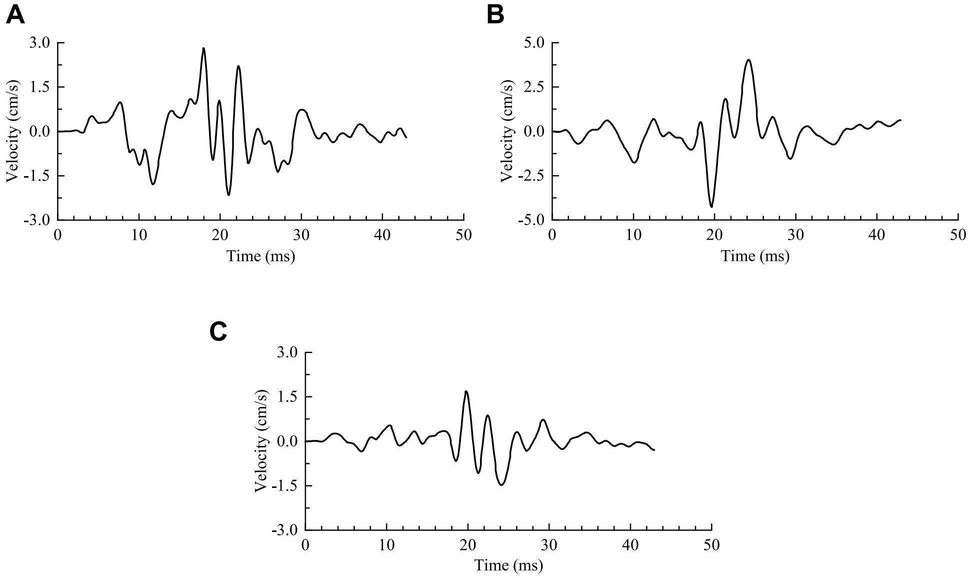

FIGURE 8 | Velocity histories monitored on site during the cut hole blasting. **(A)** Transverse component, **(B)** Vertical component, **(C)** Longitudinal component.

rock vibration, as shown in **Figure 7**. At each monitoring point, a triaxial velocity sensor is used to measure the transverse, vertical and longitudinal velocity histories. A total of five tests were carried out in the rock vibration monitoring. The distance from the monitoring points to the explosion source varies from 20 to 80 m.

The monitored vibration velocity histories at each point include seven sub-waveforms, corresponding to the seven delays of blasting mentioned above. Among these sub-waveforms, the one caused by the cut hole blasting in the first delay has the maximum vibration velocity due to its dense charge and lack of sufficient free surfaces. Furthermore, in this delay, the blasting excavation boundary (the connecting line of the blastholes in the first delay) is subjected to the highest *in situ* stress. The rock vibration resulted from the rapid stress release is also the most obvious in this delay. Therefore, the sub-waveforms produced in the cut hole blasting in the first delay are chosen for the following analysis. **Figure 8** presents the velocity histories of the sub-waveforms recorded at No. One monitoring point in the first test. These waves are body waves as the monitoring points are placed inside the surrounding rock mass. Under this scenario, the interference of surface waves on the following analysis can be eliminated.

Separation Method: Variational Mode Decomposition

The vibration waveforms presented in **Figure 8** contain explosion seismic waves and stress release-induced seismic waves. These two types of waves do not have an obvious demarcation point in the time domain, but have a significant difference in the frequency domain. Because of this, the VMD method, which is based on the frequency domain, is utilized to separate the explosion seismic waves and the stress release-induced seismic waves from the monitored vibration waveforms. The VMD method is a novel, entirely non-recursive and adaptive variational method for decomposing an input signal into a discrete number of intrinsic mode functions (Dragomiretskiy and Zosso, 2014). The VMD model looks for an ensemble of modes that reconstruct the given input signal optimally, and each mode is band-limited around a center frequency. In this model, the relevant bands are determined adaptively and the corresponding modes are estimated concurrently, thereby balancing the errors between them properly. Compared with the EMD model, the VMD model is theoretically well founded and overcomes the problems of modal aliasing and boundary effects in the EMD. In addition, it gets rid of the requirement of predefining base functions that are used in the wavelet approaches.

The goal of VMD is to decompose an input signal $f(t)$ into K discrete sub-signals (intrinsic mode functions), $u_k(t)$, which have specific sparsity properties when reconstructing the input signal. The bandwidth of each mode is chosen to be its sparsity prior. Each mode is considered to be mostly compact around a center frequency $\omega_k(t)$, which is determined along with the decomposition. The intrinsic mode function $u_k(t)$ is defined as an amplitude-modulated-frequency-modulated signal, written as:

$$u_k(t) = A_k(t)\cos\left[\varphi_k(t)\right] \quad (k = 1, \ldots, K) \tag{13}$$

where $A_k(t)$ is the instantaneous amplitude of $u_k(t)$, and $\varphi_k(t)$ is the instantaneous phase, and t is time.

In order to assess the bandwidth of each mode and reconstruct the given input signal exactly, the sum of the bandwidths of all modes is required to be minimized and the sum of all modes should be equal to the input signal. Then the resulting constrained variational problem is expressed as (Dragomiretskiy and Zosso, 2014):

$$\begin{cases} \min\limits_{\{u_k\},\{\omega_k\}} \left\{ \sum\limits_k \left\| \partial_t \left[\left(\delta(t) + \frac{j}{\pi t} \right) * u_k(t) \right] e^{-j\omega_k t} \right\|_2^2 \right\} \\ s.t. \ \sum\limits_k u_k(t) = f(t) \end{cases} \tag{14}$$

where $\{u_k\} = \{u_1, \ldots, u_K\}$ and $\{\omega_k\} = \{\omega_1, \ldots, \omega_K\}$ are respectively the shorthand notations for the sets of all modes and their center frequencies, $\delta(t)$ is the Dirac distribution function, j is the imaginary unit, and $*$denotes convolution.

In addressing the constrained problem, a quadratic penalty term α and a Lagrangian multiplier $\lambda(t)$ are introduced to render the problem unconstrained. The combination of these two terms benefits both from the nice convergence properties of the quadratic penalty and the strict execution of the constraint by the Lagrangian multiplier (Dragomiretskiy and Zosso, 2014). Consequently, the augmented Lagrangian equation La is obtained as follows:

$$\begin{aligned} La(\{u_k\}, \{\omega_k\}, \lambda) = {} & \alpha \sum_k \left\| \partial_t \left[\left(\delta(t) + \frac{j}{\pi t} \right) * u_k(t) \right] e^{-j\omega_k t} \right\|_2^2 \\ & + \left\| f(t) - \sum_k u_k(t) \right\|_2^2 + \langle \lambda(t), f(t) \\ & - \sum_k u_k(t) \rangle \end{aligned} \tag{15}$$

The solution to the original constraint problem **Eq. 14** is the saddle point of the augmented Lagrangian equation in a sequence of iterative sub-optimizations (Rockafellar, 1973). The solutions of the sub-optimizations are the following:

$$\hat{u}_k^{n+1}(\omega) = \frac{\hat{f}(\omega) - \sum_{i<k} \hat{u}_i^{n+1}(\omega) - \sum_{i>k} \hat{u}_i^{n}(\omega) + \hat{\lambda}^{n}(\omega)/2}{1 + 2\alpha\left(\omega - \omega_k^n\right)^2} \tag{16}$$

$$\omega_k^{n+1} = \frac{\int_0^\infty \omega \left| \hat{u}_k^{n+1}(\omega) \right|^2 \mathrm{d}\omega}{\int_0^\infty \left| \hat{u}_k^{n+1}(\omega) \right|^2 \mathrm{d}\omega} \tag{17}$$

$$\hat{\lambda}^{n+1}(\omega) = \hat{\lambda}^{n}(\omega) + \tau \left[\hat{f}(\omega) - \sum_k \hat{u}_k^{n+1}(\omega) \right] \tag{18}$$

where ω is the frequency, the superscript ^ denotes a Fourier transform, and τ is the update parameter of the Lagrangian multiplier.

The solutions of the sub-optimizations are plugged into the alternating direction method of multipliers (ADMM) algorithm to update the modes and their center frequencies and search for the saddle points. Then the optimal solution to the constrained variational problem is obtained, and the input signal is decomposed into an ensemble of band-limited modes and their center frequencies. The steps for the complete optimization of VMD are as follows. First, an original signal $f(t)$ and the total number of modes to be decomposed K are input. Then the mode functions $\{\hat{u}_k^1\}$, center frequencies $\{\omega_k^1\}$ and the Lagrangian multiplier $\hat{\lambda}^1$ are initialized, and $n = 0$ is assigned. The third step is to iterate $n \leftarrow n + 1$ and update $\hat{u}_k$, ω_k and $\hat{\lambda}$ respectively by using **Eq. 16–18** for $k = 1, \ldots, K$. The iteration and update processes end and K mode functions are output until the following convergence condition is satisfied,

$$\sum\nolimits_k \frac{\left\| \hat{u}_k^{n+1} - \hat{u}_k^{n} \right\|_2^2}{\left\| \hat{u}_k^{n} \right\|_2^2} < \varepsilon \tag{19}$$

where ε is the tolerance of convergence. In this study, $\varepsilon = 10^{-7}$ is considered.

Verification of the VMD Separation

The VMD is a robust signal decomposition method in the frequency domain that can adaptively seek the optimal bandwidth and center frequency for each mode. In this study, the VMD is introduced in attempt to decompose the monitored rock vibration signals mentioned above into explosion seismic waves and stress release-induced seismic waves. Before performing VMD separation on the field monitoring data, the applicability of the VMD method in the vibration separation needs to be verified. The theoretically calculated seismic waves as shown in **Figure 6A** are simple in waveforms and frequency content, which are quite different from the rock vibration measured on site. Therefore, the theoretical waveforms are incompetent to verify the applicability of VMD in the vibration separation. With regard to the field monitoring vibration, it is coupled waveforms that contain explosion seismic waves and stress release-induced seismic waves. The respective vibration waveforms cannot be measured directly and compared with the VMD separation results. In this regard, numerical modeling is an optimal approach as it can simulate both the respective vibration waves and the coupled vibration waves. Furthermore, the simulated vibration waveforms through three-dimensional modeling are more similar to the measured vibration signals. Therefore, a numerical test is conducted in this study to verify the applicability of VMD. In the verification, the simulated coupled vibration caused by the combined actions of explosion loading and rapid *in situ* stress release is first presented. Then the VMD method is employed to decompose the coupled vibration into explosion seismic waves and stress release-induced seismic waves. Finally, the separated waves are compared with the simulated vibrations respectively caused by explosion loading and stress release.

We have carried out a three-dimensional modeling of the rock vibrations caused by explosion loading, rapid stress release and their combined actions for the blasting excavation of the pilot tunnel in CJPL. The numerical modeling is performed in the FEM software ANSYS/LS-DYNA by using its implicit and explicit solutions in sequence. The initial *in situ* stress is first pre-loaded on the exterior boundaries of the numerical model. Then the implicit solver in ANSYS is launched to compute the element stress and deformation. These information is transmitted to the explicit program LS-DYNA to initialize the stress and deformation of the explicit elements. After that, the explosion load is applied and the stress initially exerted on the blast-created free surfaces is rapidly released in a specific path. The explicit solver in LS-DYNA is finally implemented to compute the element velocity under the dynamic loads. The geometric model, material parameters, loads and boundary conditions, simulation procedures and verification of the modeling have been given

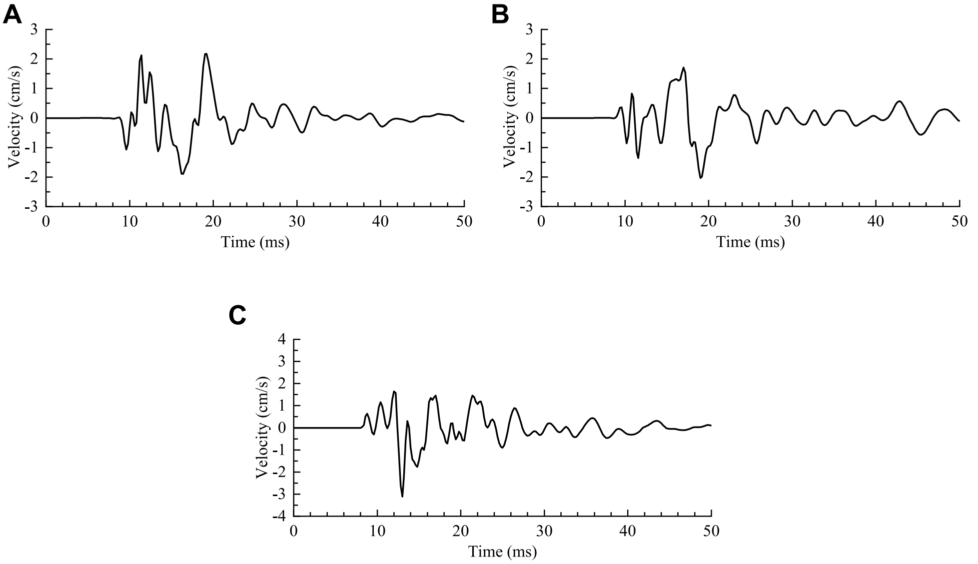

FIGURE 9 | Simulated vibration velocity histories caused by the combined actions of explosion loading and rapid stress release. **(A)** Transverse component, **(B)** Vertical component, **(C)** Longitudinal component (Yang J. et al., 2018).

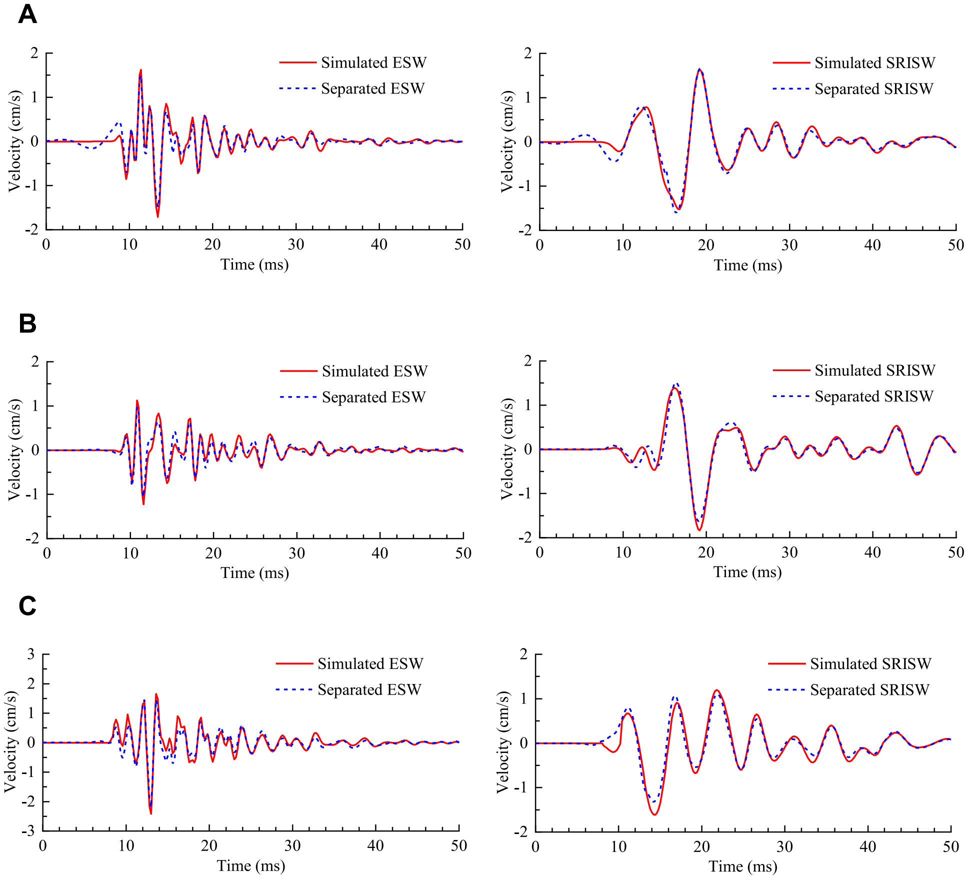

FIGURE 10 | Comparisons between the separated seismic waves based on VMD and the simulated seismic waves. **(A)** Transverse component, **(B)** Vertical component, **(C)** Longitudinal component.

TABLE 1 | PPV of the respective seismic waves obtained by the numerical modeling and the VMD separation.

Direction	Explosion seismic waves			Stress release-induced seismic waves		
	Numerical modeling (cm/s)	VMD separation (cm/s)	Relative difference (%)	Numerical modeling (cm/s)	VMD separation (cm/s)	Relative difference (%)
Transverse	1.71	1.50	−12.41	1.63	1.66	1.48
Vertical	1.23	1.06	−13.53	1.83	1.63	−11.03
Longitudinal	2.42	2.20	−9.24	1.61	1.32	−17.88

TABLE 2 | Center frequency of the respective seismic waves obtained by the numerical modeling and the VMD separation.

Direction	Explosion seismic waves			Stress release-induced seismic waves		
	Numerical modeling (Hz)	VMD separation (Hz)	Relative difference (%)	Numerical modeling (Hz)	VMD separation (Hz)	Relative difference (%)
Transverse	484.2	513.5	6.04	154.2	154.5	0.23
Vertical	545.6	581.2	6.52	162.3	165.2	1.82
Longitudinal	507.1	538.1	6.13	163.9	170.5	4.00

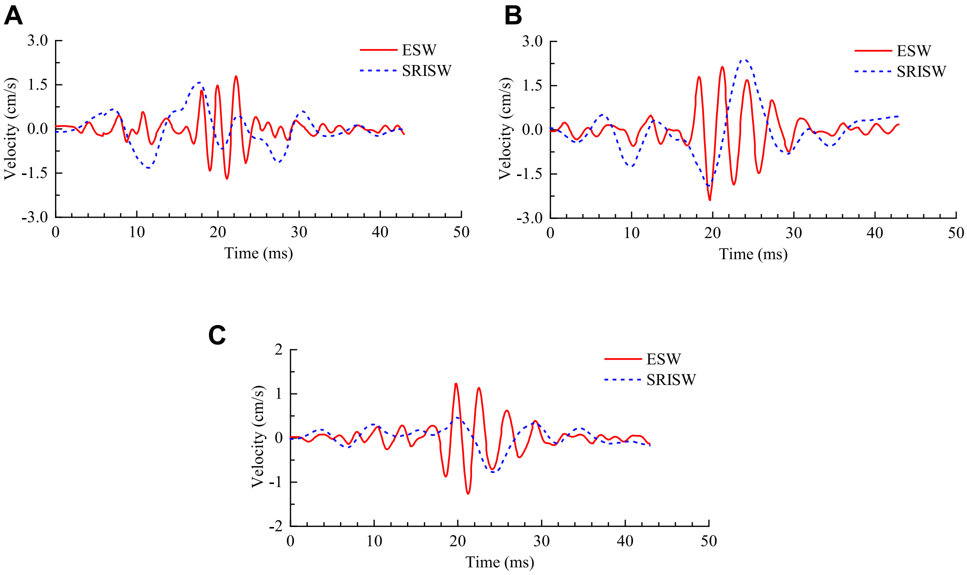

FIGURE 11 | Seismic waves separated from the monitored vibration signals. **(A)** Transverse component, **(B)** Vertical component, **(C)** Longitudinal component.

detailedly in our previous publication (Yang J. et al., 2018). Therefore, these details about the numerical modeling are not repeated in this paper.

Figure 9 presents the simulated vibration velocity histories caused by the combined actions of explosion loading and rapid *in situ* stress release for the cut hole blasting. These simulated waveforms agree well with the field monitoring vibration (Yang J. et al., 2018). These waveforms as the input signals are decomposed in the following by using the VMD method for its applicability verification. In the VMD decomposition, it is crucial to choose an appropriate K for the number of the decomposed intrinsic mode functions. If K is too small, it will result in insufficient decomposition of the input signals, and some characteristic information may be submerged. In contrast, an excessive K value will cause undue decomposition, leading to modal aliasing. According to the above theoretical analysis, the rock vibration generated in the blasting excavation of highly stressed rock masses involves two motivation sources, explosion loading and rapid stress release. Therefore, $K = 2$ is considered in this decomposition. The intrinsic mode functions obtained by the VMD decomposition are sub-signals arranged from low frequency to high frequency. The frequency of the stress release-induced vibration is much lower than that of the blasting vibration. Then the first-order intrinsic mode function is the sub-signals for the stress release-induced vibration, and the second-order mode is the sub-signals for the blasting vibration.

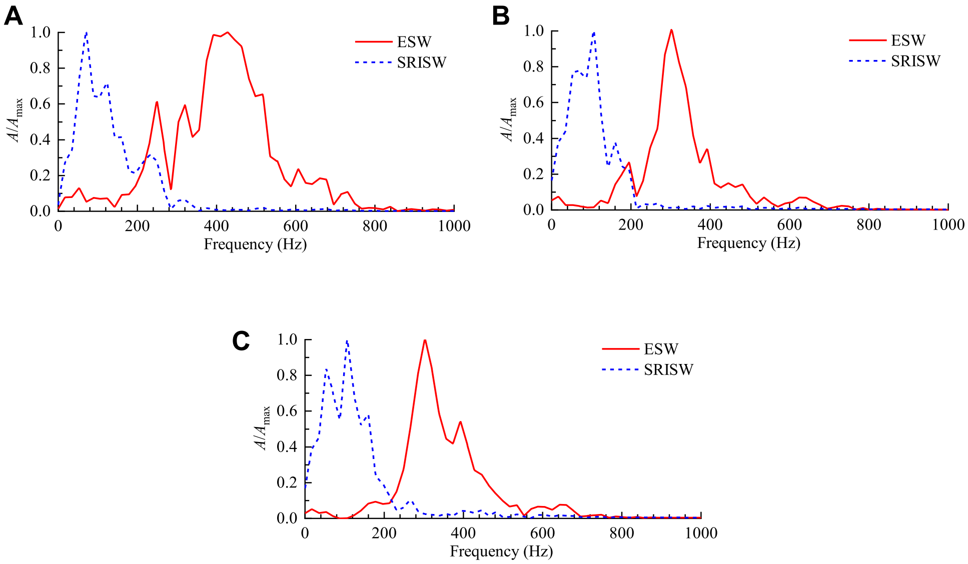

FIGURE 12 | Normalized amplitude-frequency spectra of the separated seismic waves. **(A)** Transverse component, **(B)** Vertical component, **(C)** Longitudinal component.

TABLE 3 | PPV and average center frequency of the separated seismic waves.

Number of tests	Number of monitoring points	Blasting to monitoring distance (m)	PPV (cm/s)			Average center frequency (Hz)		
			Coupled seismic waves	Explosion seismic waves	Stress release-induced seismic waves	Coupled seismic waves	Explosion seismic waves	Stress release-induced seismic waves
1	1	24	5.38	3.24	2.97	213.8	350.1	96.0
	2	33	6.46	2.00	5.69	158.9	271.2	132.3
	3	41	5.42	3.07	2.86	297.0	415.2	212.2
	4	64	3.07	1.88	1.70	263.2	378.5	168.4
2	1	24	5.23	3.37	2.19	345.8	446.8	246.9
	2	31	5.48	3.46	2.10	364.8	438.9	244.4
	3	50	1.01	0.52	0.56	242.4	405.6	119.0
	4	57	4.59	1.46	4.08	158.7	238.0	140.7
3	1	18	15.08	6.81	9.48	169.2	320.7	118.8
	2	38	8.12	4.78	4.14	144.8	286.5	71.5
	3	46	7.09	2.52	6.02	155.4	314.9	135.9
	4	78	2.81	1.82	1.14	262.5	335.3	150.3
4	1	49	2.70	1.28	1.80	173.2	277.7	119.9
	2	64	3.69	2.14	1.90	302.2	372.1	208.5
	3	73	3.87	1.60	2.87	186.9	430.0	132.8
	4	79	2.29	1.17	1.20	163.9	269.1	87.3
5	1	19	13.91	6.42	7.86	160.9	272.8	106.5
	2	41	8.91	4.97	4.34	200.2	312.1	142.4
	3	59	9.15	4.37	6.40	153.9	232.1	128.5
	4	79	2.90	1.63	1.39	230.9	331.2	140.8

Figure 10 presents the separated explosion seismic waves and stress release-induced seismic waves from the simulated coupled vibration shown in **Figure 9**. The respective vibration waves obtained by the numerical modeling are also given in this figure for comparison. It is seen that the separated waveforms based on the VMD method agree well with the numerical results, whether in vibration amplitude, frequency or duration. The PPV and center frequency of the respective vibration waves are summarized in **Tables 1**, **2** respectively. For the explosion seismic waves, the relative differences between the VMD separation and the numerical simulation do not exceed 14% in the PPV and 7% in the center frequency. For the stress release-induced seismic waves, the maximum relative differences are 18% in the PPV and 4% in the center frequency. These qualitative and quantitative comparisons show that the VMD method can realize an effective separation of explosion seismic waves and stress

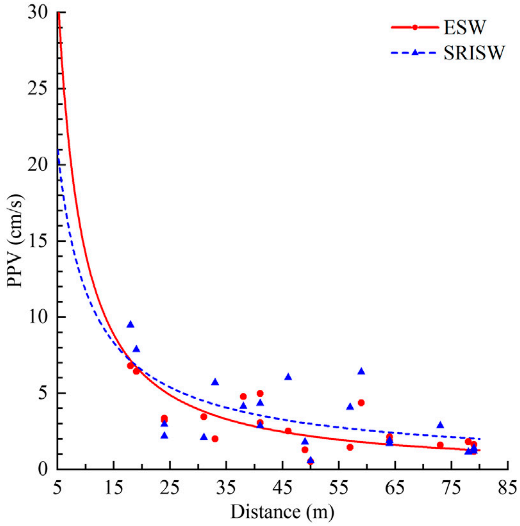

FIGURE 13 | PPV attenuation with distance of the separated seismic waves.

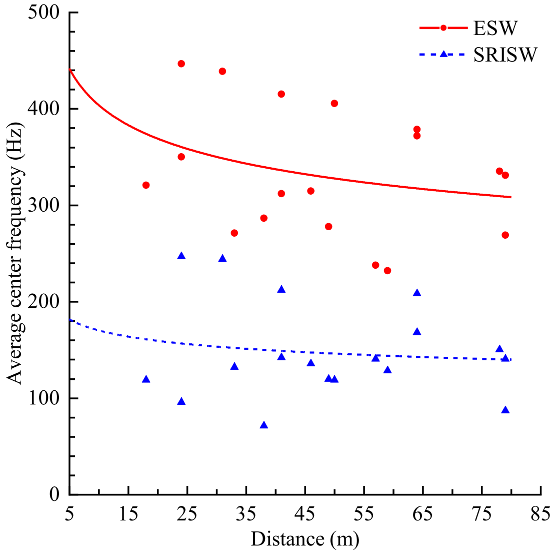

FIGURE 14 | Dependence of average center frequency on distance of the separated seismic waves.

release-induced seismic waves from the coupled vibration. In the following, this method is applied to the field monitoring vibration signals. Based on the VMD separation, the composition and characteristics of the rock vibration caused by the blasting excavation of the pilot tunnel are analyzed.

Vibration Composition and Characteristics

The VMD separation is performed on the monitored vibration signals in **Figure 8**, obtaining the velocity histories of the explosion seismic waves and the stress release-induced seismic waves, as shown in **Figure 11**. At No.1 observation point in the first test, the transverse, vertical and longitudinal PPVs of the explosion seismic waves are 1.79 cm/s, 2.38 cm/s and 1.26 cm/s, respectively. For the stress release-induced seismic waves, the corresponding PPVs are 1.57 cm/s, 2.39 cm/s and 0.77 cm/s, respectively. At this point, the vibration amplitude of the stress release related seismic waves approaches or even exceeds the amplitude of the blasting vibration. Clearly, for the blasting excavation of the deep tunnels in CJPL, the rapid *in situ* stress release occurring on blast-created free surfaces is an important motivation source that causes vibration in the surrounding rock. This is mainly due to the high *in situ* stress field in this project.

Taking Fourier transforms on the the velocity histories in **Figure 11** gives the normalized amplitude-frequency spectra of the separated seismic waves, as shown in **Figure 12**. For the explosion seismic waves, the frequency is mainly distributed in the band from 200 to 600 Hz. The center frequencies of the transverse, vertical and longitudinal components are 413.4 Hz, 310.0 Hz, and 326.9 Hz, respectively. In comparison, the frequency band of the stress release-induced seismic waves is much narrower, mainly in the band from 0 to 300 Hz. Its center frequency is lower accordingly, with 101.4 Hz, 88.9 Hz, and 97.6 Hz for the three components. In conclusion, the vibration frequency of the stress release-induced seismic waves is significantly lower than that of the explosion seismic waves. This coincides with the theoretical calculation result above.

Figures 11, **12** present the separated seismic waves and their spectra for the vibration signals recorded at No.1 monitoring point in the first test. The vibration signals monitored at the other points and tests are also decomposed into explosion seismic waves and stress release-induced seismic waves by the VMD method. After decomposition, their PPV and characteristic frequency are listed in **Table 3**. For ease of presentation and comparison, the peak velocity given in this table is the PPV of the resultant velocity, and the characteristic frequency is the average of the center frequencies of the three velocity components. Among the twenty monitoring points in the five tests, there are ten points where the stress release-induced seismic waves exceed the explosion seismic waves in the resultant PPV. The average center frequency of the explosion seismic waves is mostly higher than 250 Hz. While with regard to the stress release-induced seismic waves, the average center frequency mainly lies between 70 and 200 Hz. Admittedly, at very few monitoring points, the average center frequency of the explosion seismic waves falls between 200 and 250 Hz. The average center frequency of the stress release related seismic waves at a few points also falls within this band. However, at the same monitoring point, the average center frequency of the stress release related seismic waves is always obviously lower than that of the explosion seismic waves. This shows the conclusions obtained from **Figures 11**, **12** are also valid for the vibration signals measured at the other points.

From the comparison between the coupled seismic waves and the explosion seismic waves, it is seen that the rock vibration amplitude is increased and the vibration frequency is reduced due to the stress release-induced seismic waves. Clearly, this coupling effect causes the seismic waves arising from the blasting excavation of deep tunnels to be more harmful to structures than the shallow tunnel blasting under the same blasting design. From the perspective of the mechanical process, the explosion seismic waves are generated first, followed by the stress release-induced seismic waves. Because the two types of seismic waves arrive the monitoring points at different time and also they have different wavelengths, the peak velocity attainment time is different for the respective seismic waves. Therefore, the PPV of the coupled seismic waves is less than the sum of the PPVs of the respective seismic waves.

It is generally acknowledged that the PPV of the explosion seismic waves decays with distance as per a power function (Yilmaz, 2016; Rodríguez et al., 2021). For comparison, the PPV attenuation of the stress release-induced seismic waves is also considered to follow the power function law. Fitting the discrete PPVs at the twenty monitoring points in **Table 3** by using a power function yields the empirical attenuation laws for the respective seismic waves, as shown by the curves in **Figure 13**. It is well known that during seismic wave propagation in a rock medium, the seismic attenuation factor Q will change the relative frequency content of the spectrum as the travel distance increases. Amplitudes at high frequencies decay faster than amplitudes at low frequencies. This causes high-frequency vibration to decay faster with increasing distance. Because the vibration frequency of the stress release-induced seismic waves is lower than that of the explosion seismic waves, the PPV of the stress release-induced seismic waves decays more slowly with distance. Within 20 m distance from the explosion source, the peak velocity of the stress release-induced seismic waves is smaller than that of the explosion seismic waves. However, as the distance further increases, the stress release-induced vibration exceeds the blasting vibration due to its slower attenuation. In the far field beyond 20 m distance, the stress release-induced seismic waves become the major component of the rock vibration. It is common knowledge that low-frequency vibration is more damaged to structures than high-frequency vibration at the same PPV. Therefore, extra care should be taken for the stress release-induced rock vibration with lower frequency, particularly in the far field.

Figures 13, 14 presents the average center frequencies of the respective seismic waves at various monitoring points. Likewise, power functions are employed to best fit these discrete frequency values. The average center frequency of the stress release-induced seismic waves is significantly lower than that of the explosion seismic waves. For both, the average center frequencies decrease with an increase in the travel distance. However, the decreasing amplitudes are not significant, especially for the stress release-induced seismic waves since the distance span of vibration monitoring is only 60 m. From the comparison between the attenuation indexes of the fitted power functions, the average center frequency of the explosion seismic waves declines faster with increasing distance. This is because the explosion seismic waves have higher frequency, and rock mediums contribute to propagation of low-frequency seismic waves by filtering high-frequency seismic waves.

DISCUSSION

The above theoretical analysis and field investigation show that the stress release-induced seismic wave is an important component of the rock vibration generated in blasting excavation of deep tunnels. During the blasting excavation of the pilot tunnel in CJPL, the explosive with a density varying from 950 to 1,300 kg/m^3 and a velocity of detonation ranging from 3,500 to 5,500 m/s is used. In the cut hole blasting, the blasthole diameter is 50 mm, the explosive column diameter is 32 mm, and the space between the adjacent blastholes is 0.5 m. From these blasting parameters, it can be estimated that the equivalent explosion pressure on the blasting excavation boundary varies from 40 to 130 MPa (Yang J. et al., 2018). The *in situ* stress in this project reaches 50–70 MPa. The rock mass near the blasting work face may be subjected to higher *in situ* stress due to local stress concentration. Therefore, the rapid stress release occurring on blast-created free surfaces can produce a comparable vibration velocity to the explosion loading. Moreover, the seismic waves induced by the rapid stress release decay more slowly with distance. Then it is quite possible that the stress release-induced rock vibration exceeds the blasting vibration in the far field. Overall, the explosion seismic waves dominate the near-field rock vibration, and the stress release-induced seismic waves can become the major component of the far-field rock vibration. Therefore, during blasting excavation of deep tunnels under high *in situ* stress, the seismic waves caused by the rapid stress release cannot be ignored. Unfortunately, this concern has not attracted sufficient attention in current blasting design and vibration control for deep tunnel blasting.

In current vibration control of tunnel blasting, the widely used measures are to reduce charge weight and optimize charge structures to achieve the purpose of minimizing the explosion-induced vibration. This is certainly adequate for blasting of shallow tunnels. However, during deep tunnel blasting under high *in situ* stress, it may be necessary to reduce the stress release-induced vibration. According to the theoretical solution formula in **Eq. 10**, the rock vibration caused by the rapid stress release depends on the *in situ* stress level σ_0, the stress release period t_p, the size of blast-created free surfaces a, and the rock properties v_p. As the stress level and the size of blast-created free surfaces increase, the velocity of the stress release-induced vibration increases accordingly. The vibration velocity decreases with an increase in the period of the stress release. Intact rock masses with higher P-wave velocity generate greater vibration velocity than loose rock masses. The *in situ* stress level and the rock properties cannot be easily changed. However, the size of blast-created free surfaces and the period of the stress release can be adjusted through designing blasthole arrangements and detonation sequences.

With regard to the cut hole blasting of the pilot tunnel in CJPL in **Figure 7**, the size of blast-created free surfaces can be reduced through changing the number of the blastholes detonated in the first delay. If ten blastholes (five holes on each side) are detonated in the first delay, the vertical side length of the blast-created free surfaces will be reduced from 4.5 m to 2.0 m. The equivalent excavation radius under the same area will be shortened from 1.7 m to 1.1 m accordingly. In the theoretical model in **Section 2**, when the circular excavation radius is changed from 1.7 m to 1.1 m, the vibration PPV due to the rapid stress release decreases from 18.8 cm/s to 8.6 cm/s at 10 m distance, as shown in

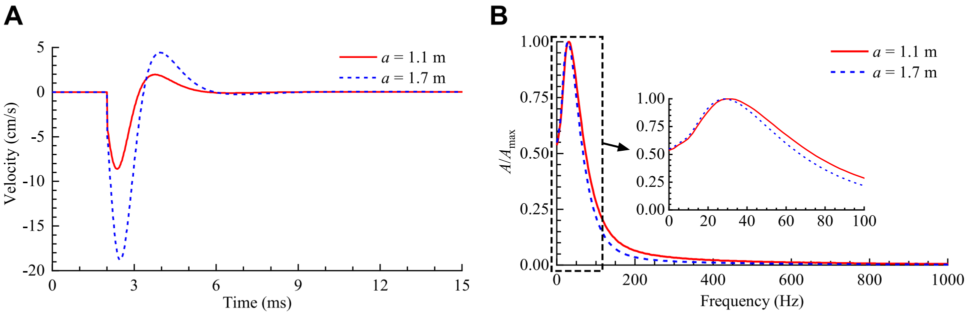

FIGURE 15 | Velocity histories and amplitude-frequency spectra of the stress release-induced vibration under different excavation radiuses. **(A)** Velocity histories at r = 10 m, **(B)** Normalized amplitude-frequency spectra of the velocity histories.

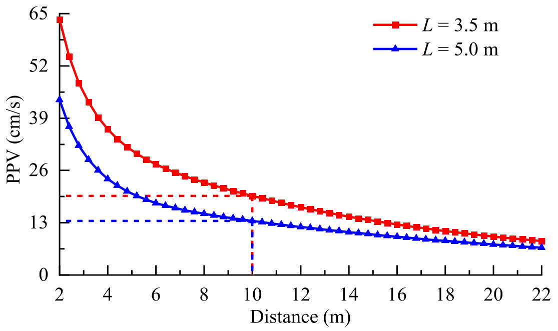

FIGURE 16 | PPV of the stress release-induced vibration under different blasthole lengths.

Figure 15A. A significant reduction of 54% is reached in the PPV. Furthermore, as the excavation radius decreases, the vibration frequency becomes higher, as presented in **Figure 15B**. This shows that reducing the size of blast-created free surfaces can achieve effective control of the stress release-induced rock vibration.

According to **Eq. 2**, the period of the rapid stress release occurring on blast-created free surfaces relies on the blasthole length and space for a given rock mass. The blasthole arrangement at a larger length and space generates a longer period, corresponding to a smaller vibration velocity. As mentioned earlier, short blastholes with a length ranging from 1.5 to 5.0 m and a space varying from 0.5 to 1.5 m are normally used in the full-face blasting of deep tunnels. The blasthole length is much greater than the blasthole space in size. Therefore, in **Eq. 2**, the period of the rapid stress release is dominated by the blasthole length. In the cut hole blasting of the pilot tunnel in CJPL, the blasthole length of 3.5 m is used. If the blasthole length is changed from 3.5 m to 5.0 m, the period of the stress release will be prolonged from 2.7 ms to 3.8 ms. Based on the theoretical model in **Section 2**, the PPV of the stress release-induced vibration under the different blasthole lengths is shown in **Figure 16**. When the blasthole length is increased from 3.5 m to 5.0 m, the PPV at 10 m distance is reduced from 19.7 cm/s to 13.4 cm/s, with a reduction of 32%. Clearly, increasing the blasthole length moderately is effective in extending the stress release period and reducing the stress release-induced rock vibration.

The above discussion indicates that in deep tunnel blasting, smaller blasting excavation boundaries and larger blasthole lengths are conducive to control the rock vibration due to the rapid *in situ* stress release. However, a larger blasthole length means a greater explosive charge weight if the charge density remains constant. It will increase the rock vibration caused by the explosion loading. Therefore, in order to determine an optimal blasthole arrangement for minimizing the coupled rock vibration, the combined effects of explosion loading and rapid stress release need to be analyzed. In this regard, the theoretical model developed in this paper is limited. For example, the detonation propagation along explosive columns and the effect of blasthole length on explosion seismic wave radiation cannot be considered. Furthermore, the interval time between the initiation of explosion loading and the start of rapid stress release cannot be accurately determined. In the similar theoretical model developed by Yang J. H. et al. (2018), it is considered that the in-situ stress release begins when the explosion pressure falls to a level equal to the initial stress on excavation boundaries. However, this is a rough estimation because the microscopic rock fracture between adjacent blastholes, which fundamentally causes in-situ stress release, is not handled properly. Alternatively, the numerical modeling is a more promising approach, in which explosive detonation, rock fracture between adjacent blastholes and *in situ* stress release on blast-created free surfaces can be reproduced.

CONCLUSION

During blasting excavation of deep tunnels under high *in situ* stress, the *in situ* stress initially exerted on blast-created free surfaces is rapidly released along with rock fragmentation by blasting. The theoretical analysis conducted in this study shows that the rapid *in situ* stress release can induce considerable seismic waves, resulting in vibration in surrounding rock masses. The vibration frequency of stress release-induced seismic waves is significantly lower than that of explosion seismic waves. The difference in the frequency content makes it possible to separate explosion seismic waves and stress release-induced seismic waves from monitored vibration signals. The VMD method is demonstrated to be an effective approach to achieve this separation. Based on the VMD separation, the composition and characteristics of the rock vibration monitored in the cut hole blasting of the pilot tunnel in CJPL are investigated. The field monitoring data investigation shows that the rock vibration amplitude is increased and the vibration frequency is reduced due to stress release-induced seismic waves. The rock vibration in the near field is dominated by explosion seismic waves. In the far field, stress release-induced seismic waves become the major composition due to their lower frequency and slower attenuation with distance. Through shortening blast-created free surface sizes and increasing blasthole lengths moderately, the rock vibration caused by the rapid stress release can be effectively reduced.

The purpose of this study is to reveal the composition and characteristics of the rock vibration generated in blasting excavation of deep tunnels through theoretical analysis and field investigation. It has been demonstrated that under high *in situ* stress, the seismic wave due to the rapid stress release is an important vibration component. The structural responses and safety criterions under the coupling of explosion seismic waves and stress release-induced seismic waves need to be studied in future research.

DATA AVAILABILITY STATEMENT

The original contributions presented in the study are included in the article/Supplementary Material, further inquiries can be directed to the corresponding author.

AUTHOR CONTRIBUTIONS

JY and JS: investigation, software, and writing original draft; YJ and YY: project administration and supervision; JY and WZ: writing, review and editing; TT: investigation. All authors have read and agreed to the published version of the manuscript.

FUNDING

This work was supported by the National Natural Science Foundation of China (51969015 and 52179102), the Open Research Program of Hubei Key Laboratory of Blasting Engineering (Jianghan University) (HKLBEF202007), and the Natural Science Foundation of Jiangxi Province (20204BCJ23002).

REFERENCES

Aydan, Ö. (2017). *Rock Dynamics*. London: CRC Press.

Blair, D. (2010). Seismic Radiation from an Explosive Column. *Geophysics* 75 (1), E55–E65. doi:10.1190/1.3294860

Cao, W., Li, X., Tao, M., and Zhou, Z. (2016). Vibrations Induced by High Initial Stress Release during Underground Excavations. *Tunn. Undergr. Space Technol.* 53, 78–95. doi:10.1016/j.tust.2016.01.017

Carter, J. P., and Booker, J. R. (1990). Sudden Excavation of a Long Circular Tunnel in Elastic Ground. *Int. J. Rock Mech. Min. Sci. Geomechanics Abstr.* 27 (2), 129–132. doi:10.1016/0148-9062(90)94861-m

Chen, H., Qiu, X., Shi, X., Zhang, J., Huo, X., and Li, D. (2022). Experimental Study on Fracturing Characteristics of Double-Hole Blasting under Static Stresses. *Front. Earth Sci.* 9, 829258. doi:10.3389/feart.2021.829258

Ding, C., Yang, R., and Yang, L. (2021). Experimental Results of Blast-Induced Cracking Fractal Characteristics and Propagation Behavior in Deep Rock Mass. *Int. J. Rock Mech. Min. Sci.* 142, 104772. doi:10.1016/j.ijrmms.2021.104772

Dragomiretskiy, K., and Zosso, D. (2014). Variational Mode Decomposition. *IEEE Trans. Signal Process.* 62 (3), 531–544. doi:10.1109/tsp.2013.2288675

Du, K., Sun, Y., Zhou, J., Wang, S.-f., Tao, M., Yang, C., et al. (2021). Low Amplitude Fatigue Performance of Sandstone, Marble, and Granite under High Static Stress. *Geomech. Geophys. Geo-energ. Geo-resour.* 7 (3), 68. doi:10.1007/s40948-021-00266-1

Fan, Y., Cui, X., Leng, Z., Zheng, J., Wang, F., and Xu, X. (2021). Rockburst Prediction from the Perspective of Energy Release: a Case Study of a Diversion Tunnel at Jinping II Hydropower Station. *Front. Earth Sci.* 9, 711706. doi:10.3389/feart.2021.711706

Feng, G.-l., Chen, B.-r., Jiang, Q., Xiao, Y.-x., Niu, W.-j., and Li, P.-x. (2021). Excavation-Induced Microseismicity and Rockburst Occurrence: Similarities and Differences between Deep Parallel Tunnels with Alternating Soft-Hard Strata. *J. Cent. South Univ.* 28 (2), 582–594. doi:10.1007/s11771-021-4623-z

He, C., and Yang, J. (2018). Dynamic Crack Propagation of Granite Subjected to Biaxial Confining Pressure and Blast Loading. *Lat. Am. J. Solids Struct.* 15 (6), e45. doi:10.1590/1679-78254463

He, M., e Sousa, L. R., Miranda, T., and Zhu, G. (2015). Rockburst Laboratory Tests Database - Application of Data Mining Techniques. *Eng. Geol.* 185, 116–130. doi:10.1016/j.enggeo.2014.12.008

He, S., Lai, J., Zhong, Y., Wang, K., Xu, W., Wang, L., et al. (2021). Damage Behaviors, Prediction Methods and Prevention Methods of Rockburst in 13 Deep Traffic Tunnels in China. *Eng. Fail. Anal.* 121, 105178. doi:10.1016/j.engfailanal.2020.105178

Huo, X., Shi, X., Qiu, X., Chen, H., Zhou, J., Zhang, S., et al. (2021). Study on Rock Damage Mechanism for Lateral Blasting under High *In Situ* Stresses. *Appl. Sci.* 11 (11), 4992. doi:10.3390/app11114992

Kaiser, P. K., and Moss, A. (2022). Deformation-Based Support Design for Highly Stressed Ground with a Focus on Rockburst Damage Mitigation. *J. Rock Mech. Geotechnical Eng.* 14 (1), 50–66. doi:10.1016/j.jrmge.2021.05.007

Li, C., Li, X., and Liang, L. (2020a). Dynamic Response of Existing Tunnel under Cylindrical Unloading Wave. *Int. J. Rock Mech. Min. Sci.* 131, 104342. doi:10.1016/j.ijrmms.2020.104342

Li, M., Mei, W., Pan, P.-Z., Yan, F., Wu, Z., and Feng, X.-T. (2020b). Modeling Transient Excavation-Induced Dynamic Responses in Rock Mass Using an Elasto-Plastic Cellular Automaton. *Tunn. Undergr. Space Technol.* 96, 103183. doi:10.1016/j.tust.2019.103183

Lu, W., Fan, Y., Yang, J., Yan, P., and Chen, M. (2017). Development of a Model to Predict Vibrations Induced by Transient Release of *In-Situ* Stress. *J. Vib. Control* 23 (11), 1828–1843. doi:10.1177/1077546315601594

Lu, W., Yang, J., Yan, P., Chen, M., Zhou, C., Luo, Y., et al. (2012). Dynamic Response of Rock Mass Induced by the Transient Release of *In-Situ* Stress. *Int. J. Rock Mech. Min. Sci.* 53, 129–141. doi:10.1016/j.ijrmms.2012.05.001

Ma, K., and Liu, G. (2022). Three-Dimensional Discontinuous Deformation Analysis of Failure Mechanisms and Movement Characteristics of Slope Rockfalls. *Rock Mech. Rock Eng.* 55 (1), 275–296. doi:10.1007/s00603-021-02656-z

Miklowitz, J. (1978). *The Theory of Elastic Waves and Waveguides*. Amsterdam: North-Holland Publishing Company.

Nex, P. A. M., and Kinnaird, J. A. (2019). “Minerals and Mining in South Africa,” in *The Geography of South Africa*. Editors J. Knight and C. Rogerson (Cham: Springer), 27–35. doi:10.1007/978-3-319-94974-1_4

Ogasawara, H., Nakatani, M., Durrheim, R., Naoi, M., Yabe, Y., Moriya, H., et al. (2014). “Observational Studies of the Rock Mass Response to Mining in

Highly Stressed Gold Mines in South Africa," in *Deep Mining 2014: Proceedings of the 7th International Conference on Deep and High Stress Mining*. Editors M. Hudyma and Y. Potvin (Perth: Australian Centre for Geomechanics), 123–137. doi:10.36487/ACG_rep/1410_06_Ogasawara

Press, F., and Archambeau, C. (1962). Release of Tectonic Strain by Underground Nuclear Explosions. *J. Geophys. Res.* 67 (1), 337–343. doi:10.1029/jz067i001p00337

Rockafellar, R. T. (1973). A Dual Approach to Solving Nonlinear Programming Problems by Unconstrained Optimization. *Math. Program.* 5 (1), 354–373. doi:10.1007/bf01580138

Rodríguez, R., García de Marina, L., Bascompta, M., and Lombardía, C. (2021). Determination of the Ground Vibration Attenuation Law from a Single Blast: a Particular Case of Trench Blasting. *J. Rock Mech. Geotechnical Eng.* 13 (5), 1182–1192. doi:10.1016/j.jrmge.2021.03.016

Si, X., Huang, L., Li, X., Ma, C., and Gong, F. (2021). Experimental Investigation of Spalling Failure of D-Shaped Tunnel under Three-Dimensional High-Stress Conditions in Hard Rock. *Rock Mech. Rock Eng.* 54 (6), 3017–3038. doi:10.1007/s00603-020-02280-3

Siren, T., Kantia, P., and Rinne, M. (2015). Considerations and Observations of Stress-Induced and Construction-Induced Excavation Damage Zone in Crystalline Rock. *Int. J. Rock Mech. Min. Sci.* 73, 165–174. doi:10.1016/j.ijrmms.2014.11.001

Talbot, A. (1979). The Accurate Numerical Inversion of Laplace Transforms. *IMA J. Appl. Math.* 23 (1), 97–120. doi:10.1093/imamat/23.1.97

Tao, J., Shi, A.-C., Li, H.-T., Zhou, J.-W., Yang, X.-G., and Lu, G.-D. (2021). Thermal-mechanical Modelling of Rock Response and Damage Evolution during Excavation in Prestressed Geothermal Deposits. *Int. J. Rock Mech. Min. Sci.* 147, 104913. doi:10.1016/j.ijrmms.2021.104913

Tao, M., Li, X., and Li, D. (2013). Rock Failure Induced by Dynamic Unloading under 3D Stress State. *Theor. Appl. Fract. Mech.* 65, 47–54. doi:10.1016/j.tafmec.2013.05.007

Toksöz, M. N., Harkrider, D. G., and Ben-Menahem, A. (1965). Determination of Source Parameters by Amplitude Equalization of Seismic Surface Waves: 2. Release of Tectonic Strain by Underground Nuclear Explosions and Mechanisms of Earthquakes. *J. Geophys. Res.* 70 (4), 907–922. doi:10.1029/jz070i004p00907

Toksoz, M. N., and Kehrer, H. H. (1972). Tectonic Strain Release by Underground Nuclear Explosions and its Effect on Seismic Discrimination. *Geophys. J. Int.* 31 (1–3), 141–161. doi:10.1111/j.1365-246x.1972.tb02364.x

Xie, G., Yin, Z., Wang, L., Hu, Z., and Zhu, C. (2017). Effects of Gas Pressure on the Failure Characteristics of Coal. *Rock Mech. Rock Eng.* 50 (7), 1711–1723. doi:10.1007/s00603-017-1194-2

Xie, H., Konietzky, H., and Zhou, H. W. (2019). Special Issue "Deep Mining". *Rock Mech. Rock Eng.* 52 (5), 1415–1416. doi:10.1007/s00603-019-01805-9

Xu, H., Yang, X.-G., Zhang, J.-H., Zhou, J.-W., Tao, J., and Lu, G.-D. (2020). A Closed-form Solution to Spherical Wave Propagation in Triaxial Stress Fields. *Int. J. Rock Mech. Min. Sci.* 128, 104266. doi:10.1016/j.ijrmms.2020.104266

Yang, C., Tang, J., Huang, D., Wang, L., Sun, Q., and Hu, Z. (2021). New Crack Initiation Model for Open-Flawed Rock Masses under Compression-Shear Stress. *Theor. Appl. Fract. Mech.* 116, 103114. doi:10.1016/j.tafmec.2021.103114

Yang, J.-h., Wu, Z.-n., Sun, W.-b., Yao, C., and Wang, Q.-h. (2022). Numerical Simulation on Radiation and Energy of Blast-Induced Seismic Waves in Deep Rock Masses. *J. Cent. South Univ.* 29 (2), 645–662. doi:10.1007/s11771-022-4908-x

Yang, J. H., Jiang, Q. H., Zhang, Q. B., and Zhao, J. (2018a). Dynamic Stress Adjustment and Rock Damage during Blasting Excavation in a Deep-Buried Circular Tunnel. *Tunn. Undergr. Space Technol.* 71, 591–604. doi:10.1016/j.tust.2017.10.010

Yang, J., Lu, W., Li, P., and Yan, P. (2018b). Evaluation of Rock Vibration Generated in Blasting Excavation of Deep-Buried Tunnels. *KSCE J. Civ. Eng.* 22 (7), 2593–2608. doi:10.1007/s12205-017-0240-7

Yilmaz, O. (2016). The Comparison of Most Widely Used Ground Vibration Predictor Equations and Suggestions for the New Attenuation Formulas. *Environ. Earth Sci.* 75 (3), 269. doi:10.1007/s12665-015-5011-5

Yin, Z., Chen, W., Hao, H., Chang, J., Zhao, G., Chen, Z., et al. (2020). Dynamic Compressive Test of Gas-Containing Coal Using a Modified Split Hopkinson Pressure Bar System. *Rock Mech. Rock Eng.* 53, 815–829. doi:10.1007/s00603-019-01955-w

Zhang, X.-L., Jia, R.-S., Lu, X.-M., Peng, Y.-J., and Zhao, W.-D. (2018). Identification of Blasting Vibration and Coal-Rock Fracturing Microseismic Signals. *Appl. Geophys.* 15 (2), 280–289. doi:10.1007/s11770-018-0682-9

Zhu, W. C., Wei, J., Zhao, J., and Niu, L. L. (2014). 2D Numerical Simulation on Excavation Damaged Zone Induced by Dynamic Stress Redistribution. *Tunn. Undergr. Space Technol.* 43 (7), 315–326. doi:10.1016/j.tust.2014.05.023

Conflict of Interest: The authors declare that the research was conducted in the absence of any commercial or financial relationships that could be construed as a potential conflict of interest.

frontiers | Frontiers in Earth Science

ORIGINAL RESEARCH
published: 26 May 2022
doi: 10.3389/feart.2022.884361

Analysis of Energy Accumulation and Dispersion Evolution of a Thick Hard Roof and Dynamic Load Response of the Hydraulic Support in a Large Space Stope

Qingwei Bu[1,2†], *Min Tu*[1*†], *Xiangyang Zhang*[1], *Ming Zhang*[3] and *Qingchong Zhao*[1]

[1]Key Laboratory of Safety and High-Efficiency Coal Mining of Ministry of Education, Anhui University of Science and Technology, Huainan, China, [2]School of Mining and Coal, Inner Mongolia University of Science and Technology, Baotou, China, [3]State Key Laboratory of Mining Response and Disaster Prevention and Control in Deep Coal Mines, Anhui University of Science and Technology, Huainan, China

Aiming at the mining disaster of a thick hard roof, based on the analysis of the mining instability influence of the thick hard roof, this study constructs the mining bearing mechanical model of the thick hard roof by using mechanical theory and obtains the mechanical distribution equation of mining bearing and energy accumulation, the mining instability energy release equation, and the dynamic load response equation of a hydraulic support in the working face, as well as the dynamic load response characteristics of the hydraulic support in the working face, putting forward the technical countermeasures for the strong dynamic pressure control of the thick hard roof in the working face. This research shows that 1) the larger the overburden load and suspension span of the thick hard roof, the more serious the mining bearing state and energy accumulation evolution; the greater the rock thickness and elastic modulus of the thick hard roof, the greater the flexural stiffness of the roof, resulting in the increase of the roof mining limit breaking span, which indirectly aggravates the mining bearing state and self-energy accumulation evolution; 2) the dynamic support resistance of the hydraulic support is composed of the dynamic support resistance caused by the release of elastic energy accumulated by mining of the thick hard roof, the work done by the overlying load, and the static support resistance caused by the direct roof gravity; 3) the dynamic support resistance caused by the work of the overlying load accounts for the highest proportion, followed by the dynamic support resistance caused by the release of mining elastic energy by the thick hard roof; the cause of mining instability and the strong dynamic pressure of the thick hard roof lie in the large span of the mining suspended roof, and the large-scale mining suspension structure of the thick hard roof leads to a high overlying load and large accumulated energy; and 4) the mining instability of the thick hard roof leads to a strong dynamic load response of the hydraulic support; adopting pre-splitting and roof cutting technology to reduce the breaking span of the thick hard roof and reducing the impact dynamic load caused by mining instability of the thick hard roof can effectively eliminate the potential safety hazard of overlimit bearing of the hydraulic support.

Keywords: large space stope, thick hard roof, mining instability, energy accumulation and dispersion, hydraulic support, dynamic pressure disaster

Edited by:
Kun Du,
Central South University, China

Reviewed by:
Liang Chen,
Guangdong University of Technology, China
Liang Chen,
China University of Mining and Technology, China

***Correspondence:**
Min Tu
mtu@aust.edu.cn

†ORCID:
Qingwei Bu
orcid.org/0000-0002-4628-856X
Min Tu
orcid.org/0000-0002-1215-9639

Specialty section:
This article was submitted to Geohazards and Georisks, a section of the journal Frontiers in Earth Science

Received: *26 February 2022*
Accepted: *24 March 2022*
Published: *26 May 2022*

Citation:
Bu Q, Tu M, Zhang X, Zhang M and Zhao Q (2022) Analysis of Energy Accumulation and Dispersion Evolution of a Thick Hard Roof and Dynamic Load Response of the Hydraulic Support in a Large Space Stope. Front. Earth Sci. 10:884361. doi: 10.3389/feart.2022.884361

INTRODUCTION

The geological conditions of the thick hard roof in coal mines are becoming more and more common, the dynamic pressure of mining instability of the thick hard roof is particularly strong, and the hidden danger of the strong dynamic pressure disaster in the working face is serious. In many coal mines in Inner Mongolia, the deep coal measure strata generally contain thick and hard strata dominated by fine sandstone and conglomerate, which have a large thickness, high strength, and no obvious bedding fissures. In the deep part of coal measure strata, the thick and hard rock stratum forms a plate beam bearing structure with a long-span suspension and is difficult to collapse; once the plate beam bearing structure reaches the bearing limit, it will cause a strong dynamic pressure impact on the stope space, which is a serious threat to the safe and efficient mining of coal mines.

In order to ensure the safe and efficient mining of coal mines, many scholars pay special attention to the problem of mining pressure disasters under thick hard roof conditions. In terms of mining disaster analysis under thick hard roof conditions and by the investigation and measurement of the ground pressure in the working face with a thick hard roof, it is concluded that a phenomenon of the strong ground pressure exists in the working face with a thick hard roof, a large number of elastic properties are accumulated in the thick and hard rock itself with the coal and rock volume under it, and the mining instability of the thick hard roof has a hidden danger of inducing rock burst and air blast disaster in the working face (Christopher and Michael, 2016; Iannacchione and Tadolini, 2016; Tan et al., 2019). Through the analysis of the stope ground pressure behavior under thick hard roof conditions, it is revealed that the instability of the thick and hard rock structure in a large space stope leads to the strong ground pressure behavior of the working face, and the classification evaluation model of the ground pressure strength is established to guide the prediction and pre-control of the ground pressure disaster in hard roof coal seam mining (Xia et al., 2017; Dou et al., 2020; Gao et al., 2020). Some scholars have carried out microseismic monitoring of the overlying rock of the stope under thick hard roof conditions, analyzed the vibration response of the mining fracture of the overlying rock of the stope, and revealed the elastic release and propagation characteristics of its accumulation caused by the mining fracture of the thick and hard roof (Lu et al., 2015; Zhang et al., 2017). Facing the disaster problem of mining instability of the thick hard roof, some scholars have carried out technical countermeasures such as solid filling and blasting roof cutting and achieved good engineering results, avoiding the disastrous disturbance of the thick hard roof structure instability on the stope and roadway (He et al., 2012; Zhang et al., 2016). The stability analysis of the working face hydraulic support under the condition of the thick hard roof was carried out Based on the key layer theory and composite beam mechanical model, a calculation method of the static resistance of the support in a fully mechanized top-coal caving face is proposed (Zhao et al., 2017). By analyzing the influence of mining instability of the thick hard roof on the stability of the hydraulic support in the working face, it is concluded that the support stiffness is positively correlated with the support resistance. Manual roof cutting is adopted to reduce the fracture length of the roof and cooperate with it to achieve the purpose of roof control (Yu et al., 2013; Song et al., 2020). By analyzing the pressure behavior characteristics of the hydraulic support of the working face when the thick hard roof is broken, this study reveals the impact dynamic pressure behavior of the mining failure of the basic roof of the thick and hard rock stratum on the lower direct roof and support and proves that the dynamic load of the working face is much greater than the pressure effect of the hydraulic support caused by the static load (Yang et al., 2017). In the analysis of the mining instability mechanism of the thick hard roof, some scholars have successively adopted the elastic foundation orthogonal beam model, fixed beam mechanical model, and composite beam structure model considering a horizontal force to study the mechanical mechanisms of mining instability of the hard roof in a stope, such as bending deformation, instability span, and stress transfer of the hard roof (Jiang et al., 2016; Zuo et al., 2017; Zhang et al., 2020). According to the bearing mechanical characteristics of the thick hard roof, scholars use the elastic foundation beam model to analyze the distribution characteristics of deflection, bending moment, and energy accumulation of the hard roof (Li et al., 2007; Gu et al., 2018). Some scholars also use the medium-thick plate theory and finite element method to analyze the mining stress and fracture evolution of the hard and thick roof in the stope space (Xie et al., 2016; Yang et al., 2020). At present, many research studies mainly analyze the hard roof slab in the stope space as a thin beam or a thin plate structure but it is not applicable to the hard rock stratum with large thickness. Although some scholars use the elastic mechanic's solution method to analyze the fixed supported thick beam or fixed supported medium and thick plate structure, the fixed support boundary is different from the clamped support boundary constraint of the actual situation, and the analyzed mining energy accumulation and fracture instability position of the thick hard roof are deviated from the actual situation; the spatial state equation analysis method and finite difference analysis method of the plate structure are complex, difficult to study in depth, and have a little advantage in popularizing and using engineering technology. Therefore, the mechanical model suitable for the analysis of the mining bearing capacity of the thick hard roof still needs to be further studied.

To sum up, many scholars have made a lot of research achievements in the study of mining disasters under thick hard roof conditions. However, the mining disasters under the conditions of a thick hard roof, such as the energy accumulation and dispersion evolution before and after the mining fracture of a thick hard roof, the mining instability of the thick hard roof, the difference between dynamic and static pressure, and the strong dynamic load response of the hydraulic support in the working face, need to be further analyzed and studied. Therefore, combined with engineering examples, based on the analysis of the mining influence characteristics of thick hard roof conditions, this study constructs the mechanical model of mining bearing structure of thick hard roof by using the mechanical analysis method of single generalized displacement thick beam and the mechanical theory of semi-infinite elastic foundation beam and

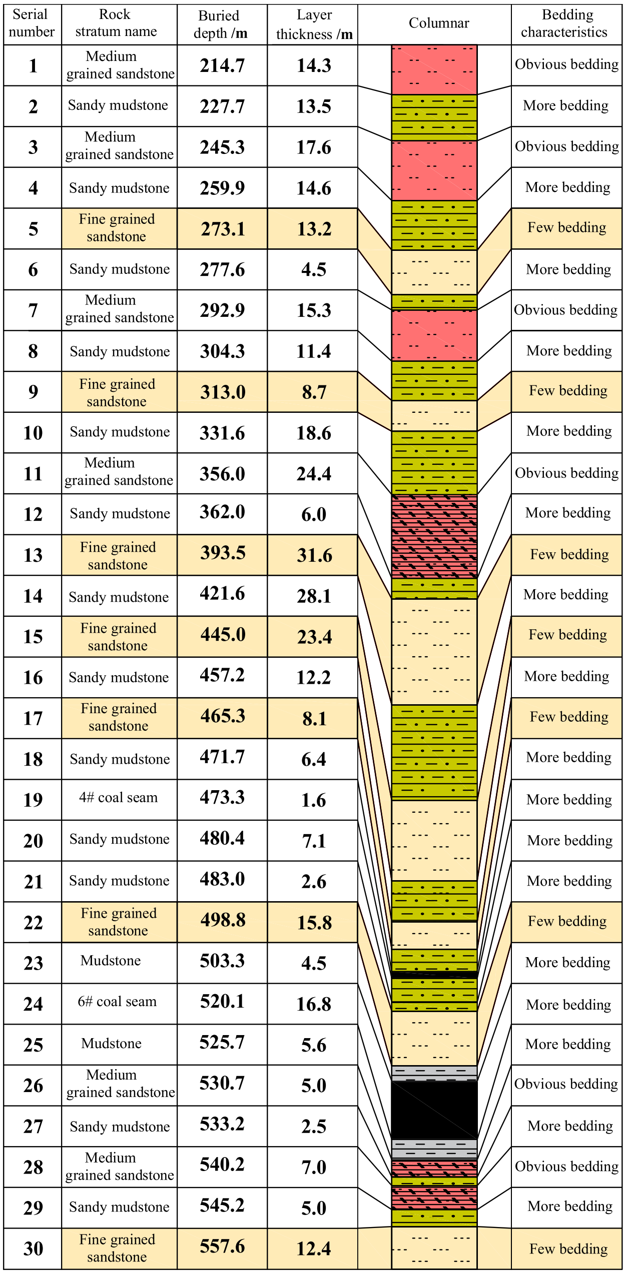

Serial number	Rock stratum name	Buried depth /m	Layer thickness /m	Columnar	Bedding characteristics
1	Medium grained sandstone	214.7	14.3		Obvious bedding
2	Sandy mudstone	227.7	13.5		More bedding
3	Medium grained sandstone	245.3	17.6		Obvious bedding
4	Sandy mudstone	259.9	14.6		More bedding
5	Fine grained sandstone	273.1	13.2		Few bedding
6	Sandy mudstone	277.6	4.5		More bedding
7	Medium grained sandstone	292.9	15.3		Obvious bedding
8	Sandy mudstone	304.3	11.4		More bedding
9	Fine grained sandstone	313.0	8.7		Few bedding
10	Sandy mudstone	331.6	18.6		More bedding
11	Medium grained sandstone	356.0	24.4		Obvious bedding
12	Sandy mudstone	362.0	6.0		More bedding
13	Fine grained sandstone	393.5	31.6		Few bedding
14	Sandy mudstone	421.6	28.1		More bedding
15	Fine grained sandstone	445.0	23.4		Few bedding
16	Sandy mudstone	457.2	12.2		More bedding
17	Fine grained sandstone	465.3	8.1		Few bedding
18	Sandy mudstone	471.7	6.4		More bedding
19	4# coal seam	473.3	1.6		More bedding
20	Sandy mudstone	480.4	7.1		More bedding
21	Sandy mudstone	483.0	2.6		More bedding
22	Fine grained sandstone	498.8	15.8		Few bedding
23	Mudstone	503.3	4.5		More bedding
24	6# coal seam	520.1	16.8		More bedding
25	Mudstone	525.7	5.6		More bedding
26	Medium grained sandstone	530.7	5.0		Obvious bedding
27	Sandy mudstone	533.2	2.5		More bedding
28	Medium grained sandstone	540.2	7.0		Obvious bedding
29	Sandy mudstone	545.2	5.0		More bedding
30	Fine grained sandstone	557.6	12.4		Few bedding

FIGURE 1 | Coal stratum histogram of the working face.

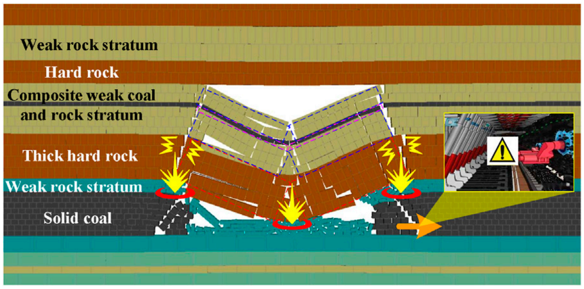

FIGURE 2 | Schematic diagram of mining dynamic pressure of the thick hard roof in the fully mechanized top-coal caving face.

analyzes the mechanical law of mining bearing and energy accumulation of thick hard roof. According to the energy principle, the mechanical equations of energy accumulation and dispersion of thick hard roof and dynamic load response of hydraulic support in a large space stope are deduced, the dynamic load response of hydraulic support for mining instability of thick hard roof in working face is analyzed, and then the technical countermeasures for the strong ground pressure control of thick hard roof are put forward. This study provides a reference for the strong dynamic pressure behavior of similar thick hard roofs and the dynamic pressure bearing analysis of hydraulic support.

ANALYSIS OF MINING INSTABILITY CHARACTERISTICS OF THE THICK HARD ROOF IN THE WORKING FACE

Engineering General Situation of the Working Face With the Thick Hard Roof

In the 61304 fully mechanized top-coal caving face in the Tangjiahui coal mine, the 6# coal seam is the main coal seam; the minable thickness of this coal seam is 16.8 m, the average dip angle of the coal seam is 2°, the strike length of the working face is 2,141 m, the dip width is 240 m, the fully mechanized mining height is 4.5 m, and the caving height is 12.3 m. The occurrence structure of the coal measure strata is shown in **Figure 1**; the direct roof of the main mining coal seam is 4.5 m thick argillaceous rock, and the overlying basic roof is 15.8 m thick fine sandstone, which is mainly composed of a 4# coal seam, sandy mudstone, medium-grained sandstone, and fine sandstone; among the aforementioned rock layers, mudstone, sandy mudstone, and medium-grained sandstone layers show obvious bedding fracture development, argillaceous weak cementation, locally mixed with loose conglomerate, and the overall strength is low but the fine sandstone layer is thick, hard and has high mechanical strength. There is a hidden danger of strong dynamic pressure disaster caused by mining instability of the long-span suspended roof.

Influence Characteristics of Mining Instability of the Working Face Under the Thick Hard Roof

By investigating the ground pressure behavior of the mined working face in the Tangjiahui coal mine, it is found that during the mining process, the direct roof of mudstone collapses with the top-coal caving mining, as shown in **Figure 2**, the thick hard roof of fine sandstone overlying it presents a plate beam suspension-bearing structure with long-span suspension and is difficult to collapse. The breaking and instability of the bearing structure of the thick hard roof cause the strong dynamic ground pressure at the moment, which poses a serious threat to the safety of mining, support equipment, and operators of the working face.

In view of the mining influence of thick hard roof conditions, combined with relevant ground pressure theory and engineering experience, the mining instability influence of the thick hard roof in the working face is analyzed from four aspects: bearing state, spatial structure, instability energy release, and dynamic and static pressure difference:

(1) From the analysis of the stope space, after mining in the longwall coal face of fully mechanized top-coal caving, spatial mining suspended roof structure with a suspended span of 60–80 m and transverse width of 240 m is formed. Once this large area of the suspended roof is unstable, it will show an air impact on the mining space.
(2) From the aspect of roof bearing, the thick and hard roof has a large thickness and relatively high strength, so it has a strong mechanical bearing capacity; in the process of on-site face mining, the thick and hard roof presents a safety risk situation of difficult collapse and large hanging span.
(3) From the analysis of the difference between the dynamic and static pressure, compared with the mining instability of the general thin and weak strata, the mining instability pressure of the thick and hard roof is strong, especially the impact dynamic load of the thick and hard roof at the low position of the stope space is particularly obvious to the dynamic pressure of the working face below.
(4) From the analysis of the pressure behavior of the working face, the instability of the long-span suspension structure will cause mining instability and dynamic load behavior of the broken rock block below and the hydraulic support of the working face, resulting in a large safety deviation between the resistance of the hydraulic support calculated according to the static load and the actual situation.

According to the above safety impact analysis, the problem of strong dynamic pressure disaster of the thick and hard roof urgently needs to be studied and solved, including how to pre-judge the mining instability impact of the thick and hard roof, how to evaluate the dynamic pressure-bearing stability of the hydraulic support in the working face, and what is the key to control the display of the strong dynamic pressure of the thick and hard roof. Therefore, the analysis of energy accumulation and dispersion evolution of the thick hard roof and dynamic load response of the hydraulic support in a large space stope is of great value to solve the problem of strong dynamic pressure disaster of this kind of a thick and hard roof.

MECHANICAL MODEL ANALYSIS OF MINING BEARING CAPACITY AND ENERGY ACCUMULATION OF THE THICK HARD ROOF

Based on the analysis of the influence characteristics of mining instability of the thick hard roof in the working face, this study considers the thick and hard rock roof as the research object, carries out the mechanical model analysis of mining bearing and energy accumulation of the thick hard roof, and reveals the characteristic law of mining bearing and energy accumulation of the thick hard roof, which provides a research basis for the analysis of mining instability and dynamic pressure influence of the thick hard roof in a large space stope.

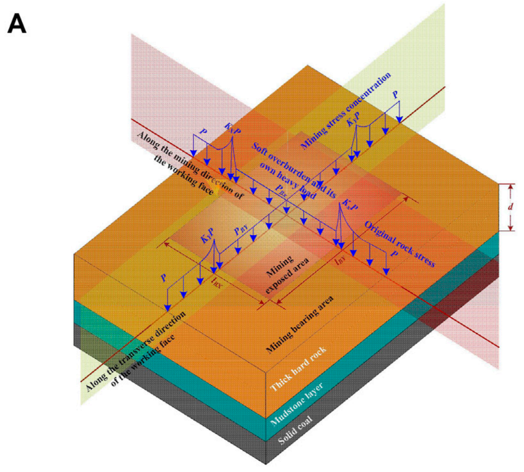

Mechanical state of mining bearing capacity of thick hard roof

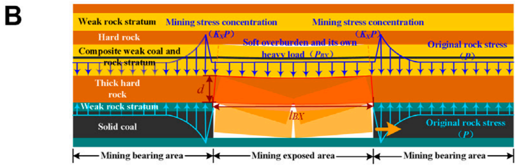

Mining bearing state of thick hard roof along the mining direction

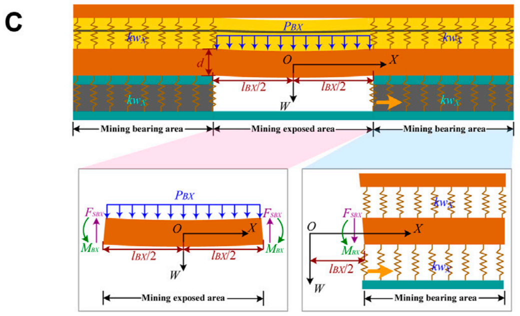

Analysis model of mining stress of thick hard roof

FIGURE 3 | Schematic diagram of the mining bearing mechanical model of the thick hard roof. **(A)** Mechanical state of the mining bearing capacity of the thick hard roof. **(B)** Mining bearing state of the thick hard roof along the mining direction. **(C)** Analysis model of mining stress of the thick hard roof.

Construction of the Mining Bearing Mechanical Model of the Thick Hard Roof

In order to reasonably analyze the mechanical evolution mechanism of mining bearing and energy accumulation of the thick hard roof, based on the MARCUS simplified algorithm, this study constructs the mechanical model of mining bearing of the thick hard roof by using the mechanical analysis method of a single generalized displacement thick beam and the mechanical theory of the semi-infinite elastic foundation beam, as shown in **Figure 3**.

In order to facilitate the solution and analysis of the mechanical model, the following basic assumptions are made for the mining bearing mechanical model of the thick hard roof:

(1) According to the analysis of the law of stope roof activity, for the longwall mining of underground coal mines, the span width ratio of the stope space roof is small and the flat strain beam structure can be used for mechanical analysis.
(2) Consider the middle of the exposed area before the mining fracture of the thick hard roof as the origin of the mechanical coordinate system; then, the mining direction along the working face is the X-coordinate axis and the vertical direction is the *W*-coordinate axis, as shown in **Figure 3B**.
(3) Set the overhang span of the thick hard roof as l_{BX} in the established mechanical coordinate system; then, the location of the mining overhang area in the stope space is $(-l_{BX}/2, l_{BX}/2)$ and the mining bearing area is $(l_{BX}/2, +\infty)$.
(4) In the mining exposed area $(-l_{BX}/2, l_{BX}/2)$, the stress state of the thick hard roof can be regarded as a beam structure under a uniform load, and the overlying load p_{BX} of the roof in the exposed area is composed of its own rock load and the overlying soft coal and rock load.
(5) Considering the large thickness span ratio of the thick hard top slab beam structure in the mining exposed area, the mechanical analysis of the thick beam structure with a single generalized displacement is carried out by using the mechanical model of the thick beam structure.
(6) In the mining bearing area $(l_{BX}/2, +\infty)$, the thick hard roof is constrained by the upper and lower strata and presents the mechanical characteristics of the sandwich bearing, as shown in **Figure 3B**; according to the analysis of the activity law of the stope roof, the upper and lower strata of the stope thick hard roof can be regarded as the elastic foundation structure and analyzed with the mechanical model of the semi-infinite elastic foundation beam structure.
(7) In the deep part of the mining bearing area, the mining stress load on the upper boundary and the foundation reaction load on the lower boundary interact with each other, so it can be regarded as the mutual balance and offset of forces in the mechanical analysis, thereby simplifying the analysis of the mining bearing mechanical model of the thick hard roof, as shown in **Figure 3C**.

Analysis of the Mining Bearing Mechanical Model of the Thick Hard Roof

According to the mechanical model shown in **Figure 3C**, the unit-wide strip of the thick hard top slab along the mining direction (*x*-axis) of the working face is considered as the research object, and the basic mechanical equation of the thick beam structure using a single generalized displacement method (Ke, 2000) is as follows:

$$\begin{cases} \theta_{BX} = \dfrac{\mathrm{d}w_{BX}}{\mathrm{d}x} + \dfrac{EI}{T}\dfrac{\mathrm{d}^3 w_{BX}}{\mathrm{d}x^3}, \\ M_{BX} = -EI\left(\dfrac{\mathrm{d}^2 w_{BX}}{\mathrm{d}x^2} + \dfrac{EI}{T}\dfrac{\mathrm{d}^4 w_{BX}}{\mathrm{d}x^4}\right), \\ F_{SBX} = -EI\dfrac{\mathrm{d}^3 w_{BX}}{\mathrm{d}x^3}, \\ -EI\dfrac{\mathrm{d}^4 w_{BX}}{\mathrm{d}x^4} = -p_{BX}, \end{cases} \tag{1}$$

where w_{BX} is the deflection of the thick hard roof in the mining exposed area along the mining direction; p_{BX} is the overlying load composed of its own gravity load and the transmission load of the overlying weak rock stratum along the mining direction; θ_{BX} is the bending angle of the thick hard roof in the mining exposed area along the mining direction; M_{BX} is the bending moment of the thick hard roof in the mining exposed area along the mining direction; F_{SBX} is the shear force of the thick hard roof in the mining exposed area along the mining direction; E is the elastic modulus of the rock stratum—in plane strain problem, $E = E/(1-v^2)$; $I\ (=bd^3/12)$ is the polar moment of inertia; b is the structural width of the thick hard roof strip, taking unit width 1; d is the thickness of the thick hard roof; $T\ (= 5Ebd/[12\ (1+v)])$ is the shear stiffness of the rectangular strip with the thick hard roof; and v is Poisson's ratio—in a plane strain problem, $v = v/(1-v)$.

From the last equation of **Eq. 1**, the deflection equation of a single generalized displacement of the thick hard roof can be established, and the general solution is as follows:

$$w_{BX} = \frac{p_{BX}}{24EI}x^4 + \frac{B_{1X}}{6}x^3 + \frac{B_{2X}}{2}x^2 + B_{3X}x + B_{4X}, \tag{2}$$

where B_{1X}, B_{2X}, B_{3X}, and B_{4X} are undetermined coefficients.

Substituting **Eq. 2** into equations (1)–(3) of **Eq. 1**, and sorting out.

$$\begin{cases} \theta_{BX} = \dfrac{p_{BX}}{6EI}x^3 + \dfrac{B_{1X}}{2}x^2 + \left(B_{2X} + \dfrac{p_{BX}}{T}\right)x + B_{3X} + \dfrac{EIB_{1X}}{T}, \\ M_{BX} = -EI\left(\dfrac{p_{BX}}{2EI}x^2 + B_{1X}x + B_{2X} + \dfrac{p_{BX}}{T}\right), \\ F_{SBX} = -EI\left(\dfrac{p_{BX}}{EI}x + B_{1X}\right), \end{cases} \tag{3}$$

In the mining exposed area $(-l_{BX}/2, l_{BX}/2)$, the stress bending of the thick hard roof is axisymmetric along the centerline ($x = 0$), which shows that $\theta_{BX}|_{x=0} = 0$, $F_{SBX}|_{x=0} = 0$.

Solution: $B_{1X} = 0$; $B_{3X} = 0$

In **Eq. 3**, only B_{2X} and B_{4X} are unknown coefficients to be determined.

In the mining bearing area of overburden $(l_{BX}/2, +\infty)$, the mechanical equation of the elastic foundation strip structure is as follows:

$$EIw_{AX}^{(4)} = -kw_{AX}, \tag{4}$$

where w_{AX} is the curvature of the thick hard roof in the mining bearing area along the mining direction and k is the elastic foundation stiffness of the upper and lower boundary strata in the mining bearing area of the thick hard roof.

Let $\alpha_A = \sqrt[4]{k/4EI}$; **Eq. 4** is sorted as follows:

$$w_{Ax}^{(4)} + 4\alpha_A^4 w_{AX} = 0, \tag{5}$$

In the mining bearing area, the general solution equation of deflection under the elastic foundation state of the thick hard roof is as follows:

$$w_{AX0} = A_{1X}[CC(x) - SC(x)] + A_{2X}[CS(x) - SS(x)], \tag{6}$$

where: $CC(x) = \cosh[\alpha_A(x - \frac{l_{BX}}{2})]\cos[\alpha_A(x - \frac{l_{BX}}{2})]$; $SC(x) = \sinh[\alpha_A(x - \frac{l_{BX}}{2})]\cos[\alpha_A(x - \frac{l_{BX}}{2})]$; $CS(x)\cosh[\alpha_A(x - \frac{l_{BX}}{2})]\sin[\alpha_A(x - \frac{l_{BX}}{2})]$; and $SC(x) = \sinh[\alpha_A(x - \frac{l_{BX}}{2})]\sin[\alpha_A(x - \frac{l_{BX}}{2})]$.

In the mining bearing area, the mechanical analysis of the semi-infinite thick hard roof can still be analyzed according to the slender strip structure of elastic foundation as follows:

$$\begin{cases} \theta_{AX} = \dfrac{\mathrm{d}w_{AX}}{\mathrm{d}x}, \\ M_{AX} = -EI\dfrac{\mathrm{d}^2 w_{AX}}{\mathrm{d}x^2}, \\ F_{SAX} = -EI\dfrac{\mathrm{d}^3 w_{AX}}{\mathrm{d}x^3}, \end{cases} \tag{7}$$

where θ_{AX} is the curvature of the thick hard roof in the mining bearing area along the mining direction; M_{AX} is the bending moment of the thick hard roof in the mining bearing area along the mining direction; and F_{SAX} is the shear force of the thick hard roof in the mining bearing area along the mining direction.

The mechanical equation of the semi-infinite thick roof strip structure in the mining bearing area is as follows:

$$\begin{cases} \theta_{AX} = \{-\alpha_A(A_{1X} + A_{2X})[CS(x) - SS(x)] + \alpha_A(A_{1X} - A_{2X})[SC(x) - CC(x)]\}, \\ M_{AX} = -2\alpha_A^2 EI\{-A_{1X}[SS(x) - CS(x)] + A_{2X}[SC(x) - CC(x)]\}, \\ F_{SAX} = -2\alpha_A^3 EI\{-(A_{1X} - A_{2X})[CS(x) - SS(x)] - (A_{1X} + A_{2X})[SC(x) - CC(x)]\}, \end{cases} \tag{8}$$

Currently, A_{1X} and A_{2X} are undetermined coefficients.

At the end of the mining exposed area, the stress and deformation of the thick hard roof meet the static equivalent, that is, on both sides of the position ($x= l_{BX}/2$).

$$\begin{cases} w_{AX}|_{x=\frac{l_{BX}}{2}} = w_{BX}|_{x=\frac{l_{BX}}{2}}, \\ \theta_{AX}|_{x=\frac{l_{BX}}{2}} = \theta_{BX}|_{x=\frac{l_{BX}}{2}}, \\ M_{AX}|_{x=\frac{l_{BX}}{2}} = M_{BX}|_{x=\frac{l_{BX}}{2}}, \\ F_{SAX}|_{x=\frac{l_{BX}}{2}} = F_{SBX}|_{x=\frac{l_{BX}}{2}}, \end{cases} \tag{9}$$

Substituting **Eqs 3** and **8** into **Eq. 9**, we obtain the following equations:

$$\begin{cases} A_{1X} = \dfrac{p_{BX}}{24EI}\left(\dfrac{l_{BX}}{2}\right)^4 + \dfrac{B_{2X}}{2}\left(\dfrac{l_{BX}}{2}\right)^2 + B_{4X} \\ -\alpha_B(A_{1X} - A_{2X}) = \dfrac{p_{BX}}{6EI}\left(\dfrac{l_{BX}}{2}\right)^3 + \left(B_{2X} + \dfrac{p_{BX}}{T}\right)\left(\dfrac{l_{BX}}{2}\right), \\ 2\alpha_B^2 EIA_{2X} = -\left[\dfrac{p_{BX}}{2}\left(\dfrac{l_{BX}}{2}\right)^2 + \left(B_{2X} + \dfrac{p_{BX}}{T}\right)EI\right] \\ -2\alpha_B^3 EI(A_{1X} + A_{2X}) = -p_{BX}\left(\dfrac{l_{BX}}{2}\right), \end{cases} \tag{10}$$

The coefficients are as follows:

$$\begin{cases} B_{2X} = \dfrac{p_{BX}l_{BX}}{8\alpha_A EI\left(-\dfrac{l_{BX}}{4\alpha_A} - \dfrac{1}{2\alpha_A^2}\right)}\left(\dfrac{1}{\alpha_A^2} + \dfrac{l_{BX}^2}{12} + \dfrac{l_{BX}}{2\alpha_A}\right) - \dfrac{p_{BX}}{T}, \\ B_{4X} = \dfrac{p_{BX}l_{BX}}{8EI}\left(\dfrac{1}{\alpha_A^3} - \dfrac{l_{BX}^2}{16\alpha_A} - \dfrac{l_{BX}^3}{48} - \dfrac{2EI}{\alpha_A T}\right) - B_{2X}\left(\dfrac{l_{BX}}{4\alpha_A} + \dfrac{l_{BX}^2}{8}\right), \\ A_{1X} = \dfrac{p_{BX}l_{BX}}{8EI}\left(\dfrac{1}{\alpha_A^3} - \dfrac{l_{BX}^2}{16\alpha_A}\right) - \dfrac{l_{BX}}{4\alpha_A}\left(B_{2X} + \dfrac{p_{BX}}{T}\right), \\ A_{2X} = \dfrac{p_{BX}l_{BX}}{8EI}\left(\dfrac{1}{\alpha_A^3} + \dfrac{l_{BX}^2}{16\alpha_A}\right) + \dfrac{l_{BX}}{4\alpha_A}\left(B_{2X} + \dfrac{p_{BX}}{T}\right), \end{cases} \tag{11}$$

The bending deformation equation of the thick hard roof in the stope space along the working face direction (X-axis) can be sorted out as follows:

$$w_{ABX} = \begin{cases} A_{1X}[CC(-x) - SC(-x)] + A_{2X}[CS(-x) - SS(-x)] & \left(-\infty, -\dfrac{l_{BX}}{2}\right] \\ \dfrac{p_{BX}}{24EI}x^4 + \dfrac{B_{2X}}{2}x^2 + B_{4X} & \left[-\dfrac{l_{BX}}{2}, \dfrac{l_{BX}}{2}\right] \\ A_{1X}[CC(x) - SC(x)] + A_{2X}[CS(x) - SS(x)] & \left[\dfrac{l_{BX}}{2}, +\infty\right), \end{cases} \tag{12}$$

$$M_{ABX} = \begin{cases} -2\alpha_A^2 EI\{-A_{1X}[SS(-x) - CS(-x)] + A_{2X}[SC(-x) - CC(-x)]\} & \left(-\infty, -\dfrac{l_{BX}}{2}\right] \\ -\left(\dfrac{p_{BX}}{2}x^2 + B_{2X}EI + \dfrac{p_{BX}EI}{T}\right) & \left[-\dfrac{l_{BX}}{2}, \dfrac{l_{BX}}{2}\right] \\ -2\alpha_A^2 EI\{-A_{1X}[SS(x) - CS(x)] + A_{2X}[SC(x) - CC(x)]\} & \left[\dfrac{l_{BX}}{2}, +\infty\right). \end{cases} \tag{13}$$

Similarly, the bending deformation equation of the thick hard roof in the stope space along the transverse direction of the working face (Y-axis) is as follows:

$$w_{ABY} = \begin{cases} A_{1Y}[CC(-y) - SC(-y)] + A_{2Y}[CS(-y) - SS(-y)] & \left(-\infty, -\dfrac{l_{BY}}{2}\right] \\ \dfrac{p_{BY}}{24EI}y^4 + \dfrac{B_{2Y}}{2}y^2 + B_{4Y} & \left[-\dfrac{l_{BY}}{2}, \dfrac{l_{BY}}{2}\right] \\ A_{1Y}[CC(y) - SC(y)] + A_{2Y}[CS(y) - SS(y)] & \left[\dfrac{l_{BY}}{2}, +\infty\right), \end{cases} \tag{14}$$

$$M_{ABY} = \begin{cases} -2\alpha_A^2 EI\{-A_{1Y}[SS(-y) - CS(-y)] + A_{2Y}[SC(-y) - CC(-y)]\} & \left(-\infty, -\dfrac{l_{BY}}{2}\right] \\ -\left(\dfrac{p_{BY}}{2}y^2 + B_{2Y}EI + \dfrac{p_{BY}EI}{T}\right) & \left[-\dfrac{l_{BY}}{2}, \dfrac{l_{BY}}{2}\right] \\ -2\alpha_A^2 EI\{-A_{1Y}[SS(y) - CS(y)] + A_{2Y}[SC(y) - CC(y)]\} & \left[\dfrac{l_{BY}}{2}, +\infty\right), \end{cases} \tag{15}$$

and

$$\begin{cases} B_{2Y} = \dfrac{p_{BY}l_{BY}}{8\alpha_A EI\left(-\dfrac{l_{BY}}{4\alpha_A} - \dfrac{1}{2\alpha_A^2}\right)}\left(\dfrac{1}{\alpha_A^2} + \dfrac{l_{BY}^2}{12} + \dfrac{l_{BY}}{2\alpha_A}\right) - \dfrac{p_{BY}}{T}, \\ B_{4Y} = \dfrac{p_{BY}l_{BY}}{8EI}\left(\dfrac{1}{\alpha_A^3} - \dfrac{l_{BY}^2}{16\alpha_A} - \dfrac{l_{BY}^3}{48} - \dfrac{2EI}{\alpha_A T}\right) - B_{2Y}\left(\dfrac{l_{BY}}{4\alpha_A} + \dfrac{l_{BY}^2}{8}\right), \\ A_{1Y} = \dfrac{p_{BY}l_{BY}}{8EI}\left(\dfrac{1}{\alpha_A^3} - \dfrac{l_{BY}^2}{16\alpha_A}\right) - \dfrac{l_{BY}}{4\alpha_A}\left(B_{2Y} + \dfrac{p_{BY}}{T}\right), \\ A_{2Y} = \dfrac{p_{BY}l_{BY}}{8EI}\left(\dfrac{1}{\alpha_A^3} + \dfrac{l_{BY}^2}{16\alpha_A}\right) + \dfrac{l_{BY}}{4\alpha_A}\left(B_{2Y} + \dfrac{p_{BY}}{T}\right), \end{cases} \tag{16}$$

Based on the Marcus simplified algorithm, the orthogonal slab structural units along the mining direction (X-axis) and the transverse direction (Y-axis) of the working face meet the following requirements:

$$w_{ABX}\big|_{x=0} = w_{ABY}\big|_{y=0}, \tag{17}$$

Substituting **Formulas 11–16**, the result is as follows:

$$\frac{p_{BX}}{p_{BY}} = \frac{\left[\frac{l_{BY}}{8}\left(\frac{1}{\alpha_A^3} - \frac{l_{BY}^2}{16\alpha_A} - \frac{l_{BY}^3}{48}\right) - \frac{EIl_{BY}}{4\alpha_A T} + \frac{\frac{l_{BY}}{8\alpha_A}\left(\frac{1}{\alpha_A^2} + \frac{l_{BY}^2}{12} + \frac{l_{BY}}{2\alpha_A}\right) + \frac{EI}{T}\left(\frac{l_{BY}}{4\alpha_A} + \frac{1}{2\alpha_A^2}\right)}{\left(\frac{l_{BY}}{4\alpha_A} + \frac{1}{2\alpha_A^2}\right)}\left(\frac{l_{BY}}{4\alpha_A} + \frac{l_{BY}^2}{8}\right)\right]}{\left[\frac{l_{BX}}{8}\left(\frac{1}{\alpha_A^3} - \frac{l_{BX}^2}{16\alpha_A} - \frac{l_{BX}^3}{48}\right) - \frac{EIl_{BX}}{4\alpha_A T} + \frac{\frac{l_{BX}}{8\alpha_A}\left(\frac{1}{\alpha_A^2} + \frac{l_{BX}^2}{12} + \frac{l_{BX}}{2\alpha_A}\right) + \frac{EI}{T}\left(\frac{l_{BX}}{4\alpha_A} + \frac{1}{2\alpha_A^2}\right)}{\left(\frac{l_{BX}}{4\alpha_A} + \frac{1}{2\alpha_A^2}\right)}\left(\frac{l_{BX}}{4\alpha_A} + \frac{l_{BX}^2}{8}\right)\right]}, \tag{18}$$

Based on the MARCUS simplified algorithm, given that $p_{BX} + p_{BY} = p_B$, let $\lambda_B = p_{BX}/p_{BY}$; then, the strip loads of the thick hard roof structure along the working face direction (X-axis) and the strip loads along the working face transverse direction (Y-axis) are respectively, as follows:

$$\begin{cases} p_{BX} = \dfrac{\lambda_B p_B}{1 + \lambda_B} \\ p_{BY} = \dfrac{p_B}{1 + \lambda_B} \end{cases} \tag{19}$$

According to the energy principle, the integral equation of the elastic energy accumulation density U of the strip structure of the thick hard roof is as follows:

$$\mathrm{d}U = \int_0^{\kappa} M \mathrm{d}\kappa, \tag{20}$$

where κ is the curvature of the strip member.

According to the physical equation of the linear elastic strip member, it can be seen that

$$M = EI\kappa, \tag{21}$$

According to the geometric equation of the strip member with a linear elastic medium, it can be seen that

$$\kappa = \mathrm{d}\theta/\mathrm{d}x, \tag{22}$$

Simultaneously, **Eqs 14–16** are sorted as follows:

$$\mathrm{d}U = \frac{EIM^2}{2}, \tag{23}$$

According to the bending moment equation under the mining bearing of the thick hard roof of the mining overburden derived from **Eqs 3** and **8**, and substituting them into **Eq. 23**, the elastic energy accumulation density equation under the mining bearing state of the thick hard roof is as follows:

$$\mathrm{d}U_{ABX} = \begin{cases} 2\alpha_A^4 EI\{-A_{1X}[SS(-x) - CS(-x)] + A_{2X}[SC(-x) - CC(-x)]\}^2 & \left(-\infty, -\frac{l_{BX}}{2}\right] \\ \frac{EI}{2}\left(\frac{p_{BX}}{2EI}x^2 + B_{2X} + \frac{p_{BX}}{T}\right)^2 & \left[-\frac{l_{BX}}{2}, \frac{l_{BX}}{2}\right] \\ 2\alpha_A^4 EI\{-A_{1X}[SS(x) - CS(x)] + A_{2X}[SC(x) - CC(x)]\}^2 & \left[\frac{l_{BX}}{2}, +\infty\right). \end{cases} \tag{24}$$

Mechanical Law of the Mining Bearing Capacity and Energy Accumulation of the Thick Hard Roof

Using the example analysis, the mechanical characteristics of the mining bearing capacity and energy accumulation evolution of the thick hard roof are revealed. The assumptions for example analysis are the following: $l_{BX} = 60$ m, $d = 10$ m, $b = 1$, $E = 4$ GPa, $\nu = 0.2$, $k = 1000$ MN/m, and $p_{BX} = 1$ MPa. The above parameters are, respectively, substituted into the deflection equation (**Eq. 12**), bending moment equation (**Eq. 13**), and elastic energy accumulation density (**Eq. 24**) to analyze the influencing factors of the mining bearing capacity of the thick hard roof. The calculation results are shown in **Figures 4–7**.

(1) Influence of the Overlying Load on the Mining Bearing Capacity of the Thick Hard Roof.

As shown in **Figure 4**, with the increase of the overburden transmission load, the mining bearing state and energy accumulation of the thick and hard roof are significantly intensified, leading to a more serious and hidden danger of mining instability of thick and hard roof; from the mechanical distribution characteristics of mining bearing, the bending force and accumulated energy of the thick and hard roof are mainly concentrated in the middle and both ends of the mining exposed area; among them, the position near the end of the suspended area (1–5 m away from the boundary of the suspended area) is the key position to judge the mining failure and instability of the thick and hard roof.

(2) Influence of the Mining Suspension Span on the Mining Bearing Capacity of the Thick Hard Roof.

As shown in **Figure 5**, with the increase of the overhang span, the bearing load of the thick and hard roof in the mining overhang area increases, and the bending degree and accumulated energy density of the thick and hard roof show an increasing evolution. The mining energy accumulation of the thick and hard roof is particularly sensitive to the increase of the overhang span.

(3) Influence of the Rock Stratum Thickness on the Mining Bearing Capacity of the Thick Hard Roof.

As shown in **Figure 6**, the greater the thickness of the rock stratum, the greater the bending stiffness of the rock stratum, making the thick and hard roof have a stronger bearing and energy accumulation capacity; although the bending degree of the

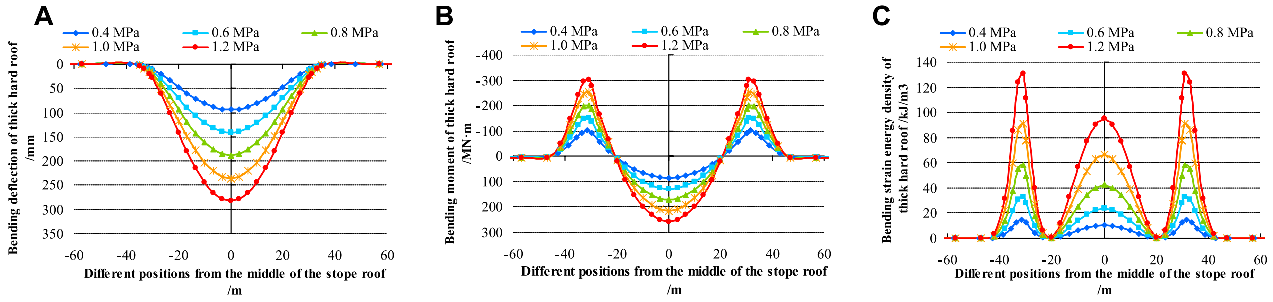

FIGURE 4 | Mechanical influence characteristics of the overlying load in the mining exposed area on the mining bearing capacity of the thick hard roof. **(A)** Distribution characteristics of bending deflection. **(B)** Distribution characteristics of stressed bending moment. **(C)** Distribution characteristics of elastic energy accumulation.

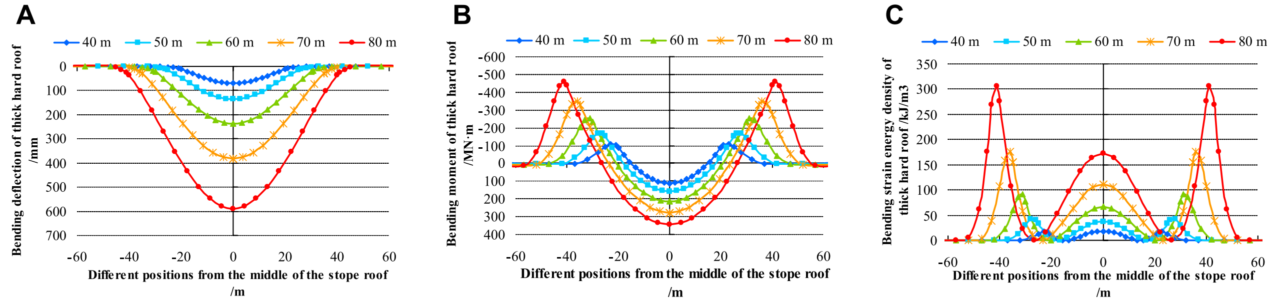

FIGURE 5 | Mechanical influence characteristics of the mining suspension span on the mining bearing capacity of the thick hard roof. **(A)** Distribution characteristics of bending deflection. **(B)** Distribution characteristics of stressed bending moment. **(C)** Distribution characteristics of elastic energy accumulation.

thick and hard roof decreases and the peak value of the bending moment does not change significantly, excessive energy accumulation will cause strong mining instability and dynamic pressure in the stope space, and the bending moment in the mining bearing area shows the characteristics of weakening convergence distribution.

(4) Influence of the Rock Elastic Modulus on the Mining Bearing Capacity of the Thick Hard Roof.

As shown in **Figure 7**, the influence of the elastic modulus of the rock stratum on the mechanical bearing capacity of the thick and hard roof is similar to the influence characteristics of the thickness of the rock stratum, and the bending stiffness of the rock stratum itself is improved, which leads to the increase of the mining breaking limit span. Accordingly, the mining instability energy and impact dynamic pressure are more intense when the mining instability occurs.

To sum up, the thick hard roof has the characteristics of a strong bearing capacity and large accumulation of mining energy, and the working face is strongly affected by the dynamic pressure; the greater the thickness and elastic modulus of the thick hard roof, the greater its flexural stiffness, and the ultimate breaking span of the thick hard roof increases; with the increase of the overhanging span and overlying load of the thick hard roof, its mining bearing state and energy accumulation are evidently intensified.

INFLUENCE OF THE ACCUMULATED ENERGY RELEASE OF THICK HARD ROOF MINING ON THE DYNAMIC LOAD OF THE HYDRAULIC SUPPORT IN THE WORKING FACE

Elastic Energy Release of Mining Failure and Instability of the Thick Hard Roof

According to the distribution characteristics of the mining bearing capacity and energy accumulation evolution of the thick hard roof given in the *Mechanical Law of Mining Bearing Capacity and Energy Accumulation of the Thick Hard Roof* section, the tensile fracture of the upper boundary of the thick hard roof is selected as the judgment condition of mining fracture instability, and its bending expression is as follows:

$$\max|M_{ABX}(x)| \geq [\sigma_t]d^2/6, \tag{25}$$

where $[\sigma_t]$ is the tensile strength of the thick hard roof rock stratum.

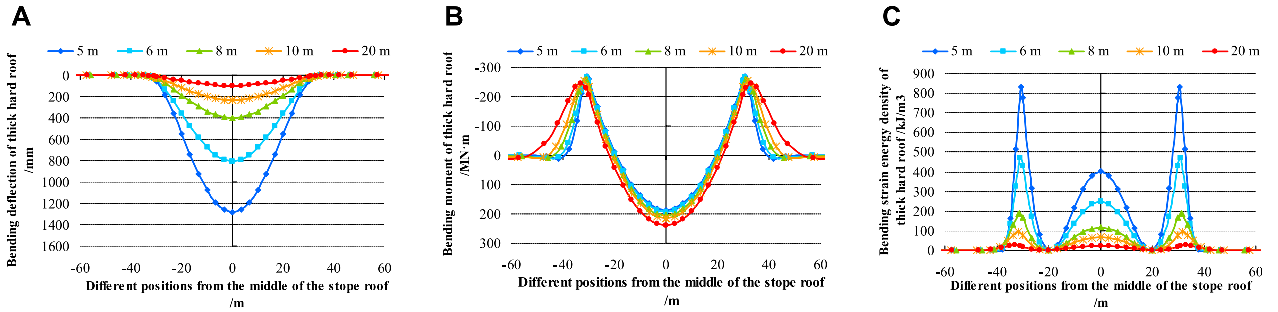

FIGURE 6 | Mechanical characteristics of the influence of the rock stratum thickness on the mining bearing capacity of the thick hard roof. **(A)** Distribution characteristics of bending deflection. **(B)** Distribution characteristics of stressed bending moment. **(C)** Distribution characteristics of elastic energy accumulation.

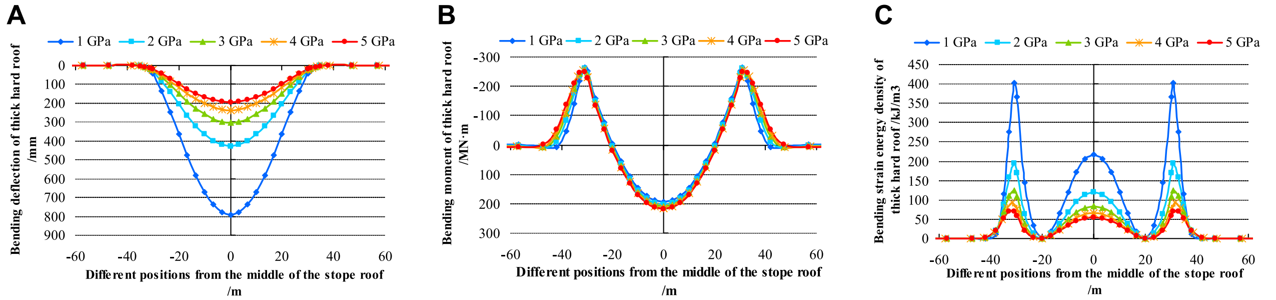

FIGURE 7 | Mechanical influence characteristics of the rock stratum elastic modulus on the mining bearing capacity of the thick hard roof **(A)** Distribution characteristics of bending deflection. **(B)** Distribution characteristics of stressed bending moment. **(C)** Distribution characteristics of elastic energy accumulation.

By substituting the bending moment equation (**Eq. 13**) of the thick hard roof into **Eq. 24**, the discrimination equation of mining failure and instability of the thick hard roof is obtained.

$$\max\left| -2k\alpha_A^2 EI\{-A_{1X}[SS(x)-CS(x)]+A_{2X}[SC(x)-CC(x)]\}\right| \geq \frac{[\sigma_t]d^2}{6}, \tag{26}$$

The example analysis shows that the mining breaking span and mining suspension span are not in the same position, and the mining limit breaking span l_{AB} of the thick hard roof can be calculated by **Eq. 26**. At the moment of mining breaking and instability, the elastic energy accumulated by the mining bearing of the thick hard roof is released due to breaking and instability, which is transformed into the instability kinetic energy of the broken block, and the mining elastic energy of the thick hard roof within the range of ($-l_{ABX}/2$, $l_{ABX}/2$) is integrated, the elastic energy release equation U_{wJBDX} of the thick hard roof breaking instability is obtained from the equation.

$$U_{wJBDX} = \int_{-\frac{l_{ABX}}{2}}^{\frac{l_{ABX}}{2}} \mathrm{d}U_{ABX}\mathrm{d}x, \tag{27}$$

By integrating the above formula, the elastic energy release equation U_{wJBDX} of mining failure and instability of the thick hard roof is obtained as follows:

$$U_{wJBDX} = \frac{p_{BX}^2 l_{BX}^5}{620EI} + \frac{p_{BX} l_{BX}^3}{24}\left(B_{2X} + \frac{p_{BX}}{T}\right) + \frac{EIl_{BX}}{2}\left(B_{2X} + \frac{p_{BX}}{T}\right)^2 + 4\alpha_A^4 EI$$
$$\cdot\left\{\begin{array}{l} \dfrac{e^{-2\alpha_A\left(\frac{l_{ABX}}{2}-\frac{l_{BX}}{2}\right)}}{8\alpha_A}\left[(2A_{1X}A_{2X}-A_{2X}^2+A_{1X}^2)\cos 2\alpha_A\left(\dfrac{l_{ABX}}{2}-\dfrac{l_{BX}}{2}\right)+(2A_{1X}A_{2X}+A_{2X}^2-A_{1X}^2)\sin 2\alpha_A\left(\dfrac{l_{ABX}}{2}-\dfrac{l_{BX}}{2}\right)\right] \\ -\dfrac{(A_{2X}^2+A_{1X}^2)}{4\alpha_A}\left[e^{-2\alpha_A\left(\frac{l_{ABX}}{2}-\frac{l_{BX}}{2}\right)}-1\right]-\dfrac{2A_{1X}A_{1X}-A_{2X}^2+A_{1X}^2}{8\alpha_A}. \end{array}\right\} \tag{28}$$

Dynamic Load Response of the Hydraulic Support in the Working Face Under Thick Hard Roof Conditions

As shown in **Figure 8**, the mining instability of a thick hard roof leads to the release of elastic energy accumulated by the thick hard roof. At the same time, with the work done by the overlying load, they are jointly converted into the mining instability kinetic energy of the thick hard roof, forming a dynamic load impact on the directly broken roof below; the impact dynamic load is transmitted to the hydraulic support of the working face along the longitudinal direction to form the dynamic pressure of the working face.

According to this force transmission characteristic, the dynamic load response of the hydraulic support in the working face with an accumulated energy release of thick hard roof mining is analyzed, and the energy balance equation before and after mining instability of the thick hard roof is established according to the energy conservation:

$$p_B l_{ABX} \Delta w_{ABX} + U_{wABX} = V_{ABX}, \tag{29}$$

where V_{ABX} is the kinetic energy of mining failure and instability of the thick hard roof, $V_{ABX} = \int_0^{\Delta w_{ABX}} K_{ZJD} w \mathrm{d}w = \frac{1}{2} K_{ZJD} \Delta w_{ABX}^2$; K_{ZJD} is the stiffness of the coal rock direct roof; Δw_{ZJDX} is the movement of the thick hard roof instability.

Solution:

$$\Delta w_{ABX} = \frac{p_{BX} l_{ABX} + \sqrt{(p_{BX} l_{ABX})^2 + 2K_{ZJD} U_{wJBDX}}}{K_{ZJD}}, \tag{30}$$

Eq. 29 is substituted into **Eq. 28**, and it is concluded that the impact dynamic load Q_{ZJD} caused by the mining instability of the thick hard roof on the direct roof is as follows:

$$Q_{ABX} = K_{ZJD} \Delta w_{ZJDX} = p_{BX} l_{ABX} \left[1 + \sqrt{1 + \frac{2K_{ZJD} U_{wABX}}{(p_{BX} l_{ABX})^2}} \right], \tag{31}$$

It should be noted that due to the mining fracture and block hinged rotation shown in **Figure 2** when the thick hard roof is unstable, part of the accumulated energy released by the thick hard roof mining is transmitted to the goaf floor and the other part is transmitted to the coal and rock direct roof at the hinged points at both ends. Therefore, the effective impact dynamic load borne by the direct roof above the working face is $Q_{ZJD} = Q_{ABX}/4$.

As shown in **Figure 9**, the dynamic load response analysis of the hydraulic support in the working face is based on the hydraulic support in the middle of the working face. In the mining space of the working face, the mining impact dynamic load at each point of the thick hard roof will have a superimposed impact on the dynamic load transmission of the hydraulic support. In view of the influence of the mining space, this study analyzes the influence of dynamic load superposition of the middle support of the working face with the idea of semi-infinite body mechanical analysis under uniformly distributed load conditions.

Considering the top of the hydraulic support in the middle of the working face as the origin o, the horizontal direction along the working face is the *Y*-axis, and the vertical direction is the *Z*-axis. The impact dynamic load Q_{ZJD} can be calculated by **Eq. 31**; considering that the hydraulic support resistance of the longwall working face is composed of the gravity load of the direct roof of coal and rock and the effective impact dynamic load transmitted from the direct roof, in which the gravity load G_{ZJD} of the inclined rectangular block of the direct roof of coal and rock carried by the roof of the support is as follows:

$$G_{ZJD} = \gamma_{ZJD} g d_{ZJD} b_{ZJ} \frac{(2l_{ZJ} + d_{ZJD} \cot \beta)}{2}, \tag{32}$$

where l_{ZJ} is the top control distance of the hydraulic support of the working face; β_{ZJD} is the direct roof breaking angle of coal and rock; r_{ZJD} is the average unit weight of the direct roof of coal and rock; g is the acceleration of gravity; and b_{ZJ} is the center distance of the support.

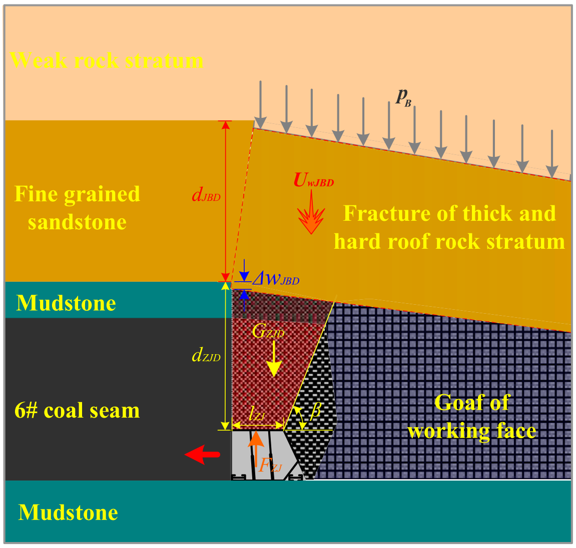

FIGURE 8 | Schematic diagram of the dynamic load response mechanical analysis of the hydraulic support in the working face.

To sum up, the dynamic load response estimation equation F_{ZJ} of the hydraulic support in the working face with the thick hard roof is established as follows:

$$\begin{aligned} F_{ZJ} &= G_{ZJD} + \int_{-\frac{L}{2}}^{\frac{L}{2}} sQ_{ZJD} b_{ZJ} \left[d_{ZJD}^2 + y^2 \right]^{-\frac{\eta}{2}} \mathrm{d}y \\ &= \gamma_{ZJD} g d_{ZJD} b_{ZJ} \frac{(2l_{ZJ} + d_{ZJD} \cot \beta)}{2} + 2sQ_{ZJD} b_{ZJ} \int_0^{\frac{L}{2}} \left[d_{ZJD}^2 + y^2 \right]^{-\frac{\eta}{2}} \mathrm{d}y, \end{aligned} \tag{33}$$

where L is the width of the working face; η is the attenuation coefficient of dynamic load transmission of the direct roof rock medium $\eta \geq 1$, and the greater the η, the greater the attenuation degree of the dynamic load (Gao et al., 2007; Jiang et al., 2015); and s is the dynamic load transfer efficiency. According to the analysis of the propagation efficiency and attenuation law of vibration energy in the literature (Gao et al., 2007; Jiang et al., 2015), the dynamic load transfer efficiency is generally 1/100–1/10.

Considering in this calculation $\eta = 1.0$ and $s = 1/20$, the dynamic load response estimation equation F_{ZJ} of the hydraulic support of the working face under the condition of a thick hard roof is obtained by integrating **Eq. 34**:

$$\begin{aligned} F_{ZJ} = \gamma_{ZJD} g d_{ZJD} b_{ZJ} \frac{(2l_{ZJ} + d_{ZJD} \cot \beta)}{2} + \frac{Q_{ZJD} b_{ZJ}}{10} \Bigg[\ln \Bigg(\frac{L}{2} \\ + \sqrt{\frac{L^2}{4} + d_{ZJD}^2} \Bigg) - \ln (d_{ZJD}) \Bigg], \end{aligned} \tag{34}$$

Dynamic Load Response Characteristics of the Hydraulic Support in the Thick Hard Roof Working Face

Based on the example analysis given in the *Analysis of the Mining Bearing Mechanical Model of the Thick Hard Roof* section, the dynamic load response characteristics of the hydraulic support in

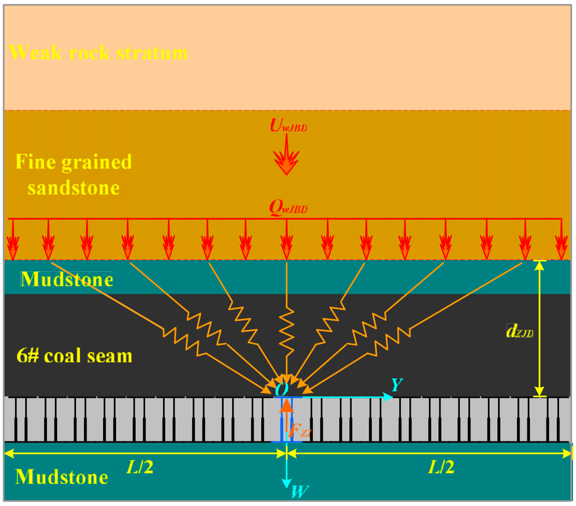

FIGURE 9 | Schematic diagram of the hydraulic support in the middle of the working face affected by impact dynamic load superposition.

the working face under thick hard roof conditions are revealed. It is assumed that l_{AB} = 60 m, l_{ZJ} = 6 m, b_{ZJ} = 1.75 m, d_{ZJD} = 16 m, $\beta_{ZJD} = 70^{\circ}$, r_{ZJD} = 1600 kg/m^3, η = 1.0, s = 1/20, L = 240 m, and g = 10 m/s^2; the above parameters are substituted into **Eqs 26**, **28**, **31**, **32**, and **34** to calculate the dynamic resistance of the hydraulic support. The calculation results are shown in **Figure 10**.

As shown in **Figure 10**, in the dynamic resistance composition of the hydraulic support, the dynamic resistance caused by the work of the overlying load accounts for the highest proportion, followed by the accumulation and release of elastic energy of the thick hard roof, and the static resistance caused by the direct top gravity accounts for the lowest proportion. The cause of formation analysis shows that the thick hard roof has a strong bearing capacity and carries a large transmission load of the overlying soft rock stratum in the process of mining.

From the analysis of the influence characteristics of various factors, as shown in **Figures 10A,B**, the dynamic resistance of the hydraulic support caused by the release of elastic energy increases with the increase of the overlying load and the span of the thick hard top plate, and the dynamic resistance caused by the work of the overlying load increases uniformly.

As shown in **Figures 10C,D**, the greater the thickness and elastic modulus of the thick hard roof, the dynamic resistance caused by the release of elastic energy shows an accelerated decreasing trend, while the increasing trend of the dynamic resistance caused by the work of the overlying load is not evident, but the greater the thickness of the rock stratum, the higher the bending stiffness of the roof, under the condition of the same rock stratum strength, the greater the limit mining breaking span of the thick hard roof, which leads to the increasing influence of the breaking instability of the thick hard roof on the dynamic resistance of the hydraulic support, as shown in **Figure 10B**.

As shown in **Figure 10E**, the thicker the direct roof of coal and rock, although the static resistance caused by the direct roof gravity is increased, it plays a prominent role in buffering and dissipating the unstable dynamic load of the thick hard roof. The dynamic resistance of the hydraulic support caused by the release of elastic energy and the work of overlying load shows a slow decreasing trend, and the dynamic resistance of the hydraulic support finally shows a slow decreasing trend, which alleviates the load of the hydraulic support of the working face to a certain extent and is conducive to improving the dynamic pressure influence of the working face.

As shown in **Figure 10F**, with the increase of the top control distance of the hydraulic support, the dynamic and static resistance of the hydraulic support increases, which increases the bearing burden of the hydraulic support.

From the aspect of rock pressure control of the thick hard roof, the overlying load, thickness, elastic modulus, and the thickness of the direct roof of the thick hard roof belong to the geological conditions of coal and the rock stratum. It is difficult to carry out artificial technical transformation and the technical and economic value is not high, while the span of the thick hard roof and the distance between hydraulic supports can be controlled by artificial technology, and the suspension span has the most serious impact on the mining instability and strong dynamic pressure of the thick hard roof. Adopting pre-splitting and roof cutting technology to regulate the suspension span is an effective technical way to realize the strong dynamic pressure control of the thick hard roof.

TECHNICAL COUNTERMEASURES FOR PREVENTION AND CONTROL OF GROUND PRESSURE IN THE THICK HARD ROOF WORKING FACE

Dynamic Load Response Analysis of the Hydraulic Support in the Thick Hard Roof Working Face

Combined with the engineering conditions of the 61304 fully mechanized top-coal caving face in the Tangjiahui coal mine, E = 4 GPa, ν = 0.2, d = 15.8 m, σ_t = 5.5 MPa, p_B = 0.94 MPa, k = 1000 MN/m, l_{ZJ} = 7.1 m, b_{ZJ} = 1.75 m, d_{ZJD} = 16 m, $\beta_{ZJD} = 70^{\circ}$, r_{ZJD} = 1600 kg/m^3, η = 1.0, s = 1/20, L = 240 m, and g = 10 m/s^2; the aforementioned parameters are substituted into **Eqs 26**, **28**, **31**, **32**, and **34** to calculate the dynamic resistance of the hydraulic support. The calculation results are shown in **Figure 10**.

The calculation results show that the dynamic resistance caused by the mining instability of the thick hard roof in a 61304 fully mechanized top-coal caving face to the hydraulic support of the working face is 20322 kN (relative pillar pressure: 52 MPa) and the working resistance of the ZF18000/28/45 working face hydraulic support selected on-site is 18000 kN, which is less than the dynamic resistance of the working face hydraulic support calculated theoretically; at present, the support does not meet the bearing stability requirements of the thick and hard basic mining instability

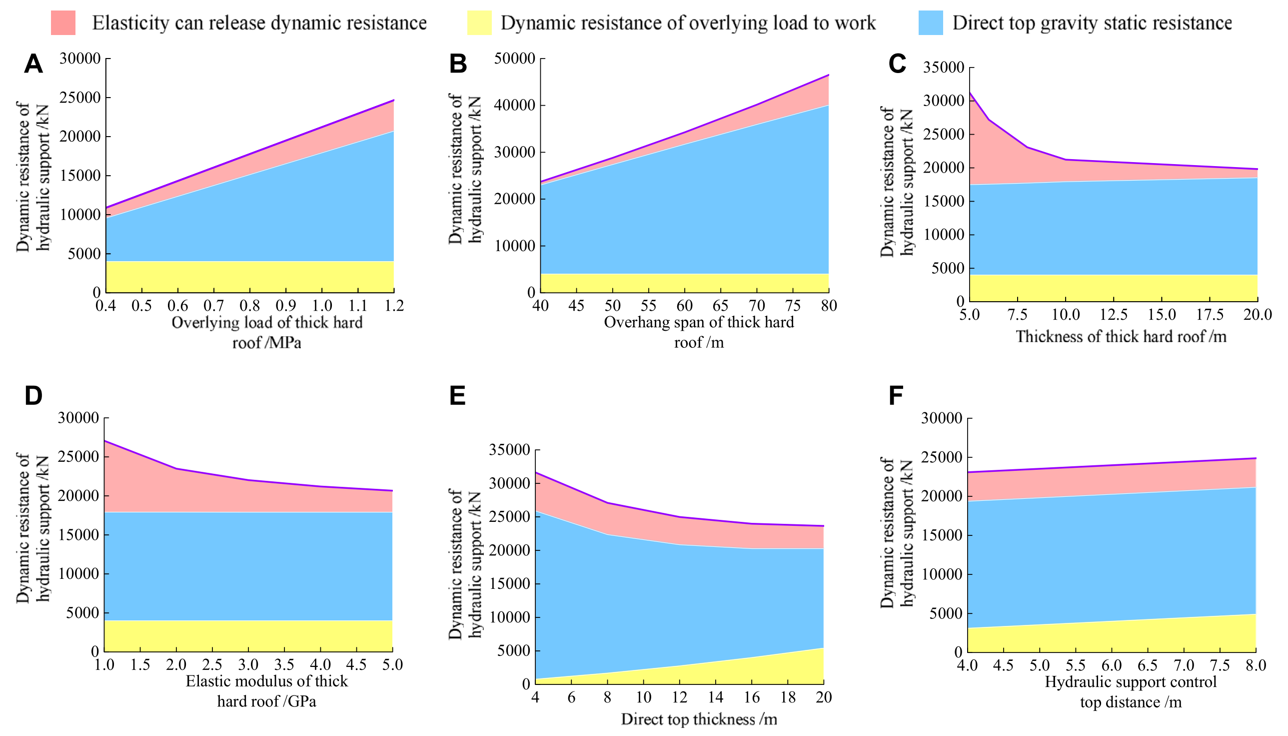

FIGURE 10 | Influence characteristics of the dynamic pressure of the working face hydraulic support under thick hard roof conditions. **(A)** Influence of the overlaying load on the thick hard roof. **(B)** Influence of the thick hard roof span. **(C)** Influence of the thick hard roof thickness. **(D)** Influence of the thick hard roof on the elastic modulus. **(E)** Influence of the direct top thickness. **(F)** Influence of the hydraulic support top control distance.

dynamic pressure. In view of the safety problems of underground coal mining engineering, this study suggests adopting pre-splitting and roof cutting technology to transform the basic mechanical bearing state of the thick hard roof, shorten the mining breaking span of the thick hard roof, and reduce the dynamic pressure appearance strength of the thick hard roof.

Technical Countermeasures for Roof Cutting and Pressure Relief of the Thick Hard Roof Working Face

Comprehensively considering the coal measures and geological conditions of a fully mechanized top-coal caving face and the actual situation of top-coal caving mining, the technical scheme of blasting top cutting in the initial mining stage of the fully mechanized top-coal caving face is designed, as shown in **Figure 11**.

The top cutting blasting drilling hole is arranged at the side of the roadway 500 mm behind the cutting hole of the working face, and within the range of the mining roadway 50 m away from the cutting hole mining coal wall and 500 mm near the side of the coal pillar with Φ 70 mm × 4000 mm and drilling spacing of 800 mm. The two-way shaped charge blasting technology is adopted. The outer diameter of the long axis of the specially shaped charge tube is 49 mm, the outer diameter of the short axis is 41 mm, and the tube length is 1500 mm. The explosive is a grade II coal mine emulsion explosive with a specification of Φ 35 × 300 mm/roll; the blasting hole is sealed with blasting mud, and the blasting network connection is connected in series with a detonating cord.

Feedback on the Bearing Effect of the On-Site Hydraulic Support

The mining starts from the cutting hole of the working face, and the pressure bearing condition of the hydraulic support of the fully mechanized top-coal caving working face after the roof cutting on-site is monitored. The hydraulic support is selected in the middle of the working face (52#, 70#) and near the end of the working face (31#, 118#), as shown in **Figure 11** to collect the ground pressure monitoring data. The data acquisition results of ground pressure monitoring are shown in **Figure 12**.

As shown in **Figure 12**, since the coal wall of the cut roadway began to be mined, the resistance of the working face 31# support increases at 27–30 m of mining, with the maximum working resistance of 37.6 MPa and the duration of the pressure of 16 h; the working face 52# support shows the phenomenon of increasing resistance at 27–29 m of mining, with the maximum working resistance of 37.3 MPa and the incoming pressure lasts for 4 h; the working face 70# support shows the phenomenon of increasing resistance at 26–28 m of mining, with the maximum working resistance of up to 38 MPa and the incoming pressure lasts for 2.5 h; the working face 118# support shows the phenomenon of increasing resistance at

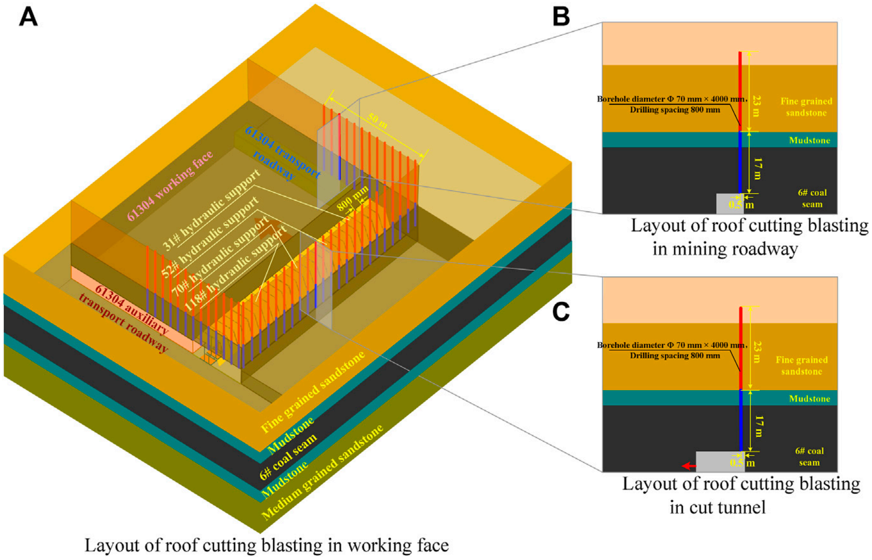

FIGURE 11 | Schematic diagram of blasting roof cutting technology at the working face **(A)** Layout of roof cutting blasting in the working face. **(B)** Layout of roof cutting blasting in the mining roadway. **(C)** Layout of roof cutting blasting in the cut tunnel.

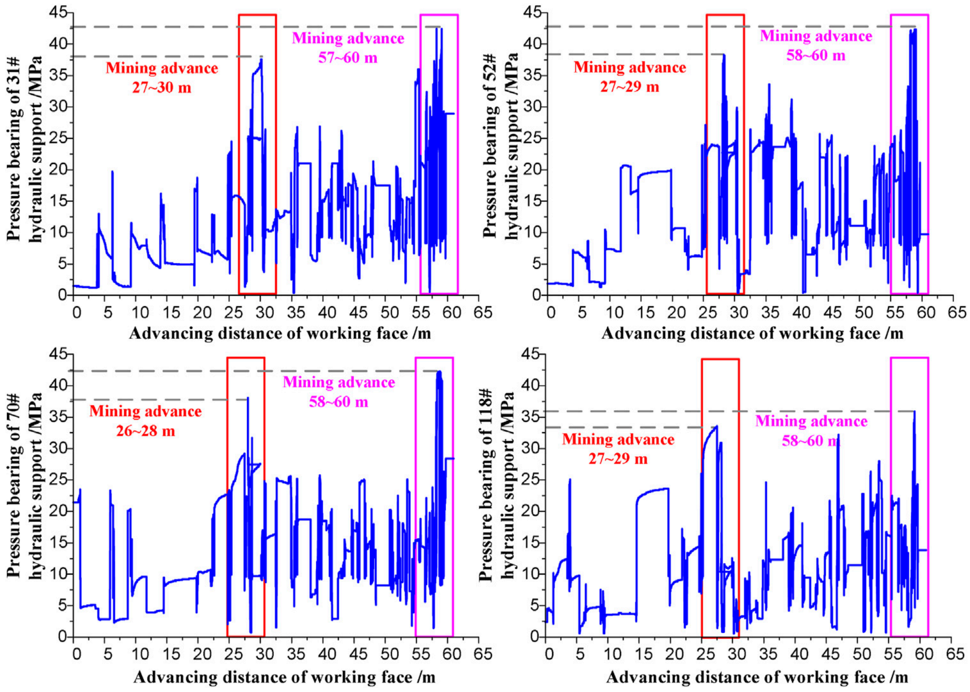

FIGURE 12 | Pressure monitoring of the working face hydraulic support (starting from the coal wall of the cut roadway).

27–29 m of mining, with the maximum working resistance of 33.6 MPa and the incoming pressure lasts for 21 h; after that, at a position of 57–60 m, the resistance of hydraulic supports increased again and the working resistance was 39–44 MPa.

The on-site monitoring results show that the ground pressure of the roof cut occurs when the mining is 26–30 m, that is, the thick hard roof of the working face is broken and unstable, and the maximum dynamic incoming pressure of the hydraulic support of the working face is 38 MPa (i.e., dynamic resistance: 14500 kN) which is less than the working resistance of the hydraulic support of the working face (working resistance of the hydraulic support of the ZF18000/28/45 working face is 18000 kN), the hydraulic support of the on-site working face has stable bearing and no equipment damage; by monitoring the subsequent mining stage, the dynamic incoming pressure of the hydraulic support of the working face is in the range of 43 MPa (i.e., dynamic resistance: 13800–16400 kN), the blasting roof cutting scheme of the fully mechanized top-coal caving face has achieved the expected ground pressure control effect and avoided the safety disaster of strong dynamic pressure caused by the mining instability of the thick hard roof.

CONCLUSION

(1) The greater the thickness and elastic modulus of the thick hard roof, the greater the flexural stiffness and the ultimate breaking span of the thick hard roof increases; with the increase of the overhanging span and overlying load of the thick hard roof, its mining bearing state and energy accumulation are obviously intensified.
(2) The dynamic resistance of the hydraulic support in the working face with a thick hard roof is composed of the dynamic resistance caused by the release of elastic energy accumulated by the mining of the thick hard roof and the work of the overlying load, as well as the static resistance caused by the direct roof gravity; among them, the dynamic resistance caused by the work of the overlying load accounts for the highest proportion, followed by the dynamic resistance caused by the release of elastic energy accumulated by the mining of the thick hard roof.
(3) The cause of mining instability and strong dynamic pressure of the thick hard roof lies in the large-span mining suspension. The long-span mining suspension structure of the thick hard roof leads to a high overlying load and serious energy accumulation and dispersion evolution, and strong dynamic load impact at the moment of mining instability.
(4) Controlling the breaking span of the thick hard roof by adopting pre-splitting and roof cutting technology reduces the impact dynamic load caused by mining instability of the thick hard roof, and effectively, eliminates the potential safety hazard of over limit bearing of the hydraulic support.

DATA AVAILABILITY STATEMENT

The original contributions presented in the study are included in the article/Supplementary Material, further inquiries can be directed to the corresponding author.

AUTHOR CONTRIBUTIONS

QB and MT carried out the mechanical analysis, and MT and XZ carried out technical design; QB, MZ, and QZ analyzed the data results, and QB and MT wrote the manuscript.

FUNDING

This research was funded by the National Natural Science Foundation of China (52074008, 52074007, and 52104114), the Natural Science Foundation of Anhui Province (2008085ME142), the Anhui Collaborative University Innovation Project (GXXT-2020-056), and the Open Research Fund Project of Key Laboratory of Safety and High-Efficiency Coal Mining of Ministry of Education (JYBSYS2019208).

ACKNOWLEDGMENTS

The authors thank Tangjiahui coal mine and the Anhui University of Technology for providing mine geological data and data analysis resources needed to complete this work.

REFERENCES

Christopher, M., and Michael, G. (2016). Evaluating the Risk of Coal Bursts in Underground Coal Mines. *Int. J. Mining Sci. Tech.* 42 (1), 42–47. doi:10.1016/j.ijmst.2015.11.009

Dou, L., Yang, K., Liu, W., Chi, X., and Wen, Z. (2020). Mining-induced Stress-Fissure Field Evolution and the Disaster-Causing Mechanism in the High Gas Working Face of the Deep Hard Strata. *Geofluids* 2020 (3), 1–14. doi:10.1155/2020/8849666

Gao, M. S., Dou, L. M., Zhang, N., Mu, Z. L., and Yang, B. S. (2007). Experimental Study on Earthquake Tremor for Transmitting Law of Rockburst in Geomaterials. *Chin. J. Rock Mech. Eng.* 26 (7), 1365–1371. doi:10.1016/S1872-2067(07)60020-5

Gao, R., Huo, B., Xia, H., and Meng, X. (2020). Numerical Simulation on Fracturing Behaviour of Hard Roofs at Different Levels during Extra-thick Coal Seam Mining. *R. Soc. Open Sci.* 7 (1), 191383. doi:10.1098/rsos.191383

Gu, S., Jiang, B., Pan, Y., and Liu, Z. (2018). Bending Moment Characteristics of Hard Roof before First Breaking of Roof Beam Considering Coal Seam Hardening. *Shock and Vibration* 2018 (2), 1–22. doi:10.1155/2018/7082951

He, H., Dou, L., Fan, J., Du, T., and Sun, X. (2012). Deep-hole Directional Fracturing of Thick Hard Roof for Rockburst Prevention. *Tunnelling Underground Space Tech.* 32, 34–43. doi:10.1016/j.tust.2012.05.002

Iannacchione, A. T., and Tadolini, S. C. (2016). Occurrence, Predication, and Control of Coal Burst Events in the U.S. *Int. J. Mining Sci. Tech.* 26 (1), 39–46. doi:10.1016/j.ijmst.2015.11.008

Jiang, J., Wang, P., Wu, Q., and Zhang, P. (2016). Evolutionary Characteristics of Fracture Laws of High-Position Hard Thick Strata with Elastic Foundation Boundary. *J. China Univ. Mining Tech.* 45 (03), 490–499. doi:10.13247/j.cnki.jcumt.000512

Jiang, J., Zhang, P., Qin, G., Li, F., Xu, B., and Xu, L. (2015). Breaking Law and Micro Seismic Energy Distribution of the High-Level Hard and Thick Key Layer on One Side Goaf. *J. Mining Saf. Eng.* 32 (4), 523–529. doi:10.13545/j.cnki.jmse.2015.04.001

Ke, G. (2000). Bending Theories for Beams and Plates with Single Generalized Displacement. *Appl. Math. Mech.* 21 (09), 1091–1098. doi:10.1007/BF02459320

Li, X., Ma, N., Zhong, Y., and Gao, Q. (2007). Storage and Release Regular of Elastic Energy Distribution in Tight Roof Fracturing. *Chin. J. Rock Mech. Eng.* 26 (S1), 2786–2793. doi:10.3321/j.issn:1000-6915.2007.z1.030

Lu, C.-P., Liu, G.-J., Liu, Y., Zhang, N., Xue, J.-H., and Zhang, L. (2015). Microseismic Multi-Parameter Characteristics of Rockburst hazard Induced by Hard Roof Fall and High Stress Concentration. *Int. J. Rock Mech. Mining Sci.* 76, 18–32. doi:10.1016/j.ijrmms.2015.02.005

Song, G., Wang, Z., and Zhong, X. (2020). Dynamic Impact Mechanism of Hard Roof Strata and Coupling Mechanism of "Constrain-Convergence" between Support and Surrounding Rock. *J. Mining Saf. Eng.* 37 (05), 951–959. doi:10.13545/j.cnki.jmse.2020.05.011

Tan, Y., Zhang, M., Xu, Q., and Shitan, G. U. (2019). Study on Occurrence Mechanism and Monitoring and Early Warning of Rock Burst Caused by Hard Roof. *Coal Sci. Tech.* 47 (01), 166–172. doi:10.13199/j.cnki.cst.2019.01.023

Xia, B., Jia, J., Yu, B., Zhang, X., and Li, X. (2017). Coupling Effects of Coal Pillars of Thick Coal Seams in Large-Space Stopes and Hard Stratum on Mine Pressure. *Int. J. Mining Sci. Tech.* 27 (06), 965–972. doi:10.1016/j.ijmst.2017.06.020

Xie, S. R., Chen, D. D., Sun, Y. D., Gao, M. M., and Shi, W. (2016). Analysis on Thin Plate Model of Basic Roof at Elastic Foundation Boundary (I): First Breaking. *J. China Coal Soc.* 41 (06), 1360–1368. doi:10.13225/j.cnki.jccs.2016.0197

Yang, S. L., Wang, J. C., and Yang, J. H. (2017). Physical Analog Simulation Analysis and its Mechanical Explanation on Dynamic Load Impact. *J. China Coal Soc.* 42 (2), 335–343. doi:10.13225/j.cnki.jccs.2016.6004

Yang, S., Wang, J., and Li, L. (2020). Deformation and Fracture Characteristics of Key Strata Based on the Medium Thick Plate Theory. *J. China Coal Soc.* 45 (8), 2718–2727. doi:10.13225/j.cnki.jccs.2020.0366

Yu, B., Liu, C. Y., Yang, J. X., and Liu, J. R. (2013). Research on the Fracture Instability and its Control Technique of Hard and Thick Roof. *J. China Univ. Mining Tech.* 42 (3), 342–348. doi:10.13247/j.cnki.jcumt.2013.03.003

Zhang, J., Li, B., Zhou, N., and Zhang, Q. (2016). Application of Solid Backfilling to Reduce Hard-Roof Caving and Longwall Coal Face Burst Potential. *Int. J. Rock Mech. Mining Sci.* 88, 197–205. doi:10.1016/j.ijrmms.2016.07.025

Zhang, M., Jiang, F., Chen, G., Jiao, Z., Hu, H., and Chen, B. (2020). A Stope Stress Transfer Model Based on the Motion State of Thick and Hard Rock Strata and its Application. *Chin. J. Rock Mech. Eng.* 39 (07), 1396–1407. doi:10.13722/j.cnki.jrme.2019.1118

Zhang, M., Jiang, F., Keqing, L., Sun, C., and Zhai, M. (2017). A Study of Surface Seismic Damage Boundary Based on the Break and Movement of Extremely Thick Key Stratum. *J. China Univ. Mining Tech.* 46 (3), 514–520. doi:10.13247/j.cnki.jcumt.000672

Zhao, T., Liu, C., Yetilmezsoy, K., Zhang, B., and Zhang, S. (2017). Fractural Structure of Thick Hard Roof Stratum Using Long Beam Theory and Numerical Modeling. *Environ. Earth Sci.* 76 (21), 1–7. doi:10.1007/s12665-017-7103-x

Zuo, J. P., Sun, Y. J., and Qian, M. G. (2017). Movement Mechanism and Analogous Hyperbola Model of Overlying Strata with Thick Alluvium. *J. China Coal Soc.* 42 (06), 1372–1379. doi:10.13225/j.cnki.jccs.2016.1164

Conflict of Interest: The authors declare that the research was conducted in the absence of any commercial or financial relationships that could be construed as a potential conflict of interest.

frontiers | Frontiers in Earth Science

ORIGINAL RESEARCH
published: 27 May 2022
doi: 10.3389/feart.2022.884974

Mechanism of Coal Burst Triggered by Mining-Induced Fault Slip Under High-Stress Conditions: A Case Study

Jinzheng Bai[1,2]*, *Linming Dou*[1,2]*, *Jiazhuo Li*[1,3], *Kunyou Zhou*[1,2], *Jinrong Cao*[1,2] *and Jiliang Kan*[1,2]

[1]*School of Mines, China University of Mining and Technology, Xuzhou, China,* [2]*State Key Laboratory of Coal Resources and Mine Safety, China University of Mining and Technology, China,* [3]*School of Mining Engineering, Anhui University of Science and Technology, Huainan, China*

Coal burst disaster is easily triggered by mining-induced fault unloading instability involving underground engineering. The high-static stress environment caused by complex geological structures increases the difficulty in predicting and alleviating such geological disasters caused by humans. At present, the mechanism of coal burst induced by mining-induced slip fault under high-stress conditions still cannot be reasonably explained. In this study, the burst accidents occurring near mining-induced slip fault under high-stress conditions were carefully combined, and the "time–space–intensity" correlation of excavation, fault, and syncline and anticline structure of the mining areas was summarized. On this basis, the rotation characteristics of the main stress field of the fault surface subjected to mining under high-stress conditions and the evolution law of stress were analyzed. Last, based on the spectrum characteristics of mining-induced tremors, the first motion of the P-wave, and the ratio of Es/Ep, the source mechanism behind mining-induced fault slip under high-stress conditions was revealed. The results demonstrate that the coal burst triggered by the fault slip instability under high-stress conditions is closely related to the excavation disturbance and the fold structure. Mining activities trigger the unloading and activation of the discontinuous structural surface of the fault, the rotation of the stress field, and the release of a large amount of elastic strain energy and cause dynamic disasters such as coal bursts. The research results in this study are helpful to enrich the cognition of the inducing mechanism of fault coal burst.

Keywords: coal burst, mining-induced stress, fault slip, stress rotation, source mechanism

Edited by:
Kun Du,
Central South University, China

Reviewed by:
Guangan Zhu,
Xi'an University of Science and Technology, China
Zhenlei Li,
University of Science and Technology Beijing, China

***Correspondence:**
Jinzheng Bai
tb19020001b4@cumt.edu.cn
Linming Dou
lmdou@126.com

Specialty section:
This article was submitted to Geohazards and Georisks, a section of the journal Frontiers in Earth Science

Received: *27 February 2022*
Accepted: *11 April 2022*
Published: *27 May 2022*

Citation:
Bai J, Dou L, Li J, Zhou K, Cao J and Kan J (2022) Mechanism of Coal Burst Triggered by Mining-Induced Fault Slip Under High-Stress Conditions: A Case Study.
Front. Earth Sci. 10:884974.
doi: 10.3389/feart.2022.884974

INTRODUCTION

Coal burst can generally be classified into three types, i.e., the fault-induced type, the coal pillar-induced type, and the strain-induced type (Kaiser et al., 2000), in which fault-induced coal burst is caused by the superposition of the mining-induced quasi-static stress in the fault coal pillar and the seismic-based dynamic stress generated by fault activation (Cai et al., 2020). Coal burst triggered by mining-induced fault slip (CBTMIFS) refers to the dynamic phenomenon that the deep excavation activities lead to the fault's transformation from a locked state to an activated state, consequently resulting in sudden instability accompanied by violent energy release (Pan, 1999). Unlike natural earthquake induced by fault activation, mining activities are a key factor in the occurrence of

CBTMIFS (Ortlepp and Stacey, 1992). A strong mining tremor of magnitude 5.2 in 1997 is considered one of the largest seismic events recorded at the Klerksdorp mine in South Africa, and the analysis result of ground motion parameters indicates that the violent earthquake was attributed to an existing fault slip in the region (McGarr et al., 2002). In 2005, 112 shallow earthquakes were recorded during the construction of the MFS Faido tunnel in Switzerland, which were felt strongly on the ground and caused considerable damage to the tunnel. The focal mechanism solution was consistent with the strike and tendency of natural fault (Husen et al., 2013). On November 3, 2011, the F16 thrust fault was activated at the Qianqiu coal mine in Yima, Henan Province, China, causing 10 fatalities and trapping 75 miners. On March 27, 2014, another devastating burst accident of magnitude 1.9 in this coal mine caused 6 fatalities and trapped 13 miners. The accident investigation report pointed out that the key factor of the accident was slip activation of the thrust fault (Cai et al., 2018). The abovementioned dynamic disasters closely related to human mining activities have attracted extensive attention from the media and the public. If the internal mechanism of CBTMIFS can be revealed, important ideas can be provided for predicting and remitting the risk of such engineering disasters.

Different from the brittle shear deformation of faults, the fold structures such as syncline and anticline reflect the continuous ductile deformation of rocks under crustal movement and sedimentation (Suppe, 1983). Both faults and folds are widely distributed in nature, often in the same tectonic unit. For large-scale crustal movements, multiple fold and fault structures interact and mutually transform through interlayer slip, uplift, and fold during the long historical tectonic movement and sedimentation process, and the specific forms include fault-related fold, fault-transition fold, fault-propagation fold, fault-detachment fold, imbricate structure, wedge structure, and interference structure(Bieniawaki, 1967). For the medium- and small-scale production range of mining areas, the frequent geological movement dominated by ancient stress leads to the complex regional tectonic stress field. Therefore, it will be more difficult to investigate the disaster-triggering mechanism of the mining-induced fault slip under a high-stress engineering background.

In order to clarify the occurrence mechanism of CBTMIFS in geological anomaly areas, plenty of studies have been carried out through theoretical analysis, laboratory experiment, numerical simulation, and field experiment,including the mechanical response and mineral composition of fault gouge (Morrow and Byerlee, 1989), hydraulic pressure and stress state of the fault zone (Segall and Rice, 1995), slip and failure criterion of fault (Fan and Wong, 2013), and energy accumulation and release law of the fault surface (Zhao and Song, 2013). On this basis, the key scientific issues condensed include the following: *1*) How engineering dynamic disturbances, such as blasting, TBM excavation, hydraulic fracturing, geological drilling and rockburst, natural earthquake, driving load, and continuous explosion, will lead to slip, failure, and even instability of faults in high-stress geological anomaly areas? *2*) What response characteristics will be caused to the stress field, vibratory field, and energy field of surrounding rock in the adjacent production area once the fault instability occurs in the high-stress geological anomaly area?

Relevant studies suggest that local high-stress concentration is likely to occur and develop when the mining working face or the excavation boundary is close to the fault in the high-stress geological anomaly area, and the corresponding burst risk increases (Cook, 1976; Blake and Hedley, 2003; Yin et al., 2014). When the fault approaches the critical stress state, the normal stress and the shear stress decrease sharply due to the reduction of intergranular force and the contact fracture of particles, and the evolution of fault state depends on the initial stress condition and excavation process (Wu et al., 2017; Yin et al., 2012). Field observations and theoretical analysis show that the development height of mining-induced fault rupture and slip is controlled by the magnitude and direction of principal stress, while the intensity of seismic events is related to the stratum matrix and local fractures involved in the rupture process (Duan et al., 2019). At the same time, many investigations have explored the response behavior of faults to static and dynamic load disturbances by changing stress conditions in laboratory tests. Marone (1998) pointed out that static friction and aging strengthening of faults are systematic responses that depend on loading rate and elastic coupling. Li et al. (2011) simplified the normal behavior of faults to elastic stiffness, adopted the coulomb-slip model to characterize the shear behavior of faults, and conducted a quantitative study on the propagation and attenuation law of seismic waves in discontinuous rock masses. Bai et al. (2021) introduced the displacement-related moment tensor method to reproduce the phenomenon of mining-induced fault slip of coal mine site in numerical simulation.

To sum up, the stress distribution and evolution characteristics of conventional fault activation instability have been well researched on. However, there are few studies on CBTMIFS under high-stress environments, and the existing research results ignore the influence of mining quasi-static loading and unloading stress paths and ground motion stress on the fault slip instability. Therefore, it is necessary to further study the mechanism of CBTMIFS under high-stress conditions, for providing guidance for the monitoring and prevention of coal bursts induced by fault instability.

SITE DESCRIPTIONS

Geological Structures

Mengcun coal mine mainly mines 4# coal seam, where is located in Binchang coal district, Shaanxi province, China, with a mining depth of 620–750 m. The 401101 working face is the first working face of the Mengcun coal mine, with a length of 2090 m and a width of 180 m. The layered fully-mechanized sub-level caving mining technology is adopted. *See* **Figure 1**, the north wing, west wing, and east wing of the working face are solid coal, and there is a 200 m protective coal pillar between it and the main entry group. The development roadway includes five main entries, which are no.2 return air main entry, no.2 belt main entry, band conveyer main entry, no.1 belt main entry, and no.1

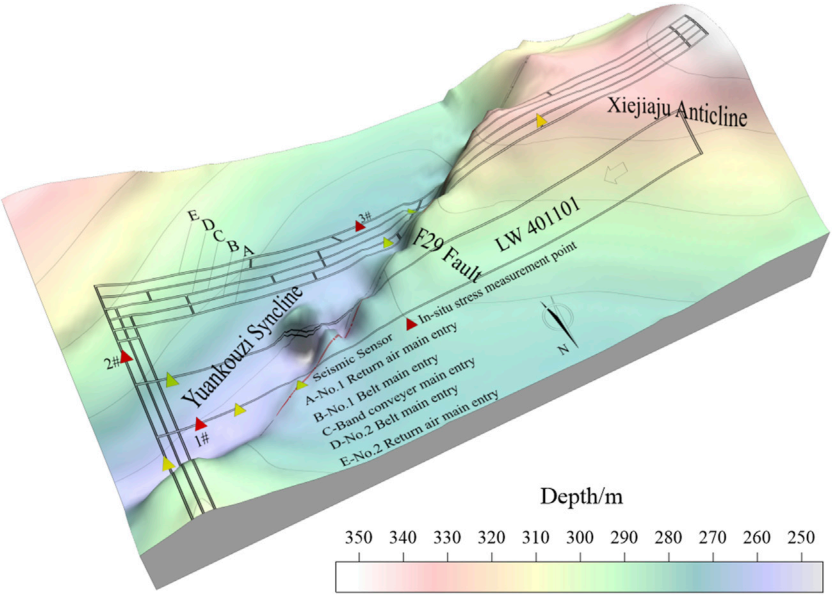

FIGURE 1 | 3D view of a mine's working face, geological structure, ground stress and microseismic measurement point.

TABLE 1 | Major geological tectonic parameters of the minefield.

Tectonic name	Occurrence		
	Dip angle (°)	Inclination angle (°)	Drop (m)
F29 normal fault	150	60–70	15–18
Yuankouzi syncline (X1)	Axial direction: NE; extending length: 1455 m; dip angle of coal seam: 5–8°		
Xiejiazui anticline (B2)	Axial direction: NEE; extending length: 2286 m; dip angle of coal seam: 3–8°		

return air main entry from north to south, with a width of coal pillars between the entries of 35 m. The average thickness of 4# coal is 20 m, and the average dip angle of the coal seam is 4°. The roof is mainly made of sandy mudstone, fine-grained sandstone, and coarse-grained sandstone, and the bottom plate is mainly made of aluminum mudstone which tends to expand when meeting water. After identification, 4# coal seam has strong burst liability, the roof has weak burst liability, while the floor has no burst liability.

Tectonic Parameters

Xiejiazui anticline (B2), Yuankouzi syncline (X1), and F29 normal fault occur from west to east in the minefield area. The faults' location between the syncline and anticline structures forms a special geological structure group, thus mainly controlling the gestation, evolution, and occurrence process of coal burst accidents in this region. Detailed geological and tectonic parameters are displayed in **Table 1**.

To further explore the influence degree of geological structure on the distribution of ground stress field in the mining area, three ground stress measurement points were arranged in the areas of central main entries, panel main entries, and the 401101 working face. Meanwhile, the ground stress of hollow inclusion was measured. As shown in **Figure 2**, the vertical stress in this area is the minimum principal stress, the results of three measurement points are basically consistent with the average stress level of the Binchang coal district and the Chinese mainland. Due to the presence of faults and fold structures, horizontal tectonic stress is the main stress component in the regional high-stress environment. The results of the three measurement points are obviously higher than the average stress levels of both the Binchang coal district and the Chinese mainland, especially the measurement point 3# is closer to the X1 axis and F29 fault, where σ_H/σ_V reaches 2.1. The results indicate that the closer it is to the fault and synclinal axis, the more abnormal its horizontal stress is.

As shown in **Figure 3**, four geological exploration boreholes, M2-1, M3-2, M4-2, and M5-2, were selected in the main entries and the 401101 working face to analyze the influence of the composite geological tectonic group on regional stratigraphic sediment characteristics. It can be concluded that: *1)* The regional strata are mainly composed of alternately deposited fine-grained sandstone, medium-grained sandstone, coarse-grained sandstone, and sandy mudstone, and no thick whole layer of hard sand-gravel rock exists. *2)* In the long process of

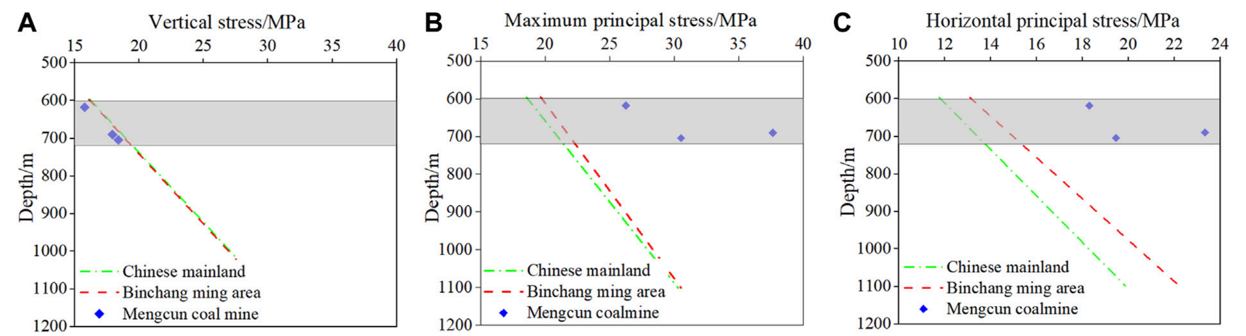

FIGURE 2 | Comparison diagram of ground stress results and *in-situ* stress values in Binchang mining area and Chinese mainland. **(A)** Vertical stress; **(B)** Max principal stress; **(C)** Horizontal principal stress.

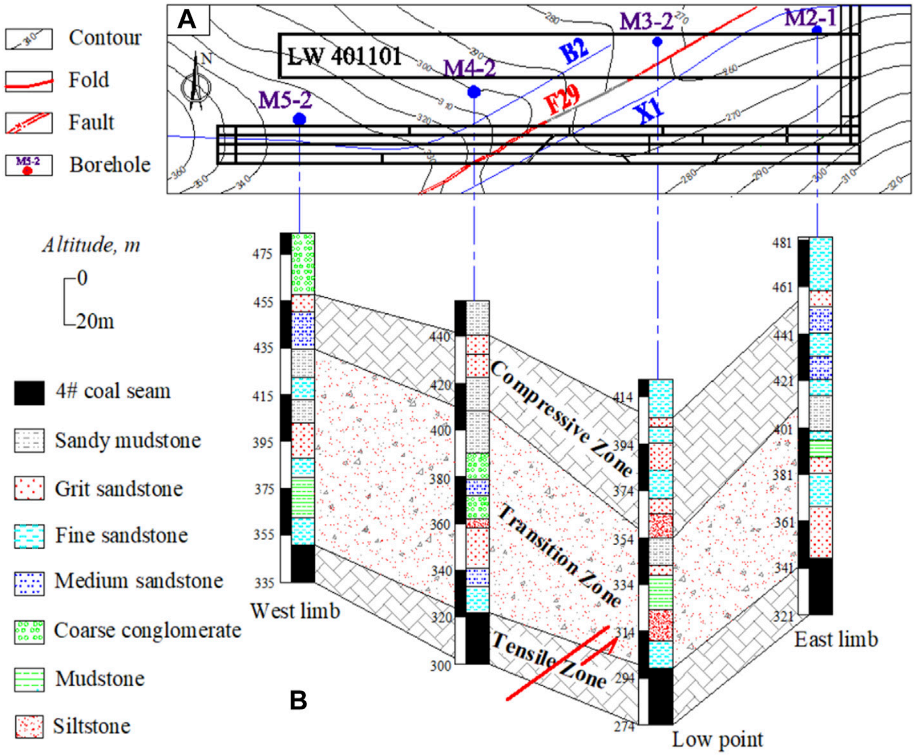

FIGURE 3 | Stratigraphic map of the coupled fault-fold region near the 401101 working face. **(A)** Geological exploration boreholes of LW 401101; **(B)** Regional stratigraphic sediment characteristics.

crustal movement and evolution, stratum inversion and deletion occur frequently among the upper overburden strata. Affected by the extrusion tectonic stress in the east and west direction, faults and relative slips occur in weak coal seams, which are upright or inverted and thus form compression-torsion faults. The strata are obviously controlled by the tectonic movement of faults and folds. *3*) Relatively, the difficulty of mining increases as the strata near the M4-2 borehole is not only squeezed by horizontal tectonic stress of fold, but also affected by vertical dislocation of the F29 normal fault, which results in the discontinuity of the strata, with stress concentration and energy accumulation. Therefore, unstable stratum deposition and phase transition provide a favorable external environment for frequent coal burst accidents in this region.

COAL BURST HISTORY

The inducing process of coal burst is very complex, which is not only affected by geological structures such as folds and faults but

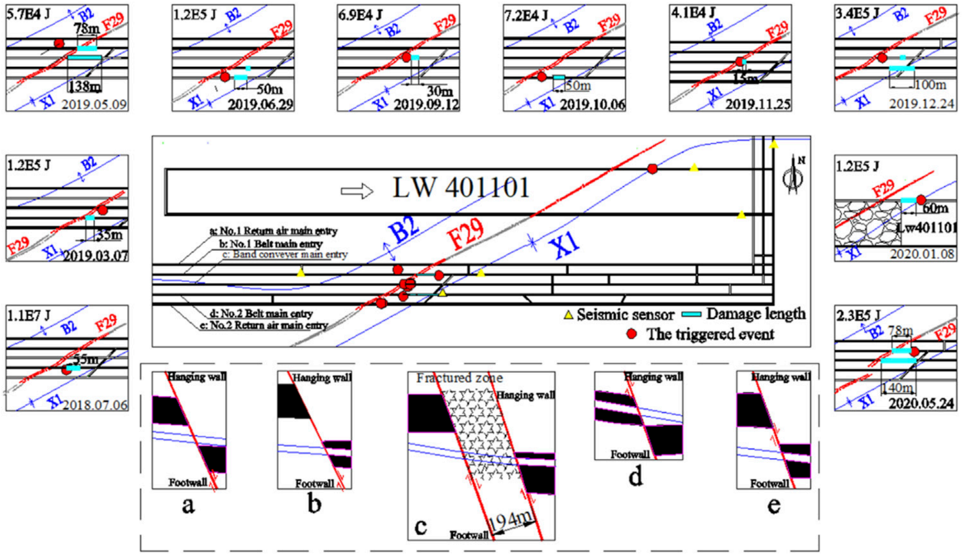

FIGURE 4 | Map of the locations of the previous bursts and the faults of each main entries.

also closely related to the mining activities involved (Zhang et al., 2017; Yin et al., 2019). Therefore, it is of great significance to clarify the relationship between coal bursts and geological structure and mining activities in this region. The mining of the 401101 working face started in June 2018 and ended in March 2020, during which a total of 10 coal burst accidents occurred. The SOS microseismic system was arranged in working face and main entries, which could monitor the vibratory signal in the mining process. The distance between the seismic source and the fault and the on-site failure range monitored when the burst occurred are presented in **Figure 4**, and the on-site burst failure is in **Figure 5**.

Figure 4 demonstrates that all previous coal burst accidents have significant common characteristics: *1*) Most of the coal bursts occurred in the main entry area, which is obviously inconsistent with the distribution law of mining-induced tremors commonly seen near the mining working face. *2*) Most of the coal bursts occurred on the hanging wall of the F19 fault, while there are relatively few occurred on the footwall of the F19 fault, showing an obvious hanging wall effect. This is in agreement with the existing research conclusions: in the field of seismology, the hanging wall's ground motion is stronger than the footwall, its vibration attenuation is weaker than the footwall, and its vibration distribution area is larger than the footwall in natural fault shear slip. *3*) The minimum destructive microseismic energy detected during a coal burst is 2.6 E+04 J, and the corresponding failure range of the entry is only 3 m; the maximum microseismic energy is 3.5 E+05 J, and the corresponding failure range of the entry is 55 m, showing that the more elastic energy released during a coal burst, the greater the influence on entry stability. *4*) The burst frequency and range of the five main entries are not completely consistent, the situation of <C> band conveyer main entry and <D> no.1 belt main entry is the most dramatic, showing the overall characteristics of multiple and repeated bursts. As shown in **Figures 4A–E**, considering different actual exposure of each entry of the F29 fault surface, especially when the band conveyer main entry passes through the fault, there is an obvious fracture zone between the hanging wall and the heading wall with a thickness of about 194 m, which has a negative effect on the stability of surrounding rock of the entry, it is speculated that the heterogeneity of coal burst frequency and intensity of each main entry is related to the heterogeneous evolution of shear stress along the F29 fault surface. *5*) The occurrence of coal bursts is significantly affected by mining disturbance. Only one coal burst accident occurs after the stoppage of mining activities, suggesting that the frequent occurrence of coal bursts on the fault surface is closely related to mining activities. *6*) The occurrence of coal burst is affected by B2 anticline to a certain extent, but it is affected by F29 fault and X1 syncline significantly. Especially in the composite area of F29 fault and X1 syncline, coal burst accidents occur intensively.

Figure 5 shows the entry damage caused by the coal burst. The overall damage characteristics can be divided into four categories: floor bulge, roof caving, support failure, and equipment damage. Floor damage can be divided into raising, side lifting, overall drum, and cracking; equipment damage can be divided into belt tilting, tub overturning, platform overturning, and pipeline falling; support failure can be divided into anchor slipping, cable overhanging, bolt shearing, and tray rushing out; roof caving can be divided into step sinking, drossy coal falling, roof separation, and roof falling. Different from conventional coal bursts, this kind of coal burst has significant shear seismic failure characteristics, with a more complex failure type, a larger failure range, and a higher failure degree.

Therefore, it is preliminarily inferred that the controlling factors of frequent coal burst accidents in the main entry area are as follows: influenced by bedding or lateral compression of

FIGURE 5 | Pictures of burst failure of coal burst on site. **(A)** Floor bulge; **(B)** Equipment damage; **(C)** Support failure; **(D)** Roof caving.

regional strata, the compound tectonic condition of B1 anticline and X1 syncline provides a high-static-stress environment for the main entry area. The F29 fault with a drop of 15–18 m crosses diagonally both main entries and the 401101 working face. Under the tectonic influence, a large amount of elastic energy is accumulated of the fault surface, which lays an energy foundation for the occurrence of coal bursts. Human activities, including excavation, mining, and entry expansion, lead to different stress adjustment ranges and intensities and result in different degrees of damage in main entries. To further verify the rationality of the hypothesis, the stress evolution law on the fault during the mining process was analyzed by numerical simulation.

STRESS FIELD MODELING OF INTERFACE IN F29

Model Setup and Constrains

FLAC^{3D} (Fast Lagrangian Analysis of Continua in 3 Dimensions) was employed to analyze the stress distribution of the fault surface

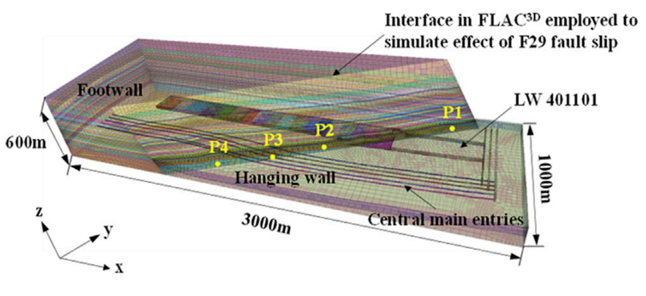

FIGURE 6 | Sketch map of initial numerical simulation and measurement points.

of F29 and in the coal pillar around the main entries of the 401101 working face during the whole stopping period. The geometric dimension of the model is 3,000 × 1,000 × 600 m. Normal displacements are fixed at the base and the sidewalls of the model. In view of the complex layout condition that five main entries cross the F29 fault as well as coal rock seam, high-precision modeling shown in **Figure 6** was realized by Rhino software, in which X1 syncline and B1 anticline generated 3D undulated strata through real coal floor contour lines for restoration. F29 fault was generated according to actual fault parameters with a fault surface dip angle of 75° and a height difference of 20 m. The strain-softening criterion was adopted to judge the yield state of materials and determine the physical mechanics parameters of both coal rock mass and fault slip surface. The parameters are listed in **Tables 2**, **3**, respectively. As displayed in **Figure 6**, four monitoring points were successively arranged along the F29 fault surface in the model.

The steps of numerical simulation are as follows:

1) According to the real ground stress test results, 30 MPa horizontal stress and 20 MPa vertical stress were applied to the model to balance the initial ground stress field and complete the excavation of the development roadway and main entries.
2) The 401101 working face was excavated step by step. The stress distribution in the coal pillar near the main entries, and the normal stress and shear stress distribution of the F29 fault surface were monitored.
3) Taking $\sigma_h = 30$ MPa, $\sigma_v = 20$ MPa, and the lateral pressure coefficient $b = 1.5$ as initial values, the effects of different horizontal ground stress on normal stress and shear stress of the fault surface in the mining process were analyzed when b equals 0.5, 1, 1.5, 2, and 2.5, respectively.

Influence of Mining Activities on the Stress Distribution of the Fault Surface

Figure 7 presents the changes in stress evolution of the fault surface at P1, P2, P3, and P4 when the lateral pressure coefficient b is 0.5. The stress at each monitoring point evolves dynamically with the advance of the working face. The change laws of normal stress and shear stress between the monitoring points are different, indicating that the stress of the fault surface is not evenly distributed due to mining disturbance, which leads to the regional difference in burst risk.

As illustrated in **Figure 7A**, due to mining disturbance, the normal stress and shear stress of the fault surface at P1 on the north side of the working face almost synchronously fluctuate sharply, in which the normal stress drops rapidly first and then recovers to a certain level with a fluctuation value of about 1.2 MPa; the shear stress first increases slightly and then decreases rapidly to a certain level, with a fluctuation value of about 3.0 MPa. As shown in **Figure 7B**, when the working face continues to advance, both the normal stress and shear stress at P2 on the south side of the working face show an upward trend, with a fluctuation value of shear stress of about 3.0 MPa, while that of normal stress of about 0.4 MPa. It suggests that the remote mining activities still have slight disturbance to the fault surface in a metastable state, which

TABLE 2 | Physical mechanics parameters of coal rock seam.

Rock property	Density/ g·cm^{-3}	Bulk modulus/ GPa	Shear modulus/ GPa	Tensile strength/ MPa	Cohesive force/ MPa	Friction angle/°	Residual cohesive forces/ MPa	Residual internal friction angle/°
Mudstone	2200	1.67	0.77	2.5	3.0	20	0.4	10
4# coal coal	1340	2.0	0.8	2.2	3.0	28	1.0	20
Coarse sandstone	2300	3.53	2.81	4.5	6.0	26	2.5	15
Medium-grained sandstone	2520	3.45	3.15	9.0	14.0	30	—	20
Fine-grained sandstone	2520	4.90	3.60	12.0	16.0	35	5.0	25
Siltstone	2520	3.2	2.8	6.3	8.67	29	4.0	20

TABLE 3 | Physical mechanics parameters of the fault interface.

Normal stiffness /GPa·m^{-1}	Shear stiffness /GPa·m^{-1}	Internal friction angle /°	Cohesive force /MPa
1.0	1.0	30	0.1

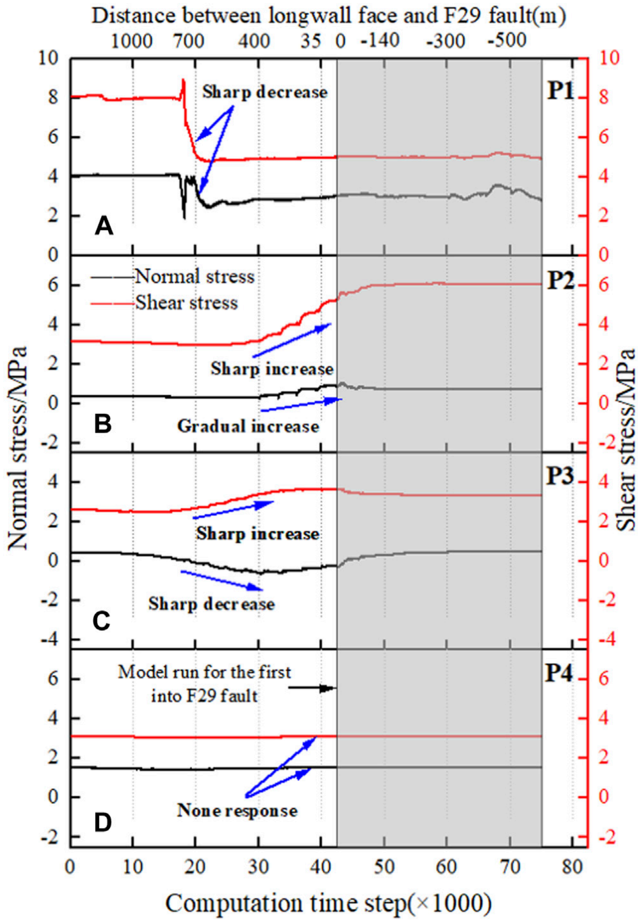

FIGURE 7 | Change laws of normal stress and shear stress with working face advance. **(A)** P1; **(B)** P2; **(C)** P3; **(D)** P4.

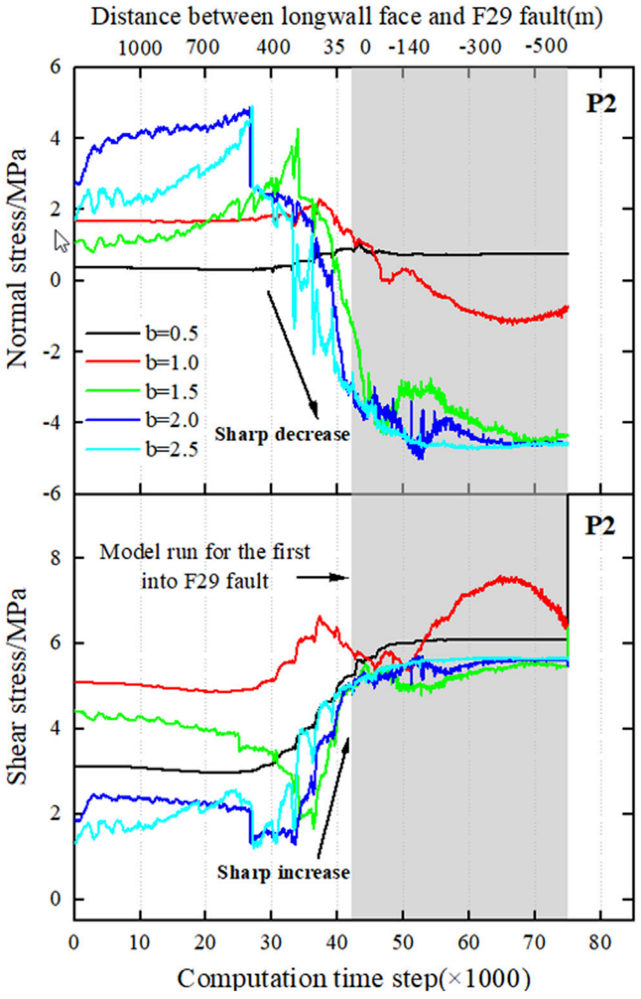

FIGURE 8 | Change laws of normal stress and shear stress with mining working face advance at different ground stress.

results in the instability of the fault with a quantity of originally accumulated strain energy, thus releasing strain energy outward, and this process is likely to induce coal burst accidents.

As illustrated in **Figure 7C**, when P3, located between no.2 return air main entry and no.2 Belt main entry, is 700 m away from the fault of the working face, the normal stress plunges, while the shear stress increases sharply. It is worth noting that the value of normal stress experiences a "positive-negative-positive" change process, suggesting that the main stress field of the fault surface rotates due to mining disturbance, which can be considered as a precursor of fault slip. As displayed in **Figure 7D**, due to the long distance between the working face and P4 located in the south of no.1 return air main entry, basically no stress response is generated during the whole mining process of the working face and the burst risk is relatively low, which is consistent with the situation that only one burst accident occurred in no.1 return air main entry.

Influence of Ground Stress on the Stress Distribution of the Fault Surface

To further investigate the inducing law of high stress caused by the fold structure to mining-induced slip fault, **Figure 8** shows the change laws of normal stress and shear stress at P2 located between the 401101 working face and the main entry group with mining advancement under different ground stress conditions (that is, when the lateral pressure coefficient b is 0.5, 1.0, 1.5, 2.0, and 2.5, respectively). As can be seen from **Figure 8**, the evolution laws of normal stress and shear stress at this measurement point are basically consistent at different ground stress levels.

When the horizontal stress is low while *b* is 0.5 and 1.0, the working face advances to about 400 m of the fault, the normal stress rises slightly, and the shear stress rises more sharply than the normal stress. When horizontal stress further rises, while *b* is 2.0 and 2.5 m, the normal stress of F29 fault shows a drastic downward trend, on the contrary, the shear stress dramatically increases, and the response time is advanced, showing that a high-stress environment provides a good condition for strain energy accumulation of the fault, which leads to a significant expansion of the range affected by mining activities. When the horizontal stress is higher, the value of the normal stress changes more from "positive value to a negative value and then to a positive value,"

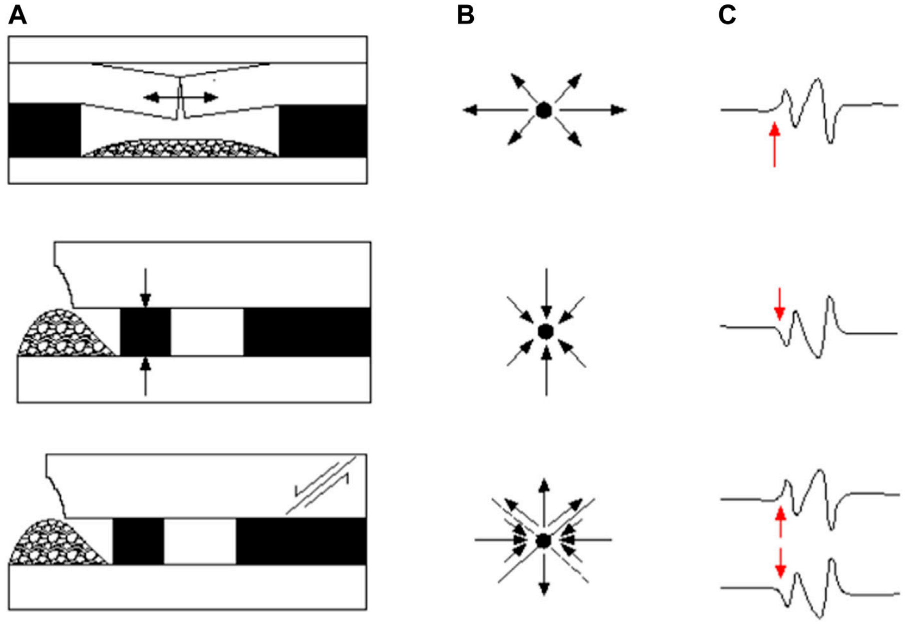

FIGURE 9 | Typical tremor model. **(A)** Types of mining-induced tremors; **(B)** Patterns of P-wave radiation; **(C)** Directions of P-wave first motion.

with higher intensity of energy accumulation and release, higher corresponding burst risk, and thus more likeliness of coal bursts. This conclusion reflects the mechanism of the fold structure on mining-induced fault slip.

MECHANISM OF COAL BURST REVEALED BY MS EVENTS

The focal rupture mechanism of coal rock spontaneous mining-induced tremors resembles that of natural earthquakes. In the past, people mainly used the occurrence mechanism of natural earthquakes to reveal the seismic source rupture process of most mining-induced tremors (McGarr, 1984; Gibowicz and Kijko, 1994). However, the geological structure, excavation environment, and overburden structure of a mine determine the particularity and complexity of the seismic source of a mining-induced tremor. Different causes of mining-induced tremors and different focal rupture mechanisms lead to the disparity in the energy release size of mining-induced tremors and in radiation modes of shake displacement wave field. As displayed in **Figure 9**, according to the seismic source acting force modes of mining-induced tremors and the relative position relationship between the coal rock failure area and the working face, mining-induced tremors can be simply divided into three types: tension type, implosion type, and shear type (Horner and Hasegawa, 1978; Hasegawa et al., 1989). The tension type and the implosion type are dominant, while the shear-type caused by a dynamic slip of fault is infrequent. At the same time, the waveform of mining-induced tremors contains abundant focal rupture mechanisms, and the application of seismology in the field of coal rock-burst rupture is beneficial for promoting the study of the focal rupture mechanism of mining-induced tremors. This section attempts to discuss the focal rupture mechanism of frequent coal bursts in the main entries from the aspects of spectrum characteristics of shake displacement, P-wave first motion, and the ratio of E_S/E_P.

Waveform and Frequency-Spectra Characteristics of Mining-Induced Tremors

The typical clear waveform monitored by the microseismic station of three typical tremor events “2019.09.12,” “2020.01.08,” and “2020.05.24” were selected to determine the main frequency segment by frequency-spectra analysis. In the process of propagation, the tremor wave carries important information that can reflect the characteristics of the stratum and the source, such as fault, fractured zone, geological acoustics characteristics, and focal mechanism characteristics, which are mainly reflected in the attenuation of seismic wave intensity, frequency structure characteristics, and local singularity of signal. In so many computing methods of fractal dimension, the box dimension index Dq is employed in this study to define the burst waveform.

Taking $N(\Delta)$ as the minimum number of a square box with a side length of Δ covering a point set, then the box dimension of the point set is defined as

$$D_q = -\lim_{\Delta\to 0}\frac{\lg N(\Delta)}{\lg\Delta}. \tag{1}$$

As shown in **Figure 10**, the spectrum of each burst event is noisy and sharp, the signal is complex, and there is a great difference between each channel, which indicates that the

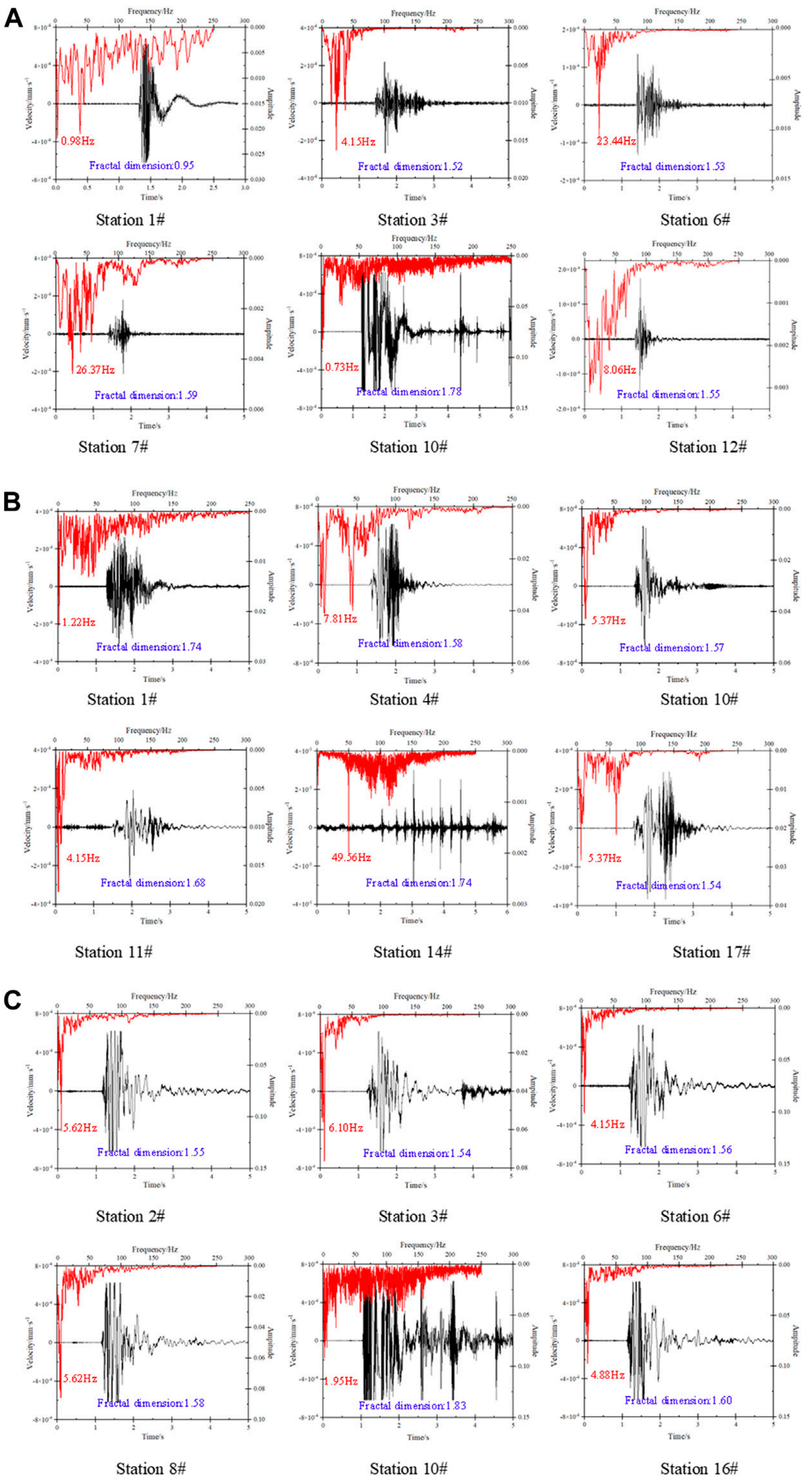

FIGURE 10 | Typical burst waveform, frequency spectrum characteristics and fractal dimension. **(A)** The "2019.09.12" burst event; **(B)** The "2020.01.08" burst event; **(C)** The "2020.05.24" burst event.

discontinuity surface of the F29 fault and the goal of the 401101 working face change the propagation characteristics of the seismic wave. Overall, the duration of typical seismic signals is about 2,500–3,500 ms, and the seismic velocity is about 2.0×10^{-4}–6.0×10^{-4} mm/s. The frequency is mainly distributed between 0–30 Hz with the main frequency mostly lower than 10 Hz, and the middle and high-frequency components attenuate notably, reflecting a characteristic of "high energy and low-frequency" of mining-induced tremor waveform. The fractal dimension D of each channel ranges from 0.95 to 1.78, which fully indicates the disorder and complexity of these burst tremors. Different from small and medium energy mining-induced tremors, the burst mining-induced tremor has a more rapid process from fracturing to receiving signal, its amplitude of P-wave first motion is weak and even difficult to identify. Furthermore, its energy release and dissipation are more violent. Another evident feature is that the shear rupture waveform reflecting the tangential deformation of coal rock units is relatively developed, and the amplitude of S-wave first motion is obvious, which accords with the common shear seismic waveform characteristics (Du et al., 2021).

Taking stations 1# and 10# in the "2019.09.12" burst event, stations 1# and 17# in the "2020.01.08" burst event, and stations 6# and 8# in the "2020.05.24" burst event as examples, the following phenomena can be observed. The coda waves of mining-induced tremor waveform monitored by them are relatively developed; the spectrum development shows a violent oscillation characteristic; the middle part of the waveform presents a shape of "inverted triangle graben"; and the whole waveform exhibits a nonlinear and multi-period disturbance characteristic. This corresponds to the ultra-low friction effect of faults and the dynamic activation instability of faults under the effect of dynamic load, which is consistent with the propagation characteristics of ultra-low-frequency, low speed, and high energy of over range pendulum-shaped waves under the effect of discontinuous and uncoordinated deformation of faults.

In addition, the waveforms monitored by station 10# in the "2019.09.12" burst event, station 14# in the "2020.01.08" burst event, and station 10# in the "2020.05.24" burst event still have secondary vibrations and even frequent vibrations after the end of the mainshock. The phenomenon of "main shock-after shock" reflects that these burst events have waveform characteristics like earthquakes induced by fault slip.

P-Wave First Motion of Mining-Induced Tremors

Byerly (1928) was the first to use the four-quadrant distribution of the compression and expansion of P-wave first motion to explore the nature of the seismic source, and he believed that the direction of P-wave first motion on the vibration sociogram was directly related to the seismic source force. As the physical image of the waveform was clear and not affected by the crustal velocity structure, it can be employed to preliminarily determine the focal mechanism solution (Herrmann, 1975). The coal rock mass fracture, such as horizontal tension fracture of the roof, longitudinal separation, and roof caving, generates the compression P-wave leaving the seismic source and the front part pushing outward. The P-wave first motion received by the microseismic station is "+," and this kind of tremor belongs to a typical tension type. The vibration, such as roof rotation instability and coal pillar compression fracture, generates the expansion P-wave pointing to the seismic source and its front part pulling outward. The P-wave first motion received by the microseismic stations is "−," and this kind of coal rock-induced tremor belongs to a typical implosion type. In coal rock tremors, such as roof shear rupture, masonry beam structure slip instability, dynamic burst of coal pillar, and mining-induced fault activation, the P-wave first motion is distributed in four quadrants in space, which is in line with the focal rupture mechanism of a typical double-couple source. They can be regarded as shear-type (Gibowicz et al., 1990; Du et al., 2020a). Mining-induced tremors of this type whose failure process is intense with more vibratory energy released and the highest burst risk.

Since the arrangement of each microseismic station is affected by the fluctuation of the coal seam and does not have a planar position relationship with the tremor events, the confirmed P-wave first motion of mining-induced tremors is not only simply upward or downward, but also should be determined according to the spatial position relationship between specific tremor events and corresponding stations.

The P-wave first motion of previous burst events is displayed in **Table 4**. It can be seen that: *1*) the P-wave first motions of the same station in different burst events are not completely the same, indicating that the microseismic waveform can fully reflect the characteristics of mine geological structure, mining environment, and overburden structure. *2*) The P-wave first motions of different stations in the same burst event are different, including compression P-waves and expansion P-waves with roughly the same proportions. Each burst event distributes in four quadrants, which is consistent with the focal rupture mechanism of a typical double-couple source. However, some channels were too far away from the source to receive an effective waveform. Moreover, as some stations were affected by mining activities with much background noise, the accurate direction of the P-wave first motion cannot be recognized.

Ratio of Es/Ep of Mining-Induced Tremors

The limitation of the P-wave first arrival method is that the closer the source is to the fault discontinuous surface, the weaker the P-wave is and the more difficult it is to identify the direction of the first motion. In the process of focal mechanism research in the Ruhr mining area, Germany, researchers found that the energy ratio of shear wave (S-wave) to compression wave (P-wave) is an important indicator to reveal the rupture mechanism of surrounding rocks. In recent years, with abundant on-site failure cases, many studies have been conducted on the discrimination criterion for determining the mechanism of coal rock mass fracture based on the distribution of the ratio of Es/Ep (Cai et al., 1998; Hudyma and Potvin, 2010; Kwiatek and Ben-Zion, 2013; Li et al., 2014). Subsequent studies demonstrate that the S-wave radiation energy is much larger than the P-wave radiation energy in earthquakes induced by fault slip (Boatwright and Fletcher, 1984), and that this kind of earthquake is dominated by shear

TABLE 4 | P-wave first motion of previous burst events.

Station number / Burst event	1#	2#	3#	4#	5#	6#	7#	8#	9#	10#	11#	12#	13#	14#	15#	16#	17#
2018.07.06	–	–	+	+	●	+	–	–	–	+	○	–	●	–	+	–	–
2019.03.07	–	+	+	●	+	+	–	–	–	+	+	–	–	–	+	–	–
2019.05.09	+	+	+	○	–	+	–	+	+	+	○	+	○	–	+	+	+
2019.06.29	–	+	–	–	+	+	+	+	+	+	+	+	–	–	–	+	+
2019.09.12	+	+	+	+	+	+	+	+	+	+	–	–	–	+	+	+	–
2019.10.06	+	+	+	+	+	+	–	–	+	+	+	+	+	–	–	+	–
2019.11.25	–	+	+	○	+	+	–	+	+	–	○	+	+	–	–	–	+
2019.12.24	+	+	–	+	+	+	+	–	–	–	–	–	+	●	+	+	+
2020.01.08	+	–	–	+	–	+	+	–	–	–	–	○	+	–	–	○	+
2020.05.24	–	+	+	+	●	–	+	–	–	+	+	+	+	+	+	–	+

+, compressed P-wave; –, expansion P-wave; ○, no valid waveform is received; ●, P-wave first motion cannot be identified due to too much background noise.

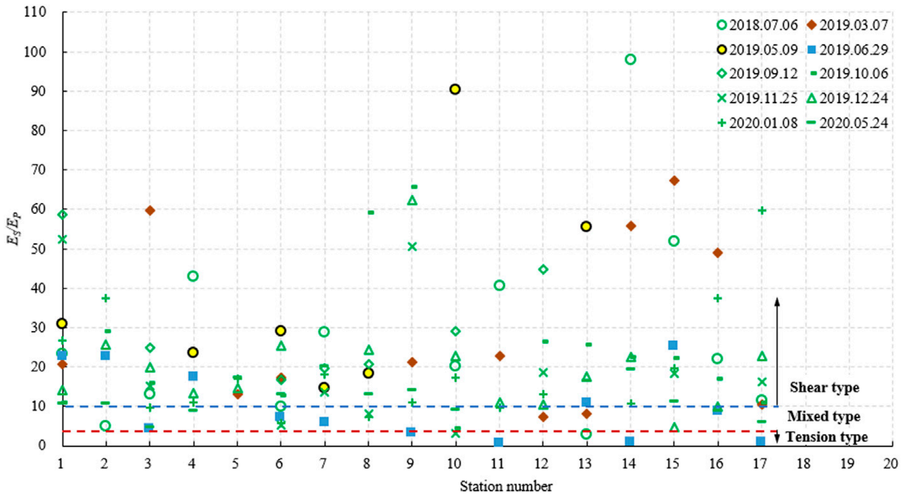

FIGURE 11 | *Es/Ep* in each channel of previous burst events.

failure. The P-wave and S-wave energies detected by the MS system can be calculated by using **the**following equation (Mendecki, 1997):

$$
\begin{aligned}
E_p &= \frac{8}{5}\pi\rho v_p R^2 \int_0^{t_s} \dot{u}^2_{corr}(t)dt,\\
E_s &= \frac{8}{5}\pi\rho v_s R^2 \int_0^{t_s} \dot{u}^2_{corr}(t)dt,\\
E_p &= \frac{8}{5}\pi\rho v_p R^2 \int_0^{t_s} \dot{u}^2_{corr}(t)dt,\\
E_s &= \frac{8}{5}\pi\rho v_s R^2 \int_0^{t_s} \dot{u}^2_{corr}(t)dt,
\end{aligned}
\tag{2}
$$

where E_p and E_s are the radiation energies of P-wave and S-wave, respectively; ρ is the rock density; v_p and v_s are the wave velocities of P-wave and S-wave, respectively; R is the distance between the station and the source; t_s is the duration of the source; and $\dot{u}^2_{corr}$ is the square of the far-field corrected radiation direction of the velocity pulse. In this study, the burst mining-induced tremors whose *Es/Ep* is larger than 10 in each channel are regarded as shear rupture; those whose *Es/Ep* is smaller than three are regarded as tension rupture and those whose *Es/Ep* ranges from three to 10 are regarded as mixed rupture (Wang et al., 2019; Du et al., 2020b; Wang et al., 2021).

Attenuation correction in the frequency domain was carried out for the body wave frequency spectrum detected in each channel of all burst events, and frequency integration was carried out for the velocity power spectrum to estimate the radiation energy fluxes of P-wave and S-wave and to further identify the rupture type. According to the results given in **Figure 11**, the basic rules are as follows: *1*) The distance and path between each station and the source are different, and the difference in attenuation of seismic wave results in different P-wave and S-wave energies at each station. The closer it is to the source, the shorter the vibration time, and the less the attenuation, therefore the higher the energy monitored by the station; otherwise, the farther away from the source, the lower the energy monitored. The energy of the same source detected in different stations can differ by up to two orders of magnitude. *2*) All the E_p in each channel of signal waveform of previous burst accidents in Mengcun coal mine are smaller than E_s with the value of E_p / E_s ranging from 3.01 to 65.69. The burst tremor waveform channels whose *Es/Ep* is smaller than three account for 1.28%, those with *Es/Ep* that lie in the range of 3–10 account for 19.23%, and those whose *Es/Ep* is greater than 10 account for 79.49%. Such a result demonstrates that the mining-induced tremors in the main entry area are mainly shear type and mixed type, which accords with the focal mechanism of CBTMIFS.

Based on the aforementioned analysis, the cause of the frequent destructive mining-induced tremors in the main entry area can be concluded as follows: The mining stress affects the F29 fault in a closed state, releasing the clamping normal stress of the long-term geological tectonic movement on the normal-line direction of the fault surface, which results in a rapid rise of shear stress of the fault surface and the "activation" of the previously stable fault. The slip dislocation of the fault surface in the main entry area gives rise to shear failure, which leads to slip instability of the fault and dynamic burst failure to the entries.

At the same time, it should be noted that different from the common burst failure induced by pushing mining across faults on the working face, this kind of burst failure mainly occurs in the main entries far from the working face, rather than on the working face. Research shows that more than 91% of coal burst events occur in the two lanes ahead of the working face, which seems to be in contradiction with the research object of this study. The coal rock mass in the fault area is weakened by pre-pressure relief measures in advances such as large diameter coal drilling, coal blasting, and roof pre-splitting blasting during entry excavation and mining, which undermines the F29 fault structure to a certain extent. The release of massive accumulated elastic energy lowers the degree of stress concentration and energy accumulation in the process of mining on the working face when crossing fault. However, the main entries, as the development roadway that needs to be used for a long time, lack the condition of frequent construction pressure relief engineering to ensure sufficient entry support effect. Consequently, coal stress becomes highly concentrated at the junction of the main entries and the fault. Under the influence of mining stress and tectonic stress, the hanging wall and the heading wall of the fault slip relative to each other, releasing massive strain energy instantly.

In addition, different from the common tension-type mining-induced tremors caused by roof stretching and implosion-type tremors by coal pillar compression, the frequency of fault slip is lower than that of the former two, but the vibration energy released is more and the failure is greater due to the volume of rock mass reaching the limit state at the source is larger (the potential source radius is larger).

CONCLUSION

Through the establishment of numerical simulation and the analysis of the microseismic signal characteristics of the burst events, the dynamic evolution characteristics of normal stress, and shear stress on the fault surface of the working face during the mining process, the influence of different horizontal stresses on the evolution of the stress field and energy field of fault slip, and the P-wave first motion and focal mechanism revealed by the ratio of E_S/E_P based on the spectrum characteristics of shake displacement are investigated, respectively. The main conclusions are as follows:

1. The geological structure leads to significant abnormal horizontal stress in the accident area, and the stratum deposition is obviously controlled by the tectonic movement of faults and folds, leading to stratum inversion, and deletion of overburden. The faults under high-stress conditions provide a favorable external environment for frequent coal burst accidents.
2. Different from common coal burst accidents in the working face, coal burst accidents induced by mining fault slip under high-stress conditions have significant shear seismic failure characteristics, i.e., with more complex failure type, larger failure scope, and higher failure degree. The failure characteristics in common are as follows: the hanging wall effect is obvious; the more energy released during a coal burst, the more destructive it will be to the entry; the heterogeneous stress evolution of the fault surface leads to the characteristics of multiple and repeated bursts of the entry.
3. The normal stress and shear stress on the fault surface show a dynamic heterogeneous evolution due to mining unloading, and the normal stress gradually decreases with mining, while the shear stress increases gradually due to shear slip, and the change rate of shear stress is greater than that of normal stress. The value of normal stress experienced a "positive-negative-positive" change process with mining, indicating that the main stress field on the fault surface rotates due to mining disturbance. This can be regarded as the precursor of fault slip. Under different initial ground stress levels, the higher the horizontal stress is, the higher the normal stress and shear stress on the fault surface will be. Besides, the greater the strain energy accumulated before the fault slip and released now of the slip is, the higher the corresponding burst risk will be.
4. The microseismic signals of burst accidents feature "high energy and low frequency," and the value of the fractal dimension D is high, and the S-wave is relatively developed, which accords with the characteristics of the shake displacement spectrum of typical shear mining-induced tremors. The P-wave first motion of each channel is distributed in four quadrants, which conforms to the focal rupture mechanism of a typical double-couple source. According to the E_S/E_P ratio of burst waveform, the destructive mining-induced tremors are mainly shear and mixed types.

Therefore, it can be concluded that frequent destructive tremors in the main entry area are caused by the mining stress affecting the F29 fault in a closed state, releasing the clamping normal stress of the long-term geological tectonic movement in the normal-line direction of the fault surface. Resultantly, the shear stress of the fault surface rises rapidly, and the previously stable fault becomes activated. The slip dislocation of the fault surface in the main entry area gives rise to shear failure, which leads to slip instability of fault and dynamic burst failure of the entries. The research conclusions disclose the mechanism of CBTMIFS under high-stress conditions, which is of great significance to further enriching the cognition of the inducing mechanism of fault coal burst.

DATA AVAILABILITY STATEMENT

The original contributions presented in the study are included in the article/Supplementary Material, further inquiries can be directed to the corresponding authors.

AUTHOR CONTRIBUTIONS

JB contributed to conceptualization, methodology, software, data curation, validation, writing—original draft, and funding acquisition. LD contributed to data curation, writing—review and editing, and funding acquisition. JL contributed to supervision, writing—review and editing, and funding acquisition. KZ contributed to writing—review and editing and funding acquisition. JC contributed to writing—review and editing. JK contributed to funding acquisition and writing—review and editing.

FUNDING

The authors gratefully acknowledge the financial support for this work provided by the Postgraduate Research & Practice Innovation Program of Jiangsu Province (Grant No. KYCX21_2342) and National Natural Science Foundation of China (Grant Nos 51874292 and 52004004).

REFERENCES

Bai, Q., Konietzky, H., Ding, Z. W., Cai, W., and Zhang, C. (2021). A Displacement-dependent Moment Tensor Method for Simulating Fault-Slip Induced Seismicity. *Geomech. Geophys. Geo-energ. Geo-resour.* 7, 79. doi:10.1007/s40948-021-00269-y

Bieniawaki, Z. T. (1967). Mechanism of Brittle Fracture of Rock, Parts I, II, III. *Int. J. Rock Mech. Min. Sci. Geomechanics Abstr.* 4 (4), 395–430. doi:10.1016/0148-9062(67)90031-9

Blake, W., and Hedley, D. G. F. (2003). *Rockbursts: Case Studies from North American Hard-Rock Mines*. Littleton: Society for Mining, Metallurgy, and Exploration, Inc.

Boatwright, J., and Fletcher, J. B. (1984). The Partition of Radiated Energy between P and S Waves. *Bull. Seismol. Soc. Am.* 74, 361–376. doi:10.1785/bssa0740020361

Byerly, P. (1928). The Nature of the First Motion in the Chilean Earthquake of November 11, 1922. *Am. J. Sci.* s5-16, 232–236. doi:10.2475/ajs.s5-16.93.232

Cai, M., Kaiser, P. K., and Martin, C. D. (1998). A Tensile Model for the Interpretation of Microseismic Events Near Underground Openings. *Pure Appl. Geophys.* 153, 67–92. doi:10.1007/978-3-0348-8804-2_5

Cai, W., Dou, L. M., Zhang, M., Cao, W., Shi, J.-Q., and Feng, L. (2018). A Fuzzy Comprehensive Evaluation Methodology for Rock Burst Forecasting Using Microseismic Monitoring. *Tunn. Undergr. Space Technol.* 80, 232–245. doi:10.1016/j.tust.2018.06.029

Cai, W., Dou, L., Si, G., and Hu, Y. (2020). Fault-Induced Coal Burst Mechanism under Mining-Induced Static and Dynamic Stresses. *Engineering* 7 (5), 687–700. doi:10.1016/j.eng.2020.03.017

Cook, N. G. W. (1976). Seismicity Associated with Mining. *Eng. Geol.* 10 (2–4), 99–122. doi:10.1016/0013-7952(76)90015-6

Du, K., Li, X.-f., Yang, C.-z., Zhou, J., Chen, S.-j., and Manoj, K. (2020b). Experimental Investigations on Mechanical Performance of Rocks under Fatigue Loads and Biaxial Confinements. *J. Cent. South Univ.* 27 (10), 2985–2998. doi:10.1007/s11771-020-4523-7

Du, K., Li, X., Tao, M., and Wang, S. (2020a). Experimental Study on Acoustic Emission (AE) Characteristics and Crack Classification during Rock Fracture in Several Basic Lab Tests. *Int. J. Rock Mech. Min. Sci.* 133, 104411. doi:10.1016/j.ijrmms.2020.104411

Du, K., Li, X., Wang, S., Tao, M., Li, G., and Wang, S. (2021). Compression-Shear Failure Properties and Acoustic Emission (AE) Characteristics of Rocks in Variable Angle Shear and Direct Shear Tests. *Measurement* 183, 109814. doi:10.1016/j.measurement.2021.109814

Duan, K., Ji, Y., Xu, N., Wan, Z., and Wu, W. (2019). Excavation-Induced Fault Instability: Possible Causes and Implications for Seismicity. *Tunn. Undergr. Space Technol.* 92, 103041. doi:10.1016/j.tust.2019.103041

Fan, L. F., and Wong, L. N. Y. (2013). Stress Wave Transmission across a Filled Joint with Different Loading/Unloading Behavior. *Int. J. Rock Mech. Min. Sci.* 60, 227–234. doi:10.1016/j.ijrmms.2012.12.046

Gibowicz, S. J., Harjes, H. P., and Schafer, M. (1990). Source Parameters of Seismic Events at Heinrich Robert Mine, Ruhr Basin, Federal Republic of Germany: Evidence for Nondouble-Couple Events. *Bull. Seism. Soc. Am.* 80, 88–109. doi:10.1016/0040-1951(90)90194-D

Gibowicz, S. J., and Kijko, A. (1994). *An Introduction to Mining Seismology*. San Diego: Academic Press.

Hasegawa, H. S., Wetmiller, R. J., and Gendzwill, D. J. (1989). Induced Seismicity in Mines in Canada?An Overview. *Pageoph* 1989 (129), 423–453. doi:10.1007/BF00874518

Herrmann, R. B. (1975). A Student's Guide to the Use of P and S Wave Data for Focal Mechanism Determination. *Seismol. Res. Lett.* 46, 29–39. doi:10.1785/gssrl.46.4.29

Horner, R. B., and Hasegawa, H. S. (1978). The Seismotectonics of Southern Saskatchewan. *Can. J. Earth Sci.* 15 (15), 1341–1355. doi:10.1139/e78-139

Hudyma, M., and Potvin, Y. H. (2010). An Engineering Approach to Seismic Risk Management in Hardrock Mines. *Rock Mech. Rock Eng.* 43, 891–906. doi:10.1007/s00603-009-0070-0

Husen, S., Kissling, E., and von Deschwanden, A. (2013). Induced Seismicity during the Construction of the Gotthard Base Tunnel, Switzerland: Hypocenter Locations and Source Dimensions. *J. Seismol.* 17 (1), 63–81. doi:10.1007/s10950-011-9261-810.1007/s10950-012-9313-8

Kaiser, P. K., Diederichs, M. S., Martin, C. D., Sharp, J., and Steiner, W. (2000). *Underground Works in Hard Rock Tunnelling and Mining. Keynote Lecture in Proceedings of GeoEng2000*, Vol. 1. Lancaster: Technomic Publishing Co., 841–926.

Kwiatek, G., and Ben-Zion, Y. (2013). Assessment ofPandSwave Energy Radiated from Very Small Shear-Tensile Seismic Events in a Deep South African Mine. *J. Geophys. Res. Solid Earth* 118, 3630–3641. doi:10.1002/jgrb.50274

Li, J., Ma, G., and Zhao, J. (2011). Analysis of Stochastic Seismic Wave Interaction with a Slippery Rock Fault. *Rock Mech. Rock Eng.* 44, 85–92. doi:10.1007/s00603-010-0109-2

Li, J., Wu, S. C., Gao, Y. T., Xie, Y., and Ji, M. (2014). Review of Slope Micro-seismic Monitoring in Open-Pit Mine. *Chin. J. Rock Mech. Eng. (in Chinese)* 33 (S2), 3998–4013. doi:10.13722/j.cnki.jrme.2014.s2.077

Marone, C. (1998). The Effect of Loading Rate on Static Friction and the Rate of Fault Healing during the Earthquake Cycle. *Nature* 391, 69–72. doi:10.1038/34157

McGarr, A. (1984). in *Some Applications of Seismic Source Mechanism Studies to Assessing Underground Hazard. Rockbursts and Seismicity in Mines*. Editors N. C. Gay and E. H. Wainwright (Johannesburg: Balkema), 1984, 199–208.

McGarr, A., Simpson, D., and Seeber, L. (2002). 40 Case Histories of Induced and Triggered Seismicity. *International Handbook of Earthquake and Engineering Seismology* 81A, 647–661. doi:10.1016/S0074-6142(02)80243-1

Mendecki, A. J. (1997). *Seismic Monitoring in Mines*. London: Chapman & Hall.

Morrow, C. A., and Byerlee, J. D. (1989). Experimental Studies of Compaction and Dilatancy during Frictional Sliding on Faults Containing Gouge. *Journal of Structural Geology* 11, 815–825. doi:10.1016/0191-8141(89)90100-4

Ortlepp, W. D., and Stacey, T. R. (1992). Rockburst Mechanisms in Tunnels and Shafts. *Tunnelling and Underground Space Technology* 30 (6), 59–65. doi:10.1016/0148-9062(93)91705-n

Pan, Y. S. (1999). *Study on Rock Burst Initiation and Failure Propagation [dissertation]Chinese*. Beijing: Tsinghua University.

Segall, P., and Rice, J. R. (1995). Dilatancy, Compaction, and Slip Instability of a Fluid-Infiltrated Fault. *J. Geophys. Res.* 100, 22155–22171. doi:10.1029/95JB02403

Suppe, J. (1983). Geometry and Kinematics of Fault-Bend Folding. *American Journal of Science* 283 (7), 684–721. doi:10.2475/ajs.283.7.684

Wang, S., Li, X., Yao, J., Gong, F., Li, X., Du, K., et al. (2019). Experimental Investigation of Rock Breakage by a Conical Pick and its Application to Non-explosive Mechanized Mining in Deep Hard Rock. *International Journal of Rock Mechanics and Mining Sciences* 122, 104063. doi:10.1016/j.ijrmms.2019.104063

Wang, S., Sun, L., Li, X., Wang, S., Du, K., Li, X., et al. (2021). Experimental Investigation of Cuttability Improvement for Hard Rock Fragmentation Using Conical Cutter. *Int. J. Geomech.* 21 (2), 06020039. doi:10.1061/(ASCE)GM.1943-5622.0001899

Wu, W., Zhao, Z., and Duan, K. (2017). Unloading-Induced Instability of a Simulated Granular Fault and Implications for Excavation-Induced Seismicity. *Tunnelling and Underground Space Technology* 63, 154–161. doi:10.1016/j.tust.2017.01.002

Yin, Z.-q., Li, X.-b., Jin, J.-f., He, X.-q., and Du, K. (2012). Failure Characteristics of High Stress Rock Induced by Impact Disturbance under Confining Pressure Unloading. *Transactions of Nonferrous Metals Society of China* 22 (1), 175–184. doi:10.1016/S1003-6326(11)61158-8

Yin, Z., Chen, W., Hao, H., Chang, J., Zhao, G., Chen, Z., et al. (2019). Dynamic Compressive Test of Gas-Containing Coal Using a Modified Split Hopkinson Pressure Bar System. *Rock Mech Rock Eng* 53 (1), 815–829. doi:10.1007/s00603-019-01955-w

Yin, Z. Q., Ma, H. F., Ma, H. F., Hu, Z. X., and Zou, Y. (2014). Effect of Static - Dynamic Coupling Loading on Fracture Toughness and Failure Characteristics in Marble. *Jestr* 7 (2), 169–174. doi:10.25103/jestr.072.25

Zhang, C., Canbulat, I., Hebblewhite, B., and Ward, C. R. (20172017). Assessing Coal Burst Phenomena in Mining and Insights into Directions for Future Research. *International Journal of Coal Geology* 179, 28–44. doi:10.1016/j.coal.2017.05.011

Zhao, Z., and Song, E.-x. (2015). Particle Mechanics Modeling of Creep Behavior of Rockfill Materials under Dry and Wet Conditions. *Computers and Geotechnics* 68, 137–146. doi:10.1016/j.compgeo.2015.04.008

Conflict of Interest: The authors declare that the research was conducted in the absence of any commercial or financial relationships that could be construed as a potential conflict of interest.

frontiers | Frontiers in Earth Science

ORIGINAL RESEARCH
published: 30 May 2022
doi: 10.3389/feart.2022.879082

Comparison of Underground Coal Mining Methods Based on Life Cycle Assessment

Haoyuan Wu[1†], **Zhiqiang Yin**[1,2*], **Yuchen Zhang**[1†], **Chao Qi**[1†], **Xian Liu**[1†] **and Jianen Wang**[1†]

[1]School of Mining Engineering, Anhui University of Science and Technology, Huainan, China, [2]Coal Mine Safety Mining Equipment Innovation Center of Anhui Province, Anhui University of Science and Technology, Huainan, China

Coal is China's main source of energy, and its production causes a certain degree of air, water, and land resource pollution. Therefore, it is necessary to compare environmental pollution caused by different mining methods. When mining underground coal resources, different mining methods have different levels of environmental impacts. To identify the mining method with the least environmental impact, different mining methods were evaluated by means of a life cycle assessment using Simapro 9.0.0 software. The Ecoinvent v3 database was used to provide background data, and the results were calculated using the Eco-indicator99 method. The findings show that for a 20 m coal column, respiratory inorganics were identified as the dominant impact category based on normalized results, followed by fossil fuels, carcinogens, and climate change. The contribution analysis indicated that electricity and coal mining are fundamental in contributing to these significant impact categories and should be of particular concern. According to the sensitivity analysis, reducing mining activities and increasing extraction efficiency and use are the primary responses to addressing environmental pollution, followed by reducing environmental pollution caused by electricity and steel production. In addition, a summary comparison of the single scores of different mining methods suggests that the environmental burden of pillarless mining is the lowest, and as the width of the coal pillar gradually increases, its single score shows a trend of increasing and then decreasing. Therefore, the single score of non-pillar mining is the lowest compared to that of other mining methods and can be the optimal mining method. This study can provide a scientific basis for the selection of green mining and underground coal resource mining methods.

Keywords: life cycle assessment, coal production, optimal mining method, environmental impact, green mining

Edited by:
Candan Gokceoglu,
Hacettepe University, Turkey

Reviewed by:
Marek Laciak,
Technical University of Košice, Slovakia
Satar Mahdevari,
Amirkabir University of Technology, Iran

***Correspondence:**
Zhiqiang Yin
zhqyin@aust.edu.cn

†ORCID:
Haoyuan Wu
orcid.org/0000-0002-6934-2493
Yuchen Zhang
orcid.org/0000-0001-5881-8989
Chao Qi
orcid.org/0000-0003-2890-6536
Xian Liu
orcid.org/0000-0003-3713-3088
Jianen Wang
orcid.org/0000-0002-6459-6865

Specialty section:
This article was submitted to Geohazards and Georisks, a section of the journal Frontiers in Earth Science

Received: 18 February 2022
Accepted: 12 May 2022
Published: 30 May 2022

Citation:
Wu H, Yin Z, Zhang Y, Qi C, Liu X and Wang J (2022) Comparison of Underground Coal Mining Methods Based on Life Cycle Assessment. Front. Earth Sci. 10:879082. doi: 10.3389/feart.2022.879082

1 INTRODUCTION

Coal mining processes in the world's major coal-producing countries are distinctive, with the negative environmental impacts caused by resource consumption and waste emissions varying among mining methods. Therefore, it is essential to choose an optimal mining method that makes the best use of resources and reduces the environmental burden. In recent years, the national demand for green and high quality industrial development has led researchers to focus on the safe and efficient production of coal. Reducing the environmental impact of the mining industry has also received increasing attention.

Coal will remain China's primary energy source in the future. For a long time, coal mining in China has generally adopted the longwall mining technology system of digging the return roadway in advance at both ends of the return workings and leaving sections of coal pillars to protect the roadway (Zhen et al., 2019). The emergence of pillarless mining technology has initiated an essential change in coal mining technology in response to the low coal extraction and high roadway boring rates of the traditional pillar retention. This technology is achieved by mining coal while maintaining the original return roadway and retaining it for continued use in the next section of the workings, without leaving section guard coal pillars, thereby resulting in pillarless mining. Evaluating these two mining processes using different methods has received national and international research interest. Dubiński and Turek (2007) argued that the absolute safety and efficiency of production should be considered while minimizing its negative impact on the environment. Therefore, it is important to establish a management system that aims to prevent pollution and comply with environmental protection laws. A key requirement of environmental management is the continuous assessment of environmental activities (Staš et al., 2015). Currently, coal mining impact assessments focus on some of the most critical impacts caused by the processes involved (Burchart-Korol et al., 2016). Methane emissions into the atmosphere, drainage, and mining waste are important negative environmental impacts of coal mining (Kugiel, 2010), and methane is one of the most significant natural hazards of underground coal mining operations (Krause and Krzemień, 2013; Krause and Smoliński, 2013; Turek, 2010). Drainage is another important environmental impact of underground coal mining. In addition to natural water inflow, water supplied to the mine for processing is also essential (Jonek-Kowalska and Turek, 2013; Pluta and Dulewski, 2006). Furthermore, the disposal of mining waste requires the consideration of multiple environmental and economic aspects (Kowalska, 2014).

Life cycle assessment (LCA) is known as the cradle-to-grave approach to environmental assessment (Ma et al., 2010; Zhu, 2004) and is one of the most standardized methods for estimating the environmental burden associated with certain products. The Society of Environmental Toxicology and Chemistry (SETAC, 1993; Fava et al., 1993) defined LCA as a process of objectively evaluating the environmental impact of products, processes, and activities by identifying and quantifying energy and material use and the resulting environmental waste emissions. It evaluates the impact of energy and materials used on the environment by identifying and quantifying the resulting environmental waste emissions to find ways to improve them. The International Organization for Standardization (ISO 14040, 2006) defines LCA as one of the branches of system evaluation that analyzes environmental impacts in three main areas, namely, resource consumption, ecological health, and human health. While these studies have addressed the direct environmental impacts of mining activities, their methods did not indicate the indirect impacts on their inputs and outputs. Compared to environmental impact assessment or environmental auditing, LCA is superior because it broadens the boundaries of the system to include the loads or impacts of a product or process throughout its lifetime rather than only the emissions and waste generated by the manufacturing process (Yingshun, 2009). LCA is an environmental assessment method that quantifies the consumption of natural resources and emissions of pollutants during the production phase of a product and also assesses the process of making raw materials and analyzes the disposal of the product as waste at a later stage (Blengini et al., 2012). Previous studies have used LCA for iron ore, uranium, gold, copper, and aluminum (Ferreira and Leite, 2015; Haque and Norgate, 2014; Awuah-Offei et al., 2008; Spitzley and Tolle, 2004), as well as copper, nickel, and zinc (Suppen et al., 2006) for mineral extraction and processing. However, as each mineral corresponds to specific geological, mining, and processing conditions, the environmental impact of extracting each mineral product differs and, therefore, requires a specific individual analysis (Norgate and Haque, 2010). Awuah-Offei and Adekpedjou (2011) provided an overview of the applications, challenges, and current applications of LCA in the mining industry; lack of awareness and tools to perform LCA; definition of different functional units; and difficulty in the scope of the purpose of the analysis and selection of environmental impact categories (Awuah-Offei and Adekpedjou, 2011). Durucan et al. (2006) developed an LCA model of mining that incorporated mine production, processing, waste treatment and disposal, rehabilitation, and aftercare into an LCA framework, a tool that enabled an integrated representation of mining systems. Burchart-Korol et al. (2016) developed a model that combined SimaPro software with the Intergovernmental Panel on Climate Change and ReCiPe methods to assess impact categories, such as greenhouse gas emissions, human health, ecosystems, and resources. Tao et al. (2021) conducted a LCA of a typical coal mine in China, which identified the main impact categories of the mine and key processes contributing to the main impact categories.

The studies described above have led to many useful conclusions, and the LCA standard approach, based on ISO 14044, reveals that impact categories vary depending on the mining process (Mahmud et al., 2018; Farjana et al., 2018; ISO 14040, 2006). In summary, there remains a lack of research on the LCA of underground coal mining processes for different mining methods; thus, an optimal mining method has not yet been identified.

2 MATERIALS AND METHODS

2.1 Life Cycle Assessment Method

The LCA methodology is a tool for assessing the environmental consequences of a product or an entire activity throughout its life. A complete LCA consists of four integral components, namely determination of purpose and scope, inventory analysis, impact assessment, and life cycle interpretation. LCA includes the following: identification and quantification of energy and resource use and environmental emissions to air, water, and land; characterization of technology quality and quantity; evaluation of the consequences of environmental impact analysis; and assessment of opportunities for environmental burden reduction and implementation. In this study, LCA was analyzed using SimaPro software, an internationally recognized database containing a large amount of data such as the Ecoinvent database and the input-output database, which is directly connected to the Eco-indicator 99 and ReCiPe Midpoint databases and contains well-known LCA calculation methods such as Eco-indicator 99 and ReCiPe Midpoint. The database provides a rich background of data, and the calculation methods are more efficient and accurate for quantitative calculations. Therefore, this software is widely used in the life cycle inventory assessment (LCIA) of coal mines.

In this study, quantitative calculations were performed using the Eco-indicator99 method, reflecting the direct and indirect environmental impacts of different mining methods. In this method, the inventory results were grouped into 11 impact categories, namely respiratory organics, respiratory inorganics, climate change, radiation, ozone layer, ecotoxicity, acidification/eutrophication, land use, minerals, and fossil fuels. When life cycle inventories of different mining methods are assigned to these impact categories, the results of the characterization analysis can reflect the relative contribution of each of these processes to the impact category. A normalized analysis reflects the specific value of each input unit in the overall environmental impact and allows for a comparison between different life cycles. Consequently, both aspects provide a clear picture of the environmental impacts of the different mining methods (**Figure 1**).

2.2 Functional Unit and System Boundary

Before an LCA evaluation, selecting functional units and delineating system boundaries are essential steps. The selection of functional units is ultimately used to compare and analyze the LCA results and provide an accurate quantitative reference for the inputs and outputs of the relevant processes that have been investigated (ISO 14040, 2006). The main role of the functional units is to provide a uniform measure of input and output in a mathematical sense, providing a frame of reference for the relevant inputs and outputs to ensure comparability of the LCA results. With reference to the measurement size of the data in the Ecoinvent database, this study used the mining of 1 kg of coal as a functional unit; thus, all inputs and outputs were based on the mining of 1 kg of coal. The study was divided into two mining methods, namely non-pillar (reserved coal pillar width of 0 m) and reserved coal pillar mining, where the reserved coal pillar width was 5, 10, 20, and 25 m. All the input and output units were determined, and the environmental impacts caused by different mining methods in coal mining were evaluated.

There are complex subsystems interconnected with a production system and interconnected as subsystems with other production systems, making it is very difficult to identify all the interconnected inputs and outputs. **Figure 2** shows the system boundary, which includes three subsystems, with the production of materials and energy within the system boundary and the production of equipment and maintenance of equipment not included within the boundary.

2.3 Life Cycle Inventory Analysis

The life cycle inventory (LCI) is the basis for LCIA and for improving and optimizing engineering practices. The inventory analysis is an iterative process. Production data and waste emissions from coal with different mining methods are monitored. Where information is insufficient, data are supplemented by referencing government planning documents and literature, in addition to background information on production materials and energy sources provided by the Ecoinvent database. All the data were measured in functional units of 1 kg of coal mining. The

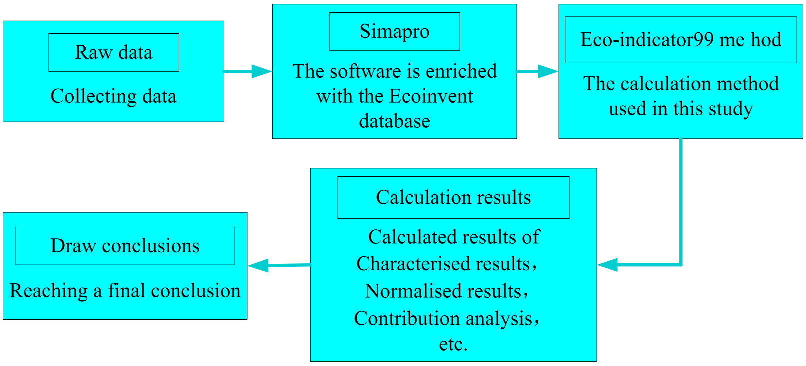

FIGURE 1 | Life cycle assessment flow chart.

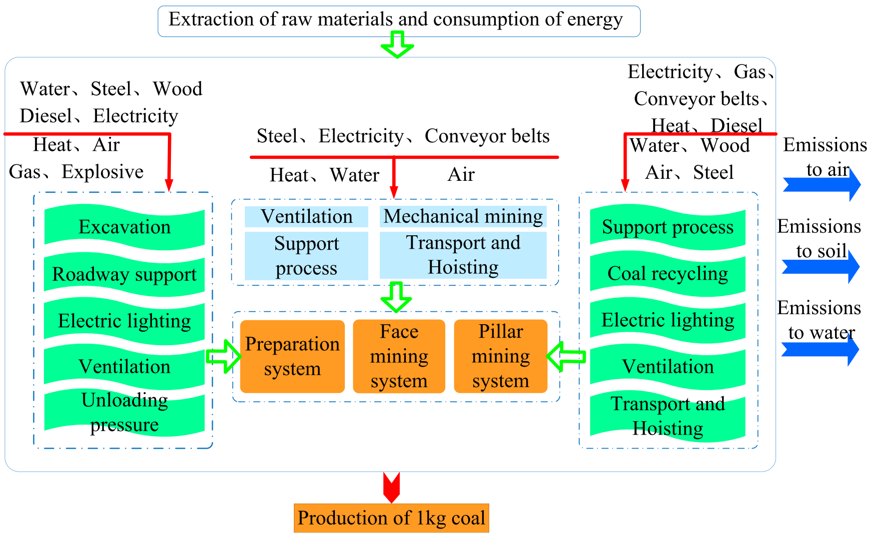

FIGURE 2 | System boundary of the coal production life cycle.

LCI is given in **Table 1**, where the data on material production, energy consumption, and direct emissions are calculated on a functional unit basis.

Daily production parameters, operating procedures, and direct emissions are the main sources of field data, which are monitored by specialist departments studying coal mines. Data, including those on steel and wood, were derived from operating procedures and emissions from direct emissions, in addition to raw data such as electricity and sulfur dioxide, which were referred from existing research in China (Tao et al., 2021). The Ecoinvent database is one of the most advanced life-cycle inventory databases, covering basic data from China and other countries and providing background data on the production of energy and raw materials (Ecoinvent Center, 2015).

The LCI is the collection of the data required at each stage of the life cycle and calculation of the data collected. The

TABLE 1 | Life cycle inventory (Values were presented per functional unit).

	Substance	Unit	Amount (0 m)	Amount (5 m)	Amount (10 m)	Amount (20 m)	Amount (25 m)
Product	Coal	kg	1	1	1	1	1
Raw materials	Steel	kg	6.506E-03	7.299E-03	7.132E-03	6.880E-03	6.753E-03
	Wood	m^3	1.684E-06	2.092E-06	2.050E-06	1.977E-06	1.940E-06
	Water	kg	3.599E-01	4.106E-01	4.007E-01	3.859E-01	3.785E-01
	Groundwater	m^3	2.261E-03	2.581E-03	2.521E-03	2.428E-03	2.381E-03
	Gas	m^3	1.105E-02	1.266E-02	1.237E-02	1.194E-02	1.171E-02
	Oxygen	kg	9.336E-03	1.058E-02	1.034E-02	9.963E-03	9.771E-03
	Occupation	m2a	1.528E-02	1.770E-02	1.731E-02	1.669E-02	1.637E-02
	Explosive	kg	2.205E-05				
Energy consumption	Electricity	kWh	3.351E-02	3.920E-02	3.826E-02	3.686E-02	3.616E-02
	Diesel	MJ	1.743E-02	2.255E-02	2.202E-02	2.123E-02	2.083E-02
	Heat	MJ	8.735E-02	9.804E-02	9.582E-02	9.240E-02	9.069E-02
Emissions to air	Carbon dioxide	kg	1.074E-02	1.268E-02	1.261E-02	1.256E-02	1.253E-02
	Carbon monoxide	kg	1.889E-04	2.183E-04	2.171E-04	2.164E-04	2.158E-04
	Methane	kg	1.084E-02	1.217E-02	1.193E-02	1.153E-02	1.133E-02
	Nitrogen oxides	kg	6.439E-05	7.288E-05	7.250E-05	7.224E-05	7.204E-05
	Particulates <2.5 μm	kg	2.303E-06	2.741E-06	2.727E-06	2.717E-06	2.710E-06
	Particulates >10 μm	kg	9.159E-05	1.046E-04	1.041E-04	1.037E-04	1.034E-04
	Particulates >2.5,and<10 μm	kg	1.207E-06	1.471E-06	1.463E-06	1.458E-06	1.454E-06
	Sulfur dioxide	kg	2.432E-05	2.951E-05	2.936E-05	2.925E-05	2.917E-05
	Water	m^3	2.190E-02	2.541E-02	2.528E-02	2.519E-02	2.512E-02
Emissions to water	Chloride	kg	1.295E-02	1.621E-02	1.612E-02	1.606E-02	1.602E-02
	Sulfur	kg	4.330E-03	5.002E-03	4.976E-03	4.958E-03	4.945E-03
	Water, CN	m^3	3.938E-04	4.612E-04	4.588E-04	4.571E-04	4.559E-04
Emissions to soil	Silicon	kg	1.640E-04	1.919E-04	1.909E-04	1.902E-04	1.897E-04
	Sulfur	kg	5.331E-05	6.183E-05	6.150E-05	6.128E-05	6.111E-05

TABLE 2 | Life cycle impact assessment results (characterized results).

Impact category	Unit	0 m	5 m	10 m	20 m	25 m
Impacts on human health						
Carcinogens	DALY	7.710E-08	8.961E-08	8.748E-08	8.429E-08	8.270E-08
Respiratory organics	DALY	1.939E-10	2.171E-10	2.126E-10	2.054E-10	2.017E-10
Respiratory inorganics	DALY	8.914E-07	1.040E-06	1.016E-06	9.789E-07	9.605E-07
Climate change	DALY	7.885E-08	8.979E-08	8.792E-08	8.496E-08	8.348E-08
Radiation	DALY	2.025E-11	2.322E-11	2.268E-11	2.187E-11	2.147E-11
Ozone layer	DALY	1.604E-12	1.860E-12	1.816E-12	1.751E-12	1.719E-12
Damage to ecosystem						
Ecotoxicity	PAF × m^2 × yr	2.953E-02	3.378E-02	3.299E-02	3.180E-02	3.121E-02
Acidification/Eutrophication	PDF × m^2 × yr	4.736E-03	5.446E-03	5.324E-03	5.145E-03	5.055E-03
Land use	PDF × m^2 × yr	1.420E-02	1.647E-02	1.610E-02	1.553E-02	1.523E-02
Natural resources depletion						
Minerals	MJ surplus	1.854E-03	2.078E-03	2.030E-03	1.958E-03	1.922E-03
Fossil fuels	MJ surplus	1.373E-01	1.591E-01	1.553E-01	1.497E-01	1.469E-01

collection process is the most labor-intensive part of the process. It involves not only the production of the materials and energy required for the different mining methods, materials, and energy consumed in various processes, but also the collection and calculation of data on various waste emissions.

3 RESULTS

3.1 Characterized Results

The LCIA directly reflects the environmental relevance of all inputs and outputs. In this study, the environmental impact results were classified into 11 impact categories according to the Eco-indicator99 method and included carcinogens, respiratory organics, and respiratory inorganics. The parameters involved in the LCI, such as material production, energy consumption, and waste emissions, were assigned to these impact categories in the SimaPro software calculations to obtain the LCIA results.

In the Eco-indicator99 method, normalization and weighting were performed in levels within the damage categories. The three damage categories were as follows:

1. HH, human health (unit: DALY = disability-adjusted life years, which means different disabilities caused by diseases are weighted).
2. EQ, ecosystem quality (unit: PDF × m^2 × yr; PDF = Potentially Disappeared Fraction of plant species).
3. R, Resources (unit: MJ surplus energy and additional energy requirement to compensate for lower future ore grade).

Table 2 provides the LCIA results, from which the potential impact of each impact category can be understood. For example, the impact values for carcinogens were 7.710E-08, 8.961E-08, 8.748E-08, 8.429E-08, and 8.270E-08 DALY for mining methods at 0, 5, 10, 15, 20, and 25 m coal pillar widths, respectively.

In the characterized results, all impact categories were counted at 100% to provide a more intuitive analysis of the proportion of each process in each impact category. However, the results of this

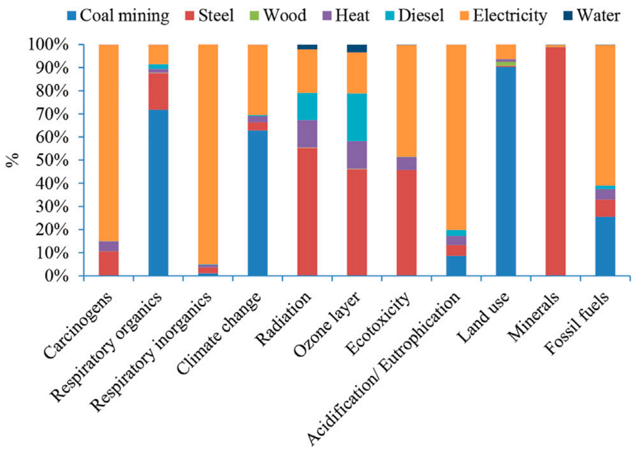

FIGURE 3 | Characterized results of LCIA taking 20 m coal pillar as an example.

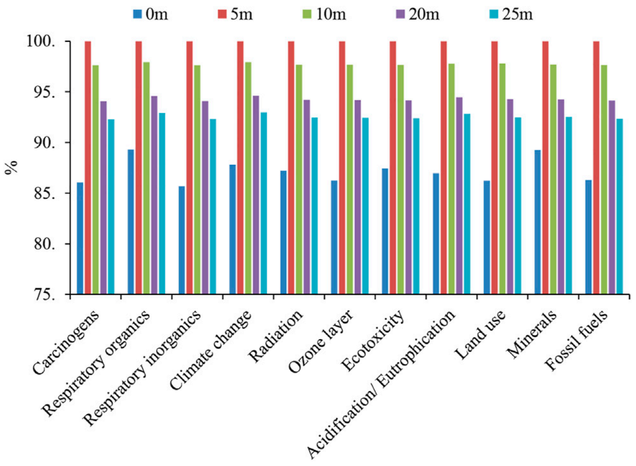

FIGURE 4 | Characterized results of LCIA (overall comparison).

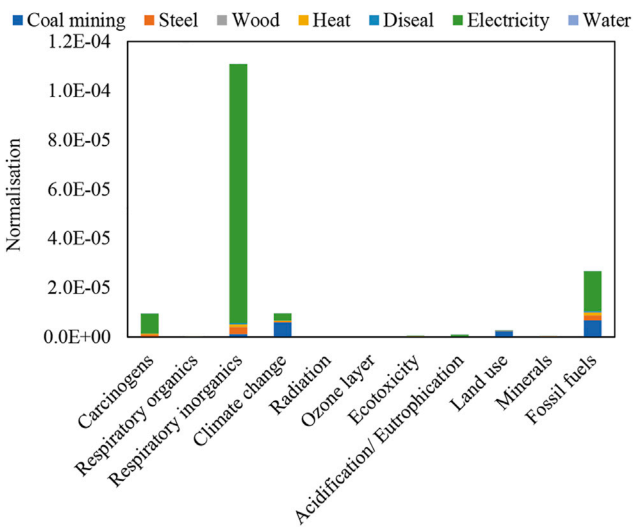

FIGURE 5 | Normalized results of LCIA taking 20 m coal pillar as an example.

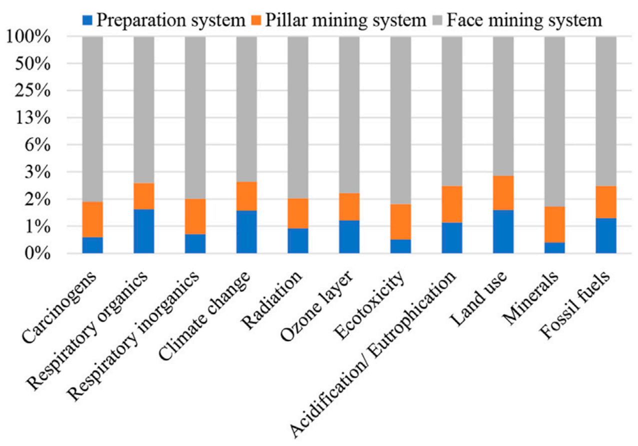

FIGURE 6 | Characterized results of LCIA (three interacting subsystems).

study do not allow for an intuitive identification of which impact category or process has the greatest impact on the overall environment. Only which unit or process contributes the most to a particular impact category can be observed. Using a 20 m coal pillar as an example, **Figure 3** shows the characterized results for each unit or process in the coal mining process. **Figure 4** shows the characterized results for coal mining at pillar widths of 0–25 m.

All units or processes contribute in some way to each of the 11 impact categories, and the share of each unit in particular impact categories is clearly demonstrated in **Figure 3**. For example, electricity was found to make a substantial contribution to the impact of carcinogens, followed by steel. Pollution is not only related to direct emissions but also to the production of materials and energy at the previous level. In this way, the magnitude of the contribution of the impact units or processes in each of the 11 impact categories could be visualized. The contributions of the impact categories, impact units, and systems for the remaining coal pillar width mining processes were similar to those for the 20 m pillar width mining process; therefore, they were not repeated here.

The 11 impact types of coal mining at five coal pillar widths were compared centrally (**Figure 4**), with the most severe mining method for each impact type being counted at 100% in the comparison process. The impact of the remaining mining methods on each impact type was compared according to the most severe mining method. The environmental impact of each mining method could only be compared for one impact type, but it was seen that the environmental impact of pillarless mining is the lowest for each impact type, and therefore, the overall environmental contribution of pillarless mining is also the lowest. Based on this method, **Figure 4** shows a comparison of the characterized results for coal mining at 0–25 m pillar widths, with each influence category increasing and then decreasing as the width of the coal column increases. The 5 m coal pillar mining method led the way for each impact type, and therefore, had the greatest overall environmental impact, followed by the 10, 20, and 25 m pillar width mining methods. The overall environmental impact of pillarless mining was the lowest. The proportion of respiratory organic impacts for each mining method was the highest compared to the other impact types in coal-free pillar mining, mainly because of organic particulate matter generated by blasting during the coal-free pillar mining process. Conversely, the 5 m coal pillar mining process had the highest impact of each category, mainly because the pillar was so small that it no longer had the capacity to carry the overlying rock seam. It required a large amount of steel, electricity, and wood to support the material in order to reach the carrying capacity of the mining and consumed a large amount of energy and material. As the width of the coal column increased, the ability to carry the overlying rock seam gradually increased, requiring less ancillary support material and energy, and the contribution to the environment from producing the corresponding energy and material gradually decreased, showing a gradual decrease in the contribution to the environment in each impact type.

3.2 Normalized Results

In the characterized results, it was not possible to directly observe the extent to which each impact category contributes to the overall impact. Therefore, a further standardized analysis was required, in which the contribution of each impact category to the overall process can be quantified and the magnitude of the contribution of the impact categories can be visually analyzed and compared. As an example of coal mining with a 20 m coal pillar width, respiratory inorganics caused the greatest environmental burden in the coal mining process, followed by fossil fuels, carcinogens, and climate change (**Figure 5**).

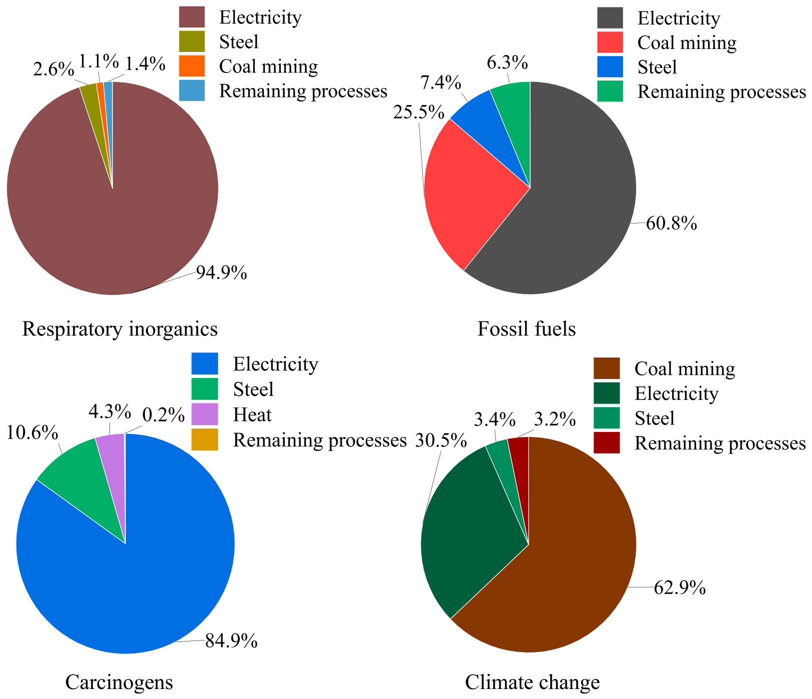

FIGURE 7 | Process contribution analysis results.

3.3 Contribution Analysis

3.3.1 Contributions of Subsystems

A contribution analysis plays an important role in an uncertainty analysis, where all contributions of individual processes are superimposed on the results of the contribution analysis calculation. By focusing on these processes, it is possible to reduce negative environmental impacts by identifying the production processes that play an important role in evaluating the results. Using a 20 m coal pillar width as an example, **Figure 6** shows the characterized results of the three interacting subsystems in the coal mining process.

The results showed that the three subsystems are responsible for most of the carcinogen, respiratory organic, respiratory inorganic, climate change, radiation, ozone layer, ecotoxicity, acidification/eutrophication, land use, mineral, and fossil fuel effects (**Figure 6**). The face mining system was responsible for the majority of these 11 impact categories and for a substantial proportion of all the impact categories. This mining system accounted for a substantial proportion of all impact categories and 98.5% of the impact in carcinogens, indicating that the face mining system is the largest contributor to each impact category of the three subsystems. In contrast to the face mining system, the preparation and pillar mining systems had a smaller environmental burden and contributed to all 11 impact categories.

3.3.2 Contributions of Processes

Respiratory inorganics, fossil fuels, and carcinogens were found to be the most significant impact categories (**Figure 5**), in addition to climate change, which has received much attention in recent years. Therefore, the categories described above were identified as key categories. In the analysis, the key processes affecting the key categories could not be accurately captured, and therefore, a process contribution analysis was conducted within the system boundary. The process contribution analysis was used to identify the critical processes within the main impact categories so that improvements can be made to reduce negative environmental impacts effectively (**Figure 7**).

According to the process contribution results (**Figure 7**), electricity was the leading cause of respiratory inorganics, fossil fuels, and carcinogens, accounting for 94.9%, 60.8%, and 84.9%, respectively. The waste generated from coal-fueled thermal power generation, whose production process uses fuels, was the leading cause of respiratory inorganic, fossil fuel, and carcinogen impacts. The main contributor to climate change was coal mining, which is caused by large amounts of polluting gases such as CO_2 and methane emitted into the air through the ventilation process.

4 DISCUSSION

4.1 Uncertainty Analysis

An uncertainty analysis examines how uncertainty in the input data affects the results of the model and helps to understand the importance of the data source or model. The dataset was drawn from the field, literature, and databases and then averaged together to create a combined dataset; therefore, it was necessary to conduct an uncertainty analysis to ensure its accuracy. The uncertainty analysis was conducted using

TABLE 3 | Uncertainty analysis results based on the Eco-indicator99 method.

Impact category	Unit	Mean	Median	SD
Carcinogens	DALY	7.89E-08	5.50E-08	1.12E-07
Respiratory organics	DALY	2.06E-10	1.99E-10	2.51E-11
Respiratory inorganics	DALY	9.85E-07	8.48E-07	5.28E-07
Climate change	DALY	8.50E-08	8.48E-08	2.14E-09
Radiation	DALY	2.17E-11	1.87E-11	1.24E-11
Ozone layer	DALY	1.74E-12	1.64E-12	5.86E-13
Ecotoxicity	PAF × m^2 × yr	0.031	0.030	0.006
Acidification/Eutrophication	PDF × m^2 × yr	0.005	0.005	0.001
Land use	PDF × m^2 × yr	0.0155	0.0154	0.0002
Minerals	MJ surplus	0.0019	0.0018	0.0003
Fossil fuels	MJ surplus	0.149	0.148	0.0175

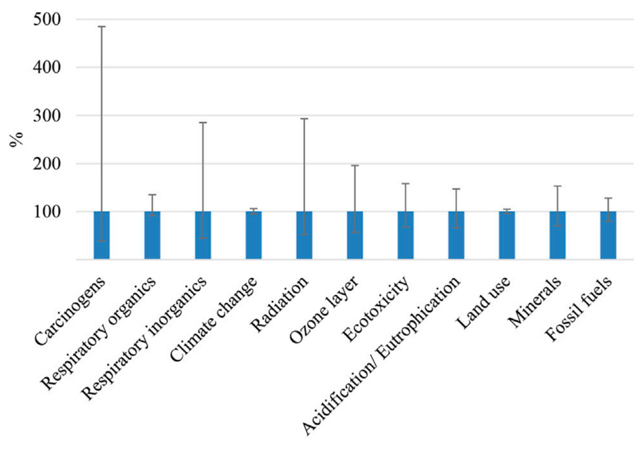

FIGURE 8 | Uncertainty analysis results using the Eco-indicator99 method.

Simapro 9.0.0 software. The input data were analyzed using the uncertainty analysis method in the Eco-indicator99 method with a 95% confidence level and displaying the mean, median, and standard deviation. The uncertainty results using a 20 m coal column and calculated using the Eco-indicator99 method are displayed in **Table 3** and **Figure 8**.

For the 20 m coal pillar mining process, the results based on **Table 3** show no significant change in the significant impact categories of carcinogens, respiratory inorganics, fossil fuels, and climate change. **Figure 8** shows the results of the Eco-indicator99 based method for the 20 m coal column mining process, with the marked categories being carcinogens, radiation, and respiratory inorganics. By comparing the uncertainty of carcinogens with the other impact types, followed by radiation and respiratory inorganics, the uncertainty results for the remaining impact types were found to be low and have high stability compared to the uncertainty results for these three impact categories. For low uncertainty data, there is a high degree of stability, whereas for high uncertainty data, double-checking is required to ensure the accuracy of the data and provide a reference for future related studies.

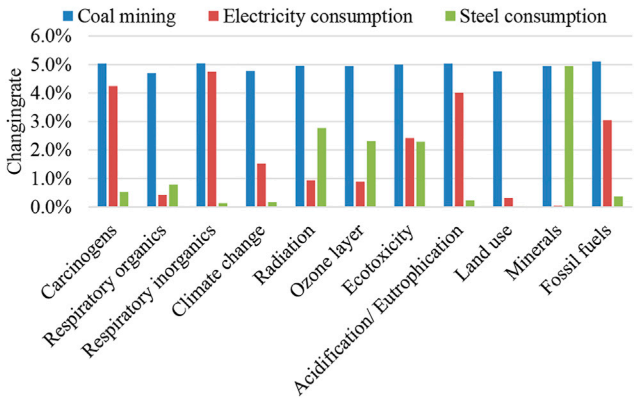

FIGURE 9 | Sensitivity analysis results of key processes.

4.2 Sensitivity Analysis

A sensitivity analysis can provide a basis for scientific decisions to reduce environmental burden. This is an indication of how changes in individual parameters and parameter sets affect the final results; that is, the importance or sensitivity of a parameter to the overall model can be determined by analyzing the impact of a change in the parameter when all other parameters are constant. The sensitivity analysis was conducted using Simapro 9.0.0 software, and the results were calculated using the Eco-indicator99 method. The results of the sensitivity analysis were calculated using the software and the methods described above. The sensitivity analysis was conducted for crucial impact categories and key processes based on functional units, reducing the input data for each key process by 5% and observing changes in the contribution of key impact categories. Taking 20 m coal pillar mining as an example, **Figure 9** shows the sensitivity analysis results for the key processes.

The graph (**Figure 9**) demonstrated that that a 5% reduction in coal mining can provide significant environmental benefits for all impact categories, such as carcinogens, respiratory organics, respiratory inorganics, and climate change, with the rates of change being 5.03%, 4.70%, 5.04%, and 4.78%, respectively. The sensitivity of the coal mining process was high and particularly important because changes in coal mining have a greater impact on all impact types. When electricity consumption was reduced by 5%, the rates of change for respiratory inorganics, carcinogens, acidification/eutrophication, fossil fuels, and climate change were 4.75%, 4.25%, 4.01%, 3.04%, and 1.52%, respectively. Therefore, changes in electricity consumption have a greater impact on the important impact types and a higher sensitivity and are crucial for the important impact categories. When steel consumption was reduced by 5%, the rate of change was 4.94%, 2.77%, and 2.30% for the minerals, radiation, and ozone layer categories, respectively, with some sensitivity and importance for some of these impact categories.

Based on the results of the sensitivity analysis, to adopt scientific countermeasures for reducing the burden on the environment, the first step is to minimize the mining of coal resources. Coal mining has a greater burden on the environment, and scientific methods should be adopted to use clean energy as much as possible and improve the efficiency of the mining and utilization of coal. The consumption of electricity also has a significant impact on the environment; therefore, we should try to use less burdensome methods of power generation, such as wind power and water power generation, and improve the efficiency of electricity use. Finally, steel consumption damages the environment, and it is necessary to reduce the environmental impact of the steel production process and improve its efficiency.

4.3 Interpretation

With rapid economic development, environmental issues have become key global topics. As one of the primary energy sources, the production and consumption of coal has caused substantial environmental pollution. As different production methods are used, their impacts on the environment vary. This study investigated the environmental impact of underground coal resources under different mining methods and identified the production method with the least burden on the environment and, consequently, the optimal mining method.

The life cycle evaluation process is similar to different coal pillar mining methods, and this study used the mining method with a 20 m coal pillar left in place as an example of a life cycle evaluation of its production process. The characterization results (**Figure 3**) provide an understanding of the extent of each process for each of the 11 impact categories and the share of each unit in a particular impact type is also shown. For example, electricity makes the largest contribution to the impact of carcinogens, followed by steel. The results of the characterization of all coal pillar widths were compared (**Figure 4**), which initially concluded that the no-pillar mining method has the least environmental burden. A standardized analysis was then used to quantify the degree of impact of each impact category on the overall environment, with respiratory inorganics, carcinogens, and fossil fuels being the most dominant impact categories. With an understanding of the main impact categories, a contribution analysis was conducted to identify the face mining system as the subsystem with the greatest environmental burden through the contributions of subsystems and processes. The main processes affecting the main categories of impact were identified, with the main processes affecting respiratory inorganics being, for example, electricity. This analysis explains the main impact categories and processes and provides a basis for scientific decisions to reduce the environmental burden. However, to verify the accuracy of the data and provide a solid scientific strategy, uncertainty and sensitivity analyses were conducted. The sensitivity analysis results showed that a 5% reduction in the input data for the main impact processes would result in a greater environmental benefit. Therefore, with the mining method of leaving a 20 m coal pillar as an example, based on the above analysis, the mining method without a coal pillar was considered to have the least negative impact on the environment. Consequently, it was initially concluded that the mining method without a coal pillar is the optimal mining method. Respiratory inorganics, carcinogens, and fossil fuels were the most important impact types, and after determining the main impact, the main impact types were identified. The face mining system was the subsystem with the greatest environmental burden. Mining, electricity, and steel were considered to have high sensitivity or importance.

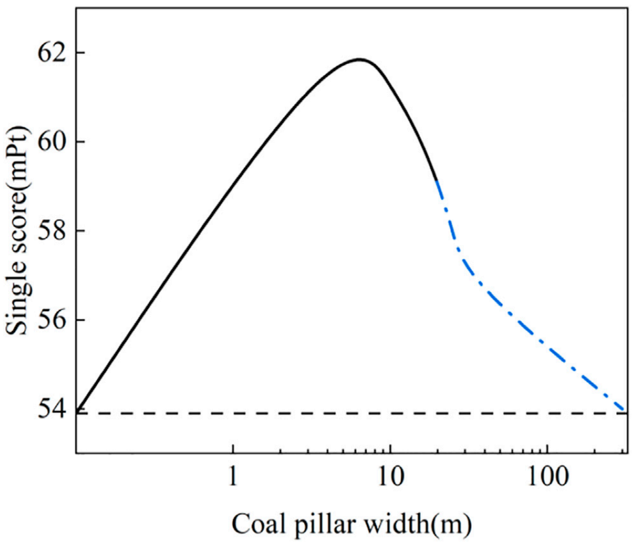

FIGURE 10 | Comparison of the single score for different mining methods.

The main objective of this study was to determine the optimal extraction method. Using the 20 m coal pillar mining method as an example, the main categories of influence and processes affecting the mining method were recognized through characterized, normalized, and contribution analyses. The influence of respiratory inorganics had a greater weighting under the non-pillar mining method (**Figure 4**), mainly because of the blasting technique used in the non-pillar mining process, which generates more organic particles. The LCA process for the other mining methods is similar to the 20 m column mining method, and there is little difference in the primary impact categories and processes. The single score value for the mining method without coal pillars, that is, 0 m pillar width, was the smallest (**Figure 10**). Combined with the results of the characterization comparison, it is clear that mining without coal pillars has the lowest level of environmental impact, and therefore, mining without coal pillars is determined to be the optimal mining method. The final single score summary comparison shows that as the width of the coal pillar increases, the degree of negative environmental impact increases and then decreases. As the width of the pillar continues to increase to a certain width, the recovery methods used because of its increased carrying capacity change and the materials and energy used are reduced accordingly, making the mining process less environmentally burdensome. It is predicted that as the width of the pillar increases to a width equal to that of the working face, the mining method will be equivalent to pillarless mining, and the level of negative environmental impact will approach that of pillarless mining (**Figure 10**).

5 CONCLUSION

This study used LCA to select the optimal mining method for different coal pillar widths. A list of input and output stream data, with 1 kg of coal mined as a functional unit, was created using the SimaPro software and Ecoinvent database, and impact analyses were evaluated based on the list analysis. The Eco-indicator 99 method was used to assign the input and output data in the LCI to 11 different environmental impact types. Characterized, normalized, and contribution analyses were conducted using a 20 m coal pillar width mining method as an example. To verify the accuracy of the data and scientific decisions, an uncertainty analysis and summary comparison of the single scores of the different mining methods were conducted to obtain the optimal mining method and the environmental impact variations between the different mining methods. The following conclusions were obtained.

(1) Through characterized and normalized analyses, the degree of impact of each process on 11 impact types was obtained. It is tentatively concluded that mining without coal pillars has the lowest negative impact on the environment, and using the mining method with a 20 m pillar width as an example, it was found that respiratory inorganics, carcinogens, and fossil fuels are the most dominant impact types. The contribution analysis shows that the face mining system has the greatest environmental burden. The main influencing processes for respiratory inorganics, carcinogens, and fossil fuels is electricity, accounting for 94.9%, 60.8%, and 84.9%, respectively. The main process influencing climate change is coal mining, which accounted for 62.9% of the total.

(2) Uncertainty and sensitivity analyses were used to verify the accuracy of the data and provide accurate scientific decisions. The uncertainty analysis provides a basis for data accuracy. The sensitivity analysis results showed that when the coal mining process unit data are reduced by 5%, the rate of change of carcinogens, respiratory organics, and respiratory inorganics are 5.03%, 4.70%, and 5.04%, respectively. For a 5% reduction in electricity consumption process data, the rates of change for respiratory inorganics, carcinogens, and acidic/eutrophication are 4.75%, 4.25%, and 4.01%, respectively. For a 5% reduction in consumption process data for steel, the rates of change for minerals, radiation, and ozone layer are 4.94%, 2.77%, and 2.30%, respectively. A 5% reduction in input data for these three main impact types resulted in greater rates of change for the main impact categories, all of which would result in greater environmental benefits.

(3) A comparative analysis of the single score values for environmental burden shows that non-pillar mining had the lowest environmental burden and was determined to be the optimal mining method. As the width of the coal pillar gradually increases, the single score value for the environmental burden increases and then decreases. As the width of the coal pillar gradually increases to approach the width of the working face, the degree of negative environmental impact gradually approaches that of non-pillar mining.

DATA AVAILABILITY STATEMENT

The original contributions presented in the study are included in the article/supplementary material, further inquiries can be directed to the corresponding author.

AUTHOR CONTRIBUTIONS

HW: conceptualization, methodology, software, data curation, validation, and writing-original draft. ZY: supervision, writing-review and editing, and funding acquisition. YZ, CQ, XL, and JW: data curation.

FUNDING

This work was supported by the National Natural Science Foundation of China (Grant Nos 51874006 and 51774009), and Anhui Provincial Natural Science Foundation (Grant No. 2008085QE226), and Key Research and Development Projects in Anhui Province (Grant No. 202004a07020045), which are gratefully acknowledged.

REFERENCES

Awuah-Offei, K., and Adekpedjou, A. (2011). Application of Life Cycle Assessment in the Mining Industry. *Int. J. Life Cycle Assess.* 16, 82–89. doi:10.1007/s11367-010-0246-6

Awuah-Offei, K., Checkel, D., and Askari-Nasab, H. (2008). Evaluation of Belt Conveyor and Truck Haulage Systems in an Open Pit Mine Using Life Cycle Assessment [J]. *Cim. Bull.* 102 (8), 1–6.

Blengini, G. A., Garbarino, E., Šolar, S., Shields, D. J., Hámor, T., Vinai, R., et al. (2012). Life Cycle Assessment Guidelines for the Sustainable Production and Recycling of Aggregates: The Sustainable Aggregates Resource Management

Project (SARMa). *J. Clean. Prod.* 27, 177–181. accessed 10.12.13. doi:10.1016/j.jclepro.2012.01.020

Burchart-Korol, D., Fugiel, A., Czaplicka-Kolarz, K., and Turek, M. (2016). Model of Environmental Life Cycle Assessment for Coal Mining Operations[J]. *Sci. Total Environ.* 562, 61–72. doi:10.1016/j.scitotenv.2016.03.202

Dubiński, J., and Turek, M. (2007). "Szanse Rozwojowe Przedsiębiorstw Górniczych Winnowacjach," in *Polski Kongres Górniczy*. Sesja 5. (Innowacyjne Górnictwo. Research Re-ports of Central Mining Institute) No. I (in Polish).

Durucan, S., Korre, A., and Munoz-Melendez, G. (2006). Mining Life Cycle Modelling: A Cradle-To-Gate Approach to Environmental Management in the Minerals Industry[J]. *Clean. Prod.* 14 (12-13), 1057–1070 (Euracoal.eu [accessed on: 15/03/2016]). doi:10.1016/j.jclepro.2004.12.021

Ecoinvent Centre (2018). Introduction to Ecoinvent Version 3. Available at: https://www.ecoinvent.org/database/introduction-to-ecoinvent-3/introduction-to-ecoinvent-version-3.html.

Farjana, S. H., Huda, N., Mahmud, M. A. P., and Lang, C. (2018). Comparative Life-Cycle Assessment of Uranium Extraction Processes. In Australia[J]. *J. Clean. Prod.* 202, 666–683. doi:10.1016/j.jclepro.2018.08.105

Fava, J., Consoli, F., and Dennison, R. (1993). *A Conceptual Framework for Life-Cycle Impact Assessment*. Pensacola: SETAC and SETAC Foundation for Environmental Education.

Ferreira, H., and Leite, M. G. P. (2015). A Life Cycle Assessment Study of Iron Ore Mining[J]. *J. Clean. Prod.* 108, 1081–1091. doi:10.1016/j.jclepro.2015.05.140

Haque, N., and Norgate, T. (2014). The Greenhouse Gas Footprint of *In-Situ* Leaching of Uranium, Gold and Copper in Australia. *J. Clean. Prod.* 84, 382–390. doi:10.1016/j.jclepro.2013.09.033

ISO 14040 (2006). *Environmental Management-Life Cycle Assessment-Principles and Frame Work*. Geneva, Switzerland: International Organization for Standardization.

Jonek-Kowalska, I., and Turek, M. (2013). Cost Rationalization of Maintaining Post-industrial Regions. *Pol. J. Environ. Stud.* 22 (3), 727–740.

Kowalska, I. J. (2014). Risk Management in the Hard Coal Mining Industry: Social and Environmental Aspects of Collieries' Liquidation. *Resour. Policy* 41, 124–134. doi:10.1016/j.resourpol.2014.05.002

Krause, E., and Krzemień, K. (2013). Methane Risk Assessment in Underground Mines by Means of a Survey by the Panel of Experts (SOPE). *J. Sustain. Min.* 13 (2), 6–13. doi:10.46873/2300-3960.1262

Krause, E., and Smoliński, A. (2013). Analysis and Assessment of Parameters Shaping Methane Hazard in Longwall Areas. *J. Sustain. Min.* 12 (1), 13–19. doi:10.7424/jsm130104

Kugiel, M. (2010). Activities of Kompania Węglowa S.A. In the Sphere of Environment Pro-tection, with Particular Emphasis on Commercial Exploitation of Methane[J]. *Górnictwoi Geologia* 5 (1), 73–87 (in Polish)

Li, Y. (2009). Environmental Impact Assessment Study of Copper Recovery from Copper Slag [D]. Dissertaiton. Beijing: China University of Mining and Technology.

Ma, F., Wang, J., and Zhang, Y. (2010). Knowledge Map of Domestic Life Cycle Theory Studies. *Inf. Sci.* 28 (3), 334–340.

Mahmud, M., Huda, N., Farjana, S., Lang, C., Mahmud, M. A. P., Huda, N., et al. (2018). Environmental Impacts of Solar-Photovoltaic and Solar-Thermal Systems with Life-Cycle Assessment. *Energies* 11, 2346. doi:10.3390/en11092346

Norgate, T., and Haque, N. (2010). Energy and Greenhouse Gas Impacts of Mining and Mineral Processing Operations. *J. Clean. Prod.* 18, 266–274. doi:10.1016/j.jclepro.2009.09.020

Pluta, I., and Dulewski, J. (2006). Mine Waters in the Light of Old and Current Terminology and Their Classification Obeying in Coal Mining [J]. *Min. News* 57 (1), 37–41. (in Polish)

Society of Environmental Toxicology and Chemistry (SETAC) (1993). *Guidelines for Life-Cycle Assessment: A Code of Practice*. Brussels: SETAC Europe, 11.

Spitzley, D. V., and Tolle, D. A. (2004). Evaluating Land-Use Impacts: Selection of Surface Area Metrics for Life-Cycle Assessment of Mining[J]. *Ind. Ecol.* 8 (1-2), 11–21. doi:10.1162/1088198041269481

Staš, D., Lenort, R., Wicher, P., and Holman, D. (2015). Green Transport Balanced Scorecard Model with Analytic Network Process Support[J]. *Sustainability* 7, 15243–15261. doi:10.3390/su71115243

Suppen, N., Carranza, M., Huerta, M., and Hernandez, M. (2006). Environmental Management and Life Cycle Approaches in the Mexican Mining Industry[J]. *Clean. Prod.* 14 (12-13), 1101–1115. doi:10.1016/j.jclepro.2004.12.020

Tao, M., Cheng, W., Nie, K., Zhang, X., and Cao, W. (2021). Life Cycle Assessment of Underground Coal Mining in China [J]. *Sci. Total Environ.* 804. doi:10.1016/j.scitotenv.2021.150231

Turek, M. (2010). *Fundamentals of Underground Coal Mining*. first ed. Katowice: Publishing House of the Central Mining Institute. (in Polish).

Yingshun, L. (2009). *Environmental Impact Assessment Study of Copper Recovery From Copper Slag [D]*. China University of Mining and Technology (Beijing).

Zhu, X. (2004). Study on Life Cycle Methodology. *Stud. Sci. Sci.* 22, 566–571.

Zhen, Z., He, M., Wang, Q., Wang, E, Zhang, J, and Sun, Y (2019). An Innovative Non-Pillar Mining Method Formation Automatically and its Application in Ningtiaota Coal Mine [J]. *J. China Univ. Min. Technol.* 48(1): 46–53.

Conflict of Interest: The authors declare that the research was conducted in the absence of any commercial or financial relationships that could be construed as a potential conflict of interest.

frontiers | Frontiers in Earth Science

BRIEF RESEARCH REPORT
published: 23 June 2022
doi: 10.3389/feart.2022.908032

BIM Digital Shadow Technology and Risk Assessment Method of the Deep Foundation Pit's Behavior for Zibo Light Rail

Minghui Yuan[1], *Changfeng Yuan*[1]*, *Fu Chen*[1], *Liang Li*[1], *Yong Hong*[1], *Guangming Yu*[1] *and Jun Lei*[2]

[1]School of Civil Engineering, Qingdao University of Technology, Qingdao, China, [2]China Construction Fifth Engineering Bureau Co., Changsha, China

With the shortage of land resources, there has been a trend toward increasingly deep foundation pit engineering in urban areas. It is extremely important to reflect on the behavior and safety of deep foundation pits and conduct risk assessments in time. A nonhomologous and multi-indicator deep foundation pit risk assessment model was studied for nine types of nonhomologous on-site data monitored in the deep foundation pit. Based on the BIM (Building Information Modeling) technology, a family of monitored points was created that reflects the information on site from a deep foundation pit. The data visualization module was redeveloped by using Visual Studio 2019 to map the on-site data monitored to the components in the BIM model, which can visualize the data monitored in the BIM model of deep foundation pits. On this basis, the assessment of the safety level of deep foundation pits was realized in combination with a risk assessment model. Through the instance of the deep foundation pit of Zibo light rail, the analysis shows that the new visualization and risk assessment method can help construction workers locate dangerous units and formulate corresponding prevention and control measures better and faster.

Keywords: bim, deep foundation pit, digital shadow, visualization, risk assessment

Edited by:
Zhiqiang Yin,
Anhui University of Science and Technology, China

Reviewed by:
Zhigang Tao,
China University of Mining and Technology, China
Dan Meng,
Qingdao Agricultural University, China
Jun Hu,
Hainan University, China
Xiaolei Wang,
Hebei University of Engineering, China

****Correspondence:***
Changfeng Yuan
yuanchangfeng@qut.edu.cn

Specialty section:
This article was submitted to Geohazards and Georisks, a section of the journal Frontiers in Earth Science

Received: *30 March 2022*
Accepted: *11 May 2022*
Published: *23 June 2022*

Citation:
Yuan M, Yuan C, Chen F, Li L, Hong Y, Yu G and Lei J (2022) BIM Digital Shadow Technology and Risk Assessment Method of the Deep Foundation Pit's Behavior for Zibo Light Rail.
Front. Earth Sci. 10:908032.
doi: 10.3389/feart.2022.908032

1 INTRODUCTION

By the end of 2019, China's urbanization rate had reached 60.6%. With a large number of people moving into cities, a large amount of infrastructure development is required. However, land resources are becoming increasingly scarce in cities. As a result, there are more and more deep foundation pits in the construction of infrastructure projects. Urban deep foundation pit engineering has two main characteristics: the first is that urban deep foundation pits are often adjacent to complex surrounding environments such as rail transit infrastructure, old buildings, and integrated underground pipelines; the second is the complex geological conditions, such as water-rich soft soil, soil-gravel composite stratum, fault zones, and intrusive rocks. The behavior and impact of urban deep foundation pit engineering on the surrounding environment have been studied by many scholars. Research has been carried out through theoretical calculations, on-site monitored, and numerical simulation (Yuan et al., 2019) on the stability of deep foundation pits during excavation and their impact on the surrounding environment; the results of these studies have guided the safe construction of urban deep foundation pits. The research approach of this study is to map the information of deep foundation pits to BIM through secondary development based on the BIM technology and to further visualize the behavior of deep foundation pits and assess the risk level of foundation pit engineering.

Building information modeling (BIM), is described as a shared digital representation of any built object's physical and functional properties that serves as a trustworthy basis for decisions (ISO, 2016), has been transforming the architecture, engineering, and construction (AEC) business in many nations (Azhar, 2011). A construction project, in general, entails a number of stages, ranging from planning and design to building and upkeep. Because of its 3D modeling capability, data utilization and modification, and visualization capabilities, BIM may be used as a data management tool at any stage of the process. Practitioners in the AEC business began to use BIM in projects in the mid-2000s. Various studies on technical BIM challenges have been undertaken over the previous decade to increase BIM adoption. BIM research has become more diverse over the previous decade, with more developing technologies being integrated into BIM. For example, BIM can help with 3D printing implementation (Arayici et al., 2012) and has been used in the 3D printing of small-scale models and large-scale buildings (Wu et al., 2016). By combining 3D laser scanning with BIM, (Mahdjoubi et al., 2013) created a model to aid in the delivery of real estate services. (Wang et al., 2013) established a conceptual framework that combines BIM and augmented reality (AR) to allow for real time visualization of the physical context of any construction activity or task. (Tang et al., 2010) investigated strategies for automating the process of recreating as-built building information models from laser-scanned point clouds. (Cerovsek, 2011) reviewed the data exchange standards and features of over 150 AEC/O (Architecture, Engineering, Construction, and Operations) tools and digital models, and offered a framework for improving both BIM tools and schemata. However, limited efforts have been made to research the application of BIM visualization technology to practical engineering.

At present, the application of the BIM technology in the architectural field is mainly in the design stage to conduct top-down design, for detecting pipeline collisions, for engineering calculations, and for visual construction management at the construction stage. These functions are mainly realized by the built-in functions of the BIM software and users only need to learn how to use the software. (Oscar and Zhang, 2021) used the BIM model to analyze architectural design information; (Qi et al., 2021) conducted BIM modeling and UAV aerial oblique photography data collection for Huali Expressway; Furthermore, researchers have connected BIM and the Internet of Things (IoT) so that BIM can display on-site conditions (Lu et al., 2020; Zhao and Liu, 2021), perform a series of functions such as seismic assessment (Chen et al., 2020), and the mutual calling between finite elements (Wen et al., 2020) based on the BIM technology. The aforementioned applications have greatly promoted the digital and informatization development of intelligent engineering activities. With the further promotion and application of BIM, its existing conventional functions cannot serve current engineering requirements. The Construction Standard Regulation [2020] No. 8 issued by the Ministry of Housing and Urban-Rural Development in 2020 pointed out that the integrated application of the BIM technology should be accelerated during the total life cycle of new buildings. The development trend of BIM is to model the behavior of the buildings and perform safety assessments throughout their life cycle (Su et al., 2021). It is necessary to visualize monitored information obtained through sensors in the digital shadow created from a BIM. Meanwhile, it is necessary to further study the safety risk assessment methods and visualize the research results during the total life of the BIM digital shadow. It requires users to gain better capabilities to further develop the software platform. As an emerging technology, the BIM digital shadow technology can collect various data from a physical model in the real world, and map the information to an accurate digital model in the digital space to update the data with the physical model. It can not only achieve modeling but also a simulation of the life cycle. The application of BIM digital shadow for the assessment and visualization of the project's behavior has rarely been reported.

This study aims to use the BIM digital shadow technology to map the on-site monitoring information to the BIM model of the deep foundation pit in real time, and to make the behavior assessment of the deep foundation pit through the relevant risk assessment model. In this study, an on-site family of monitored points of the deep foundation pits is created in a BIM model, and the Revit software is used to re-develop the data visualization module of the on-site monitored data; a risk assessment model considering conditional information entropy was established and embedded in the visualization development module; this module allows for the visualization of the deep foundation pit's abnormal units and enables the comprehensive assessment of the risk grade. It has broken through the current application of calculation and collision in BIM and realized the visualization techniques of the deep foundation pits' behavior, which can better provide support for the safety assessment throughout the construction's life cycle.

2 PROJECT OVERVIEW

Zibo rail transit station can seamlessly transfer to a high-speed rail station. The embedded section of the station is about 740 m long and 23 m wide. The standard section excavation depth is 16.05–18.2 m and the end well excavation depth is 19.5–20.8 m. The deep foundation pit of the station has been constructed through the open-cut method. The north side of the site is the construction site of the high-speed railway station, and the rest is farmland. Concurrent construction projects around the site include a drop-off platform, a ramped bridge, a square east-west road, a station-overlying steel structure, and a bus station. The safety level of the deep foundation pit is level Ⅰ.

According to the design documents, the standard section of the main deep foundation pit enclosure structure in the field adopts the form of φ800@1000 bored pile plus an internal support enclosure. The station is equipped with three supports along the longitudinal direction and one support replacement is added to the end well. The first support adopts an 800 mm × 800 mm concrete support with a support spacing of about 5.0–9.0 m. The other supports are steel pipe supports with a diameter of 609 mm and a wall with a thickness of 16 mm and a spacing of about 3 m. The foundation pit

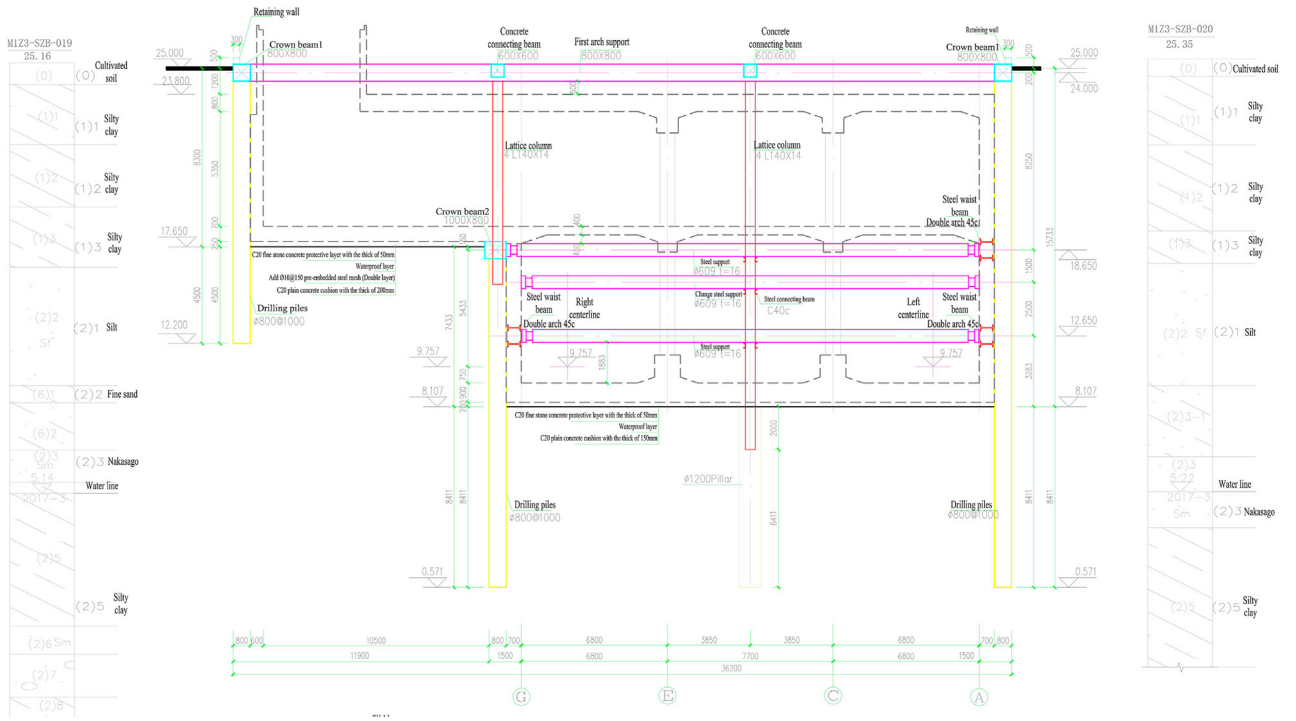

FIGURE 1 | The borehole histogram and support design of the standard section.

at the entrance of the underground first floor adopts the structure of a pile plus anchor cable with a horizontal spacing of about 2 m. A double-row pile with a φ800@1000 enclosure structure is adopted near the pile foundation of the high-speed railway station building. The borehole histogram and support design of the standard section are shown in **Figure 1**.

The lithological composition of the soil layer in the field is complex and the soil layer changes significantly, being cultivated soil, silty clay, silt, fine sand, medium sand, and round gravel soil (Li et al., 2022). According to the stratum distribution characteristics of the site, the permeability of the stratum in the site also varies significantly. The groundwater is slightly low confined (Zhu et al., 2022) and primarily recharged by lateral underground runoff with secondary downward surface water percolation (Wang et al., 2022). The stable groundwater table is at a depth of 19.48–20.34 m and the stable groundwater elevation is 4.93–5.66 m. Judging from the on-site excavation, no obvious groundwater was seen until the foundation pit was excavated to the bottom.

3 DIGITAL SHADOW AND VISUALIZATION TECHNOLOGY OF DEEP FOUNDATION PIT BEHAVIOR IN BIM

3.1 Creating a Family of Monitored Points in the BIM of the Deep Foundation Pit

At present, the monitoring of deep foundation pits is carried out by setting on-site monitored points (Wang et al., 2019). During the establishment of the deep foundation pit model in BIM, the monitored points and sensors cannot be displayed in the model (Tong et al., 2019). To reflect the monitored point information in the established BIM digital shadow, it is necessary to load the on-site monitored points and sensor information into BIM in the form of a family of monitored points. It is necessary to create a monitored family of points in the BIM of the deep foundation pit. According to deep foundation pit support design documents and monitored requirements, deep foundation pit monitored information generally includes data on pile deformation, the vertical and horizontal displacement of the pile top, subsidence (Wang et al., 2021), the horizontal and vertical displacement of the slope top, the axial force of the internal support, ground subsidence (Su et al., 2021), groundwater (Wu et al., 2021), and the subsidence of surrounding buildings, pipelines, and roads (Dou et al., 2021), etc. In this study, the family of monitored points was categorized as foundation pit slope top displacement, surrounding building subsidence, road and pipeline subsidence, deep soil displacement, and anchor rod (an anchor cable) axial force. All the aforementioned monitored points are collectively called monitored nails in the BIM. First, the plane coordinates and elevation of the monitored nails were set according to the geometric and spatial relationships of the components in the design drawings. Second, the monitored nails were assigned the material parameters of the different supporting components, and then the definitions were saved as a new monitored nails family. Third, the saved files of each of the families were loaded into the project file and the refined modeling was completed by changing the position of the axis net

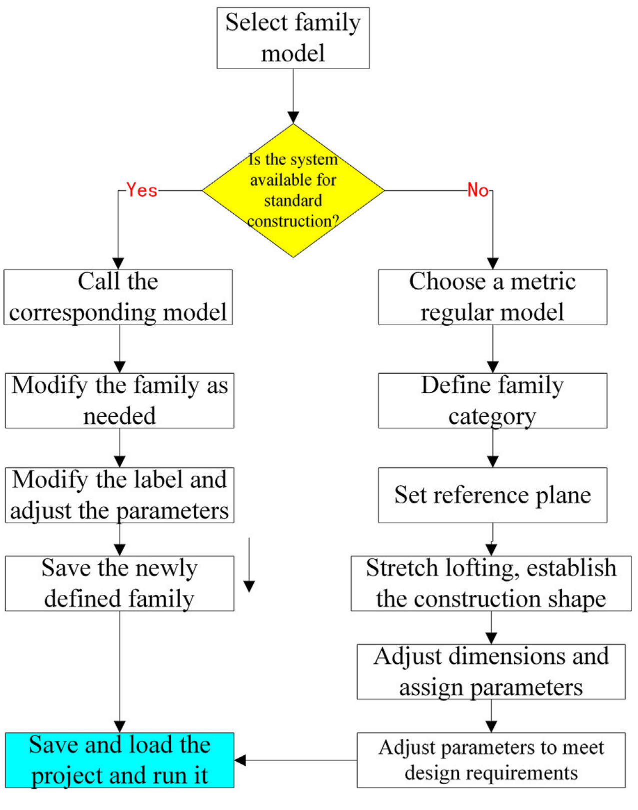

FIGURE 2 | The creation process of the Revit family file.

and the specific values of the elevation. The file of the family of monitored points in the BIM of the foundation pit was created according to the process shown in **Figure 2**. Based on the family file, the AutoCAD plan of the deep foundation pit supporting structure and the monitored point layout were imported into the Revit software to create a BIM digital shadow model of the deep foundation pit.

3.2 Visualization of the Early Warning System for the Deep Foundation Pit Based on the Secondary Development of Revit

Revit provides a packaged API interface. By using Visual Studio 2019 and Revit SDK, the corresponding programming environment was selected to create the function plug-in. The specific steps are as follows:

1. In Visual Studio 2019, the source program of the visualization plug-in was compiled for the early warning alerts of the foundation pit and then files in the *. dll format was generated.
2. The external plug-in loading tool, Addin-In Manager, was added to the Revit software by installing the Revit SDK software. Then, the external plug-in loading tool was used to load the *. dll file and generate the plug-in loading files in the *. addin format.
3. The plug-in installation package was converted to the *.exe format using the Visual Studio 2019 software and the *. dll file and *. addin file were integrated into the plug-in installation package.
4. The created plug-in was installed.
5. The plug-in was used to import the data from MS Excel into the database of the BIM three-dimensional visualization model to provide on-site data support for visualization and risk assessment. The specific implementation path and key technologies of the aforementioned steps are shown in **Figure 3**.

4 COMPREHENSIVE RISK ASSESSMENT AND RESULT VISUALIZATION OF THE DEEP FOUNDATION'S BEHAVIOR

4.1 Comprehensive Risk Assessment of the Deep Foundation Pit's Behavior

When monitoring the behavior of the deep foundation pit, the arrangement of all the monitored points is discrete (Liu et al., 2014). When only one of the multiple monitored indicators requires early warning at a certain point, further studies need to be performed to understand how to assess the risk level at the monitored point and categorize the warning level (Zheng et al., 2016). This study proposes a comprehensive assessment method considering information entropy and embeds the assessment model into the assessment module through secondary development to assess the risk of deep foundation pits and to visualize the assessment results. The effect is apparently obvious through on-site observation.

The steps to comprehensively assess the risk grade of deep foundation pit behavior are as follows:

1. For the deep foundation pit to be assessed, the monitored assessment indexes that affect the safety level of the foundation pit need to be determined to classify them.

Each assessment index is classified according to the corresponding foundation pit safety monitored specifications (GB 50911-2013, 2012) and actual conditions. The 9 indexes are shown in **Table 1**. The result of the safety classification of each index is shown in **Table 1** (*H* is the depth of the foundation pit excavation; *F* is the prestress control value).

1. Then, we calculate the conditional information entropy, attribute significance, and weight of each assessment index according to **Eqs 1**, **2**, and **Eq. 3** to obtain a normalized weight matrix considering information entropy $A_{1\times n}$.

$$I(D|C) = \sum_{i=1}^{n} \frac{|C_i|^2}{|U|^2} \sum_{j=1}^{k} \frac{|C_i \cap D_j|}{|C_i|} \left(1 - \frac{|C_i \cap D_j|}{|C_i|} \right), \tag{1}$$

$$\sigma_{CD}(C_i) = I(D|C - \{C_i\}) - I(D|C) + \frac{\left(\sum_{\alpha \in C} |\alpha(x)| - \sum_{\alpha \in C - \{C_i\}} |\alpha(x)| \right)}{\sum_{\alpha \in C} |\alpha(x)|}, \tag{2}$$

$$\boldsymbol{W}_i = \frac{\sigma_{CD}(C_i) + I(D|\{C_i\})}{\sum_{i=1}^{n} [\sigma_{CD}(C_i) + I(D|\{C_i\})]}. \tag{3}$$

2. The normalized weight matrix is $\boldsymbol{A}_{1\times n} = [\boldsymbol{W}_i]$.

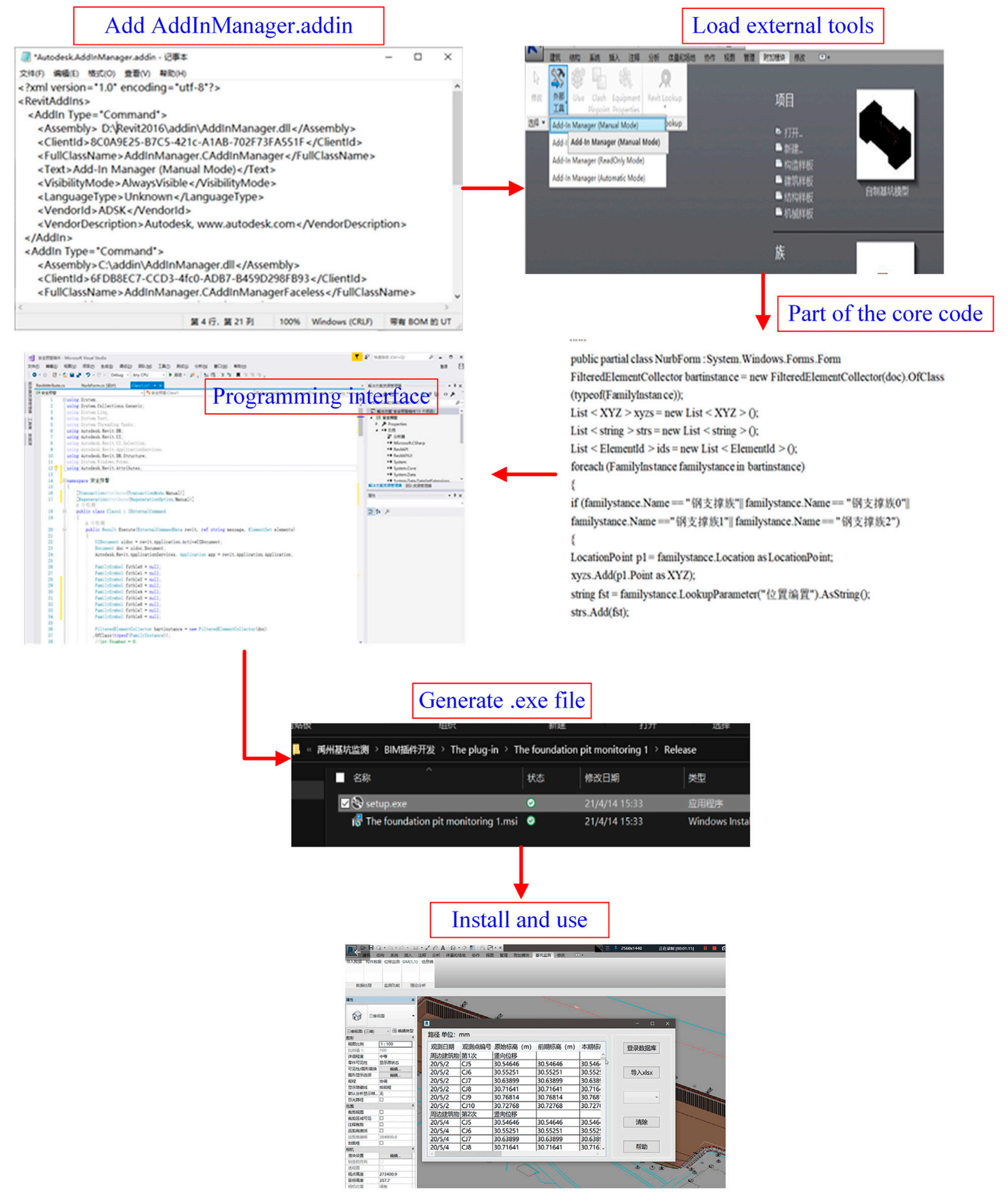

```
*Autodesk.AddInManager.addin - 记事本
<?xml version="1.0" encoding="utf-8"?>
<RevitAddIns>
  <AddIn Type="Command">
    <Assembly> D:\Revit2016\addin\AddInManager.dll</Assembly>
    <ClientId>8C0A9E25-B7C5-421c-A1AB-702F73FA551F</ClientId>
    <FullClassName>AddInManager.CAddInManager</FullClassName>
    <Text>Add-In Manager (Manual Mode)</Text>
    <VisibilityMode>AlwaysVisible</VisibilityMode>
    <LanguageType>Unknown</LanguageType>
    <VendorId>ADSK</VendorId>
    <VendorDescription>Autodesk, www.autodesk.com</VendorDescription>
  </AddIn>
  <AddIn Type="Command">
    <Assembly>C:\addin\AddInManager.dll</Assembly>
    <ClientId>6FDB8EC7-CCD3-4fc0-ADB7-B459D298FB93</ClientId>
    <FullClassName>AddInManager.CAddInManagerFaceless</FullClassName>
第 4 行，第 21 列    100%    Windows (CRLF)    带有 BOM 的 UT
```

```
……
public partial class NurbForm :System.Windows.Forms.Form
FilteredElementCollector bartinstance = new FilteredElementCollector(doc).OfClass
(typeof(FamilyInstance));
List < XYZ > xyzs = new List < XYZ > ();
List < string > strs = new List < string > ();
List < ElementId > ids = new List < ElementId > ();
foreach (FamilyInstance familystance in bartinstance)
{
if (familystance.Name == "钢支撑族"|| familystance.Name == "钢支撑族0"||
familystance.Name =="钢支撑族1"|| familystance.Name == "钢支撑族2")
{
LocationPoint p1 = familystance.Location as LocationPoint;
xyzs.Add(p1.Point as XYZ);
string fst = familystance.LookupParameter("位置编置").AsString();
strs.Add(fst);
```

禹州基坑监测 › BIM插件开发 › The plug-in › The foundation pit monitoring 1 › Release

名称	状态	修改日期	类型
☑ setup.exe	✓	21/4/14 15:33	应用程序
The foundation pit monitoring 1.msi	✓	21/4/14 15:33	Windows Insta

路径 单位：mm

观测日期	观测点编号	原始标高（m）	前期标高（m）	本期标
周边建筑物	第1次	竖向位移		
20/5/2	CJ5	30.54646	30.54646	30.546
20/5/2	CJ6	30.55251	30.55251	30.552
20/5/2	CJ7	30.63899	30.63899	30.638
20/5/2	CJ8	30.71641	30.71641	30.716
20/5/2	CJ9	30.76814	30.76814	30.768
20/5/2	CJ10	30.72768	30.72768	30.727
周边建筑物	第2次	竖向位移		
20/5/4	CJ5	30.54646	30.54646	30.546
20/5/4	CJ6	30.55251	30.55251	30.552
20/5/4	CJ7	30.63899	30.63899	30.638
20/5/4	CJ8	30.71641	30.71641	30.716

FIGURE 3 | The specific implementation path of the secondary development based on Revit.

Among them, U is a set of non-empty finite sets, called the domain of discourse; C is a conditional attribute, which is expressed as an index that affects the safety state of the foundation pit in this paper, and the corresponding factor subset C_i is the equivalence class obtained by dividing the domain of discourse U with respect to C; D is a decision-

TABLE 1 | Classification of the safety levels of each assessment index.

Assessment index	I	II	III	IV	V
Displacement of pile deformation	(0, 0.3%H)	(0.3%H, 0.4%H)	(0.4%H, 0.45%H)	(0.45%H, 0.5%H)	>0.5%H
Steel support axial force	(30%F, 50%F)	(50%F, 70%F)	(70%F, 85%F)	(85%F, 100%F)	>100%F
Concrete support axial force	(30%F, 50%F)	(50%F, 70%F)	(70%F, 85%F)	(85%F, 100%F)	>100%F
Pit bottom upheaval	(0, 0.1%H)	(0.1%H, 0.2%H)	(0.2%H, 0.25%H)	(0.25%H, 0.3%H)	>0.3%H
Surface subsidence	(0, 0.2%H)	(0.2%H, 0.3%H)	(0.3%H, 0.35%H)	(0.35%H, 0.4%H)	>0.4%H
Groundwater level	Anhydrous	Poor water	Weakly abundant water	Relatively abundant water	Abundant water
Horizontal displacement of pile top	(0, 0.1%H)	(0.1%H, 0.2%H)	(0.2%H, 0.25%H)	(0.25%H, 0.3%H)	>0.3%H
Vertical displacement of pile top	(0, 0.1%H)	(0.1%H, 0.2%H)	(0.2%H, 0.25%H)	(0.25%H, 0.3%H)	>0.3%H
Column subsidence	(0, 0.1%H)	(0.1%H, 0.2%H)	(0.2%H, 0.25%H)	(0.25%H, 0.3%H)	>0.3%H

making attribute, which is the safety state of the foundation pit in this study, and the corresponding factor subset D_j is the equivalence class obtained by dividing the domain of discourse U with respect to D; $C \cap D = \phi$; $I(D|C)$ is the conditional information entropy of the decision-making attribute D relative to the conditional attribute C; $\sigma_{CD}(C_i)$ represents the significance of the conditional attribute C_i; $\alpha(x) = U|\{\alpha\}$; W_i represents the weight of the conditional attribute C_i, reflecting the importance of C_i relative to the overall attribute in the entire assessment system; $I(D|\{C_i\})$ represents the conditional information entropy of D relative to C_i. The weight indexes calculated according to the 9 indexes are shown in **Table 2**.

Then, the normalized weight matrix can be obtained:

$$A_{1\times 9} = \left[0.1482 \quad 0.1245 \quad 0.1137 \quad 0.1075 \quad 0.1012 \quad 0.1088 \quad 0.1163 \quad 0.0887 \quad 0.0911\right].$$

3. Then, we identify whether each assessment index is a quantifiable factor and select the corresponding membership function to obtain the membership assessment matrix $R_{n\times 5}$.

The selected assessment indexes are classified based on whether they are quantitative or qualitative. For the qualitative indexes, the Karwowski membership function (Ning et al., 2020) is used for classification while for the quantitative indexes, **Eq. 4** is used. To unify the qualitative and quantitative classifications, a five-level classification is adopted, corresponding to the following: normal, basically normal, slightly abnormal, seriously abnormal, and malignantly abnormal.

$$f\left(C_{ij}\right) = \begin{cases} 0 & x_j \le 20 \\ \dfrac{x-20}{10} & 20 < x_j \le 30 \\ 1 & 30 < x_j \le 35 \\ \dfrac{40-x}{5} & 35 < x_j \le 40 \\ 0 & 40 < x_j \end{cases} . \tag{4}$$

$$\left(i = 1, 2, \cdots, m;\ j = 1, 2, 3, 4, 5\right)$$

Among them, $f(C_{ij})$ is the trapezoidal membership function of the quantitative index x_j, indicating the degree of membership of x_j to the conditional attribute C_i, and the closer $f(C_{ij})$ is to 1, the higher the degree of membership; the closer $f(C_{ij})$ is to 0, the lower the degree of membership; m is the number of selected n indexes minus the number of qualitative indexes.

Among the 9 indicators selected, only the groundwater level is not quantified according to the specifications so that qualitative methods are used to assess the membership degree of this index. Combining on-site geological conditions and on-site monitored data, the other indexes are classified according to **Eq. 4** and the 9 selected assessment indexes are finally obtained as shown in **Table 3**.

4. According to **Table 3**, the membership degree assessment matrix is obtained: $R_{9\times 5} = (r_{ij}) i = 1, 2, \cdots, 9;\ j = 1, 2, 3, 4, 5$.

$$R_{9\times 5} = \begin{bmatrix} 0.25 & 1 & 0.75 & 0 & 0 \\ 0 & 0.4 & 1 & 0.6 & 0 \\ 0 & 0.7 & 1 & 0.3 & 0 \\ 1 & 0.8 & 0 & 0 & 0 \\ 0.7 & 1 & 0.7 & 0.3 & 0.1 \\ 0.75 & 1 & 0.7 & 0.3 & 0.1 \\ 0 & 0.3 & 1 & 0.7 & 0 \\ 0.6 & 1 & 0.4 & 0 & 0 \\ 0.34 & 1 & 0.66 & 0 & 0 \end{bmatrix}.$$

From the second and third steps, the comprehensive assessment matrix of the safety level of the deep foundation pit can be obtained by $C_{1\times 5} = A_{1\times n} \times R_{n\times 5}$.

$$\begin{aligned} C_{1\times 5} &= \left[0.1482 \quad 0.1245 \quad 0.1137 \quad 0.1075 \quad 0.1012 \quad 0.1088 \quad 0.1163 \quad 0.0887 \quad 0.0911\right] \\ &\quad \times \begin{bmatrix} 0.25 & 1 & 0.75 & 0 & 0 \\ 0 & 0.4 & 1 & 0.6 & 0 \\ 0 & 0.7 & 1 & 0.3 & 0 \\ 1 & 0.8 & 0 & 0 & 0 \\ 0.7 & 1 & 0.7 & 0.3 & 0.1 \\ 0.75 & 1 & 0.7 & 0.3 & 0.1 \\ 0 & 0.3 & 1 & 0.7 & 0 \\ 0.6 & 1 & 0.4 & 0 & 0 \\ 0.34 & 1 & 0.66 & 0 & 0 \end{bmatrix}, \\ &= \left[0.3812 \quad 0.7882 \quad 0.6593 \quad 0.2205 \quad 0.0102\right]. \end{aligned}$$

5. Combining the principle of the maximum membership degree, the maximum value of the foundation pit safety grade assessment matrix $C_{1\times 5}$ obtained is 0.7882. And combined with the assessment grade interval where the maximum value is located, the safety grade of the foundation pit can finally be determined. This study selects the assessment interval as shown in **Table 4.**

It is seen in **Table 4** that the comprehensive assessment of the foundation pitfalls within the interval (0.8, 0.6], which is relatively safe.

TABLE 2 | Weight calculation.

Assessment index	Displacement of pile deformation	Steel support axial force	Concrete support axial force	Pit bottom upheaval	Surface subsidence	Water level	Horizontal displacement of pile top	Vertical displacement of pile top	Column subsidence
Conditional information entropy	0.1452	0.1171	0.1098	0.0913	0.0902	0.1091	0.0976	0.0731	0.0644
Attribute significance	0.1526	0.1326	0.1186	0.1246	0.1132	0.1095	0.1358	0.1054	0.1186
Normalized weight	0.1482	0.1245	0.1137	0.1075	0.1012	0.1088	0.1163	0.0887	0.0911

TABLE 3 | Assessment table of membership degree of the nine selected assessment indexes.

Assessment index	Normal	Basically normal	Slightly abnormal	Seriously abnormal	Malignantly abnormal
Displacement of pile deformation	0.25	1	0.75	0	0
Steel support axial force	0	0.4	1	0.6	0
Concrete support axial force	0	0.7	1	0.3	0
Pit bottom upheaval	1	0.8	0	0	0
Surface subsidence	0.7	1	0.7	0.3	0.1
Groundwater level	0.75	1	0.7	0.3	0.1
Horizontal displacement of pile top	0	0.3	1	0.7	0
Vertical displacement of pile top	0.6	1	0.4	0	0
Column subsidence	0.34	1	0.66	0	0

TABLE 4 | Division of the deep foundation pit safety grade interval.

Safety level	Safe	Relatively safe	Early warning	Dangerous	Very dangerous
Subordinate interval	(1, 0.8)	(0.8, 0.6)	(0.6, 0.4)	(0.4, 0.2)	(0.2, 0)

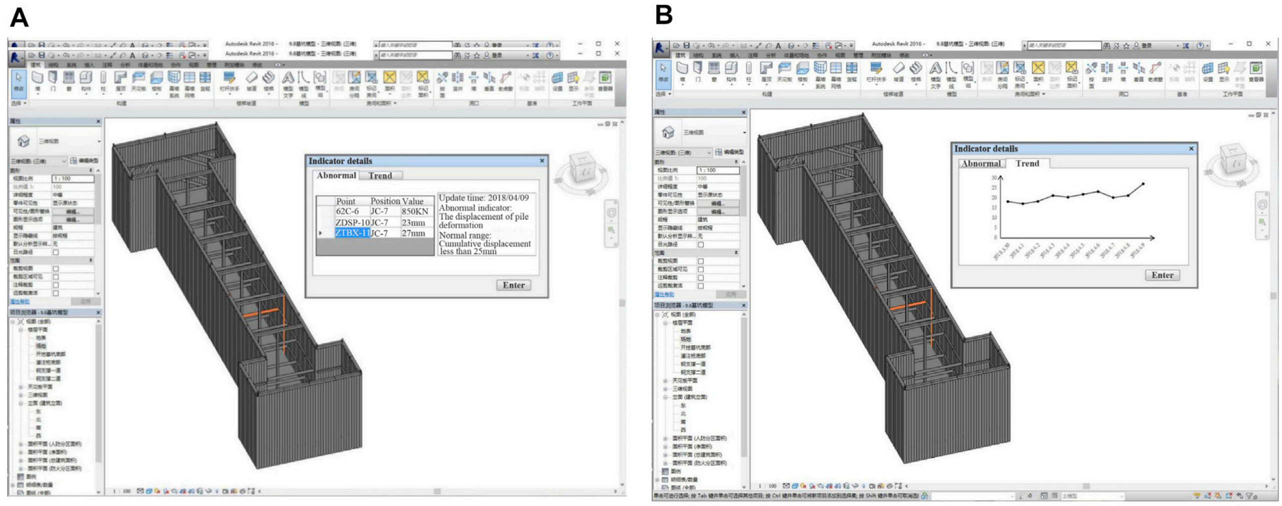

Point	Position	Value
62C-6	JC-7	850KN
ZDSP-10	JC-7	23mm
ZTBX-11	JC-7	27mm

Update time: 2018/04/09
Abnormal indicator:
The displacement of pile deformation
Normal range:
Cumulative displacement less than 25mm

Indicator details

Indicator change trend

FIGURE 4 | Details of the abnormal units and trend diagram of the abnormal units. **(A)** Indicator details, **(B)** Indicator change trend.

4.2 Visualization of the Comprehensive Risk Assessment of the Deep Foundation Pit's Behavior

A deep foundation pit model was established in Revit and the secondary development plug-in, including monitored nails, foundation pit monitored, and management modular presented in **Section 3** of this study, was loaded. The on-site monitored data was imported into BIM through the plug-in. The abnormal status of the foundation pit's supporting unit caused by the deformation of the foundation pit due to excavation was displayed on the three-dimensional model after rendering, as shown in brown in **Figure 4**.

In the safety risk assessment and early warning interface, the monitored indexes were clicked to get the details of the monitored data; this data can effectively help construction staff locate dangerous units and take timely and correct remedial measures. In the 7th supporting unit of this foundation pit, the steel support axial force, horizontal displacement of the pile top, and displacement of the pile deformation exceed the specified range values, as shown in **Figure 4**. Clicking the trend on the interface allows one to see the trend of the abnormal unit in the next few days, which can help construction staff identify and analyze possible dangerous situations and take protective measures in time. The reason for the abnormality at the location of the 7th unit of the foundation pit was analyzed on-site. It may be that the inner steel support was not installed in time during the excavation of the foundation pit, resulting in excessive stress on the inner support at the adjacent location. Meanwhile, the vertical cast-in-place pile has no horizontal internal support force to restrict its lateral deformation so that the pile has a corresponding lateral displacement. Although the 7th monitored unit is abnormal, the results of the comprehensive risk assessment of the deep foundation pit based on conditional information entropy proposed in this study show that the foundation pit is in a relatively safe state on the whole. However, construction staff should combine the visualization method and the safe early warning system rendered through the BIM technology to install the internal steel support at the abnormal unit as soon as possible and apply sufficient prestress. In addition, the rate of on-site construction should be reduced, especially the speed of earth excavation, and then restored to a normal speed after the supporting measures have been put in place.

5 CONCLUSION

In this study, a comprehensive risk assessment method considering conditional information entropy through secondary development of Revit was developed; this risk assessment method can better facilitate application on-site. The conclusions are as follows:

(1) By establishing a connection between the monitored nails and the on-site monitored points in BIM, the deep foundation pit behavior could be reproduced in real time, and the true meaning of a deep foundation pit's digital shadow based on the BIM technology was realized.

(2) Using the Revit software, an early warning management plug-in of the deep foundation pit was developed through Visual Studio 2019 and Revit SDK tools. The plug-in could achieve 3D modeling, data import, foundation pit calculation, safety level assessment, and visualization of abnormal units.

(3) The comprehensive assessment method based on conditional information entropy effectively and comprehensively assessed the risk of the monitored area of the deep foundation pit; some alerts were generated by a few individual monitored components; these alerts can effectively help the construction staff to identify and analyze possible dangerous situations and take protective measures in time.

DATA AVAILABILITY STATEMENT

The original contributions presented in the study are included in the article/Supplementary Material; further inquiries can be directed to the corresponding author.

AUTHOR CONTRIBUTIONS

CY was responsible for the original concept. All authors then contributed to the development of the concept as is presented in this manuscript. FC and LL developed software and ran simulations. MY wrote the first draft of the manuscript. CY wrote sections of the manuscript. YH, GY, and JL contributed to the figures. All authors contributed to manuscript revision and have approved the submitted version.

FUNDING

This study was supported by the Natural Science Foundation of Shandong Province (ZR2017MEE017), Key R&D Project of Shandong Province (Public Welfare Projects) (2018GSF120005), and National Natural Science Foundation of China (51174124).

ACKNOWLEDGMENTS

The authors would like to acknowledge the funding for support. Finally, they would also like to thank the associate editor of this special edition and the reviewers who provided constructive feedback that has, without doubt, improved this manuscript.

REFERENCES

Arayici, Y., Egbu, C., and Coates, P. (2012). Building Information Modelling (BIM) Implementation and Remote Construction Projects: Issues, Challenges, and Critiques. *J. Inf. Technol. Constr.* 17, 75–92.

Azhar, S. (2011). Building Information Modeling (BIM): Trends, Benefits, Risks, and Challenges for the AEC Industry. *Leadersh. Manage. Eng.* 11 (3), 241–252. doi:10.1061/(asce)lm.1943-5630.0000127

Cerovsek, T. (2011). A Review and Outlook for a 'Building Information Model' (BIM): A Multi-Standpoint Framework for Technological Development. *Adv. Eng. Inf.* 25 (2), 224–244. doi:10.1016/j.aei.2010.06.003

Chen, P., Shi, J., and Jiang, L. (2020). Research on Evaluation Method of Building Seismic Performance Based on BIM and Ontology. *China Civ. Eng. J.* 53 (09), 52–59+67. doi:10.15951/j.tmgcxb.2020.09.006

Dou, Z., Tang, S., Zhang, X., Liu, R., Zhuang, C., Wang, J., et al. (2021). Influence of Shear Displacement on Fluid Flow and Solute Transport in a 3D Rough Fracture. *Lithosphere* 2021, 1569736. doi:10.2113/2021/1569736

GB 50911-2013 (2012). *Code for Monitoring Measurement of Urban Rail Transit Engineering (GB 50911-2013)*. Beijing: China Architecture Publishing & Media Co.,Ltd.

ISO (2016). *ISO 29481-1: 2016 Building Information Models - Information Delivery Manual - Part 1: Methodology and Format*. Geneva, Switzerland: International Organization for Standardization.

Li, X. S., Li, Q. H., Hu, Y. J., Chen, Q. S., Peng, J., Xie, Y., et al. (2022). Study on Three-Dimensional Dynamic Stability of Open-Pit High Slope under Blasting Vibration. *Lithosphere* 2022. Article ID 6426550, 17 pages. doi:10.2113/2022/6426550

Liu, J., Ou, X., Zhang, X., Liang, Q., Yang, J., and Liu, X. (2014). Study on Effects of Group Foundation Pits Excavation on Heaving/Settlement of Adjacent Metro Tunnel in Operation. *Mod. Tunn. Technol.* 51 (4), 81–87. doi:10.13807/j.cnki.mtt.2014.04.012

Lu, Y., Zhuo, Y., Si, J., and Zhang, J. (2020). Research on BIM Construction Application of Gaoligongshan Tunnel on Dali-Ruili Railway. *Tunn. Constr.* 40 (10), 1516–1524. doi:10.3973/j.issn.2096-4498.2020.10.016

Mahdjoubi, L., Moobela, C., and Laing, R. (2013). Providing Real-Estate Services through the Integration of 3D Laser Scanning and Building Information Modelling. *Comput. Industry* 64 (9), 1272–1281. doi:10.1016/j.compind.2013.09.003

Ning, X., Li, J., Wang, L., Yang, B., and Wang, X. (2020). Research on Calculation Method of Finite Element Model Transformation Based on BIM Design. *Highway* 65 (09), 107–113.

Oscar, W. C., and Zhang, J. (2021). Logic Representation and Reasoning for Automated BIM Analysis to Support Automation in Offsite Construction. *Automation Constr.* 129, 103756. doi:10.1016/j.autcon.2021.103756

Qi, Z., Xu, Y., Wang, Q., and Huang, G. (2021). Application of Monitored Platform Based on BIM and Oblique Photography Technology in Huali Expressway. *Highway* 66 (06), 284–287.

Su, Y.-q., Gong, F.-q., Luo, S., and Liu, Z.-x. (2021). Experimental Study on Energy Storage and Dissipation Characteristics of Granite under Two-Dimensional Compression with Constant Confining Pressure. *J. Cent. South Univ.* 28 (3), 848–865. doi:10.1007/s11771-021-4649-2

Tang, P., Huber, D., Akinci, B., Lipman, R., and Lytle, A. (2010). Automatic Reconstruction of As-Built Building Information Models from Laser-Scanned Point Clouds: A Review of Related Techniques. *Automation Constr.* 19 (7), 829–843. doi:10.1016/j.autcon.2010.06.007

Tong, Y., Yang, M., Kong, X., Liu, S., and Li, Y. (2019). Application of BIM Technology in Deep and Large Foundation Pit and Super High-Rise Projects. *Build. Technol.* 50 (10), 1265–1268.

Wang, F., Huang, Q., Xu, D., and Tao, Y. (2019). Application and Analysis of BIM Technology in the Whole Process of Building Construction. *Eng. Sci.* 22, 32–33. doi:10.19537/j.cnki.2096-2789.2019.22.014

Wang, Q., He, M. C., Li, S. C., Jiang, Z. H., Wang, Y., Qin, Q., et al. (2021). Comparative Study of Model Tests on Automatically Formed Roadway and Gob-Side Entry Driving in Deep Coal Mines. *Int. J. Min. Sci. Technol.* 31 (04), 591–601. doi:10.1016/j.ijmst.2021.04.004

Wang, X., Love, P. E. D., Kim, M. J., Park, C.-S., Sing, C.-P., and Hou, L. (2013). A Conceptual Framework for Integrating Building Information Modeling with Augmented Reality. *Automation Constr.* 34, 37–44. doi:10.1016/j.autcon.2012.10.012

Wang, Y., Yang, H. N., Han, J. Q., and Zhu, C. (2022). Effect of Rock Bridge Length on Fracture and Damage Modelling in Granite Containing Hole and Fissures under Cyclic Uniaxial Increasing-Amplitude Decreasing-Frequency (CUIADF) Loads. *Int. J. Fatigue* 158, 106741. doi:10.1016/j.ijfatigue.2022.106741

Wen, Y., Chen, J., and Yang, Y. (2020). Application Research on Lean Project Management of Cross-Bao-Mao Expressway Bridge Based on BIM. *Highway* 65 (10), 245–252.

Wu, P., Wang, J., and Wang, X. (2016). A Critical Review of the Use of 3-D Printing in the Construction Industry. *Automation Constr.* 68, 21–31. doi:10.1016/j.autcon.2016.04.005

Wu, Z.-j., Wang, Z.-y., Fan, L.-f., Weng, L., and Liu, Q.-s. (2021). Micro-failure Process and Failure Mechanism of Brittle Rock under Uniaxial Compression Using Continuous Real-Time Wave Velocity Measurement. *J. Cent. South Univ.* 28 (2), 556–571. doi:10.1007/s11771-021-4621-1

Yuan, C., Yu, H., Yuan, Z., and Wang, Y. (2019). Numerical Simulation of Impact Caused by Construction of High-Rise Building upon Adjacent Tunnels. *Geotech. Geol. Eng.* 37 (4), 3171–3181. doi:10.1007/s10706-019-00834-z

Zhao, F., and Liu, G. (2021). Research and Application of Prefabricated Assembly Building Information Management Platform Based on BIM and Internet of Things. *J. Inf. Technol. Civ. Eng. Archit.* 13 (03), 101–106. [2021-07-04]. doi:10.16670/j.cnki.cn11-5823/tu.2021.03.15

Zheng, G., Zhu, H., Liu, X., and Yang, G. (2016). Control of Safety of Deep Excavations and Underground Engineering and its Impact on Surrounding Environment. *China Civ. Eng. J.* 49 (6), 53–65. doi:10.15951/j.tmgcxb.2016.06.001

Zhu, C., Karakus, M., He, M., Meng, Q., Shang, J., Wang, Y., et al. (2022). Volumetric Deformation and Damage Evolution of Tibet Interbedded Skarn under Multistage Constant-Amplitude-Cyclic Loading. *Int. J. Rock Mech. Min. Sci.* 152, 105066. doi:10.1016/j.ijrmms.2022.105066

Conflict of Interest: Author JL is employed by China Construction Fifth Engineering Division Corp.

The remaining authors declare that the research was conducted in the absence of any commercial or financial relationships that could be construed as a potential conflict of interest.

frontiers | Frontiers in Earth Science

TYPE Original Research
PUBLISHED 04 August 2022
DOI 10.3389/feart.2022.936029

EDITED BY
Zhiqiang Yin,
Anhui University of Science and Technology, China

REVIEWED BY
Yuan Benqing,
CCTEG Chongqing Research Institute, China
Chun Wang,
Henan Polytechnic University, China
Chao Yuan,
Hunan University of Science and Technology, China
Lei Fan,
Hunan University of Science and Engineering, China

*CORRESPONDENCE
Jun Li,
ustblijun@126.com

SPECIALTY SECTION
This article was submitted to Geohazards and Georisks, a section of the journal Frontiers in Earth Science

RECEIVED 04 May 2022
ACCEPTED 30 June 2022
PUBLISHED 04 August 2022

CITATION
Li J, Lian X, Li C, Wu Z and Wang J (2022), Failure mechanism and support system of roofs in advance areas affected by mining under the condition of soft rock stratum.
Front. Earth Sci. 10:936029.
doi: 10.3389/feart.2022.936029

Failure mechanism and support system of roofs in advance areas affected by mining under the condition of soft rock stratum

Jun Li[1]*, Xiaoyong Lian[1], Chen Li[2], Zheng Wu[1] and Jun Wang[1]

[1]School of Energy and Mining Engineering, China University of Mining and Technology (Beijing), Beijing, China, [2]CCTEG Wuhan Engineering Company, Wuhan, China

The advance area affected by mining (AAAM) of the Lijiahao coal mine is influenced by the superposition of the side and advance abutment pressure, and the roadway roof is considerably damaged. General support technology and equipment cannot economically and effectively maintain the stability of the roadway roof of AAAM. Through field detection, theoretical analysis, and numerical simulation, this study analyzes the structure of the surrounding rock, the evolution characteristics of the regional stress field, the distribution of the surrounding rock plastic zone, and the influencing factors of the plastic zone in the AAAM of the Lijiahao mine. The results show the following: 1) the direct roof and floor of the roadway comprise coal, siltstone, and sandy mudstone, which has low strength and can be easily broken. 2) The maximum and minimum principal stresses in the AAAM reach 2.3 and 1.5 times of *in situ* stress, respectively, and the ratio of the two stresses reaches 2–8, which causes the shape of the plastic zone of the surrounding rock to turn into a butterfly shape. 3) The principal stress direction of AAAM deflects at a large angle, which causes the deepest failure direction of the surrounding rock to rotate to the roof and floor of the roadway. Accordingly, a self-moving foldable support system is proposed to support the AAAM of the Lijiahao coal mine. The system will not support the roof repeatedly and is suitable for soft rock stratum. In addition, it can also adapt to the heave of roadway floor and avoid dumping. The mechanized operation of the system makes the roof support in AAAM more efficient and safer.

KEYWORDS

support system, failure mechanism, advance area affected by mining, plastic zone, soft rock stratum

1 Introduction

In underground mines, the advance areas affected by mining (AAAM) are an important channel for pedestrians, ventilation, and equipment transportation (Du et al., 2014; Kang et al., 2016a). However, due to the superposition influence of the advance and side abutment pressures of the goaf, the roadway is often deformed and seriously damaged, and secondary support is required (Qian et al., 2010; Cai, 2020; Zhang et al., 2020). Numerous scholars have studied the stress evolution and failure characteristics of roadway surrounding rock in detail and have proposed the corresponding control technology and equipment. For example, Ma et al. (2015a, 2015b) and Zhao (2014) studied the partial stress field of deep mining roadways and revealed the asymmetric deformation failure mechanism of roadways. Moreover, they proposed the use of extendable anchor bolts and flexible anchor cables to support the roadways. Based on the stress evolution law of roadways under repeated mining and the asymmetric evolution characteristics of the plastic zone in the Shendong mining area, (Wu, 2018), (Wu, 2020), and Lv et al. (2019) revealed the malignant expansion mechanism of the plastic zone of the roadway surrounding rock and presented a hierarchical stability control system of the roadway surrounding rock. Yu et al. (2021) studied the fracture mode and abutment pressure distribution of a thick and hard rock roof with a weak interlayer. (Kang and Zhong (2016b) studied the influence of working face abutment pressure on the stability of roof rock that was strengthened using a bolt through physical and numerical simulation. Li et al. (2019, 2020) studied the non-uniform failure mechanism of roadways under the influence of secondary mining and presented a roof stability control technology based on plastic zone evolution. Jia et al. (2019) studied the failure mechanism of a soft rock roadway and multi-layer combined rock roadway and determined that the plastic zone has “penetration characteristics,” i.e., the plastic zone can pass through a hard rock stratum and redistribute in the soft rock. Thus, they presented the corresponding control technology. Liu et al. (2021) studied the stress evolution and surrounding rock failure of roadways and coal pillars under the influence of repeated mining in a double-roadway layout system through UDEC (Universal Distinct Element Code) numerical simulation software. Zhu et al. (2022) analyzed the stress distribution law caused by mining under different roof strengths through FLAC 3D (Fast Lagrangian Analysis of Continua) and obtained the influence area range of the working face pressure. Yao et al. (2020) introduced the technical idea of using an active support (reinforced anchor bolt and anchor cable) to replace a passive support (hydraulic powered support, HPS) in AAAM. In terms of the support research of HPS, Xu et al. (2020) analyzed the support resistance and support mode of HPS and proposed that HPS in AAAM should be coordinated with the roadway roof and anchorage system. Zhang (2013) studied a new type of HPS in AAAM, which can not only realize the overall support of the roof up to 12 m but also support the two sides of a roadway. Kang et al. (2019) analyzed the stress distribution characteristics of a roadway in front of the working face, presented the support concepts of “low initial support, high work resistance” and “unequal support,” and realized the automatic control of HPS in AAAM.

The aforementioned analysis shows that few studies currently exist on the stress distribution and plastic zone characteristics of roadway surrounding rock in AAAM and that the research on the advance support scheme is still limited to increasing the support resistance of bolts and cables or expanding the support range of HPS, which does not solve the problem of repeatedly supporting the roof. Furthermore, the support resistance makes it difficult to collapse roofs and increases the support cost.

In the AAAM of the Lijiahao coal mine, surrounding rocks of the roadway are relatively soft and prone to deformation and damage. In this case, the HPS system is easy to dump, and the repeated support of the HPS system to the roof often causes roof fall accidents. In addition, the traditional single hydraulic prop requires a lot of labor to erect and remove support units, which is difficult and unsafe. This study analyzes the advance area affected by the secondary mining of the Lijiahao coal mine, explores failure characteristics of the roadway, reveals its failure mechanism, and puts forward the corresponding support system to provide a reference for AAAM support under similar conditions.

2 Engineering background

2.1 Geological survey of the mining area

The Lijiahao coal mine of the Shenhua Baotou energy group is located in the Dongsheng coalfield, Inner Mongolia, China. The coal seams in the mining area are shallow and geological conditions are complex. Rocks of roof and floor of the coal seam are mainly layered clastic rocks, sandy mudstone, and siltstone. Rock strength is low and its stability is poor. The ratio of the horizontal stress to vertical stress in the regional stress field is about 1.2. Recently, with the continuous increase of the mining intensity, problems of AAAM support are becoming increasingly serious, and it needs to be urgently solved.

2.2 Project profile

Currently, the Lijiahao mine is mining 31# coal seam 31,115 working face, with an average coal thickness of 6 m. The thickness of the coal seam in the entire working face is relatively uniform. The thickness of the overlying loose layer of the coal seam in the working face ranges from 10 to 30 m and that of the overlying bedrock ranges from 150 to 220 m. The strike length of the 31,115 working face under mining is 2,600 m and the dip length is 300 m. It is close to the 31,114 goaf in the north and the 31,116 working face are planned to be arranged in the south. The 31,115 working face adopt a three roadways layout mode, as shown in Figure 1. The ventilation roadway of the 31,115 working face was once an auxiliary roadway of the 31,114 working face, the roadway section is 5.2 m wide × 3.56 m high; the section of the 31,115 haulage roadway is 5.4 m wide × 3.66 m high, and that of the 31,115 auxiliary roadway is 5.2 m wide × 3.56 m high. The coal pillar between the haulage and auxiliary roadways is 20 m in width. According

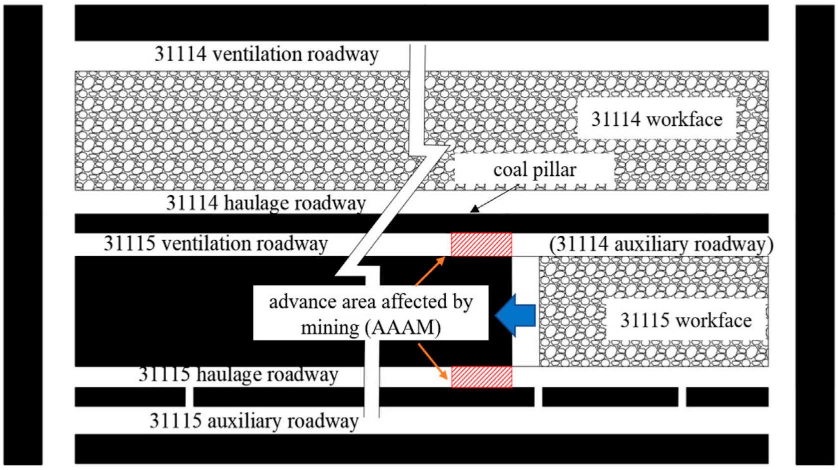

FIGURE 1
Roadway layout of the working face.

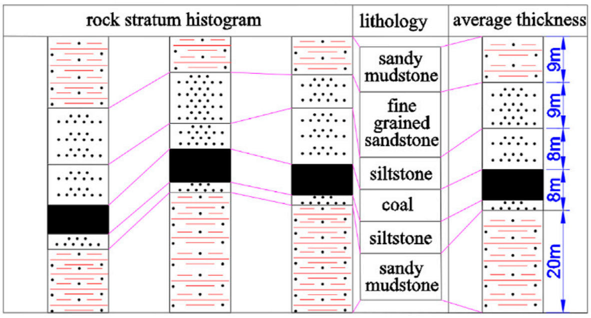

FIGURE 2
Sketch of the rock stratum structure.

to China's coal mine safety production regulations, the area within 20 m ahead of the working face is the AAAM, and the roof support equipment needs to be arranged (red area in Figure 1). Currently, the mine adopts HPS for roof support.

2.3 Coal and rock mass structure

Through borehole detection and rock sample analysis, the rock structure of the Lijiahao 31,115 working face was obtained, as shown in Figure 2. The direct roof of the coal seam is mainly siltstone and fine-grained sandstone, wherein the thickness of the siltstone is 5–11 m with an average thickness of 8 m. The thickness of fine-grained sandstone is 6–11 m, with an average thickness of 9 m. The main roof is sandy mudstone, with a thickness of 6–14 m and an average thickness of 9 m. The direct floor is sandy mudstone and siltstone. The thickness of siltstone is 1–3 m, with an average thickness of 2 m. The thickness of sandy mudstone is 12–27 m, with an average thickness of 20 m. According to the mechanical measurement results, the physical and mechanical properties of each rock are shown in Table 1.

3 Methodology

3.1 Analysis of the stress field in AAAM

After the previous working face is mined, the stress in the goaf is relieved, yielding a low-stress area. Furthermore, the abutment pressure on the side of the goaf forms a stress-increasing area. Based on the existing research, the peak stress in the stress-increasing area can reach 3–5 times the *in situ* rock stress (Guo et al., 2021a; 2021b). As it is far away from the goaf, the stress field is less disturbed by mining, i.e., it is a stress stable area. During the mining process of the working face, the surrounding rock stress will be redistributed. Under the superposition of the lateral abutment pressure of the goaf and the advance abutment stress in front of the working face (Figure 3), AAAM will form a non-uniform stress field called the deviatoric stress field.

3.2 Failure characteristics of roadway surrounding rock under the non-uniform stress field

3.2.1 Asymmetric distribution of plastic zone of surrounding rock

Kastner (1962) conducted an elastic–plastic analysis on the stress and deformation of the roadway surrounding rock under

TABLE 1 Lithology and rock physical and mechanical parameters.

Lithology	Density (kg/m^3)	Bulk modulus × 10^3 (MPa)	Shear modulus × 10^3 (MPa)	Friction angle (°)	Cohesion (MPa)	Tensile strength (MPa)
Sandy mudstone 2	2,200	2.7	1.6	29	1.2	1.06
Fine-grained sandstone	2,600	4.5	2.8	31	5.6	2.1
Siltstone 2	2,600	3.9	1.9	31	1.5	1.3
coal	1,350	2.5	1.2	28	0.5	0.6
Siltstone 1	2,600	3.9	1.9	31	1.5	1.3
Sandy mudstone 1	2,400	3.8	1.8	28	1.6	1.2

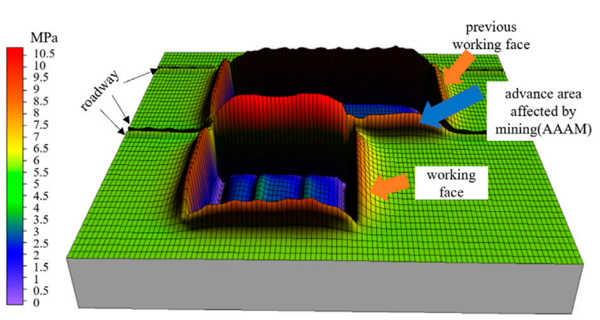

FIGURE 3
Stress distribution in AAAM.

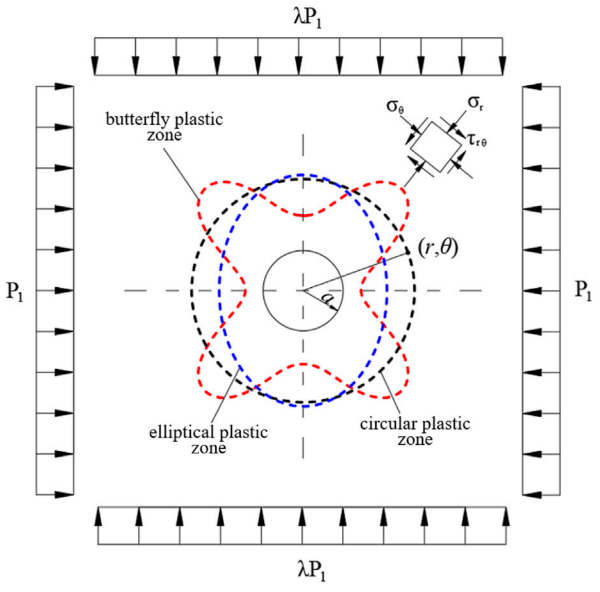

FIGURE 4
Stress model of roadway in a non-uniform stress field.

the condition of two-way uniform pressure and obtained the boundary equation of the surrounding rock plastic zone. Later, Guo et al. (2019, 2020) deduced the boundary equation of the surrounding rock plastic zone of a homogeneous circular roadway under the condition of a non-uniform stress field (Eq. (1)) (Zhao et al., 2018). Moreover, based on the hole plane strain model in the theory of elasticity (Figure 4) and taking the Mohr–Coulomb criterion, they proposed that the plastic zone of the roadway surrounding rock generally has three forms, i.e., circle, ellipse, and butterfly (Guo et al., 2019,2020) (Figure 5A). This reveals the failure mechanism of the roadway surrounding rock, such as asymmetric deformation (Zhao, 2014), roof fall (Zhao et al., 2016), and floor heave (Li et al., 2018).

$$f\left(\frac{a}{r}\right) = K_1\left(\frac{a}{r}\right)^8 + K_2\left(\frac{a}{r}\right)^6 + K_3\left(\frac{a}{r}\right)^4 + K_4\left(\frac{a}{r}\right)^2 + K_5 = 0, \quad (1)$$

where $K_1 = 9(1-\eta)^2$

$$K_2 = -12(1-\eta)^2 + 6(1-\eta^2)\cos 2\theta,$$

$$K_3 = 10(1-\eta)^2\cos^2 2\theta - 4(1-\eta)^2\sin^2\varphi\cos^2 2\theta - 2(1-\eta)^2\sin^2 2\theta - 4(1-\eta^2)\cos 2\theta + (1+\eta)^2,$$

$$K_4 = -4(1-\eta)^2\cos 4\theta + 2(1-\eta^2)\cos 2\theta - 4(1-\eta^2)\sin^2\varphi\cos 2\theta - \frac{4C(1-\eta)\sin 2\varphi\cos 2\theta}{P_3},$$

$$K_5 = (1-\eta)^2 - \sin^2\varphi\left(1+\eta+\frac{2C\cos\varphi}{P_3\sin\varphi}\right)^2.$$

Here, P$_1$ and P$_3$ are the maximum and minimum principal stresses, respectively. Additionally, a is the roadway radius, η is the ratio of the maximum principal stress to the minimum principal stress (also known as the lateral pressure coefficient), φ is the friction angle, and R and θ are the polar coordinates of any point in the coordinate system.

3.2.2 Directional rotation of the butterfly plastic zone

According to Eq. (1), when the direction of the maximum and minimum principal stresses of the regional stress field

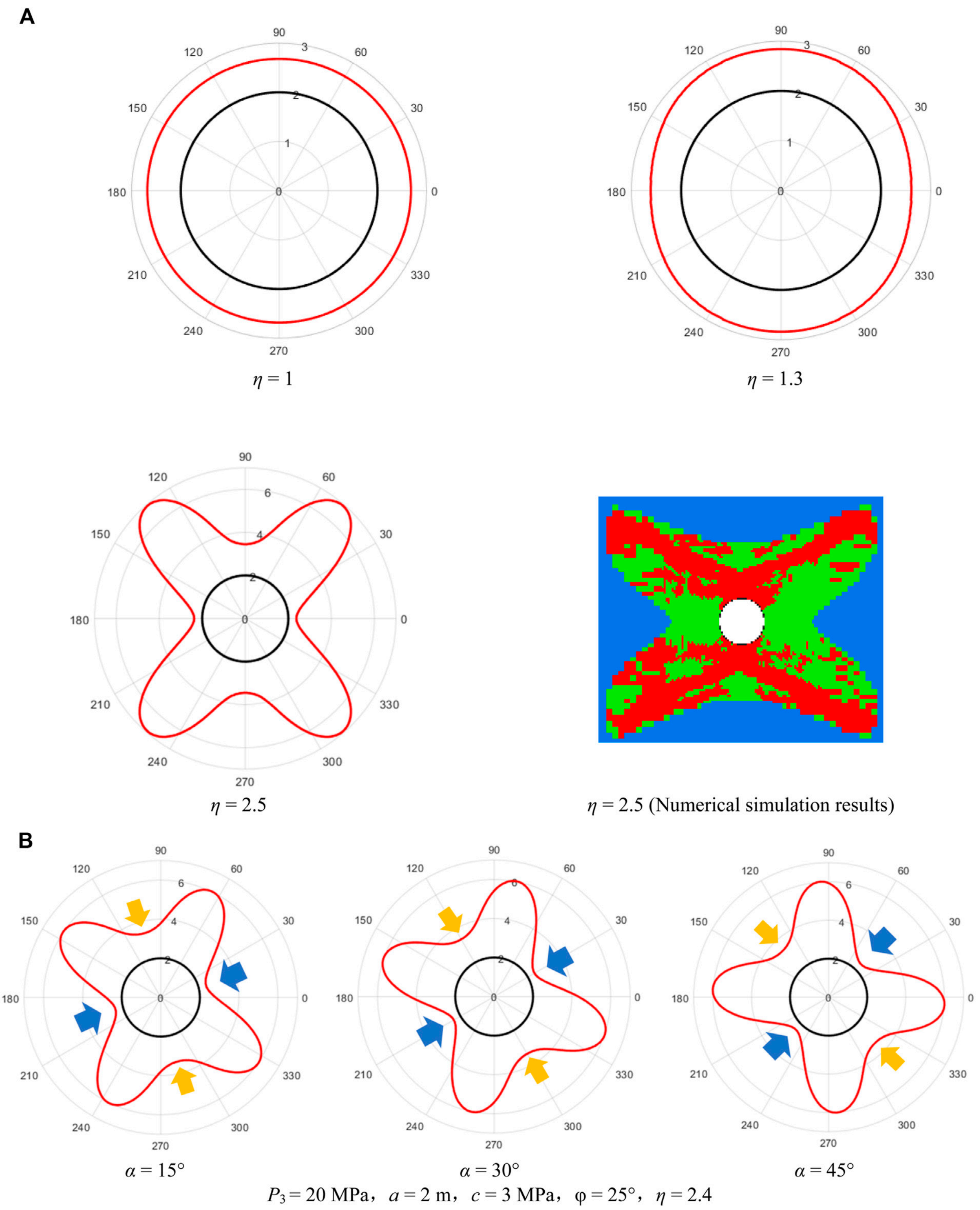

$\eta = 1$ $\eta = 1.3$

$\eta = 2.5$ $\eta = 2.5$ (Numerical simulation results)

$\alpha = 15°$ $\alpha = 30°$ $\alpha = 45°$

$P_3 = 20$ MPa， $a = 2$ m， $c = 3$ MPa， $\varphi = 25°$， $\eta = 2.4$

FIGURE 5
Plastic zone shape of the surrounding rock. **(A)** Shape of the plastic zone under different lateral pressure coefficients. **(B)** Rotation of the butterfly plastic zone.

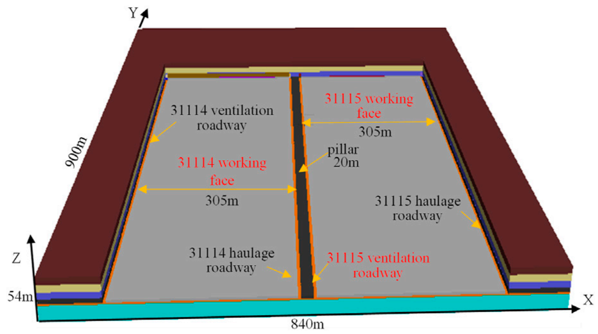

FIGURE 6
Numerical simulation model.

deflects, the plastic zone shape of the roadway surrounding rock rotates at a corresponding angle, as shown in Figure 5B (defining the horizontal direction as 0° and the counterclockwise and clockwise rotations as positive and negative, respectively).

4 Numerical simulation

4.1 Model construction

FLAC 3D can accurately simulate the distribution characteristics of stress and the plastic zone after continuous medium excavation using the dynamic motion equation. Therefore, this study uses FLAC 3D software to simulate and analyze the Lijiahao coal mine. A model X × Y × Z = 840 m × 900 m × 54 m is established, and a 4.15 MPa equivalent load is applied above the model to compensate for the vertical stress of overburden. The grid is 5 m/grid, and the AAAM is refined to 0.5 m/grid. The numerical simulation model is shown in Figure 6 rock stratum parameters are shown in Table 1. The lateral pressure coefficient is 1.2, and the model adopts the Mohr–Coulomb criterion.

4.2 Model excavation and filling

To more truly simulate the on-site engineering environment, the 31,114 working face and its two adjacent roadways are excavated and the goaf is filled with the double yield model. After balancing, the model is saved and named the basic calculation model. Then, the 31,115 working face is excavated in the basic calculation model, and the goaf is filled. After calculation, the axial stress at the ventilation roadway of 31,115 working face is extracted for analysis. Finally, according to the actual engineering excavation process, the 31,114 working face, its two adjacent working roadways, and the 31,114 auxiliary roadway (31,115 ventilation roadway) are re-excavated, and the 31,114 working face and its two adjacent roadways are filled. After the calculation, the 31,115 working face and the roadway on its right side shall be excavated and filled. After the model is balanced, the distribution of the surrounding rock plastic zone at different positions of the mining roadway is obtained by slicing the mining roadway in the model. The parameters of the double yield model in goaf are shown in Table 2.

4.3 Results

4.3.1 Stress distribution characteristics of surrounding rock in mining roadway

The maximum and minimum principal stresses at the roadway centerline under the conditions of different mining distances of the working face are shown in Figures 7A,B. The figure shows that the maximum and minimum principal stresses of the original rock stress field (before being affected by mining) are about 5.9 and 4.9 MPa, respectively. Due to the influence of mining-induced stress (superposition of abutment pressure at the side of goaf and advance abutment pressure at this working face), the maximum and minimum principal stresses reach extreme values near the working face and the open cut hole, respectively. The peak value of the maximum principal stress is about 12–13 MPa, and the peak value of the minimum principal stress is about 6–7.5 MPa. Due to the difference in the spatial distribution of the main roof structure of the coal seam, the peak stress of the roadway is different under different mining distances. With increasing distance from the open cut hole and the working face, the principal stresses exhibit a decreasing trend. The figure also shows that the stress distribution characteristics are independent of the mining distance of the working face.

When the coal seam is mined 300 m, the maximum and minimum principal stresses in AAAM are shown in Figure 7C. With the increasing distance from the working face, the maximum and minimum principal stress increase rapidly at first, and then decrease gradually. This is because the stress near the working face is concentrated due to the influence of mining, and surrounding rocks adjacent to the working face have been damaged, where the stress has been released. The maximum and minimum principal stress peaks of surrounding rocks are about 13.5 and 5.5 MPa. It can be seen from Figure 7C that the principal stress ratio gradually decreases from 8.0 to 2.0 as it is away from the working face. At 5, 10, and 20 m in front of the working face, the principal stress ratios are 3, 2.3, and 2.1, respectively.

4.3.2 Failure characteristics of the surrounding rock in the advance area of the working face

The aforementioned analysis shows that the stress variation law of the AAAM is basically the same at different mining

TABLE 2 Parameters of the double yield model in goaf.

Density (kg/m^3)	Bulk modulus × 10^3 (MPa)	Shear modulus × 10^3 (MPa)	Friction angle (°)	Dilation angle (°)
1800	5.53	4.62	20	7

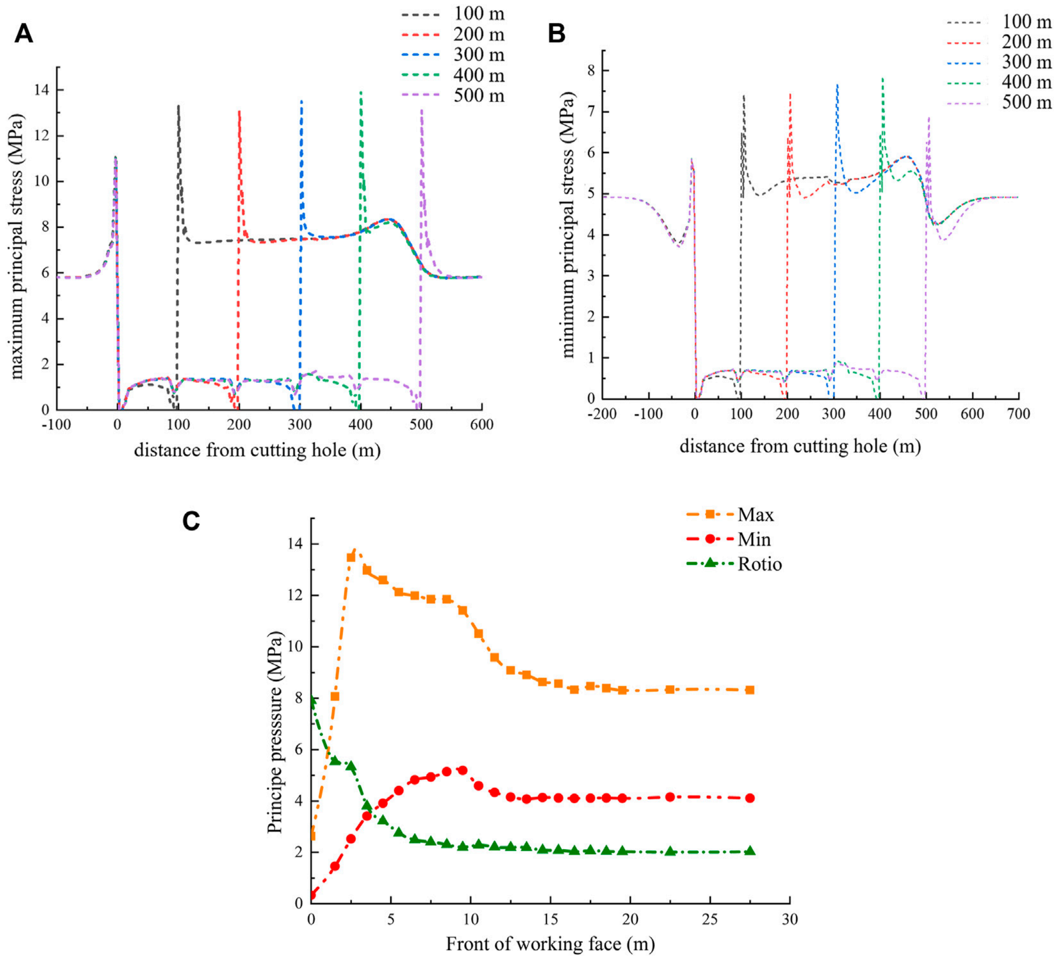

FIGURE 7
Distribution characteristics of the principal stress of surrounding rocks under different mining distances. **(A)** Maximum principal stress. **(B)** Minimum principal stress. **(C)** Maximum principal stress and minimum principal stress in AAAM.

distances of the working face. Therefore, taking the 300 m of the working face as an example, the distribution characteristics of the plastic zone of surrounding rocks in the advance area are analyzed.

Figure 8 shows the plastic zone of the roadway surrounding rock at different positions in the advance area of the working face when the mining distance of the working face is 300 m. Near 1 m in front of the working face (Figure 8A), the surrounding rock of the roadway is seriously damaged, the plastic zone exhibits asymmetric deformation characteristics, the right side of the roadway and the roof are penetrated, and the maximum failure depth on the left side of the roadway (coal pillar side) is about 4 m. About 5 m in front of the working face (Figure 8B), the overall range of the plastic zone of the roadway surrounding rock is reduced, the right side of the roadway is still damaged, and the maximum damage depth of the roadway roof is 4.5 m. Near 10 m

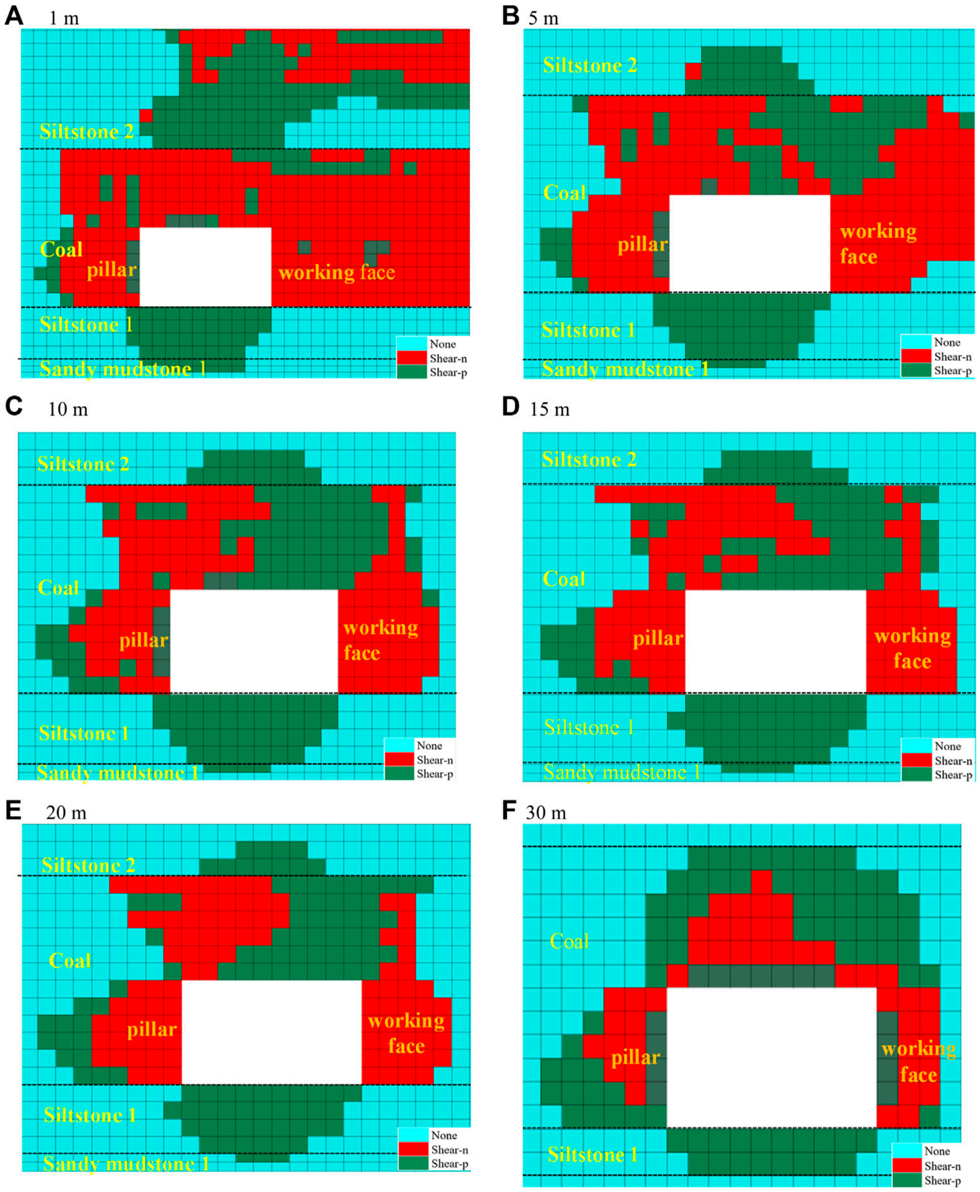

FIGURE 8
Failure characteristics of surrounding rock in the advance area.

in front of the working face (Figure 8C), the range of the plastic zone of the roadway surrounding rock decreases, but it still exhibits asymmetric characteristics. The roof of the roadway has the largest failure range, and the failure depth is about 4 m. The failure depth on the left and right sides of the roadway is 4 and 3 m, respectively. At 15 m and 20 m in front of the working face (Figures 8D,E), the failure range and failure characteristics of the roadway surrounding rock are almost identical. The maximum failure position is still the roof, and the failure depth is 4 m. The maximum failure depths on the left and right sides of the roadway are 4 and 2.5 m, respectively. Near 30 m in front of the working face (Figure 8F), the plastic zone of the surrounding rock decreases, but the distribution characteristics of the plastic zone do not change. The plastic zone of the surrounding rock still exhibits an asymmetric distribution. The largest failure part of the roadway is still the roadway roof, and the failure of the left side of the surrounding rock is more serious than that of the right side.

The aforementioned analysis shows that the plastic zone of the roadway surrounding rock near the working face is large and

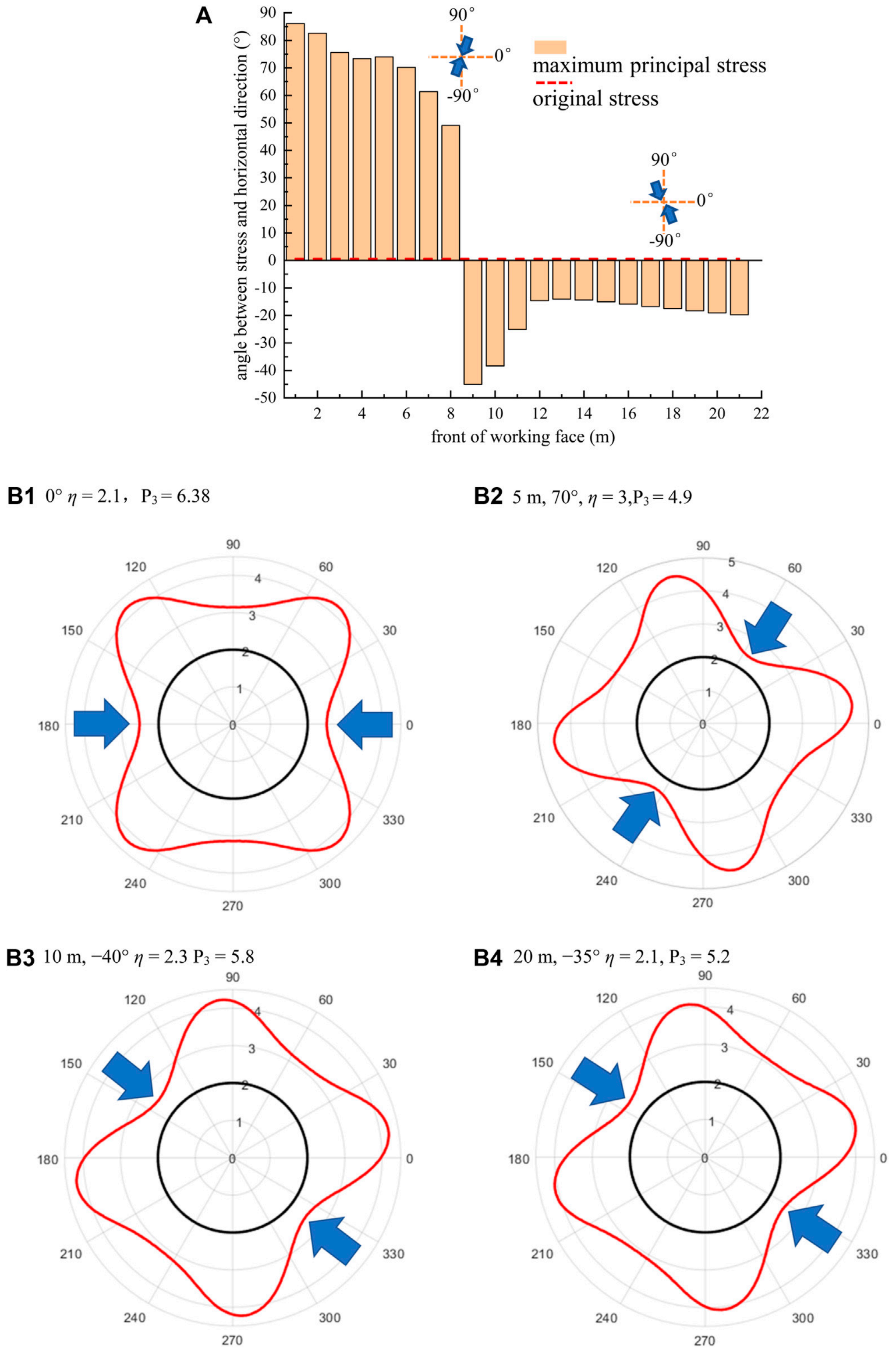

FIGURE 9
(A) Variation of the principal stress direction. **(B)** Influence of principal stress direction on the plastic zone of the surrounding rock.

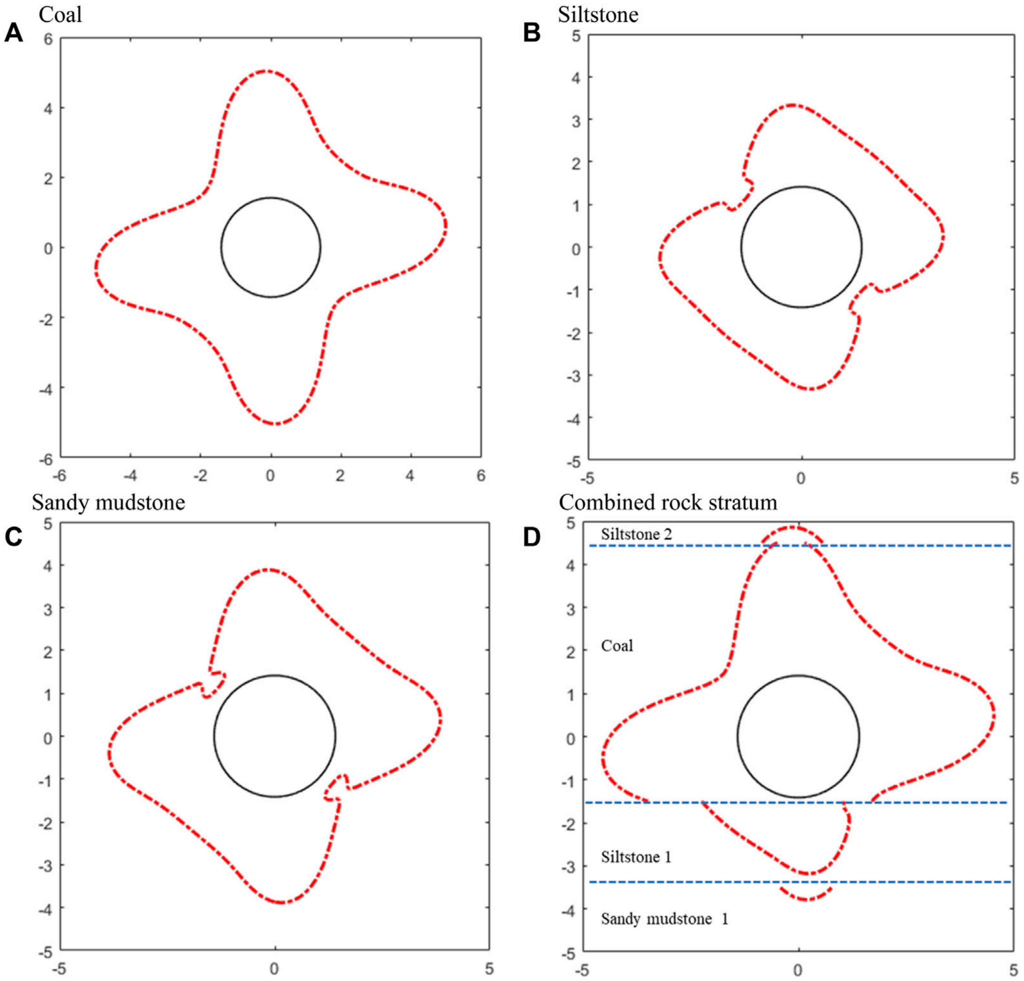

FIGURE 10
Influence of different rock structures on the plastic zone of the surrounding rock.

the damage is serious. As the distance from the working face increases, the plastic zone of the roadway surrounding rock gradually decreases, i.e., the failure zone of the roadway gradually decreases. The plastic zone of the roadway surrounding rock exhibits asymmetric distribution characteristics. Although a certain range of the plastic zone is present on the roof, floor, and two sides of the roadway, the plastic zone of the roadway roof is the largest. Furthermore, the plastic zone of the surrounding rock on the left side of the roadway is larger than that on the right side of the roadway.

4.4 Discussion

The shape and distribution characteristics of the roadway plastic zone stem from the interaction between the regional stress field vector and surrounding rock. Therefore, the influence of the size and direction of the regional stress field and the structure and strength of the surrounding rock on the plastic zone needs to be analyzed.

4.4.1 Influence of the stress rotation angle

Taking the working face distance of 300 m as an example, the direction of the maximum principal stress within 20 m in front of the working face (Figure 9A) is determined by using the numerical model. The horizontal direction is defined as 0°, and the counterclockwise and clockwise rotations are defined as positive and negative, respectively. The direction of the stress field in the AAAM considerably changes from the original stress of about 0° to about 85°, then rapidly changes to about −40° with increasing distance from the working face, and finally gradually decreases to about −20°. At about 0–8 m ahead of the working face, due to the influence of the mining of the working face, the overlying strata fracture and collapse, resulting in the change of

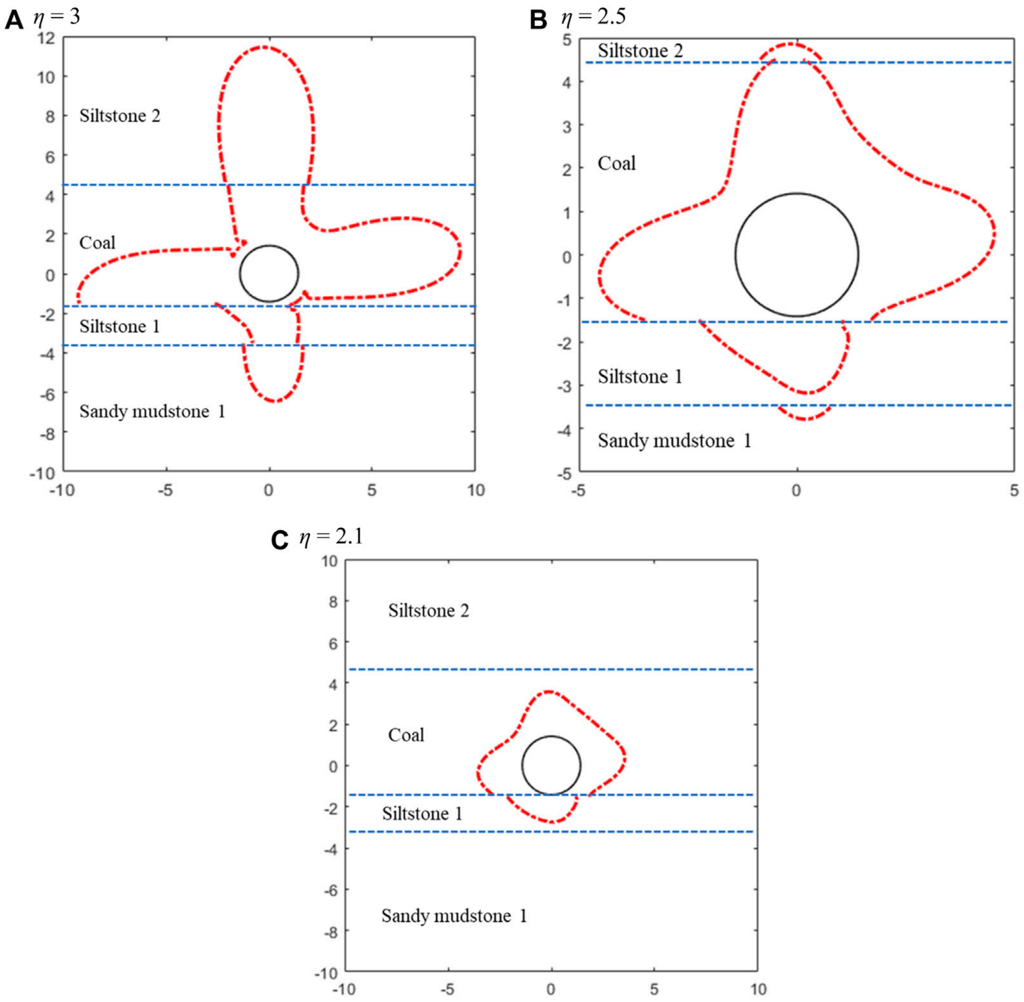

FIGURE 11
Influence of the stress ratio on the plastic zone of the surrounding rock.

the stress direction. Therefore, the direction of the maximum principal stress changes from approximately horizontal (about 0°) to approximately vertical (about 85°). Clearly, after 8 m, the surrounding rock of the roadway is less affected by the mining of this working face but is greatly affected by the mining of the previous working face. After the mining of the previous working face, the overburden breaks and collapses, and the abutment stress of the goaf is transmitted to the coal pillar side. Therefore, the stress direction changes from the positive to the negative direction and the angle between the maximum principal stress and the horizontal direction ranges between about −45° and −15°.

When the stress field is not affected by mining, the direction of the maximum principal stress is approximately horizontal while that of the minimum principal stress is approximately vertical. In this case, the shape of the plastic zone of the surrounding rock is shown in Figure 9B1 and the plastic zone in the four corner directions of the roadway is the largest. Taking the mechanical parameters of coal as an example, the boundary of the surrounding rock plastic zone at 5, 10, and 20 m in front of the working face is calculated, as shown in Figures 9B2–B4. The figures show that AAAM is affected by the successive mining of the two working faces and that the direction of the regional stress field dramatically changes, causing the deflection of the plastic zone of the surrounding rock at the corresponding angle. Within 20 m ahead of the working face, the maximum damage direction of the plastic zone changes from the four corners of the roadway to the roof, floor, and both sides of the roadway.

4.4.2 Influence of rock structure and strength

According to the borehole detection results (Figure 2), the direct roof of the coal seam is siltstone, and the direct floor is siltstone and sandy mudstone. Taking the stress environment of 10 m in front of the working face ($\eta = 2.3$, $P_3 = 5.8$, the maximum principal stress direction is −40°) as an example, the plastic zone

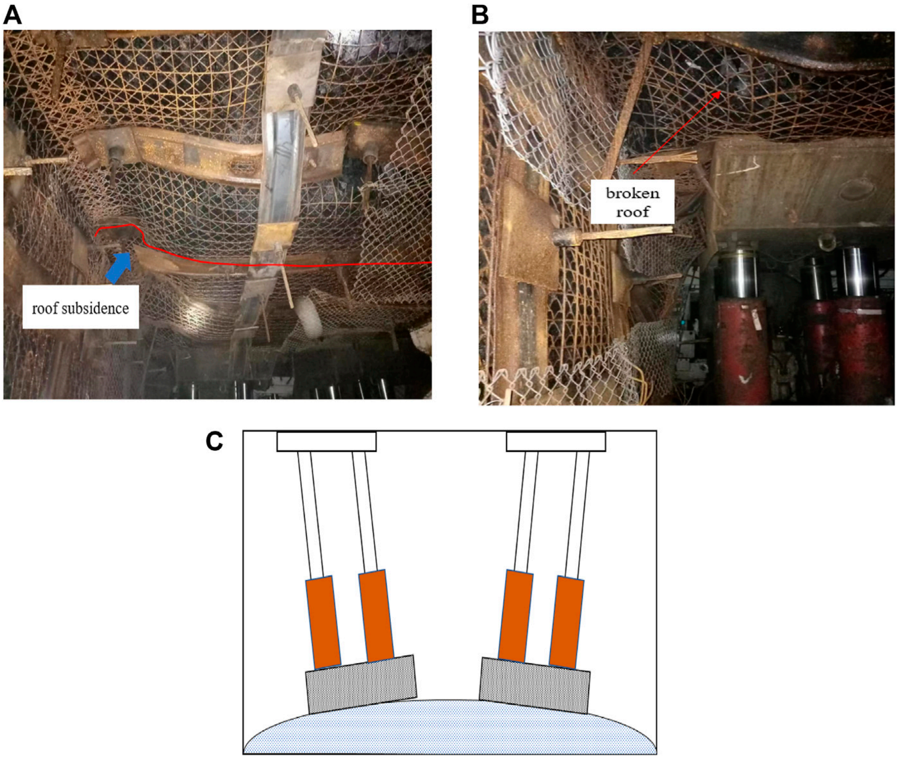

FIGURE 12
Problems faced by the Lijiahao advance support. **(A)** Roof deformation. **(B)** Broken roof. **(C)** Hydraulic support dumping.

boundary of roadway surrounding rock under different rock stratum conditions is calculated by Eq. (1) (Figure 10). The figure shows that under the same stress conditions, when the surrounding rock of the roadway is coal, the plastic zone is the largest, followed by sandy mudstone, and siltstone affords the smallest plastic zone. When the roadway surrounding rock comprises three lithological rocks, the plastic zone of the roadway surrounding rock is the superposition and combination of three plastic zone forms. The shape of the plastic zone in Figure 10D is basically consistent with that in Figure 8C. The failure range of the roadway roof is the largest, followed by that of the side of the roadway, and the roadway floor affords the smallest failure range. The aforementioned analysis shows that the range of surrounding rock plastic zone will be different due to different rock structures and the strength of each rock stratum. The direct roof and both sides of the roadway are coal, and its strength is small, so the plastic zone is large. The direct floor of the roadway is sandstone, which is stronger than coal, and the range of the plastic zone is relatively small.

4.4.3 Influence of the principal stress ratio

With increasing distance from the working face, the ratio of the maximum to the minimum principal stresses in AAAM gradually decreases from 8 to about 2.1. Similarly, taking the distance of 10 m ahead of the working face as an example (η = 2.5, P_3 = 5.8, and the maximum principal stress direction is −40°), the boundary of the surrounding rock plastic zone under different principal stress ratios is analyzed (Figure 11). Under the same conditions, when the stress ratio changes from 2.5 to 3, the range of the butterfly plastic zone sharply increases and the plastic zone of the roadway roof is the largest. When the stress ratio changes from 2.5 to 2.1, the plastic zone of the surrounding rock still exhibits a butterfly shape, but the failure range decreases.

The aforementioned analysis shows that under the same conditions, the ratio of the maximum to minimum principal stresses is positively correlated with the range of the plastic zone of the roadway surrounding rock. When the ratio of principal stress is larger, the range of surrounding rock plastic zone is larger, and the failure range of roadway roof is larger. The magnitude of the stress ratio does not affect the maximum failure direction (position) of surrounding rocks. Under the three conditions, the damage range of the roadway roof is the largest.

In summary, the AAAM of the Lijiahao coal mine is affected by the continuous mining of two working faces, and the rotation angle of the direction of the regional stress field is large, leading to the occurrence of butterfly plastic zone in the roof and floor of the roadway. In addition, the roadway roof strata are relatively soft.

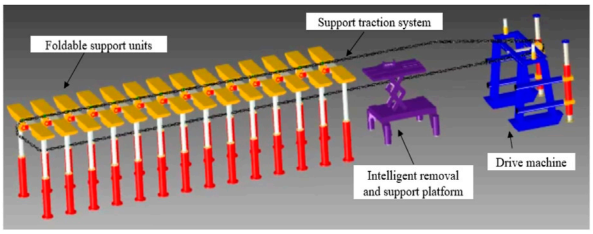

FIGURE 13
Schematic of the self-moving foldable support system.

What is more, the superposition of goaf advance pressure and side abutment pressure results in the ratio of the maximum to the minimum principal stress exceeding 2, and the plastic zone evolves into a butterfly shape. The aforementioned reasons lead to a large range of plastic zone in the roadway roof.

5 Support strategy and system

5.1 Factors considered in advance support

The roof of AAAM needs to be stable during mining, and it also needs to collapse in time after mining. Therefore, secondary supplementary support of bolt and anchor cable not only increases the cost but also not conducive to roof caving. The roof and floor in the AAAM of the Lijiahao mine are coal and sandstone, with low strength. The plastic zone of the roadway roof is large, and the roadway roof has step subsidence (Figure 12A). Thus, when an HPS system is been used, the broken coal can easily fall (Figure 12B) and cause accidents. The deformation of the roadway floor is large, and HPS may topple when a floor bulge occurs (Figure 12C). Therefore, supplementary supports and HPS in AAAM are not suitable for the Lijiahao coal mine.

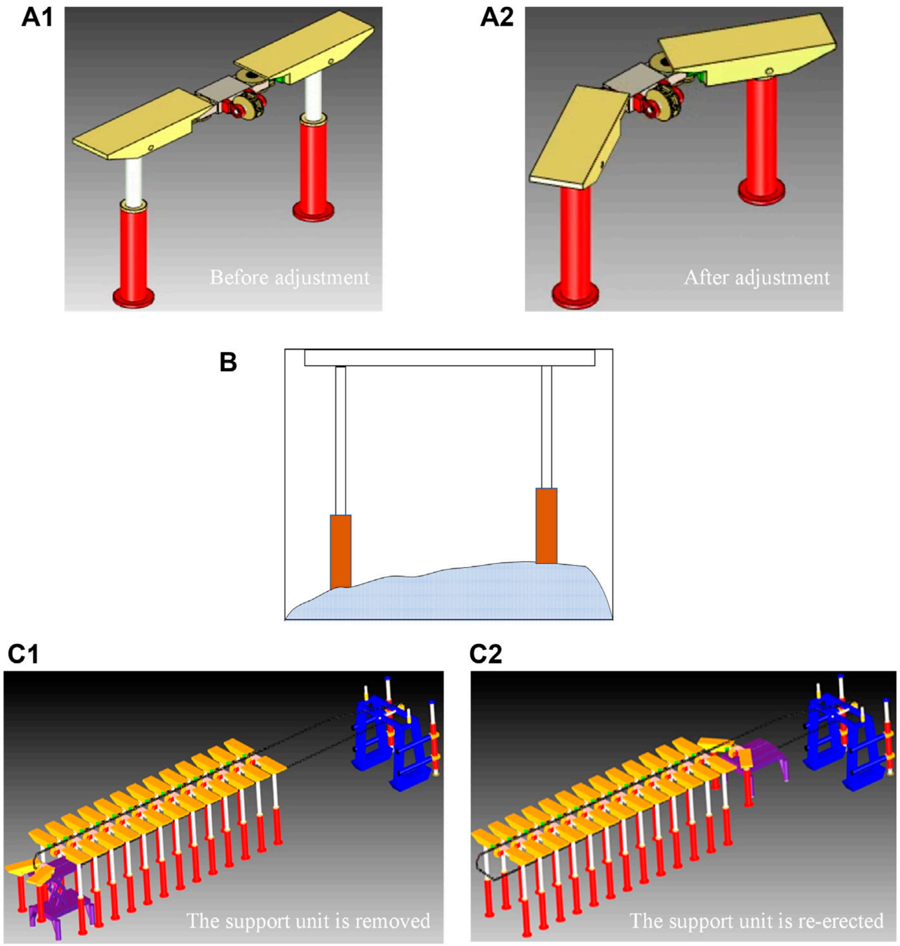

FIGURE 14
Features of the support system. **(A)** Foldable support unit. **(B)** Support unit adapted to floor heave. **(C)** Removal and erection of the support units.

5.2 System of advance support

Considering the geological conditions that the roof of the Lijiahao mine is seriously broken and the floor is deformed to a certain extent, a self-moving foldable support system (Figure 13) in AAAM is recommended. The system includes a foldable support unit, an intelligent support and withdrawal platform, a self-driving machine head, and a traction system.

The system includes the following features:

(1) The system does not support the roadway roofs repeatedly and can fully adapt to roofs' deformation. The foldable support unit is small, so roadway roofs will not be repeatedly supported when the support unit is erected and removed. Furthermore, the direction of the support unit can be adjusted (Figure 14A), which improves its adaptability to the deformation of the roof and prevents damage to the roof bolt, anchor cable, and reinforcement mesh.

(2) It is suitable for roadway floor heave and will not dump. The support system comprises multiple support units, and each support unit is supported by two hydraulic rods. In case of a non-uniform deformation of the roadway floor, the support height can be adjusted by adjusting the lifting of the hydraulic rod to adapt to the deformation of the roadway floor. Additionally, the support unit is small, which can prevent dumping (Figure 14B).

(3) The system operates mechanically, which is safe and efficient. As mining progresses, the support unit is removed from the rear of the system, transported to the front of the system, and then re-erected by an intelligent support and withdrawal platform (Figure 14C). The system is pulled by a driving machine, which can realize the safety and efficiency of the support erection, removal, and transportation.

6 Conclusion

(1) The roof and floor of the mining roadway in the Lijiahao coal mine are sandstone and sandy mudstone, which are relatively soft and prone to roof fall and asymmetric deformation. In AAAM, the HPS and the secondary supplementary support of bolt and anchor cable cannot maintain the stability of the roadway roof economically and effectively. These technologies are not suitable for this condition.

(2) Affected by the successive mining of the two working faces, maximum and minimum principal stresses reach 2.3 and 1.5 times the original stress, respectively, and the ratio of the two stresses reaches 2–8. The regional non-uniform stress field makes the shape of the plastic zone of the surrounding rock change from circular to oval and butterfly, and the plastic zone also deflects at a certain angle (the largest part of the plastic zone rotates to the roof and floor of the roadway). These are the reasons for the roof failure in AAAM of the Lijiahao coal mine.

(3) A self-moving foldable support system is proposed for AAAM support in the Lijiahao coal mine. As the working face moves forward, the support unit will not repeatedly support the roof during erection and removal. Furthermore, the support unit can adapt to the floor heave and prevent dumping. The field test shows that the system can better adapt to the geological conditions of roof crushing and floor deformation.

Data availability statement

The original contributions presented in the study are included in the article/supplementary material; further inquiries can be directed to the corresponding author.

Author contributions

All authors listed have made substantial, direct, and intellectual contributions to the work and approved it for publication.

Funding

This work was partially supported by the National Natural Science Foundation of China (Grant Nos. 52004289 and 51704294), and Fundamental Research Funds for the Central Universities (Grant No. 2022YJSNY10).

Conflict of interest

CL was employed by the Wuhan Engineering Company of CCTEG. The remaining authors declare that the research was conducted in the absence of any commercial or financial relationships that could be construed as a potential conflict of interest.

Publisher's note

References

Cai, M. F. (2020). Key theories and technonogies for surrounding rock stability and ground control in deep mining. *J. Min. Strat. Control. Eng.* 2, 5–13. doi:10.13532/j.jmsce.cn10-1638/td.20200506.001

Du, J. P., and Meng, X. R. (2014). *Mining science*. Xuzhou, China: China University of mining and Technology Press.

Guo, X. F., Guo, L. F., Ma, N. J., Zhao, Z. Q., and Li, C. (2020). Applicability analysis of the roadway butterfly failure theory. *J. China Univ. Min. Technol.* 49, 646–653. 660. doi:10.13247/j.cnki.jcumt.001169

Guo, X. F., Li, C., and Huo, T. H. (2021b). A quantitative evaluation method on the stability of roadway surrounding rock in partial con-fining stress based on plastic zone shapes. *Geomech. Eng.* 25, 405–415. doi:10.12989/gae.2021.25.5.405

Guo, X. F., Li, C., and Huo, T. H. (2021a). Shapes and formation mechanism of the plastic zone surrounding circular roadway under partial confining stress in deep mining. *Geomech. Eng.* 25, 509–520. doi:10.12989/gae.2021.25.6.509

Guo, X. F., Zhao, Z. Q., Gao, X., Wu, X., and Ma, N. (2019). Analytical solutions for characteristic radii of circular roadway surrounding rock plastic zone and their application. *Int. J. Min. Sci. Technol.* 29, 263–272. doi:10.1016/j.ijmst.2018.10.002

Jia, H. S., Wang, L. Y., Fan, K., Peng, B., and Pan, K. (2019). Control technology of soft rock floor in mining roadway with coal pillar protection: A case study. *Energies* 12, 3009. doi:10.3390/en12153009

Kang, H. P., Xu, G., Wang, B. M., Wu, Y. Z., Jiang, P. F., Pan, J. F., et al. (2019). Forty years development and prospects of underground coal mining and strata control technologies in China. *J. Min. Strat. Control. Eng.* 1, 7–39. doi:10.13532/j.jmsce.cn10-1638/td.2019.02.002

Kang, H. P. (2016a). Sixty years development and prospect of rock bolting technology for underground coal mine roadways in China. *J. China Univ. Min. Technol.* 45, 1071–1081. doi:10.13247/j.cnki.jcumt.000583

Kang, H. P., Zhong, J., Yang, J., and Gao, F. (2016b). Investigation on the influence of abutment pressure on the stability of rock bolt reinforced roof strata through physical and numerical modeling. *Rock Mech. Rock Eng.* 50, 387–401. doi:10.1007/s00603-016-1114-x

Kastner, H. (1962). *Statik des Tunel und Stollenbauess*. Berlin/Heidelberg, Germany: Springer.

Li, C., Guo, X. F., Lian, X. Y., and Ma, N. (2020). Failure analysis of a pre-excavation double equipment withdrawal channel and its control techniques. *Energies* 13, 6368. doi:10.3390/en13236368

Li, C., Zhang, W. L., Wang, N., and Hao, C. (2019). Roof stability control based on plastic zone evolution during mining. *J. Min. Saf. Eng.* 36, 753–761. doi:10.13545/j.cnki.jmse.2019.04.014

Li, Y. E., Ma, N. J., and Ma, J. (2018). Surrounding rock's failure characteristic and rational location of floor gas drain-age roadway above deep confined water. *J. China Coal Soc.* 43, 2491–2500.

Liu, S. G., Bai, J. B., Wang, X. Y., Wang, G. H., Wu, B., Li, Y., et al. (2021). Study on the stability of coal pillars under the disturbance of repeated mining in a double-roadway layout system. *Front. Earth Sci.* 9, 1–9. doi:10.3389/feart.2021.754747

Lv, K., Feng, Z. G., Feng, J. C., Xuan, Z. T., Xiao, J., and Wu, X. Y. (2019). Surrounding rock failure mechanism of reserved roadway under superimposed mining and its control technology. *J. Min. Saf. Eng.* 36, 685–695. doi:10.13545/j.cnki.jmse.2019.04.006

Ma, N. J., Li, J., and Zhao, Z. Q. (2015a). Distribution of the deviatoric stress field and plastic zone in circular roadway surrounding rock. *J. China Univ. Min. Technol.* 44, 206–213. doi:10.13247/j.cnki.jcumt.000309

Ma, N. J., Zhao, X. D., Zhao, Z. Q., Li, Q., and Guo, X. F. (2015b). Stability analysis and control technology of mine roadway roof in deep mining. *J. China Coal Soc.* 40, 2287–2295. doi:10.13225/j.cnki.jccs.2015.6011

Qian, M. G., Shi, P. W., and Xu, J. L. (2010). *Mining pressure and strata control*. Xuzhou, China: China University of Mining and Technology Press.

Wu, X. Y. (2018). *Evolutionary regularity of plastic zone and stability control in repetitive mining roadway in Shendong mining area*. Beijing, Chinna: Doctoral dissertation, China University of Mining and Technology.

Wu, X. Y., Liu, H. T., Li, J. W., Guo, X. F., and Lv, K. (2020). Space-time evolutionary regularity of plastic zone and stability control in repetitive mining roadway. *J. China Coal Soc.* 45, 3389–3400. doi:10.13225/j.cnki.jccs.2019.1051

Xu, Y. J., Zhang, K., Li, D. Y., and Zhang, D. S. (2020). Theory and application of self-adaptive support for advanced powered support. *J. China Coal Soc.* 45, 3615–3624. doi:10.13225/j.cnki.jccs.2019.1207

Yao, Q. L., Wang, X. H., Xia, Z., Li, L. H., Zhu, L., and Li, X. H. (2020). Key technology and application of active fore poling for longwall coal mining in coal mine. *J. Min. Saf. Eng.* 37, 289–297.

Yu, M., Zuo, J., Sun, Y., Mi, C., and Li, Z. (2021). Investigation on fracture models and ground pressure distribution of thick hard rock strata including weak interlayer. *Int. J. Min. Sci. Technol.* 32, 137–153. doi:10.1016/j.ijmst.2021.10.009

Zhang, P. C. (2013). *Doctoral dissertation*. Beijing), Beijing, China: China University of Mining and Technology.Research on key technology and equipments for advanced support used in the ends of fully mechanized mine face

Zhang, T., and Wang, Y. L. (2020). Study on deformation evolution law and support technology of surrounding rock in multiple mining roadway. *J. Min. Strat. Control. Eng.* 2, 66–73. doi:10.13532/j.jmsce.cn10-1638/td.20200106.001

Zhao, Z. Q., Ma, N. J., Guo, X. F., and Zhao, X. D. (2016). Falling principle and support design of butterfly-failure roof in large deformation mining roadways. *J. China Coal Soc.* 14, 2932–2939. doi:10.13225/j.cnki.jccs.2016.1146

Zhao, Z. Q., Ma, N. J., Liu, H. T., and Guo, X. F. (2018). A butterfly failure theory of rock mass around roadway and its application prospect. *J. China Univ. Min. Technol.* 47, 969–978. doi:10.13247/j.cnki.jcumt.000922

Zhao, Z. Q. (2014). *Doctoral dissertation*. Beijing, Beijing, China: China University of Mining and Technology.Mechanism of surrounding rock deformation and failure and control method research in large deformation mining roadway

Zhu, Z. J., Wu, Y. L., and Liang, Z. (2022). Mining-induced stress and ground pressure behavior characteristics in mining a thick coal seam with hard roofs. *Front. Earth Sci.* 10, 1–12. doi:10.3389/feart.2022.843191

Frontiers in Earth Science

TYPE Original Research
PUBLISHED 09 August 2022
DOI 10.3389/feart.2022.949043

EDITED BY
Kun Du,
Central South University, China

REVIEWED BY
He Deyin,
Henan Polytechnic University, China
Xiaoliang Wang,
China University of Mining and Technology, China
Wang Wei,
Northeastern University, China

*CORRESPONDENCE
Ke Yang,
keyang2003@163.com

SPECIALTY SECTION
This article was submitted to Geohazards and Georisks, a section of the journal Frontiers in Earth Science

RECEIVED 20 May 2022
ACCEPTED 27 June 2022
PUBLISHED 09 August 2022

CITATION
Fang J, Yang K, Lyu X, Tang J and Zhang J (2022), Mechanical properties and instability analysis of concrete specimens with horizontal holes of different diameters.
Front. Earth Sci. 10:949043.
doi: 10.3389/feart.2022.949043

Mechanical properties and instability analysis of concrete specimens with horizontal holes of different diameters

Juejing Fang[1,2], Ke Yang[3]*, Xin Lyu[1,2], Jinzhou Tang[1,2,4] and Jiqiang Zhang[1,2]

[1]State Key Laboratory of Mining Response and Disaster Prevention and Control in Deep Coal Mines, Anhui University of Science and Technology, Huainan, China, [2]Coal Mine Safety Mining Equipment Innovation Center of Anhui Province, Anhui University of Science and Technology, Huainan, China, [3]Institute of Energy, Hefei Comprehensive National Science Center, Hefei, China, [4]Guizhou Provincial Key Laboratory of Rock and Soil Mechanics and Engineering Safety, Guizhou University, Guiyang, China

Uniaxial compression tests were carried on 12 concrete specimens with six different diameter holes using a rigid test machine, and the stress–strain relationship was analyzed in different hole diameter specimens. The effects of different hole diameters on specimen compression strength, elastic modulus, and Poisson’s ratio were studied, and the failure form and instability mode of concrete specimens with holes of different diameters were evaluated. The results show that the larger the compression strength of the specimen, the larger the axial and horizontal strains. As the hole diameter increased from 0 to 50 mm, the compression strength and elastic modulus reduced. The decreasing trend slowed down, and the relationships between the hole diameter and compression strength, and elastic modulus could be represented by negative liner functions. The Poisson ratio of the specimen increased in waves with the increase in hole diameter from 0 to 50 mm. A crack in the concrete specimen with 0–20 mm diameter hole started at the upper and lower diagonal angles of the hole wall; a crack in the concrete specimen with 30–50 mm diameter hole started at the left and right parts of the hole wall. The instability mode of concrete specimens with horizontal holes of different diameters was divided into shear dislocation instability and planar splitting instability.

KEYWORDS

horizontal hole, concrete specimen, failure form, pressure relief hole, uniaxial compression

Introduction

The surrounding rock is transformed from brittle to plastic with increasing mining depth due to high stress (Li et al., 2019; Xie et al., 2021). The main methods used to control the gateway surrounding rock include a combination of releasing surrounding rock stress and using a low-cost support instead of improving the support strength involving increasing costs (He et al., 2021; Kang 2021; Wu et al., 2021; Wang et al., 2022b). Pressure-relief drill parameters affect the release of surrounding rock stress and the continuous deformation; selecting proper pressure-relief drill diameters is an important step to control deep gateway surrounding rocks (Gao et al., 2020; Zhang et al., 2022).

Recently, studies on the drilling pressure-relief of high-stress weak gateway surrounding rocks have improved (Pu et al., 2020; Zuo et al., 2021). Based on the analysis of the mechanism of drill pressure-relief in deep gateway surrounding rocks, a method determining drill parameters was developed, and the precrack failure of gateway sides' surrounding rock could be realized by the rational distribution of pressure-relief drills. The unloading effect within a surrounding rock was studied under cyclic excavation; the mechanism of pressure relief and structural stability of hard roof along the roadway was elucidated; and elastic stress analysis and plastic zone estimation in pressure-relief gateway were carried out using the complex variable method (Xu et al., 2019; Zhao et al., 2020; Kan et al., 2022). Based on the impact of energy dissipation by pre-excavation pressure release, technologies combining the reinforcing of surrounding rock and pressure relief, anchoring grouting, and floor pressure relief were proposed to prevent the rock burst in deep gateway (Zhai et al., 2018; Wang et al., 2022a). The failure characteristics of rocks with different holes and fractures have been studied in the laboratory (Gou et al., 2007; You et al., 2020). The strength and fracturing of rocks with inclining cracks and holes in different locations and shapes were also studied (Wu et al., 2017; Wang et al., 2020). The failure processes of intact, single-hole, double-hole, single-hole double-crack, double-hole single-crack, and defect specimens were analyzed (Zhao et al., 2017; Fan et al., 2018; Chen et al., 2020; Wu et al., 2020), and the mechanism of crack coalescence in surrounding rocks with different holes was elucidated. With the improvement of monitoring and experimental level, the relationship between creep failure stress and horizontal hole was studied (Xin et al., 2018; Wang et al., 2019); acoustic emission monitoring and digital imaging systems were used to conduct uniaxial compression tests of sandstone specimens with cracks and elliptical holes (Liu et al., 2019; Du et al., 2020; Fan et al., 2022); and the surface potential change characteristics of the concrete wall with holes under uniaxial compression were tested (Liu et al., 2014). With studies on the characteristics of concrete and application of concrete technology in coal mines (Gao et al., 2015; Lyu et al., 2021), attention has been paid to the characteristics of concrete holes, which undoubtedly provides a good research basis for this test.

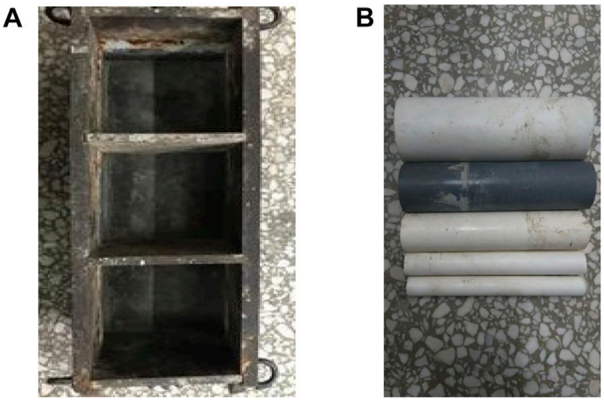

FIGURE 1
Molds for concrete specimens. **(A)** Filling mold. **(B)** Perforated tubes.

In the study, uniaxial compression tests were carried out on 12 concrete specimens with six different diameter holes using a rigid test machine, and the stress–strain relationship of different hole diameter specimens was analyzed. The effects of different hole diameters on specimen compression strength, elastic modulus, and Poisson's ratio, were studied, and the failure form and instability mode of concrete specimens with holes of different diameters were evaluated. The results provide references for selecting the hole diameter and sealing-hole design of deep gateway surrounding rocks.

Test design

Specimen preparation

The concrete specimens were prepared from C32.5 cement and water with a ratio of 1:0.3 in a square standard mold of 100 mm × 100 mm × 100 mm (Figure 1A). The holes in the specimens were reserved using PVC tubes (Figure 1B) with diameters of 10, 20, 30, 40, and 50 mm, which were immobilized in the center of the square mold (Figure 2). Before preparing concrete specimens, the inside of the molds and the surface of the tubes were greased to release the specimens easily.

Eighteen specimens were tested. According to the hole diameter, these specimens were divided into six groups, namely, group A, group B, group C, group D, group E, and group F; each group had three specimens. The prefabricated concrete specimens were demolded after 24 h, and water was sprayed for 28 days (Figure 3). The loading roughness end of the specimens was grinded well to a nonparallelism of less than 0.02 mm. The prefabrication influenced the hole height and inclination; for accuracy, two specimens with less dissimilarity were selected from each group for the uniaxial compression test.

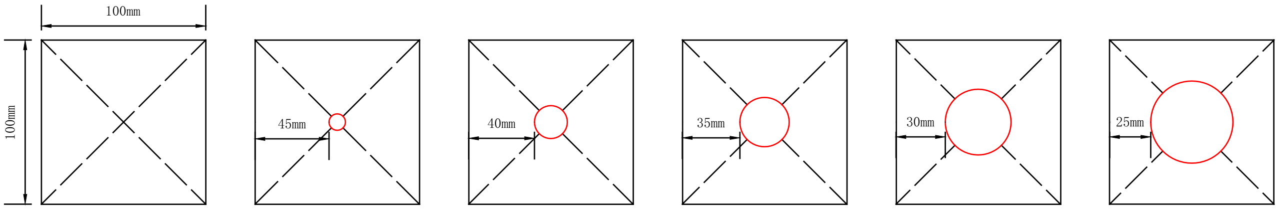

FIGURE 2
Hole design in concrete specimens.

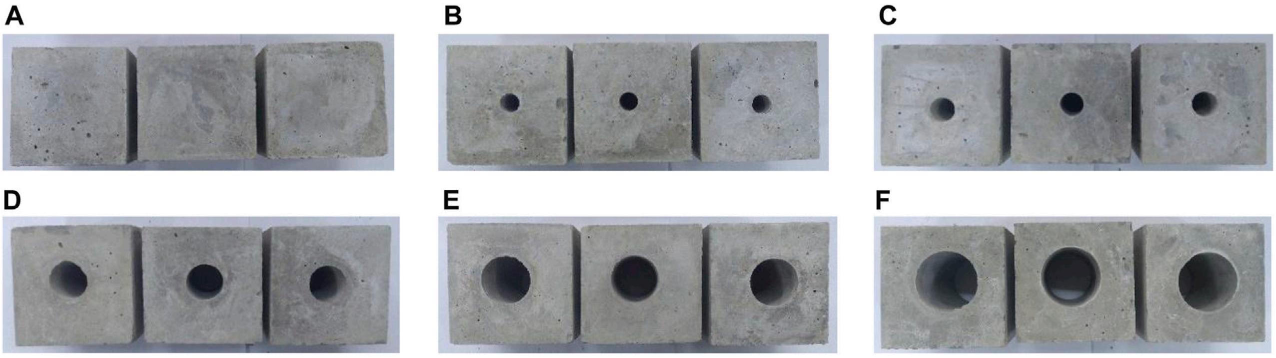

FIGURE 3
Prefabricated concrete specimens. **(A)** 0 mm, **(B)** 10 mm, **(C)** 20 mm, **(D)** 30 mm, **(E)** 40 mm, and **(F)** 50 mm.

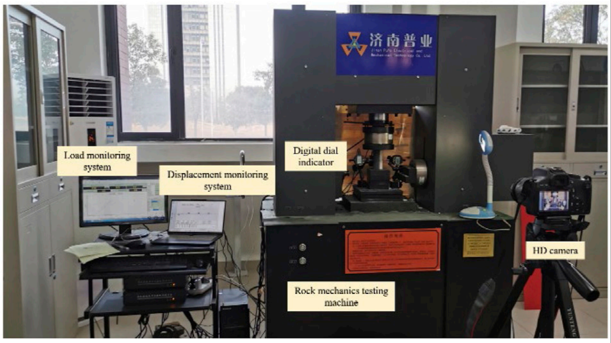

FIGURE 4
Test process.

Test mothed

The displace loading test was conducted using a full-servo test system controlled using a computer, and the loading rate was 0.03 mm/s. The axial and lateral deformations of the specimens were acquired using digital micrometers. The load was controlled and collected using a software, and all the test data were recorded and saved automatically using a computer. The whole stress–strain curve of uniaxial compression concrete specimens with holes of different diameters could be obtained.

Test result analysis

The specimen B2 was not analyzed because of more data difference, which was reloaded after being damaged. The other specimens were subjected to the whole uniaxial compression (Figure 4); the uniaxial compression data are shown in Table 1.

Analysis of test results

Characteristics of stress–strain curves

Figure 5 shows that the whole stress–strain curve of uniaxial compression concrete specimen with holes of different diameters has five stages: origin void compaction, linear elasticity, elastic–plastic transition, plastic, and failure. The linear elasticity stage was longer, and the elastic–plastic transition and plastic stage were not obvious. It was found that concrete specimens had good elastic deformation.

TABLE 1 Uniaxial compression data.

Group number	Hole diameter/ mm	Number	Compression strength/MPa	Axial strain/ %	Horizontal strain/%	Poisson ratio	Elasticity modulus/ GPa	Remarks
Group A	0	A1	64.7155	0.8864	0.0402	0.0454	10.7429	
		A2	72.5987	0.8372	0.0426	0.0509	10.9584	
Group B	10	B1	57.6887	0.9212	0.2606	0.2829	9.6182	
		B2	—	—	—	—	—	Secondary loading
Group C	20	C1	47.3769	0.8176	0.2347	0.2870	8.0156	
		C2	62.4426	0.9399	0.2426	0.2581	12.8199	
Group D	30	D1	46.9829	0.6711	0.1244	0.1853	10.0846	
		D2	44.9703	1.0191	0.4230	0.4151	10.3112	
Group E	40	E1	40.0070	0.8010	0.2734	0.3413	8.1103	
		E2	33.1267	0.5980	0.2517	0.4209	7.7638	
Group F	40	F1	32.6251	0.5839	0.1538	0.2635	6.9240	
		F2	32.2700	0.7565	0.2034	0.2688	7.2626	

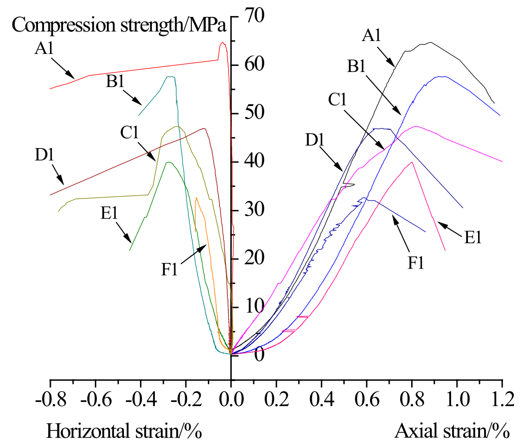

FIGURE 5
Stress–strain curves of uniaxial compression on specimens.

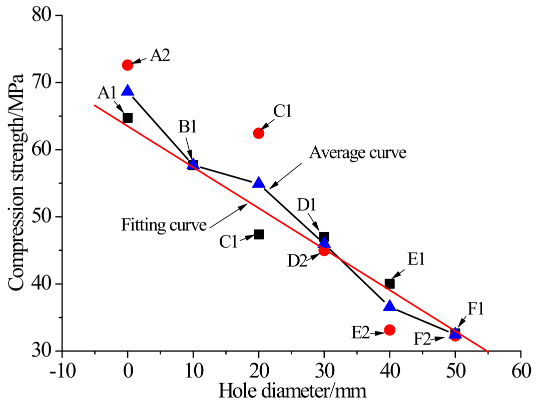

FIGURE 6
Relationship between the hole diameter and compression strength.

The higher the compression strength, the larger the axial strain and horizontal strain on the concrete specimen with holes of different diameters. The axial strain was more than the horizontal strain in the same-hole specimen, while the axial strain growth was less than the horizontal strain growth. The average axial strain decreased with increasing hole diameter. When the hole diameter increased from 0 to 30 mm, the axial strain was less, and the horizontal strain first increased and then decreased. When the hole diameter was 30 mm, the horizontal strain reached the maximum and then decreased.

Relationship between horizontal-hole diameter and compression strength

Figure 6 shows the relationship between the hole diameter and compression strength of concrete specimens. When the hole diameter increased from 0 to 50 mm, the average compression strength of the concrete specimen with different hole diameters decreased from 68.6571 to 57.6887, 54.9098, 45.9766, 36.5669, and 32.4476 MPa, and the average compression damping range was 52.74%. This shows that the larger the hole diameter, the lower the strength of concrete specimen.

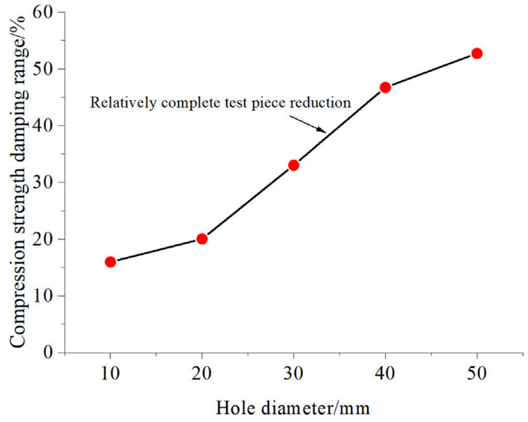

FIGURE 7
Relationship between the hole diameter and compression strength damping range.

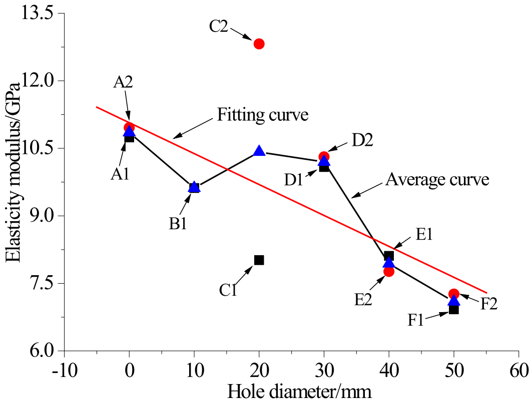

FIGURE 8
Relationship between the hole diameter and elasticity modulus.

Figure 7 shows the relationship between the hole diameter and compression damping of concrete specimens. The hole diameter increased from 0 to 50 mm, and the compression damping range of hole specimens increased more linearly than that of intact specimens. The average decrease rate of the compression strength of concrete specimens with holes of different diameters to the specimen with previous hole diameter was, in turn, 15.9756%, 4.8171%, 16.2689%, 20.4663%, and 11.2651%, i.e., the average increasing rate of compression strength compared to the previous hole diameter specimen is 13.7586%. When the hole diameter was 20 mm, the decrease in compression strength was the least, which could explain why the hole slightly affected the compression strength of concrete specimens when the hole diameter was less than 20 mm. When the hole diameter increased from 20 to 30 mm, a large decrease in the compression strength of concrete specimens was observed, and the failure form was obviously different.

The fitting relationship between the hole diameter and compression strength of concrete specimens can be expressed as follows:

$$\boldsymbol{\sigma_c} = -\mathbf{0.7238}\boldsymbol{d} + \mathbf{67.4710}, \tag{1}$$

where $\boldsymbol{\sigma_c}$ is the compression strength of concrete specimens in MPa and $\boldsymbol{d}$ is the hole diameter in mm.

The correlation coefficient was $R^2 = 0.9820$. Therefore, the linear function could characterize the relationship between the pore size and the peak strength of the concrete specimen, that is, as the pore size increased, the strength of the concrete specimen decreased.

Relationship between horizontal-hole diameter and elasticity modulus

The elasticity modulus of the concrete specimen with holes of different diameters was obtained by fitting and calculating the approximate linear data of the whole stress–strain curve, which occurred before specimen failure.

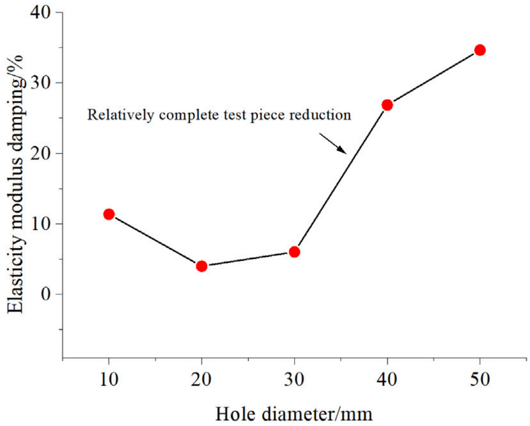

FIGURE 9
Relationship between the hole diameter and elasticity modulus damping.

Figure 8 shows the relationship between the hole diameter and elasticity modulus of concrete specimens. The elasticity modulus of the concrete specimen with the same hole diameter was similar except that with a 20 mm diameter hole, which was larger than that with a 10 mm diameter hole. The elasticity modulus of the concrete specimen with a 0–30 mm diameter hole was little difference, indicating that the 0–30 mm diameter hole slightly affected the elastic modulus of concrete specimens. When the hole diameter was more than 30 mm, the elasticity modulus damping increased, and the most damping rate was 22.1693% of the previous hole diameter specimen. The elasticity modulus damping rate of concrete specimens decreased when the hole diameter was 50 mm. In the whole, the average elasticity modulus of concrete specimens with holes of different diameters decreased with the increase in hole diameter from 0 to 50 mm.

Figure 9 shows the relationship between the hole diameter and elasticity modulus damping of concrete specimens. The elasticity modulus damping range of hole specimens to the intact specimen first decreased and then increased with the increase in hole diameter from 0 to 50 mm. The elasticity modulus of the concrete specimen slightly changed when the hole diameter was 0–30 mm, and the damping rate was 6.0162%, indicating that the hole diameter slightly affected the elasticity modulus of the concrete specimen. When hole diameter increased from 30 to 50 mm, the elasticity modulus damping range was 30.4435%, indicating that 30–50 mm hole diameter affected the elasticity modulus of concrete specimens.

On the whole, 20–30 mm hole diameter was the key range affecting the mechanics parameters. When the hole diameter increased from 0 to 50 mm, the elasticity modulus damping was 34.6282%, indicating that the larger the hole diameter of concrete specimen, the lower the elasticity modulus.

The fitting relationship between the hole diameter and elasticity modulus can be expressed as follows:

$$\boldsymbol{E_c} = \mathbf{-0.0687}\boldsymbol{d} + \mathbf{11.07}, \tag{2}$$

where E_c is the compression strength of concrete specimens in MPa.

The correlation coefficient R^2 is 0.7331. The negative-leaner functional equation could still express the relationship between the hole diameter and elasticity modulus of concrete specimens, while the correlation between the hole diameter and elastic modulus is less than that between the hole diameter and compression strength.

Relationship between horizontal-hole diameter and Poisson's ratio

Figure 10 shows the relationship between the hole diameter and Poisson ratio of concrete specimens. When the hole diameter increased from 0 to 50 mm, the Poisson ratio first increased and then decreased, and the whole increasing range was 452.2822%. The Poisson ratio of no-hole concrete specimens was the least, and that of 50 mm hole diameter specimens was the second. When the hole diameter increased from 10 to 50 mm except no-hole concrete specimens, the Poisson ratio slightly changed, so the hole diameter slightly affected the Poisson ratio of concrete specimens.

Figure 11 shows the relationship between the hole diameter and Poisson ratio of concrete specimens. Poisson's ratio of hole concrete specimens increased with the increase in hole diameter from 0 to 50 mm, and the increasing range of 40 mm diameter concrete specimens was larger. The increasing ranges of the other specimens (10 mm, 20 mm, 30 mm, and 50 mm) were 486.9295%, 465.5620%, 522.8216%, and 452.2822%, respectively. The largest change rate was 15.60%, indicating that the hole diameter slightly affected Poisson's ratio of concrete specimens.

The fitting relationship between the hole diameter and Poisson ratio of concrete specimens can be expressed using the following equation:

$$\boldsymbol{\mu_c} = \mathbf{0.3276} - \frac{\mathbf{0.2796}}{\mathbf{1} + \left(\frac{\boldsymbol{d}}{\mathbf{1.5972}}\right)^{\mathbf{0.8282}}}, \tag{3}$$

where μ_c is the Poisson ratio of concrete specimens.

The correlation coefficient R^2 is 0.8666. The results mentioned above showed that the relationship between the pore diameter and Poisson's ratio of concrete specimens could be expressed by Logistic.

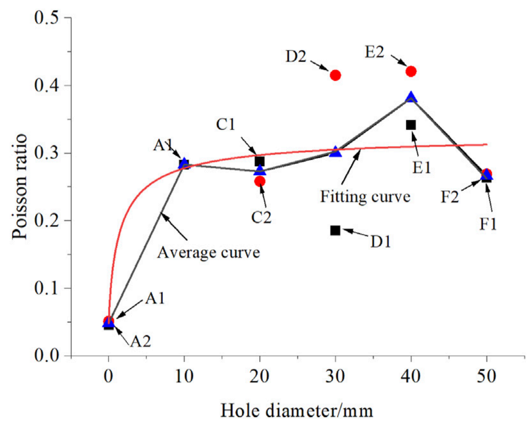

FIGURE 10
Relationship between the hole diameter and Poisson ratio.

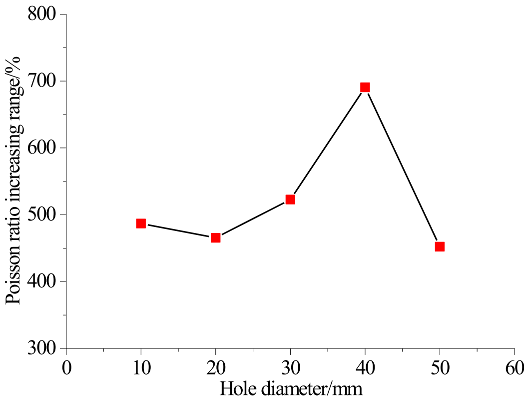

FIGURE 11
Relationship between the hole diameter and Poisson ratio increasing range.

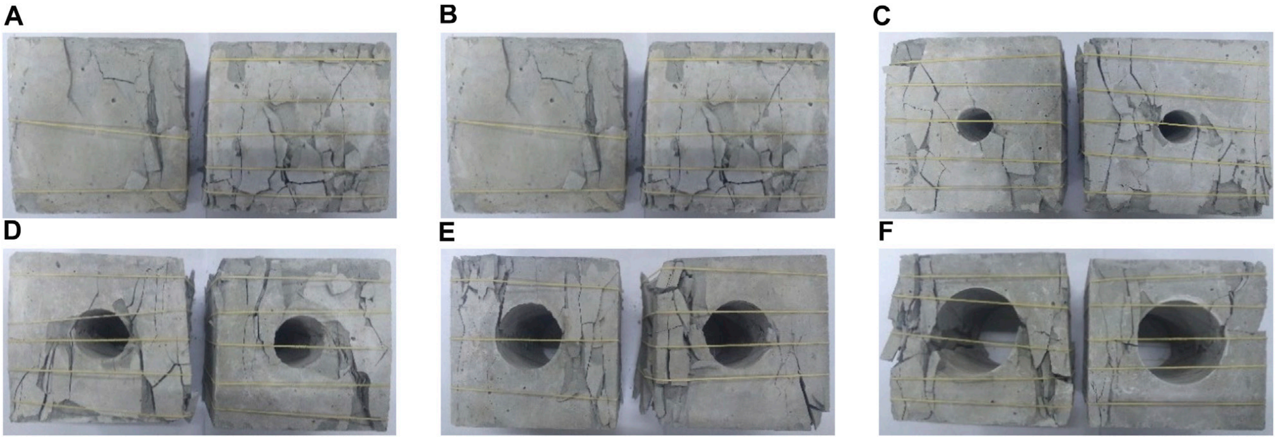

FIGURE 12
Failure forms of concrete specimens with holes of different diameters. **(A)** 0 mm, **(B)** 10 mm, **(C)** 20 mm, **(D)** 30 mm, **(E)** 40 mm, and **(F)** 50 mm.

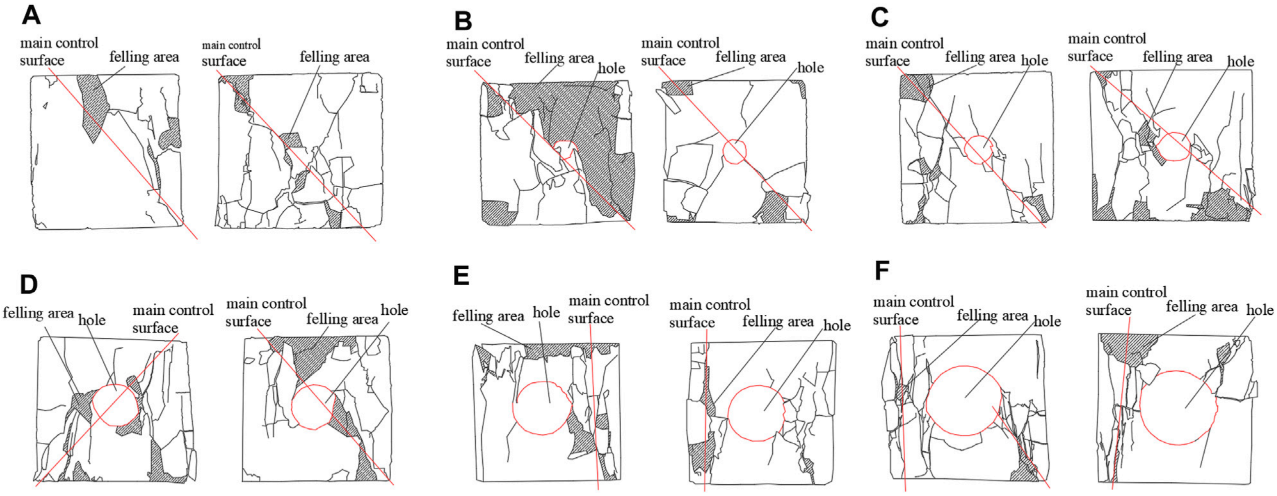

FIGURE 13
Failure-mode sketch of concrete specimens with holes of different diameters. **(A)** 0 mm, **(B)** 10 mm, **(C)** 20 mm, **(D)** 30 mm, **(E)** 40 mm, and **(F)** 50 mm.

With the increase of the aperture, Poisson's ratio increased slowly, and the presence of pore size had a great influence on the specimen.

Relationship between horizontal-hole diameter and failure mode

Failure mode of concrete specimen with holes of different diameters

Figure 12 shows the failure mode of concrete specimens with holes of different diameters. Figure 13 shows the failure mode. Figures 12, 13 show some common and different characteristics of failure mode. The common characteristics are that the main fracture surface occurred in all failure concrete specimens and controlled failure mode; all concrete specimens were damaged along the hole diameter, which controlled the specimen failure mode. The different characteristics are as follows: The main fracture surface angle of concrete specimens with holes of different diameters was different; the failure mode of concrete specimens with holes of different diameters failed differently along the hole diameter.

In summary, as the hole diameter increased from 0 to 50 mm, the concrete specimens failed from near-friction-angle compression shear to vertical compression splitting.

The concrete specimen with 0–30 mm diameter hole showed shear failure along the diagonal of hole diameter. The larger the hole diameter, the smaller the fracture block, the less surface fell off, the more obvious the main control surface, the second control surface initiated, the number of reverse crack increased, the hole displaced along the transverse direction, and the failure mode of concrete specimens became complex.

The concrete specimen with 40–50 mm diameter hole showed flake splitting failure from multiple cracks in the left and right sides of hole, indicating that the cracks easily initiated in the stress-concentrated points during uniaxial compression on large-hole concrete specimens. In the concrete specimens with holes of 40 and 50 mm diameters, the boundary of the main and second failure surface was vague, the number of reverse tensile cracks gradually decreased, and the hole collapsed. The larger the hole diameter of concrete specimens, the smaller the fracture blocks, the more severe the hole collapsed.

Figure 14 shows the failure mode of holes of the wall of different diameters. In the small hole (the hole diameter was less than 20–30 mm), the hole wall displaced to fail along one direction, the upper and the lower parts of the failure hole dislocated, and the rupture surface run through the whole hole. In the large hole (the hole diameter was more than 20–30 mm), the hole wall was compressed to fail along the loaded direction, the upper and lower parts of hole did not dislocate, mainly compression failure occurred, the upper compression wall was larger than the lower compression wall, and the compression offshoring instability was observed in the upper part of the hole.

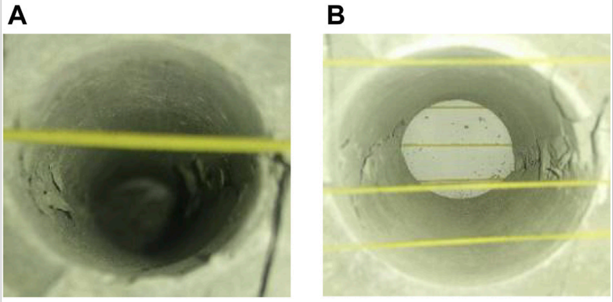

FIGURE 14
Hole-wall failure modes of concrete specimens with holes of different diameters. **(A)** 20 mm and **(B)** 50 mm.

Instability mode of concrete specimens with holes of different diameters

According to the hole diameter, the instability modes of concrete specimens were divided into two types (Figure 15): small-diameter-hole shear displaced instability and large-diameter-hole flake splitting stability.

Small-diameter-hole shear displaced instability. When the hole diameter of concrete specimens was small, the concrete specimens were transformed into plastic stage, and cracks occurred with the increase in stress. In the concrete specimens with holes of 0 or 20 mm diameters, the cracks initiated at the upper and lower inclined angles of the hole wall, the upper and lower cracks extended to the upper and lower angles of concrete specimens with the increase in axial stress, and partial microcracks initiated to break through the upper and lower parts of hole wall angles to fail, i.e., small-diameter-hole shear displaced instability. Group C belonged to small-diameter-hole shear displaced instability.

Large-hole-diameter flake splitting instability: When the hole diameter of concrete specimens was large, the concrete specimens were transformed into the plastic stage, and cracks occurred with the increase in stress. In concrete specimens with holes of 30 or 50 mm diameter, the crack initiated in the left and right sides of the hole, and extended vertically to the upper and lower surfaces of concrete specimens, and then

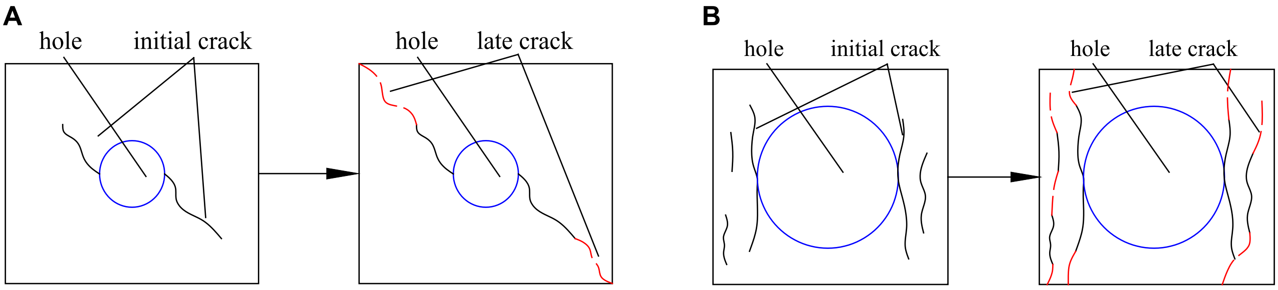

FIGURE 15
Failure modes of concrete specimens with holes of different diameters. **(A)** Small-diameter-hole shear displaced instability. **(B)** Large-hole-diameter flake splitting instability.

collapsed to fail vertically along the left and right wall of hole, indicating large-diameter-hole flake splitting instability. Group E belonged to the large-diameter-hole flake splitting instability.

Conclusion

In this study, the mechanical properties of concrete specimens with different pore sizes were studied from the aspects of stress–strain relationship, compressive strength, elastic modulus, Poisson's ratio, failure mode, and instability mode. The following conclusions can be drawn based on the experimental analysis and discussion.

1) The whole uniaxial compression stress–strain curve of concrete specimens with horizontal holes of different diameters had five stages similar to intact specimens. The larger the compression strength of the hole of concrete specimens, the higher the axial and horizontal strains.
2) With the increase in hole diameter from 0 to 50 mm, the compression strength and elasticity modulus of concrete specimens decreased, and the trend slowed down. The damping rates were 52.7396% and 34.6282%, and the relationships between hole diameter and compression strength, and elasticity modulus could be expressed using a negative linear formula.
3) With the hole diameter increasing from 0 to 50 mm, Poisson's ratio of concrete specimens increased wholly wave. Poisson's ratio increased slowly with increasing hole diameter. Holes with different diameters had little effect on Poisson's ratio of concrete specimens, but the existence of pore diameters had a great influence on the specimens.
4) In the concrete specimens with 0–30 mm diameter holes, the crack passed through the hole along the diagonal; the larger the diameter, the smaller the fracture block, the less the surface shedding, and the more obvious the main control surface, showing the shear displacement instability of the small-diameter-hole. In the concrete specimens with holes of 40–50 mm diameter, the crack occurred around the hole and flake splitting occurred in the hole; the larger the diameter, the smaller the fracture block, and the more severe hole failed, which is manifested as large-diameter-hole flaky splitting instability.

Data availability statement

The original contributions presented in the study are included in the article/Supplementary Material; further inquiries can be directed to the corresponding author.

Author contributions

Conceptualization, JF and KY; methodology, JF and XL; software, JF, KY, and XL; validation, JT and JZ; writing—original draft preparation, JF; writing—review and editing, KY, XL, and JT; and project administration, JZ. All authors have read and agreed to the published version of the manuscript.

Funding

This work was supported by the Institute of Energy, the Hefei Comprehensive National Science Center Project (21KZS215), the National Program on Key Basic Research Project of China (2019YFC1904304), the Graduate Innovation Fund project of Anhui University of Science and Technology (2021CX 2016), the Key Research and Development Plan of Anhui Province (202104a07020009), the Anhui Provincial Department of Science and Technology University Research Project (YJS20210391), and the Guizhou Provincial Science and Technology Projects ([2020]2004).

Conflict of interest

The authors declare that the research was conducted in the absence of any commercial or financial relationships that could be construed as a potential conflict of interest.

Publisher's Note

References

Chen, S., Xia, Z., and Feng, F. (2020). Numerical simulation of strength, deformation, and failure characteristics of rock with fissure hole defect. *Adv. Mater. Sci. Eng.* 2020, 1–15. doi:10.1155/2020/7048645

Du, K., Li, X., Tao, M., and Wang, S. (2020). Experimental study on acoustic emission (AE) characteristics and crack classification during rock fracture in several basic lab tests. *Int. J. Rock Mech. Min. Sci.* 133, 104411. doi:10.1016/j.ijrmms.2020.104411

Fan, J., Zhu, X., Hu, J. W., Tang, Y., and He, C. L. (2022). Experimental study on crack propagation and damage monitoring of sandstone using three-dimensional digital image correlation technology. *Rock Soil Mech.* 43, 1009–1019. doi:10.16285/j.rsm.2021.1132

Fan, X., Chen, R., Lin, H., Lai, H., Zhang, C., and Zhao, Q. (2018). Cracking and failure in rock specimen containing combined flaw and hole under uniaxial compression. *Adv. Civ. Eng.* 2018, 1–15. doi:10.1155/2018/9818250

Gao, X. J., Li, Y. Y., Zhang, Z. J., Zhang, Z. Y., Yu, H. T., Huang, Z. Z., et al. (2020). Prevention and control technology of pre-splitting roof by dual active advanced blasting in soft rock large deformation roadway. *J. China Coal Soc.* 45, 589–598. doi:10.13225/j.cnki.jccs.2020.0425

Gao, Y. F., Liu, K. M., Feng, S. W., Zhao, W., Qu, G. L., and Xie, H. (2015). Early strength concrete experiment and applied research of early strength concrete-filled steel tubular supports in extremely soft rock roadways. *J. Min. Saf. Eng.* 32, 537–543. doi:10.13545/j.cnki.jmse.2015.04.003

Gou, Y., Su, C. D., and Qin, G. Z. (2007). Size effect of hollowed marble cylinder specimen. *J. Min. Saf. Eng.* 24, 302–305.

He, D., Liu, S., Fu, M., Peng, B., and Ren, Y. (2021). Experimental study on resin-anchored bolt concentricity Including a device for More consistent bolt centering. *Int. J. Rock Mech. Min. Sci.* 148, 104962. doi:10.1016/j.ijrmms.2021.104962

Kan, J., Dou, L., Li, J., Li, X., Bai, J., and Wang, M. (2022). Characteristics of microseismic waveforms induced by underground destress blasting: comparison with those induced by ground blasting and coal mining. *Front. Earth Sci.* 10, 797358. doi:10.3389/feart.2022.797358

Kang, H. P. (2021). Seventy years development and prospects of strata control technologies for coal mine roadways in China. *Chin. J. Rock Mech. Eng.* 40, 1–30. doi:10.13722/j.cnki.jrme.2020.0072

Li, C. Y., Zhang, Y., Zuo, J. P., Tang, S. J., and Liu, S. F. (2019). Floor failure mechanical behavior and partition characteristics under the disturbance of voussoir beam instability in deep coal mining. *J. China Coal Soc.* 44, 1508–1520. doi:10.13225/j.cnki.jccs.2019.6006

Liu, X., Zhang, H., Wang, X., Zhang, C., Xie, H., Yang, S., et al. (2019). Acoustic emission characteristics of graded loading intact and holey rock samples during the samage and failure process. *Appl. Sci.* 9, 1595. doi:10.3390/app9081595

Liu, Z. T., Li, X. L., Li, Z. H., Liu, Y. J., Yang, Y. L., and Feng, J. J. (2014). Electric potential of the hole wall of concrete under uniaxial compression. *J. China Coal Soc.* 39, 372–377. doi:10.13225/j.cnki.jccs.2013.1762

Lyu, X., Yang, K., Liu, Q. J., Fu, Q., and Fang, J. J. (2021). Characteristics of early-Damaged cement stone and the creep behavior after damage. *Constr. Build. Mater.* 303, 124484. doi:10.1016/j.conbuildmat.2021.124484

Pu, H. P., Jiang, P. F., Huang, B. X., Guan, X. M., Wang, Z. G., Wu, Y. Z., et al. (2020). Roadway strata control technology by means of bolting-modification-destressing in synergy in 1000 M deep coal mines. *J. China Coal Soc.* 45, 845–864. doi:10.13225/j.cnki.jccs.SJ20.0204

Wang, J., Wu, Q. Q., Guan, J. F., Zhang, P., Fang, H. Y., and Hu, S. W. (2020). Numerical simulation on size effect of fracture toughness of concrete based on mesomechanics. *Materials* 13, 1370. doi:10.3390/ma13061370

Wang, M., Zheng, D. J., Wang, X. Y., Xiao, T. Q., Shen, W. L., and Song, Z. F. (2019). Deformation characteristics and creeping control of deep roadway with pressure-relief borehole. *J. Min. Saf. Eng.* 36, 437–445. doi:10.13545/j.cnki.jmse.2019.03.002

Wang, W., Pan, Y. S., and Xiao, Y. H. (2022a). Synergistic mechanism and technology of cable bolt resin anchoring for roadway roofs with weak interlayers. *Rock Mech. Rock Eng.* 55, 3451–3472. doi:10.1007/s00603-022-02817-8

Wang, W., Pan, Y. S., and Xiao, Y. H. (2022b). Synergistic resin anchoring technology of rebar bolts in coal mine roadways. *Int. J. Rock Mech. Min. Sci.* 151, 105034. doi:10.1016/j.ijrmms.2022.105034

Wu, Q. H., Li, X. B., Zhao, F. J., Tao, M., Dong, L. J., and Chen, L. (2017). Failure characteristics of hollow cylindrical specimens of limestone under hole pressure unloading. *Chin. J. Rock Mech. Eng.* 36, 1424–1433. doi:10.13722/j.cnki.jrme.2016.1498

Wu, T. H., Gao, Y. T., Zhou, Y., and Li, J. W. (2020). Experimental and numerical study on the interaction between holes and fissures in rock-like materials under uniaxial compression. *Theor. Appl. Fract. Mech.* 106, 102488. doi:10.1016/j.tafmec.2020.102488

Wu, Y. Z., Fu, Y. K., He, J., Chen, J. Y., Chu, X. W., and Meng, X. Z. (2021). Principle and technology of "pressure relief-support-protection" collaborative prevention and control in deep rock burst roadway. *J. China Coal Soc.* 46, 132–144. doi:10.13225/j.cnki.jccs.yg20.1821

Xie, H. P., Li, C. B., Gao, M. Z., Zhang, R., Gao, F., and Zhu and, J. B. (2021). Conceptualization and preliminary research on deep *In situ* rock mechanics. *Chin. J. Rock Mech. Eng.* 40, 217–232. doi:10.13722/j.cnki.jrme.2020.0317

Xin, Y. J., Hao, H. C., Lv, X., and Ji, H. Y. (2018). Creep characteristics and instability analysis of concrete specimens with horizontal holes. *Comput. Concr.* 22, 563–572. doi:10.12989/cac.2018.22.6.56310.1080/19648189.2016.1229223

Xu, M. F., Wu, S. C., Gao, Y. T., Ma, J., and Wu, Q. L. (2019). Analytical elastic stress solution and plastic zone estimation for a pressure relief circular tunnel using complex variable methods. *Tunn. Undergr. Space Technol.* 84, 381–398. doi:10.1016/j.tust.2018.11.036

You, B., Xu, J. X., Shi, S. L., Liu, H. Q., Lu, Y., and Li, H. (2020). Effect of stress and water pressure on permeability of fractured sandstone based on response surface method. *Front. Earth Sci.* 8, 11. doi:10.3389/feart.2020.00011

Zhai, X. X., Huang, G. S., Chen, C. Y., and Li, R. B. (2018). Combined supporting technology with bolt-grouting and floor pressure-relief for deep chamber: an underground coal mine case study. *Energies* 11, 67–83. doi:10.3390/en11010067

Zhang, H., Li, T. C., Wu, S., Zhang, X. T., Gao, W. L., and Shi, Q. P. (2022). A study of innovative cut blasting for rock roadway excavation based on numerical simulation and field tests. *Tunn. Undergr. Space Technol.* 119, 104233. doi:10.1016/j.tust.2021.104233

Zhao, H., Hu, G., Wang, F., and Ju, N. (2017). Quantitative analysis of crack expansion in specimens of coal having a single pre-existing hole. *J. China Coal Soc.* 42, 860–870.

Zhao, J., Guo, G. T., Xu, D. P., Huang, X., Hu, C., Xia, Y. L., et al. (2020). Experimental study of deformation and failure characteristics of deeply-buried hard rock under triaxial and cyclic loading and unloading stress paths. *Rock Soil Mech.* 41, 1521–1530. doi:10.16285/j.rsm.2019.1604

Zuo, J. P., Sun, Y. J., Wen, J. H., Wu, G. S., and Yu, M. L. (2021). Full-space collaborative control technology and its application for deeply buried roadways. *J. Tsinghua Univ. Sci. Technol.* 61, 853–862. doi:10.16511/j.cnki.qhdxxb.2021.25.018

frontiers | Frontiers in Earth Science

TYPE Original Research
PUBLISHED 10 August 2022
DOI 10.3389/feart.2022.960812

Strain rate effects on characteristic stresses and acoustic emission properties of granite under quasi-static compression

Lu Liu[1,2,3], Sijing Wang[1,2]* and Wencheng Yang[2,4]

[1]Key Laboratory of Shale Gas and Geoengineering, Institute of Geology and Geophysics, Chinese Academy of Sciences, Beijing, China, [2]Innovation Academy for Earth Science, Chinese Academy of Sciences, Beijing, China, [3]University of Chinese Academy of Sciences, Beijing, China, [4]Key Laboratory of Petroleum Research, Institute of Geology and Geophysics, Chinese Academy of Sciences, Beijing, China

OPEN ACCESS

EDITED BY
Zhiqiang Yin,
Anhui University of Science and Technology, China

REVIEWED BY
Baohua Guo,
Henan Polytechnic University, China
Wanchun Zhao,
Northeast Petroleum University, China

*CORRESPONDENCE
Sijing Wang,
Wangsijing@126.com

SPECIALTY SECTION
This article was submitted to Geohazards and Georisks, a section of the journal Frontiers in Earth Science

RECEIVED 03 June 2022
ACCEPTED 12 July 2022
PUBLISHED 10 August 2022

CITATION
Liu L, Wang S and Yang W (2022), Strain rate effects on characteristic stresses and acoustic emission properties of granite under quasi-static compression. *Front. Earth Sci.* 10:960812.
doi: 10.3389/feart.2022.960812

In order to further investigate the strain rate effects on characteristic stresses and acoustic emission parameters of rock under quasi-static compression, uniaxial compressive tests were conducted on cylindrical specimens measuring 50 mm in diameter and 100 mm in height using a rock material testing machine and a multi-channel acoustic emission monitoring system at strain rates ranging from 10^{-6} s^{-1} to 10^{-2} s^{-1}. The stress-strain curves of rock samples, characteristic stresses, energy data, and temporal and spatial distribution of acoustic emission signals were obtained and analyzed. The experimental results certified a linearly positive correlation between characteristic stresses and the logarithm of strain rates, despite the fact that the linear correlation varies for different characteristic stresses, whereas the ratios of characteristic stresses essentially do not change with increasing strain rates. The input energy and elastic strain energy at the damage point, UCS point and failure stress point exhibit a linearly positive correlation with the logarithm of strain rates when the strain rate exceeds 10^{-5} s^{-1}. Meanwhile, the characteristics of energy conversion between input energy and elastic strain energy or the dissipated energy at different characteristic stresses points were explored. Based on this, the energy conversion process of rock under quasi-static compression can be divided into three stages: energy accumulation, energy dissipation, and energy release, respectively. Besides, it is noted that the total number of the located AE events decreases as strain rates increase when the strain rate exceeds 10^{-5} s^{-1}, and the majority of located AE events occur during the crack closure stage and unstable crack growth stage. Finally, based on the perspective of energy conversion and the structural properties of multi-scale defects in rock, the mechanism of the increase of characteristic stresses with the increase of strain rates was proposed: that is, when rock is subjected to quasi-static compression, the higher strain rates can activate the small-scale defects, which necessitates more input energy from the external load via continuous work and causes an increase in the associated characteristic stresses.

KEYWORDS

strain rate effects, characteristic stresses, acoustic emission, energy conversion, multi-scale defects

1 Introduction

Rock is a type of special solid material generated by long-term tectonic geological movement. It is heavily fractured and contains numerous joints, fissures, and microflaws. Consequently, when rock is subjected to a variety of loading conditions, such as different strain rates, confining pressures, or loading paths, its mechanical properties may significantly vary. This implies that investigating the relationship between external loading conditions and rock mechanical properties is crucial, as the results of this research can help us better comprehend the process of rock deformation and failure, as well as provide more precise mechanical parameters of rock for use in practical engineering designs.

According to the magnitude of the strain rate, loading conditions can be roughly categorized into five groups: creep loading, quasi-static loading, intermediate strain rate loading, high strain rate loading and ultra-high strain rate loading (Zhang and Zhao, 2014). It is commonly acknowledged that the mechanical characteristics and corresponding fracture process of brittle rock can be influenced by varying loading strain rates under quasi-static loading conditions, such as blasting, explosion and seismic stress (Brace and Jones, 1971; Lindholm et al., 1974; Lajtai et al., 1991; Zhao et al., 1999; Li et al., 2005; Li et al., 2014; Liang C. et al., 2015; Hokka et al., 2016). A series of laboratory tests on granite samples were conducted at loading strain rates ranging from $10^{-4}\ s^{-1}$ to $10^{0}\ s^{-1}$, and the results of these tests indicated that the compressive strength of rock samples increased with the increase of the strain rate and confining pressure, whereas elastic modulus and Poisson's ratio had no rate-dependence on loading strain rates (Li et al., 1999). When the loading strain rate exceeds $5 \times 10^{-4}\ s^{-1}$, Liang C. et al. (2015) found that the uniaxial compressive strength (UCS) of granite samples was dependent on strain rates. In addition, the uniaxial compressive strength of shale (Mahanta et al., 2018), marble (Li et al., 2014) and sandstone (Zhao Z. et al., 2021) exhibits a substantial dependence on strain rates, but the variation differs slightly from that of granite. The uniaxial compressive strength of rock, an essential parameter for evaluating rock mechanical characteristics, is a function of rock stress state (Martin and Chandler, 1994) and is easily affected by the size of rock samples, confining pressure, the shape of rock samples and other factors. Therefore, in addition to the uniaxial compressive strength of rock, characteristic stresses, including crack initiation stress, damage stress and failure stress, should be adopted to systematically analyze the strain rate effects on rock mechanical properties during rock deformation and failure. Wang C. et al. (2011) found that the varation between the crack initiation stress and damage stress of red sandstone samples and strain rates ranging from 10^{-6}-$10^{-3}\ s^{-1}$ was irregualr, while the ratio between the crack initiation stress and damage stress and the uniaxial compressive strength decreased as strain rates increased. Jaczkowski (2018) also determined that there was no significant relationship between the crack initiation stress, damage stress or uniaxial compressive strength of argillaceous limestone and axial strain rate. However, Liang C. Y. et al. (2015) discovered that the crack initiation stress, damage stress or uniaxial compressive strength of granite increased as strain rates increased, and silimar results were determined using grain-based finite-discrete element method (Li et al., 2020). In light of the aforementioned review of literature, a unified understanding of the variation of strain rate effects on charactersitic stress has not yet emerged, and the mechanism underlying these effects requires further investigation.

The essence of rock deformation and failure, from the viewpoint of thermodynamics, is the result of energy input, energy accumulation, and energy conversion (Xie et al., 2009). The input energy and elastic strain energy are typically calculated by integrating stress and strain, which can characterize the process of rock deformation and failure more comprehensively and systematically than stress or strain alone. Zhang et al. (2000) conducted dynamic compression tests on Gabbro samples and marble samples and discovered that rock samples can absorb more energy as strain rates increase. The greater the strain energy accumulated by rock samples under quasi-static compression prior to the peak point of the stress-strain curve, the greater the intensity of rock fracture (Li et al., 2014). Liang C. et al. (2015) provided an explanation for why rock samples can absorb more energy when strain rates increase: that is, at low strain rates, the predominant micro-fracture pattern of rock is the intergranular fracture, which consumes less energy. At the high strain rate, the process of energy input is rapid. Consequently, the transgranular fracture develops gradually. Due to the difficulty of the transgranular fracture, this mode will require more energy than the mode of the intergranular fracture. The variation trend of energy parameters of rock subjected to quasi-static compression is the primary focus of the aforementioned studies. Moreover, these studies are only limited to qualitative descriptions or simple data fitting between energy data, mechanical parameters, and strain rates, and there are a few investigations into the root cause of this phenomenon. In addition, the structural properties of multi-scale defects in rock have not been taken into account in the energy conversion during rock deformation and failure, necessitating further investigation.

Acoustic emission technology (AE), as an excellent approach for real-time and non-destructive monitoring of microscopic damage features, has been widely adopted in rock mechanics throughout recent decades (Lei et al., 2000; Cai et al., 2007; Meng et al., 2016; Wang et al., 2018). Several investigations have demonstrated that AE activities correlate well with the process of rock deformation and failure under quasi-static compression

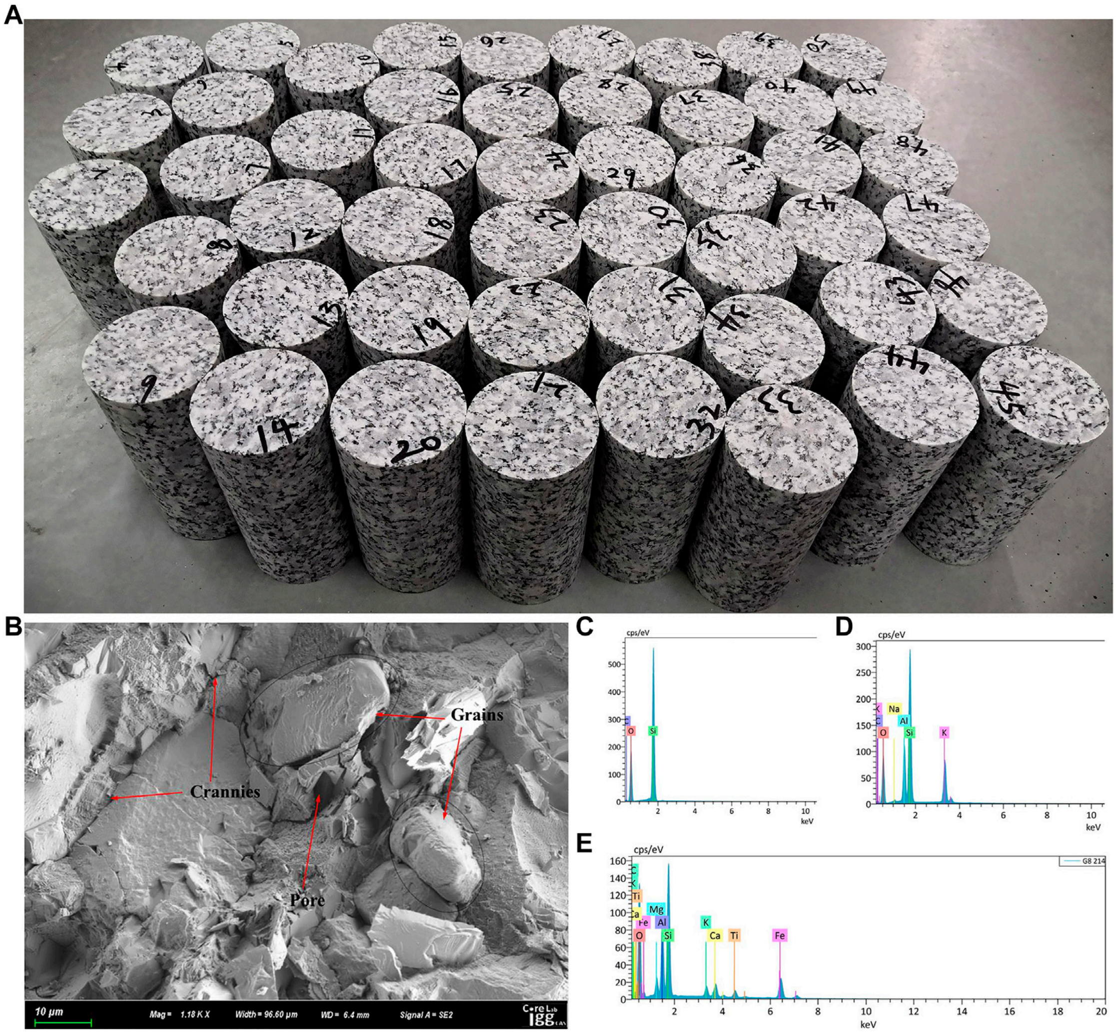

FIGURE 1
Rock samples. **(A)** Cylindrical specimens; **(B)** rock sample SEM; **(C)** quartz XRD; **(D)** potassium feldspar XRD; **(E)** biotite XRD.

(Sirdesai et al., 2018; Zhao Z. et al., 2021). AE events decrease as the strain rates increase (Zhang et al., 2017), while the maximum AE ring rate and the maximum AE energy rate correlate positively with strain rates (Zhao et al., 2018). Using the AE location technology, Zhao Z. et al. (2021) determined that under high strain rates, AE events of rock samples occurred predominately along the axial loading direction, and their spatial distribution was more dispersed than under low strain rates. Despite the fact that the current studies have yielded significant results regarding the AE characteristics at various strain rates, additional research into the spatial distribution of AE events and the mechanism underlying the strain rate effect on AE properties is necessary.

According to the above review, numerous studies on the strain rate effects of rock mechanical properties and AE features have been conducted under quasi-static compression. However, the energy conversion in the process of rock deformation and failure and the structural properties of multi-scale defects in rock are rarely considered when investigating the mechanism of the increase of characteristic stresses with increasing strain rates. In this paper, uniaxial compressive tests of different strain rates in the range from $10^{-6}\,\mathrm{s}^{-1}$ to $10^{-2}\,\mathrm{s}^{-1}$ were comprehensively performed to investigate the mechanical behaviors and AE characteristics of granite samples subjected to quasi-static compression. Then, the stress-strain curves of rock samples, characteristic stresses, energy data, and temporal and spatial distribution of AE events were analyzed. Finally, the mechanism underlying the increase of characteristic stresses with the increasing strain rates was discussed from the perspective of energy conversion and rock intrinsic properties.

TABLE 1 Physical parameters of rock samples.

Samples	Strain rate/s^{-1}	Diameter/mm	Height/mm	Quality/g	Volume/cm^3	Density/g.cm^{-3}
GS-1-1	1×10^{-6}	49.87	100.31	525.10	195.94	2.68
GS-1-2		49.81	100.20	526.30	195.25	2.70
GS-1-3		49.90	100.47	524.70	196.48	2.67
GS-2-1	1×10^{-5}	49.85	100.30	525.80	195.76	2.69
GS-2-2		49.87	100.45	524.30	196.21	2.67
GS-2-3		49.89	100.25	525.10	195.98	2.68
GS-3-1	5×10^{-5}	49.81	100.20	522.10	195.25	2.67
GS-3-2		49.88	100.33	526.20	196.05	2.68
GS-3-3		49.96	100.15	524.40	196.33	2.67
GS-4-1	1×10^{-4}	49.92	100.59	525.10	196.88	2.67
GS-4-2		49.87	100.56	525.80	196.42	2.68
GS-4-3		49.79	100.49	523.80	195.66	2.68
GS-5-1	5×10^{-4}	49.91	100.60	526.60	196.82	2.68
GS-5-2		49.92	100.40	524.50	196.50	2.67
GS-5-3		49.93	100.34	525.20	196.47	2.67
GS-6-1	7.5×10^{-4}	49.87	100.25	523.90	195.82	2.68
GS-6-2		49.91	100.41	525.10	196.45	2.67
GS-6-3		49.93	100.48	526.00	196.74	2.67
GS-7-1	1×10^{-3}	49.81	100.52	524.10	195.87	2.68
GS-7-2		49.92	100.49	524.60	196.68	2.67
GS-7-3		49.86	100.82	524.90	196.85	2.67
GS-8-1	2.5×10^{-3}	49.89	100.32	525.60	196.11	2.68
GS-8-2		49.85	100.69	524.00	196.52	2.67
GS-8-3		49.84	100.36	524.80	195.80	2.68
GS-9-1	5×10^{-3}	49.88	100.29	525.50	195.97	2.68
GS-9-2		49.94	100.46	526.40	196.78	2.68
GS-9-3		49.84	100.67	524.60	196.40	2.67
GS-10–1	7.5×10^{-3}	49.89	100.66	524.60	196.78	2.67
GS-10–2		49.81	100.60	523.60	196.03	2.67
GS-10–3		49.87	100.77	525.00	196.83	2.67
GS-11–1	1×10^{-2}	49.93	100.24	525.10	196.27	2.68
GS-11–2		49.94	100.52	525.10	196.90	2.67
GS-11–3		49.88	100.48	523.80	196.50	2.67

2 Rock samples and tests

2.1 Rock samples and testing system

The natural granite blocks were extracted from northern China, as shown in Figure 1A. It is noted from the microscopic structure in Figure 1B that the irregular mineral grains, tiny micro-pores and crannies are intertwined, which may have an effect on the macroscopic mechanical properties of granite samples. The X-ray Diffractometer (XRD) results of rock flakes are shown in Figures 1C–E, which represent quartz, potassium feldspar and biotite respectively, indicating that these minerals are the primary constituents of the testing samples. In accordance with the standard testing procedure of the International Society for Rock Mechanics (Kovari et al., 1983), the rock blocks were drilled and polished into cylindrical specimens measuring 50 mm in diameter and 100 mm in height, as shown in Figure 1A. The flatness of the specimen end surface must be less than 0.02 mm, and the parallelism of the upper and lower surfaces must be less than 0.05 mm. The physical parameters of rock samples were listed in Table 1, and the thirty-three processed specimens were randomly divided into eleven groups containing three specimens each. These specimens were numbered GS-1-1, GS-1-2, GS-1-3, GS-2-1, GS-2-2, and GS-2-3, etc., in accordance with the “GS-A-B″ naming convention.

As shown in Figure 2A, uniaxial compressive tests were conducted in the Key Laboratory of Rock Mechanics and

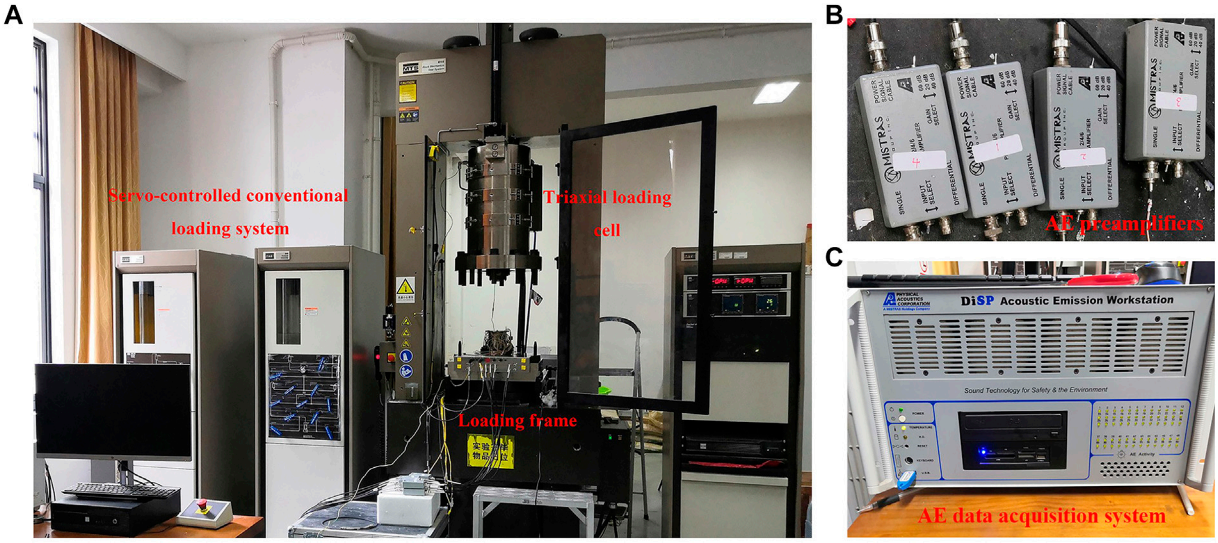

FIGURE 2
Schematic diagram of the testing system. **(A)** material testing system; **(B)** AE signals preamplifier; **(C)** AE signals acquisition system.

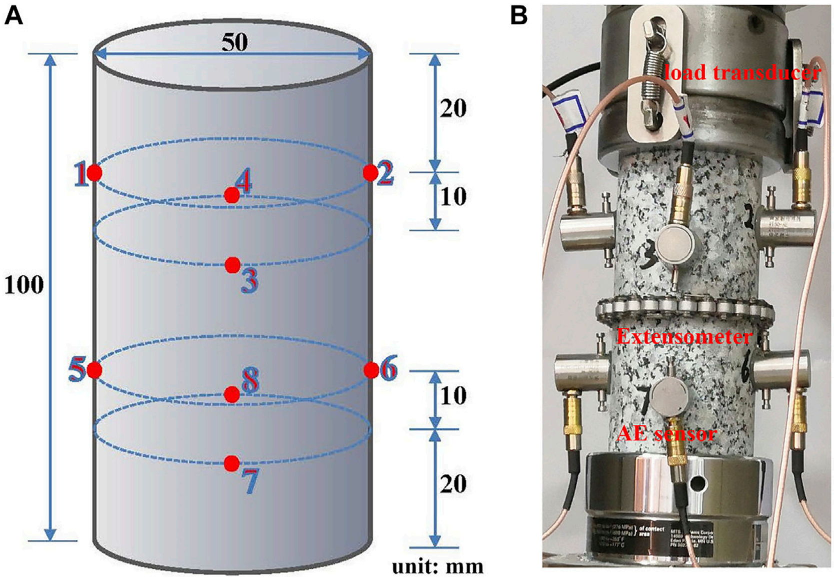

FIGURE 3
Schematic diagram of sensor installation. **(A)** The installation layout of AE sensors; **(B)** the layout of mechanical transducers.

Geohazards of Zhejiang Province using the mechanics testing system MTS815.04 with strain rates ranging from 10^{-6} s^{-1} to 10^{-2} s^{-1} over eleven levels. AE signals were acquired using a digital AE monitoring system (12CHsPCI-2) with 32 channels manufactured by Physical Acoustic Company, and this test utilized eight of these channels, as shown in Figures 2B,C.

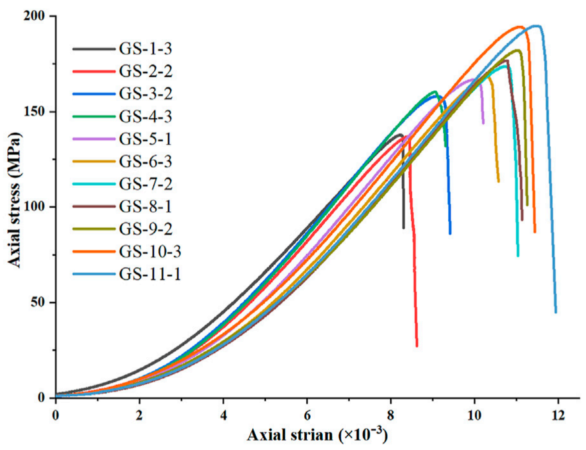

FIGURE 4
Stress-strain curves of a portion of granite samples at various strain rates.

2.2 Procedures for testing

The quasi-static strain rates utilized in this paper ranged from 10^{-6} s^{-1} to 10^{-2} s^{-1} and were divided into three stages containing eleven levels (Li et al., 2014; Liang C. et al., 2015). As shown in Table 1, testing was undertaken on three replicates for each strain rate level to reduce the dispersion of experimental results. The three stages of strain rates were as follows: The first stage of the strain rate consists of two levels ranging from 10^{-6} s^{-1} to 10^{-5} s^{-1}; the second stage of the strain rate has three levels: 10^{-5} s^{-1} to 5×10^{-4} s^{-1}; six levels comprise the third stage of the strain rate: 5×10^{-4} s^{-1} to 10^{-2} s^{-1}. Detailed procedures for testing include: First, eight AE sensors were adhered to the surface of the rock sample using hot adhesive according to the position designed in Figure 3A; Next, as illustrated in Figure 3B, the loading transducer and extensometer were mounted on the bottom and middle of the samples, respectively, ensuring that they did not come into contact with any AE sensors; Then, the acquisition parameters of the AE monitoring software were configured. In order to avoid erroneous interference from surrounding noise, the external amplifiers were set to 45 dB, which aided in amplifying the AE signals originating from the cracks within the rock samples. The operating frequency of the sensors was 300 kHz, and the sampling frequency was 1,000 kHz; Afterwards, 4 kN axial pre-stress was applied in the load-controlled mode of 0.5 kN per second, and then maintained for 30 s; Finally, uniaxial compressive tests of different strain rates were carried out at a loading rate ranging from 0.006 mm per minute to 60 mm per minute in displacement-controlled mode.

3 Experimental results and analysis

3.1 Stress-strain curves

Figure 4 depicted the stress-strain curves of rock at various strain rates, ranging from 10^{-6} s^{-1} to 10^{-2} s^{-1}. To make Figure 4 appear more concise, one sample was selected from three samples at each strain rate level. It can be observed that when strain rates increase, peak stress and associated strain also increase. However, despite the fact that rock samples are subjected to different strain rates, the shape of their stress-strain curves is essentially identical. In general, different shapes of rock's stress-strain curves can characterize various modes of rock deformation. Therefore, the above results mean that increasing the strain rate only increases the peak stress and other related mechanical parameters of rock samples, but does not change the fundamental mode of rock deformation.

3.2 Strain rate effects on characteristic stresses

The status of all micro-cracks within a compressed rock frequently determines its macroscopic mechanical properties. In other words, the process of rock deforamtion and failure is the process of microcrack development in rock (Liang C. et al., 2015). Thus, the process of rock deforamtion can be divided into five stages based on the process of microcracks development (Hoek and Bieniawski, 1965; Brace et al., 1966; Bieniawski, 1967; Martin and Chandler, 1994): 1) crack closure stage; 2) elastic stage; 3) stable crack growth stage; 4) unstable crack growth stage; 4) post-peak stage, as shown in Figure 5A. The division of each stage depends on three important stress thresholds, which are crack initiation stress σ_{ci}, damage stress σ_{cd}, and uniaxial compressive strength σ_p. Crack initiation, the oneset of dilation and the beginning of crack growth, is attributed to local tensile stress concentration at the tips of pre-existed flaws, inclusions and other heterogeneities (Li et al., 2020); hence, the axial stress corresponding to the onset of micro-cracks in rock was referred to as the crack initiation stress (Martin and Chandler, 1994). The axial stress level at which the total volumetric strain reversal occurs marks the beginning of the unstable crack growth stage (Bieniawski, 1967). In other words, the axial stress corresponding to the maximum value of the axial stress-volumetric strain curve was designated as the damage stress, or dilatancy stress. The uniaxial compressive strength of rock correpsonding to the maximum value of the axial stress-axial strain marks the beginning of post-peak stage.

The axial stress is the failure stress when rock loses its bearing capacity and appears to fail as a whole when subjected to external compression. The overall failure of rock samples was defined in this paper based on laboratory data as follows: when the external load exceeds the uniaxial compressive strength of rock samples,

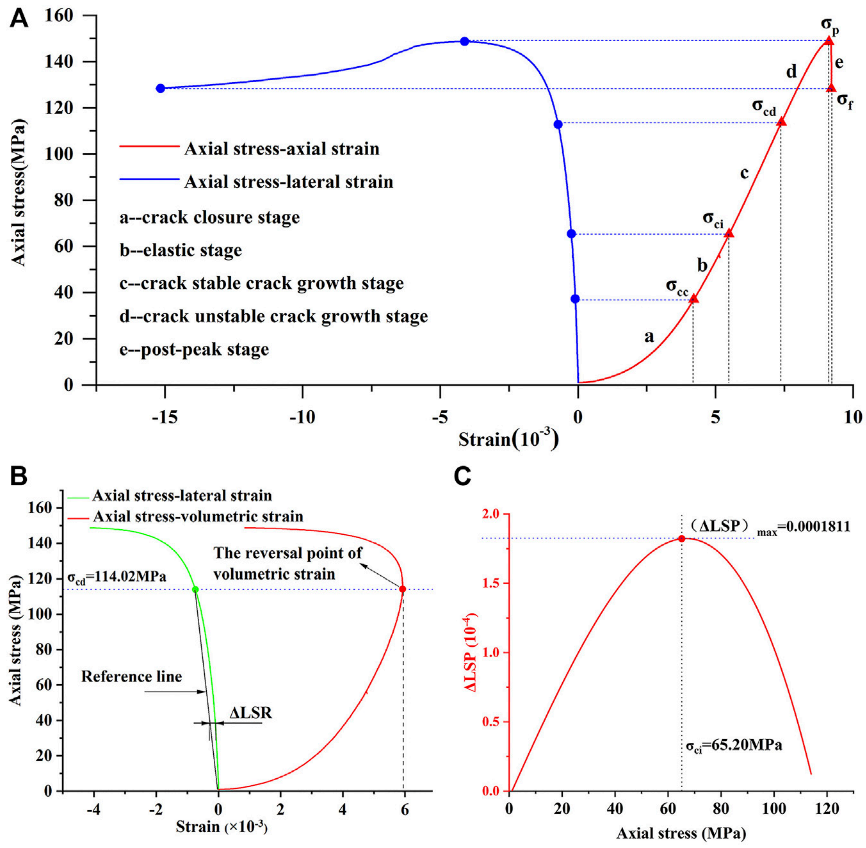

FIGURE 5
An example used to determine the crack initiation stress using the LSR method. **(A)** Stress-strain curves of the sample GS-2-3 (strain rate: 10^{-5} s^{-1}); **(B)** the curves of axial stress-strain; **(C)** the curve of △LSP-axial stress.

the drop of axial stress between two adjacent points of MTS loading transducers is more than 30%, and the corresponding lateral strain increases as well. At this point, the entire failure of rock samples can be considered, and the failure stress σ_f is the axial stress corresponding to this failure.

The value of crack initiation stress is difficult to determine in comparison to damage stress, uniaxial compressive strength and failure stress of rock. There are many methods to determine the value of crack initiation stress, including the crack volumetric strain method (Martin and Chandler, 1994), AE method (Zhao Z. et al., 2021), and the lateral strain response method (LSR method) (Nicksiar and Martin, 2012). In this paper, the LSR method was applied to determine the crack initiation stress, with the following procedures: First, determining the point of damage stress in the axial stress-lateral strain curve, as shown in Figure 5B; second, connecting the point of damage stress to the curve's origin as the reference line, as shown in Figure 5B; and third, drawing the curve based on the difference value between the curve of axial stress-lateral strain and the reference line, where the peak point of this curve corresponding to the axial stress is the crack initiation stress, as shown in Figure 5C.

The characteristic stresses of rock samples were determined using the aforementioned method, as shown in Table 2. Figure 6A depicted the relationship between three kinds of characteristic stresses and strain rates, including crack initiation stress, damage stress and uniaxial compressive strength of rock samples. It can be observed that the characteristic stresses are significantly strain rate-dependent, while there are differences in the magnitude and trend of the increase. The growth process of characteristic stresses corresponding to the strain rate can be divided into two stages: stage I and stage II, as shown in Figure 6A. When the strain rate is less than 10^{-4} s^{-1}, the crack initiation stress grows rapidly, but the stress increases slowly when the strain rate is greater than 10^{-4} s^{-1}. Nevertheless, the strain rate for the damage stress and uniaxial compressive corresponding to the preceding trend is 2.5×10^{-3} s^{-1}. Besides, the threshold strain rate between static loading and quasi-static loading should be mentioned as a key issue. There are numerous results for this value, such as

TABLE 2 Characteristic stresses of rock samples within different strain rates (σ_{ci}-crack initiation stress; σ_{cd}-damage stress; σ_p-uniaxial compressive stress; σ_f-failure stress).

Granite samples	Strain rate/s^{-1}	σ_{ci}/MPa	σ_{cd}/MPa	σ_p/MPa	σ_f/MPa	σ_{ci}/σ_p	σ_{cd}/σ_p	σ_{ci}/σ_{cd}
GS-1-1	1×10^{-6}	73.53	115.90	140.82	101.32	0.52	0.82	0.63
GS-1-2		77.99	115.50	136.89	79.80	0.57	0.84	0.68
GS-1-3		78.04	117.62	137.75	89.08	0.57	0.85	0.66
GS-2-1	1×10^{-5}	70.87	111.58	132.84	37.25	0.53	0.84	0.64
GS-2-2		70.02	112.09	136.98	59.79	0.51	0.82	0.62
GS-2-3		65.20	114.02	148.73	62.55	0.44	0.77	0.57
GS-3-1	5×10^{-5}	80.71	133.54	163.81	79.52	0.49	0.82	0.60
GS-3-2		65.52	120.16	158.14	86.22	0.41	0.76	0.55
GS-3-3		76.06	126.31	157.71	80.15	0.48	0.80	0.60
GS-4-1	1×10^{-4}	73.01	125.75	158.90	110.59	0.46	0.79	0.58
GS-4-2		86.36	134.97	167.54	143.72	0.52	0.81	0.64
GS-4-3		81.20	133.12	160.31	131.96	0.51	0.83	0.61
GS-5-1	5×10^{-4}	76.53	128.63	166.80	144.05	0.46	0.77	0.59
GS-5-2		75.38	129.07	162.53	131.27	0.46	0.79	0.58
GS-5-3		83.60	136.14	172.28	110.31	0.49	0.79	0.61
GS-6-1	7.5×10^{-4}	74.72	130.59	165.22	120.51	0.45	0.79	0.57
GS-6-2		85.33	134.59	163.74	108.76	0.52	0.82	0.63
GS-6-3		95.96	139.41	168.24	113.60	0.57	0.83	0.69
GS-7-1	1×10^{-3}	81.72	139.69	176.61	135.74	0.46	0.79	0.59
GS-7-2		87.49	139.67	173.67	121.31	0.50	0.80	0.63
GS-7-3		83.29	136.47	172.46	131.23	0.48	0.79	0.61
GS-8-1	2.5×10^{-3}	88.07	139.96	176.76	114.48	0.50	0.79	0.63
GS-8-2		83.27	141.46	180.93	143.37	0.46	0.78	0.59
GS-8-3		72.85	136.29	168.39	120.39	0.43	0.81	0.53
GS-9-1	5×10^{-3}	89.42	148.48	186.16	143.93	0.48	0.80	0.60
GS-9-2		88.59	144.75	182.11	160.20	0.49	0.79	0.61
GS-9-3		90.92	143.80	179.81	162.07	0.51	0.80	0.63
GS-10-1	7.5×10^{-3}	108.78	161.83	196.00	181.34	0.56	0.83	0.67
GS-10-2		94.90	148.15	174.78	127.67	0.54	0.85	0.64
GS-10-3		92.34	156.16	194.40	173.56	0.48	0.80	0.59
GS-11-1	1×10^{-2}	87.69	150.36	195.00	175.16	0.45	0.77	0.58
GS-11-2		58.12	140.38	178.44	157.82	0.33	0.79	0.41
GS-11-3		84.47	154.66	193.50	177.97	0.57	0.80	0.55

$10^{-5}\,s^{-1}$ (Zhang and Zhao, 2014), $5 \times 10^{-4}\,s^{-1}$ (Liang C. et al., 2015), $10^{-3}\,s^{-1}$ (Tarasov, 1990). However, comparing the variation of damage stress and the uniaxial compressive strength of rock samples in Figure 6B, a noticeable increase in the stresses occurred between $10^{-5}\,s^{-1}$ and $5 \times 10^{-5}\,s^{-1}$, and the increments for damage stress and uniaxial compressive strength are 12.29 and 20.36 MPa, respectively, which are the maximum increments between the adjacent strain rate level in this test. Therefore, it may be inferred that the threshold strain rate of granite between static loading and quasi-static loading was $5 \times 10^{-5}\,s^{-1}$.

The variation of the averaged characteristic stresses with the logarithm of strain rates at each level of strain rates was shown in Figure 6B. In the quasi-static strain rates ranging from $10^{-6}\,s^{-1}$ to $10^{-2}\,s^{-1}$, a linear relation can be expressed between the averaged characteristic stresses and the logarithm of strain rates, as illustrated in Figure 6B and Table 3. It can be seen that the damage stress and the uniaxial compressive strength both show a strong linear correlation with strain rates, and their mean values increase by approximately 32.79 and 50.49 MPa, respectively, as the strain rate rises from $10^{-6}\,s^{-1}$ to $10^{-2}\,s^{-1}$. However, the crack initiation stress presents a weak linear correlation with the logarithm of strain rates, and the correlation coefficient is only 76%, whereas the corresponding values for the damage stress and the uniaxial compressive strength are 85 and 96%, respectively.

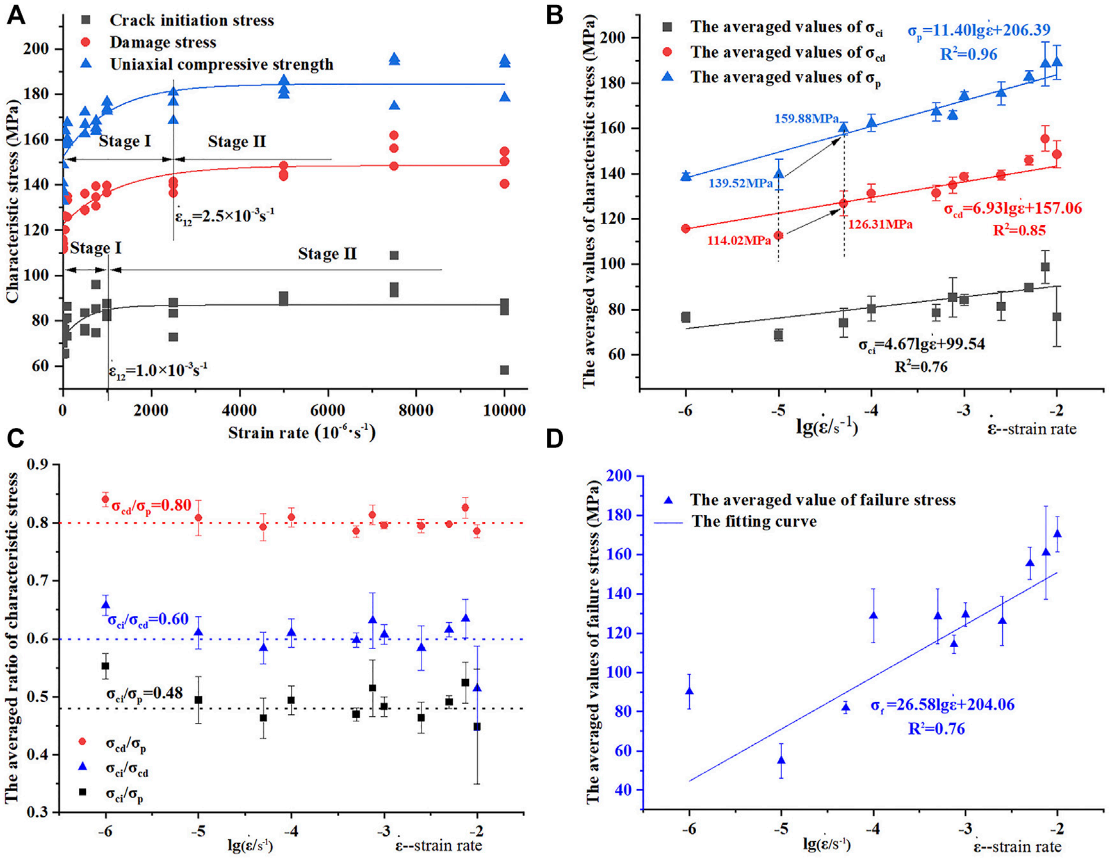

FIGURE 6
The relationship between characteristic stresses and strain rates. **(A)** The variation trend of characteristic stresses with the increase of strain rates; **(B)** the linear fitting of characteristic stresses versus the denary logarithm of strain rates; **(C)** the averaged ratios of characteristic stresses versus the denary logarithm of strain rates; **(D)** the linear fitting of the averaged failure stress versus the denary logarithm of strain rates (error bars at each data point represent the standard deviations).

TABLE 3 Fitting equations of characteristic stresses with the logarithm of strain rates.

Characteristic stress	Fitting equation	Correlation coefficient (R^2)
Crack initiation stress	$\sigma_{ci} = 4.67lg\dot{\varepsilon} + 99.54$	0.76
Damage stress	$\sigma_{cd} = 6.93lg\dot{\varepsilon} + 157.06$	0.85
Uniaxial compressive strength	$\sigma_p = 11.40lg\dot{\varepsilon} + 206.39$	0.96
Failure stress	$\sigma_f = 26.58lg\dot{\varepsilon} + 204.06$	0.76

Furthermore, the averaged values of the crack initiation stress only increased from 76.52 to 76.76 MPa as the strain rate rises from 10^{-6} s^{-1} to 10^{-2} s^{-1}, indicating that the strain rate had a minimal effect on the crack initiation stress within the spectrum of quasi-static strain rates. The definition of crack initiation stress is that the stress corresponds to the time when the micro-cracks begin to initiate, so this stress can reflect the condition of native defects or micro-cracks in rock. Consequently, the intrinsic properties of rock may have a greater impact on the crack initiation stress than external factors, such as the strain rate.

Figure 6C depicted the ratio of characteristic stresses to the denary logarithm of strain rates. It can be observed that, with the increase of the strain rates, the characteristic stress ratios neither exhibit a linear increase like the characteristic stresses, nor a clear downward trend, but instead fluctuate up

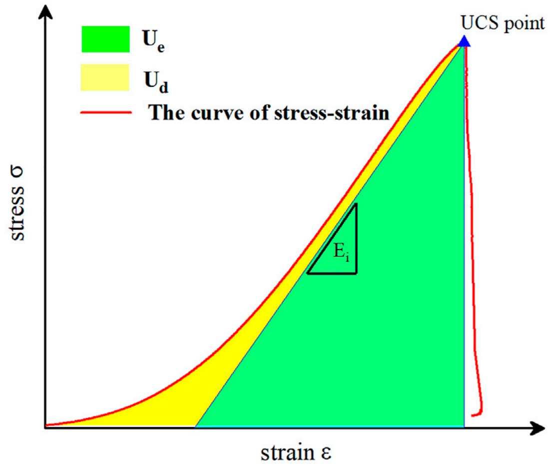

FIGURE 7
The relationship between elastic strain energy and dissipated energy.

and down a value, with σ_{ci}/σ_p, σ_{ci}/σ_{cd} and σ_{cd}/σ_p having values of 0.48, 0.60, and 0.80, respectively. This indicates that the strain rate has a significant effect on the magnitude of the values of characteristic stresses but a negligible effect on the ratios. Thus, it can be inferred that the ratio of characteristic stresses can be used to characterize the fundamental mode of rock deformation since strain rate does not change the mode when rock is under quasi-static compression, just like the shape of the stress-strain curves. In addition, the optimum option is the ratio between damage stress and uniaxial compressive strength if selecting one of those ratios to characterize the mode of rock deformation, because the deviation of σ_{cd}/σ_p is less than that of the other two ratios.

Figure 6D depicted the relationship between the averaged values of failure stress and the logarithm of strain rates. It can be seen that the averaged failure stress shows a certain rate of sensitivity, and as the strain rate increases, the averaged failure stress also increases. The reason for this increasing trend can be attributed to the diffrence in crack propogation speeds at various strain rates. Rock deformation will enter the post-peak stage once the external force exceeds its uniaxial compressive strength, as shown in Figure 5A. At this stage, the macroscopic fracture plane of rock is forming, resulting in the instability of elastic strain energy stored in rock. The higher the loading strain rate, the faster the crack propagation speed (Alneasan and Behnia, 2021), and thus, the formation speed of rock's fracture plane increases as strain rates rise. This implies that the time between the UCS point and the failure point decreases as strain rates increase, which is supported by experimental results: the time for $10^{-6}\ s^{-1}$ is 109.33 s, whereas the time for $10^{-2}\ s^{-1}$ is only 0.013 s. As a result, the stress drop between the UCS point and the failure point of rock decreases as the time between these two points decreases, causing the failure stress to increase as strain rates increase. On the other hand, the increase of failure stress as strain rates increase exhibits greater dispersion than the increase in damage stress or uniaxial compressive strength. The reason for this variation is that once the loading process exceeds the UCS point, the state of rock samples becomes unstable. In this condition, the overall failure of rock may occur at any time due to a minute change in external conditions or the coalescence of internal cracks. It is therefore reasonably straightforward to predict the mechanical characteristics before the UCS point when rock samples are subjected to quasi-static compression, whereas it is difficult and quite random to predict rock failure.

3.3 Energy conversion characteristics in the process of rock deformation and failure

The energy in the process of rock deformation and failure consists of three parts: input energy, elastic strain energy and dissipated energy. According to the first law of thermodynamics, the relationship between these three parts is shown in Eq. 1 and Figure 7:

$$U = U_e + U_d \tag{1}$$

Where U is the input energy; U_e is the elastic energy; U_d is the dissipated energy.

The value of input energy can be calculated under uniaxial compression using Eq. 2 (Solecki and Conant, 2003). Combining Eqs 3, 4, the value of elastic strain energy can be expressed as the middle part of Eq. 4. Due to the fact that there is little difference between the unloading elastic modulus and the loading modulus of rock under unxiaxial compression, E_i in the middle part of Eq. 4 can be replaced by E (David et al., 2020). Thus, the elastic strain energy of rock can be calculated by the right part of Eq. 4. The dissipated energy can be expressed as Eq. 6:

$$U = \int_0^\varepsilon \sigma d\varepsilon \tag{2}$$

$$U_e = \frac{1}{2}\sigma\varepsilon^e \tag{3}$$

$$\varepsilon^e = \frac{1}{E_i}\sigma \tag{4}$$

$$U_e = \frac{\sigma^2}{2E_i} = \frac{\sigma^2}{2E} \tag{5}$$

$$U_d = U - U_e \tag{6}$$

Where σ and ε are the stress and strain, respectively; ε^e is the total elastic strain; E_i is the unloading modulus; E is the loading modulus, as illustrated in Figure 7.

TABLE 4 The energy values at different stress points (enery unit: J/cm^3).

Granite samples	Strain rate/s^{-1}	Crack initiation stress point (σ_{ci})			Damage stress point (σ_{cd})			Uniaxial compressive strength point (σ_p)			Failure stress point (σ_f)		
		U	U_e	U_d	U	U_e	U_d	U	U_e	U_d	U	U_e	U_d
GS-1-1	1×10^{-6}	0.165	0.116	0.049	0.341	0.289	0.052	0.496	0.426	0.070	0.510	0.221	0.289
GS-1-2		0.174	0.128	0.045	0.328	0.281	0.047	0.458	0.395	0.064	0.469	0.134	0.335
GS-1-3		0.165	0.127	0.038	0.318	0.278	0.040	0.458	0.395	0.064	0.470	0.165	0.305
GS-2-1	1×10^{-5}	0.137	0.102	0.034	0.288	0.253	0.035	0.411	0.359	0.052	0.464	0.028	0.436
GS-2-2		0.132	0.097	0.036	0.285	0.248	0.037	0.439	0.370	0.068	0.457	0.071	0.386
GS-2-3		0.116	0.082	0.034	0.287	0.250	0.037	0.511	0.425	0.086	0.532	0.075	0.457
GS-3-1	5×10^{-5}	0.161	0.123	0.038	0.375	0.336	0.039	0.584	0.505	0.079	0.612	0.119	0.493
GS-3-2		0.115	0.082	0.033	0.311	0.275	0.036	0.569	0.477	0.092	0.611	0.142	0.470
GS-3-3		0.149	0.111	0.038	0.346	0.305	0.041	0.565	0.476	0.089	0.591	0.123	0.468
GS-4-1	1×10^{-4}	0.144	0.102	0.042	0.348	0.303	0.045	0.578	0.483	0.095	0.607	0.234	0.373
GS-4-2		0.184	0.140	0.044	0.388	0.341	0.047	0.623	0.526	0.098	0.640	0.387	0.253
GS-4-3		0.161	0.123	0.038	0.371	0.331	0.040	0.555	0.480	0.075	0.594	0.325	0.269
GS-5-1	5×10^{-4}	0.157	0.113	0.044	0.364	0.318	0.046	0.647	0.535	0.113	0.685	0.399	0.286
GS-5-2		0.159	0.110	0.048	0.374	0.323	0.051	0.605	0.512	0.092	0.650	0.334	0.316
GS-5-3		0.176	0.133	0.043	0.396	0.352	0.045	0.656	0.563	0.093	0.705	0.231	0.474
GS-6-1	7.5×10^{-4}	0.174	0.112	0.062	0.411	0.342	0.069	0.670	0.548	0.122	0.698	0.291	0.407
GS-6-2		0.191	0.140	0.051	0.401	0.349	0.053	0.618	0.516	0.102	0.664	0.228	0.437
GS-6-3		0.232	0.177	0.055	0.430	0.374	0.056	0.651	0.544	0.107	0.685	0.248	0.437
GS-7-1	1×10^{-3}	0.176	0.126	0.050	0.421	0.369	0.052	0.714	0.590	0.123	0.760	0.349	0.411
GS-7-2		0.206	0.148	0.058	0.438	0.377	0.060	0.703	0.584	0.119	0.740	0.285	0.455
GS-7-3		0.204	0.137	0.067	0.438	0.367	0.071	0.708	0.586	0.122	0.735	0.339	0.396
GS-8-1	2.5×10^{-3}	0.205	0.147	0.058	0.432	0.372	0.060	0.709	0.593	0.115	0.761	0.249	0.512
GS-8-2		0.192	0.130	0.061	0.442	0.377	0.065	0.743	0.616	0.127	0.783	0.387	0.396
GS-8-3		0.174	0.106	0.068	0.451	0.372	0.079	0.685	0.568	0.117	0.718	0.290	0.428
GS-9-1	5×10^{-3}	0.220	0.154	0.066	0.493	0.423	0.069	0.788	0.665	0.122	0.840	0.398	0.443
GS-9-2		0.217	0.151	0.066	0.473	0.403	0.070	0.760	0.637	0.122	0.788	0.493	0.294
GS-9-3		0.236	0.162	0.074	0.483	0.405	0.078	0.768	0.634	0.134	0.802	0.515	0.288
GS-10–1	7.5×10^{-3}	0.286	0.220	0.066	0.555	0.486	0.068	0.852	0.713	0.139	0.878	0.611	0.267
GS-10–2		0.252	0.174	0.078	0.507	0.425	0.082	0.704	0.592	0.112	0.765	0.316	0.449
GS-10–3		0.220	0.159	0.061	0.520	0.455	0.065	0.848	0.705	0.143	0.893	0.562	0.331
GS-11–1	1×10^{-2}	0.204	0.145	0.059	0.490	0.426	0.064	0.857	0.717	0.140	0.900	0.579	0.321
GS-11–2		0.108	0.062	0.046	0.427	0.364	0.064	0.698	0.588	0.110	0.722	0.460	0.262
GS-11–3		0.219	0.150	0.069	0.572	0.504	0.068	0.873	0.789	0.083	0.894	0.668	0.227

The energy values at the crack initiation stress point, damage stress point, UCS point and failure stress point were determined using the method described above, as shown in Table 4. Figure 8 depicted the energy values at various characteristic stress points in relation to the denary logarithm of strain rates. The results indicate that as strain rates increase, the variations of input energy, elastic strain energy and dissipation energy are drastically different at various characteristic stress points. The values of input energy and elastic strain energy at the crack initiation stress point greatly fluctuate as stain rates increase and essentially do not exhibit any rate-dependence, as shown in Figure 8A. However, the variation of input energy and elastic strain energy at the damage stress point and UCS point exhibit a positive correlation with the logarithm of strain rates when the strain rate exceeds 10^{-5} s^{-1}, as shown in Figures 8B,C. The dissipated energy prior to the UCS point varies little with the increase of strain rates, and the values at the crack initiation stress point, damage stress point and UCS point are significantly less than the corresponding values of elastic energy. A hypothesis can be derived from the analysis presented above: the values of elastic strain energy are substantially greater than the dissipated energy prior to the UCS point, indicating that elastic strain energy may

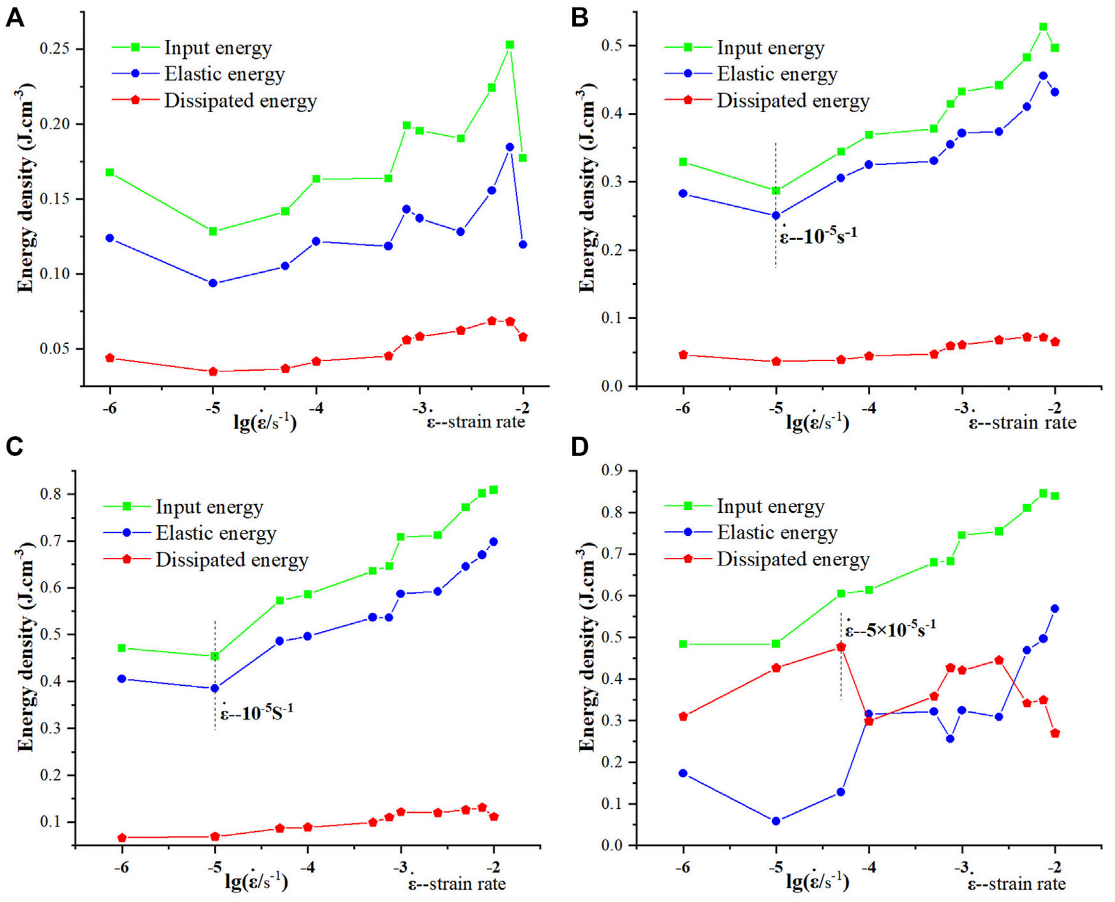

FIGURE 8
The energy values at different characteristic stress points versus the denary logarithm of strain rates. **(A)** Crack initiation stress; **(B)** damage stress; **(C)** uniaxial compressive strength; **(D)** failure stress.

govern the deformation process of rock before the UCS point, which may be the primary reason for brittle deformation of granite. The input energy and elastic strain energy at the failure stress point continue to exhibit a positive correlation with the logarithm of strain rates, similar to the trend at the damage stress point and UCS point, whereas the variation in the dissipated energy is completely different from the previous trend, as shown in Figure 8D. This difference is reflected in two aspects: First, the values of the dissipated energy at various strain rates are 2–14 times greater than the dissipated energy at the crack initiation stress point, damage stress point and UCS point; second, the dissipated energy increases as strain rates increase when the strain rate is less than $5 \times 10^{-5}\ \text{s}^{-1}$ and reaches its maximum at this strain rate. Then, the value of the dissipated energy greatly fluctuates as stain rates increase and essentially shows no rate dependence once the strain rate exceeds $5 \times 10^{-5}\ \text{s}^{-1}$.

The input energy generated by work performed by an external force is primarily converted into two components: elastic strain energy stored in rock and dissipated energy through crack initiation, crack propagation, friction heat, etc. Thus, the faster the external force is applied, or the higher the strain rate, the input energy is greater. Figure 9 depicted the relationship between input energy and elastic strain energy at different characteristic stress points. The relationship between input energy and elastic strain energy can be fitted by the linear equation, as depicted by the red lines in Figure 9, and the correlation coefficients of linear equations for the crack initiation stress point, damage stress point and UCS point are 0.94, 0.99, and 0.98, respectively, indicating a strong linear correlation between input energy and elastic strain energy. The slope of the linear equations in Figure 9 is 0.74, 0.84, and 0.83, respectively, representing the ratios of energy conversion between input energy and ealstic strain erergy (Gong et al., 2019a; Gong et al., 2019b). Based on this, energy conversion ratio was defined, and in Figure 10, K_a, K_b, and K_c represent the respective ratios at different characteristic stress points. As shown in Figure 10, the energy conversion ratio at stage III increased

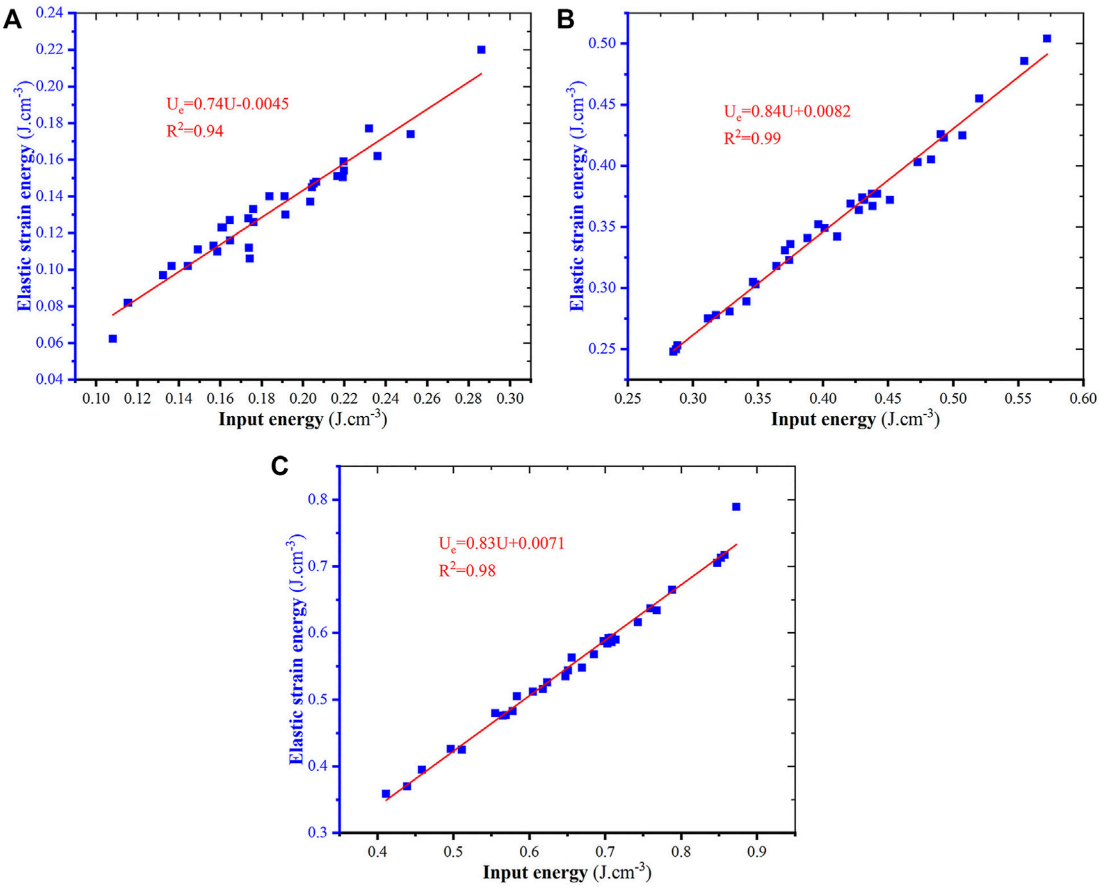

FIGURE 9
The relationship between the input energy and elastic strain energy at different characteristic stress points **(A)** crack initiation stress; **(B)** damage stress; **(C)** uniaxial compressive strength.

from 0.74 to 0.84, despite the fact that this stage may dissipate more input energy than the ealstic stage. More energy is dissipated at stage IV due to the crack propagation and coalescence, resulting in the energy conversion ratio decreasing from 0.84 to 0.83, but the decline is only 1.1%, indicating that unstable crack growth does not alter the primary mode of energy conversion. Therefore, it can be concluded that, although the energy conversion ratios differ prior to the UCS point, the values are all greater than 0.74 and that the input energy is primarily stored as elastic strain energy in rock during the pre-peak stage. When the stress exceeds the UCS point of rock, its deformation enters into the post-peak stage, and the dissipated energy increases sharply due to the formation of the macro-fracture surface, as shown in Figure 8D. The dissipated energy at the strain rate level of 5 × 10^{-5} s^{-1} even increased 13.12 times, 12.37 times and 5.54 times, respectively, than the dissipated energy at the crack initiaiton stress point, damage stress point and UCS point, indicating that the primary characteristic of energy conversion during the post-peak stage is the dissipated energy transferred from the elastic strain energy stored in rock. Nonetheless, this stage only lasts a brief period, and its duration decreases as the strain rate increases. Finally, the elastic strain energy stored in rock is abruptly released when rock fails, accompanied by the ejection of rock fragments and loud noises. Based on the analysis of energy conversion features at different deforamtion stages, it can be concluded that the energy conversion process of rock under quasi-static compression can be divided into three stages: energy accumulation, energy dissipation, and energy release, respectively, as shown in Figure 10, which differs from other rock types, such as mudstone (Zhang et al., 2020), sandstone (Zhao H. et al., 2021).

3.4 Acoustic emission properties

Rock deformation and failure are always accompanied by the release of strain energy in the form of elastic waves, which

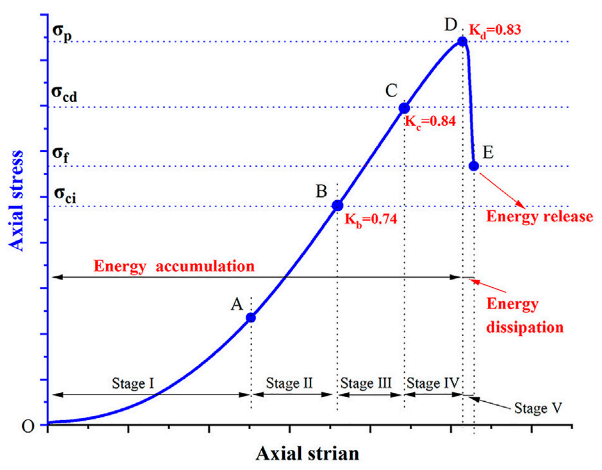

FIGURE 10
The typical stress-strain curve of granite: stage I (OA)—crack closure stage; stage II (AB)—elastic stage; stage III (BC)—stable crack growth stage; stage IV (CD)—unstable crack growth stage; stage V (ED)—post-peak stage.

is referred to as acoustic emission (Meng et al., 2016). With five different strain rates as represented strain rates, as depicted in Figure 11, it is evident that the AE energy rate around different characteristic stress points varies significantly. The values of the AE energy rate around the crack initiaiton stress point and damage stress point are in the tens to hundreds when strain rates range from 10^{-6}-10^{-3} s^{-1}, as depicted by the enlarged figures in Figures 11A–D. However, the value around the UCS point is three to four orders of magnitude greater than the above two characteristic stress points, increasing to hundreds of thousands or even millions, indicating the number and magnitude of AE events occurred around the crack initiation stress and damage stress ponit being greatly lower than that around the UCS point. There is a strong correlation between AE activity and the process of crack development (Sirdesai et al., 2018). Thus, this difference implies that the internal damage caused by crack propagation and crack coalescence occurs primarily near the UCS point, reflecting the brittle characteristics of granite deformation and failure. In addition, there is an obvious increase of AE energy rate around the crack initiation stress point and damage stress point when the strain rate is 10^{-2} s^{-1}, as depicted by the enlarged figures in Figure 11E, indicating that the AE events or magnitudes resulting from the cracking development are beginning to increase. Nonetheless, as the strain rate is 10^{-2} s^{-1}, the maximum value of AE energy rate around the UCS point is roughly dozens of times greater than that around the crack initiation stress point and damage stress point. This means that when the strain rate increase from 10^{-6} to 10^{-2} s^{-1}, the mode of crack development does not fundamentally change.

Figure 12 depicted the spatial location and energy intensity of AE events at different deformation stages and strain rates. It can be observed that the number of the located AE events varies significantly under various strain rates or at different deformation stages. Table 5 depicted the statistical results from Figure 12. There is a great difference in the total number of the located AE events between 10^{-6} s^{-1} and 10^{-5} s^{-1}, but energy rate varies little between 10^{-6} s^{-1} and 10^{-5} s^{-1}, as shown in Figures 11A,B. This difference can be explained by the AE location principle. In order to confirm the spatial location of an AE event, at least four sensors in different positions that can receive the AE signal are necessary to determine the event's three-dimensional coordinates and arrival time. Consequently, the AE events with a low magnitude may lack sufficient energy to propagate over a greater distance, preventing them from being received by more than four sensors and preventing the AE monitoring system from locating them. Based on the above principle, it is concluded that the number of low-magnitude AE events of 10^{-6} s^{-1} is greater than that of 10^{-5} s^{-1}, and this quantitative variation may be indicative of a transition from 10^{-6} s^{-1} to 10^{-5} s^{-1} in the rock's microscopy failure pattern. The total number of the located AE events decreases as strain rates increase when the strain rate exceeds 10^{-5} s^{-1}. It is noted that when the strain rate exceeds 7.5×10^{-3} s^{-1}, the number of the located AE events is less than 10. This variation may be due to the high loading strain rate and the limitation of the AE sensors' resonant frequency. The loading time is only 2.22 and 1.17 s, corresponding to 7.5×10^{-3} s^{-1} and 10^{-2} s^{-1}, respectively, and the resonant frequency of AE sensors is 300 kHz. Even though a large number of AE events can occur in a short period of time, the acquisition mode of the AE sensor is time-triggered and it takes a certain amount of time to receive an AE signal. This means that AE monitoring system can only receive the limited number of AE signal during the given time period. In addition, more than four sensors must receive the signal simultaneously for an AE event to be located, which further increases the difficulty of determining the spatial location of an AE event under high strain rate loading. Obviously, the solution to this issue is to use a more sensitive AE sensor, which is also the direction of future research. It is also possible to conclude that 10^{-5} s^{-1} is the optimal strain rate for acoustic emission testing of granite samples, given that the number of the located AE events is greatest for this strain rate in the range of 10^{-6} s^{-1} to 10^{-2} s^{-1}. In comparison to the difference in the number of the located AE events at different deformation stages, it is found that the majority of located AE events occur during the unstable crack growth stage and prior to the crack initiation stress. In general, almost no AE activity is present during the elastic stage. Thus, it can be concluded that the majority of located AE events occur during the crack closure stage and unstable crack growth

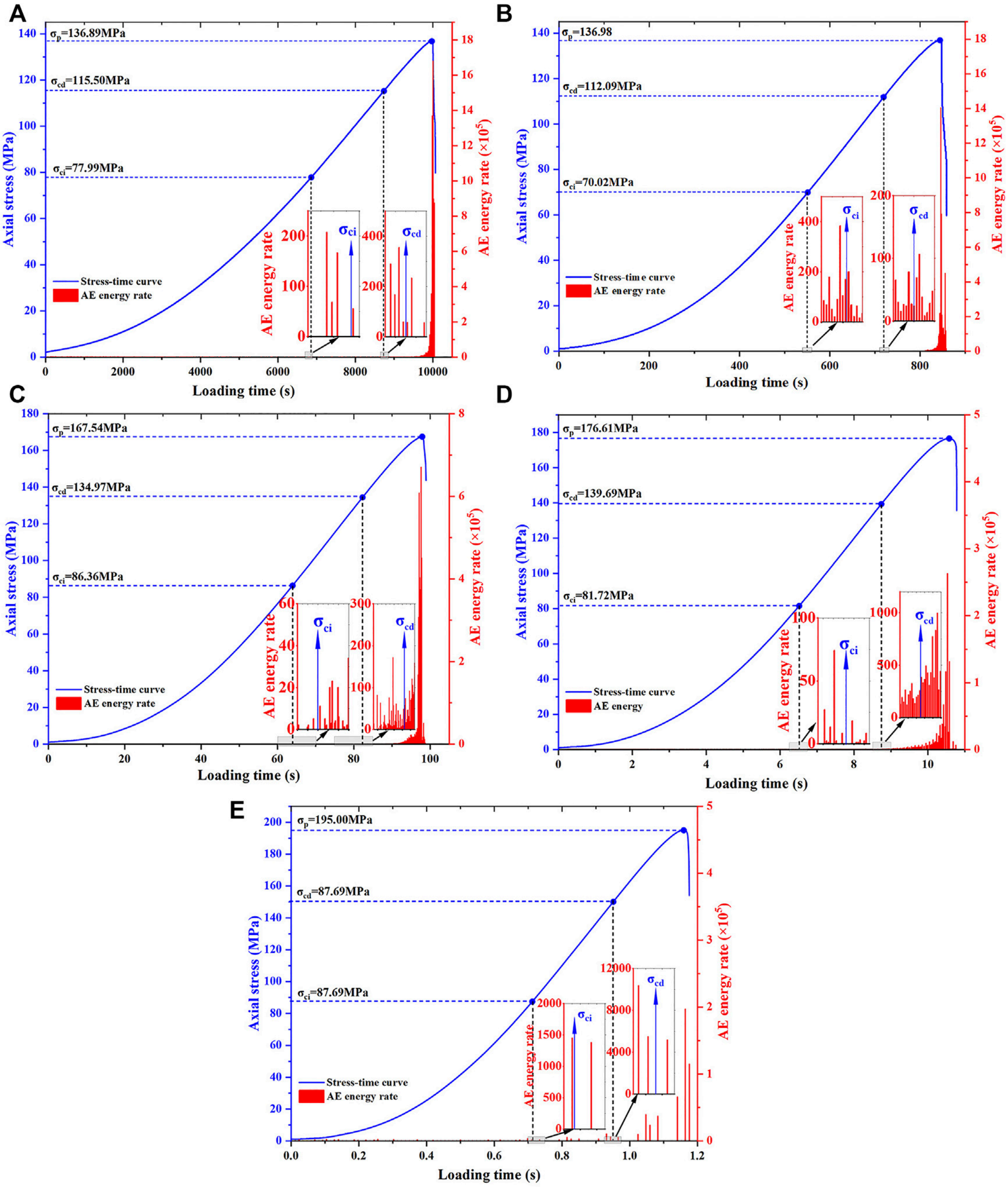

FIGURE 11
AE energy rate and stress versus loading time under different strain rates. **(A)** 1 × 10^{-6} s^{-1}; **(B)** 1 × 10^{-5} s^{-1}; **(C)** 1 × 10^{-4} s^{-1}; **(D)** 1 × 10^{-3} s^{-1}; **(E)** 1 × 10^{-2} s^{-1}.

stage. The AE events during the crack closure stage are frictional AE caused by the closure of original cracks and friction between the particles of rock, where the AE events during the unstable crack growth stage are cracking AE produced by the new failure extension or dislocation (Wang X. et al., 2011).

4 Discussion

The preceding analysis of experimental results suggests that characteristic stresses exhibited a positive correlation with strain rates, with this correlation being relatively high for damage stress and uniaxial compressive strength, but

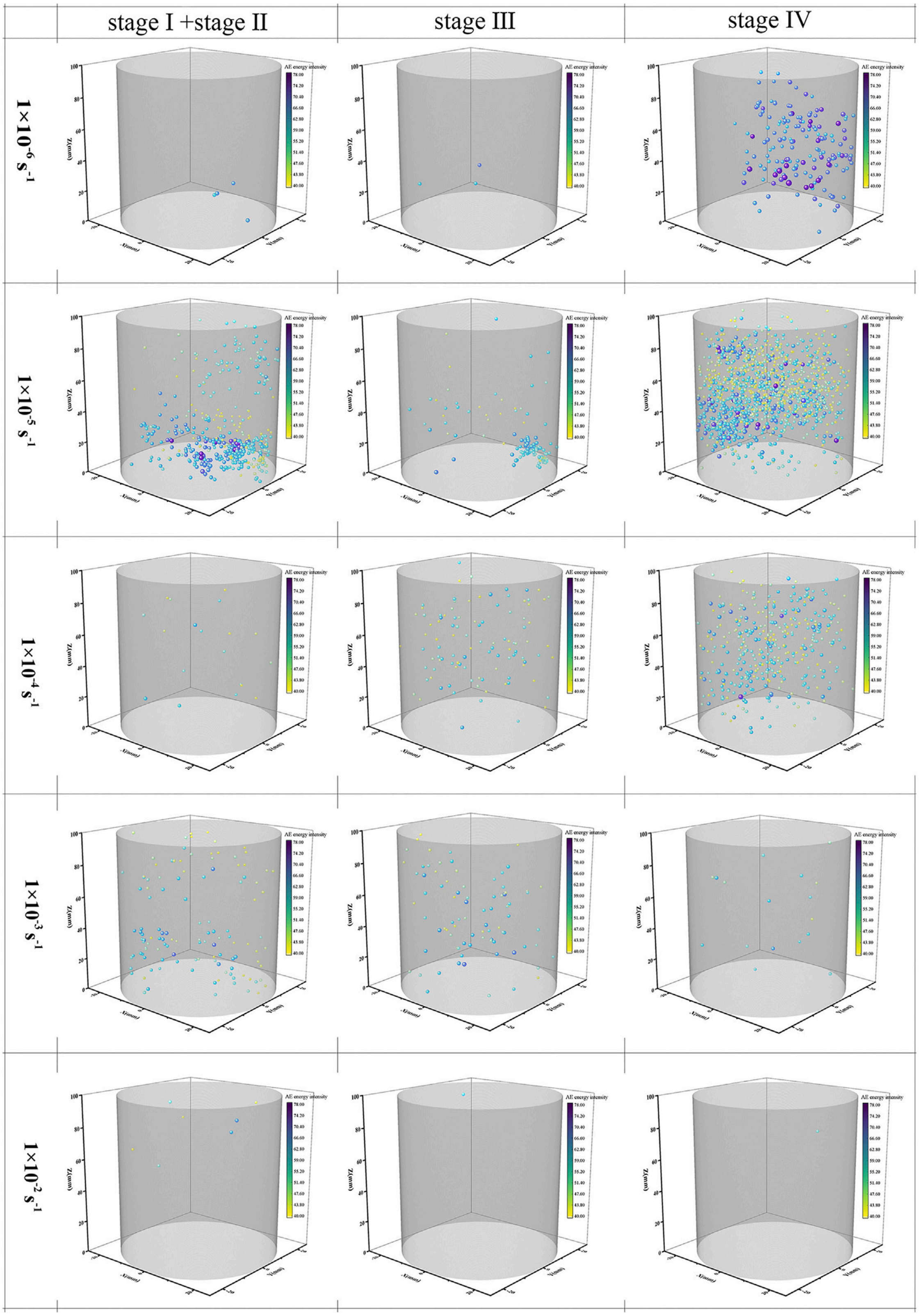

FIGURE 12
Spatial distribution and energy intensity of the located AE events at different deformation stages under various strain rates: stage I– crack closure; stage II– elastic stage; stage III– stable crack growth; stage IV– unstable crack growth.

TABLE 5 The number of the located AE events at different deformation stages and various strain rates before the UCS point.

Stain rate (s^{-1})	The number of the located AE events			
	Stage I+II	Stage III	Stage IV	Total
1×10^{-6}	4	3	165	172
1×10^{-5}	497	149	1,338	1984
5×10^{-5}	645	59	692	1,396
1×10^{-4}	20	105	389	514
5×10^{-4}	110	36	95	241
7.5×10^{-4}	201	144	90	435
1×10^{-3}	131	86	17	234
2.5×10^{-3}	27	27	20	74
5×10^{-3}	49	16	9	74
7.5×10^{-3}	2	1	2	5
1×10^{-2}	7	1	1	9

relatively low for crack initiation stress. There are several explanations for this increasing trend, such as the thermal reactivation effect (Qi et al., 2009), the micromechanics-based effect (Zhang and Zhao, 2014), the Stefan effect (Rossi, 1991), energy dissipation (Pan, 2017) and the inertia effect (Ožbolt et al., 2011). These perspectives revealed the mechanisms of the rock's rate effect to some extent, whereas we argue the explanation for why the characteristic stresses of rock increase with increasing strain rates should depend on the rock's intrinsic properties and the perspective of energy conversion.

Figure 13 depicted the relationship between characteristic stresses and input energy. The correlation coefficients for the linear positive relationship between three kind of characteristic stresses and their corresponding input energy are 0.91, 0.93, and 0.97, respectively, indicating that there is a strong positive correlation between characteristic stress and

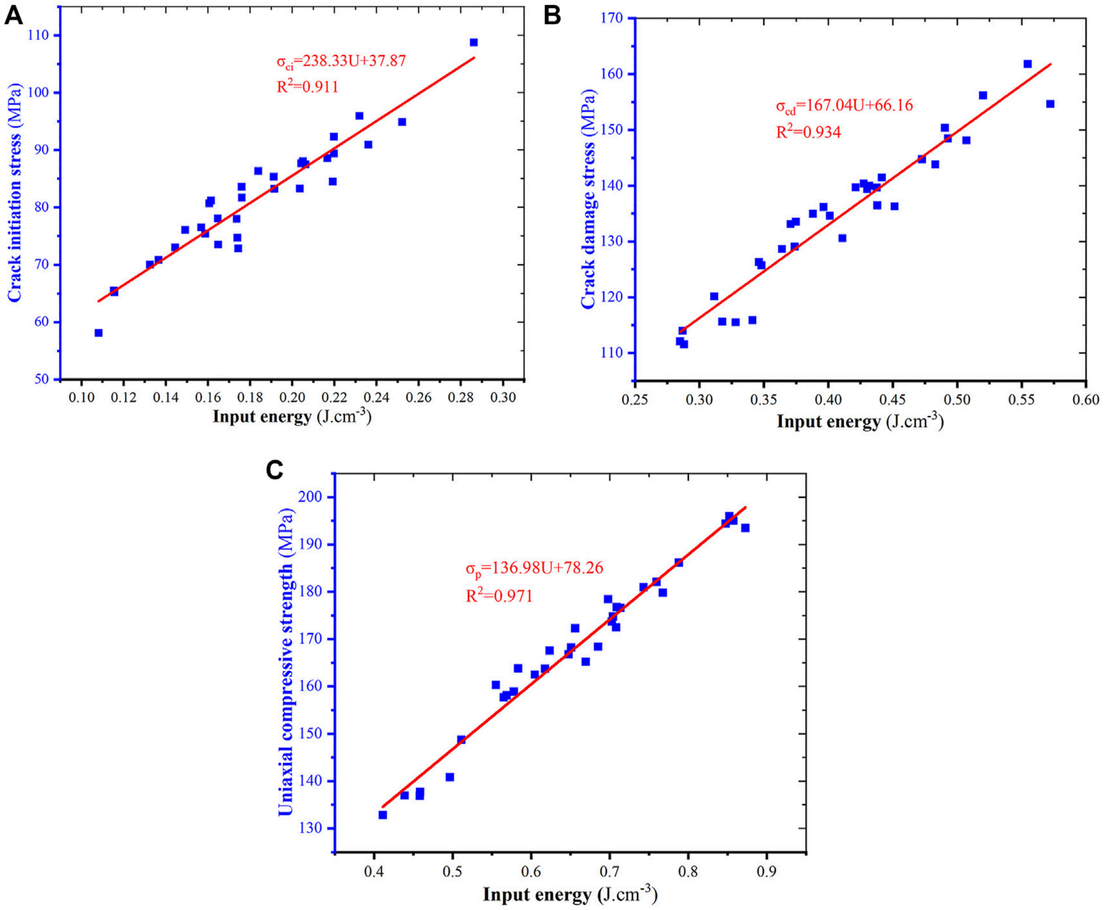

FIGURE 13
The relationship between the characteristic stresses and input energy. **(A)** Crack initiation stress; **(B)** damage stress; **(C)** uniaxial compressive strength.

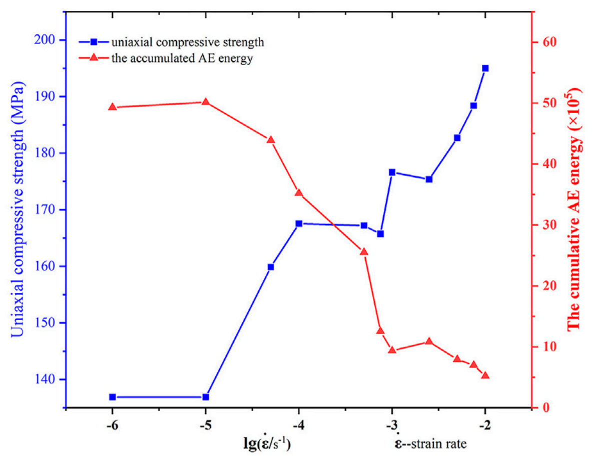

FIGURE 14
The averaged values of uniaxial compressive strength and the cumulative AE energy prior to the UCS point versus the denary logarithm of strain rates.

input energy. This relationship allows us to explain the strain rate effects of characteristic stresses through energy conversion between input energy and elastic strain energy. In general, a portion of the input energy is dissipated by crack initiation, crack propagation, and crack coalescence, while the remaining portion of the input energy is stored in rock as elastic strain energy. Consequently, the variation in the dissipated energy and elastic strain energy transferred from input energy correlate strongly with the increase of characteristic stresses. In addition, it is interesting to note that the intercept of the *Y* axis of the fitting equation in Figure 13C is 78.26 MPa, which is the corresponding uniaxial compressive strength when the input energy is zero. This value may be the intrinsic strength of rock.

Figure 14 shows the relationship between uniaxial compressive strength, the cumulative AE energy prior to the UCS point and strain rates. Contrary to the variation trend of rock's uniaxial compressive strength, the cumulative AE energy has a negative correlation with the logarithm of strain rates. The cumulative AE energy can indicate the damage degree of rock (Meng et al., 2016). As strain rates increase, the damage degree of rock decreases, indicating that the dissipated energy also decreases indirectly. Considering the discussion of the preceding paragraph, it can be determined that, as the strain rate increases, a greater proportion of the input energy is transferred primarily into the elastic strain energy, which is the main reason for the increase in characteristic stresses.

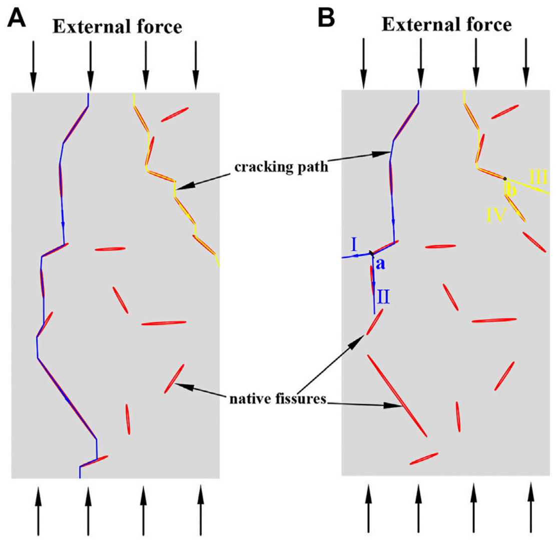

FIGURE 15
The schematic diagram of the cracking process in rock under different strain rates. **(A)** Lower strain rate; **(B)** higher strain rate.

It is commonly known that rock is a type of heterogeneous material, consisting of mineral grains of various sizes and multi-scale defects. In fact, the size of rock defects extends from a few nanometers to thousands of kilometers with a strong hierarchy if the crust is considered a specific type of rock. Table 6 depicted the range in size of rock defects in rock mechanics and rock engineering, from a few microns to several hundred meters (Feng and Zhao, 2008). Consequently, when rock is compressed at varying strain rates, its defects on different scales are activated, and the interaction of these defects determines rock deformation and failure. The overall stress state of rock is relatively uniform under the lower strain rate loading, and the area harboring native defects on a large scale begins to crack once the stress exceeds its strength

TABLE 6 Scale distribution of rock defects.

Type	Mirco-pore	Pore	Micro-crack	Crack	Fissure	Fault
Size range/m	10^{-6}	10^{-5}	10^{-4}	10^{-3}-10^{-2}	10^{-1}-10^{1}	$>10^{2}$

limit. Based on the principle of minimal dissipative energy, as the external load slowly increases, the cracks will preferentially propagate to the sections with the weakest structure in rock, such as native fissures, mineral boundaries, etc. These defects then join to form a macro-fracture surface, resulting in the loss of the rock's bearing capacity, as shown in Figure 15A. The accumulated elastic stain energy is dissipated during the process of crack development, resulting in a drop of the elastic strain energy stored in rock and a decrease in the values of the characteristic stresses. In contrast, due to the rapid rise in input energy, the cumulative elastic strain energy increases when the rock is compressed at a higher strain rate. As a result, the accumulated elastic strain energy at the extremities of some cracks, such as the point a and b in Figure 15B, grows dramatically. In addition to guaranteeing the consumption of crack propagation along the path II and the path IV, residual energy remains, but it may be insufficient to initiate cracks on a small scale because the energy required to initiate a small crack is significantly greater than that required to initiate a large crack. Therefore, the elastic strain energy continues to accumulate at these two points until it reaches the threshold energy required to initiate the small-scale cracks and then propagate it down the path I and path III, as shown in Figure 15B. Prior to that, the accumulated energy has to be transferred from the external load through continuous work, resulting in a rise in the corresponding characteristic stresses. Some studies can attest to the validity of the preceding explanation. Kipp et al. (1980) found that smaller cracks get activated as strain rate increases, resulting in an increase in the material's ultimate strength. Liang C. Y. et al. (2015) discovered that uniaxial compressive strength of rock decreased with an increase in the ratio between the height and radius of cylindrical samples at various strain rates. In general, the size of rock samples increases as the ratio increases. This indicates that these samples may contain more large-scale defects than small-size samples. Therefore, the large-scale defect is easier to be initiated than the smalle-scale defect under uniaxial compression, causing the uniaxial strength of the large-size samples to be lower than that of the small-size samples.

In a word, rock is a special material with multi-scale defects, and the threshold energy required to activate the defect varies depending on the scale of the defects. In general, the smaller the scale of cracks, the higher the threshold energy for crack initiation. Therefore, due to the difficulty in initiating small-scale cracks, the elastic strain energy transferred from input energy increases as strain rates increase within the range of quasi-static strain rates, resulting in an increase in the values of the associated characteristic stresses.

5 Conclusion

In this paper, uniaxial compressive tests of various strain rates within quasi-static strain rates of $10^{-6}\ s^{-1}$–$10^{-2}\ s^{-1}$ were carried out using a rock material testing system and a multi-channel acoustic emission monitoring system. The stress-strain curves of rock samples, characteristic stresses, energy data, and temporal and spatial distribution of AE signals were analyzed. According to the experimental results, the following conclusions can be drawn:

1 The characteristic stresses of rock samples, including crack initiation stress, damage stress, uniaxial compressive strength and failure stress, increase as strain rates increase. The relationship between characteristic stresses and the logarithm of strain rates can be described by linear equations with respective correlation coefficients of 0.76, 0.85, 0.96, and 0.76. In addition, the ratios of characteristic stresses are 0.48, 0.60, and 0.80, respectively, and essentially do not vary when strain rates increase. The ratios can therefore be used to characterize the fundamental mode of rock deformation, as the loading of various strain rates cannot change the mode when rock is under quasi-static compression.

2 As strain rates increase, the variations of input energy, elastic strain energy and dissipation energy are drastically different at various characteristic stress points. The input energy and elastic strain energy at the damage point, UCS point and failure stress point exhibit a linearly positive correlation with the logarithm of strain rates when the strain rate exceeds $10^{-5}\ s^{-1}$, whereas the dissipated energy prior to the UCS point varies little with the increase of strain rates. The input energy is converted primarily into elastic strain energy stored in rock during the pre-peak stage, and the ratios of energy conversion between input energy and elastic strain energy corresponding to the crack initiation stress point, damage stress point and UCS point, are 0.74, 0.84, and 0.83, respectively. However, the primary characteristic of energy conversion during the post-peak stage is the dissipated energy transferred from the elastic strain energy stored in rock, and the elastic strain energy stored in rock is abruptly released when rock fails. Based on those, the energy conversion process of rock under quasi-static compression can be divided into three stages: energy accumulation, energy dissipation, and energy release, respectively.

3 AE energy rate around different characteristic stress points varies significantly. This difference can be summarized as follows: the AE energy rate around the UCS point is considerably greater than the AE energy rate around the crack initiation stress point or damage stress point, and this relationship does not change as strain rates increase. The total number of the located AE events decreases as strain rates increase when the strain rate exceeds $10^{-5}\ s^{-1}$, and the majority of the located AE events occur during the crack closure stage and the unstable crack growth stage. Besides, $10^{-5}\ s^{-1}$ may be the optimal strain rate for acoustic emission testing of granite samples, given that the number of the

located AE events is greatest for this strain rate in the range of 10^{-6} s^{-1} to 10^{-2} s^{-1}.

4 It is certified that there is a strong linearly positive correlation between input energy and characteristic stresses. Consequently, based on the perspective of energy conversion and the structural properties of multi-scale defects in rock, the mechanism of the increase of characteristic stresses with the increase of strain rates was proposed: that is, when rock is subjected to a lower strain rate, native defects on a large scale are initially activated and then propagate toward the weak section of rock, resulting in a decrease in the elastic strain energy stored in rock and a reduction in characteristic stress values. Nonetheless, the cumulative elastic strain energy increases when the rock is compressed at a higher strain rate, so it is able to initiate more small-scale defects, which necessitates more input energy from the external load via continuous work and causes an increase in the associated characteristic stresses.

Data availability statement

The original contributions presented in the study are included in the article/Supplementary Material, further inquiries can be directed to the corresponding author.

Author contributions

SW contributed to the conception of the study; LL performed the experiment and data analysis; SW and LL contributed significantly to analysis and manuscript preparation; LL wrote the first draft of the manuscript; SW provided the thought of discussion; WY performed the AE data analysis and guided the AE tests; All authors contributed to manuscript revision, read, and approved the submitted version.

Funding

This work was supported by the Opening Fund of State Key Laboratory of Geohazard Prevention and Geoenvironment Protection (Chengdu University of Technology) No. SKLGP2016K001.

Conflict of interest

Publisher's note

References

Alneasan, M., and Behnia, M. (2021). Strain rate effects on the crack propagation speed under different loading modes (I, II and I/II): Experimental investigations. *Eng. Fract. Mech.* 258, 108118. doi:10.1016/j.engfracmech.2021.108118

Bieniawski, Z. T. (1967). Mechanism of brittle fracture of rock: Parts I-theory of the fracture process. *Int. J. Rock Mech. Min. Sci. Geomechanics Abstr.* 4 (4), 395–406. doi:10.1016/0148-9062(67)90030-7

Brace, W., and Jones, A. (1971). Comparison of uniaxial deformation in shock and static loading of three rocks. *J. Geophys. Res.* 76 (20), 4913–4921. doi:10.1029/JB076i020p04913

Brace, W., Paulding, B., Jr, and Scholz, C. (1966). Dilatancy in the fracture of crystalline rocks. *J. Geophys. Res.* 71 (16), 3939–3953. doi:10.1029/JZ071i016p03939

Cai, M., Morioka, H., Kaiser, P., Tasaka, Y., Kurose, H., Minami, M., et al. (2007). Back-analysis of rock mass strength parameters using AE monitoring data. *Int. J. Rock Mech. Min. Sci.* 44 (4), 538–549. doi:10.1016/j.ijrmms.2006.09.012

David, E. C., Brantut, N., and Hirth, G. (2020). Sliding crack model for nonlinearity and hysteresis in the triaxial stress-strain curve of rock, and application to antigorite deformation. *J. Geophys. Res. Solid Earth* 125 (10), e2019JB018970. doi:10.1029/2019JB018970

Feng, Z., and Zhao, Y. (2008). Control effect of fissure scale on deformamtion and failure of rock mass. *Chin. J. Rock Mech. Eng.* 27 (1), 78–83. (in Chinese).

Gong, F., Yan, J., Li, X., and Luo, S. (2019a). A peak-strength strain energy storage index for rock burst proneness of rock materials. *Int. J. Rock Mech. Min. Sci.* 117, 76–89. doi:10.1016/j.ijrmms.2019.03.020

Gong, F., Yan, J., Luo, S., and Li, X. (2019b). Investigation on the linear energy storage and dissipation laws of rock materials under uniaxial compression. *Rock Mech. Rock Eng.* 52 (11), 4237–4255. doi:10.1007/s00603-019-01842-4

Hoek, E., and Bieniawski, Z. (1965). Brittle fracture propagation in rock under compression. *Int. J. Fract.* 1 (3), 137–155. doi:10.1007/BF00186851

Hokka, M., Black, J., Tkalich, D., Fourmeau, M., Kane, A., Hoang, N. H., et al. (2016). Effects of strain rate and confining pressure on the compressive behavior of Kuru granite. *Int. J. Impact Eng.* 91, 183–193. doi:10.1016/j.ijimpeng.2016.01.010

Jaczkowski, E. L. (2018). *Laboratory strength testing of argillaceous limestone under varying saturation, scale, loading rate, and confinement conditions*. Kingston: Dissertation thesis, Queen's University.

Kipp, M., Grady, D., and Chen, E. (1980). Strain-rate dependent fracture initiation. *Int. J. Fract.* 16 (5), 471–478. doi:10.1007/BF00016585

Kovari, K., Tisa, A., and Einstein, H. (1983). Suggested methods for determining the strength of rock materials in triaxial compression: revised version. *Int. J. Rock Mech. Min. Sci.* 20 (6), 283–290. doi:10.1016/0148-9062(83)90598-3

Lajtai, E. Z., Duncan, E., and Carter, B. (1991). The effect of strain rate on rock strength. *Rock Mech. Rock Eng.* 24 (2), 99–109. doi:10.1007/BF01032501

Lei, X., Kusunose, K., Rao, M., Nishizawa, O., and Satoh, T. (2000). Quasi-static fault growth and cracking in homogeneous brittle rock under triaxial compression using acoustic emission monitoring. *J. Geophys. Res.* 105 (B3), 6127–6139. doi:10.1029/1999JB900385

Li, H., Zhao, J., and Li, T. (1999). Triaxial compression tests on a granite at different strain rates and confining pressures. *Int. J. Rock Mech. Min. Sci.* 36 (8), 1057–1063. doi:10.1016/S1365-1609(99)00120-3

Li, X., Li, H., Liu, L., Liu, Y., Ju, M., and Zhao, J. (2020). Investigating the crack initiation and propagation mechanism in brittle rocks using grain-based finite-discrete element method. *Int. J. Rock Mech. Min. Sci.* 127, 104219. doi:10.1016/j.ijrmms.2020.104219

Li, X., Lok, T., and Zhao, J. (2005). Dynamic characteristics of granite subjected to intermediate loading rate. *Rock Mech. Rock Eng.* 38 (1), 21–39. doi:10.1007/s00603-004-0030-7

Li, Y., Huang, D., and Li, X. a. (2014). Strain rate dependency of coarse crystal marble under uniaxial compression: strength, deformation and strain energy. *Rock Mech. Rock Eng.* 47 (4), 1153–1164. doi:10.1007/s00603-013-0472-x

Liang, C., Wu, S., Li, X., and Xin, P. (2015a). Effects of strain rate on fracture characteristics and mesoscopic failure mechanisms of granite. *Int. J. Rock Mech. Min. Sci.* 76, 146–154. doi:10.1016/j.ijrmms.2015.03.010

Liang, C. Y., Zhang, Q. B., Li, X., and Xin, P. (2015b). The effect of specimen shape and strain rate on uniaxial compressive behavior of rock material. *Bull. Eng. Geol. Environ.* 75 (4), 1669–1681. doi:10.1007/s10064-015-0811-0

Lindholm, U., Yeakley, L., and Nagy, A. (1974). The dynamic strength and fracture properties of dresser basalt. *Int. J. Rock Mech. Min. Sci. Geomechanics Abstr.* 11 (5), 181–191. doi:10.1016/0148-9062(74)90885-7

Mahanta, B., Singh, T. N., Ranjith, P. G., and Vishal, V. (2018). Experimental investigation of the influence of strain rate on strength; failure attributes and mechanism of Jhiri shale. *J. Nat. Gas. Sci. Eng.* 58, 178–188. doi:10.1016/j.jngse.2018.08.001

Martin, C., and Chandler, N. (1994). The progressive fracture of Lac du Bonnet granite. *Int. J. Rock Mech. Min. Sci. Geomechanics Abstr.* 31 (6), 643–659. doi:10.1016/0148-9062(94)90005-1

Meng, Q., Zhang, M., Han, L., Pu, H., and Nie, T. (2016). Effects of acoustic emission and energy evolution of rock specimens under the uniaxial cyclic loading and unloading compression. *Rock Mech. Rock Eng.* 49 (10), 3873–3886. doi:10.1007/s00603-016-1077-y

Nicksiar, M., and Martin, C. D. (2012). Evaluation of methods for determining crack initiation in compression tests on low-porosity rocks. *Rock Mech. Rock Eng.* 45 (4), 607–617. doi:10.1007/s00603-012-0221-6

Ožbolt, J., Sharma, A., and Reinhardt, H.-W. (2011). Dynamic fracture of concrete–compact tension specimen. *Int. J. Solids Struct.* 48 (10), 1534–1543. doi:10.1016/j.ijsolstr.2011.01.033

Pan, F. (2017). *Study on the mechanism of the enhancement of dynamic strength for concrete material considering the meso-structure. Dissertation thesis*. Xi'an: Xi'an Technological University. (in Chinese).

Qi, C., Wang, M., and Qian, Q. (2009). Strain-rate effects on the strength and fragmentation size of rocks. *Int. J. Impact Eng.* 36 (12), 1355–1364. doi:10.1016/j.ijimpeng.2009.04.008

Rossi, P. (1991). A physical phenomenon which can explain the mechanical behaviour of concrete under high strain rates. *Mat. Struct.* 24 (6), 422–424. doi:10.1007/BF02472015

Sirdesai, N. N., Gupta, T., Singh, T. N., and Ranjith, P. (2018). Studying the acoustic emission response of an Indian monumental sandstone under varying temperatures and strains. *Constr. Build. Mat.* 168, 346–361. doi:10.1016/j.conbuildmat.2018.02.180

Solecki, R., and Conant, R. J. (2003). *Advanced mechanics of materials*. Oxford: Oxford University Press.

Tarasov, B. (1990). Simplified method for determining the extent to which strain rate affects the strength and energy capacity of rock fracture. *Soviet Min. Sci.* 26 (4), 315–320. doi:10.1007/BF02506510

Wang, C., Fan, P., and Wang, M. (2011a). Influence of strain rate on progressive failure process and characteristic stresses of red sandstone. *Rock Soil Mech.* 32 (5), 1340–1346. (in Chinese). doi:10.16285/j.rsm.2011.05.008

Wang, X., Ge, H., and Song, L. (2011b). Experimental study of two types of rock sample acoustic emission events and kaiser effect point recognition approach. *Chin. J. Rock Mech. Eng.* 30 (3), 580–588. (in Chinese).

Wang, X., Wen, Z., Jiang, Y., and Huang, H. (2018). Experimental study on mechanical and acoustic emission characteristics of rock-like material under non-uniformly distributed loads. *Rock Mech. Rock Eng.* 51 (3), 729–745. doi:10.1007/s00603-017-1363-3

Xie, H., Li, L., Peng, R., and Ju, Y. (2009). Energy analysis and criteria for structural failure of rocks. *J. Rock Mech. Geotechnical Eng.* 1 (1), 11–20. doi:10.3724/SP.J.1235.2009.00011

Zhang, Q. B., and Zhao, J. (2014). A review of dynamic experimental techniques and mechanical behaviour of rock materials. *Rock Mech. Rock Eng.* 47 (4), 1411–1478. doi:10.1007/s00603-013-0463-y

Zhang, Y., Chen, Y., Yu, R., Hu, L., and Irfan, M. (2017). Effect of loading rate on the felicity effect of three rock types. *Rock Mech. Rock Eng.* 50 (6), 1673–1681. doi:10.1007/s00603-017-1178-2

Zhang, Z., Deng, M., Bai, J., Yu, X., Wu, Q., and Jiang, L. (2020). Strain energy evolution and conversion under triaxial unloading confining pressure tests due to gob-side entry retained. *Int. J. Rock Mech. Min. Sci.* 126, 104184. doi:10.1016/j.ijrmms.2019.104184

Zhang, Z., Kou, S., Jiang, L., and Lindqvist, P. A. (2000). Effects of loading rate on rock fracture: fracture characteristics and energy partitioning. *Int. J. Rock Mech. Min. Sci.* 37 (5), 745–762. doi:10.1016/S1365-1609(00)00008-3

Zhao, F., Li, Y., Ye, Z., Fan, Y., Zhang, S., Wang, H., et al. (2018). Research on acoustic emission and electromagnetic emission characteristics of rock fragmentation at different loading rates. *Shock Vib.* 2018, 1–8. doi:10.1155/2018/4680879

Zhao, H., Song, Z., Zhang, D., Liu, C., and Yu, B. (2021a). True triaxial experimental study on mechanical characteristics and energy evolution of sandstone under various loading and unloading rates. *Geomech. Geophys. Geo-energ. Geo-resour.* 7 (1), 22. doi:10.1007/s40948-020-00212-7

Zhao, J., Li, H., Wu, M., and Li, T. (1999). Dynamic uniaxial compression tests on a granite. *Int. J. Rock Mech. Min. Sci.* 36 (2), 273–277. doi:10.1016/S0148-9062(99)00008-X

Zhao, Z., Jing, H., Shi, X., Wu, J., and Yin, Q. (2021b). Experimental investigation on fracture behaviors and acoustic emission characteristics of sandstone under different strain rates. *Environ. Earth Sci.* 80 (3), 85. doi:10.1007/s12665-020-09351-2

Frontiers in Earth Science

TYPE Original Research
PUBLISHED 26 August 2022
DOI 10.3389/feart.2022.963973

OPEN ACCESS

EDITED BY
Zhiqiang Yin,
Anhui University of Science and Technology, China

REVIEWED BY
Jianguo Ning,
Shandong University of Science and Technology, China
Runsheng Lv,
Henan Polytechnic University, China
Ningbo Zhang,
China University of Mining and Technology, China

*CORRESPONDENCE
Ying Chen,
56724647@qq.com
Xiufeng Zhang,
415690468@qq.com

SPECIALTY SECTION
This article was submitted to Geohazards and Georisks, a section of the journal Frontiers in Earth Science

RECEIVED 08 June 2022
ACCEPTED 30 June 2022
PUBLISHED 26 August 2022

CITATION
Chen Y, Wang Z, Hui Q, Zhu Z, Sun D, Chen Y, Zhang X, Wang Z, Wang J and Zhao J (2022), Overlying rock movement and mining pressure in a fully mechanized caving face with a large dip angle.
Front. Earth Sci. 10:963973.
doi: 10.3389/feart.2022.963973

Overlying rock movement and mining pressure in a fully mechanized caving face with a large dip angle

Ying Chen[1,2]*, Zhiwen Wang[1], Qianjia Hui[1], Zhijie Zhu[1], Dequan Sun[2,3], Yang Chen[4], Xiufeng Zhang[4]*, Zhaoyi Wang[5], Jian Wang[5] and Jian Zhao[6]

[1]Mining Engineering School, Liaoning Technical University, Fuxin, China, [2]Engineering Laboratory of Deep Mine Rockburst Disaster Assessment, Jinan, China, [3]Shandong Provincial Research Institute of Coal Geology Planning and Exploration, Jinan, China, [4]Shandong Energy Group Co. Ltd, Jinan, China, [5]Liangbaosi Energy Co. Ltd, Shandong Energy Group Luxi Mining Co. Ltd, Jining, China, [6]Shandong Energy Group Luxi Mining Co. Ltd, Jining, China

The overlying rock movement and mining pressure in the fully mechanized caving face with a large dip angle were systematically investigated according to theoretical analysis, similar material simulation, numerical calculation, and field monitoring. The following conclusions were obtained: 1) the theoretical analysis showed that the roof movement characteristics at different positions of the working face are quite different. The mining pressure in the upper section of the working face is primarily controlled by the structural instability of the main roof. The stable structure of the main roof is easily formed in the middle and lower sections of the working face, and the mining pressure is mostly controlled by the collapse of the immediate roof. 2) The results of similar material simulations indicated that the height of the fracture zone in different areas of the working face is different due to the influence of a large dip angle. The height of the fracture zone formed in the upper section of the working face is significantly larger than that formed in the lower section of the working face. 3) The numerical calculation suggested that the residual coal pillar of the overlying coal seam has a certain influence on the mining pressure of the 9-301 working face, making the advanced abutment pressure in the range of 80 m close to the main gate under the coal pillar more obvious. 4) The field pressure monitoring results demonstrated that the influence range of the advanced abutment pressure close to the upper part of the working face is greater than that close to the lower part of the working face, and the peak point is closer to the mining rib. Affected by the overlying residual coal pillar, the hydraulic support resistance and the peak value of advanced abutment pressure in the lower part of the working face are greater than those in the upper part. Both the initial and periodic pressure intervals of the upper section of the working face are smaller than those of the lower section. The results of this research will provide a scientific basis for the reasonable determination of the control measures for the mining pressure.

KEYWORDS

top coal caving, large dip angle, overlying rock movement, abutment pressure, numerical calculation

1 Introduction

Based on the studies on the nearly horizontal and gentle-dip coal seam, many achievements have been obtained on the overlying strata breakage and movement characteristics and mining pressure occurrence over the large-dip coal seam working face.

Since the 21st century, due to the impact of the coal market, many countries have gradually ceased the extraction of the large-dip coal seam. For instance, Great Britain and France have already closed their coalmines; thus, the research progress on the large-dip coal seam mining is slow (Singh and Gehi, 1993; Kulakov, 1995; Wang 2014; Wu et al., 2020c). Wu et al. (2020a), Luo et al. (2021), and Zhang and Wu (2020) utilized theoretical analysis, physical modeling, and field measurements to examine the breakage law of the main roof of a large-dip coal seam working face and pointed out that the asymmetrical space is easily formed due to the roof breakage, collapse sequence, and non-uniform backfilling of the gouge into the goaf. Moreover, they proposed that the main roof breakage commences from the middle and upper parts, followed, finally, by the lower part, leading to the corresponding sequence of the working face mining pressure. Wang et al. (2015a), Wang et al. (2015b), Xiao et al. (2019), and Zhang et al. (2014) built the mechanical model of the first weighting and periodic weighting of the main roof, derived the instability judgment of the roof breakage, and stated that the sequential breakage of the strata in the dip direction is mainly responsible for the formation of the asymmetrical bearing arch within the overlying strata. Combining numerical simulation and physical modeling, Xie et al. (2019) and Xie et al. (2021) found that the stress distribution and displacement of the roof of the large-dip coal seam working face were non-symmetrical, and the roof exhibited asymmetrical “O-X”-shaped breakage.

Huang (2002) stated that during the overlying strata movement of the large-dip coal seam working face, a small voussoir beam is easily formed due to the backfilling support of the caved gouge of the immediate roof, whereas a large inclined voussoir beam is easily developed for the main roof. Chai et al. (2019), Luo et al. (2018), Wu et al. (2020b), and Zhang and Wang (2014) reported that the roof deformation over the large-dip coal seam working face is non-symmetrical with higher deformation in the upper middle part than in the lower part, and the eventual caving of the overlying strata displayed non-symmetrical distribution. Zhang et al. (2010) pointed out that the overlying strata movement of the large-dip coal seam working face is non-symmetrical, and when the overlying strata break and collapse, a non-systematical backfilling zone is formed due to the downward movement along the dipping strata. Lin et al. (2015) and Luan et al. (2015) studied the dynamic evolution of the spatial structure of the overlying strata of the large-dip coal seam working face and pointed out that the active region of the structural movement of the main roof primarily locates in the upper section over the working face; the overlying strata structure will evolve into several main roof beams at different levels and a “non-symmetrical fractured arch”. Sun et al. (2008), Rong et al. (2012), and Xie et al. (2012) investigated the “three-zone” evolution of the overlying strata of the large-dip coal seam working face. The sequential and non-uniform breakage of the overlying strata resulted in a remarkable difference in “three-zone” evolution characteristics between the lower region and the middle and upper regions of the working face; the “three zones” are highly developed in the middle and upper regions, whereas those in the lower region are less noticeable. Wang et al. (2005), Yang et al. (2010), Cheng and Li (2009), Liu et al. (2017), Men et al. (2014), Du et al. (2020a), and Du et al. (2022) also made efforts to the overlying strata movement and structural characteristics of the large-dip coal seam mining. Xiong et al. (2022), Liu et al. (2021), and Li et al. (2020) studied mining pressure caused by coal rib spalling.

Through the monitoring and analysis of mining pressure, Gao et al. (2020) stated that the periodic weighting of the large-dip, extra-thick coal seam has an obvious sequence, and the mining pressure in the middle of the working face is more severe. Zhang (2007) concluded that the support pressure at the lower end of the large-dip coal seam working face depends on the backfilling degree of the caved rock in the lower goaf, and the support pressure at the upper end depends on the roof caving when the working face is advanced. Li and Liu (2016) analyzed the mining pressure monitoring data on the large-dip coal seam working face and found that the roof stress at the lower end is larger than that of the upper end, and the upper part of the working face is loaded earlier due to the unbalanced force on the beam. Sun (2015) established a multi-section numerical model along the dip direction of the large-dip coal seam working face and obtained the distribution characteristics of the abutment pressure and the damage range of the plastic zone in the upper, middle, and lower parts of the working face in the dip direction. Yin et al. (2010), Qin et al. (2015), and Wang (2017) pointed out that the support load distribution and the weighting distance of the large-dip coal seam working face are different in the dip direction and found that the weighting period and distance were larger in the lower part than those in the upper part. Song et al. (2018) studied the mining pressure occurrence in the fully mechanized caving working face with a large dip angle and thick coal seam and obtained the mining pressure evolution of the upper, middle, and lower parts of the roof. Through the analysis of mining pressure monitoring data and numerical simulation, Xing et al. (2018) pointed out that mining pressure occurs at both ends of the working face with the mining height along the dip direction of the working face before the middle part. Zhu et al. (2014) discussed the mining pressure in the

TABLE 1 Roof and floor of the working face.

Roof and floor	Lithology	Thickness(m)
Main roof	Sandy mudstone	6–9
Immediate roof	Limestone	5–7
Immediate floor	Mudstone	1–2
Main floor	Fine sandstone	1–3

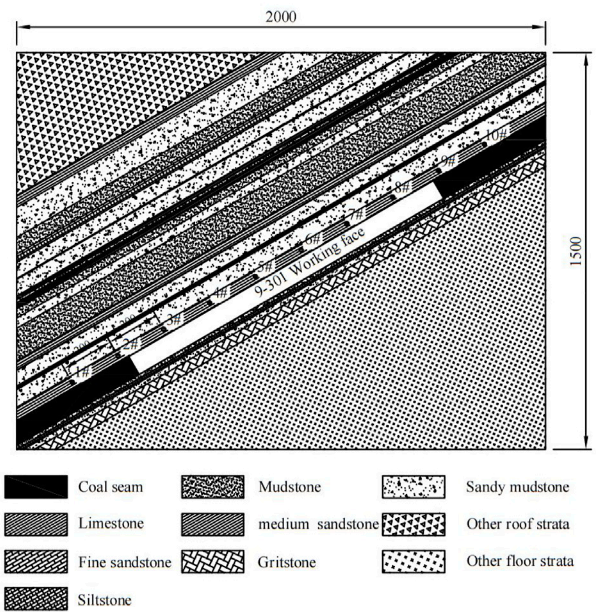

FIGURE 1
Monitoring points' layout (Unit: mm).

fully mechanized caving working face of soft coal seams with large dip angles and pointed out that the mining pressure in the upper, middle, and lower sections of the working face gradually weakened, and the pressure at both ends comes later than that at the middle.

Taking the 9-301 fully mechanized top coal caving working face with a large dip angle and extra-thick coal seam as the object, the overlying rock movement and mining pressure are systematically investigated by the use of theoretical analysis, similar simulation experimentation, numerical calculation, and mining pressure monitoring.

2 Field conditions

The thickness of the No. 9 coal seam in a coal mine is 10.8–12.4 m, with an average thickness of 11.8 m. The dip angle is 26°–34°, and the proctor's coefficient f is 1. The upper distance from the No. 5 coal seam is 40.90–56.15 m, with an average distance of 50.63 m. The coal seam structure is complex, containing 1–4 interlayers of gangue; the thickness of the gangue is 0.10–0.38 m; and the gangue is mostly carbonaceous mudstone.

The 9-301 working face adopts the fully mechanized top coal caving, mining the overall height at one time, with a mining height of 3.2 m, the top coal caving thickness of 8.6 m, and a mining/caving ratio of 1:2.69. The caving interval is "two cuttings and one caving," and the caving method is single-round sequential caving. The inclined length of the working face is 200 m, and the advancing length of the strike is 2002 m. The depth of the working face is 435–540 m. The roof and floor of the working face are reported in Table 1.

3 Analysis of overlying rock movement characteristics in coal seam mining with a large dip angle

3.1 Analysis of movement characteristics of immediate roof strata

The collapse of the immediate roof of the fully mechanized top coal caving face with a large dip angle is different from that in a horizontal (or near horizontal) coal seam. Along the inclination and strike of the working face, the collapse state and structure of the immediate roofs are quite different.

With the release of top coal, the immediate roof loses its support and reaches the strength limit under the action of the overburden rock layer. Under the condition of a large dip angle, the broken immediate roof moves down along the dip of the working face, resulting in the accumulation of gangue in the lower section of the goaf. The immediate roof of the upper section of the working face will generally collapse sufficiently and move downward. The immediate roof of the middle section of the working face is usually characterized by stratification. The lower stratification can be fully caved, while different degrees of fracture and large-sized blocks can be formed in the upper stratification. Due to the filling and supporting effect of the falling gangue in the upper and middle sections, damage and falling in the lower section of the working face can only be formed in the lower stratification of the immediate roof.

The immediate roof in the upper part of the working face will form small fragments; thus, it will not form a stable bearing structure. The immediate roof in the middle of the working face will be broken into large pieces and will be arranged neatly, and it is easy to form a small structure of a "masonry beam" along the strike. Due to the filling support, the space for deformation and caving of the immediate roof in the lower part of the working face is limited; therefore, it is easier to form a "masonry arch" structure with a certain span in the lower part than in the middle part of the working face.

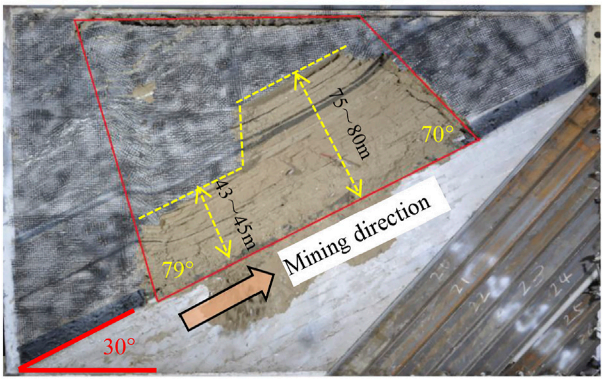

FIGURE 2
Final caving pattern of overburden.

3.2 Analysis of the main roof structure and movement characteristics

The “masonry beam” structure can be easily formed not only in the strike of the immediate roof but also in the middle and lower parts of the working face in the dip direction due to the rock gravity component (Guo et al., 2012). The “masonry beam” structure formed by the immediate roof promotes the formation of the “large structure” of the main roof.

The “large structure” formed by the main roof in the strike presents different mechanical states in the upper, middle, and lower parts of the working face. In the upper part, due to the movement and accumulation of the immediate roof falling to the middle and lower parts of the working face, the main roof cannot be fully supported, and fracture instability occurs when the suspension length exceeds its limit deflection. Therefore, the mining pressure in the upper part of the large dip working face is affected and controlled by the instability of the main roof.

In the middle and lower parts of the working face, the main roof can maintain the structural balance and stability for a long time under the support of the immediate roof and its own structural characteristics. At the same time, it can also maintain the stability of the “masonry beam” formed by the immediate roof. Thus, the mining pressure in the middle and lower parts of the large dip working face is chiefly affected and controlled by the lower stratification collapse of the immediate roof. When the “masonry beam” formed by the immediate roof is unstable, it accelerates the damage of the main roof; thus, it affects the strength of the mining pressure.

4 Similarity experiment

4.1 Similarity parameters

The similarity method is utilized to study the overburden movement and failure process after simplifying the physical model under the ensuring similar conditions. According to the actual situation and test conditions, the following similar conditions were introduced to achieve the simulation results.

It was determined that the geometric similarity scale α_L =150, that is,

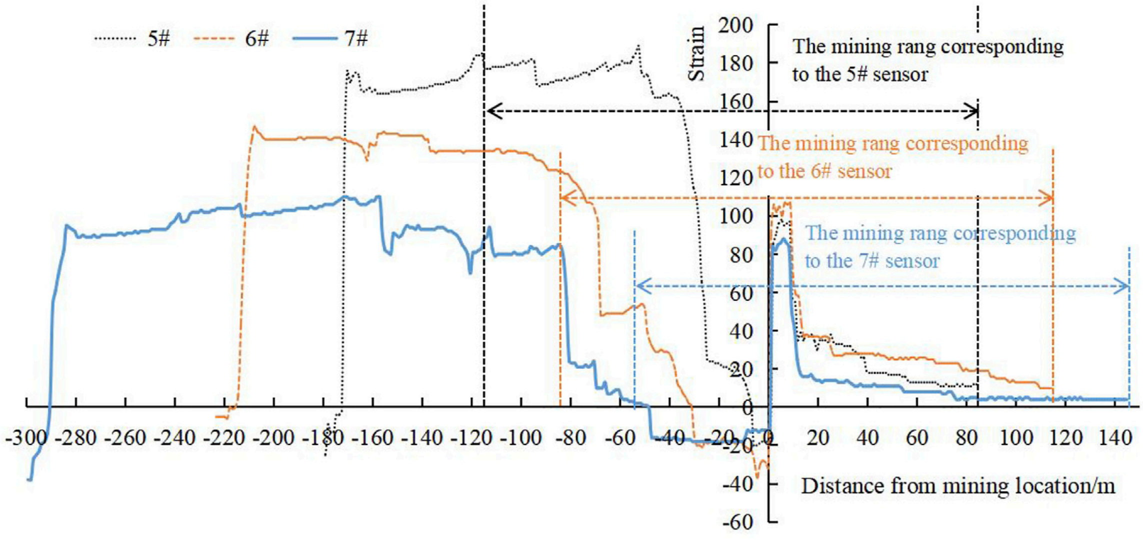

FIGURE 3
Variation curves of strain values of No. 5, No. 6, and No. 7 pressure sensors.

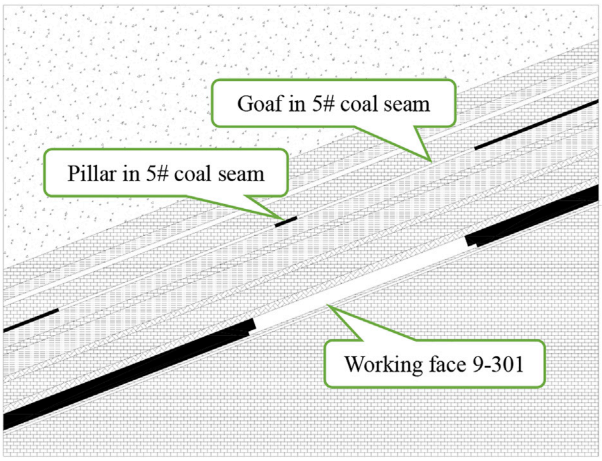

FIGURE 4
Mining model.

$$\alpha_L = \frac{L_H}{L_M} = 150, \tag{1}$$

where L_H and L_M represent the length of the prototype and the model, respectively.

Based on geometric similarity, gravity similarity is required to be constant, that is,

$$\alpha_\gamma = \frac{\gamma_H}{\gamma_M} = 1.67, \tag{2}$$

where α_γ represents the gravity similarity scale. γ_H and γ_M are the apparent densities of the rock stratum of the prototype and the model, considered to be 2.5 g/m^3 and 1.5 g/m^3, respectively.

From geometric and gravity similarities, the stress or strength scale α_σ can be obtained as follows:

$$\alpha_\sigma = \frac{\sigma_H}{\sigma_M} = \frac{\gamma_H}{\gamma_M} \cdot \alpha_L = \frac{2.5}{1.5} \times 150 = 250, \tag{3}$$

where σ_H and σ_M are the uniaxial compressive strength of the rock stratum of the prototype and the model, respectively.

For satisfying the motion similarity, the motion of all corresponding points in the model has to be similar to that in the prototype. In other words, the speed, acceleration, and motion time of each corresponding point should be in a certain proportion. The time scale α_t is defined and obtained as follows:

$$\alpha_t = \frac{t_H}{t_M} = \sqrt{\alpha_L} = \sqrt{150} = 12.25, \tag{4}$$

where t_H and t_M represent the time of the prototype and model, respectively.

4.2 Model fabrication

The tendency model of the working face was established in a similar material experiment. The model size was length × width × height = 2,000 mm × 240 mm × 1,500 mm (Figure 1). The model frame adopted channel steel, with two sides closed. The front and rear of the model were shaped with 240 mm-wide removable channel steel guard plates. Silica sand was selected as the aggregate, calcium carbonate and gypsum were used as cement, and mica powder was utilized for stratification. The aggregate, cement, and water were mixed evenly according to a similar proportion, and then, the mixed material was filled into the similar material model frame. In total, 10 stress monitoring points were arranged in the model (1#~10# in Figure 1). After the model was filled, it was dried for 20 days under constant temperature and humidity, and then, it was mined according to the length scale (α_L) and time scale (α_t) determined by Eqs 1, 2.

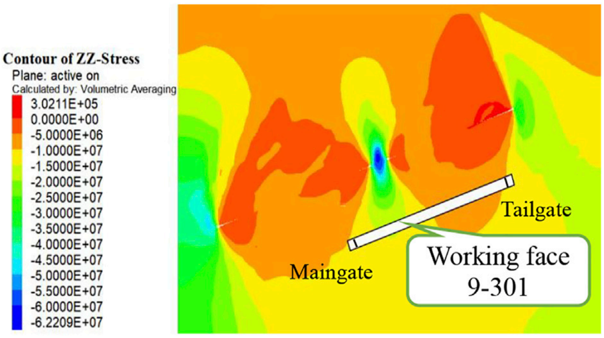

FIGURE 5
Stress distribution of the surrounding rock before mining in the 9-301 working face.

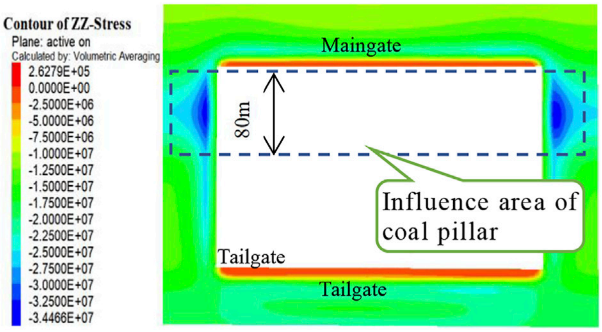

FIGURE 6
Stress distribution of the surrounding rock when mining advanced to 300 m.

4.3 Analysis of experimental results

4.3.1 Overburden movement and failure characteristics

The geometric similarity scale chosen in the similar model is 1:150. The actual thickness of the 5# coal seam is 3.0 m, and the converted thickness in the model is 20 mm. Since the thickness is too small, the simulation mining cannot be implemented in the model. Therefore, the influence of five coal seams on the working face 9-301 is not considered in the similarity experiment.

The process of the experiment was the same as the mining of coal seam. To eliminate the boundary effect, the position of 65 cm away from the model boundary was set as the initial mining position. The mining direction of the working face was from the bottom to the top along the inclination. Considering the recovery of top coal, 93% of the thickness of the coal seam was mined in the model.

When the working face retreated to 52.5 m, the roof collapsed for the first time. The roof collapsed periodically with continuous mining. Figure 2 exhibits the final collapse form of overburden when the mining reached 200 m. The damage range of overburden caused by mining developed to the model boundary. It can be observed that because of the effect of the dip angle, the affected boundary angle of the goaf is asymmetric, the movement angle in the uphill direction is 79°, and the movement angle in the downhill direction is 70°. In the process of mining, it was found that the collapsed gangue from the upper part of the working face slipped and accumulated toward the lower part of the working face due to the influence of the dip angle, which supported and restricted the roof, causing the height of the overburden fracture zone in the lower part of the working face to be smaller than that in the upper part of the working face. The total height of the fracture zone on the working surface is 75–80 m, and the height of the fracture zone in the lower section of the working face is 43–45 m. The difference in the height of the fracture zone will lead to different mining pressures in different areas of the working face.

4.3.2 Analysis of pressure distribution in front of the working face

By embedding a BW5 micro-pressure sensor in the model, a YJZ-32A intelligent digital strain gauge was employed to monitor the real-time strain. The strain data on the sensor reflect the stress change. The strain data on some pressure

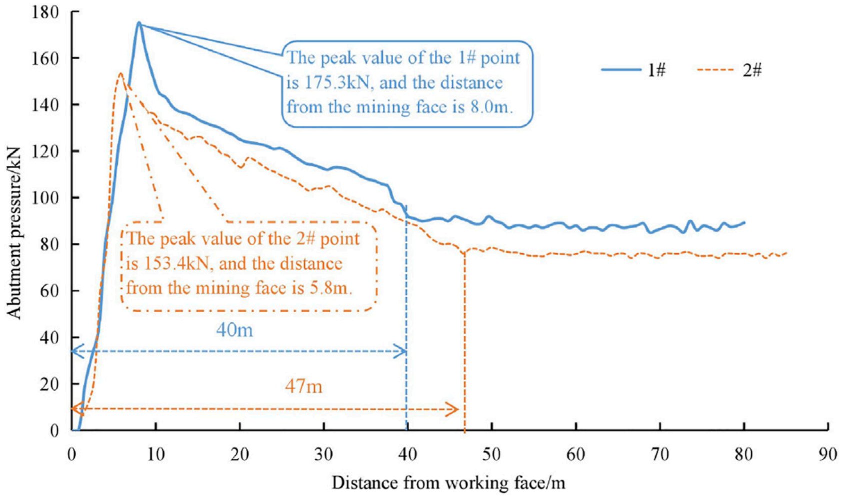

FIGURE 7
Variation curve of the advanced abutment pressure.

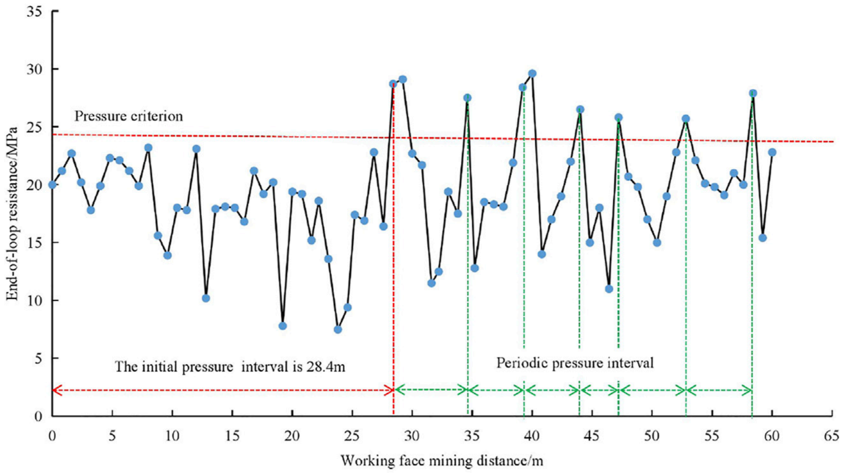

FIGURE 8
Curve of the end-of-loop resistance of the No. 15 hydraulic support.

boxes were selected, and the monitoring curve was drawn (Figure 3). The variation in the strain value of the sensor was utilized to qualitatively reflect the change in stress in the roof of the working face. The variation curves of the No. 5, No. 6, and No. 7 sensor strain values with the movement of the mining location are displayed in Figure 3. As can be observed from the figure, the strain value of the sensor gradually became larger as the mining location approached the sensor. When the position of mining was 5–7 m away from the sensor, the strain value was the largest. After that, the strain value of the sensor started to decrease. When the mining position passed through the sensor, with subsidence deformation and stress unloading of the roof, the strain of the sensor rebounded and showed a negative value. After some distance behind the mining position, the strain value of the sensor began to rise again. This means the rock stratum collapsed and recompacted, and the sensors were loaded again. When the sensors at different positions were loaded again, the distance behind the mining position and the magnitude of stress (reflected by the magnitude of strain value) were different. With the mining of the working face from the bottom to top, the starting point of the sensor was farther and farther away from the mining position, and the No. 5, No. 6, and No. 7 sensors lagged behind the mining position by 10 m, 31 m, and 51 m, respectively. After mining, with the increase in model placement time, the strain value of sensors at each position tended to become stable after reaching a certain value. The closer to the lower part of the coal seam, the greater is the strain value (i.e., the greater the bearing stress). The experimental data indicated that the activity of the roof near the lower part of the working face is weak. It will be re-loaded after a short time of adjustment, while the roof strata located at the upper part of working face are more likely to collapse with a larger range, and the new equilibrium state requires a longer adjustment time.

The No. 1, No. 2, No. 9, and No. 10 sensors were located outside the mining district (Figure 1). Except for the strain value of the No. 9 sensor changing during mining, the strain of

TABLE 2 Statistics of the abutment pressure of the working face.

Advance/m	Abutment pressure/MPa		Peak position ahead of the working face/m	Influence range/m
	Pillar	Non-pillar		
50	28.4	14.3	6.5	30
100	30.2	19.5	6.5	37
150	30.9	22.5	6.5	40
200	31.9	24.7	6.5	47
250	32.4	25.1	6.5	47
300	32.3	25.2	6.5	49

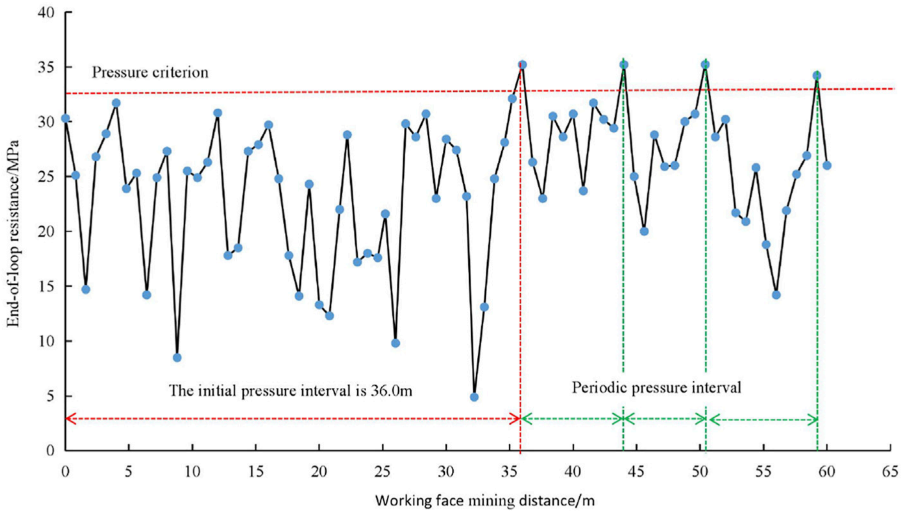

FIGURE 9
Curve of the end-of-loop resistance of the No. 40 hydraulic support.

other sensors did not change significantly (that is, mining had no impact on them). The abrupt change in the strain value of the No. 9 sensor was about 6.6 m away from the mining position, indicating that the roof strata here were affected by mining, resulting in the change in stress distribution, but the influence was small. The No. 1 and No. 2 sensors located at the bottom of the coal seam exhibited no significant change in the whole process, indicating that there was no large movement of the roof strata here, and the stress was stable. Due to the large dip angle, the mining of the working face had an impact on the side abutment pressure in the upper part of the working face, but the impact on the side abutment pressure at the lower part was not obvious.

5 Numerical simulation

5.1 Model and parameters

The numerical calculation model was established by FLAC3D. We considered the influence of the No. 5 coal seam goaf and pillar on the surrounding rock stress of the 9-301 working face (Figure 4). The model size was length × width × height = 500 m × 400 m × 250 m, and a total of 6,48,960 units and 6,83,995 nodes were established. The physical and mechanical parameters of coal and rock in the model were estimated according to the data on the mine and measured in a laboratory.

5.2 Calculation results

5.2.1 Stress distribution of the surrounding rock in the working face

Figure 5 displays the stress distribution of the surrounding rock before mining in the 9-301 working face. This figure shows that the lower part of the working face is in the stress influence area of the residual coal pillar, and the stress reaches 12–18 MPa. The upper part of the working face is located in the pressure relief area of the upper goaf, and the stress value is between 8 and 12 MPa. Figure 6 exhibits the stress distribution of the surrounding rock when mining advanced to 300 m. The working face within 80 m near the main gate is obviously affected by the concentrated stress of the coal pillar, and the abutment stress near the tailgate is small.

Table 2 shows the distribution of the advanced abutment pressure of the working face in the mining process. It can be seen that with the mining of the working face, the peak value and influence range of abutment stress gradually increase. When the working face advanced to 200 m, the peak values of the pressure under the coal pillar area and non-coal pillar area are 31.9 and 24.7 MPa, respectively. The peak point is located 6.5 m in front of the working face, and the influence range of the abutment pressure is 47 m. The mining continues in the working face, and the peak value and influence range of abutment stress tend to be stable. Affected by the coal pillar of the upper No. 5 coal seam, the lower section (near the main gate) of the 9-301 working face is affected by concentrated stress, the advanced abutment pressure is large, and the peak pressure reaches 32.4 MPa.

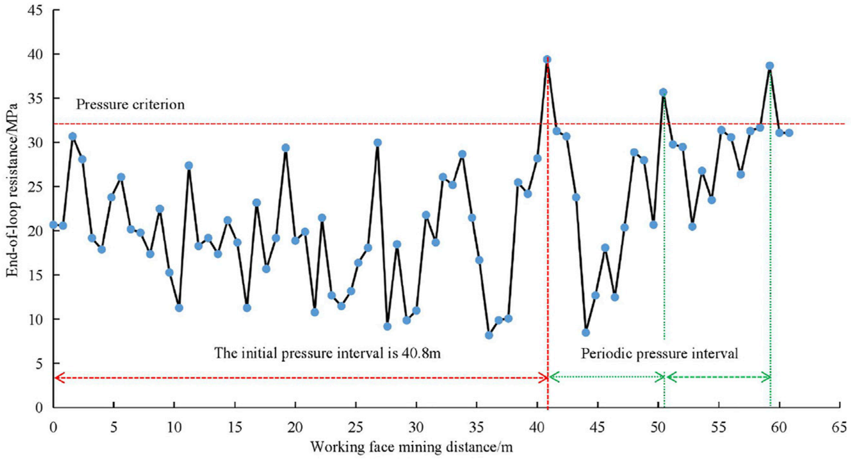

FIGURE 10
Curve of the end-of-loop resistance of the No. 65 hydraulic support.

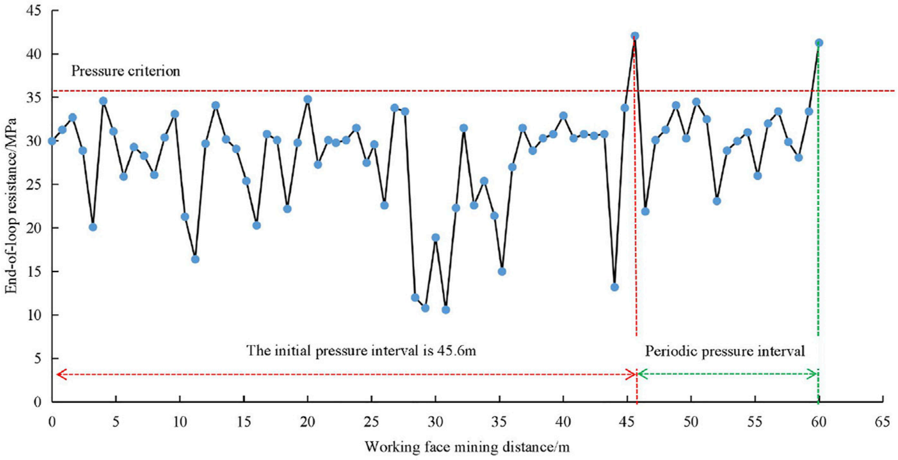

FIGURE 11
Curve of the end-of-loop resistance of the No. 90 hydraulic support.

6 Monitoring and analysis of the mining pressure

6.1 Monitoring scheme of the mining pressure

(1) The distribution and variation of the advanced abutment pressure of the working face were monitored by installing stress sensors in boreholes of the advanced coal body. To eliminate the effect of concentrated stress around the roadway, the depths of the stress sensors were determined to be 15 m. One monitoring point was set in the main gate and another one was set in the tailgate of the 9-301 working face. A strain-type stress sensor was used on site to observe the vertical stress. The monitoring point No. 1 in the main gate of the 9-301 working face was 80 m away from the working face, and the monitoring point No. 2 in the tailgate of the 9-301 working face was 85 m away from the working face.

(2) The stress monitor installed on the hydraulic support was employed to collect the working resistance of the support in real-time. Through the filtering and statistics of the

monitoring data, the disciplines of initial and periodic pressures and the stress changes in different areas of the working face were obtained.

6.2 Analysis of the advanced abutment pressure of the working face

Statistical analysis and mapping were performed according to the monitoring data (Figure 7). As can be observed from Figure 7, the influence ranges of the advanced abutment pressure of the working face reflected by the No. 1 and No. 2 measuring points are 40 and 47 m, respectively. The position of the peak value of the measuring point No. 1 is 8 m away from the working face, with a peak value of 175.3 kN. The position of the peak value of the measuring point No. 2 is 5.8 m away from the working face, with a peak value of 153.4 kN. The measuring point No. 2 is located at the upper section along the dip of the 9-301 working face. Based on the analyses mentioned in Section 3.1 and Section 3.2, the activity of the roof in the upper section of the working face is higher than that in the lower section, owing to the large dip angle. The immediate roof and the main roof are prone to fracture and rotation deformation, resulting in structural instability. This makes the influence range of the advanced abutment pressure of the No. 1 measurement point larger and causes the peak point to occur closer to the working face. Since the measuring point No. 1 is situated within the influence range of the residual coal pillar of the overlying No. 5 coal seam, the peak value at this location is greater, which is in line with the numerical simulation results presented in Section 5.2.

6.3 Analysis of working resistance of the support of the working face

The judgment index of the periodic pressure of the working face is the sum of the average resistance at the end of the cycle of the support and its mean square deviation (Qian et al., 2021). The calculation formula is as follows:

$$\sigma_p = \sqrt{\frac{1}{n}\sum_{i=1}^{n}\left(P_{ti} - \bar{P}_t\right)^2}, \tag{5}$$

$$\bar{P}_t = \frac{1}{n}\sum_{i=1}^{n} P_{ti}, \tag{6}$$

$$P'_t = \bar{P}_t + \sigma_P. \tag{7}$$

In the aforementioned equations:

σ_p is the mean square deviation of the average value of the end of the cycle resistance;

n is the measured number of cycles;

P_{ti} is the measured value of the end-of-loop resistance (kN);

$\bar{P}_t$ is the average value of the end-of-loop resistance (kN);

P'_t is the pressure criterion of the working face (kN).

If the measured value of the end-of-loop resistance is greater than the pressure criterion of the working face, the working face is under pressure; otherwise, it is in a non-pressure state.

A total of 101 caving hydraulic supports were arranged in the 9-301 working face, and the serial number of the supports was counted from the tailgate of the working face. The working resistance data on the No. 15, No. 40, No. 65, and No. 90 hydraulic supports were selected for statistical analysis (Figures 8–11), and the pressure criterion was employed to determine the pressure appearance of the working face. The analysis results are as follows:

(1) The initial pressure intervals of the working face reflected by the No. 15, No. 40, No. 65, and No. 90 hydraulic supports are 28.4, 36.0, 40.8, and 45.6 m, respectively. The initial pressure at different positions of the working face is non-synchronous, which is closely related to the non-uniformity of the roof movement caused by the large dip angle of the coal seam. The gangue from the upper and middle roof of the working face moves and accumulates to the goaf at the lower part of the working face, forming support and restriction to the roof so that the roof at the lower part of the working face cannot easily fracture. Because of the lack of support of the caving gangue, the roof in the upper and middle parts of the working face breaks after the main roof reaches the limit span, resulting in the initial pressure.

(2) The periodic pressure characteristics of each support are consistent with the initial pressure. The periodic pressure interval of the roof near the upper and middle parts of the working face (No. 15 and No. 40 supports) is about 6–9 m, and the periodic pressure interval of the roof near the lower part of the working face (No. 65 and No. 90 supports) is about 11–14 m. The phenomenon of non-synchronous pressure is also related to the large dip angle of the coal seam.

(3) By comparing Figures 8–11, we observed that the resistance at the end of circulation of supports in the lower part of the working face (No. 65 and No. 90 supports) is generally larger than that in the upper part of the working face (No. 15 and No. 40 supports). This indicates that the stress generated by the residual coal pillar of the overlying No. 5 coal seam has a certain influence on the pressure behavior of the 9-301 working face, which is consistent with the numerical calculation results.

6.4 Application of the research results

Based on theoretical analyses, similar material simulation, numerical calculation, and field observation, several research results have been gained. The research results can be applied in the following aspects:

(1) The results obtain the law of mining pressure interval and strength in different areas of the working face, which provided a basis for taking differentiated mine pressure control measures for different areas.
(2) The results obtained the distribution of the advanced abutment pressure of the working face, which can be used to optimize and determine the advanced support range and select the appropriate support form.
(3) The results obtained the movement and breaking characteristics of the roof, which can provide a basis for the selection of anti-fall and anti-skid measures for working face equipment.
(4) The results provide an important reference for future research on the migration features of top coal.

7 Conclusion

(1) The results of theoretical analyses demonstrated that the mining pressure in the middle and lower sections of the working face is mostly affected and controlled by the layered collapse of the immediate roof. The main roof of the upper section of the working face is more likely to be broken due to the lack of support of the immediate roof, and the mining pressure is mostly affected and controlled by falling of the main roof.
(2) A similarity experiment was conducted with a coal seam inclination of 30°. The experiments proved that the height of the overburden fracture zone in the lower part of the working face is smaller than that in the upper part of the working face. When the pressure sensor in the roof was 5–7 m away from the mining position, the stress increased rapidly. After some distance behind the mining position, the sensor was loaded again. The closer to the upper section of the working face, the longer is the distance behind the mining position when the sensor is reloaded, indicating that the roof activity is stronger.
(3) The numerical model of a fully mechanized coal caving face with a large dip angle was established by using FLAC3D. The calculation suggested that the residual coal pillar in the upper 5-108 face has an impact on the mining pressure of the 9-301 face, and the working face within 80 m near the main gate is obviously affected by the concentrated stress of the coal pillar. The peak values of the advanced abutment pressure in the coal pillar area and non-coal pillar area are 32.4 and 25.1 MPa, respectively. The peak point is 6.5 m in front of the face, and the influence range of the advanced abutment pressure is 47 m.
(4) The advanced abutment pressure and hydraulic support resistance in the 9-301 working face were monitored on site. The monitoring results demonstrated that the mining pressure at different positions of the working face was asynchronous. The (initial and periodic) pressure intervals of the upper, middle, and lower sections of the working face increase successively. The influence range, peak value, and peak position of the advanced abutment pressures in the upper and lower sections of the working face are distinct. The advanced abutment pressure in the upper section of the working face has a larger influence range, and its peak position is closer to the working face. Due to the residual coal pillar, the peak value of the advanced abutment pressure in the lower section of the working face is greater.
(5) The results will provide a scientific basis for reasonable determination of the control measures for the mining pressure in the 9-301 working face and can also provide a reference for research on mining pressure in a fully mechanized caving face with a large dip angle.

Data availability statement

The original contributions presented in the study are included in the article/Supplementary Material; further inquiries can be directed to the corresponding authors.

Author contributions

Chen determined the structure of the manuscript, gave ideas, and conducted theoretical analysis. Wang was in charge of experiments and data analysis of similar materials. Hui was in charge of numerical modeling and calculations. Zhu performed text calibration and language polishing. Sun formulated an on-site monitoring program. Zhang was responsible for the analysis of mine pressure monitoring data. YC was in charge of data curation and graphing. ZW, JW, and JZ were responsible for monitoring instrument installation and data collection.

Funding

This work was supported by the National Natural Science Foundation of China (Grant No. 51874164), the Open Projects of the Engineering Laboratory of Deep Mine Rockburst Disaster Assessment (Grant Nos. (2020) 011 and 2021 (003)), the Major scientific and technological innovation projects in Shandong Province (Grant No. 2019SDZY02), and the Innovative Talent Support Program for Higher Education Institutions in Liaoning Province.

Conflict of interest

YC and XZ were employed by Shandong Energy Group Co., Ltd. ZW and JW were employed by Liangbaosi Energy Co., Ltd and Shandong Energy Group Luxi Mining Co., Ltd. JZ was employed by Shandong Energy Group Luxi Mining Co., Ltd.

The remaining authors declare that the research was conducted in the absence of any commercial or financial relationships that could be construed as a potential conflict of interest.

Publisher's note

References

Chai, J., Du, W. G., Zhang, D. D., and Lei, W. L. (2019). Study on roof activity law in steeply inclined seams based on BOTDA sensing technology. *Chin. J. Rock Mech. Eng.* 38 (09), 1809–1818. doi:10.13722/j.cnki.jrme.2018.1464

Cheng, W. D., and Li, J. M. (2009). Stope wall rock activity law of long-wall fully mechanized caving mining on strike of steep dipping seam. *China Min. Mag.* 18 (05), 56–58

Du, K., Li, X. F., Yang, C. Z., Zhou, J., Chen, S. J., Manoj, K., et al. (2020a). Experimental investigations on mechanical performance of rocks under fatigue loads and biaxial confinements. *J. Cent. South Univ.* 27 (10), 2985–2998. doi:10.1007/s11771-020-4523-7

Du, K., Yang, C. Z., Su, R., Tao, M., and Wang, S. F. (2020b). Failure properties of cubic granite, marble, and sandstone specimens under true triaxial stress. *Int. J. Rock Mech. Min. Sci.* 130, 104309. doi:10.1016/j.ijrmms.2020.104309

Du, K., Li, X. F., Su, R., Tao, M., Lv, S. Z., Luo, J., et al. (2022). Shape ratio effects on the mechanical characteristics of rectangular prism rocks and isolated pillars under uniaxial compression. *Int. J. Min. Sci. Technol.* 32 (2), 347–362. doi:10.1016/j.ijmst.2022.01.004

Guo, D. M., Fan, J. M., Zhu, Y. L., and Zhu, X. L. (2012). Mining pressure characteristics and control technology in fully mechanized caving face in the soft and thick coal seam with a large dip angle. *Metallurgical Industry Press*.

Gao, L. S., Zhang, E. H., Zhu, Q. J., Shi, J. J., and Wang, Y. C. (2020). Strata-pressure behavior in fully mechanized caving face with large dip angle and extra-large thickness. *J. Xi'an Univ. Sci. Technol.* 40 (04), 615–620+657

Huang, J. G. (2002). Structural analysis for roof mov ement for steep coal seams. *J. China Univ. Min. Technol.* (05), 74–77.

Kulakov, V. N. (1995). Stress state in the face region of a steep coal bed. *J. Min. Sci.* 31 (3), 161–168. doi:10.1007/bf02047661

Li, X. M., and Liu, F. (2016). Analysis of overlying strata structure and strata behavior characteristics of stope in steep coal seam. *Coal Eng.* 48 (05), 80–83.

Li, L., Yu, L., Zhang, S. Q., and Zhang, S. Y. (2020). Spalling mechanism of coal wall in large-angle and high-cutting coal mining face. *Coal Eng.* 52 (12), 102–107.

Lin, D. C., Wang, G. Z., Luan, H. J., Jia, C. Y., and Dai, M. M. (2015). Experimental study on roof failure mechanism in dip mining of large inclination coal seam. *Coal Eng.* 47 (05), 98–100.

Liu, Y. Q., Jiang, J. Q., Zhang, P. P., Gao, L., and Kong, P. (2017). Numerical simulation research on strata movement regularity of large dip angle coal seam mining. *Coal Technol.* 36 (02), 84–87. doi:10.13301/j.cnki.ct.2017.02.033

Liu, S., Yang, K., and Tang, C. N. (2021). Mechanism and integrated control of "rib spalling:roof collapse-support instability" hazard chains in steeply dipping soft coal seams. *Adv. Mater. Sci. Eng.* 2021, 1–20. doi:10.1155/2021/5524591

Luan, H. J., Lin, D. C., Jia, C. Y., Shi, Y. K., and Zhang, P. S. (2015). Similar simulation for overlying strata movement laws in large inclined coal seam with dip mining. *Saf. Coal Mines* 46 (09), 51–53. doi:10.13347/j.cnki.mkaq.2015.09.014

Luo, S. H., Wu, Y. P., Liu, K. Z., Xie, P. S., and Wang, H. W. (2018). Asymmetric load and instability characteristics of coal wall at large mining height fully-mechanized face in steeply dipping seam. *J. China Coal Soc.* 43 (07), 1829–1836. doi:10.13225/j.cnki.jccs.2018.0134

Luo, S. H., Tian, C. Y., Wu, Y. P., Xie, P. S., and Wang, H. W. (2021). Characteristics of loading and failure of overlying rock at working face advancing direction in longwall mining of steeply inclined seam. *J. China Coal Soc.* 46 (07), 2227–2236. doi:10.13225/j.cnki.jccs.2020.0379

Men, J. G., Wang, S., Yuan, R. F., Li, X. J., Jiao, Z. H., and Peng, S. P. (2014). Study on overburden strata structure features and stress distribution law of coal pillar in inclined seam. *Coal Sci. Technol.* 42 (05), 21–24. doi:10.13199/j.cnki.cst.2014.05.006

Qian, M. G., Xu, J. L., Wang, J. C., and Wu, Y. P. (2021). Mine pressure and rock control. *China University of Mining and Technology Press*.

Qin, Z. C., Zhou, S. T., and Liu, M. Q. (2015). Study on stability of surrounding rock in uphill mining stope with large inclination. *Coal Eng.* 47 (07), 86–88+92

Rong, H. R., Wang, L. G., Wang, Z. S., Zhou, D. L., and Huang, J. H. (2012). Analysis on overburden structure in the mining of deeply inclined coal seam. *Min. Res. Dev.* 32 (02), 18–21. doi:10.13827/j.cnki.kyyk.2012.02.016

Singh, T. N., and Gehi, L. D. (1993). "State behavior during mining of steeply dipping thick seams-a case study," in The 27th international symposium on thick seam mining, Dhanbad (India), 311–315

Song, P., Pang, X. K., and Liu, B. Z. (2018). Behavior laws of mine pressure of steep thick coal seam with stagger roadway layout in tangshan mine. *Saf. Coal Mines* 49 (12), 221–224. doi:10.13347/j.cnki.mkaq.2018.12.055

Sun, X., Lin, C. B., and Lin, B. Q. (2008). Cracking development variation low of overlying strata over fully-mechanized coal caving mining face during exploitation process. *Saf. Coal Mines* (04), 21–24+28.

Sun, S. L. (2015). Analysis on numerical simulation of strata behavior law of fully mchanized caving face in large dip angle. *Coal Technol.* 34 (08), 25–27. doi:10.13301/j.cnki.ct.2015.08.010

Wang, S. R., Wang, J. A., and Dai, Y. (2005). Distinct element analysis on coal movement law and failure mechanism during mechanized top-coal caving in steep tinck seam. *J. Univ. Sci. Technol. Beijing* 27 (01), 5–8. doi:10.13374/j.issn1001-053x.2005.01.002

Wang, J. A., Zhang, J. W., Gao, X. M., Wen, J. D., and Gu, Y. D. (2015a). Fracture mode and evolution of main roof stratum above longwall fully mechanized top coal caving in steeply inclined thick coal seam (I)—initial fracture. *J. China Coal Soc.* 40 (06), 1353–1360. doi:10.13225/j.cnki.jccs.2015.0407

Wang, J. A., Zhang, J. W., Gao, X. M., Wen, J. D., and Gu, Y. D. (2015b). Fracture mode and evolution of main roof stratum above fully mechanized top coal caving longwall coalface in steeply inclined thick coal seam (II): periodic fracture. *J. China Coal Soc.* 40 (08), 1737–1745. doi:10.13225/j.cnki.jccs.2015.0408

Wang, H. W. (2014). *Research on evolution of stress and structural stability of surrounding rock in the longwall mining of steeply dipping seam*. Xi'an, China: Xi'an University of Science and Technology.

Wang, C. M. (2017). Study on overburden movement and strata behavior law in fully mechanized face in thick coal seam with large angle. *Min. Saf. Environ. Prot.* 44 (04), 14–18.

Wu, Y. P., Wang, H. W., Xie, P. S., and Zeng, Y. F. (2011). Numerical analysis on influencing factors of fractured zone height in overburden strata above high inclined seam. *Coal Eng.* 3, 63–66.

Wu, Y. P., Liu, W. H., Xie, P. S., and Tian, S. (2020a). Stress evolution and roof breaking characteristics of surrounding rock in oblique longwall mining area of steeply dipping seam. *Saf. Coal Mines* 51 (09), 222–227. doi:10.13347/j.cnki.mkaq.2020.09.047

Wu, Y. P., Liu, W. H., Zhang, Y. L., and Yang, W. B. (2020b). Deformation and failure characteristics of overburden in working face with steeply-angle and large mining height in the roof of interbedded coal gangue. *Min. Res. Dev.* 40 (09), 66–70. doi:10.13827/j.cnki.kyyk.2020.09.013

Wu, Y. P., Yun, D. F., Xie, P. S., Wang, H. W., Lang, D., and Hu, B. S. (2020c). Progress, practice and scientific issues in steeply dipping coal seams fully-mechanized mining. *J. China Coal Soc.* 45 (1), 24–34. doi:10.13225/j.cnki.jccs.YG19.0494

Xiao, J. P., Yang, k., Liu, S., and Zhou, B. (2019). Study on breaking mechanism of overlying strata in deeply inclined coal seam. *J. Saf. Sci. Technol.* 15 (03), 75–80.

Xie, P. S., Wu, Y. P., Wang, H. W., and Ren, S. G. (2012). Study on space activity law of overburden strata above longwall coal mining face in high inclined seam. *Coal Sci. Technol.* 40 (09), 1–5. doi:10.13199/j.cst.2012.09.7.xiepsh.019

Xie, P. S., Tian, S. Q., and Duan, J. J. (2019). Experimental study on the movement law of roof in pitching oblique mining area of steeply dipping seam. *J. China Coal Soc.* 44 (10), 2974–2982. doi:10.13225/j.cnki.jccs.2019.0602

Xie, P. S., Zhang, Y. Y., Zhang, Y. L., Chen, J. J., Zhang, X. B., and Duan, J. J. (2021). Instability law of the coal-rock interbedded roof and its influence on supports in large mining height working face with steeply dipping coal seam. *J. China Coal Soc.* 46 (2), 344–356. doi:10.13225/j.cnki.jccs.xr20.1866

Xing, D. S., Wang, L. G., and Liu, X. M. (2018). Mine pressure behavior of fully mechanized mining face with large mining height for steeply dipping coal seam. *Min. Metallurgical Eng.* 38 (05), 16–19+24.

Xiong, Y., Kong, D. Z., Yang, S. L., Wu, G. Y., Zuo, Y. J., and Cheng, Z. B. (2022). Cloud model identification of coal face stability in steeply inclined working faces. *China Saf. Sci. J.* 32 (03), 144–151. doi:10.16265/j.cnki.issn1003-3033.2022.03.020

Yang, Z. M., Zhang, J. H., Lai, X. P., and Lv, Z. H. (2010). Localized character of strata movement for complicated super-thick water-rich coal seam with large mining height. *J. China Coal Soc.* 35 (11), 1868–1872. doi:10.13225/j.cnki.jccs.2010.11.019

Yin, G. Z., Li, X. S., and Guo, W. B. (2010). Photo-elastic experimental and field measurement study of ground pressure of surrounding rock of large dip angle working coalface. *Chin. J. Rock Mech. Eng.* 29 (S1), 3336–3343.

Zhang, Y. X., and Wang, K. (2014). Roof broken features at fully mechanized caving mining stope in steep inclined and specially thick seam. *Saf. Coal Mines* 45 (07), 187–191. doi:10.13347/j.cnki.mkaq.2014.07.056

Zhang, H., and Wu, Y. P. (2020). Timing failure mechanism of basic roof of large mining height stope in steeply dipping coal seam. *Saf. Coal Mines* 51 (03), 211–215. doi:10.13347/j.cnki.mkaq.2020.03.045

Zhang, Y. L., Li, K. F., and Ren, S. G. (2010). Overlying strata movement property of fully mechanized caving mining in steep inclined seam. *J. Xi'an Univ. Sci. Technol.* 30 (02), 150–153. doi:10.13800/j.cnki.xakjdxxb.2010.02.010

Zhang, C. L., Zhang, S. Q., Zhao, J. J., Li, Z. F., and Ma, Y. (2014). Law of overburden strata above longwall coal mining face in high inclined seam based on FLAC3D. *J. Liaoning Tech. Univ. Nat. Sci.* 33 (06), 736–740. doi:10.3969/j.issn.1008-0562.2014.06.004

Zhang, L. M. (2007). Research on ground behavior law of fully mechanized caving mining face in deep inclined seam of Wangjiashan Mine. *Coal Sci. Technol.* (12), 22–26. doi:10.13199/j.cst.2007.12.26.zhanglm.008

Zhu, X. L., Yang, R. S., Cai, Z. Y., and Qi, H. J. (2014). Study on strata pressure behavior features of fully-mechanized top coal mining in soft large inclined angle seam. *Coal Sci. Technol.* 42 (05), 25–28. doi:10.13199/j.cnki.cst.2014.05.007

Advantages of publishing in Frontiers

OPEN ACCESS
Articles are free to read
for greatest visibility
and readership

FAST PUBLICATION
Around 90 days
from submission
to decision

HIGH QUALITY PEER-REVIEW
Rigorous, collaborative,
and constructive
peer-review

TRANSPARENT PEER-REVIEW
Editors and reviewers
acknowledged by name
on published articles

Frontiers
Avenue du Tribunal-Fédéral 34
1005 Lausanne | Switzerland

Visit us: www.frontiersin.org
Contact us: frontiersin.org/about/contact

REPRODUCIBILITY OF RESEARCH
Support open data
and methods to enhance
research reproducibility

DIGITAL PUBLISHING
Articles designed
for optimal readership
across devices

FOLLOW US
@frontiersin

IMPACT METRICS
Advanced article metrics
track visibility across
digital media

EXTENSIVE PROMOTION
Marketing
and promotion
of impactful research

LOOP RESEARCH NETWORK
Our network
increases your
article's readership